Transactions of the ASME

Journal of Applied Mechanics

Published Quarterly by The American Society of Mechanical Engineers

VOLUME 49 • NUMBER 2 • JUNE 1982

Journal of Applied Mechanics (ISSN 0021-8936) is edited and published quarterly at the offices of the American Society of Mechanical Engineers, United Engineering Center, 345 E. 47th St., New York, N.Y. 10017. ASME-TWX No. 710-581-5267, New York. Second Class postage paid at New York, N.Y., and at additional mailing offices.

CHANGES OF ADDRESS must be received at Society headquarters seven weeks before they are to be effective. Please send old label and new address.

PRICES: To members, $30.00, annually; to nonmembers, $60.00. Single copies, $20.00 each. Add $5.00 for postage to countries outside the United States and Canada.

INDEXED by the Engineering Index, Inc.

TECHNICAL PAPERS

(Contents continued on Inside Back Cover)

CONTENTS (CONTINUED)

DESIGN DATA AND METHODS

BRIEF NOTES

DISCUSSIONS

BOOK REVIEWS

ERRATA

Contact Problems Involving the Flow Past an Inflated Aerofoil

J.-M. Vanden-Broeck[1]
Department of Mathematics,
Stanford University,
Stanford, Calif. 94305

Steady potential flow around a two-dimensional inflated airfoil is considered. The aerofoil consists of a flexible and inextensible membrane which is anchored at both leading and trailing edges. The flow and the aerofoil shape are determined as functions of the angle of attack α, the cavitation number γ, and the Weber number λ. When γ decreases to a critical value γ_0 (α, λ), opposite sides of the membrane become tangent to each other at the trailing edge. For $\gamma < \gamma_0$ the aerofoil is partially collapsed near the trailing edge. The length of the region of collapse increases as γ decreases and for $\gamma = -\infty$, the aerofoil is completely collapsed. The shape of the aerofoil and the value of γ_0 are determined analytically by a perturbation solution for λ small. Graphs of the results are presented.

1 Introduction

We consider the deformation of a two-dimensional inflated aerofoil due to the steady potential flow of an incompressible fluid around it. The aerofoil consists of a flexible and inextensible membrane anchored at both leading and trailing edges (see Fig. 1). This configuration can serve as a model for various pneumatic structures, such as those sometimes used to cover sport arenas.

The aerofoil is characterized by its internal pressure p_b, its constant tension σ, and its chord length c, while the fluid has density ρ, pressure p_∞ at infinity, and velocity U at infinity. As we shall see, the shape of the aerofoil is determined by the angle of attack α, the cavitation number

$$\gamma = (p_b - p_\infty - \frac{1}{2}\rho U^2) / \frac{1}{2}\rho U^2, \tag{1}$$

and the Weber number

$$\lambda = 2\rho c U^2 / \sigma. \tag{2}$$

This problem was first considered by Newman and Tse [1] who obtained approximate solutions for $\alpha = 0$, by using thin aerofoil theory. Nonlinear results for $\alpha = 0$ were obtained by Vanden-Broeck and Keller [2], who considered the flow past a two-dimensional bubble attached to a wall. Their solution, when reflected in the wall, also describes the flow past an inflated aerofoil at zero angle of attack.

In the present paper we solve the problem for arbitrary values of α by a perturbation solution for λ small. Our results can be described as follows.

As γ tends to infinity, the membrane consists of two circular arcs. As γ decreases, the aerofoil becomes thinner. When γ reaches a critical value $\gamma_0(\alpha, \lambda)$, opposite sides of the membrane are tangent to each other at the trailing edge (see Fig. 2). This family of solutions becomes physically unacceptable for $\gamma < \gamma_0$ because then opposite sides of the aerofoil cross over. Similar difficulties were encountered before by Flaherty, Keller, and Rubinow [3], Flaherty and Keller [4], and Vanden-Broeck and Keller [5]. (See Keller [6] for a review of these problems.)

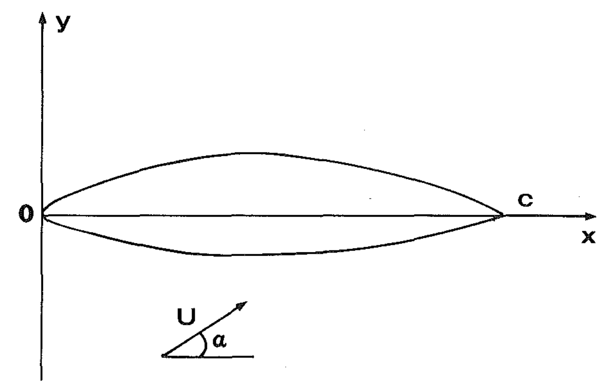

Fig. 1 Sketch of the inflated aerofoil. The coordinates and the flow direction are also shown. The aerofoil is anchored at $x = 0, y = 0$, and at $x = c, y = 0$.

Following the general philosophy of the methods used by these authors, we redetermine the shape of the aerofoil by preventing crossing but allowing contact. This leads to a new family of solutions for $\gamma < \gamma_0$ in which the aerofoil is partially collapsed near the trailing edge (see Fig. 3). The length of the region of collapse increases as γ decreases, and for $\gamma = -\infty$, the aerofoil is completely collapsed. The limiting configuration for $\gamma = -\infty$ is the single membrane or sail considered by Thwaites [7], Vanden-Broeck and Keller [8], and others.

The solutions before and after contact are described, respectively, in Sections 2 and 3.

2 Solution Before Contact

We introduce the dimensionless variables by using c as the unit length and U as the unit velocity. Let the aerofoil shape

[1] Currently, Professor of Mathematics, Mathematics Department, Mathematics Research Center, University of Wisconsin-Madison, Madison, Wis. 53706.

Contributed by the Applied Mechanics Division for Publication in the JOURNAL OF APPLIED MECHANICS.

Discussion on this paper should be addressed to the Editorial Department, ASME, United Engineering Center, 345 East 47th Street New York, N.Y. 10017, and will be accepted until two months after final publication of the paper itself in the JOURNAL OF APPLIED MECHANICS. Manuscript received by ASME Applied Mechanics Division, April, 1981.

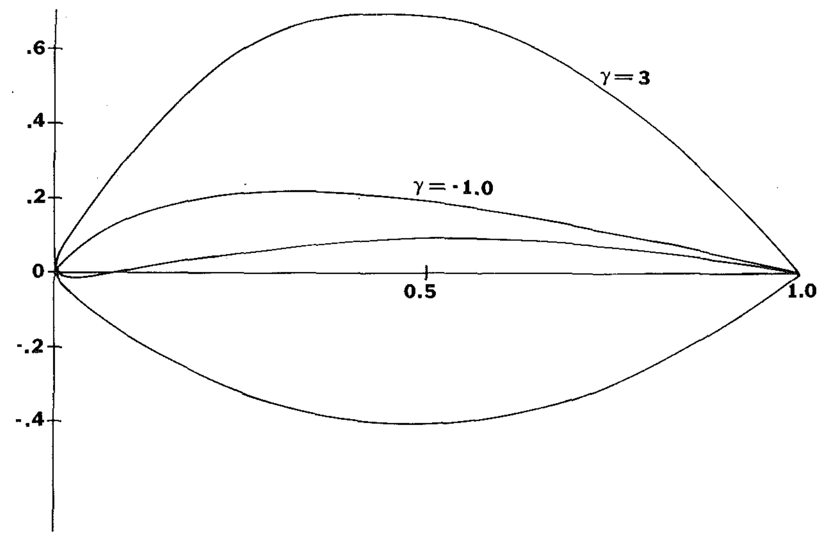

Fig. 2 The shape of the aerofoil is shown for two different values of γ with $\alpha = \pi/4$ in units of $\lambda c/4$ based on (9). The unit along the x-axis is c. For $\gamma = -1$ opposite sides of the aerofoil are tangent to each other at $x = 1$.

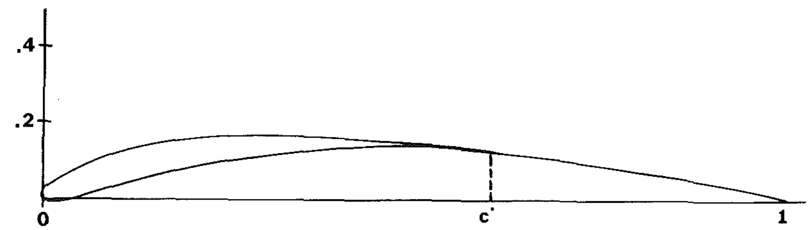

Fig.3 The shape of the aerofoil is shown for $\gamma = -1.666$ with $\alpha = \pi/4$ in units of $\lambda c/4$ based on (18)–(20). The unit along the x-axis is c.

be $y = \eta^{\pm}(x)$, $0 \le x \le 1$. Here "+" and "−" correspond, respectively, to the top and bottom parts of the aerofoil. The conditions of attachment at the leading and trailing edges imply

$$\eta^{\pm}(0) = \eta^{\pm}(1) = 0. \qquad (3)$$

On the aerofoil surface, the Bernoulli equation and the pressure jump due to the tension σ yield

$$p_\infty + \frac{\rho U^2}{2} - \frac{\rho(q^{\pm})^2}{2} + \sigma\kappa^{\pm} = p_b, \qquad 0 \le x \le 1. \qquad (4)$$

Here q is the flow velocity and κ the curvature of the aerofoil. In dimensionless variables this becomes

$$(q^{\pm})^2 + \gamma = \frac{4}{\lambda}\kappa^{\pm}, \qquad (5)$$

where γ and λ are defined in (1) and (2).

The flow velocity is assumed to be $\nabla\phi$ where ϕ is a harmonic function. At infinity we require that the flow have unit velocity and direction α:

$$\nabla\phi \sim (\cos\alpha, \sin\alpha) \text{ at } \infty.$$

In addition, on both sides of the aerofoil, $\nabla\phi$ must be tangent to it, and the Kutta condition requires the velocity to be finite at the trailing edge $x = 1$.

We shall solve the problem for λ small, which corresponds to the tension σ being large. When $\lambda = 0$ or $\sigma = \infty$, (5) shows that $\kappa^{\pm}(x) = 0$ so the aerofoil is a straight line segment. It follows from (3) that this segment must lie on the x-axis from $x = 0$ to $x = 1$ so $\eta_0^{\pm}(x) = 0$. The subscript "0" denotes $\lambda = 0$. The complex velocity $u - iv$ is given in terms of $z = x + iy$ by (Carrier, Krook, and Pierson [9], p. 158)

$$u_0 - iv_0 = \cos\alpha - i\sin\alpha[(z-1)/z]^{1/2}. \qquad (6)$$

We have chosen the circulation to be $-\pi\sin\alpha$ to satisfy the Kutta condition at $x = 1, y = 0$.

Next we set $\lambda = 0$ in (5). Then the right side of (5) becomes $\mp 4(\eta_\lambda^{\pm})''$. The left side can be evaluated by using (6), in which we choose the negative square root on the top part of the aerofoil and the positive one on the bottom part, and note that $v_0 = 0$ on the aerofoil. In this way we get from (5)

$$\mp 4(\eta_\lambda^{\pm})''(x) = \gamma + \cos 2\alpha + \sin^2\alpha/x \pm \sin 2\alpha[(1-x)/x]^{1/2}. \qquad (7)$$

Now we differentiate (3) with respect to λ at $\lambda = 0$ to obtain

$$\eta_\lambda^{\pm}(0) = \eta_\lambda^{\pm}(1) = 0. \qquad (8)$$

We next integrate (7) twice and use (8) to get $\eta_\lambda^{\pm}(x)$. Then $\eta^{\pm}(x) = \eta_0^{\pm}(x) + \lambda\eta_\lambda^{\pm}(x) + 0(\lambda^2)$. On using $\eta_0^{\pm} = 0$, and the result for $\eta_\lambda^{\pm}$, we can write this in the form

$$\frac{4}{\lambda}\eta^{\pm}(x) = \pm(\gamma + \cos 2\alpha)(x - x^2)/2 \mp \sin^2\alpha x \ln x$$
$$- \sin 2\alpha[(4x-1)\sin^{-1}(2x-1)/8$$
$$- \pi(2x+1)/16 + (2x+1)(x-x^2)^{1/2}/4] + 0(\lambda). \qquad (9)$$

The result (9) is illustrated in Fig. 2 for various values of γ with $\alpha = \pi/4$.

As γ tends to infinity, the nonlinear condition (5) shows that $\kappa^{\pm} \sim \lambda\gamma/4$. Thus for γ large, the shape of the aerofoil on either side is a circular arc of radius $4/\lambda\gamma$. For λ small, (9) shows that these circular arcs can be approximated by the parabolas $\pm\gamma\lambda(x - x^2)/8$.

From (9) it can be shown easily that

$$(\eta_\lambda^{+})'_{x=1} = (\eta_\lambda^{-})'_{x=1}, \quad \text{for } \gamma = -1. \qquad (10)$$

Thus the critical value $\gamma_0(\alpha,\lambda)$ of γ, at which opposite sides of the membrane are tangent to each other at the trailing edge, is given asymptotically by

$$\gamma_0(\alpha,\lambda) \sim -1 + 0(\lambda^2). \tag{11}$$

For $\gamma < -1$, equation (9) yields unphysical profiles in which opposite sides of the aerofoil cross over. In the next section we construct a physically acceptable family of solutions for $\gamma < -1$ by preventing crossing but allowing contact.

3 Solution With an Interval of Contact

To obtain solutions for $\gamma < \gamma_0$, we require the aerofoil to be collapsed between $x = c^*$ and $x = 1$ (see Fig. 3). The value of c^* is to be found as part of the solution. Let the shape of the aerofoil be described by the equations $y = f^{\pm}(x)$, $0 \le x \le c^*$, and $y = f^{s}(x)$, $c^* \le x \le 1$. We shall solve the problem for λ small. By proceeding as in Section 2, we obtain for the profile of the aerofoil the following differential equations

$$\mp 4(f_\lambda^{\pm})''(x) = \gamma + \cos 2\alpha + \sin^2\alpha/x \pm \sin 2\alpha[(1-x)/x]^{1/2}, \tag{12}$$

$$4(f_\lambda^{s})''(x) = -\sin 2\alpha[(1-x)/x]^{1/2}. \tag{13}$$

The condition of attachment at the trailing and leading edges imply

$$f_\lambda^{\pm}(0) = 0, \tag{14}$$

$$f_\lambda^{s}(1) = 0. \tag{15}$$

In addition we impose continuity of the profile and of the slope at $x = c^*$, i.e.,

$$f_\lambda^{\pm}(c^*) = f_\lambda^{s}(c^*), \tag{16}$$

$$(f_\lambda^{\pm})'(c^*) = (f_\lambda^{s})'(c^*). \tag{17}$$

We next integrate twice (12) and (13). The six constants of integration and the value of c^* are evaluated by using the seven conditions (14)–(17). Thus we obtain after some algebra

$$c^* = -2\sin^2\alpha/(\gamma + \cos 2\alpha), \tag{18}$$

$$\begin{aligned} \frac{4}{\lambda} f^{\pm}(x) = {} & \mp(\gamma + \cos 2\alpha)x^2/2 \mp \sin^2\alpha(x \ln x - x) \\ & - \sin 2\alpha[(4x-1)\sin^{-1}(2x-1)/8 \\ & - \pi(4x+1)/16 + (2x+1)(x-x^2)^{1/2}/4] \\ & + x[-\frac{\pi}{8}\sin 2\alpha \pm c^*\cos 2\alpha \pm \ln c^* \sin^2\alpha \pm \gamma c^*] + 0(\lambda), \\ & 0 \le x \le c^* \end{aligned} \tag{19}$$

$$\begin{aligned} \frac{4}{\lambda} f^{s}(x) = {} & -\sin 2\alpha[(4x-1)\sin^{-1}(2x-1)/8 \\ & - \pi(2x+1)/16 + (2x+1)(x-x^2)^{1/2}/4] + 0(\lambda), \\ & c^* \le x \le 1. \end{aligned} \tag{20}$$

The results (18)–(20) are illustrated in Fig. 3 for $\gamma = -1.666$ and $\alpha = \pi/4$.

For $\gamma = -1$, (18) shows that $c^* = 1$ and the solution (19) reduces to the solution (9). For $\gamma = -\infty$, $c^* = 0$ and the aerofoil is completely collapsed. The limiting configuration for $\gamma = -\infty$ is the single membrane or sail considered by Vanden-Broeck and Keller [8]. Equation (20) is then identical to the formula (11) given by these authors. It is interesting to note the right-hand side of (20) does not depend on γ. Therefore as γ varies between -1 and $-\infty$, the point of the aerofoil with abcissa $x = c^*$ moves continuously along the curve $y = 4/\lambda f^{s}(x)$.

Finally let us mention that the inflated aerofoil in Fig. 1 can be viewed as a sailwing aerofoil. Murai and Maruyama [10] considered a more general sailwing in which the leading edge is replaced by a rounded closed curve. The upper and lower membranes were required to separate smoothly from this curve. They reported that the upper and lower membranes sometimes cross each other. Although their numerical scheme appears to handle this difficulty, the present method could be used to resolve it in a more systematic way. This would lead to sailwing profiles that are partially collapsed near the trailing edge.

Acknowledgments

I wish to thank Professor J. B. Keller for some very helpful discussions of the problem. This work was supported in part by the Air Force Office of Scientific Research, the Office of Naval Research, the Army Research Office, and the National Science Foundation.

References

1 Newman, B. G., and Tse, M.-C., "Flow Past a Thin, Inflated Lenticular Aerofoil," *J. Fluid Mech.*, Vol. 100, 1980, pp. 673–689.

2 Vanden-Broeck, J.-M., and Keller, J. B., "Deformation of a Bubble or Drop in a Uniform Flow," *J. Fluid Mech.*, Vol. 101, 1980, pp. 673–686.

3 Flaherty, J. E., Keller, J. B., and Rubinow, S. I., "Post-Buckling Behavior of Elastic Tubes and Rings With Opposite Sides in Contact," *SIAM J. Appl. Math.*, Vol. 23, 1972, pp. 446–455.

4 Flaherty, J. E., and Keller, J. B., "Contact Problems Involving a Buckled Elastica," *SIAM J. Appl. Math.*, Vol. 24, 1973, pp. 215–225.

5 Vanden-Broeck, J.-M., and Keller, J. B., "A New Family of Capillary Waves," *J. Fluid Mech.*, Vol. 98, 1980, pp. 161–169.

6 Keller, J. B., "Some Bubble and Contact Problems," *SIAM Rev.*, Vol. 22, 1980, pp. 442–458.

7 Thwaites, B., "The Aerodynamic Theory of Sails, I. Two-Dimensional Sails," *Proc. Roy. Soc.*, Series A, Vol. 261, 1961, pp. 402–422.

8 Vanden-Broeck, J.-M., and Keller, J. B., "Shape of a Sail in a Flow," *Phys. Fluid*, Vol. 24, 1981, pp. 552–553.

9 Carrier, G. F., Krook, M., and Pierson, C. E., *Functions of a Complex Variable*, McGraw-Hill, New York, 1966.

10 Murai, H., and Maruyama, S., "Theoretical Investigation of the Aerodynamics of Double Membrane Sailing Airfoil Sections," *Journal of Aircraft*, Vol. 17, 1980, pp. 294–299.

Natural Convection Past Inclined Porous Layers

N. Rudraiah

V. Wilfred

UGC-DSA Centre in Fluid Mechanics,
Department of Mathematics,
Central College
Bangalore University,
Bangalore 560001, India

This paper describes a study of combined Rayleigh-Bénard convection and Tollmien-Schlichting type of instability of a fluid in an inclined layer bounded by two permeable beds. Several types of flows, depending on the value of the Prandtl number, Pr, are studied using a fast convergent power series technique. Two different convective movements, longitudinal and transverse rolls, based on different Prandtl numbers, are reported. The effect of slip at the nominal surface is to augment the instability and change the critical Grashof number, Gr, and critical Rayleigh number, Ra, markedly for small permeability parameter σ, being independent of Gr and Ra for large σ. The effect of inclination ϕ is to inhibit the onset of instability in the case of air and to augment it in the case of mercury. It is shown that at maximum inclination (i.e., $\phi = \pi/2$), the instability sets in as transverse rolls, irrespective of the value of Pr. In the case of mercury, the transverse rolls exist for all ϕ, whereas in the case of air, they are limited only to certain ϕ. The cell pattern changes dramatically in the range $\phi = \pi/6$–$\pi/4$.

1 Introduction

The instability of an inclined layer of fluid bounded on both sides by permeable beds, due to combined thermal stratification and viscous shear is investigated in this paper because of its natural occurrence and its importance in the process of technology (for example, chemical engineering and some oil recovery techniques). It is also of interest in many geophysical problems (for example, the determination of reservoir characteristics in the geothermal region) and biomechanical problems (for example, blood flow in pulmonary alvelor sheet, see Fung and Tang [1, 2]) where the layer is bounded on both sides by porous material. In the geothermal region, the main mechanism of transfer of heat from the deep igneous rocks to shallow depths is buoyancy induced convection. Meteoric liquid percolating down to depth in a permeable formation is heated directly or indirectly by the intruded magma and is then driven buoyantly upward to the top of the aquifer where it can be trapped through drill holes. A viable geothermal reservoir usually consists of a sloping layer bounded on both sides by porous beds. Therefore, the criterion for the onset of convection in such a model considered in this paper may shed some insight on the study of transport processes in geothermal reservoirs.

The instability of a layer of fluid due to thermal stratification (known as Rayleigh-Bernard problem, see Chandrasekhar [3]) or due to viscous shear (known as Tollmien-Schlichting type of oscillations, see Betchov and Criminal, Jr. [4]) has been extensively investigated when the layer is bounded by impermeable rigid boundaries. Much attention has also been given to the study of instability of an inclined layer of fluid bounded on both sides by rigid impermeable plates (see Hart [5], Ruth [6], and Unny [7]). Natural convection in an inclined porous layer is also given considerable attention (see Bories and Combarnous [8], Kaneko, et al. [9], and Combarnous and Aziz [10]). However, we know relatively little about the instability of an inclined layer of fluid bounded on both sides by a porous material, which is considered in this paper.

The core problem here is to specify the proper boundary conditions at the permeables boundaries, since the vertical transport of heat depends strongly on what happens near the boundaries. Until recently, it was assumed that the no-slip boundary conditions are valid at the permeable boundaries. However, Beavers and Joseph ([11], hereafter called BJ) have shown that this no-slip condition is no longer valid at the porous boundaries and postulated the slip boundary condition called the BJ slip condition and verified it experimentally. This BJ condition was later confirmed experimentally by others (Beavers et al. [12], Taylor [13], and Rajasekhara [14]). Recently Channabasappa and Ranganna [15] have established the existence of a slip even in the case of an inclined channel. This velocity slip not only causes skewing of the main flow velocity profile in the channel but also permits a nonzero, streamwise disturbance velocity at the walls. The existence of the slip at the permeable boundary is based on the assumption of laminar flow. Therefore it is of interest to determine the condition for the transition from conduction to convective flow, which is the object of this paper. Here, we study the linear stability of a laminar flow in a channel bounded on both sides by a permeable material and inclined at an angle ϕ to the horizontal (Fig. 1). The novel feature of the linear stability problem considered here is the coupling between

Contributed by the Applied Mechanics Division for publication in the JOURNAL OF APPLIED MECHANICS.

Discussion on this paper should be addressed to the Editorial Department, ASME, United Engineering Center, 345 East 47th Street, New York, N.Y. 10017, and will be accepted until two months after final publication of the paper itself in the JOURNAL OF APPLIED MECHANICS. Manuscript received by ASME Applied Mechanics Division, April 1981; final revision, Spetember 1981.

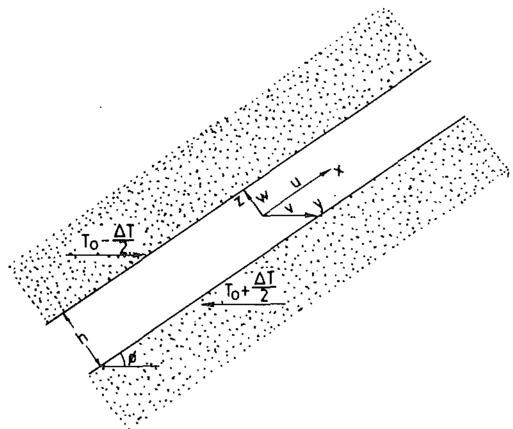

Fig. 1 Physical model

Rayleigh-Bénard type of instability due to uniform heating from below and cooling from above and Tollmien-Schlichting wave-like instability due to shear.

When the channel is horizontal and bounded on one side by a permeable bed, Sparrow, et al. [16] have investigated the linear stability using finite-difference technique. We note that the difficulty and the computer time required in solving the stability equation using finite difference technique has precluded a detailed study of the present problem. Hence the solution technique used in the present study is the classical power series method (Sparrow, et al. [17], and Ruth [6]) which is found to be a fast converging method. It is shown that the instability sets in at a lower Grashof number than that of the fluid in the channel bounded on both sides by rigid impermeable boundaries due to reduction in friction at the bounding surfaces. In particular, it is shown that there exists a fairly close analogy between convective motions in the present problem and in a fluid layer bounded by rigid boundaries.

2 Mathematical Formulation

The physical configuration of the problem under study is shown in Fig. 1. The fluid is contained between two parallel, porous layers of infinite extent, separated by a distance "h" apart and inclined at an angle ϕ to the horizontal. The temperature difference between the layers is ΔT, the upper layer having temperature $T_0 - \Delta T/2$ and the lower $T_0 + \Delta T/2$. Cartesian coordinate system (x, y, z) is taken as shown in Fig. 1, with corresponding velocity components (u, v, w).

For this configuration, the governing equations of motion for a Boussinesq fluid, made dimensionless using h for length scale, ν/h for velocity scale, ΔT for temperature, and $\rho g h$ for pressure, are

$$\nabla \cdot \mathbf{q} = 0 \tag{2a}$$

$$\frac{\partial \mathbf{q}}{\partial t} + (\mathbf{q} \cdot \nabla)\mathbf{q} = -\eta \nabla p + \eta \mathbf{a} - \mathrm{Gr}(T - T_0)\mathbf{a} + \nabla^2 \mathbf{q} \tag{2b}$$

$$\frac{\partial T}{\partial t} + (\mathbf{q} \cdot \nabla)\mathrm{T} = \frac{1}{\mathrm{Pr}} \nabla^2 T \tag{2c}$$

where $\mathbf{q}$ is the velocity, T the temperature, T_0 the ambient temperature, p the pressure, ρ the density, $\mathbf{a} = -(\sin\phi, 0, \cos\phi)$, the gravity vector,

$\eta = gh^3/\nu^2$

$\mathrm{Gr} = \eta\beta\Delta T$, the Grashof number,

$\mathrm{Pr} = \dfrac{Cp\mu}{K}$ the Prandtl number

g the gravitational acceleration, μ the viscosity, ν the kinematic viscosity, β the thermal expansion coefficient, C_p the constant pressure specific heat and K is the thermal conductivity. Equations (2a)–(2c) reduce to those given by Hart [5] when $\phi = 90\text{-}\delta$ and with suitable dimensionless parameters.

The boundary conditions are,

$$\frac{du}{dz} = -\alpha\sigma(u_{B1} - Q_1) \text{ at } z = \frac{1}{2} \tag{2d}$$

$$\frac{du}{dz} = \alpha\sigma(u_{B2} - Q_2) \text{ at } z = -\frac{1}{2} \tag{2e}$$

$$v = w = 0 \text{ at } z = \pm\frac{1}{2} \tag{2f}$$

$$T = T_0 \pm \frac{1}{2} \text{ at } z = \pm\frac{1}{2} \tag{2g}$$

$$p = 0 \text{ at } x = 0, z = 0 \tag{2h}$$

where u_{B1} and u_{B2} are the slip velocities at the upper and lower interfaces, respectively, and Q_1 and Q_2 are the Darcy velocities at the edge of the boundary layers, i.e., $z = \pm 1/2 \pm 1/\sigma$ (see Rudraiah and Veerbhadraiah [18] where they have shown that the boundary layer is of order $1/\sigma$).

The Darcy velocity in the bed is given by,

$$Q = -\frac{\eta}{\sigma^2}\left[\frac{\partial p}{\partial x} + \left\{1 - \frac{\mathrm{Gr}}{\eta}(T - T_0)\right\}\sin\phi\right] \tag{2i}$$

where $\sigma = h/\sqrt{k}$ is the permeability parameter, k is the permeability of the porous material, and α is the slip parameter. This Darcy velocity is valid away from the nominal surface (see Rudraiah and Masuoka [19]).

Conditions (2d) and (2e) are the BJ slip conditions and conditions (2g) imply that the boundaries are isothermal. The Darcy equation (2i) is obtained under the assumption of the same pressure and temperature in the flows above and in the bed.

2.1 Basic Flow. The flow is due to an imbalance between the pressure and buoyancy forces when $\mathrm{Gr} \neq 0$. At low Gr, this motion forms the base flow, in which the velocity u is only in the axial direction and is a function of z and inclination ϕ only. The corresponding temperature is a function of z only and pressure is a function of both x and z. Thus the required basic flow satisfying the boundary conditions (2d)–(2h) is,

$$u_b = \frac{\mathrm{Gr}\sin\phi}{6}\left[z^3 - \left(\frac{1}{4} + f\right)z\right] \tag{2j}$$

$$u_{B2} = -u_{B1} = \frac{\mathrm{Gr}\sin\phi}{12} f \tag{2k}$$

$$T_b = T_0 - z \tag{2l}$$

$$P_b = -\left(z + \frac{\mathrm{Gr}}{2}z^2\right)\cos\phi - x\sin\phi \tag{2m}$$

$$Q = -\frac{\mathrm{Gr}\sin\phi}{2} z \tag{2n}$$

$$Q_2 = -Q_1 = \frac{\mathrm{Gr}\sin\phi}{2}\left(\frac{1}{2} + \frac{1}{\sigma}\right) \tag{2o}$$

$$f = \frac{\sigma + 6\alpha}{\sigma(2 + \alpha\sigma)}\left[1 + \frac{12\alpha}{\sigma(6\alpha + \sigma)}\right] \tag{2p}$$

where the sufffix b denotes the base flow.

2.2 The Perturbation Equations. At sufficiently large Gr, the conduction base flow regime, discussed in Section 2.1, becomes unstable and suffers a transition to convection regime. Transitions resulting in transverse rolls with their axes in the y-direction are considered in this paper. For this, we

Table 1 Critical a, Gr, and Ra for Pr = 0.025 and 0.71.

Pr	σ	$\phi = 10$ deg			$\phi = 30$ deg		
		a_c	$(\mathrm{Gr})_c$	$(\mathrm{Ra})_c$	a_c	$(\mathrm{Gr})_c$	$(\mathrm{Ra})_c$
	∞	2.889	31100.413	777.5103	2.773	13661.636	341.5409
	10,000	2.883	30869.604	771.7401	2.767	13555.529	338.8882
	2000	2.861	29988.052	749.7013	2.744	113149.011	328.7253
0.025	1000	2.833	28973.359	724.3340	2.715	12679.048	316.9762
	250	2.663	24460.890	611.5223	2.542	10581.099	264.5473
	100	2.373	20016.291	501.5323	2.237	8551.1534	213.7788
	∞	3.095	2527.4172	1794.4662	2.822	5596.4447	3973.4757
	10,000	3.087	2511.0511	1782.8462	2.816	5521.6223	3920.3518
	2000	3.073	2449.1400	1738.8894	2.793	5248.7324	3726.60
0.71	1000	3.050	2378.9218	1689.0344	2.766	4958.8829	3520.8068
	250	2.943	2072.4968	1471.4727	2.622	3925.1275	2786.8405
	100	2.787	1749.1672	1241.9087	2.388	3181.1417	2258.6109
			$\phi = 50$ deg			$\phi = 90$ deg	
	∞	2.783	9449.1286	236.2282	2.702	7657.120	191.428
	10,000	2.732	9374.8320	234.3708	2.695	7596.1617	189.9040
	2000	2.709	9089.9037	227.2476	2.674	7362.1555	184.0539
	1000	2.681	8760.0795	219.002	2.646	7090.8989	177.2725
0.025	250	2.508	7286.0908	182.1523	2.471	5877.2908	146.9323
	100	2.201	5866.5191	146.663	2.164	4713.9528	117.8488
	∞	2.868	7644.4398	5427.5523	2.810	8037.5955	5706.6928
	10,000	2.860	7599.8691	5381.7070	2.803	7973.2631	5661.0168
	2000	2.833	7334.8705	5207.7580	2.780	7726.7036	5485.9595
0.71	1000	2.80	7056.1279	5009.8508	2.749	7441.6597	5283.5783
	250	2.601	5861.8610	4161.9231	2.557	6176.4118	4385.2523
	100	2.267	4777.4387	3391.9814	2.219	4981.0913	3536.5748

superimpose on the flow a small symmetrical disturbance of the form

$$
\begin{aligned}
u &= u_b(z) + u'(x, y, z, t) \\
v &= v'(x, z, t),\ w = w'(x, z, t) \\
T &= T_b(z) + T'(x, z, \mathrm{t}) \qquad (2q)\\
p &= p_b(x, z) + p'(x, z, t)
\end{aligned}
$$

where the primes denote the perturbed quantities which are assumed to be very small compared to the base flow. Substituting (2q) into the equations (2a) - (2c), linearizing and assuming that all the perturbed quantities vary in the form

$$(\text{function of } z)\ \mathrm{Exp}\,(iax + ct) \qquad (2r)$$

we get,

$$
\begin{aligned}
&(D^2 - a^2 - c)(D^2 - a^2)W - a^2 \mathrm{Gr} \cos\phi\Theta - ia\,\mathrm{Gr}\sin\phi D\Theta \\
&\quad + (ia^3 u_b + ia\,D^2 u_b)W - iau_b D^2\ W = 0 \qquad (2s)
\end{aligned}
$$

and

$$(D^2 - a^2 - \mathrm{Pr}\,c)\Theta + \mathrm{Pr}\,W - \mathrm{Pr}\ iau_b\Theta = 0 \qquad (2t)$$

where W is the velocity, Θ the temperature, $c(= cr + ici)$ the wave velocity, a the horizontal wave number, and $D = d/dz$. The corresponding boundary conditions are,

$$\Theta = W = DW \pm \frac{1}{\alpha\sigma} D^2 W = 0 \text{ at } z = \pm\frac{1}{2} \qquad (2u)$$

We note that when $u_B = 0$ (i.e., quiescent state) and $\phi = 0$ equations (2s) and (2t) tend to the usual Rayleigh-Benard equations given by Chandrasekhar [3].

3 Marginal Stability Analysis

Since there are no external constraints like magnetic field, rotation, or salinity gradient on the motion, we assume that the marginal state is valid immediately after transition so that $c = 0$ in equations (2s) and (2t).

We shall consider the cases:

(i) Pr = 0 (Pure Tollmien-Schlichting instability)
(ii) Pro, $\phi = 0$ (Rayleigh-Benard Problem)
(iii) Pr $\neq$ 0 (combined Rayleigh Bénard and Tollmien-Schlichting instability)

3.1 The Case When Pr = 0. In this case shear would be dominant and it corresponds to thermally perfectly conducting fluids. Then equation (2t) becomes,

$$(D^2 - a^2)\Theta = 0 \qquad (3a)$$

The solution of this equation satisfying the condition (2a) is $\Theta = 0$.

That is, the temperature perturbation vanishes and the instability is strictly due to shearing. In this case, equation (2s) using equation (2j), takes the form

$$
\begin{aligned}
&(D^2 - a^2)^2 W + \left[\frac{ia^3 \mathrm{Gr}'}{6}\left\{z^3 - \left(\frac{1}{4} + f\right)z\right\} + ia\mathrm{Gr}'\,z\right]W \\
&\quad - \frac{ia\mathrm{Gr}'}{6}\left\{z^3 - \left(\frac{1}{4} + f\right)z\right\}D^2 W = 0 \qquad (3b)
\end{aligned}
$$

where $\mathrm{Gr}' = \mathrm{Gr}\sin\phi$.

We note that, since Gr scales with $\sin\phi$, a solution for one particular angle will provide stability condition for all angles. A solution of equation (3b) is obtained in Section 4 using the power series method.

3.2 The case when $\phi = 0$. This is the usual Rayleigh-Bénard problem with porous boundaries. In this case equations (2s) and (2t) take the form,

$$(D^2 - a^2)^2 W - a^2 \mathrm{Gr}\ \Theta = 0 \qquad (3c)$$

and

$$(D^2 - a^2)\Theta + \mathrm{Pr}\ W = 0 \qquad (3d)$$

These simplify to the form

$$(D^2 - a^2)^3 W + a^2 \mathrm{Ra}\ W = 0 \qquad (3e)$$

where Ra = Pr•Gr, is the Rayleigh number and Pr does not appear explicitly. The eigenvalues of equation (3e) are determined using the power series method as explained in Section 4.

3.3 The Case When Pr $\neq$ 0. Here we have the coupling between Tollmien-Schlichting wave-like instability due to shear and Rayleigh-Bénard type of instability due to uniform heating from below and cooling from above. Equations (2s) and (2t) using equation (2j) take the form,

$$
\begin{aligned}
&(D^2 - a^2)^2 W - a^2 \mathrm{Gr}\cos\phi\Theta - ia\,\mathrm{Gr}\sin\phi\, D\Theta \\
&\quad + \left[\frac{1}{6} ia^3 \mathrm{Gr}\sin\phi\left\{z^3 - \left(\frac{1}{4} + f\right)z\right\} + ia\,\mathrm{Gr}\sin\phi z\right]W \\
&\quad - \frac{1}{6} ia\,\mathrm{Gr}\sin\phi\left\{z^3 - \left(\frac{1}{4} + f\right)z\right\}D^2 W = 0 \qquad (3f)
\end{aligned}
$$

and

$$(D^2 - a^2)\Theta + \Pr W - \frac{1}{6} ia \Pr \mathrm{Gr} \sin\phi \left\{ z^3 - \left(\frac{1}{4} + f\right) z \right\} \Theta = 0 \tag{3g}$$

4 The Power Series Solution

In this section, the power series solution for equations (3*f*) and (3*g*) are obtained for $\Pr \neq 0$. The solutions for $\Pr = 0$ and $\phi = 0$ can be obtained as particular cases.

A general solution of equations (3*f*) and (3*g*) can be constructed in the form

$$W(z) = \sum_{k=1}^{\infty} b_k z^{k-1} \tag{4a}$$

$$\Theta(z) = \sum_{k=1}^{\infty} c_k z^{k-1} \tag{4b}$$

where b_k and c_k are arbitrary constants. These constants are determined by substituting equations (4*a*) and (4*b*) into equations (3*f*) and (3*g*).
Assuming,

$$b_k = Sb_{kn} G_n, \; c_k = Sc_{kn} G_n \tag{4c}$$

where

$$G_n = (b_1, b_2, b_3, b_4, c_1, c_2) \tag{4d}$$

is the general solution vector Sb_{kn} and Sc_{kn} are particular solution vectors, we obtain

$$Sb_{kn} = (\delta_{k1}, \delta_{k2}, \delta_{k3}, \delta_{k4}, 0, 0) \text{ for } 1 \le k \le 4$$

$$Sc_{kn} = (0, 0, 0, 0, \delta_{k1}, \delta_{k2}) \text{ for } 1 \le k \le 2$$

where δ_{ki} is the Kronecker delta.
For $k > 4$,

$$\begin{aligned} Sb_{kn} = \frac{1}{(k-1)(k-2)(k-3)(k-4)} \Big[& 2a^2(k-3)(k-4) Sb_{k-2,n} \\ & - a^4 Sb_{k-4,n} + a^2 \mathrm{Gr} \cos\phi Sc_{k-4,n} \Delta_{1,k-4} \\ & + ia \,\mathrm{Gr} \sin\phi (k-4) Sc_{k-3,n} \Delta_{1,k-3} \\ & - \mathrm{Gr} \sin\phi \Big\{ \frac{1}{6} ia^3 Sb_{k-7,n} \Delta_{1,k-7} - \Big(\frac{1}{6} ia^3 \Big(\frac{1}{4} + f\Big) \\ & - ia + \frac{1}{6} ia (k-6)(k-7) \Big) Sb_{k-5,n} \Delta_{1,k-5} \\ & + \frac{1}{6} ia \Big(\frac{1}{4} + f\Big) (k-4)(k-5) Sb_{k-3,n} \Big\} \Big] \end{aligned} \tag{4e}$$

and for $k > 2$,

$$\begin{aligned} Sc_{kn} = \frac{1}{(k-1)(k-2)} \Big[& a^2 Sc_{k-2,n} - \Pr Sb_{k-2,n} \\ & + \frac{1}{6} ia \Pr \mathrm{Gr} \sin\phi Sc_{k-5,n} \Delta_{1,k-5} \\ & - \frac{1}{6} ia \Pr \mathrm{Gr} \sin\phi \Big(\frac{1}{4} + f\Big) Sc_{k-3,n} \Delta_{1,k-3} \Big] \end{aligned} \tag{4f}$$

where

$$\Delta_{nm} = 0, \; m < n$$
$$\Delta_{nm} = 1, \; m \ge n$$

Since G_n is arbitrary and nonzero when the solution is nontrivial, it has been removed from the preceding equations. The constants b_i ($i = 1-4$) and c_j ($j = 1, 2$) must be chosen to satisfy the boundary conditions (2*u*). The condition for the nontrivial solution of these constants leads to the characteristic equation,

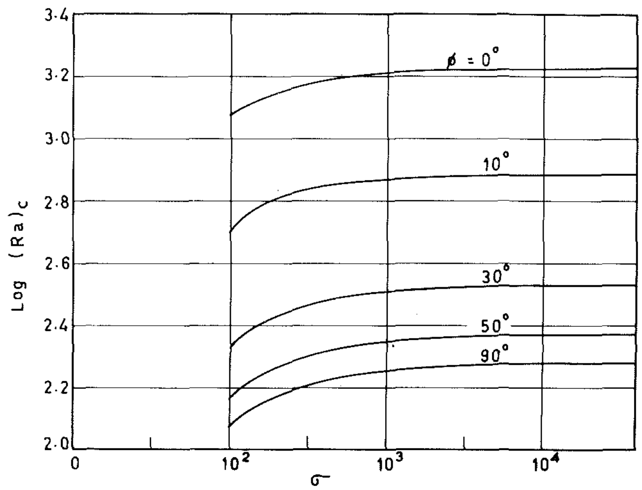

Fig. 2 Effect of σ on $(\mathrm{Ra})_c$ for Pr = 0.025

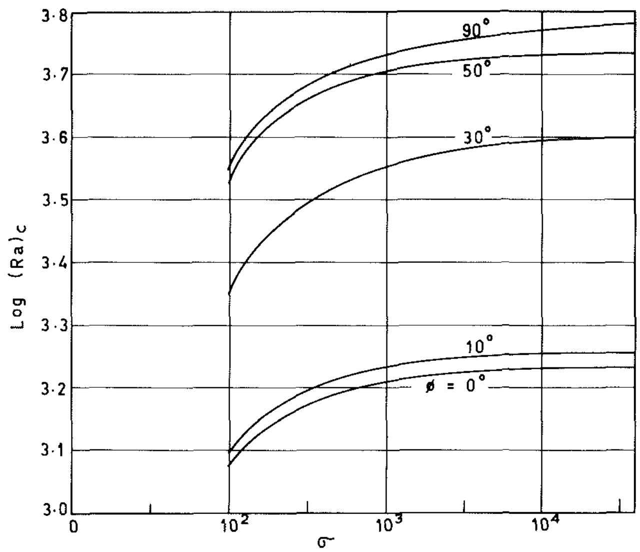

Fig. 3 Effect of σ on $(\mathrm{Ra})_c$ for Pr = 0.71

$$|A_{mn}| = 0 \tag{4g}$$

where

$$\begin{aligned} A_{1n} &= Sb_{kn}(0.5)^{k-1} \\ A_{2n} &= Sb_{kn}(-0.5)^{k-1} \\ A_{3n} &= Sb_{kn}\Big[(k-1)(0.5)^{k-2} + \frac{1}{\alpha\sigma}(k-1)(k-2)(0.5)^{k-3}\Big] \\ A_{4n} &= Sb_{kn}\Big[(k-1)(-0.5)^{k-2} \\ & \quad - \frac{1}{\alpha\sigma}(k-1)(k-2)(-0.5)^{k-3}\Big] \\ A_{5n} &= Sc_{kn}(0.5)^{k-1} \\ A_{6n} &= Sc_{kn}(-0.5)^{k-1} \end{aligned} \tag{4h}$$

where k ranges from $1-\infty$.

The required eigenvalues are determined using the following numerical procedure. For a particular value of a, Gr is given a guess value and $|A_{mn}|$ is calculated. Using an appropriate iteration technique Gr is varied until $|A_{mn}| = 0$ up to a certain approximation. To find the critical value of Gr, its value is calculated for a range of values of a. The minimum value of Gr is taken as Gr_c and the corresponding a, a_c.

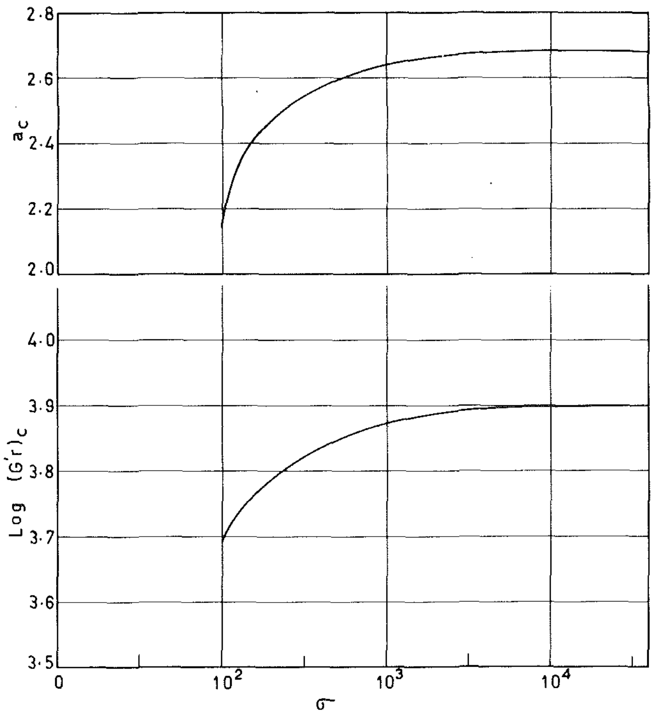

Fig. 4 Effect on σ on $(G'r)_c$ and a_c for Pr = 0

The same procedure is adopted to find the eigenvalues in the particular cases for Pr = 0 and $\phi = 0$ and the results are discussed in the following section.

5 Discussions

The stability of flow in an inclined channel bounded on both sides by porous layers with uniform heating from below and cooling from above has been studied for various inclinations ϕ, when Pr = 0 (absence of buoyancy force, i.e., pure shear), 0.025 (mercury), and 0.71 (air), for different values of σ, using a simple, fast convergent power series technique. Gr is iterated on using Newton-Raphson method up to an accuracy of 10^{-8}. The accuracy of the results depends on the number of terms used in the power series. It has been found that convergence in Gr to 8 figures accuracy requires 70 terms.

5.1 The Case When Pr $\neq$ 0. In Table 1, we have the critical Rayleigh numbers $(Ra)_c$ and critical wave numbers, a_c, for different inclinations ϕ and various values of σ when Pr = 0.025 and 0.71, with shear dominating in the former case and thermal gradient predominant in the latter case. The critical Rayleigh numbers are plotted against different σ's in Figs. 2 and 3. We note that there is a considerable decrease in $(Ra)_c$ for values of σ between 100 and 400 due to the slip at the bed, with no appreciable change for large values of σ. For large values of σ the $(Ra)_c$ tends to the values of fluid layer bounded by impermeable boundaries considered by Ruth [6]. It is interesting to note that with increase in ϕ $(Ra)_c$ decreases for Pr = 0.025 and increases for Pr = 0.71. This is because of different nature of buoyancy force phenomena in mercury and air. In the case of mercury (small Pr = 0.025) the control of convection is due to the tangential component of buoyancy which decreases with a decrease in inclination from the vertical. Hence convection sets in at a higher critical Rayleigh number as evident from Fig. 2. In the case of air, however, the normal component of buoyancy force is dominating and a very different kind of flow drive arises. This sets up a secondary flow in addition to the base flow. Hence the system becomes more unstable and a reverse phenomena to that in mercury occurs (see Fig. 3).

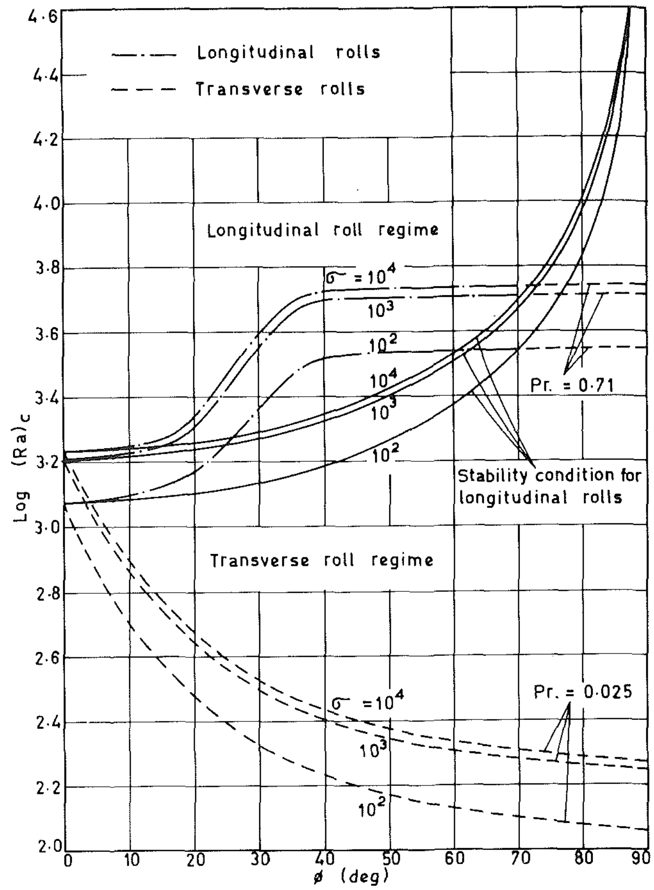

Fig. 5 Critical Ra for $\sigma = 10^2, 10^3$ and 10^4

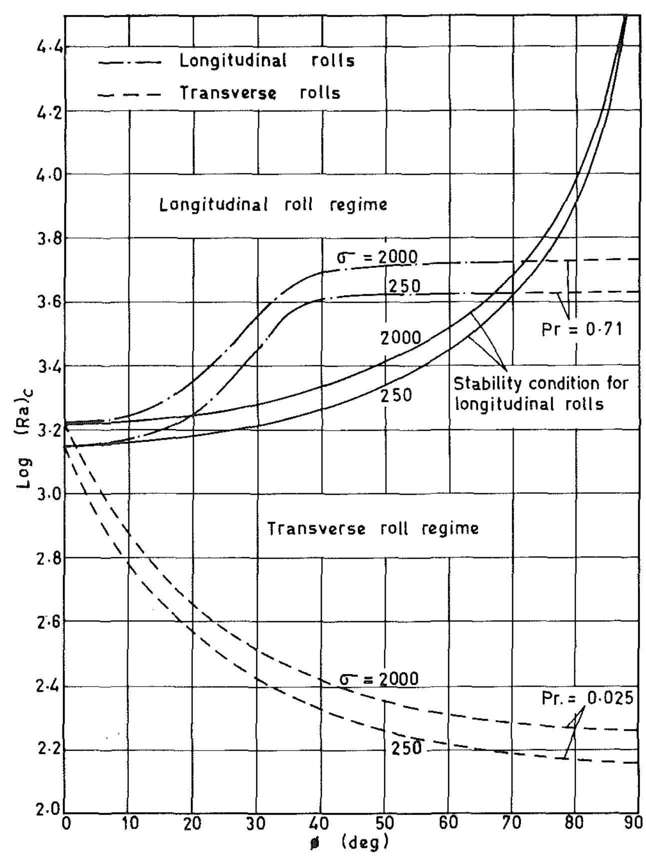

Fig. 6 Critical Ra for $\sigma = 250, 2 \times 10^3$

Table 2 Critical a and $\acute{\mathrm{Gr}}$ (= Gr sin ϕ) for Pr = 0

σ	a_c	$(\acute{\mathrm{Gr}})_c$
∞	2.688	7930.055
10,000	2.682	7867.1273
2000	2.661	7625.4095
1000	2.633	7345.0095
250	2.456	6090.8115
100	2.145	4900.4230

Table 3 Critical a, Gr, and Ra, $\phi = 0$

σ	a_c	$(\mathrm{Gr})_c$	$(\mathrm{Ra})_{c0}$
∞	3.117	2405.2982	1707.7617
10,000	3.112	2390.0779	1696.9553
2000	3.095	2332.4242	1656.0211
1000	3.076	2266.8695	1609.4773
250	2.971	1978.7683	1404.9254
100	2.824	1670.5023	1186.0566

5.2 The Case When Pr = 0. As Gr scales with sin ϕ in this case, $(\acute{\mathrm{Gr}})_c$ the critical $\acute{\mathrm{Gr}}$(= Gr sin ϕ) for various values of σ have been calculated and are given along with the critical wave numbers in Table 2. These provide the stability conditions for all angles.

For examples:

$$(i) \text{ for } \sigma \rightarrow \infty, (\mathrm{Gr})_c = \frac{7930.055}{\sin \phi} \quad (5a)$$

$$(ii) \text{ for } \sigma = 10^4, (\mathrm{Gr})_c = \frac{7867.1273}{\sin \phi} \quad (5b)$$

and

$$(iii) \text{ for } \sigma = 10^2, (\mathrm{Gr})_c = \frac{4900.4230}{\sin \phi} \quad (5c)$$

Figure 4 shows the variation of $(\acute{\mathrm{Gr}})_c$ and a_c with respect to σ. As in Section 5.1, we note that $(\mathrm{Gr})_c$ decreases considerably for small values of σ and tends to a constant value for large σ because of the existence of the slip. From equations (5*a*)-(5*c*), it is clear that $(\mathrm{Gr})_c$ is minimum for ϕ = 90 deg and these equations are not valid for $\phi = 0$. The case $\phi = 0$ is treated separately in the following section.

5.3 The Case When ϕ = 0. The critical Rayleigh numbers and critical wave numbers, in this case, are computed and are shown in Table 3. The critical Rayleigh numbers are denoted as (Ra)*c*o. Following Birikh, et al. [20], stability condition for longitudinal rolls is derived in the form

$$(\mathrm{Ra})_c = \frac{(\mathrm{Ra})_{c0}}{\cos \phi} \quad (5d)$$

where $(\mathrm{Ra})_{c0}$ = (Ra) when $\phi = 0$.

Transverse rolls will occur only if their $(\mathrm{Ra})_c$ is less than the $(\mathrm{Ra})_c$ in equation (5*d*). Figures 5 and 6 show the regimes where transverse and longitudinal rolls occur for various Pr and σ. For ϕ = 90 deg, the instability results in transverse rolls irrespective of Pr. For Pr = 0.025, the transverse rolls occur for all inclinations. For Pr = 0.71, the regions where the transverse rolls occur are limited. The physical explanation for the existance of longitudinal rolls for most angles (≤ 70 deg) in the case of Pr = 0.71 (air) and for the existence of transverse rolls for all angles in the case of Pr = 0.025 (mercury) is the same as the different nature of components of buoyancy force phenomena explained in Section 5.1. It is interesting to note that although the effect of porous boundaries is to lower the critical Rayleigh numbers, the inclinations for transverse rolls to occur are almost unaffected by σ when Pr = 0.71.

5.4 The Critical Wave Number, a_c. It is found that, in general, $(\mathrm{Gr})_c$ had to be calculated to 8 figure accuracy in order to find a_c to 4 figure accuracy. The effect of Pr and σ on

Table 4 Comparison of critical Gr for Pr = 0.71

ϕ	Hart [5]	Ruth [6]	Present case
	$(\mathrm{Gr})_c\ (\sigma \rightarrow \infty)$	$(\mathrm{Gr})_c\ (\sigma \rightarrow \infty)$	$(\mathrm{Gr})_c\ (\sigma = 10^5)$
0°	2363	2405.2983	2390.0779
10°	2420	2527.4172	2511.0511
30°	6793	5596.4447	5521.6223
50°	7059	7644.4398	7579.8691
90°	8230	8037.5955	7973.2631

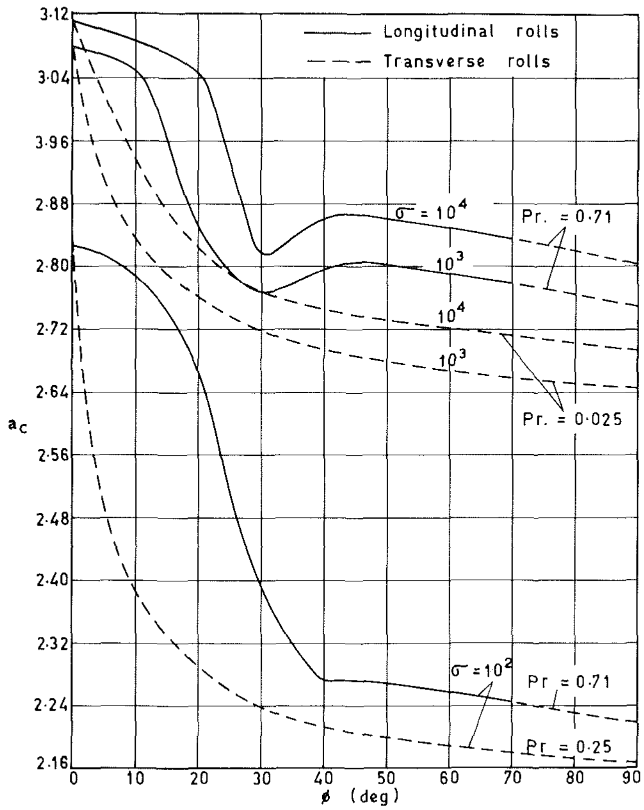

Fig. 7 Critical a for $\sigma = 10^2, 10^3$ and 10^4

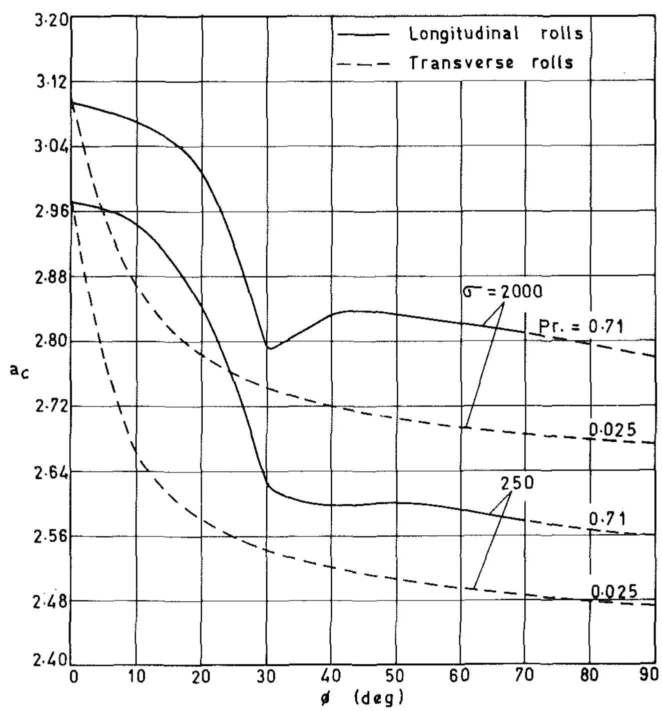

Fig. 8 Critical a for $\sigma = 250, 2 \times 10^3$

the critical wave number a_c for various inclinations are shown in Figs. 7 and 8. As σ decreases a_c also decreases. We see that in Fig. 7, the difference in a_c for $\sigma = 10^2$ and $\sigma = 10^3$ is quite large. So, as σ decreases, the wave lengths are increased. Thus, for smaller values of σ, the convection cells are elongated. Also, there is a notable change in a_c between $\phi = 30$ and $\phi = 40$ for Pr = 0.71, σ = 100,250. For these values of σ, a_c decreases in this region whereas for higher values of σ, a_c increases between ϕ = 30 deg and ϕ = 40 deg. We note that at Pr = 0.025, the shear would be very important and the indirect convective instability exhibiting transverse rolls with low wave numbers prevail. At Pr = 0.71 instability results in the form of longitudinals rolls having larger wave numbers.

Comparison of the results for $\sigma \to \infty$ with those for other values of σ reported in Tables 1-3 reveals that the effect of decrease in σ is to make the system less stable because of the reduction in friction at the boundaries. It is also of interest to compare our results with those of Hart [5] and Ruth [6] for $\sigma \to \infty$. This is done in Table 4 for Pr = 0.71. In this table, we have not reported the results of Unny [7] since they do not agree well with our results. Although agreement with Unny [7] is not obtained, the good agreement with Hart [5] and Ruth [6] can be interpreted as validation of the power series method employed in this paper.

6 Conclusion

The power series method employed in this paper to study convection in an inclined channel bounded on both sides by porous beds reveals a close analogy between the results of the present problem and those of a fluid layer studied by Hart [5] and Ruth [6]. Two main conclusions are as follows:

(*i*) The convective movements in the case of mercury (Pr = 0.025) are in the form of transverse rolls for all angles. In the case of air (Pr = 0.71), however, the convective movements are in the form of longitudinal rolls for the range of inclination 0 deg $\leq \phi \leq$ 70 deg and transverse rolls exist only in the narrow region of 70 deg $< \phi \leq$ 90 deg. The physical explanation for the existence of these different convective movements is given based on the dominant role of the components of buoyancy force.

(*ii*) The effect of porous boundaries is to make the system less stable due to the existence of the slip at the nominal surfaces. Further, the critical Grashof, Rayleigh, and wave numbers vary considerably with the porous parameter σ, decreasing with decreasing σ because of the reduction in friction at the porous boundaries. In the case of air, two different behaviors of critical numbers a_c are observed (Figs. 7 and 8). For 30 deg $< \phi <$ 40 deg, and for σ = 100,250, a_c decreases in this region and the convection cells are elongated. For higher values of σ, however, a_c increases for 30 deg $< \phi <$ 40 deg.

Acknowledgment

This work was sponsored by the U.G.C., India, under the DSA programme.

References

1 Fung, Y. C., and Tang, H. T., "Solute Distribution in the Flow in a Channel Bounded by Porous Layers," ASME JOURNAL OF APPLIED MECHANICS, Vol. 42, Series E, No. 3, 1975, pp. 531-535.

2 Fung, Y. C., and Tang, H. T., "Longitudinal Dispersion of Tracer Particles In the Blood Flowing in a Pulmonary Alveolar Sheet," ASME JOURNAL OF APPLIED MECHANICS, Vol. 42, Series E, No. 3, 1975, pp. 536-540.

3 Chandrasekhar, S., "Hydrodynamic and Hyrdomagnetic Stability," Claredon Press, Oxford, 1961.

4 Betchov, R., and Criminal, W. O., Jr., "Stability of Parallel Flows," Academic Press, New York, 1967.

5 Hart, J. E., "Stability of Flow in a Differently Heated Inclined Box," *Journal of Fluid Mechanics,* Vol. 47, 1971, pp. 547-576.

6 Ruth, D. W., "The Stability Criteria Governing the Transition From the Base Flow-Conduction Regime to the Transverse Roll Regime," Department of Mechanical Engineering, University of Calgary, Report 129, 1978.

7 Unny, T. E., "Thermal Instability in Differentially Heated Inclined Fluid Layers," ASME JOURNAL OF APPLIED MECHANICS, Vol. 39, 1972, pp. 41-46.

8 Bories, S. A., and Combarnous, M., "Natural Convection in a Sloping Porous Layer," *Journal of Fluid Mechanics*, Vol. 57, 1973, pp. 63-79.

9 Kaneko T., Mohtadi, M. F., and Aziz, K., "An Experimental Study of Natural Convection in an Inclined Porous Media," *International Journal of Heat and Mass Transfer*, Vol. 17, 1974, pp. 485-496.

10 Combarnous, M., and Aziz, K., "Influence of Natural Convection in Oil and Gas Reservoirs," Revnue, Institute Fr. Petrole, Vol. 25, 1970, pp. 1335-1353.

11 Beavers, G. S., and Joseph, D. D., "Boundary Conditions at a Naturally Permeable Wall," *Journal of Fluid Mechanics*, Vol. 30, 1967, pp. 197-207.

12 Beavers, G. S., Sparrow, E. M., and Magnuson, R. A., "Experiments on Coupled Parallel Flows in a Channel and a Bounding Porous Medium," ASME *Journal of Basic Engineering*, Vol. 92, Series D, 1970, pp. 845-848.

13 Taylor, G. I., "A Model for the Boundary Condition of a Porous Material," Part 1, *Journal of Fluid Mechanics*, Vol. 49, 1971, pp. 319-326.

14 Rajasekhara, B. M., 1974, Ph.D. Thesis, Bangalore University, India.

15 Channabasappa, M. N., and Ranganna, G., "Transition from Laminar Flow to Turbulence," Private Communication, 1980.

16 Sparrow, E. M., Beavers, G. S., Chen, T. S., and Lloyd, J. R., "Breakdown of the Laminar Flow Regime in Permeable Walled Ducts," ASME JOURNAL OF APPLIED MECHANICS, Vol. 40, Series E, 1973, pp. 337-342.

17 Sparrow, E. M., Golstein, R. J., and Johsson, V . K., "Thermal Instability in a Horizontal Fluid Layer: Effect of Boundary Conditions and Nonlinear Temperature Profile," *Journal of Fluid Mechanics*, Vol. 18, Part 4, 1964, pp. 513-528.

18 Rudraiah, N., and Veerabhadraiah, R., "Buoyancy Effect on the Couette Flow Past a Permeable Bed," *Journal of Mathematical and Physical Sciences*, Vol. 13, No. 6, 1979, pp. 523-539.

19 Rudraiah, N., and Masuoka, T., "Asymptotic Analysis of Natural Convection Through Horizontal Porous Layers," *International Journal of Engineering Sciences*, 1981, (accepted for publication).

20 Birikh, R. V., Gershuni, G. Z., Zhukovitskii, E. M., and Rudakov, R. N., "Hydrodynamic and Thermal Instability of a Steady Convective Flow," *Prikl, Mat. i Mekh.*, Vol. 32, No. 2, pp. 256-263.

Calculation of Unsteady Transonic Pressure Distributions by the Indicial Method

G. D. Kerlick
Research Scientist.

D. Nixon
Manager, Computational Fluid Dynamics Department.

Nielsen Engineering and Research, Inc., Mountain View, Calif. 94043

A method for the rapid estimation of complete unsteady transonic pressure distributions is developed. The two key elements of this method are (1) the indicial method and (2) the strained coordinate technique. The indicial method permits the determination of the response of a system to an arbitrary schedule of perturbations once the response of the system to a step change in one of the perturbing variables (the indicial response) is known. The strained coordinate permits the movement of discontinuities in the solution (e.g., shock waves) to occur as the solution develops in time. Together, these two techniques provide detailed information on the time development of pressure distributions over an airfoil that is of use in aeroelastic applications such as control surface flutter and active control design. Examples of both oscillatory and transient perturbations are given, as well an example that demonstrates the potential of this method for aeroelastic tailoring and active control. In all cases, the agreement with more expensive finite-difference calculations is good, and the time savings is about an order of magnitude.

1 Introduction

Aeroelastic effects on aircraft flying at transonic speeds are extremely important, but very difficult to estimate. The main difficulty lies in calculating unsteady aerodynamic loads with sufficient accuracy to permit flutter prediction. Moreover, such a calculation should be fast enough to allow its repeated use by designers in parametric studies.

Although recent advances in numerical and analytical techniques have permitted fairly routine calculations of the steady aerodynamic loads in transonic flow, even in three dimensions, corresponding techniques for unsteady loading have yet to be developed. Presently available numerical techniques are too slow and costly to be used repetitively by designers.

There have been two basic approaches to unsteady transonic flow calculations. Ballhaus and Goorjian [1] integrate the flow field numerically in the time domain, using finite differences. This method can be combined with an aeroelastic program to yield a direct numerical simulation of the unsteady motion of the airfoil. The principal drawback to this method is its cost in computing time. Since the simulation must be repeated for every new choice of flight parameter, repetitive design calculations are prohibitively expensive.

Traci, Albano, and Farr [2] and Weatherill, Ehlers, and Sebastian [3] analyze the aerodynamic problem in the frequency domain. Frequency domain methods have also been extended to three-dimensional flows. The drawback here is that only the harmonics of a chosen fundamental frequency are considered in the calculation and are available for coupling to the aeroelastic calculation. It is therefore expensive to run the calculation for all frequencies of interest. Furthermore, in the absence of a shock-fitting algorithm, the frequency domain method constrains the shock position to its mean, steady location, which is a serious disadvantage, especially for modern supercritical wings in which the physical shock motions can be considerable.

Clearly, there is a need for a rapid, repeatable, sufficiently accurate method for computing unsteady transonic airloads. The indicial method, described in Section 2, is a most promising approach to this problem. Ballhaus and Goorjian [4] have used this method to estimate unsteady lifts and moments such as would be needed in a flutter calculation. In many cases of interest, only integrated quantities such as lifts and moments are needed, and their method provides the needed rapid estimation of these forces.

There are cases where a more detailed knowledge of the pressure distribution is necessary. The design of control surfaces requires that the unsteady forces on the surface, both for infinitesimal motions (onset of flutter) and for larger amplitude motions (associated with the design of active controls) be calculated. Airfoil design optimization procedures, which include unsteady effects, require estimates of the complete unsteady pressures. Additionally, knowledge of the distribution of unsteady forces gives insight into the mechanisms of unsteady flow.

In the extended indicial method described in the following, after two initial finite-difference calculations have been performed, it is possible to obtain complete unsteady pressures for additional transonic flows for essentially the same cost as for obtaining lifts and moments, and at far less

Contributed by the Applied Mechanics Division for Publication in the JOURNAL OF APPLIED MECHANICS.

Discussion on this paper should be addressed to the Editorial Department, ASME United Engineering Center, 345 East 47th Street, New York, N.Y. 10017, and will be accepted until two months after final publication of the paper itself in the JOURNAL OF APPLIED MECHANICS. Manuscript received by ASME Applied Mechanics Division, April, 1981; final revision, December, 1981.

cost than an additional finite-difference calculation. Large shock excursions are permitted and predictable, even those of the order of 30 percent chord or more, because of the use of a strained coordinate technique.

2 Comments on the Indicial Method

For the aeroelastic applications we just mentioned, we want to be able to predict, rapidly and accurately, the pressures on an airfoil that undergo a small disturbance in one or more of its flight parameters, such as angle of attack or profile shape. Such changes may be either oscillatory (as in flutter) or transient (as in gusts). For transonic flows, these phenomena are described by the low-frequency transonic small disturbance (TSD) equation

$$\frac{2kM_\infty^2}{\delta^{2/3}}\phi_{xt}=\left[\frac{(1-M_\infty^2)}{\delta^{2/3}}-(\gamma+1)M_\infty^q\phi_x\right]\phi_{xx}+\phi_{yy} \qquad (1)$$

Here, ϕ is the velocity potential, U_∞ and M_∞ are the free stream velocity and Mach number, respectively, $k \equiv \omega c/U_\infty$ is the reduced frequency, c is the chord length, γ is the ratio of specific heats, δ is the thickness-to-chord ratio, and q is a transonic scaling parameter. The quantities x, y, t, ϕ have been scaled by c, $c\delta^{-1/3}$, ω^{-1}, and $c\delta^{2/3}U_\infty$, respectively.

Unfortunately, equation (1) is nonlinear. When dealing with these small disturbances, it would be a tremendous advantage for us, both conceptually and computationally, to be able to linearize this equation in the neighborhood of some exact or numerical steady solution, since we could then construct new solutions via the principle of superposition.

Transonic flows present an obstacle to such linearization because they possess discontinuities (shocks) that move in response to the disturbance. In the region where the shock moves, the effect of a small perturbation in, say angle of attack will be a large change in pressure. A means of overcoming this obstacle is to introduce strained coordinates that move with the shock. The shock motion is assumed to vary linearly with the perturbation parameter. In these coordinates, the unsteady perturbations to pressure are indeed small compared to steady values and the TSD equation can be split into a nonlinear steady equation and a linear unsteady equation. Since the unsteady effects are represented by a linear equation, the principle of superposition can be applied.

In this paper, we shall construct solutions of the unsteady component of the split TSD equation in strained coordinates by the indicial method (see also [1]). We wish to find a solution $u(t)$ to the equation

$$L[u]=\epsilon(t), \qquad (2)$$

where $L[u]$ is a linear operator.

Here $\epsilon(t)$ represents the disturbance and can be considered either as a right-hand side of the differential equation or as a change to the boundary condition. It may be an arbitrary function that vanishes for times $t<0$. Now, we assume that we can construct a solution $u(t)$ of the equation

$$L[u]=\theta(t-t_0) \qquad (3)$$

where $\theta(t_0)$ is a unit step function at time t_0. The solution $u_\epsilon(t-t_0)$ is called the indicial response of the system. In our work, the indicial response will be obtained by a finite-difference calculation.

Since the function $\epsilon(t)$ can be represented by the identity

$$\epsilon(t)\equiv\int_0^t \frac{d\epsilon}{dt}\bigg|_{t-t_0}\theta(t_0)dt_0+\epsilon(0)\theta(t), \qquad (4)$$

we can obtain by superposition the solution

$$u(t)=\int_0^t \frac{d\epsilon}{dt}\bigg|_{t-t_0}u_\epsilon(t_0)dt_0+\epsilon(0)u_\epsilon(t). \qquad (5)$$

This type of convolution integral is known as Duhamel's integral [6]. We shall find that constructing a solution by means of these convolution integrals represents a very substantial savings of computation time over a finite-difference calculation.

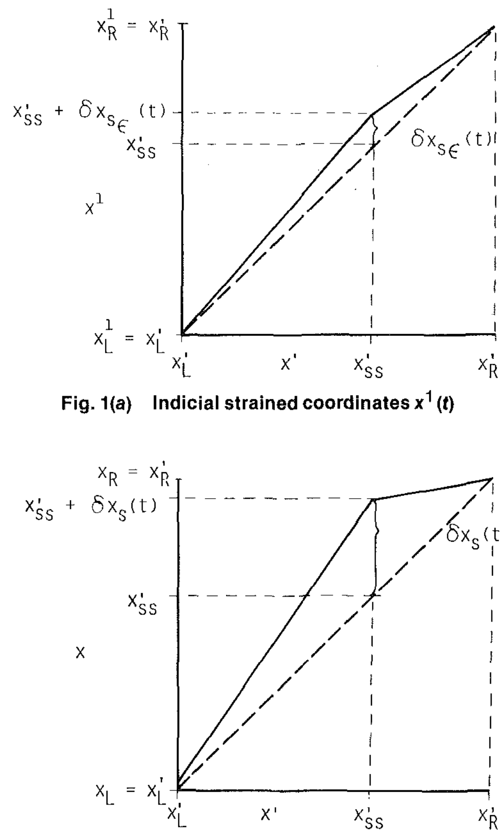

Fig. 1(a) Indicial strained coordinates $x^1(t)$

Fig. 1(b) Convolved strained coordinates x(t)

Fig. 1

We have written a computer code, CONVOL, to construct unsteady solutions of the TSD equaion via Duhamel's integral in strained coordinates. The details of this program follow. For a fuller analysis, see Nixon [5].

2.1 Computational Aspects of the Problem: Steady Solution. Before we can apply the indicial method, we need the results of two calculations, namely (1) a time-independent (steady-state) solution about which to perturb, and (2) a time-dependent (unsteady) solution of the TSD equation for an indicial (step) change in the perturbation parameter (e.g., angle of attack).

In the present work, the finite-difference code LTRAN2 [1] was used to solve for the steady and indicial upper surface pressures. Lower surface pressures are, of course, handled the same way. We shall denote the upper surface-pressure coefficient as $C_p(x')$, where x' is the physical coordinate scaled to the airfoil chord. The pressure coefficient is here defined as $C_p(x') = -2\delta^{2/3}u_0(x')$, where $u_0(x') = d\phi(x')/dx'$ is the velocity and ϕ is the velocity potential. Note that the physical coordinate x' does not depend on time.

We may easily obtain the shock position from any C_p distribution, so long as there is a single shock only (which is true for all cases considered here). We merely interpolate the curve to find the point where C_p reaches its critical value C_p^* and dC_p/dx' is positive. We shall denote the steady shock position as x_{ss}'.

2.2 Indicial Response Function. We also use the finite-difference code LTRAN2 to generate the indicial responses we need. A restriction on the applicability of our results comes from the choice of the low frequency TSD equation (1). Here, and in LTRAN2 as well, we should restrict our consideration

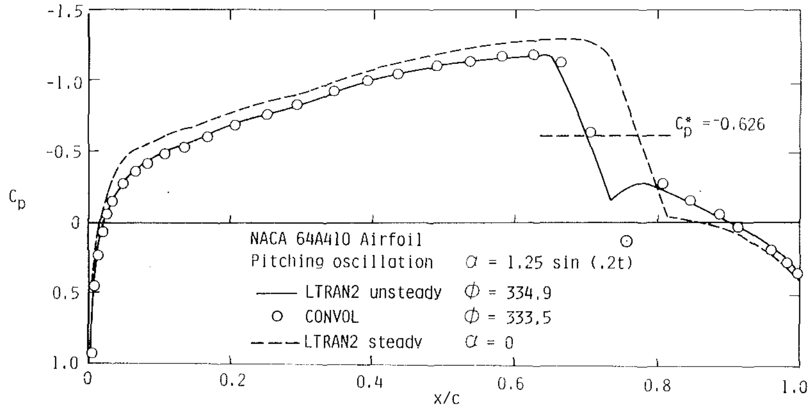

Fig. 2(a) Near forwardmost position

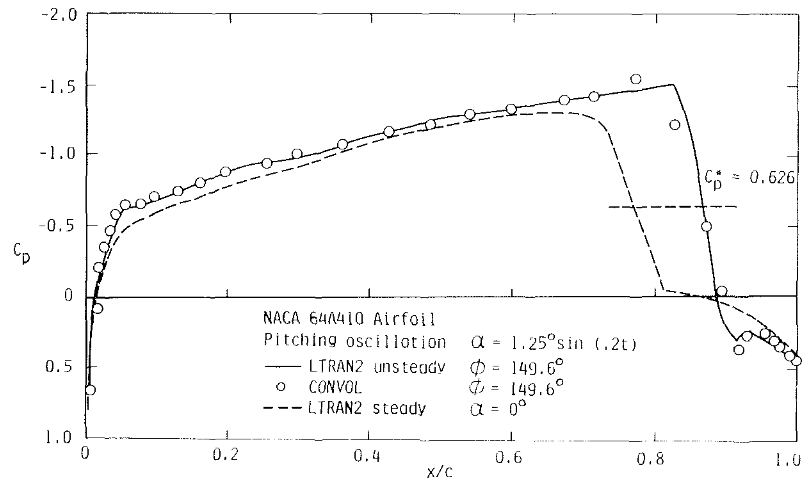

Fig. 2(b) Near aftmost shock position

Fig. 2 Comparison of CONVOL and LTRAN2 unsteady upper surface pressures

to cases where k is less than about 0.2 (see [7]). Similarly, the ranges of the perturbation parameters for which the indicated method is here applied cannot exceed the ranges over which LTRAN2 is valid. Of course, these restrictions are not inherent in the indicial method itself, but rather in the equations and numerical schemes whereby we generate the indicial response function.

3 The Convolution Code CONVOL

First, we need to obtain the indicial response $\delta x_{s\epsilon}(t)$ for the shock motion and $C_p(x^1, t)$ for the pressures, where x^1 is a strained coordinate, defined in the following, chosen so that the indicial shock position remains fixed.

To find the indicial shock excursion $\delta x_{s\epsilon}(t)$ we merely repeat the shock-finding algorithm which we used to find the steady shock location, and subtract the steady shock position, thus

$$\delta x_{s\epsilon}(t) = x_s'(t) - x_{ss}' \tag{6}$$

Now we compute, for each iteration, strained coordinates $x^1(t)$ according to the prescription

$$x^1(t) = x' + \delta x_s(t) f(x') \tag{7}$$

Here, $f(x')$ is a piecewise linear straining function given by

$$f(x') = \begin{cases} (x' - x_L)/(x_{ss} - x_L) & x_L \leq x' \leq x_{ss}' \\ (x_R - x')/(x_R - x_{ss}) & x_{ss}' \leq x' \leq x_R \end{cases} \tag{8}$$

The straining function vanishes outside the fixed points x_L and x_R, which are the boundaries of the strained region. They must be chosen so as to include the full range of the shock motion; it is usually best to choose them as the coordinates of the leading and trailing edges of the airfoil ($x_L = 0$ and $x_R = 1$), respectively. The relation between the "indicial" strained coordinates x^1 and the physical coordinates x' for a typical value of $\delta x_{s\epsilon}(t)$ is shown in Fig. 1(a). Note that Nixon [5] uses a parabolic straining function instead of the piecewise linear one used here. However, Nixon [8] has shown that the method is insensitive to the particular straining chosen.

The next step is to interpolate the unsteady C_p distribution obtained from LTRAN2 into these strained coordinates. We have found that quasi-Hermite piecewise polynomials are superior to cubic spline functions for our purposes, because they allow the second derivative of the interpolating curve to be discontinuous in the region of the shock. Cubic splines, by enforcing continuity of the second derivative, induce an artificial "wiggle" in the curve.

Having interpolated the unsteady C_p's, we subtract the steady pressure, in physical coordinates, corrected for the shock motion, obtaining thereby the indicial response for C_p:

$$C_{p_\epsilon}(x', t) = C_p(x^1, t) - C_{p_0}(x')[1 - f'(x')\delta x_{s\epsilon}(t)] \tag{9}$$

Here, $f'(x')$ is just the derivative of the straining function defined in equation (8) and is piecewise constant.

3.1 Convolution Integrals. The total shock displacement due to any arbitrary schedule of the perturbation parameter as a function of time, $\epsilon(t)$, can be written in terms of Duhamel's integral as follows:

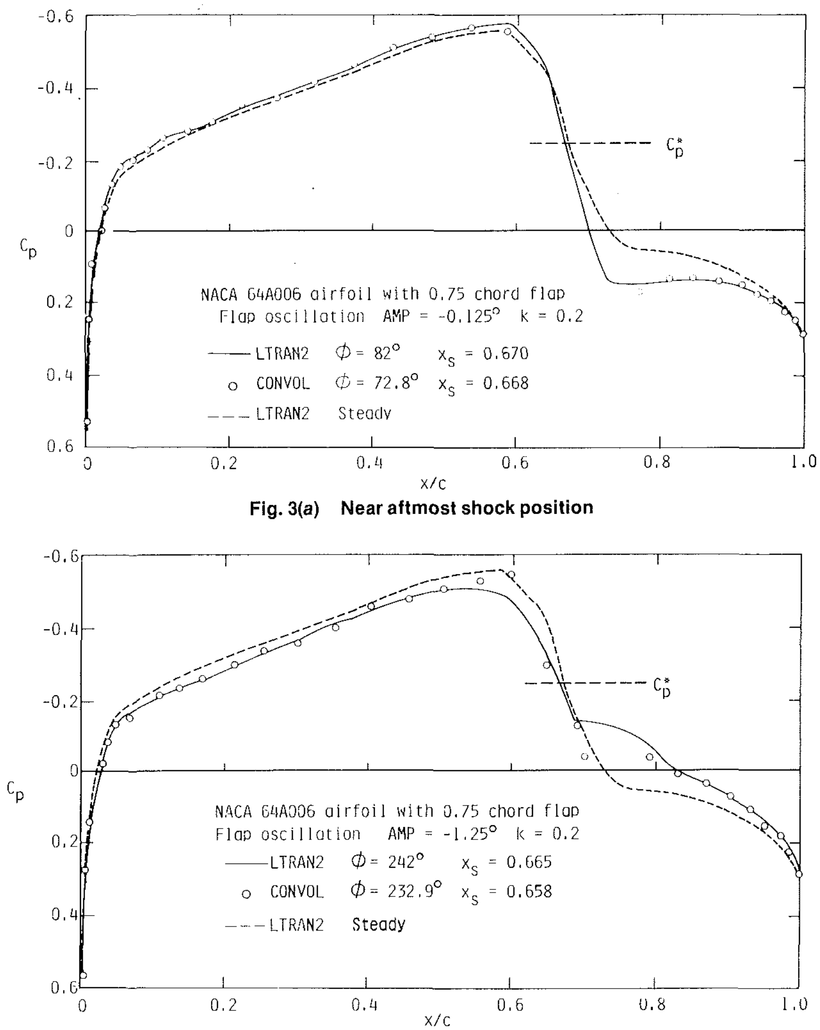

Fig. 3(*a*) Near aftmost shock position

Fig. 3(*b*) Near foremost shock position

Fig. 3 Unsteady pressures due to motion of 0.75 chord flap

$$\delta x_s(t) = \delta x_{s_\epsilon}(t)\,\epsilon(0) + \int_0^t \delta x_{s_\epsilon}(\tau) \quad \epsilon'(t-\tau)\,d\tau \tag{10}$$

A similar convolution integral is computed for C_p, but we must also account for the (convolved) shock motion and express the answer in convolved strained coordinates which are given by

$$x = x' + \delta x_s(t) f(x') \tag{11}$$

(see Fig. 1(*b*)). The straining function used here is the same as that used before (equation (8)). However, the total shock displacement computed in equation (10) replaces the indicial shock displacement used in equation (7).

Thus, we obtain for the total unsteady pressure due to the time-dependent perturbation $\epsilon(t)$ the expression (compare Nixon [4], equation (13)):

$$C_p(x,t) = C_{p_\epsilon}(x',t)\,\epsilon(0) + \int_0^t C_{p_\epsilon}(x',t)\,\epsilon'(t-\tau)\,d\tau$$

$$+ C_{p_0}(x')[1 - \delta x_s(t) f'(x')] \tag{12}$$

3.2 Multiparameter Convolution. It is simple and straightforward to generalize this method to two or more independent modes of perturbation. We start with a steady-state solution and set of indicial responses $\delta x_s{}^{(k)}$ and $C_p{}^{(k)}(x'^{(k)},t)$ for each mode (here the kth). Then the total convolved shock excursion is the sum over the modes

$$\delta x_s(t) = \sum_k \delta x_s^{(k)}(t)$$

where

$$\delta x_s^{(k)} = \epsilon^{(k)}(0) \quad \delta x_{s_\epsilon}^{(k)}(t) + \int_0^t \frac{d}{d\tau}\epsilon^{(k)}(t-\tau) \quad \delta x_{s_\epsilon}^{(k)}(\tau)\,d\tau \tag{13}$$

Of course, $\epsilon^{(k)}(t)$ is just the schedule of the kth perturbation. Note that no summation is implied by the repeated indices in equation (13).

A similar formula obtains for the pressure coefficients, namely

$$C_p(x,t) = \sum_k \left[C_{p_\epsilon}^{(k)}(x',t)\epsilon^{(k)}(0) + \int_0^t \frac{d}{d\tau}\epsilon^{(k)}(t-\tau)\, C_{p_\epsilon}^{(k)}(\tau)d\tau \right]$$

$$+ C_{p_0}(x')\left[1 - f'(x') \sum_k \delta x_s^{(k)}(t)\right] \tag{14}$$

The convolved coordinate is here given by

$$x = x' + f'(x') \sum_k \delta x_s^{(k)} \tag{15}$$

4 Results

Results of running CONVOL were compared to finite-difference (LTRAN2) calculations for two, single-parameter oscillatory cases and one, two-parameter case, as well as a transient disturbance of Gaussian shape.

Case 1: NACA 64A410 airfoil at $M_\infty = 0.74$ oscillating in angle of attack with amplitude 1.25 deg and reduced

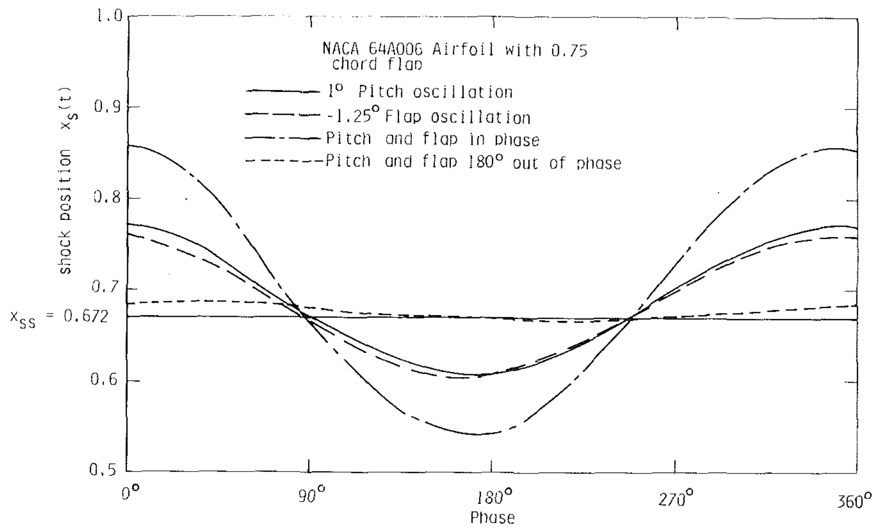

Fig. 4 Shock motion due to superimposed pitching and flap motions

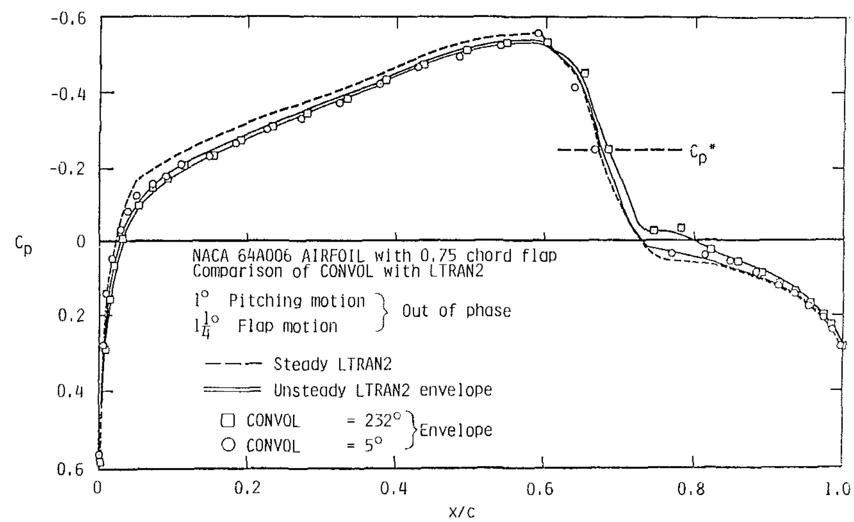

Fig. 5 CONVOL and LTRAN2 unsteady pressures for out-of-phase pitching and flap motions

frequency $k = 0.2$. The steady-state solution and solution for 1/4 deg indicial motion were stored on tape. Looking first at the oscillatory motion we found good agreement, both in the amplitude and phase of the shock motion, between CONVOL and LTRAN2. We then chose two cases for pressure plots, one near the forwardmost shock position (Fig. 2(*a*)) and one near the aftmost shock position (Fig. 2(*b*)). The angle ϕ in the figures is the phase ωt of the current cycle of angle of attack motion. Generally, the agreement is excellent, especially considering the large (25 percent chord) shock motion. Note that the dashed line represents the steady shock position. There is some discrepancy near the foot of the shock (resulting in a different shock strength) but this appears traceable to the error introduced by capturing, rather than fitting, the shock.

Case 2: NACA 64A006 airfoil with 0.75 chord trailing edge flap, $M_\infty = 0.875$. Flap oscillation with amplitude 1.25 deg and reduced frequency (based on chord) $k = 0.2$. The indicial response for a 1/4 deg flap motion was calculated along with the steady-state solution. Once again, there is excellent agreement in both shock position (Fig. 5) and upper surface-pressure coefficients near the maximum and minimum shock positions (Figs. 3(*a*) and (*b*), respectively).

Case 3: Two-parameter perturbation. In this case, a NACA 64A006 airfoil with a 0.75 chord flap undergoes simultaneous oscillations in angle of attack and flap motion. The reduced frequency is $k = 0.2$, and the free-stream Mach number is 0.875.

We ran several combinations of pitching and flap motions, a few of which are noted in Fig. 4. Note that the shock motions are indeed superimposable; this has been confirmed by conparison with LTRAN2. Figure 4 illustrates this point for the cases of (*a*) a pitching oscillation of amplitude 1 deg, (*b*) a flap motion of amplitude 1.25 deg, (*c*) pitching and flap motion in phase (shock excusion amplitudes add), and (*d*) pitching and flap motion out of phase (shock excursions cancel out).

In the out-of-phase case, we see that the two motions, which separately account for a shock excursion of about 18 percent chord each, can be cancelled so as to restrict the shock motion to within less than 1.5 percent of chord. This cancellation also applies to the C_p distribution as shown in Fig. 5, where it is also verified by a corresponding run of LTRAN2. It should be noted that the required magnitude and phase lag of the flap motion, relative to the angle of attack motion, to remove the shock oscillation of the pitching airfoil are given by a simple algebraic equation.

Case 4: A transient disturbance. In order to demonstrate

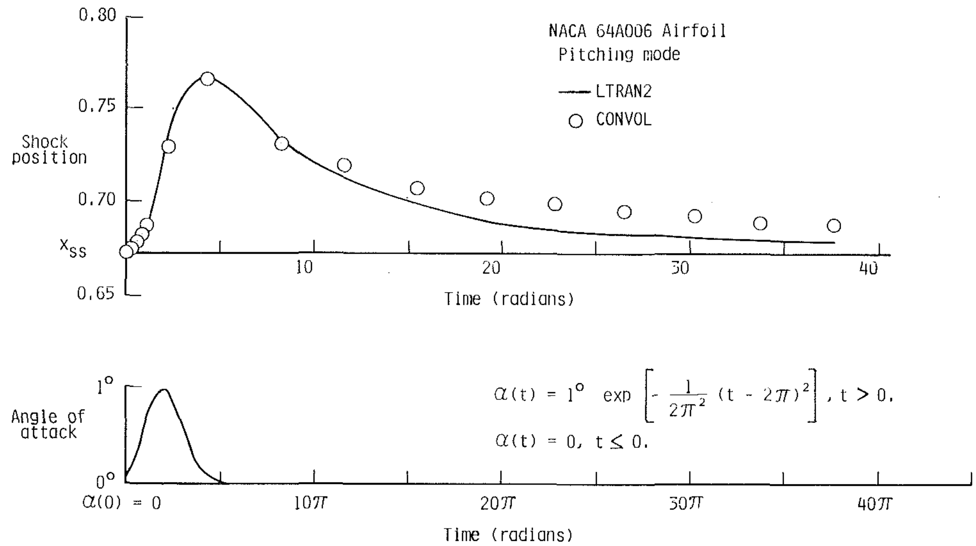

Fig. 6 Motion of the upper surface shock in response to a transient disturbance in angle of attack.

the capabilities of CONVOL for transient as well as oscillatory small disturbances, we applied the indicial method to the case of angle-of-attack variation according to the schedule:

$$\alpha(t) = 1 \text{ deg} \cdot \exp[-(t-2\pi)^2/2\pi^2], \quad t \geq 0$$

for a NACA 64A006 airfoil, $M_\infty = 0.875$. A comparison of the shock motions computed by LTRAN2 and CONVOL is given in Fig. 6. Note that the indicial response of this airfoil seems to have two predominant components, a decaying exponential with time scale of about three cycles, and a decaying exponential with a time scale about 10 times longer.

4.1 Savings in Computing Time. CONVOL requires a steady-state solution and an unsteady indicial response. For a fine grid solution, LTRAN2 requires approximately 350 sec of CPU time on the CDC 7600 computer to produce these. With these data on hand, CONVOL requires about 4 sec of time for the various interpolation steps and about 0.25 sec for each C_p distribution per time and frequency. By comparison, LTRAN2 requires 3–4 sec of time for each C_p per time and frequency.

Hence, using CONVOL can result in a very substantial savings in computation time, particularly if a range of frequencies are to be run. In fact, the pressure distributions for about 10 frequencies can be computed in the time that LTRAN2 requires for one.

In the case of multiparameter perturbations, the potential for savings is even greater, since an entire n-parameter space of solutions can be run for little more than the time required for $(n + 1)$ finite-difference calculations.

The indicial method is also immediately generalizable to three dimensions. The only new problem concerns the more complicated straining of coordinates, but such methods have already been worked out [8] and present no new difficulties of principle.

The multiparameter capability, together with the reduced computation times, opens up the possibility for using CONVOL to fit the aerodynamic response to the structural model in a combined program. This "tailoring" capability ought to be of particular value in the development of active control technology for aircraft.

It is probably worth repeating that the indicial method is very general in its applicability, since it will work for any schedule of parameter changes to any flow field equation, providing that it is locally linearizable by freezing the discontinuities in appropriately strained coordinates.

Two additional studies of interest which relate to this one are those of Yang et al. [9] who have done a flutter analysis of the NACA 64A006 airfoil using finite differences, and of Guruswamy [10] who has used the strained coordinate technique to generate steady solutions that are then used as initial conditions in a calculation of transrail divergence speeds.

The work was sponsored by the Air Force Office of Scientific Research under Contract No. F49620-79-C-0054.

References

1 Ballhaus, W. F., and Goorjian, P. M., "Implicit Finite-Difference Computations of Unsteady Transonic Flows About Airfoils Including the Effect of Irregular Shock Motions," *AIAA Journal*, Vol. 15, No. 12, Dec. 1977, pp. 1728–1735.

2 Traci, R. M., Albano, E. D., and Farr, T. L., "Small Disturbance Transonic Flows About Oscillating Airfoils and Planar Wings," Air Force Flight Dynamics Lab, AFFDL-TR-75-10, 1975.

3 Weatherill, W. H., Ehlers, F. E., and Sebastian, J. H., "Computation of the Transonic Perturbation Flow Fields Around Two and Three-Dimensional Oscillating Wings," NASA CR2599, 1975.

4 Ballhaus, W. F., and Goorjian, P. M., "Computation of Unsteady Transonic Flows by the Indicial Method," *AIAA Journal*, Vol. 16, No. 2, Feb. 1978, pp. 117–124.

5 Nixon, D., "Notes on the Transonic Indicial Method," *AIAA Journal*, Vol. 16, 1978, p. 613.

6 Courant, R., and Hilbert, D., *Methods of Mathematical Physics*, Vol. II, Wiley-Interscience, New York, 1962, pp. 511–515.

7 Rizzetta, D. P., and Yoshihara, H., "Computations of the Pitching Oscillation of a NACA 64A-0010 Airfoil in the Small Disturbance Limit," AIAA Paper No. 80-0128, AIAA 18th Aerospace Sciences Meeting, Pasadena, Calif., Jan. 1980.

8 Nixon, D., "Perturbation in Two and Three Dimensional Transonic Flows," *AIAA Journal*, Vol. 16, No. 7, July 1978, pp. 699–709.

9 Yang, T. Y., Guruswamy, P., Striz, A. G., and Olsen, J. J., "Flutter Analysis of NACA 64A006 Airfoil in Small Disturbance Transonic Flow," *Journal of Aircraft*, Vol. 17, Apr. 1980, pp. 225–232.

10 Guruswamy, P., "Use of Strained Coordinate Perturbation Method in Transonic Aeroelastic Computations," Air Force Flight Dynamics Lab, AF-FDL-TR-80-3102, Oct. 1980.

Torque on Eccentric Spheres Flowing in Tubes

H. Tözeren
Department of Engineering Sciences,
Middle East Technical University,
Ankara, Turkey

The steady flow of an eccentric sphere in a circular cylindrical tube filled with viscous fluid is considered as a regular perturbation of the axisymmetric problem. A sequence of boundary value problems are formulated involving Stokes equations and some linear boundary conditions. Solution of the first-order problem yields the leading term in the perturbation series of the torque on the sphere.

1 Introduction

This paper presents a perturbation solution for the off-axis motion of a sphere of arbitrary size translating and rotating in a circular cylinder in the limit where the eccentricity of the sphere is small. Previous off-axis solutions have been presented for two limiting flow geometries: (*i*) Happel and Brenner [4] considered the case where the sphere diameter was very small compared to the tube diameter but the eccentricity was arbitrary. (*ii*) The flow of eccentric, closely fitting spheres is treated by Bungay and Brenner [1] by using singular perturbation techniques. The solution by Happel and Brenner [4] was based on the method of reflections which requires the particle to be small and far removed from the boundaries if the solution is to converge after a few terms. The present solution is based on the boundary collocation technique described in [5] which is applicable in a wide range of particle-to-tube diameter ratios.

The flow of a spherical particle placed slightly off axis is treated herein as a perturbation of the axisymmetric flow of a sphere in a tube. Assuming regular perturbation expansions for velocities and pressure in terms of the eccentricity ϵ, as ϵ approaches zero, a sequence of boundary value problems are obtained involving Stokes equations and some linear boundary conditions. The zero-order perturbation solution is the exact solution for the motion of a sphere along the axis of a circular cylinder. This solution is given for a single sphere in Haberman and Sayre [3] and also in Leichtberg et al. [5] as a special case of the more general problem of the flow past a finite coaxial array of spheres. The first-order solution for a particle translating and rotating is obtained herein using the results of [5]. This solution gives the leading term in the perturbation expansion of the torque on the particle, but yields no information about the drag on the particle and the pressure drop. Higher order solutions are required to evaluate the corrections to zero-order terms in these variables.

The perturbation scheme and the solutions for the first-order fields are given in Section 2. The numerical results are presented and compared with the results of [1], [4], and [5] in Section 3.

Contributed by the Applied Mechanics Division for publication in the JOURNAL OF APPLIED MECHANICS.

Discussion on this paper should be addressed to the Editorial Department, ASME, United Engineering Center, 345 East 47th Street, New York, N.Y. 10017, and will be accepted until two months after final publication of the paper itself in the JOURNAL OF APPLIED MECHANICS. Manuscript received by ASME Applied Mechanics Division, May, 1981; final revision, December, 1981.

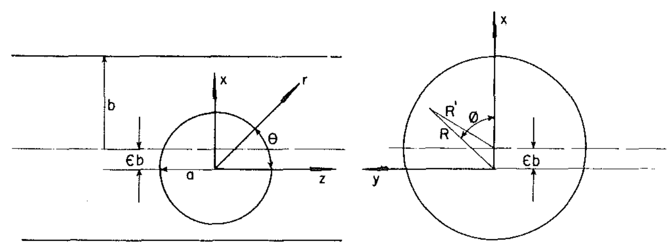

Fig. 1 The flow of an eccentric sphere in a tube

2 Formulation

Consider the slow, steady motion of a sphere placed eccentrically in a circular cylindrical tube filled with viscous fluid. The radius of the sphere is taken to be equal to a, the tube radius b and the distance between the sphere center and the tube axis is equal to ϵb where ϵ is small compared to unity. A coordinate system stationary relative to the cylinder is introduced taking the sphere center as the origin of coordinates as shown in Fig. 1. With respect to this coordinate system, the particle translates parallel to the tube axis with velocity U, rotates in $x-z$ plane with an angular velocity $\epsilon\,\Omega$ and the viscous fluid flows with an average velocity $V/2$.

The velocities and pressure are treated as a regular perturbation of the axisymmetric problem

$$\mathbf{u}=\sum_{n=0}^{\infty}\mathbf{u}^{(n)}\,\epsilon^{n}\ \text{and}\ p=\sum_{n=0}^{\infty}p^{(n)}\,\epsilon^{n}, \tag{2.1}$$

where each field $u^{(n)}$ and $p^{(n)}$ satisfies the Stokes equations and equation of continuity

$$\nabla^{2}\mathbf{u}^{(n)}=\nabla p^{(n)},\quad \nabla\cdot\mathbf{u}^{(n)}=0. \tag{2.2}$$

The boundary conditions are

$$\mathbf{u}=U\mathbf{k}+\epsilon\,\Omega\,a\mathbf{j}\times\mathbf{e}_r\quad\text{at}\quad r=a,\quad \mathbf{u}=0\quad\text{at}\quad R'=b,$$

$$\mathbf{u}=V\left(1-\frac{R'^{2}}{b^{2}}\right)\mathbf{k}\quad\text{at}\quad z=\pm\infty, \tag{2.3}$$

where $\mathbf{j}$, $\mathbf{k}$, and $\mathbf{e}_r$ are unit vectors in y, z, and r directions. The relation between R' and R in Fig. 1 (the radial coordinates with respect to the cylinder axis and the $z-$axis passing through the center of the sphere) is obtained by applying the law of cosines

$$R'^2 = R^2 - 2Rb\,\epsilon\cos\phi + b^2\epsilon^2. \tag{2.4}$$

The equation of the circular cylindrical surface $R' = b$ is then

$$R = b(1+\epsilon\cos\phi) + 0(\epsilon^2), \quad \text{as} \quad \epsilon \to 0. \tag{2.5}$$

Substituting equations (2.1) and (2.4) into equation (2.3), the boundary conditions for zero and first-order velocity fields on the particle and at infinity are obtained:

$$\mathbf{u}^{(0)} = U\mathbf{k},\ \mathbf{u}^{(1)} = \Omega\, a\,\mathbf{j}\times\mathbf{e}_r \quad \text{at} \quad r = a,$$

$$\mathbf{u}^{(0)} = V\left(1 - \frac{R^2}{b^2}\right)\mathbf{k}, \quad \mathbf{u}^{(1)} = 2V\frac{R}{b}\cos\phi\,\mathbf{k} \quad \text{at} \quad z = \pm\infty. \tag{2.6}$$

Expanding the no-slip condition, $\mathbf{u} = \mathbf{u}^{(0)} + \epsilon\,\mathbf{u}^{(1)} + \ldots = 0$, in Taylor series about $R = b$ and computing the terms at the cylindrical surface $R = b(1 + \epsilon\cos\phi)$

$$\mathbf{u}^{(0)} = 0, \quad \mathbf{u}^{(1)} = -b\cos\phi\frac{\partial\mathbf{u}^{(0)}}{\partial R} \quad \text{at} \quad R = b. \tag{2.7}$$

The zero-order perturbation solution is the exact solution for the motion of a sphere along the axis of a circular cylinder. This solution which satisfies the boundary conditions (2.6) and (2.7) (for zero-order fields) is extensively obtained by Leichtberg et al. [5] as a special case of the more general problem of the flow of an array of concentric spheres in a tube. In the remainder of this section, the first-order solution is developed using the results of [5].

The solution $\mathbf{u}^{(1)}$ is found by superposition of two solutions: (*i*) the solution $\mathbf{v}$ of Stokes equations which satisfies conditions on the tube but not on the sphere

$$\mathbf{v} = -b\cos\phi\frac{\partial\mathbf{u}^{(0)}}{\partial R} \ \text{at}\ R = b, \quad \mathbf{v} = 2V\frac{R}{b}\cos\phi\,\mathbf{k}\ \text{at}\ z = \pm\infty \tag{2.8}$$

and (*ii*) the solution $\mathbf{w}$, which satisfies no-slip condition on the tube

$$\mathbf{w} = 0 \quad \text{at} \quad R = b, \quad \mathbf{w} = 0 \quad \text{at} \quad z = \pm\infty,$$

$$\mathbf{w} = -\mathbf{v} + \Omega\,a\,\mathbf{j}\times\mathbf{e}_r \quad \text{at} \quad r = a. \tag{2.9}$$

In the following, all variables having dimensions of length are made dimensionless with respect to the tube diameter b.

The velocity field $\mathbf{v}$ is found as follows: using

$$u_R{}^{(0)} = u_z{}^{(0)} = \frac{\partial u_z{}^{(0)}}{\partial z} = 0 \quad \text{at} \quad R = 1,$$

the continuity equation gives

$$\frac{\partial u_R{}^{(0)}}{\partial R} = 0$$

and therefore

$$v_R = v_\phi = 0, \quad v_z = -\cos\phi\frac{\partial u_z{}^{(0)}}{\partial R} \quad \text{at} \quad R = 1. \tag{2.10}$$

The $u_z^{(0)}$ is given by Leichtberg et al. [5] as

$$u_z^{(0)} = V(1-R^2) + \int_0^\infty \{A(t)\,t\,I_0(Rt) + B(t)\,(Rt\,I_1(Rt) + 2I_0(Rt))\}\cos zt\,dt + \sum_{n=2}^{\infty}\{C_n P_n(\mu)r^{-n-1} + D_n(P_n(\mu) + 2F_n(\mu))r^{-n+1}\} \tag{2.11}$$

where $P_n(\mu)$ and $F_n(\mu)$ are Legendre and Gegenbauer functions with argument $\mu = \cos\theta$. The coefficients C_n and D_n and the functions $A(t)$ and $B(t)$ are calculated and used as defined in [5]. (Numerical accuracy is discussed and compared with the results of Leichtberg et al. [5] and Wang and Skalak [6] in Section 3.) Differentiating equation (2.11)

$$\frac{\partial u_z^{(0)}}{\partial R} = -2RV + \sum_{n=2}^{\infty}\left\{C_n\frac{\partial}{\partial R}(P_n(\mu)r^{-n-1}) + D_n\frac{\partial}{\partial R}((P_n + 2F_n(\mu))r^{-n+1})\right\} + \int_0^\infty\{t^2 I_1(Rt)\,A(t) + (Rt^2\,I_0(Rt) + 2t\,I_1(Rt))\}\cos zt\,dt. \tag{2.12}$$

At $R = 1$, equation (2.12) can be written as an inverse Fourier cosine transform

$$\frac{\partial u_z^{(0)}}{\partial R} + 2V = \frac{2}{\pi}\int_0^\infty F(t)\cos zt\,dt \quad \text{at} \quad R = 1,$$

$$\begin{aligned} F(t) = \sum_{n=2}^{\infty}(-1)^{n/2}\frac{1}{n!}\{&C_n(t^{n+1}K_0(t) + t^n K_1(t)) \\ &- D_n((n^2-3n+3)t^{n-1}K_0(t) - (2n-3)t^n K_1(t) \\ &+ (n-2)(n-3)t^{n-2}K_1(t))\} \\ &+ \frac{\pi}{2}\{t^2 I_1(t)A(t) + (t^2 I_0(t) + 2tI_1(t))\,B(t)\} \end{aligned} \tag{2.13}$$

where K_0, K_1, and I_0, I_1 are Macdonald and modified Bessel functions of zero and first orders.

Substituting (2.13) into (2.10) and using equation (7-3.51) of Happel and Brenner [4] the $\mathbf{v}$ is found as

$$\begin{Bmatrix} v_R \\ v_\phi \\ v_z \end{Bmatrix} = \begin{Bmatrix} 0 \\ 0 \\ 2RV\cos\phi \end{Bmatrix} - \int_0^\infty [I(R,t)][I^{-1}(1,t)] \begin{Bmatrix} 0 \\ 0 \\ \frac{2}{\pi}F(t) \end{Bmatrix} \begin{matrix} \cos\phi\sin zt \\ \sin\phi\sin zt\,dt \\ \cos\phi\cos zt \end{matrix} \tag{2.14}$$

After carrying out the matrix multiplication, the terms found in each row are multiplied with ϕ and z dependent functions in the same row. The matrix $[I(R,t)]$ is given by Happel and Brenner [4] for the term proportional to $\cos\phi$ in the Fourier series as

$$[I(R,t)] = \begin{bmatrix} I_1(Rt)/(Rt), & I_1'(Rt), & RtI_1''(Rt) \\ -I_1'(Rt), & -I_1(Rt)/(Rt), & I_1(Rt)/(Rt) - I_1'(Rt) \\ 0, & I_1(Rt), & I_1(Rt) + tRI_1'(Rt) \end{bmatrix} \tag{2.15}$$

The $\mathbf{v}$ defined in equation (2.14) satisfies Stokes equations and boundary conditions (2.10). This can be verified directly by substituting $R = 1$ in (2.14) and comparing with equation (2.13).

Having obtained the solution $\mathbf{v}$, it is now required to find $\mathbf{w}$ which satisfies boundary conditions (2.9). The solution consists of (*i*) the solution of Stokes equations in spherical coordinates, which are used to satisfy the conditions on the particle, and (*ii*) the solution in cylindrical coordinates chosen to satisfy the no-slip condition on the tube surface.

The series solution in spherical coordinates proportional to $\cos\phi$ (or $\sin\phi$) is

$$w_R = \cos\phi\sum_{n=1}^{\infty}\left\{a_n\frac{r^{-n}}{R(2n+1)}(nP_{n+1}^1 + (n+1)P_{n-1}^1)\right.$$

$$+ \frac{1}{2} b_n (r^{-n-2} P_{n+1}^2 - n(n+1) r^{-n-2} P_{n+1})$$

$$+ \frac{1}{n(2n-1)} c_n \Big[- \frac{(n-2)}{4} r^{-n} (P_{n+1}^2$$

$$- n(n+1)P_{n+1}) + (n+1) R r^{-n-1} P_n^1 \Big] \Big\},$$

$$w_\phi = \sin\phi \sum_{n=1}^{\infty} \Big\{ a_n \Big[-nRr^{-n-2} P_{n+1}^1 - \frac{1}{2(2n+3)} r^{-n-1}$$

$$(nP_{n+2}^2 + (n+3)P_n^2 - n(n+1)(n+2)P_{n+2}$$

$$- n(n+1)^2 P_n) \Big] - \frac{1}{R} b_n r^{-n-1} P_n^1$$

$$+ \frac{n-2}{2nR(2n-1)} c_n r^{-n+1} P_n^1 \Big\},$$

$$w_z = \cos\phi \sum_{n=1}^{\infty} \Big\{ -a_n r^{-n-1} P_n^1 - b_n n r^{-n-2} P_{n+1}^1$$

$$+ c_n \Big[\frac{n}{2(2n+1)} r^{-n} P_{n+1}^1$$

$$+ \frac{(n+1)^2}{n(2n-1)(2n+1)} r^{-n} P_{n-1}^1 \Big] \Big\}. \qquad (2.16)$$

Due to the symmetry about the $x-y$ plane, the w_z contains the components involving $P_n^m(\mu)$ even in μ and the w_ϕ and w_R involve odd terms. Therefore, $a_n = 0$ if n = even and $b_n = c_n = 0$ if n = odd. In obtaining equation (2.16), equation (3.2.31) of Happel and Brenner [4] and the following equations involving a solid spherical harmonic $\chi = r^{-(n+1)} P_n^1(\mu)\cos\phi$ are extensively used:

$$\frac{\partial \chi}{\partial z} = -nr^{-n-2} P_{n+1}^1(\mu),$$

$$\frac{\partial \chi}{\partial R} = \frac{1}{2} [r^{-n-2} P_{n+1}^2 - n(n+1) r^{-n-2} P_{n+1}] \cos\phi, \qquad (2.17)$$

$$\mu P_n^m(\mu) = \frac{(n-m+1) P_{n+1}^m + (n+m) P_{n-1}^m}{2n+1}.$$

The following solution in cylindrical coordinates used in addition to the solution in spherical coordinates (2.16) satisfies the no-slip condition on the tube surface:

$$\mathbf{w} = -\frac{2}{\pi} \int_0^\infty [I(R,t)]\,[I^{-1}(1,t)] \Big\{ \sum_{n=1}^{\infty} [A^n(t)] \Big\} \begin{matrix} \sin zt \\ \sin zt \\ \cos zt \end{matrix} \, dt, \qquad (2.18)$$

where the elements of $[A^n(t)] = [A_1^n, A_2^n, A_3^n]^T$ are the Fourier cosine (or sine) transforms of w_R, w_ϕ, and w_z in (2.16).

$$A_1^n(t) = \frac{(-1)^{n/2}}{(n-1)!} \Big[a_{n-1}(n-1)\{ -(n-2)t^{n-2} K_1(t)$$

$$+ t^{n-1} K_0(t) \} - \frac{b_n}{2} \{ t^{n+1} K_2(t) + t^{n+1} K_0(t) \}$$

$$+ \frac{c_n}{(2n-1)} \Big\{ - \frac{(n-2)^2(n-1)}{4n} t^{n-1} K_2(t)$$

$$+ \frac{2n-1}{2} t^n K_1(t) - \frac{(n+1)(n-2)}{4} t^{n-1} K_0(t) \Big\} \Big] \cos\phi,$$

$$A_2^n(t) = \frac{(-1)^{n/2}}{(n-1)!} \Big[-\frac{a_{n-1}}{2} (n-1) \{ (n-2) t^{n-1} K_2(t)$$

$$+ n t^{n-1} K_0(t) \} - b_n t^n K_1(t) + \frac{c_n (n-2)}{2n(2n-1)}$$

$$\{ -(n-2)(n-1) t^{n-2} K_1(t)$$

$$+ (2n-1) t^{n-1} K_0(t) \} \Big] \sin\phi,$$

$$A_3^n(t) = \frac{(-1)^{n/2}}{(n-1)!} \Big[-a_{n-1}(n-1) t^{n-1} K_1(t)$$

$$+ b_n t^{n+1} K_1(t) + \frac{c_n}{2} \Big\{ \frac{(n-1)(n^2+2)}{n(2n-1)} t^{n-1} K_1(t)$$

$$- t^n K_0(t) \Big\} \Big] \cos\phi, \; n = 2, 4, 6, \ldots \qquad (2.19)$$

Table 1 Tests of convergence for zero-order perturbation solutions for various diameter ratios a/b

a/b	Number of collocation points	$\lambda^{(U)}$
0.2	11	1.6796
	15	1.6796
	19	1.6796
0.4	11	3.5927
	15	3.5926
	19	3.5926
0.6	11	11.108
	15	11.109
	19	11.109

In developing equation (2.19), the following equations obtained from equations (8.77.5) and (6.69.4) of Gradstein and Ryhzik [2] are used

$$r^{-(n+1)} P_n^m(\mu)$$

$$= \frac{2(-1)^{\frac{m+n}{2}}}{\pi(n-m)!} \int_0^\infty t^n K_m(t) \cos zt \, dt, \; m+n = \text{even},$$

$$= \frac{2(-1)^{\frac{m+n-1}{2}}}{\pi(n-m)!} \int_0^\infty t^n K_m(t) \sin zt \, dt, \; m+n = \text{odd} \qquad (2.20)$$

$$r^2 r^{-(n+1)} P_n^m(\mu)$$

$$= \frac{2(-1)^{\frac{m+n}{2}}}{\pi(n-m)!} \int_0^\infty \{ -(n-m-1)(n-m)\, t^{n-2} K_m(t)$$

$$+ (2n-1) t^{n-1} K_{m-1}(t) \} \cos zt \, dt, \; m+n = \text{even},$$

$$= \frac{2(-1)^{\frac{m+n-1}{2}}}{\pi(n-m)!} \int_0^\infty \{ -(n-m-1)(n-m)\, t^{n-2} K_m(t)$$

$$+ (2n-1) t^{n-1} K_{m-1}(t) \} \sin zt \, dt, \; m+n = \text{odd}, \qquad (2.21)$$

where computed for $R = 1$, the r is a function of z alone.

The collocation method is used to determine the unknown coefficients a_n, b_n, and c_n by applying the boundary conditions on the particle (2.9) to the summation of the solutions in spherical coordinates (2.16) and in cylindrical coordinates (2.18). How to use these coefficients to compute important variables such as drag and the torque on the particles and the accuracy of the numerical calculations are discussed in Section 3.

Table 2 Comparison of additional drag coefficients $\lambda^{(U)}$ and $\lambda^{(V)}$ with results of Leichtberg et al. [5] and Wang and Skalak [6]

a/b	Leichtberg et al.		Wang and Skalak			
	$\lambda^{(U)}$	$\lambda^{(V)}$	$\lambda^{(U)}$	$\lambda^{(V)}$	$\lambda^{(U)}$	$\lambda^{(V)}$
0.1	1.263	1.255	1.263	1.255	1.263	1.255
0.2	1.680	1.636	1.680	1.635	1.680	1.635
0.3	2.373	2.231	2.370	2.229	2.371	2.229
0.4	3.599	3.223	3.593	3.216	3.593	3.216
0.5	5.973	5.017	5.949	4.996	5.952	4.999
0.6	11.20	8.696	11.10	8.617	11.11	8.627
0.7	25.29	17.91	24.70	17.49	24.77	17.54

Table 3 Tests of convergence of first-order perturbation solutions for various diameter ratios a/b

a/b	Number of collocation points	a_1
0.2	11	−.003302
	15	−.003303
	19	−.003303
0.4	11	−.09817
	15	−.09819
	19	−.09819
0.6	11	−1.258
	15	−1.260
	19	−1.260

3 Results and Discussion

Numerical tests are performed to determine the accuracy of C_n, D_n and a_n, b_n, c_n coefficients computed by the boundary collocation procedure. The C_n, D_n coefficients giving the zero-order solution are previously determined (but not tabulated) by Leichtberg et al. [5]. In the present computations their results are extensively used: The angle δ is taken as 0.8 deg and 15 collocation points are chosen uniformly distributed along the semicircle. The tests for convergence given in Table 1 show that by using 15 collocation points five significant figures in $\lambda^{(U)}$ are obtained for a/b values between 0.001-0.6. A comparison of the present results with that of Leichtberg et al. [5] and Wang and Skalak [6] are given in Table 2. The quantities compared in the table, $\lambda^{(U)}$ and $\lambda^{(V)}$, are the coefficients of additional drag for $U \neq 0$, $V = 0$ and $U = 0$, $V \neq 0$ cases, respectively. There is a small but increasing difference (with increasing a/b) between the present results and the results of [5]. But the agreement is good between the present results and that of Wang and Skalak [6] as can be seen from the table. (The Wang and Skalak [6] solutions are presented for infinite chains of spheres uniformly distributed along the axis and the numerical results given in Table 1 are for the largest spacing of 40 tube radii.) Same collocation points as zero-order solution are used for the calculation of a_n, b_n, and c_n coefficients of the first-order perturbation solution. The accuracy of these calculations are discussed later in this section.

In the series solution of Stokes equations in spherical coordinates as given in [4], the only term that contributes to the drag on the particle is the solid spherical harmonic p_{-2}. In the first-order solution subject to the boundary conditions (2.8), the surface spherical harmonic in p_{-2} is necessarily of the form $P_l^1(\mu)\cos\phi$. However, the velocity components derived from such a term violates the symmetry requirements mentioned in Section 2, and therefore its coefficient c_1 in equation (2.16) must be zero.

A simple relation is also available to calculate the torque on the particle as given in [4]

$$\mathbf{T} = -8\pi\mu\nabla(r^3\chi_{-2}). \tag{3.1}$$

In contrast to p_{-2} harmonic, the solid spherical harmonic $\chi_{-2} = a_1 r^{-2} P_1^1(\mu)\sin\phi$ is present in the series (2.16) and yields a torque on the sphere

$$\mathbf{T} = 8\pi\mu b^2 a_1 \epsilon \mathbf{j} \tag{3.2}$$

where μ is the viscosity of the fluid and ϵ is as defined in Section 2. The torque $\mathbf{T}$ given by (3.2) is the leading term in the perturbation expansion of the torque on the particle exerted by the fluid.

The coefficients a_n, b_n, and c_n in (2.16) are determined in three cases: (*i*) a sphere moving steadily in a tube through a viscous fluid that is at rest at infinity ($U \neq 0$, $\Omega = 0$, $V = 0$), (*ii*) steady flow of fluid past a stationary sphere ($U = 0$, $V \neq 0$, $\Omega = 0$), and (*iii*) pure rotation of the sphere ($\Omega \neq 0$, $U = V = 0$).

Tests are performed to determine the rate of convergence of solutions as a function of number of collocation points used. Table 3 gives the coefficient a_1 for different a/b values and numbers of collocation points. Up to $a/b = 0.6$, four significant figures are obtained by using 15 points uniformly distributed along the semicircle.

In cases (*i*) and (*ii*) mentioned in the preceeding paragraph, the torque is due to the eccentricity of the sphere. However, in the case of rotating sphere, the leading term is the solution for a concentric sphere rotating in an otherwise quiescent fluid in a tube. The values of the coefficient a_1 is computed for all these three cases for various a/b values and tabulated in Table 4 as A_U, A_V, A_Ω coefficients. The torque in more general cases can be calculated using

$$T = 8\pi\mu b^2 \mathbf{j}(A_U U + A_V V + bA_\Omega \Omega)\epsilon \tag{3.3}$$

The results of the present treatment may be compared with the results of the work by Happel and Brenner [4] when a/b is small and that of Bungay and Brenner [1] when a/b approaches unity. The torque $\mathbf{T}$ is given by Happel and Brenner [4] as

$$\mathbf{T} = \mathbf{j}8\pi\mu a^2[V(a/b)\epsilon + \{V(1-\epsilon^2) - U\}g(\epsilon)\ (a/b)^2]$$

$$\text{as} \quad a/b \to 0, \tag{3.4}$$

where the function $g(\epsilon)$ is approximately $1.296\epsilon + 0(\epsilon^3)$, as ϵ tends to zero. The result $A_U = 1.299$ for $a/b = 0.001$ given in Table 4 is in fairly good agreement with this value and the discrepancy in the fourth digit is partly due to the omission of the terms of order $(a/b)^3$ in equation (3.5).

Bungay and Brenner [1] determined the drag and the torque on closely fitting spheres using singular perturbation techniques. The range of (a/b) considered in the present paper is probably out of the range of application of their work [1]. Still, there is a fair comparison between these results for larger values of (a/b). Equations (3.6), (4.67), and (6.9) of Bungay and Brenner [1] give $A_U = 1.377$, $A_V = 1.308$ for $a/b = 0.6$; and $A_U = 4.85$, $A_V = 3.792$ for $a/b = 0.7$. The corresponding values given in Table 4 are 1.26, 1.207, 4.689, and 3.637.

The series solutions for zero and first-order velocity fields were particularly simple involving axisymmetric terms for zero-order fields and terms proportional to $\cos\phi$ (or $\sin\phi$) for first-order fields. The higher order solutions require the consideration of all surface harmonics of corresponding order due to the boundary conditions on the tube. This complicates

Table 4 The coefficients A_U, A_V, A_Ω for several different values of diameter ratio a/b

a/b	A_U	A_V	A_Ω
0.001	-1.299×10^{-12}	1.0013×10^{-9}	-1.10^{-9}
0.01	-1.324×10^{-8}	1.0132×10^{-6}	-1.000001×10^{-6}
0.1	-1.615×10^{-4}	1.160×10^{-3}	-1.00074×10^{-3}
0.2	-3.303×10^{-3}	1.122×10^{-2}	-0.0080473
0.3	-2.219×10^{-2}	4.799×10^{-2}	-0.02755
0.4	-9.819×10^{-2}	1.527×10^{-1}	-0.06722
0.5	-3.607×10^{-1}	4.318×10^{-1}	-0.1381
0.6	-1.260	1.207	-0.2592
0.7	-4.689	3.637	-0.4703

the formulation and increases the amount of the computational work considerably. However, the higher order corrections to the drag are relatively easier to obtain, knowing that only p_{-2} harmonic contributes to the drag. Among the surface harmonics in p_{-2}, $P_1(\mu)$ is the only term to be considered since the other harmonic P_1^1 (μ) $\cos\phi$ violates the symmetry requirements. Therefore, the higher order terms in the drag can be calculated by solving a series of axisymmetric problems which involve prescribed velocities on the tube (various derivatives of lower order velocity fields with respect to R). Currently, the work is in progress to extend the present analysis to second and third-order perturbation solutions.

Acknowledgment

This research was supported by Turkish Scientific Research Institute Grant No. MAG 559 and by NATO Research Grant No. 110.80.

References

1 Bungay, P. M., and Brenner, H., "The Motion of a Closely Fitting Sphere in a Fluid Filled Tube," *Int. J. Multiphase Flow*, Vol. 1, 1973, pp. 25-56.

2 Gradshteyn, I. F., and Ryzhik, I. W., *Tables of Integrals, Series and Products*, Academic Press, 1965.

3 Haberman, W. L., and Sayre, R. M., "David Taylor Model Basin," Report No. 1143, U.S. Navy Dept., 1958.

4 Happel, J. and Brenner, H., *Low Reynolds Number Hydrodynamics*, Prentice-Hall, Englewood Cliffs, N.J., 1965.

5 Leichtberg, S., Pfeffer, R., and Weinbaum, S., "Stokes Flow Past Finite Coaxial Clusters of Spheres in a Circular Cylinder," *Int. J. Multiphase Flow*, Vol. 3, 1976, pp. 147-169.

6 Wang, H., and Skalak, R., "Viscous Flow in a Cylindrical Tube Containing a Line of Spherical Particles," *J. F. Mech.*, Vol. 38, 1969, pp. 75-96.

The Growth of Localized Disturbances in Unstable Flows

A. D. D. Craik
Department of Applied Mathematics,
University of St. Andrews,
St. Andrews, Fife KY16 9SS,
Scotland

The development of three-dimensional localized disturbances in unstable flows was recently studied by Craik [1] using a model dispersion relation. The adoption of such an approximate formula for the linear dispersion relation allows a dramatic reduction in computational effort, in comparison with more precise calculations (e.g., Gaster [3], [5]), yet may still yield quite accurate results. Craik [1] gives simple analytical solutions for various limiting cases of his chosen model. Here, this model is further investigated. Numerical results are given which are free of previous scaling assumptions and the accuracy of the proposed model is assessed by comparison with known exact computations for plane Poiseuille flow. Certain improvements are made by including further terms in the model dispersion relation and the influence of these additional terms is determined. A further model is investigated which yields "splitting" of the wave packet into two regions of greatest amplitude, one on either side of the axis of symmetry. Such behavior may be characteristic of many flows at sufficiently large Reynolds numbers. Extension of this work to three-dimensional and slowly varying flows seems a practical possibility.

1 Introduction

Precise calculation of the evolution of an initially localized disturbance in unstable flows is an exceedingly laborious task. For the Blasius boundary layer, Gaster [3] admirably performed this task and found good agreement with the experiments of Gaster and Grant [2] throughout the early stages of growth. Gaster's solution consisted of a superposition of many wave modes, each with its characteristic (real) frequency and spatial growth or decay rate, as determined by the eigenvalues of a reduced Orr-Sommerfeld problem.

An alternative approach, based on an asymptotic saddle-point analysis, is known to give accurate results for all but very small times after initiation of the disturbance (Gaster [5]). However, the computational effort required to locate the saddle points in the complex frequency/wave-number planes is very great, if one seeks to work with the precise eigenvalues. Indeed, Gaster [5] does so only for two-dimensional disturbances, and the complexity of the three-dimensional problem is much greater. Two-dimensional packets are also considered by Itoh [8], who attempts to extend the method of ray trajectories to dissipative flows.

An alternative and much simpler procedure, described by Craik [1], may yield satisfactory approximations, though with some loss of accuracy. The essential simplifying feature is the adoption of an algebraic formula for the complex dispersion relation, which by suitable choice of parameters, fits quite closely to the exact dispersion relation for all the unstable modes of the system. The application of the saddle-point method to this *model* dispersion relation readily yields the desired solution.

In Craik [1], hereafter denoted by Part 1, a model dispersion relation

$$\omega = \cos\vartheta[\omega_0 + a_1(\gamma-\alpha_0) - ia_2(\gamma-\alpha_0)^2 + i\delta(1 - R_c/R\cos\vartheta)] \qquad (1.1)$$

was employed to investigate the linear evolution of localized three-dimensional disturbances in unstable flows. Such a disturbance is assumed to have the form

$$\psi(\mathbf{x},t) = \int_{-\infty}^{\infty}\int_{-\infty}^{\infty} \bar{\psi}(\alpha,\beta;y)\exp i(\alpha x + \beta z - \omega t)d\alpha d\beta$$

characteristic of primary flows $\mathbf{u} = (U(y),0,0)$ where $\omega = \omega(\alpha,\beta)$, $\alpha = \gamma\cos\vartheta$ and $\beta = \gamma\sin\vartheta$. Thus, the wave-number vector of each Fourier component has magnitude γ and direction θ relative to the downstream x-axis and maximum temporal amplification occurs when (γ,θ) equals $(\alpha_0,0)$. Also, a_1 is a real constant, precisely equal to the downstream group velocity $\partial\omega/\partial\alpha$ of the component $(\alpha_0,0)$ when the Reynolds number R equals its critical value R_c for marginal stability. The constants a_2 and δ are complex with positive real parts a_{2r} and δ_r. The model dispersion relation (1.1) satisfies Squire's theorem and is assumed to hold for complex as well as real values of γ and θ.

Supposing that time $t \to \infty$ while x/t and z/t remain fixed, saddle points of the respective α and β integrals yield the dominant contribution to $\psi(\mathbf{x},t)$. These saddle points are located at the complex values $\alpha = \alpha^*$, $\beta = \beta^*$ where

$$\frac{\partial\omega}{\partial\alpha} = \frac{x}{t}, \quad \frac{\partial\omega}{\partial\beta} = \frac{z}{t}$$

Contributed by the Applied Mechanics Division for publication in the JOURNAL OF APPLIED MECHANICS.
Discussion on this paper should be addressed to the Editorial Department, ASME United Engineering Center, 345 East 47th Street, New York, N.Y. 10017, and will be accepted until two months after final publication of the paper itself in the JOURNAL OF APPLIED MECHANICS. Manuscript received by ASME Applied Mechanics Division, May, 1981; final revision, October, 1981.

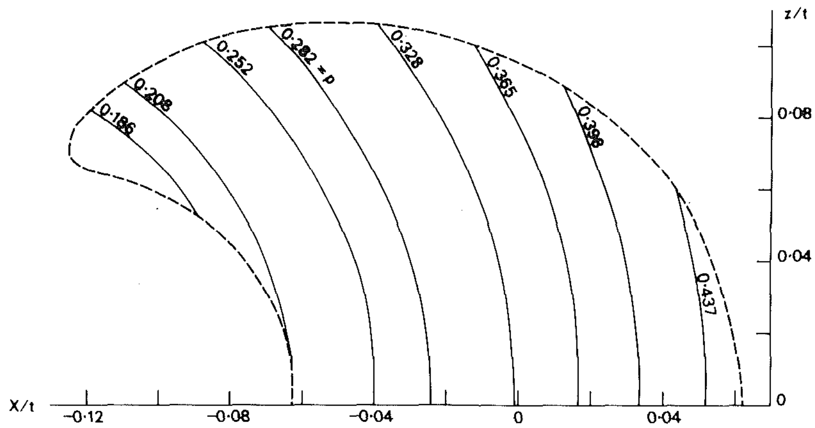

Fig. 1 Lines of constant phase from (2.7) with data as in (2.9). The dashed boundary denotes the extent of the growing disturbance when R = 11,110.

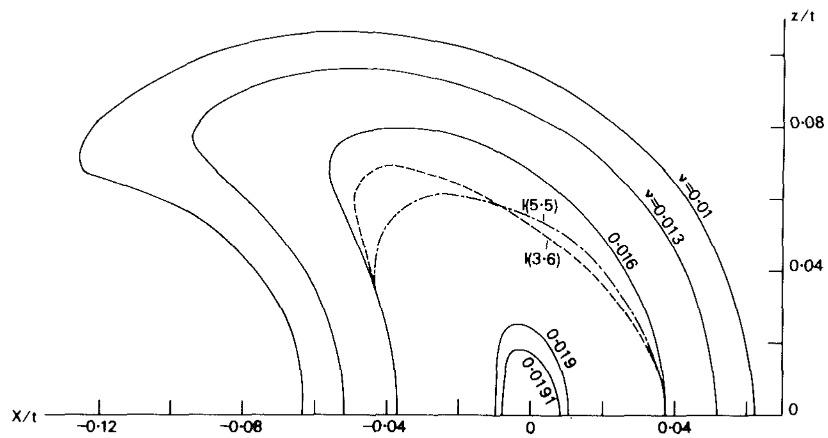

Fig. 2 Lines of constant amplification from (2.8) with data as in (2.9). Also shown are the analytic solutions, Part 1 (3.6), Part 1 (5.5) for the neutral boundary at R = 6944 with data (2.9), corresponding to ν = 0.016.

Correspondingly, these saddle points are situated at $\gamma = \gamma^*$, $\theta = \theta^*$ defined by

$$\gamma^* = \alpha_0 + \frac{i}{2a_2}\left(\frac{X}{t} + \frac{z}{t}\tan\theta^*\right)$$

$$\frac{2(z/t)}{\sin\theta^*\cos\theta^*} = \left(\frac{X}{t} + \frac{z}{t}\tan\theta^* - 2i\alpha_0 a_2\right) + \frac{4ia_2(\omega_0 + i\delta - \alpha_0 a_1 - i\alpha_0^2 a_2)}{\left(\frac{X}{t} + \frac{z}{t}\tan\theta^* - 2i\alpha_0 a_2\right)} \qquad (1.2a,b)$$

(c.f. Part 1, equations (2.4), (2.5)) where $X \equiv x - a_1 t$ denotes downstream distance measured from an origin moving with velocity a_1.

The saddle-point method yields the dominant contribution

$$\psi(\mathbf{x},t) \sim \frac{f(\gamma^*,\theta^*;y)(\pi/t)}{\left(\frac{1}{2}a_2\cos\theta^* K^*_{\theta\theta}\right)^{1/2}}\exp tK(\theta^*),$$

$$K(\theta^*) \equiv \cos\theta^*\left[-i(\omega_0 - \alpha_1\alpha_0) + \delta - \alpha_0^2 a_2 - \frac{1}{4a_2}\left(\frac{X}{t} + \frac{z}{t}\cos\theta^* - 2i\alpha_0 a_2\right)^2\right] - \frac{\delta R_c}{R},$$

$$f(\gamma^*,\theta^*;y) \equiv \gamma^*\bar{\psi}(\gamma^*\cos\theta^*,\gamma^*\sin\theta^*;y) \qquad (1.3)$$

where $K^*_{\theta\theta}$ denotes $d^2K/d\theta^2$ evaluated at $\theta = \theta^*$.

Of course, the model dispersion relation does not precisely represent any particular flow, but it incorporates qualitative features of many flows and considerable insight is gained from studying this simplified model. Furthermore, under certain circumstances, results using (1.1) may in fact give quantitatively accurate results (see Section 3). Other than adoption of the model (1.1) the only assumptions made in deducing (1.3) are that $t \to \infty$ and

$$\mathrm{Re}\{a_2\cos\theta^*\gamma^{*2}\} > 0. \qquad (1.4)$$

This last condition is necessary to ensure that the dominant contribution does, indeed, come from the saddle points, rather then the end point $\gamma = 0$; and it is certain to be satisfied in all cases of practical interest.

In Part 1, various remarkably simple, closed-form approximate solutions were deduced for the wave packet, on making further assumptions regarding the relative magnitudes of the constants $\omega_0, \alpha_0, a_1, a_2, \delta$ and R/R_c. The purpose of the present paper is threefold. First, in Section 2, numerical results based on (1.3) are presented, which are free from the additional scaling assumptions used in Part 1. Second, in Section 3, the accuracy of the model dispersion relation is assessed by comparison with computed eigenvalues for plane Poiseuille flow, and the consequences of discrepancies are evaluated. Conditions are established under which the model calculation should yield accurate quantitative results. Third, in Section 4, an alternative model is proposed which exhibits features qualitatively different from

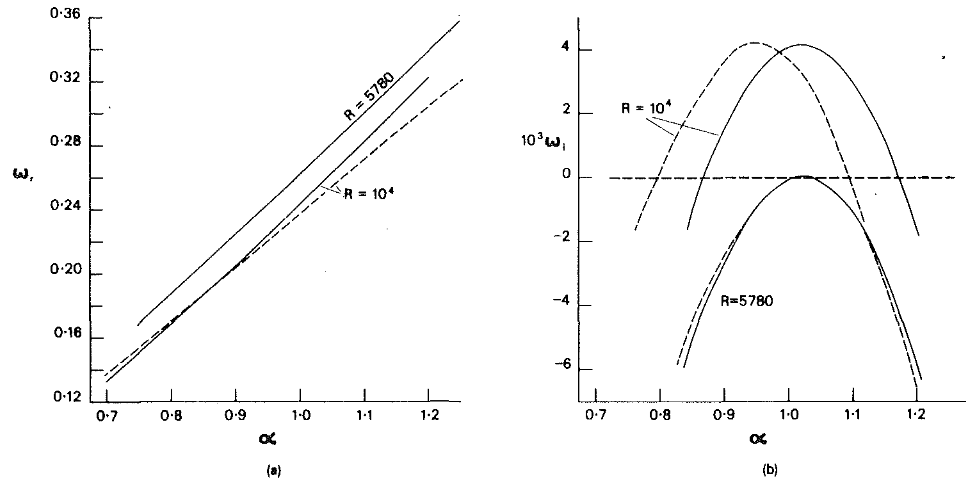

Fig. 3 Comparison of model (1.1) (solid curves) and computed eigenvalues (dashed curves) for temporal instability of plane Poiseuille flow at R = 5780 and 10,000. Figures 3(*a*) and 3(*b*) show ω_r and ω_i, respectively, versus wave number α.

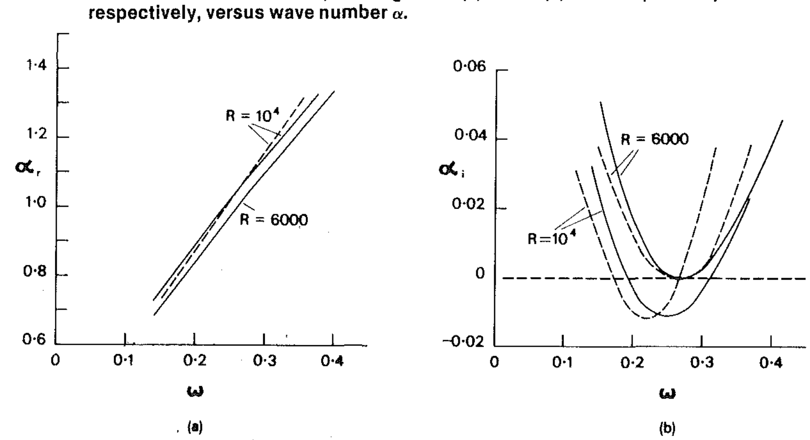

Fig. 4 Comparison of model (1.1) (solid curves) and computed eigenvalues (dashed curves) for spatial instability of plane Poiseuille flow at R = 6000 and 10,000. Figures 4(*a*) and 4(*b*) show α_r and α_i, respectively, versus frequency ω.

those resulting from (1.1). This new model is relevant to certain flows at Reynolds numbers substantially above critical, which have a maximum growth rate at some finite value $R=R_1(>R_c)$. For this model, it is found that when $R>R_1$ the maximum amplitude may no longer occur on the x-axis; but, rather, two maxima may exist, one on either side of the center line $z=0$. This "splitting" of the packet may be a general feature of many flows.

2 Numerical Results

On defining

$$\varphi \equiv \frac{X}{t} + \frac{z}{t}\tan\theta^* - 2i\alpha_0 a_2,$$

$$\Lambda \equiv 4a_2(-i\omega_0 + i\alpha_0 a_1 - \alpha_0^2 a_2 + \delta),$$

results (1.2*a*,*b*) may be re-expressed as

$$\gamma^* = i\varphi/2a_2, \quad \sin 2\theta^* = 4(z/t)\varphi(\varphi^2-\Lambda)^{-1} \qquad (2.1a,b)$$

and the dominant exponential term of (1.3) becomes

$$\exp tK(\theta^*) = \exp t\left[-\frac{\delta R_c}{R} + \frac{\cos\theta^*}{4a_2}\left(\Lambda-\varphi^2\right)\right]. \qquad (2.2)$$

Accordingly, lines of constant phase, for each t, are given to good approximation by

$$Im\left\{\frac{\cos\theta^*}{4a_2}\left(\Lambda-\varphi^2\right)\right\} = \text{constant} \qquad (2.3)$$

and lines of constant temporal amplification rate σ are

$$-\frac{\delta_r R_c}{R} + \mathrm{Re}\left\{\frac{\cos\theta^*}{4a_2}(\Lambda-\varphi^2)\right\} = \sigma. \qquad (2.4)$$

On introducing the (complex) quantity $v \equiv \tan\theta^*$ and writing $\mu \equiv 2\alpha_0 a_2$, expressions for X/t and z/t are found from (2.1*a*) to be

$$X/t = \varphi_r - \mu_i - (v_r/v_i)(\varphi_i + \mu_r) \qquad (2.5a)$$

$$z/t = v_i^{-1}(\varphi_i + \mu_r) \qquad (2.5b)$$

where subscripts r and i denote real and imaginary parts. Also, result (2.1*b*) may be written as

$$\left(\frac{v}{1+v^2}\right)\left(\frac{\varphi^2-\Lambda}{\varphi}\right) = \frac{2(\varphi_i+\mu_r)}{v_i}; \qquad (2.6)$$

a complex equation connecting the unknown complex v and φ which has a real right-hand side. Finally (2.3) and (2.4) may be expressed in terms of φ and v only as the two real equations

$$Im\left\{\frac{(\Lambda-\varphi^2)}{\mu(1+v^2)^{1/2}}\right\} = \text{constant} \equiv p \qquad (2.7)$$

$$\mathrm{Re}\left\{\frac{(\Lambda-\varphi^2)}{\mu(1+v^2)^{1/2}}\right\} = \frac{2}{\alpha_0}\left(\sigma + \frac{\delta_r R_c}{R}\right) \equiv 4\nu. \qquad (2.8)$$

This form is now suitable for computation, according to the following scheme. Starting values of $\varphi_r, \varphi_i, v_r$ and v_i may be chosen as

$$\varphi_r = (X/t)_0 + \mu_i, \quad \varphi_i = -\mu_r, \quad v_r = v_i = 0,$$

corresponding to a specified point $X/t=(X/t)_0$, $z/t=0$ of the $X/t-z/t$ plane. On altering φ_r slightly, new values of φ_i, v_r, and v_i may be found by iterative solution of (2.6) and (2.7), or of (2.6) and (2.8), depending on whether lines of constant phase or constant amplification are sought. Corresponding values of X/t and z/t are then established from (2.5*a*,*b*). Continuing in this way, curves of constant phase or amplification through the chosen starting point may be traced out. Note that the curves so obtained are independent of the Reynolds number R; but that, since R_c/R occurs on the right-hand side of (2.8), the value of amplification (or damping) rate associated with a curve of constant amplification varies with R. The independence from R of these curves is of course a consequence of the particular model (1.1) and *not* a general feature of unstable wave packets. No convergence problems were encountered with the ad hoc iteration scheme adopted. The programs were written and all the computations performed by Mrs. M. F. McCall using the St. Andrews University computer.

Values of ω_0, α_0, a_1, a_2, and δ must be assigned. These were chosen to be

$$\omega_0=0.26933, \quad \alpha_0=1.0202, \quad a_1=0.384,$$
$$a_2=0.183+0.070i, \quad \delta=0.00982+0.04621i, \tag{2.9}$$

which are the values appropriate for plane Poiseuille flow at Reynolds numbers near $R_c=5774$, taken from Hocking, Stewartson and Stuart [6]. However, we do *not* claim that the results shown here are necessarily quantitatively accurate representations of unstable wave packets in plane Poiseuille flow. A fuller appreciation of the range of validity of the results is provided in Fig. 3.

The solid curves shown in Fig. 1 denote constant phase lines calculated as described. The dashed boundary is a line of constant amplification, which would represent the neutral case $\sigma=0$ if $R=11{,}110$. Curves are shown only for $z/t \geq 0$, the portion with $z/t < 0$ being identical, by symmetry. Figure 2 shows lines of constant amplification. The labels indicate constant values of ν, as defined in (2.8). The neutral boundary at given $R>R_c$ is therefore the curve on which $\nu=\delta_r R_c/2\alpha_0 R=27.8\ R^{-1}$. The maximum possible value of ν is $\nu_{\max}=\delta_r/2\alpha_0=0.01924$, which corresponds to a maximum growth rate $\sigma=\delta_r(1-R_c/R)$, located at the origin $X/t=z/t=0$. The curves labeled $\nu=0.019, 0.016, 0.013, 0.010$ would be neutral boundaries ($\sigma=0$) for $R=5848$, 6944, 8547 and 11,110, respectively. The results display similar features in those shown in Figs. 2 and 4(*a*) of Part 1, which relate to analytic solutions obtained by making additional scaling assumptions.

To enable comparison of these analytic approximations with the computed solutions, Fig. 2 also shows results (3.6) and (5.5) of Part 1 for neutral boundary at $R = 6944$ ($\nu=0.016$). Both analytic solutions underestimate the size of the unstable wave packet in this case. Since result Part 1 (3.6), requires $1-R_c/R << 1$ and Part 1 (5.5) that $|a_2|$ is large, close agreement was not to be expected.

3 The Model Dispersion Relation

Gaster [4] has advocated the use of a series representation of the exact dispersion relationship and has shown that great accuracy is obtained on retaining a sufficient number of terms. Such accuracy is not to be expected from the simple model (1.1). In order to test the accuracy of (1.1), it has been compared with two situations for which precise numerical calculations are available; namely, the temporal and spatial instability of two-dimensional disturbances in plane Poiseuille flow. Results for the temporal problem have been computed by various authors, with good agreement. Those obtained by Sen and Venkateswarlu [1976 private communication] for $R = 5780$ and 10,000 and used here. For the spatial problem, we use the results of Itoh [7] for $R = 6000$ and 10,000.

Figure 3(*a*) and (*b*) displays the temporal results, the crosses denoting computed values of ω_r and ω_i and the solid curves the model estimates, plotted against real wave number α. The values of the various constants in (1.1) were chosen as in (2.9), with $R_c = 5774$, $\theta=0$, and $\gamma=\alpha$. Agreement at $R = 5780$ is nearly perfect, as might have been expected. For $R = 10{,}000$, agreement is predictably less good. The most notable discrepancies are a shift of about 7 percent in the most unstable wave number, and an overestimate by the model of the (virtually constant) gradient $\partial\omega_r/\partial\alpha$ amounting to around 14 percent. In contrast, results for maximum growth rate are in substantial agreement, and the greatest error in ω_r is only about 6 percent for α in the range 0.7–1.2.

Figure 4(*a*) and (*b*) shows a similar comparison between the model (solid curves) and Itoh's results for spatial growth (dashed curves), the real and imaginary parts of α being plotted against real frequency ω. In solving (1.1) for α, it is necessary to disregard one (spurious) root of the quadratic equation. For $R = 6000$, results for α_r are virtually identical and no dashed curve is shown. For $R = 10{,}000$, the slopes $\partial\alpha_r/\partial\omega$ are nearly constant but disagree by around 12 percent. With ω_r in the range 0.15–0.35, the greatest discrepancy in α_r is about 3 percent. There is some discrepancy in $\alpha_i(\omega)$ at $R = 6000$, and more for $R = 10{,}000$. For the latter, the model overestimates the frequency of the most unstable mode by around 11 percent and predicts a range of unstable frequencies 20 percent wider than actually occurs; but, again, the estimate of maximum growth rate is quite good.

At first sight, it looks as though calculations based on (1.1) might give good accuracy at Reynolds numbers between 5774 and 6000 and acceptable approximations at much higher values, even up to 10,000. However, a closer examination is required.

The greatest discrepancies between the model (1.1) and the computed eigenvalues are in $\partial\omega_r/\partial\alpha$ (or$\partial\alpha_r/\partial\omega$) and in the most unstable wave number (or frequency). Improved agreement may be effected by adding to the expression (1.1) for ω the additional terms

$$\cos\theta\left(-\frac{R_c}{R\cos\theta}\right)\left[b(\gamma-\alpha_0)-\frac{ib_i^2}{4a_{2r}}\left(1-\frac{R_c}{R\cos\theta}\right)\right] \tag{3.1}$$

where $b=b_r+ib_i$ is some complex constant. The real and imaginary parts of ω, for $\theta=0$ and γ real, then become

$$\omega_r=\omega_0+a_{1r}(\gamma-\alpha_0)-\delta_i(1-R_c/R)$$
$$+b_r(\gamma-\alpha_0)(1-R_c/R)+a_{2i}(\gamma-\alpha_0)^2$$
$$\omega_i=\delta_r(1-R_c/R)-a_{2r}\left[\gamma-\alpha_0-\frac{b_i}{2a_{2r}}(1-R_c/R)\right]^2.$$

Accordingly, the temporally most unstable wave number with $\theta=0$ is

$$\gamma=\alpha_0+\frac{b_i}{2a_{2r}}(1-R_c/R),$$

with unchanged growth rate, and the real part of the group velocity is

$$\frac{\partial\omega_r}{\partial\gamma}=a_{1r}+b_r(1-R_c/R)+2a_{2i}(\gamma-\alpha_0).$$

The term $2a_{2i}(\gamma-\alpha_0)$ in the latter expression is small for wave numbers of interest. Clearly, values of b_r and b_i may be chosen to give a better fit with the exact temporally growing eigenvalues. An associated improvement in the spatially growing eigenvalues also follows. Values giving rather good agreement with the computed eigenvalues in Figs. 3 and 4 are

$$b_r\approx-0.10, \quad b_i\approx-0.052. \tag{3.2}$$

It is necessary to investigate the consequences of these additional terms in the model dispersion relation.

First we consider the situation investigated in Sections 3 and 6 of Part 1, but modified to include these extra terms. That is to say, we introduce the scaling assumptions

$$\delta=\epsilon\bar{\delta},\quad 1-R_c/R=\epsilon\mu,\quad \frac{X}{t}=\epsilon\xi,\quad \frac{z}{t}=\epsilon^{1/2}\eta,$$

and calculate the dominant exponential term exp $tK(\theta^*)$as described in Part 1. In this connection, we note that a local expansion of the exact dispersion relation about the critical Reynolds number R_c and wave number α_0 is now entirely consistent with the chosen model. Indeed, the incorporation of the terms in b is necessary for this to be so and this improvement establishes the model as a formally valid approximation to the exact dispersion relation sufficiently close to R_c and α_0.

It is found that

$$K(\theta^*)=i(\alpha_0a_1-\omega_0)+i\alpha_0\epsilon\left[\xi-\frac{\alpha_0\eta^2}{2(\omega_0-\alpha_0a_1)}\right]$$

$$+\epsilon^2\left[\mu\bar{\delta}-\frac{\bar{\delta}\alpha_0^2\eta^2}{2(\omega_0-\alpha_0a_1)^2}\right.$$

$$-\frac{i\alpha_0^3\eta^2}{2(\omega_0-\alpha_0a_1)^2}\left(\xi-\frac{\alpha_0\eta^2}{4(\omega_0-\alpha_0a_1)}\right)-\frac{b_i^2\mu^2}{4a_{2r}}$$

$$\left.-\frac{1}{4a_2}\left\{\xi-b\mu+\frac{\alpha_0\eta^2}{(\alpha_0a_1-\omega_0)}\left(1+\frac{b\alpha_0}{2(\alpha_0a_1-\omega_0)}\right)\right\}^2\right]+0(\epsilon^3).$$

Comparison with (3.4) of Part 1 shows that the new terms enter at $0(\epsilon^2)$. Accordingly, the $0(\epsilon)$ approximation for lines of constant phase remains as

$$\xi=\frac{\alpha_0\eta^2}{2(\omega_0-\alpha_0a_1)}+\text{constant},$$

but curves of constant amplification, at $0(\epsilon^2)$, are modified by terms in b. Making the change of variables

$$\tilde{\xi}\equiv\frac{\alpha_0\bar{\delta}_r}{2(\alpha_0a_1-\omega_0)(\mu\bar{\delta})_r}\,\frac{[\xi-\mu(b_r+a_{2i}b_i/a_{2r})]}{\left[1+\dfrac{\alpha_0(a_{2r}b_r+a_{2i}b_i)}{2a_{2r}(\alpha_0a_1-\omega_0)}\right]}$$

$$\tilde{\eta}\equiv\frac{\alpha_0\eta}{(\alpha_0a_1-\omega_0)}\left(\frac{\bar{\delta}_r}{2(\mu\bar{\delta})_r}\right)^{1/2},\tag{3.3}$$

$$K\equiv\frac{|a_2|\alpha_0\bar{\delta}_r}{(\alpha_0a_1-\omega_0)[a_{2r}(\mu\bar{\delta})_r]^{1/2}}\left[1+\frac{\alpha_0(a_{2r}b_r+a_{2i}b_i)}{2a_{2r}(\alpha_0a_1-\omega_0)}\right]^{-1}$$

these curves of constant amplification rate σ are [c.f. Part 1 (3.9)]

$$\tilde{\xi}=-\tilde{\eta}^2\pm\left\{K^2(1-\tilde{\sigma}-\tilde{\eta}^2)+M^2\tilde{\eta}^2(2-\tilde{\eta}^2)\right\}^{1/2}\tag{3.4}$$

where

$$\tilde{\sigma}\equiv\sigma/(\mu\bar{\delta})_r,M\equiv\frac{|a_2|\alpha_0b_i}{2a_{2r}(\alpha_0a_1-\omega_0)+\alpha_0(a_{2r}b_r+a_{2i}b_i)}.$$

Compared with the definitions of $\tilde{\xi}$, $\tilde{\eta}$, and K in Part 1, it is seen that $\tilde{\eta}$ is unchanged, the origin of $\tilde{\xi}$ is moved to

$$\frac{x-a_1t}{t}=\frac{X}{t}=\left(1-\frac{R_c}{R}\right)\left(b_r+\frac{a_{2i}b_i}{a_{2r}}\right)$$

(in part to accommodate the variation in group velocity with R), and both $\tilde{\xi}$ and K include the further scaling factor

$$\left[1+\frac{\alpha_0(a_{2r}b_r+a_{2i}b_i)}{2a_{2r}(\alpha_0a_1-\omega_0)}\right]^{-1}.$$

Because this factor occurs in both $\tilde{\xi}$ and K, the length (as measured by x) of the unstable packet on the axis of symmetry $\tilde{\eta}=0$ is identical to that found in Part 1. In addition to these changes of scale, the term in M^2 of (3.4) influences the shape of the packet. Since M is a constant for a given flow even though R may change, and K is proportional to $(1-R_c/R)^{-1/2}$, it is clear that the term in M^2 will be insignificant for values of R sufficiently close to R_c, but that its influence will be increasingly apparent as R increases beyond R_c. For the values given in (2.9) and (3.2), which are typical for plane Poiseuille flow, it is found that

$$\left(\frac{K}{M}\right)^2\approx\frac{2.66}{1-R_c/R}\tag{3.5}$$

which is 15.2 at R = 7000 and 6.3 at R = 10,000. Since the maximum allowable value of $\tilde{\eta}$ is approximately unity (for real roots $\tilde{\xi}$), it is clear that the omission from (3.4) of the term in M^2 incurs only quite small errors. For example, the neutral boundary $\tilde{\sigma}=0$ at R = 10,000 has a maximum value of $\tilde{\eta}$ equal to 1.075 including the M^2 term and unity without it. Accordingly, there seemed little point in plotting curves based on (3.4): these will differ only slightly from those shown in Fig. 3 of Part 1 for the case $M=0$.

Of course, the analysis leading to (3.4) cannot be expected to remain valid for R as large as 10,000, since it was assumed that $1-R_c/R$ is $0(\epsilon)$ when ϵ is small. The results of Section 2 introduced no such scaling assumption, and the work described may also be extended to include the additional terms (3.1) in the dispersion relation. It is found that the dominant exponential is then exp $tK_1(\theta^*)$ where

$$K_1(\theta^*)=-\frac{\delta R_c}{R}+\frac{\cos\theta^*}{4a_2}(\Lambda-\varphi^2)$$

$$-\frac{b_i^2\cos\theta^*}{4a_{2r}}\left(1-\frac{R_c}{R\cos\theta^*}\right)^2-\frac{i\alpha_0bR_c}{R},$$

$$\sin2\theta^*=\frac{4z}{t}\varphi\left\{\varphi^2-\Lambda+\frac{a_2b_i^2}{a_{2r}}\left[1-\left(\frac{R_c}{R\cos\theta^*}\right)^2\right]\right.$$

$$\left.-2b\varphi\left(2-\frac{R_c}{R\cos\theta^*}\right)\right\}^{-1}$$

and Λ, φ are redefined as

$$\Lambda\equiv4a_2[-i\omega_0+\delta+i\alpha_0(a_1+b_1)-\alpha_0^2a_2],$$

$$\varphi\equiv\frac{X}{t}+\frac{z}{t}\tan\theta^*-2i\alpha_0a_2-b\left(1-\frac{R_c}{R\cos\theta^*}\right),$$

which may be compared with results (2.1) and (2.2). When z and θ^* are set equal to zero, corresponding to points on the x-axis, it is readily confirmed that

$$\text{Re}\,\{K_1(0)\}=\delta_r\left(1-\frac{R_c}{R}\right)$$

$$-\frac{a_{2r}}{4|a_2|^2}\left[\frac{X}{t}-\left(1-\frac{R_c}{R}\right)\left(b_r+\frac{a_{2i}b_i}{a_{2r}}\right)\right]^2$$

which is consistent with result (3.4) in the foregoing with $\tilde{\eta}$ = 0.

It may be anticipated that, provided $1-R_c/R$ is fairly small, the dominant effects of the b-terms will be similar to those discovered for the small $-\epsilon$ expansion. These are [c.f. results (3.3)]: (*i*) a shift of origin, following the "center" of the disturbance, to

$$\frac{X_0}{t}=\frac{x-a_1t}{t}=\left(1-\frac{R_c}{R}\right)\left(b_r+\frac{a_{2i}b_i}{a_{2r}}\right),$$

(*ii*) a magnification, whereby X/t for the case b = 0 is replaced by $S^{-1}(X-X_0)/t$ with

$$S\equiv1+\frac{\alpha_0(a_{2r}b_r+a_{2i}b_i)}{2a_{2r}(\alpha_0a_1-\omega_0)},$$

and (*iii*) a change in the effective value of a_2 to $a_2 S^{-2}$ which ensures that the "length" of the disturbance on the x-axis is identical with that when $b = 0$. Since the ratio $(M/K)^2$ is fairly small even for values of R as large as 10,000, further Reynolds-number-dependent variations are expected to be comparatively slight. Curves of constant amplification and phase may be computed from the foregoing relations if required. For plane Poiseuille flow, S turns out to be approximately 0.5 and the influence of the b terms is significant at *all* values of $R > R_c$ since S is independent of R. The results presented in Figs. 1 and 2 of Part 1 and in Figs. 1 and 2 of the present paper must be interpreted accordingly. In particular, the shape of the unstable packet, in physical $(X-X_0)/t - z/t$ space, is somewhat less "swept-back" than predicted by the theory with $b = 0$, because of items (*ii*) and (*iii*) in the foregoing. For flows in which $|b| << |a_1 - \omega_0/\alpha_0|$, S is close to unity and results for b equal to zero yield good approximations without need for reinterpretation.

At the opposite extreme, flows for which S is close to zero will exhibit little sweepback of unstable wave packets; because as $S \to 0$, result (3.4) simplifies to

$$(\xi/K)^2 + \eta^2 = 1 - \tilde{\sigma} + (M/K)^2 \tilde{\eta}^2 (2 - \tilde{\eta}^2)$$

which is close to an ellipse when $(M/K)^2 << 1$. Also, flows with

$$a_1 - \omega_0/\alpha_0 + \frac{1}{2}[b_r + b_i(a_{2i}/a_{2r})] < 0$$

must have wave packets that are concave downstream rather than upstream.

4 A Model For "Splitting" Packets

It is well known that the greatest possible growth rate of a two-dimensional Fourier mode frequently occurs at some *finite* value of $R = R_1 (> R_c)$. Consequently, when $R > R_1$, the most unstable mode need not be two-dimensional. In such cases, the possibility arises that a localized disturbance need not remain centered on the x-axis, but may "split" into two regions of maximum amplitude. To demonstrate this phenomenon, we adopt the model dispersion relation

$$\omega = \cos\theta[\omega_0 + a_1(\gamma - \alpha_0) - ia_2(\gamma - \alpha_0)^2 + i\delta_1 - i\delta_2(1 - R_1/R\cos\theta)^2]. \tag{4.1}$$

Here, α_0 is the wave number of the most unstable mode at $R = R_1$. Of course, this model may not accurately represent a particular flow and further terms might have to be incorporated, much as in the foregoing, to achieve better accuracy. But, for simplicity, attention is here restricted to (4.1).

Here, the critical Reynolds number R_c and another, higher, Reynolds number R_1 are related by

$$R_1/R_c = 1 + (\delta_{1r}/\delta_{2r})^{1/2}$$

where a_2, δ_1, and δ_2 are complex constants with positive real parts and ω_0, α_0, a_1 are real constants as before. Now, temporally growing modes have a maximum possible growth rate $\omega_i = \delta_{1r}$ when $\theta = 0$, $\gamma = \alpha_0$, and $R = R_1$, and when $R > R_1$, the disturbance that grows most rapidly may be an *oblique* wave with $\theta \neq 0$. More precisely, for real γ and θ, $\partial\omega_i/\partial\gamma = 0$ when $\gamma = \alpha_0$, and $\partial\omega_i/\partial\theta = 0$ both when $\theta = 0$ and when $\theta = \theta_m \equiv \cos^{-1}\{(R_1/R)(1 - \delta_{1r}/\delta_{2r})^{-1/2}\}$, the latter solution existing provided $\delta_{1r} < \delta_{2r}$ and $R > R_1(1 - \delta_{1r}/\delta_{2r})^{-1/2}$. For $\gamma = \alpha_0$ and $\theta = 0$,

$$\omega_i = \delta_{1r} - \delta_{2r}(1 - R_1/R)^2,$$

while for $\gamma = \alpha_0$, $\theta = \theta_m$,

$$\omega_i = 2\delta_{2r}(R_1/R)\{1 - (1 - \delta_{1r}/\delta_{2r})^{1/2}\}.$$

The latter exceeds the former for all $R > R_1(1 - \delta_{1r}/\delta_{2r})^{-1/2}$; that is, whenever the latter root exists.

The model dispersion relation (4.1) is thus an instance of the situation first envisaged by Watson [9] for temporal instability, where oblique modes may be most unstable at sufficiently large R. The nature of the development of localized disturbances in such cases is very different from that found in the foregoing.

The saddle-point method may be applied as in Part 1, Section 2, and in Sections 1-2 of the present paper with the following results. On defining

$$\varphi \equiv \frac{X}{t} + \frac{z}{t}\tan\theta^* - 2i\alpha_0 a_2, \quad \Lambda_1 \equiv 4a_2[-i\omega_0 + i\alpha_0 a_1 - \alpha_0^2 a_2 + \delta_1 - \delta_2 + \delta_2(R_1/R\cos\theta^*)^2]$$

the dominant exponential term is $\exp tK_2(\theta^*)$ where

$$K_2(\theta^*) = \frac{\cos\theta^*}{4a_2}(\Lambda_1 - \varphi^2) + \frac{2\delta_{2r}R_1}{R} - \frac{2\delta_2}{\cos\theta^*}\left(\frac{R_1}{R}\right)^2 \tag{4.2}$$

and

$$\sin 2\theta^* = 4(z/t)\varphi(\varphi^2 - \Lambda_1)^{-1}. \tag{4.3}$$

These are the counterparts, for the dispersion relation (4.1), of the results shown in (2.1) and (2.2). The real part of $K_2(\theta^*)$ yields the equation for curves of constant amplification rate σ,

$$\sigma = \frac{2\delta_{2r}R_1}{R} + \mathrm{Re}\left\{\frac{\cos\theta^*}{4a_2}(\Lambda_1 - \varphi^2) - \frac{2\delta_2}{\cos\theta^*}\left(\frac{R_1}{R}\right)^2\right\}; \tag{4.4}$$

while the imaginary part gives lines of constant phase

$$Im\left\{\frac{\cos\theta^*}{4a_2}(\Lambda_1 - \varphi^2) - \frac{2\delta_2}{\cos\theta^*}\left(\frac{R_1}{R}\right)^2\right\} = \text{constant}. \tag{4.5}$$

Results (4.2)-(4.5) may be used to find computed solutions as was done in Fig. 2. However, since the dispersion relation (4.1) is proposed only as an instructive qualitative model, rather than as a basis for precise results, attention is here restricted to a particular case when simple analytical solutions can be found.

This case is the analogue of that presented in Section 5 of Part 1 for situations where δ is small but a_2 is large. Accordingly, we write

$$\delta_2 = \delta_1 d_2, \quad a_2^{-1} = \delta_1 \lambda$$

and consider δ_1 to be a small (complex) parameter and d_2, λ to be 0 (1) complex quantities independent of δ_1. To leading order in δ_1, result (4.3) yields

$$\tan\theta^* = \frac{z/t}{X/t + a_1 - \omega_0/\alpha_0} + 0(\delta_1)$$

which may be re-expressed as

$$\theta^* = \theta_0 + \delta_1\theta_1, \quad \theta_0 = \tan^{-1}\frac{z/t}{X/t + a_1 - \omega_0/\alpha_0}.$$

Letting $\eta_1 \equiv z/t$, $\xi_1 \equiv X/t + a_1 - \omega_0/\alpha_0$ as in Part 1, Section 5, result (4.2) reduces to

$$K_2(\theta^*) = i\alpha_0(\xi_1^2 + \eta_1^2)^{1/2} + 0(\delta_1),$$

which yields constant phase lines which are circles in the $X/t - z/t$ plane with center $X/t = \omega_0/\alpha_0 - a_1$, $z/t = 0$. That is, the center of the circles travels with the phase velocity ω_0/α_0, such that $x/t = X/t + a_1 = \omega_0/\alpha_0$. This was also the case for the solution found in Part 1, Section 5.

To the next order,

$$K_2(\theta^*) = i\alpha_0(\xi_1^2 + \eta_1^2)^{1/2} + \delta_1\left(\frac{2d_2R_1}{R}\right) + \frac{\delta_1\xi_1}{(\xi_1^2 + \eta_1^2)^{1/2}}\left[1 - d_2 - \frac{\lambda}{4}\left(\frac{\xi_1^2 + \eta_1^2}{\xi_1} - a_1 + \frac{\omega_0}{\alpha_0}\right)^2 - \left(\frac{d_2R_1^2}{R^2}\right)\left(\frac{\xi_1^2 + \eta_1^2}{\xi_1^2}\right)\right] + 0(\delta_1^2),$$

the terms in θ_1 vanishing identically at $0(\delta_1)$. Taking the real part, the amplification rate σ is given by

$$\sigma = \frac{2R_1}{R}(\delta_1 d_2)_r + \frac{\xi_1}{(\xi_1^2 + \eta_1^2)^{1/2}}\left[\delta_{1r} - (\delta_1 d_2)_r\right.$$

$$- \frac{(\delta_1\lambda)_r}{4}\left(\frac{\xi_1^2+\eta_1^2}{\xi_1} - a_1 + \frac{\omega_0}{\alpha_0}\right)^2$$

$$-(\delta_1 d_2)_r\left(\frac{R_1}{R}\right)^2\left(\frac{\xi_1^2+\eta_1^2}{\xi_1^2}\right)\Bigg] + 0(\delta_1^2). \qquad (4.6)$$

On introducing polar coordinates ρ_1, ϕ_1 defined as

$$\xi_1 = \rho_1\cos\phi_1, \quad \eta_1 = \rho_1\sin\phi_1,$$

this result may be rewritten as

$$\frac{\rho_1}{a_1 - \omega_0/\alpha_0} = \cos\phi_1 \pm M\left\{\cos\phi_1\left(\cos\phi_1 - \frac{\sigma}{\delta_{1r}}\right) - \Delta\left(\cos\phi_1 - \frac{R_1}{R}\right)^2\right\}^{1/2} \qquad (4.7)$$

where

$$M \equiv \frac{2|a_2|}{(a_1 - \omega_0/\alpha_0)}\left(\frac{\delta_{1r}}{a_{2r}}\right)^{1/2}, \quad \Delta \equiv \frac{(\delta_1 d_2)_r}{\delta_{1r}} = \frac{\delta_{2r}}{\delta_{1r}}.$$

Here, the growth rate σ cannot exceed δ_{1r}. This result may be compared with Part 1, equation (5.5). When both conditions

$$R/R_1 \geq \left(\frac{\Delta}{\Delta - 1}\right)^{1/2}, \quad \Delta > 1 \qquad (4.8)$$

are satisfied, the growth rate σ has an absolute maximum value

$$\sigma_{\max} = 2\delta_{1r}(R_1/R)\Delta[1-(1-\Delta^{-1})^{1/2}] \qquad (4.9)$$

at two points

$$\rho_1 = \frac{(R_1/R)(a_1 - \omega_0/\alpha_0)}{(1-\Delta^{-1})^{1/2}},$$

$$\phi_1 = \pm\cos^{-1}\left[\frac{R_1/R}{(1-\Delta^{-1})^{1/2}}\right]. \qquad (4.10)$$

Otherwise, a maximum value of

$$\sigma_{\max} = \delta_{1r}[1 - \Delta(1 - R_1/R)^2]$$

is obtained at

$$\rho_1 = a_1 - \omega_0/\alpha_0, \quad \phi_1 = 0.$$

This point is a saddle point of $\sigma(\rho_1, \phi_1)$ when (4.8) is satisfied. Conditions (4.8) are precisely those that ensure that the temporally most unstable mode is an oblique wave.

The shapes of curves of constant amplification σ are readily found from (4.7). In some cases, ρ_1 becomes zero and there is a cusp at the origin. This also occurred in Part 1, Section 5, where it was pointed out that the saddle-point method may break down near $\rho_1 = 0$ because of violation of condition (1.4). If $\Delta(1 - R_1/R)^2 > 1$, the neutral boundary does not intersect the x/t-axis and there are two distinct unstable regions, one on either side of it. Curves of constant amplification $\sigma/\delta_{1r} = 0$, 0.6, and 0.8 were calculated for the particular case $R_1/R = 0.8$, $\Delta = 10$, $M = 0.5$, and are shown in Fig. 5. The corresponding lines of constant phase are circles with their centers at the origin.

It is clear that the dispersion relation (4.1) yields results dramatically different from those found previously. Now a splitting of the wave packet yields greatest amplitudes at two peaks on either side of the x/t axis, whenever conditions (4.8) are satisfied. For R/R_1 less than $(1-\Delta^{-1})^{-1/2}$ or $\Delta < 1$, no splitting takes place and the results would then be qualitatively similar to those described in Part 1, Section 5, and in Section 2 in the present paper.

Since R_1/R_c is around 10 for both Blasius and plane Poiseuille flow, $\Delta < 1$ in the present model and no splitting is then predicted; but firm conclusions must await more accurate representation of the dispersion relation for $R >> R_c$. The occurrence of two amplitude maxima in the experiments of Gaster and Grant [2] was almost certainly due to nonlinear effects. But it is conceivable that initially small, local

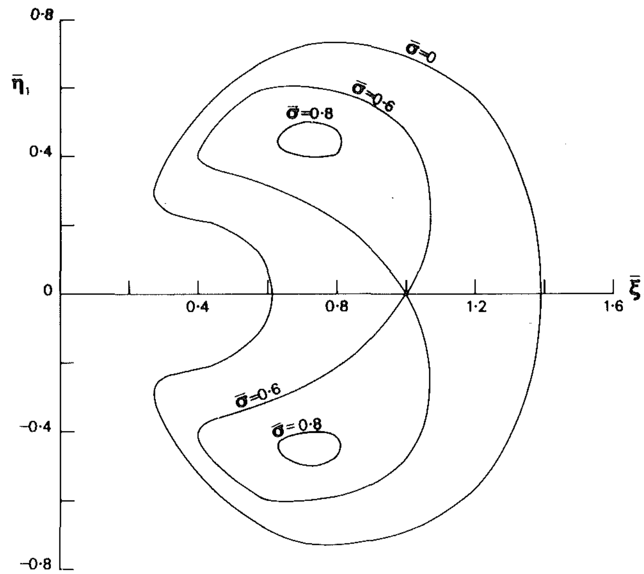

Fig. 5 Lines of constant amplification from (4.7) for $R_1/R = 0.8$, $\Delta = 10$, $M = 0.5$, showing splitting of packet. Values of $\sigma/\delta_{1r} = \bar{\sigma}$ shown are 0, 0.6, and 0.8. Coordinates are $\bar{\xi}_1 \equiv \xi_1(a_1 - \omega_0/\alpha_0)^{-1}$, $\bar{\eta}_1 \equiv \eta_1(a_1 - \omega_0/\alpha_0)^{-1}$.

disturbances in Blasius flow may ultimately exhibit a "two peak" structure at sufficiently large R owing to linear effects alone. Gaster's [3] computations, involving linear superposition of many discrete modes with real frequencies and spanwise wave numbers, did not reveal a two-peak structure, but his representation cannot remain adequate at very large times and distances, on account of the ever-increasing spanwise extent of the wavepacket.

The approximate technique described here and in Part 1 appears capable of fruitful extension to three-dimensional and spatially varying mean flows, for which precise computations are impractical but which are of great practical interest.

Acknowledgment

I am grateful to Mrs. M. F. McCall for carrying out the computations described in Section 2, and to Dr. Pradeep Sen for making available the computational results shown in Fig. 3, also to a referee for helpful comments.

References

1 Craik, A. D. D., "The Development of Wave Packets in Unstable Flows," *Proceedings of the Royal Society of London*, Vol. A373, 1981, pp. 457–476.

2 Gaster, M., and Grant, I., "An Experimental Investigation of the Formation and Development of a Wave Packet in a Laminar Boundary Layer," *Proceedings of the Royal Society of London*, Vol. A347, 1975, pp. 253–269.

3 Gaster, M., "A Theoretical Model of a Wave Packet in the Boundary Layer on a Flat Plate," *Proceedings of the Royal Society of London*, Vol. A347, 1975, pp. 271–289.

4 Gaster, M., "Series Representation of the Eigenvalues of the Orr-Sommerfeld Equation," *Journal of Computational Physics*, Vol. 29, 1978, pp. 147–162.

5 Gaster, M., "The Propagation of Linear Wave Packets in Laminar Boundary Layers—Asymptotic Theory for Nonconservative Wave Systems," A.I.A.A. Paper 79-1492, 1979.

6 Hocking, L. M., Stewartson, K., and Stuart, J. T., A Nonlinear Instability Burst in Plane Parallel Flow," *Journal of Fluid Mechanics*, Vol. 51, 1972, pp. 705–735.

7 Itoh, N., "A Power Series Method for the Numerical Treatment of the Orr-Sommerfeld Equation," *Transactions of the Japan Society for Aeronautical and Space Science*, Vol. 17, 1974, pp. 65–75.

8 Itoh, N., "Linear Stability Theory for Wave-Packet Disturbances in Parallel and Nearly Parallel Flows," *Proceedings of I.U.T.A.M. Symposium on Laminar-Turbulent Transition*, Stuttgart, Eppler, R., and Fasel, H., eds., Springer, 1980, pp. 86–95.

9 Watson, J., "Three-Dimensional Disturbances in Flow Between Parallel Planes," *Proceedings of the Royal Society of London*, Vol. A254, 1960, pp. 562–569.

A Nonlinear Constitutive Model for Granular Materials: Application to Gravity Flow

D. F. McTigue[1]

Geology Department,
Stanford University,
Stanford, Calif. 94305

The form of the dissipative part of the stress in flowing granular materials is motivated by considering momentum exchange due to intergranular collisions. Both shear and normal stresses are predicted that are quadratic in the rate of deformation. The equilibrium part of the stress is assumed to include a thermodynamic pressure and a term compatible with the Coulomb failure criterion in the limit of vanishing deformation. Solutions for the volume fraction and velocity fields in steady gravity flow down a slope are found. The volume fraction increases linearly downward through the shearing layer at a rate that decreases with increasing slope. The velocity profile develops an inflection near the lower boundary at smaller slopes, and becomes fully convex downstream as it approaches a critical maximum slope for steady flow. The results are in qualitative agreement with available experimental measurements.

Introduction

Interest in the flow behavior of granular materials is primarily motivated by design problems in the bulk handling of grain, sand and gravel, powders, and other particulate solids. Flowing granular materials also represent a limiting case of two-phase flow at high solids concentrations and high solid-to-fluid density ratios. Their understanding is thus pertinent to slurry transport and perhaps to certain natural sediment transport problems. Despite the practical importance of such flows, no general and completely satisfying mechanical theory for their description has emerged.

This work is directed toward developing and exploring some of the implications of a nonlinear continuum model for flowing granular materials. As with most similar efforts at this juncture, the theory must be regarded as speculative, particularly in the absence of an extensive body of relevant experimental data. Previous continuum theories generally fall into two broad categories: plastic and viscous. The former, exemplified by the work of Shield [22], Spencer [23], and Mandl and Fernandez-Luque [12], depart from the stress relations for a frictional-cohesive material at failure, leading to rate-independent constitutive equations. Viscous, or rate-dependent theories imply momentum fluxes within the deforming material due to particle interactions. Goodman and Cowin [4, 5] have advanced a linear theory of this type. The present work includes features of both the plastic and viscous models.

A successful theory must embody several features characteristic of granular materials. An assemblage of close-packed grains must undergo volumetric expansion for any deformation to occur, a phenomenon known as *dilatancy* [16]. Similarly, it can be anticipated that in fully developed flow beyond failure, the volume fraction of solids will respond to the dynamics of the flow, and the stresses will vary strongly with the volume fraction. Granular materials can sustain finite shear stresses in the absence of any deformation, and the critical stress at which shearing begins depends on the normal stress. A theory for the flow beyond this initial failure should, in the limit of vanishing deformation, predict stresses that resemble those at failure. Finally, it is noted that the experimental work of Bagnold [1] and Savage [18] suggests nonlinear rate dependence. It is these features that the following developments endeavor to accommodate. Savage [19] has independently worked toward a similar end, but his approach is somewhat different, particularly in posing the equilibrium stress.

Structure of the Theory

It is assumed that a granular material can be treated as a material continuum. Implicit in this assumption is the caveat that the theory is expected to be valid only at length scales that are large relative to the particle scale.

The model material considered here is comprised of grains of uniform solid density, γ, and voids with no mass. Thus, the bulk density, ρ, can be written

$$\rho = \gamma \nu, \tag{1}$$

where ν = volume fraction of solids[2] [5].

Employing (1), the usual balance laws for mass, momentum, and moment of momentum in a purely mechanical ("isothermal") theory become

$$\dot{\nu} + \nu \nabla \cdot \mathbf{u} = 0, \tag{2}$$

[1] Presently at Sandia National Laboratories, Albuquerque, N. Mex. 87185, a U. S. Department of Energy facility.

Contributed by the Applied Mechanics Division for publication in the Journal of Applied Mechanics.

Discussion on this paper should be addressed to the Editorial Department, ASME, United Engineering Center, 345 East 47th Street, New York, N.Y. 10017, and will be accepted until two months after final publication of the paper itself in the Journal of Applied Mechanics. Manuscript received by ASME Applied Mechanics Division, May, 1980; final revision, October, 1981.

[2] The volume fraction, ν, is the ratio of solids volume to total volume, and is related to the porosity, η, and the void ratio, e, by $\nu = 1 - \eta = 1/(1+e)$.

$$\gamma\nu\dot{\mathbf{u}} = \nabla \cdot \mathbf{T} + \gamma\nu\mathbf{b}, \tag{3}$$

$$\mathbf{T} = \mathbf{T}', \tag{4}$$

where $\mathbf{u}$ = velocity, $\mathbf{T}$ = stress, and $\gamma\nu\mathbf{b}$ = body force per unit volume. A superposed dot indicates the material derivative. Equation (4) assumes no couple stresses or external body couples.

Closure to the system (2)–(4) is sought in the form of a constitutive equation,

$$\mathbf{T} = \mathbf{T}(\nu, \mathbf{D}), \tag{5}$$

where $\mathbf{D} = [\nabla \mathbf{u} + (\nabla u)']$ = rate of deformation. The total stress, $\mathbf{T}$, may be decomposed into an *equilibrium* part, $\mathbf{T}^\circ$, and a *dissipative* part, $\mathbf{T}^*$ [4]:

$$\mathbf{T} = \mathbf{T}^\circ + \mathbf{T}^*, \tag{6}$$

where $\mathbf{T}^\circ$ is of order zero in $\mathbf{D}$, and thus can remain finite in the absence of deformation. Goodman and Cowin [4, 5] and Savage [19] include $\nabla\nu$ among the independent constitutive variables in (5) in order to include the effect of microstructure.

Collisional Momentum Exchange

The dependence of the macroscopic stress on the rate of deformation is expected to somehow reflect the mechanisms of momentum exhange within the material at a microscopic scale. A simple model for momentum exchange by interparticle collisions is examined here to provide some intuitive motivation for the choice of rate-dependent terms in the constitutive equation adopted. A preliminary version of this development was presented by McTigue [13].

Consider a system of spheres of uniform radius and density in a steady two-dimensional shear flow. It is assumed that both the concentration of particles and the velocity vary smoothly across the flow. A low concentration of solids is assumed, so that only single collisions are considered, and particles can be assumed to approach a reference grain parallel to the flow direction at a relative velocity that is related to the mean motion. Fluctuations of the particles about the mean velocity are ignored.

The flow is defined relative to a Cartesian coordinate system fixed at the center of an arbitrary reference particle in the flow. A cylindrical coordinate system is also centered on the reference grain (Fig. 1). The reference particle, of radius a, will interact only with grains whose centers lie within a "collision cylinder" of radius $2a$ with its axis aligned with the flow (Fig. 1).

Consider now a single perfectly elastic collision between two grains. The change in momentum, $\Delta\mathbf{m}$, of the reference grain is

$$\Delta\mathbf{m} = \frac{4}{3}\pi a^3 \gamma (\mathbf{n} \cdot \mathbf{v}_r)\mathbf{n}, \tag{7}$$

where $\mathbf{n}$ = inward-directed contact normal, and $\mathbf{v}_r$ = relative velocity. The contact normal is given by

$$\mathbf{n} = -\frac{r\cos\theta}{2a}\mathbf{e}_1 - \frac{r\sin\theta}{2a} - \mathbf{e}_2 \pm \frac{\sqrt{4a^2 - r^2}}{2a}\mathbf{e}_3, \tag{8}$$

where the $\pm$ in the x_3 component holds in the lower and upper hemispheres, respectively. The relative velocity is approximated by the leading terms in the expansion about $x_2 = 0$:

$$\mathbf{v}_r(x_2) = (u_0' x_2 + \frac{1}{2}u_0'' x_2^2 + \cdots)\mathbf{e}_3, \tag{9}$$

where, for brevity, u_0' has been written for the derivative $u_{3,2}$ evaluated at $x_2 = 0$.

The collision frequency, f, is given by

$$f = \frac{3}{a}\nu|\mathbf{v}_r|. \tag{10}$$

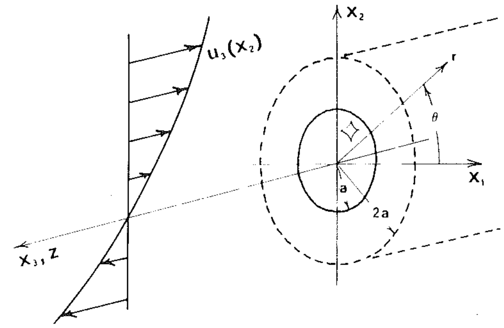

Fig. 1 Definition sketch for collisional momentum exchange

The volume fraction, ν, is approximated by the leading terms in the series

$$\nu(x_2) = \nu_0 + \nu_0' x_2 + \frac{1}{2}\nu_0'' x_2^2 + \cdots. \tag{11}$$

The net force, $\mathbf{F}(0)$, exerted on the reference grain is found by integrating the rate of change of momentum, $f\Delta\mathbf{m}$, found by combining (7)–(11), over all possible collisions, where each is assumed to be equally probable. The result, after dropping fifth- and sixth-order products of derivatives, is

$$\mathbf{F}(0) = -\frac{64\gamma a^5}{35}[\nu_0 u_0' u_0'' + \nu_0'(u_0')^2]\left(\pi\mathbf{e}_2 + \frac{8}{3}\mathbf{e}_3\right). \tag{12}$$

The force per unit volume, $\mathbf{F}(0)$, is obtained by multiplying $\mathbf{F}(0)$ by the number density, $3\nu_0/4\pi a^3$:

$$\mathbf{F}(0) = -\frac{48\gamma a^2}{35}[\nu_0^2 u_0' u_0'' + \nu_0\nu_0'(u_0')^2]\left(\mathbf{e}_2 + \frac{8}{3\pi}\mathbf{e}_3\right) \tag{13}$$

The choice of the reference particle is arbitrary so that, in general, $\mathbf{F}(x_2)$ is given by (13) with ν, u_3, and their derivatives evaluated at x_2.

Consider now an arbitrary control volume, R, bounded by the surface S. The total force, $\Sigma\mathbf{F}$, acting on R due to the shearing is given by

$$\Sigma\mathbf{F} = \frac{-48\gamma a^2}{35}\iiint_R [\nu^2 u_{3,2}u_{3,22} + \nu\nu_{,2}(u_{3,2})^2]\left(\mathbf{e}_2 + \frac{8}{3\pi}\mathbf{e}_3\right)dR, \tag{14}$$

where the full indicial notation is again employed.

For this flow, in which only gradients in x_2 exist, (14) can be written in terms of a tensor quantity $\mathbf{T}^*$:

$$\Sigma\mathbf{F} = \iiint_R \nabla \cdot \mathbf{T}^* \, dR, \tag{15}$$

where

$$T_{22}^* = \frac{-24\gamma a^2}{35}\nu^2(u_{3,2})^2, \tag{16}$$

and

$$T^*_{23} = \frac{-64\gamma a^2}{35\pi}\nu^2(u_{3,2})^2. \tag{17}$$

By Gauss' divergence theorem, equation (15) can be rewritten

$$\Sigma\mathbf{F} = \iint_S \mathbf{n} \cdot \mathbf{T}^* \, dS, \tag{18}$$

where $\mathbf{n}$ is here the normal to the surface S. This expression is equal to the total rate of change of momentum within S due to the action of the surface forces imposing the shear. But this quantity is also identified with the surface integral of the stress, so the tensor $\mathbf{T}^*$ is seen to represent the stresses associated with collisional momentum exchange in a flowing granular material.

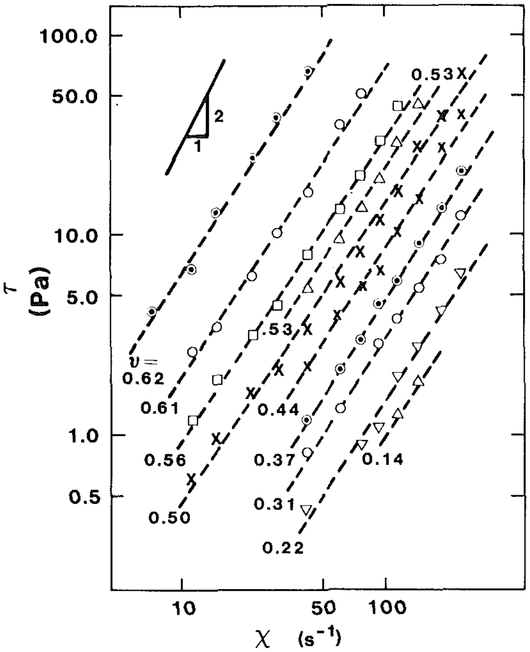

Fig. 2 Shear stress (τ) versus shear rate (χ) for various values of the volume fraction of solids. Data from Bagnold [1], for neutrally buoyant spheres in viscous fluid. Dashed lines are fit to data by eye.

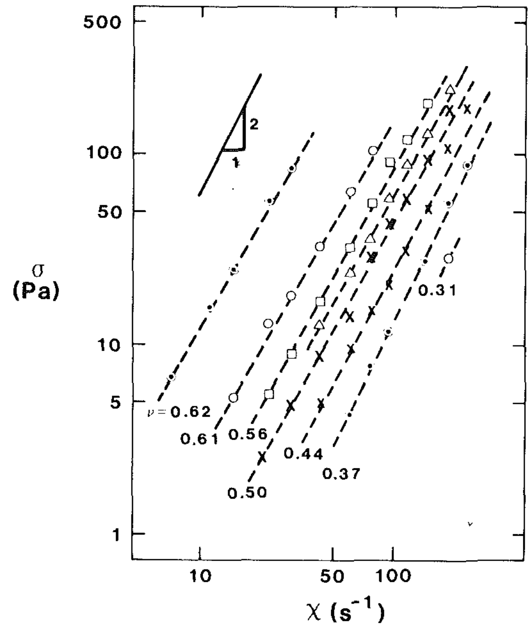

Fig. 3 Normal stress (σ) versus shear rate (χ) for various values of the volume fraction of solids. Data from Bagnold [1].

Reversing the flow direction and repeating the analysis will change the sign of the shear stress, but not that of the normal stress. Hence, (17) should be written

$$T_{23}^{*} = \frac{64\gamma a^2}{35\pi} \nu^2 \, |u_{3,2}| \, u_{3,2}. \tag{19}$$

Similar results have been obtained by Bagnold [1] and Kanatani [10]. Bagnold [1] performed extensive experimental measurements of shear and normal stresses in concentrated suspensions of neutrally buoyant spheres, assuming that the stresses arise dominantly from particle-particle interactions. His findings for the shear rate dependence are shown in Figs. 2 and 3, and show excellent agreement with the quadratic relation predicted by (16) and (19) over the entire range of shear rates tested. To examine the dependence of the stresses on ν, Bagnold's data are replotted in Fig. 4. The predicted quadratic dependence is reasonable for lower values of ν, say from $\nu \simeq 0.2$–0.4. However, at higher volume fractions, the theory is clearly not valid. This result is not surprising, for it is obvious that at very high concentrations interaction mechanisms such as multiple collisions and sliding friction become important. In fact, at some large value of ν, the grains will become "locked" and continuous deformation cannot occur. Indeed, Bagnold's data show the stresses becoming very large as ν approaches a value of approximately 0.63. An empirical modification to the predictions of (16) and (19) that is consistent with the available data may be written in the form

$$T_{22}^{*} \sim -(\nu-\nu_m)^{-2}(u_{3,2})^2, \tag{20}$$

$$T_{23}^{*} \sim (\nu-\nu_m)^{-2} \, |u_{3,2}| \, u_{3,2}, \tag{21}$$

where ν_m = maximum volume fraction for flow. The ν-dependence suggested in (20) and (21) is shown in Fig. 4. These expressions also compare favorably with the more recent data of Savage [18].

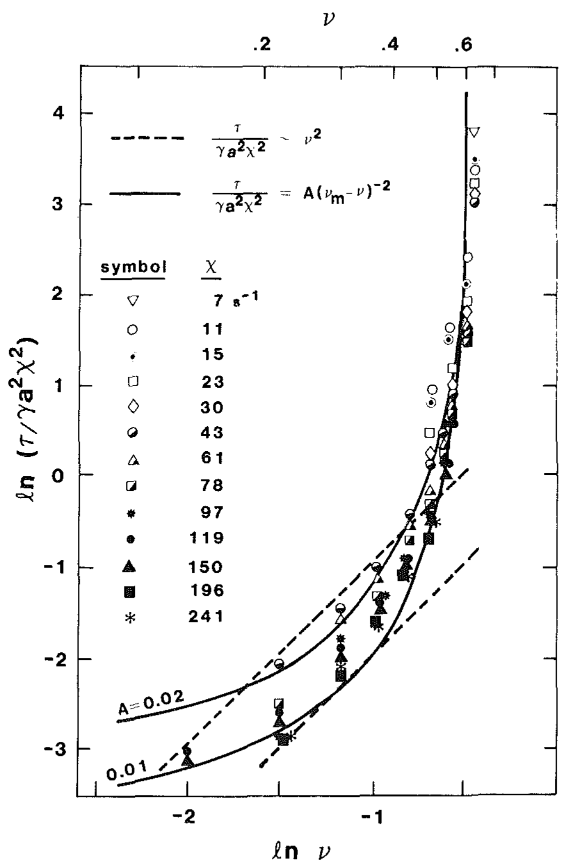

Fig. 4 Dimensionless shear stress versus volume fraction of solids. Data from Bagnold [1].

The Form of T*

A properly invariant constitutive equation is now sought such that it reduces to the form of (20) and (21) for the special case of unidirectional plane shear flow. The *principle of material indifference* [25], along with the constitutive assumption given in (5), requires that $\mathbf{T}$ be an isotropic tensor function of the symmetric tensor $\mathbf{D}$, the most general representation of which is easily shown to be

$$\mathbf{T} = f_0 \mathbf{1} + f_1 \mathbf{D} + f_2 \mathbf{D}^2, \tag{22}$$

where f_0, f_1, and f_2 are functions of ν and I, II, and III, the principal invariants of $\mathbf{D}$:

$$\mathrm{I}=tr\mathbf{D},\quad \mathrm{II}=\frac{1}{2}[(tr\mathbf{D})^2-tr\mathbf{D}^2],\quad \mathrm{III}=\det\mathbf{D}. \tag{23}$$

Equation (22) defines a Reiner-Rivlin fluid [17]. Experimental work with nonlinear fluids exhibiting normal stress effects has led most investigators to abandon constitutive equations of this form (e.g., Truesdell [24]). However, the view is adopted here that there are as yet insufficient data for granular materials to justify moving beyond the simple constitutive assumption of (5).

An expression for $\mathbf{T}^*$ that is of the form of (22) and reduces to (20) and (21) for plane shear flow is

$$\mathbf{T}^*=\eta_1(\nu-\nu_m)^{-2}\mathrm{II}'^{1/2}\mathbf{D}-\eta_2(\nu-\nu_m)^{-2}\mathbf{D}^2, \tag{24}$$

where η_1 and η_2 are non-negative material constants, and

$$\mathrm{II}'=\frac{1}{2}\mathrm{I}-\mathrm{II}=\frac{1}{2}tr\mathbf{D}^2. \tag{25}$$

Savage [19] has suggested a similar generalization of the findings of Bagnold. This choice of terms for the dissipative stress is not without some ambiguity, and is discussed in detail by Jenkins and Cowin [9] and McTigue [14].

The Form of T°

Attention is now turned toward determining an appropriate form for the equilibrium stress, $\mathbf{T}^\circ$. In particular, it is anticipated that $\mathbf{T}^\circ$ must include an isotropic thermodynamic pressure, p, and a term that allows finite shear stresses at incipient failure. This latter term is taken in a form introduced by Hohenemser and Prager [7], and is included in the function f_1 in equation (22), giving

$$\mathbf{T}^\circ=-p\mathbf{1}+\kappa\mathrm{II}'^{-1/2}\mathbf{D} \tag{26}$$

where p and κ are functions of ν, to be further discussed in the following.

In the limit, as $\mathbf{D}$ vanishes, equation (26) must give the stresses in a granular material that is everywhere at failure, here taken to correspond to the *critical state* of the soil mechanics literature. This is defined as a condition in which continuous deformation takes place under constant applied shear stress and at constant volume fraction [21]. Thus, in the critical state, $tr\,\mathbf{D}\equiv 0$.

The relationship between shear and normal stresses for granular materials at failure is well represented by the Mohr-Coulomb criterion, which is given in a familiar form for plane stress by

$$\tau=c-\sigma\tan\phi, \tag{27}$$

where τ = magnitude of critical shear stress, c = cohesion, σ = normal stress (assuming zero pore pressure), and ϕ = angle of internal friction. By requiring (26) to embody (27), and knowing p, the failure function, κ, can be determined.

Determination of $p(\nu)$. An equation of state for the thermodynamic pressure, p, under isothermal conditions is determined following Goodman and Cowin [5], leading to

$$p=\gamma\nu^2\frac{\partial\psi}{\partial\nu}, \tag{28}$$

where ψ = Helmholtz free energy per unit mass. After arguments similar to those of Goodman and Cowin [6], but neglecting constitutive dependence on $\nabla\nu$, the free energy per unit volume, $\gamma\nu\psi$, is taken in the form

$$\gamma\nu\psi=\alpha(\nu-\nu_c)^2, \tag{29}$$

which for $\alpha\geq 0$ is non-negative for all ν, and has a minimum at $\nu=\nu_c$ (see also Passman, et al. [15]). Substituting (29) into (28),

$$p=\alpha(\nu^2-\nu_c{}^2). \tag{30}$$

Note that this is identical to the form of $p(\nu)$ found empirically by Jenike [8], although he suggests that the exponent in (30) is much larger (>10).

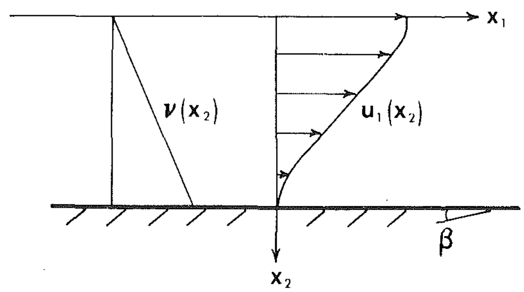

Fig. 5 Definition sketch for gravity flow

Determination of $\kappa(\nu)$. The function $\kappa(\nu)$ can now be determined. Drucker and Prager [2] have offered an invariant generalization of the Mohr-Coulomb failure criterion (27):

$$\frac{1}{3}\sin\phi J_1+J_2'^{1/2}-c\cos\phi=0, \tag{31}$$

where J_1 and J_2' are the first invariant of $\mathbf{T}^\circ$ and the second invariant of the deviatoric equilibrium stress, $\mathbf{T}^\circ-1/3(tr\mathbf{T}^\circ)\mathbf{1}$, respectively. From (26), these are given by

$$J_1=-3p+\kappa\mathrm{II}'^{-1/2}tr\mathbf{D}, \tag{32}$$

$$J_1'=\frac{1}{2}\kappa^2\mathrm{II}'^{-1}tr(\mathbf{D}'^2), \tag{33}$$

where $\mathbf{D}'=\mathbf{D}-1/3(tr\mathbf{D})\mathbf{1}$. Recalling that in the critical state $tr\,\mathbf{D}$ vanishes, (32) and (33) reduce to

$$J_1=-3p,\quad J_2'=\kappa^2. \tag{34}$$

Substituting (34) into (31), and using (30),

$$\kappa=c\cos\phi+\alpha\sin\phi\ (\nu^2-\nu_c{}^2). \tag{35}$$

A similar form has been derived by Kanatani [11], departing from an associated flow rule in plasticity theory. Finally, collecting (26), (30), and (35),

$$\mathbf{T}^\circ=-\alpha(\nu^2-\nu_c{}^2)\mathbf{1}+[c\cos\phi$$
$$+\alpha\sin\phi(\nu^2-\nu_c{}^2)]\mathrm{II}'^{-1/2}\mathbf{D}. \tag{36}$$

It is noted here that (36) is consistent with the observation (e.g., [21]) that the specific volume $(1/\nu)$ of a granular material in the critical state decreases nonlinearly with increasing confining stress.

Gravity Flow

The boundary value problem for steady flow of a cohesionless ($c=0$) granular material down a slope is now considered (Fig. 5). The momentum balance (3) reduces to

$$0=T_{21,2}+\gamma\nu g\sin\beta, \tag{37}$$

$$0=T_{22,2}+\gamma\nu g\cos\beta, \tag{38}$$

where β = slope. From (24) and (36), the stress components of interest are

$$T_{21}=-\alpha\sin\phi(\nu^2-\nu_c{}^2)-\eta_1(\nu_m-\nu)^{-2}(u_{1,2})^2, \tag{39}$$

$$T_{22}=-\alpha(\nu^2-\nu_c{}^2)-\eta_2(\nu_m-\nu)^{-2}(u_{1,2})^2, \tag{40}$$

having accounted for the particular choice of coordinates shown in Fig. 5 in writing the second term in (39).

Substituting (39) and (40) into (37) and (38) and nondimensionalizing with respect to a characteristic velocity U and the flow depth d, the equations of motion are

$$0=-N_1\sin\phi\nu\nu_{,2}-N_2N_3[(\nu_m-\nu)^{-2}(u_{1,2})^2]_{,2}$$
$$+N_4\nu\sin\beta, \tag{41}$$

$$0 = -N_1 \nu \nu_{,2} - N_3 [(\nu_m - \nu)^{-2} (u_{2,1})^2]_{,2} + N_4 \nu \cos\beta, \tag{42}$$

where u_1 and x_2 are now dimensionless, and

$$N_1 = \frac{2\alpha}{\gamma U^2},\ N_2 = \frac{\eta_1}{\eta_2},\ N_3 = \frac{\eta_2}{\gamma d^2},\ N_4 = \frac{gd}{U^2}. \tag{43}$$

The appropriate boundary conditions for the free surface are, from (39) and (40),

$$\nu(0) = \nu_c, \tag{44}$$

$$u_{1,2}(0) = 0. \tag{45}$$

A no-slip condition is assumed at the bed:

$$u_1(1) = 0. \tag{46}$$

The last condition has been substantiated experimentally for a sufficiently rough boundary [19].

The terms in the velocity gradient are easily eliminated between (41) and (42), giving an uncoupled equation for the volume fraction. Integrating and using (44),

$$\nu = \nu_c + \Gamma x_2. \tag{47}$$

where

$$\Gamma = \frac{N_4}{N_1} \frac{N_2 \cos\beta - \sin\beta}{N_2 - \sin\phi} \tag{48}$$

Thus, the volume fraction of solids simply increases linearly downward through the flowing layer at a rate that decreases with increasing bed slope, β. At the critical slope, $\beta_c = \tan^{-1}(\eta_1/\eta_2)$, Γ vanishes and the volume fraction of solids is uniform across the flow.

Recalling that ν cannot exceed the maximum value ν_m, equation (47), in dimensional form, gives a maximum flow depth, d_m, for any fixed flow conditions:

$$d_m = \frac{2\alpha}{\gamma g \cos\beta} \frac{\dfrac{\eta_1}{\eta_2} - \sin\phi}{\dfrac{\eta_1}{\eta_2} - \tan\beta} (\nu_m - \nu_c). \tag{49}$$

A similar observation has been made by Savage [19]. Note that as $\tan\beta$ approaches the maximum value η_1/η_2, d_m becomes unbounded.

Finally, (47) is substituted into (42), and integration applying (45) and (46) yields:

$$u_1 = \frac{2}{3} N_5^{1/2} [F_1(x_2)^3 - F_1(1)^3] - \frac{\nu_m N_5^{1/2}}{2\Gamma} \Big[F_1(x_2) F_2(x_2) - F_1(1) F_2(1) - \frac{\nu_c^2}{\Lambda} \ln \frac{\Lambda F_1(x_2) + F_2(x_2)}{\Lambda F_1(1) + F_2(1)} \Big], \tag{50}$$

where $F_1 = (\nu_c x_2 + 1/2 \Gamma x_2^2)$, $F_2 = \nu_c + \Gamma x_2$, $\Lambda = (2\Gamma)^{1/2}$, and $N_5 = (N_4 \cos\beta - N_1 \Gamma)/N_3$. This result is shown in Fig. 6, normalized to the surface velocity, u_s, for various values of ν_c and Γ, assuming $\nu_m = 0.63$. Note that (47) requires $\Gamma \le \nu_m - \nu_c$, a limit accounted for in Fig. 6. For increasing slope, Γ goes from its minimum value $\Gamma = \nu_m - \nu_c$ to zero, and the velocity profile becomes fully convex downstream, losing the inflection point near the bed. Consideration of (39) reveals that as ν approaches ν_m, the velocity gradient must vanish in order that the shear stress remain finite, resulting in the inflection in the velocity profile. For $\Gamma = 0$, ν is uniform, and the velocity gradient need not vanish near the bed. Note that because of the change in bulk density across the flow (47), the shear stress distribution is, in general, nonlinear.

The velocity profile (50) is more easily visualized through several limiting cases of interest. First, consider flow at the critical maximum slope, for which Γ vanishes (48) and ν becomes uniform (47). Integrating the resulting equation of motion, applying the boundary conditions, and normalizing to the free surface velocity gives

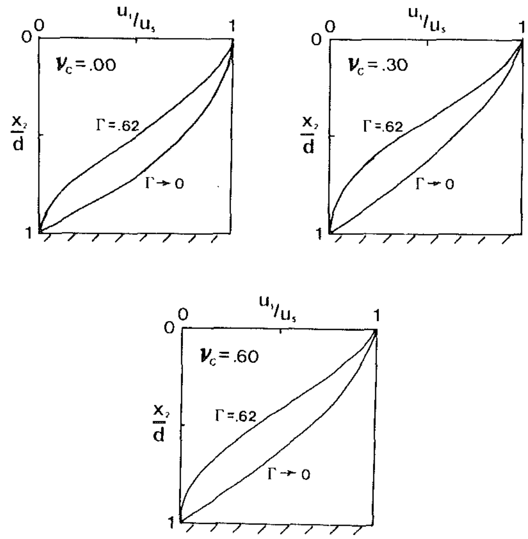

Fig. 6 Velocity profiles for gravity flow (50), normalized to surface velocity, u_s. Maximum Γ corresponds to minimum bed slope, vanishing Γ to maximum slope. Value $\nu_m = 0.63$ used in calculations.

$$\frac{u_1}{u_s} = 1 - x_2^{3/2}, \tag{51}$$

shown in Fig. 7. This is precisely the velocity field found by Bagnold [1]. Thus, his result emerges as a special case of the model presented here that can be obtained at only one slope.

A second special case is for flows at the maximum depth (49). In this case, $\Gamma = \nu_m - \nu_c$, and (42) can be integrated at once to give

$$u_{1,2} = -N_5 (\nu_m - \nu_c) [\nu_c x_2 + \frac{1}{2} (\nu_m - \nu_c) x_2^2](1 - x_2). \tag{52}$$

It is immediately apparent that the velocity gradient vanishes both at the free surface ($x_2 = 0$) and at the base of the flow ($x_2 = 1$). The effect of different values of ν_c can now be examined. The possible extreme values are $\nu_c \to 0$, for which

$$\frac{u_1}{u_s} = 3(1 - x_2^2) - 2(1 - x_2^3), \tag{53}$$

and $\nu_c \to \nu_m$, for which

$$\frac{u_1}{u_s} = \frac{5}{2}(1 - x_2^{3/2}) - \frac{3}{2}(1 - x_2^{5/2}), \tag{54}$$

shown in Fig. 7. In the latter case, of course, the flow depth becomes vanishingly small (49) and the entire flow is arrested.

Savage [18, 19] has performed a series of elegant experiments to measure velocity profiles in gravity flows of granular materials. He used polystyrene beads with a mean diameter of 1.22 mm and a specific gravity of 1.03, in a channel 3.86 cm wide with smooth side walls and a rough bottom. Velocities were measured at the side wall by means of fiber-optic probes. Steady flows of about 1.5 cm depth were obtained on slopes between 30 deg and 40 deg with surface velocities on the order of 100 cm/s. The no-slip condition was verified by extrapolation of measured velocities near the bed.

There is substantial qualitative agreement of the theoretical velocity field (50) with the results of Savage. The measured profiles exhibit inflections, with the gradient becoming small near the bed. The profiles become fuller for increasing slope, corresponding to increasing Γ in the theory. Again, this is the behavior predicted by (50).

Summary and Discussion

A constitutive equation for flowing granular materials has been posed that consists of an equilibrium part, of zero order in the rate of deformation, $\mathbf{D}$, and a dissipative part that vanishes as $\mathbf{D}$ vanishes. The equilibrium part, $\mathbf{T}^{\circ}$, includes a thermodynamic pressure and a failure term. The latter is determined by assuming that in the limit as $\mathbf{D} \rightarrow 0$, $\mathbf{T}^{\circ}$ must give the stresses in a Coulomb material at failure. A nonlinear representation for the dissipative stress is motivated by a simple model for collisional momentum exchange in a plane shear flow and by available experimental data. The model predicts both shear and normal stresses that are quadratic in the rate of deformation, because the change in momentum per collision and the collision rate are each proportional to the velocity gradient.

Since this work was completed, Savage and Jeffrey [20] have presented results for a statistical mechanical analysis of collisional momentum exchange in which the fluctuating motion of the particles about their mean translation is explicitly accounted for. The mean shearing gives rise to shear and normal stresses quadratic in the velocity gradient, as discussed in the foregoing. The fluctuating part of the particle motion gives rise to an isotropic normal stress independent of the mean shearing, giving motivation to the pressure, p, introduced here. Note, however, that the volume fraction dependence predicted by the more complete analysis of Savage and Jeffrey [20] is different. In the limit of small ν, they obtain stresses linear in ν, whereas the model presented here predicts ν^2 dependence [equations (16) and (19)]. At larger ν, their results are more realistic and predict magnitudes consistent with experimentally measured stresses.

The boundary value problem for gravity flow predicts that the volume fraction of solids increases linearly downward through the flowing layer. The flow thickness is thus limited to the depth at which ν reaches the maximum value for which continuous deformation can occur. The downward increase in ν is less rapid with increasing slope, until at a critical slope ν is uniform, and the maximum flow thickness is unlimited.

Near the minimum slope, the velocity profile exhibits an inflection near the bed, because the velocity gradient must vanish as ν increases in order that the stresses remain finite. As the slope approaches its maximum value for steady flow, and the grains are dilated across the entire layer, the velocity profile becomes fully convex downstream.

Of particular interest in this model is the prediction of normal stresses, which have been noted experimentally by Bagnold [1] and Savage [19]. In the gravity flow problem, a nonuniform gradient of the normal stress balances the normal component of the body force (42), resulting in variation of ν across the flowing layer. Other normal stress effects can be anticipated in granular materials, particularly in three-dimensional flow. Indeed, Savage [19] has observed secondary flows in a rectangular channel (cf. Green and Rivlin [6]).

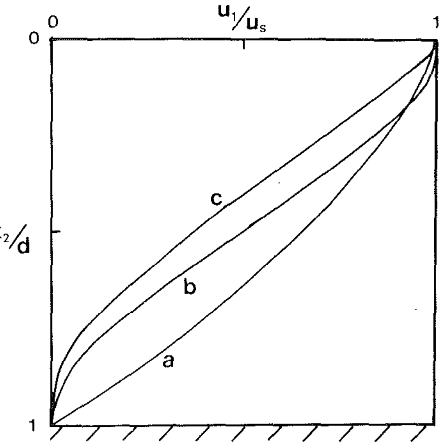

Fig. 7 Velocity profiles for special cases. a: $\Gamma = 0$, ν uniform. b: $\Gamma = \nu_m - \nu_c$, $\nu_c \rightarrow 0$. c: $\Gamma = \nu_m - \nu_c$, $\nu_c \rightarrow \nu_m$.

Acknowledgments

The author wishes to thank J. T. Jenkins for invaluable discussion. Acknowledgment is made to the donors of the Petroleum Research Fund, administered by the American Chemical Society, for the support of this research.

References

1 Bagnold, R. A., "Experiments on Gravity-Free Dispersion of Large Solid Spheres in a Newtonian Fluid Under Shear," *Proceedings of the Royal Society of London*, Series A, Vol. 225, 1954, pp. 49-63.

2 Drucker, D. C., and Prager, W., "Soil Mechanics and Plastic Analysis or Limit Design," *Quarterly of Applied Mathematics*, Vol. 10, 1952, pp. 157-165.

3 Goodman, M. A., *A Continuum Theory for the Dynamical Behavior of Granular Materials*, Ph.D. dissertation, Tulane University, New Orleans, 1970.

4 Goodman, M. A., and Cowin, S. C., "Two Problems in the Gravity Flow of Granular Materials," *Journal of Fluid Mechanics*, Vol. 45, 1971, pp. 321-339.

5 Goodman, M. A., and Cowin, S. C., "A Continuum Theory for Granular Materials," *Archive for Rational Mechanics and Analysis*, Vol. 44, 1971/1972, pp. 249-266.

6 Green, A. E., and Rivlin, R. S., "Steady Flow of Non-Newtonian Fluids Through Tubes," *Quarterly of Applied Mathematics*, Vol. 14, 1956, pp. 299-308.

7 Hohenemser, K., and Prager, W., "Uber die Ansatze der Mechanik Isotroper Kontinua," *Zeitschrift für Angewandte Mathematik*, Vol. 12, 1932, pp. 216-226.

8 Jenike, A. W., "Steady Gravity Flow of Frictional-Cohesive Solids in Converging Channels," ASME Journal of Applied Mechanics, Vol. 86, 1964, pp. 5-11.

9 Jenkins, J. T., and Cowin, S. C., "Theories for Flowing Granular Materials," in: Cowin, S. C., ed., *Mechanics Applied to the Transport of Bulk Materials*, Applied Mechanics Division, ASME, AMD 31, 1979, pp. 79-90.

10 Kanatani, K., "A Micropolar Continuum Theory for the Flow of Granular Materials," *International Journal for Engineering Science*, Vol. 17, 1979, pp. 419-432.

11 Kanatani, K., "A Plasticity Theory for the Kinematics of Granular Materials," to appear.

12 Mandl, G., and Fernandez-Luque, R., "Fully Developed Plastic Flow of Granular Materials," *Geotechnique*, Vol. 20, 1970, pp. 277-307.

13 McTigue, D. F., "A Model for Stresses in Shear Flow of Granular Materials," in: Cowin, S. C., and Satake, M., eds., *Proceedings of the U.S.-Japan Seminar on Continuum Mechanical and Statistical Approaches in the Mechanics of Granular Materials*, Gakujutsu Bunken Fukyu-kai, Tokyo, 1978, pp. 258-265.

14 McTigue, D. F., *A Nonlinear Continuum Model for Flowing Granular Materials*, Ph. D. dissertation, Stanford University, Palo Alto, 1979.

15 Passman, S. L., Nunziato, J. W., Baily, P. B., and Thomas, J. P., Jr., "Shearing Flow of Granular Materials," *Journal of the Engineering Mechanics Division*, ASCE, Vol. 106, 1980, pp. 773-783.

16 Reynolds, O., "On the Dilatancy of Media Composed of Rigid Particles in Contact," *Philosophical Magazine*, Fifth Series, 1885, pp. 469-481.

17 Rivlin, R. S., "The Hydrodynamics of Non-Newtonian Fluids," *Proceedings of the Royal Society of London*, Series A, Vol. 193, 1948, pp. 260-281.

18 Savage, S. B., "Experiments on Shear Flow of Cohesionless Granular Materials," in: Cowin, S. C., and Satake, M., eds., *Proceedings of the U.S.-Japan Seminar on Continuum Mechanical and Statistical Approaches in the Mechanics of Granular Materials*, Gatujutsu Bunken Fukyu-kai, Tokyo, 1978, pp. 241-254.

19 Savage, S. B., "Gravity Flow of Cohesionless Granular Materials in Chutes and Channels," *Journal of Fluid Mechanics*, Vol. 92, 1979, pp. 53-96.

20 Savage, S. B., and Jeffrey, D. J., "The Stress Tensor in a Granular Flow at High Shear Rates," *Journal of Fluid Mechanics*, to appear.

21 Schofield, A., and Wroth, P., *Critical State Soil Mechanics*, McGraw-Hill, New York, 1968, p. 310.

22 Shield, R. T., "Stress and Velocity Fields in Soil Mechanics," *Journal of Mathematical Physics*, Vol. 33, 1955, pp. 144-156.

23 Spencer, A. J. M., "A Theory of the Kinematics of Ideal Soils Under Plane Strain Conditions," *Journal of the Mechanics and Physics of Solids*, Vol. 12, 1964, pp. 337-351.

24 Truesdell, C., "Second Order Effects in the Mechanics of Materials," in: Reiner, M., and Abir, D., eds., *Second Order Effects in Elasticity, Plasticity, and Fluid Dynamics*, Macmillan, New York, 1964, pp. 1-50.

25 Truesdell, C., and Noll, W., "The Non-Linear Field Theories of Mechanics," *Handbuch der Physik*, Vol III/3, Springer, Berlin, 1965.

Creep and Plastic Strains of 304 Stainless Steel at 593°C Under Step Stress Changes, Considering Aging

U. W. Cho
Assistant Professor of
Mechanical and Aerospace Engineering,
University of Missouri-Columbia,
Columbia, Mo. 65211
Assoc. Mem. ASME

W. N. Findley
Professor of Engineering,
Brown University
Providence, R.I. 02912
Fellow ASME

Nonlinear constitutive equations for varying stress histories are developed and used to predict the creep behavior of 304 stainless steel at 593°C (1100°F) under variable tension or torsion stresses including reloading, complete unloading, step-up, and step-down stress changes. The strain in the constitutive equations (a viscous-viscoelastic model) consists of: linear elastic, time-independent plastic, time-dependent-recoverable viscoelastic, and time-dependent-nonrecoverable viscous components. For variable stressing, the modified superposition principle, derived from the multiple integral representation, and the strain hardening theory were used to represent the recoverable and nonrecoverable components, respectively, of the time-dependent strain. Time-independent plastic strains were described by a flow rule of similar form to that for nonrecoverable, time-dependent strains. The material constants of the theory were determined from constant stress creep and creep recovery data. Considerable aging effects were found and the effects on the strain components were incorporated in each strain predicted by the theory. Some modifications of the theory for the viscoelastic strain component under step-down stress changes were made to improve the predictions. The final predictions combining the foregoing features made satisfactory agreements with the experimental creep data under step stress changes.

Introduction

The need for experimental creep studies under multiaxial stresses varying with time has been emphasized [1, 2]. Advanced theories proposed suffer from a lack of experimental data to evaluate them.

The experimental work in this field was reviewed in reference [3]. Preliminary study of 304 stainless steel (reference heat 9T2796) at 593°C (1100°F) was reported in [4]. A study of the microstructure of the same reference heat of 304 stainless steel over a wide range of temperature and stress was reported in [5–7]. In recent papers [8, 9] creep and creep recovery data of the same 304 stainless steel was analyzed by using a viscous-viscoelastic model in which the strain was resolved into four components; elastic ϵ^E, time-independent plastic ϵ^P, time-dependent recoverable viscoelastic ϵ^{VE}, and time-dependent-nonrecoverable viscous strain ϵ^V. Also, considerable aging effects were found [9]. From creep and creep recovery experiments under combined tension and torsion, the time and stress dependence of these components was evaluated for constant stress.

In this paper, constitutive equations for changes in state of combined tension and torsion are developed and used to predict, from the relations determined from constant stress tests in [8, 9], the creep and plastic behavior under abrupt step-up and step-down changes in tension or torsion including reloading and complete unloading. The results are compared with experiments reported in this paper.

Future work will consider abrupt changes in the state of combined tension and torsion, and stress reversal in torsion with or without constant tension.

Material, Specimen, Apparatus, and Procedure

Type 304 stainless steel (reference heat no. 9T2796), supplied by Oak Ridge National Laboratory, was reannealed and tested at 593°C (1100°F). The melting temperature was about 1407°C (2565°F). A more complete description of material and specimens is given in [4, 8, 9]. The combined tension and torsion machine used for these experiments was described in [10]. Some modifications for high temperature use were described in [8]. The testing procedure was described in [8, 9].

Experimental Results

Nine creep experiments including pure tension and pure torsion under step stress changes are shown in Figs. 1–9. The loading programs and resulting total strain-time data as measured are also shown as inserts in Figs. 1–9.

Figure 1 shows the results of a pure-tension creep ex-

Contributed by the Applied Mechanics Division for publication in the Journal of Applied Mechanics.

Discussion on this paper should be addressed to the Editorial Department, ASME, United Engineering Center, 345 East 47th Street, New York, N.Y. 10017, and will be accepted until two months after final publication of the paper itself in the Journal of Applied Mechanics. Manuscript received by ASME Applied Mechanics Division, May, 1981; final revision, December, 1981.

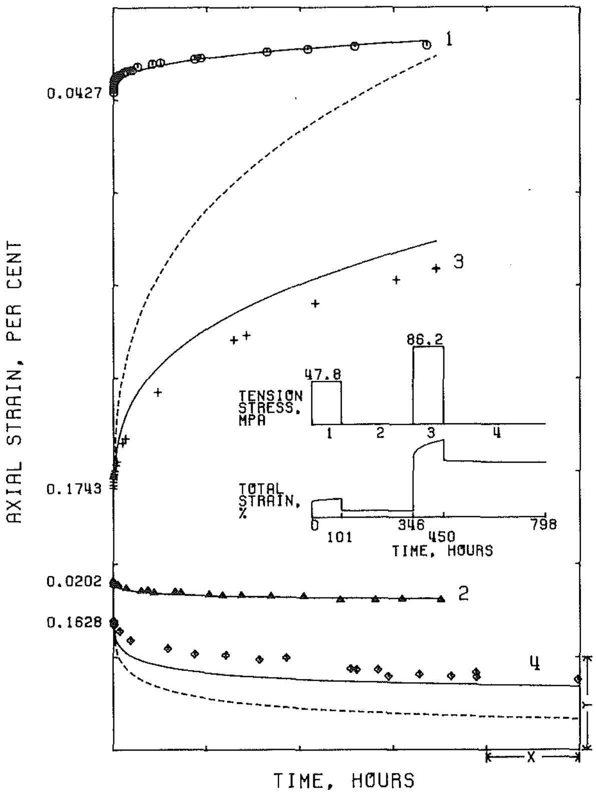

Fig. 1 Test no. A43. Axial creep strain for pure tension creep of 304 stainless steel at 593°C under complete unloading and reloading. Numbers 1-4 indicate periods on insert. Scales are $X = 30$h, $Y = 0.02$ percent for periods 1 and 3, and $X = 70$h, $Y = 0.01$ percent for periods 2 and 4.

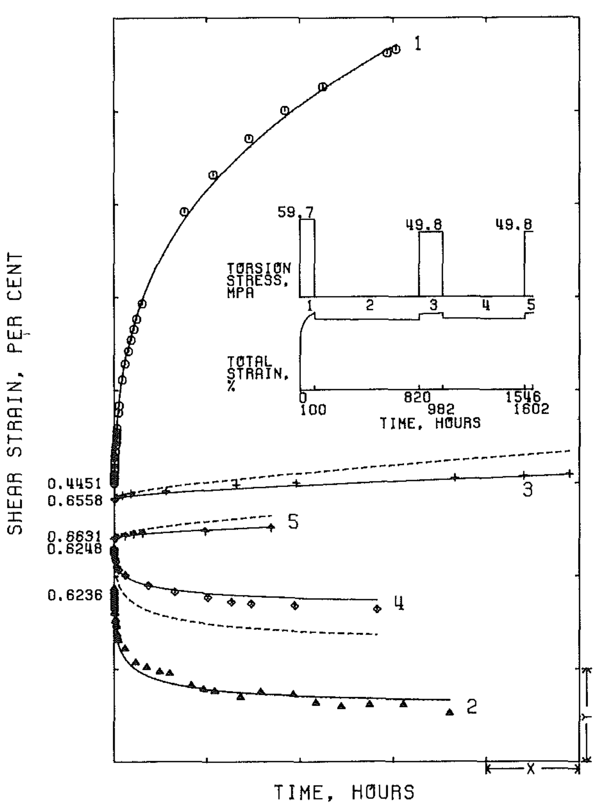

Fig. 2 Test no. T29. Shear creep strain for pure torsion creep of 304 stainless steel at 593°C under complete unloading and reloading. Numbers 1-5 indicate periods on insert. Scales are $X = 33$h, $Y = 0.05$ percent for periods 1,3, and 5, and $X = 200$h, $Y = 0.01$ percent for periods 2 and 4.

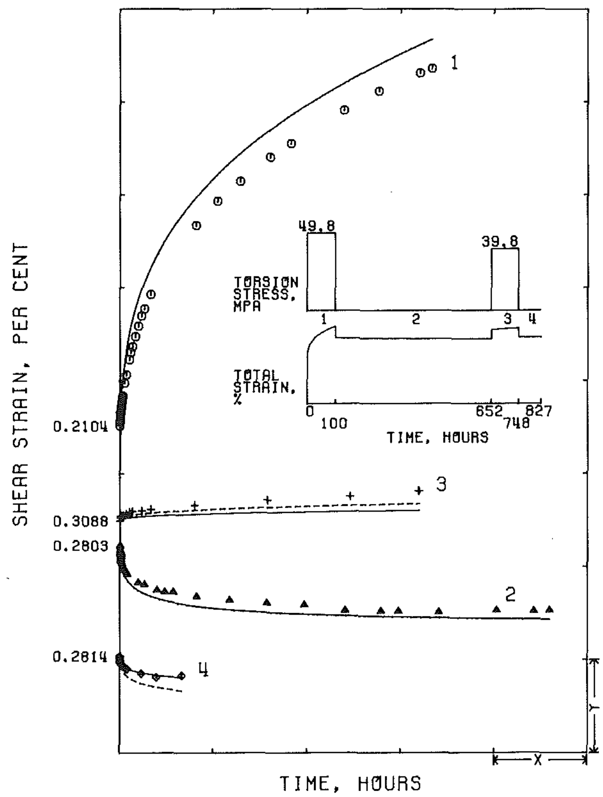

Fig. 3 Test no. T32. Shear creep strain for pure torsion creep of 304 stainless steel at 593°C under complete unloading and reloading. Numbers 1-4 indicate periods on insert. Scales are $X = 30$h, $Y = 0.03$ percent for periods 1 and 3, and $X = 120$h, $Y = 0.01$ percent for periods 2 and 4.

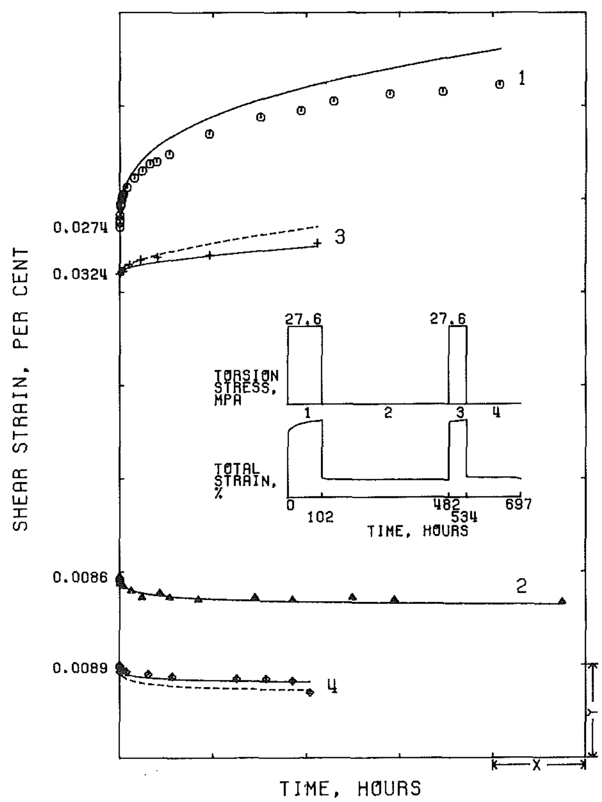

Fig. 4 Test no. T35. Shear creep strain for pure torsion creep of 304 stainless steel at 593°C under complete unloading and reloading. Numbers 1-4 indicate periods on insert. Scales are $X = 25$h, $Y = 0.04$ percent for periods 1 and 3, and $X = 80$h, $Y = 0.004$ percent for periods 2 and 4.

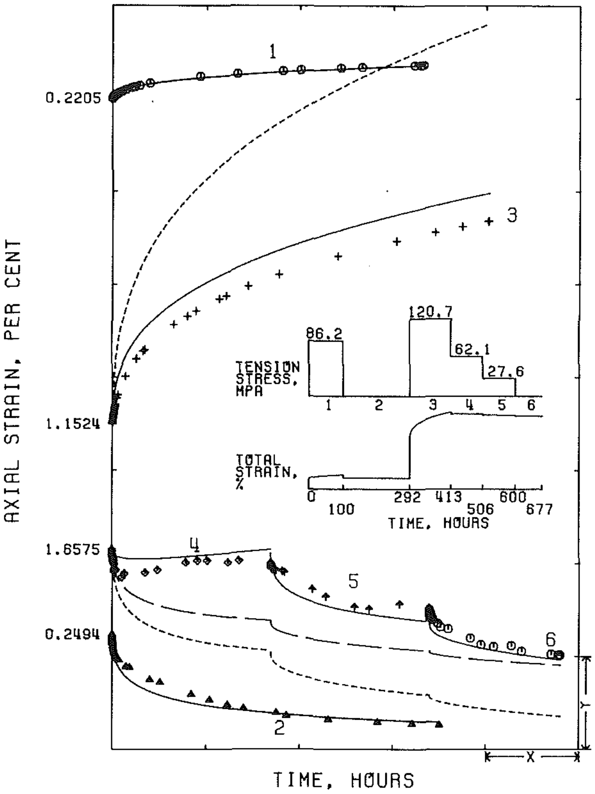

Fig. 5 Test no. A38. Axial creep strain for pure tension creep of 304 stainless steel at 593°C under step-down stress changes following complete unloading and reloading. Numbers 1-6 indicate periods on insert. Scales are X = 30h, Y = 0.25 percent for periods 1 and 3, and X = 55h, Y = 0.01 percent for periods 2 and 4-6.

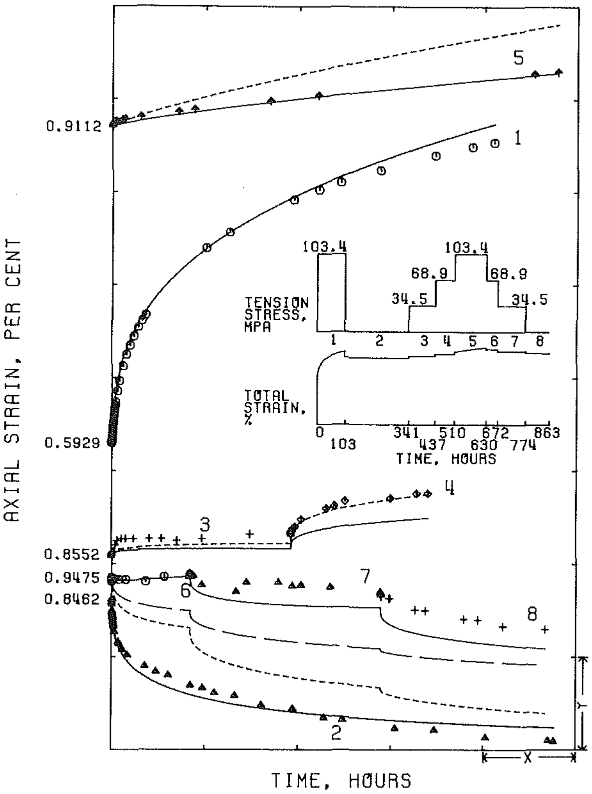

Fig. 6 Test no. A39. Axial creep strain for pure tension creep of 304 stainless steel at 593°C under step-up and step-down stress changes following complete unloading. Numbers 1-8 indicate periods on insert. Scales are X = 25h, Y = 0.1 percent for periods 1 and 5, and X = 50h, Y = 0.01 percent for periods 2-4 and 6-8.

periment and Figs. 2–4 show pure torsion experiments. These include complete unloading and reloading to a higher stress or lower stress than the first loading or the same stress, followed by complete unloading.

Figures 5–9 show the results of pure tension (Figs. 5–7) or pure torsion (Figs. 8, 9) experiments consisting of multiple step changes of stress. The step changes included several steps of reloading and partial unloading or partial unloading and reloading followed by complete unloading.

It is noted that periods 1 and 2 (creep and creep recovery data) of all the tests shown in Figs. 1–9 except test T47 (Fig. 8) were used to determine the constants of the constitutive equations at constant stresses in [8, 9].

Constitutive Equations for Constant Stress

By a viscous-viscoelastic model [8, 9] the total creep strain at constant stress was represented by the sum of four components; an elastic strain, ϵ_{ij}^E, a plastic strain, ϵ_{ij}^P, a viscoelastic strain, ϵ_{ij}^{VE}, and a viscous strain, ϵ_{ij}^V

$$\epsilon_{ij} = \epsilon_{ij}^E + \epsilon_{ij}^P + \epsilon_{ij}^{+VE} t^n + \epsilon_{ij}^{+V} t^n, \tag{1}$$

where ϵ_{ij}^E, ϵ_{ij}^P, ϵ_{ij}^{+VE}, and ϵ_{ij}^{+V} are all functions of stress. The time-dependent components, ϵ_{ij}^{VE} and $_{ij}^{V}$ were well described by a power function of time with a constant exponent n for both components [8, 9].

The stress dependence of ϵ_{ij}^P, ϵ_{ij}^{+VE}, and ϵ_{ij}^{+V} was described by a third-order multiple integral representation [11]. Incorporating the concept of limit stresses, the relation yielded the following forms for axial and shear creep strain under constant pure tension and pure torsion, respectively [8],

$$\epsilon_{11} = F(\sigma) = F_1(\sigma - \sigma^*) + F_2(\sigma - \sigma^*)^2 + F_3(\sigma - \sigma^*)^3, \tag{2}$$

$$\epsilon_{12} = G(\tau) = G_1(\tau - \tau^*) + G_2(\tau - \tau^*)^3, \tag{3}$$

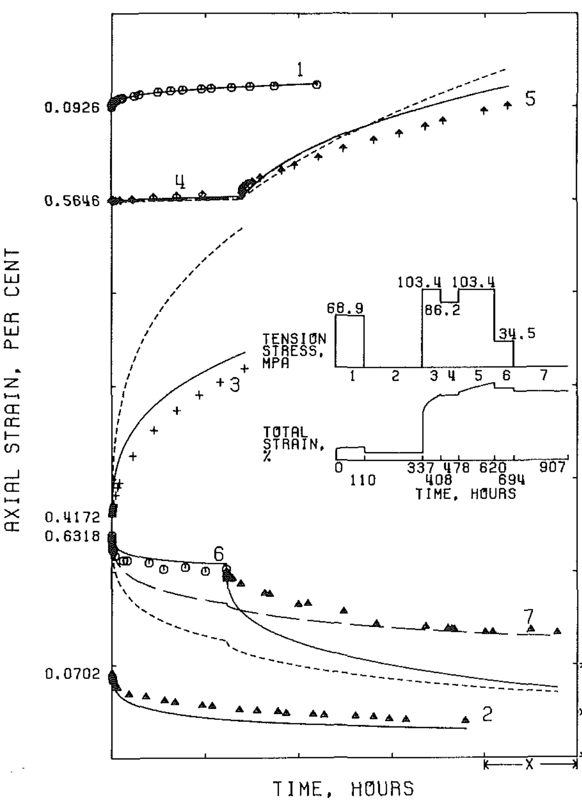

Fig. 7 Test no. A40. Axial creep strain for pure tension creep of 304 stainless steel at 593°C under mixed step-up and step-down stress changes following complete unloading. Numbers 1-7 indicate periods on insert. Scales are X = 50h, Y = 0.1 percent for periods, 3–5, and X = 60h, Y = 0.01 percent for periods 2, 6, and 7.

where ϵ_{ij}, F_i, and G_i assume superscripts P, VE, or V according to whether plastic, P, viscoelastic, VE, or viscous, V, strains are being described; where σ^*, τ^*were the yield limits for ϵ_{ij}^P and creep limits for ϵ_{ij}^{+VE} and ϵ_{ij}^{+V}; and where $F(\sigma) = G(\tau) = 0$, for $-\sigma^* \le \sigma \le \sigma^*$, $-\tau^* \le \tau \le \tau^*$. The values σ^* and τ^* had a Mises' relation, i.e., $\sigma^* = \sqrt{3}\,\tau^*$, and different values for each component. The values of σ^* and τ^* and material constants F_i and G_i were determined as given in Table 1 of reference [8]. Superscripts P, VE, and V were used to identify the constants for ϵ_{ij}^P, ϵ_{ij}^{+VE}, ϵ_{ij}^{+V}, respectively.

Recent experimental results [9] at low stresses (below the creep limits) showed that the time-dependent creep strain ϵ_{ij}^{VE} and ϵ_{ij}^{V} were not negligible, particularly at stress levels just below the creep limits. They had linear stress-strain relations up to stresses somewhat above the creep limits found in [8]. For convenience of representation, transition points σ^T or τ^T were introduced to divide the high stress region described by equations (2) and (3) and the low stress region described by linear relations as follows,

$$\epsilon_{11} = F(\sigma) = F_0\sigma, \quad \sigma < \sigma^T, \tag{4}$$

$$\epsilon_{12} = G(\tau) = G_0\tau, \quad \tau < \tau^T, \tag{5}$$

where the values of F_0, G_0, σ^T, and τ^T for ϵ_{ij}^{+VE} and ϵ_{ij}^{+V} were determined as shown in the text of reference [9].

Constitutive Equations for Variable Stress

Plastic Strain, ϵ_{ij}^P: The instantaneous response (time-independent strain) at each stress change in Figs. 1-9 consisted of the sum of the elastic strain ϵ_{ij}^E, and the plastic strain, ϵ_{ij}^P. The plastic strain occurs on initial loading when the stress level is above the yield limit as described in equations (2) and (3). On subsequent loading, plastic strain was considered to occur only when the stress was larger than the maximum of the previous stresses. The new plastic strain increment was determined as the amount of ϵ^P given by equation (2) or (3) minus the accumulated plastic strain up to that time of loading. That is, the stress-strain curve given by equation (2) or (3) was a flow rule for variable stresses under pure tension or pure torsion. For unloading or reloading to stresses less than the maximum of the previous stresses, only elastic strain was produced, a fact that was well supported by the experimental results. For a review of plastic strain determination see reference [13].

Viscoelastic Strain, ϵ_{ij}^{VE}: By the modified superposition principle (MSP) [11, 12] the viscoelastic strain for a varying stress is given by

$$\epsilon = \int_0^t \frac{\partial f[\sigma(\xi), t-\xi]}{\partial \sigma(\xi)}\,\dot{\sigma}(\xi)\,d\xi, \tag{6}$$

where the strain at constant stress is given by $\epsilon = f(\sigma, t)$.

For a series of m steps in stress as in the present test programs, the strain was described by the following form from equation (6)

$$\begin{aligned}\epsilon_{11}^{VE} &= F^{VE}(\sigma_1)[t^n - (t-t_1)^n] + \ldots \\ &\quad + F^{VE}(\sigma_{m-1})[(t-t_{m-2})^n - (t-t_{m-1})^n] \\ &\quad + F^{VE}(\sigma_m)(t-t_{m-1})^n, \; t_{m-1} < t.\end{aligned} \tag{7}$$

Similarly, ϵ_{12}^{VE} was obtained by replacing $F^{VE}(\sigma)$ by $G^{VE}(\tau)$ in equation (7).

Viscous Strain, ϵ_{ij}^{V}: The nonrecoverable (viscous) strain was described by a strain-hardening theory (SH). The (SH) relation for variable stresses has the following form for axial strain [14],

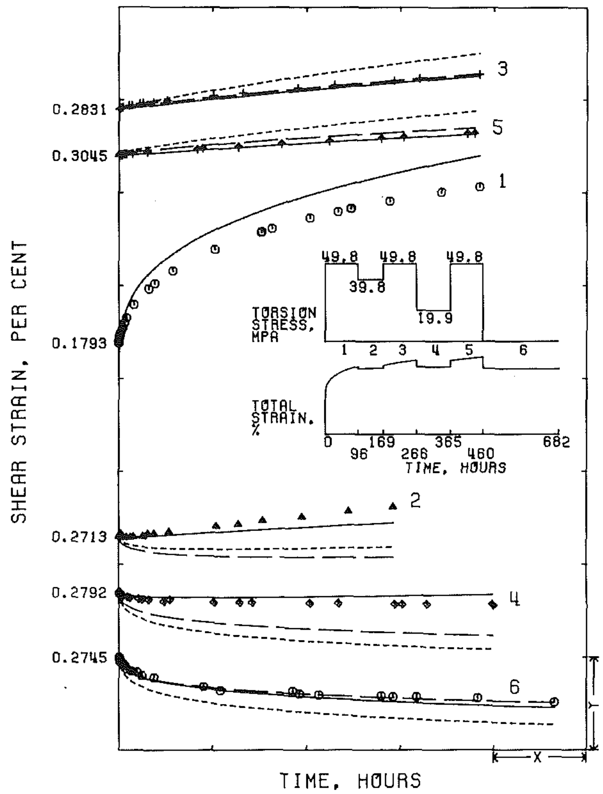

Fig. 8 Test no. T45. Shear creep strain for pure torsion creep of 304 stainless steel at 593°C under mixed step-up and step-down stress changes followed by complete unloading. Numbers 1-6 indicate periods on insert. Scales are X = 25h, Y = 0.06 percent for periods 1, 3, and 5, and X = 25h, Y = 0.01 percent for periods 2, 4, and 6.

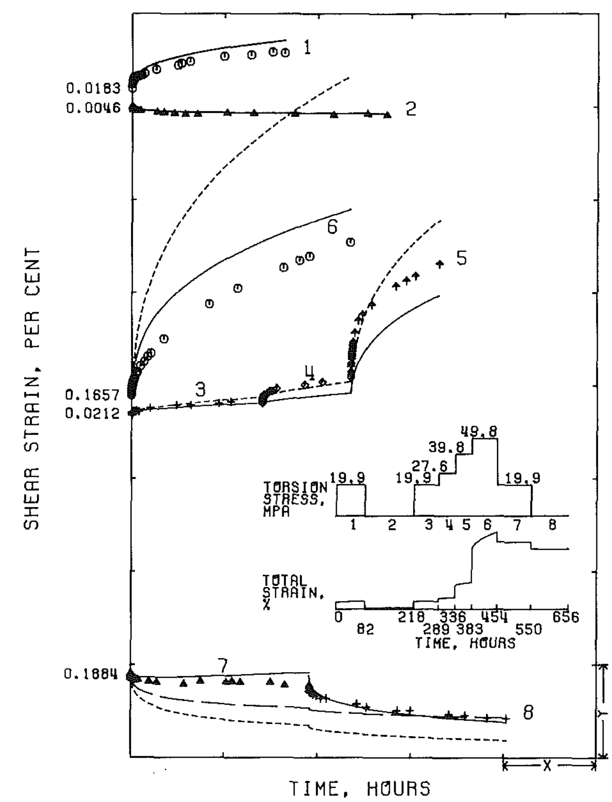

Fig. 9 Test no. T47. Shear creep strain for pure torsion creep of 304 stainless steel at 593°C under step-up and step-down stress changes following complete unloading. Numbers 1-8 indicate periods on insert. Scales are X = 50h, Y = 0.01 percent for periods 1-5, 7, and 8, and X = 30h, Y = 0.03 percent for period 6.

Table 1 Total time-independent strain data

Test (Fig. no.)	Period	Stress, σ or τ MPa	Stress, σ or τ ksi	Strain, percent
A43 (Fig. 1)	1	47.8	6.928	0.0434
	2	−47.8	−6.928	−0.0325
	3	86.2	12.5	0.1558
	4	−86.2	−12.5	−0.0585
T29 (Fig. 2)	1	59.7	8.66	0.4147
	2	−59.7	−8.66	−0.0541
	3	49.8	7.217	0.0448
	4	−49.8	−7.217	−0.0447
	5	49.8	7.217	0.0448
T32 (Fig. 3)	1	49.8	7.217	0.1940
	2	−49.8	−7.217	−0.0450
	3	39.8	5.773	0.0355
	4	−39.8	−5.773	−0.0368
T35 (Fig. 4)	1	27.6	4.0	0.0272
	2	−27.6	−4.0	−0.0268
	3	27.6	4.0	0.0249
	4	−27.6	−4.0	−0.0248
A38 (Fig. 5)	1	86.2	12.5	0.2085
	2	−86.2	−12.5	−0.0599
	3	120.7	17.5	0.9062
	4	−58.6	−8.5	−0.0406
	5	−34.5	−5.0	−0.0240
	6	27.6	−4.0	−0.0184
A39 (Fig. 6)	1	103.4	15.0	0.5499
	2	−103.4	−15.0	−0.0696
A39 (Fig. 6)	3	34.5	5.0	0.0243
	4	34.5	5.0	0.0227
	5	34.5	5.0	0.0265
	6	−34.5	−5.0	−0.0234
	7	−34.5	−5.0	−0.0240
	8	−34.5	−5.0	−0.0234
A40 (Fig. 7)	1	68.9	10.0	0.0918
	2	−68.9	−10.0	−0.0457
	3	103.4	15.0	0.3292
	4	−17.2	−2.5	−0.0111
	5	17.2	2.5	0.0118
	6	−68.9	−10.0	−0.0457
	7	−34.5	−5.0	−0.0236
T45 (Fig. 8)	1	49.8	7.217	0.1596
	2	−10.0	−1.444	−0.0087
	3	10.0	1.444	0.0087
	4	−29.9	−4.33	−0.0264
	5	29.9	4.33	0.0267
	6	−49.8	−7.217	−0.0442
T47 (Fig. 9)	1	19.9	2.887	0.0180
	2	−19.9	−2.887	−0.0174
	3	19.9	2.887	0.0175
	4	7.7	1.113	0.0071
	5	12.2	1.773	0.0299
	6	10.0	1.444	0.0910
	7	−29.9	−4.33	−0.0265
	8	−19.9	−2.887	−0.0176

$$\epsilon^V = \left[\int_0^t \{F^V[\sigma(\xi),(t-\xi)]\}^{1/n} d\xi \right]^n, \tag{8}$$

when the strain at constant stress is represented by $\epsilon_{11}^V = F^V(\sigma)t^n$. In equation (8) it was assumed, in accordance with the usual strain-hardening concept, that the same function $F^V(\sigma)$ applied for variable stress $F^V[\sigma(\xi)]$ as for constant stress $F^V(\sigma)$.

For a series of m steps in stress the axial strain was described by the following form from equation (8) by employing the Dirac delta function,

$$\begin{aligned}\epsilon_{11}^V = \{ & [F^V(\sigma_1)]^{1/n}(t_1) + \ldots \\ & + [F^V(\sigma_{m-1})]^{1/n}(t_{m-1}-t_{m-2}) \\ & + [F^V(\sigma_m)]^{1/n}(t-t_{m-1})\}^n, \quad t_{m-1}<t.\end{aligned} \tag{9}$$

Similarly, ϵ_{12}^V was obtained by replacing $F^V(\sigma)$ by $G^V(\tau)$ in equation (8) and (9).

Predictions by the Theory and Comparison With Experimental Data

In the present analysis, the time-independent strain and the time-dependent strain were treated separately for predictions and comparison with experimental data.

The predictions of the time-independent strain ($\epsilon_{ij}^E + \epsilon_{ij}^P$) were made by the sum of the elastic strain (see [9]) and the plastic strain given by equations (2) and (3) as illustrated in the preceding section. The predictions of the time-dependent strain ($\epsilon_{ij}^V + \epsilon_{ij}^{VE}$) were obtained by the sum of equations (7) and (9). For example, the calculation of the time-dependent strain $\epsilon_{11}(t)$ for the third step of a three-step sequence in pure tension with stress changes at t_1 and t_2 are as follows,

$$\begin{aligned}\epsilon_{11}(t) = & F^{VE}(\sigma_1)\{t^n-(t-t_1)^n\} \\ & + F^{VE}(\sigma_2)\{(t-t_1)^n-(t-t_2)^n\} + F^{VE}(\sigma_3)(t-t_2)^n \\ & + \{[F^V(\sigma_1)]^{1/n}t_1 + [F^V(\sigma_2)]^{1/n}(t_2-t_1) \\ & + [F^V(\sigma_3)]^{1/n}(t-t_2)\}^n, \quad t_2<t.\end{aligned} \tag{10}$$

For comparison of the predictions by equation (10) with experimental data, the time-dependent creep strain data was extracted from the measured, total strain data as follows.

The first datum, following the instantaneous response upon changing the stress, was usually observed several seconds after completion of the change in load. Thus an allowance was made for the strain occurring during this interval. For simplicity and consistency the allowance was the strain calculated from the theory, equation (10), as having occurred in the interval between the end of the instantaneous response following completion of the load change and the first data reading. This amounts to making the first data point and theory coincide at the time of the first data reading. Then the data for the time-independent strain at each stress change was obtained as the amount of strain change from the last data point of the previous period (just before load change) to the zero time data of the creep strain of the current period (just after load change) corrected as just described. The resulting time-independent strain data are shown in the fifth column of Table 1. The data for plastic strain shown in column 5, Table 2, was obtained by the total time-independent strain minus the elastic strain. The predictions of time-independent plastic strain by equations (2) and (3) are also shown in column 8 ("prediction without aging") of Table 2. The data of the time-dependent strain are shown using different ordinates for each period in Figs. 1–9.

The theory curves predicted by equation (10) are shown as short-dash lines in Figs. 1–9. If the theory curves are the same as the other theory curves described later, only solid lines are shown. The data and theory curves for a given test period are plotted in the scales specified in the figure captions. Two different scales are used for different periods because the difference of strain magnitudes between periods are usually

Table 2 Plastic strain

Test (Fig. no.)	Period	Stress, σ or τ MPa	ksi	Data,[a] percent	Aging time, t_s,h	Aging factor, $g^P(t_s)$	Prediction without aging, percent	Prediction with aging, percent
A43 (Fig. 1)	3	86.2	12.5	0.0976	366	0.714	0.1489	0.1063
T29 (Fig. 2)	1	59.7	8.66	0.3610	20	1.000	0.3614	0.3614
T32 (Fig. 3)	1	49.8	7.217	0.1492	20	1.000	0.1480	0.1480
A38 (Fig. 5)	1	86.2	12.5	0.1503	20	1.000	0.1489	0.1489
	3	120.7	17.5	0.8247	312	0.728	1.1293	0.8221
A39 (Fig. 6)	1	103.4	15.0	0.4801	20	1.000	0.4806	0.4806
A40 (Fig. 7)	1	68.9	10.0	0.0452	20	1.000	0.0512	0.0512
	3	103.4	15.0	0.2594	357	0.716	0.4294	0.3075
T45 (Fig. 8)	1	49.8	7.217	0.1148	20	1.000	0.1480	0.1480
T47 (Fig. 9)	5	12.2	1.773	0.0189	356	0.716	0.0427	0.0306
	6	10.0	1.444	0.0820	404	0.706	0.1053	0.0743

[a] Data of plastic strain = total time-independent strain minus elastic strain.

too large to be properly included in one plot. Scales are grouped for similar periods and some continuous periods. The time and strain axes of each period were arbitrarily shifted so that data of all periods could be shown in one plot without confusion. The data and theory curves are drawn so as to be matched at zero time of each period (as described previously) starting from the left end of the figure. For some continuous sequences of periods, such as periods 4–6, Fig. 5, the time-dependent strains are only connected for each period. The actual difference between the data and the prediction of the theory at the end of a given period may be determined by accumulating all the differences for each prior period. In the present analysis the comparison between theory and data are usually based on each individual period – rather than the accumulated effect.

As shown in Figs. 1–9 and Table 2, the predicted strains without consideration of aging were much larger than the data, which indicated that aging effects should be included in the present analysis as found in [9].

Consideration of Aging

In [9], aging effects were found to be considerable for all strain components except the elastic strain. The aging time-strain relation was well represented by a power function, appearing as a factor inserted as a coefficient of each of the last three terms of equation (1), as follows,

$$g^P(t_s) = 1.4147\ t_s^{-0.1158}, \tag{11}$$

$$g^{VE}(t_s) = 1.5197\ t_s^{-0.1397}, \tag{12}$$

$$g^V(t_s) = 1.8293\ t_s^{-0.2016}, \tag{13}$$

where $g^P(t_s) = g^{VE}(t_s) = g^V(t_s) = 1.0$ at $t_s = 20$ h, t_s is the aging time in hours at 593°C (1100°F) from heating of the specimen up to the first time of loading.

This method of treating aging was an approximation in that it did not account for the fact that aging occurred continuously during each of the several creep tests from which the aging functions were determined. The viscoelastic strain component, ϵ^{VE} during creep was determined in [9] from recovery data following 100 h of creep. Since the amount of recovery strain following creep was considered to depend on the recoverable viscoelastic component accumulated during creep, the aging time for $g^{VE}(t_s)$ was taken to be the time up to load application rather than the time up to unloading following creep. Therefore, in both $g^{VE}(t_s)$ and $g^V(t_s)$, t_s was taken to be the aging time prior to start of the creep test. The same concept was used in the following analysis of creep data under multiple step changes of stress.

Since all the present tests had about 20 h aging time at the test temperature before the initial loading, the aging factor $g(t_s)$ was taken equal to unity at $t_s = 20$ h. And as the material constants were determined from the tests of 20 h aging, the results of 20 h aging were taken as reference.

Several ways of including aging in the theory for changes in stress state were tried. The following yielded the best results for step changes in stress. For example, the calculation of ϵ_{11}^{VE} and ϵ_{11}^{V} for the third step of a three-step sequence in pure torsion with stress changes at t_1 and t_2 are as follows,

$$\begin{aligned}\epsilon_{11}^{VE}(t) \;=\; & g^{VE}(20)F^{VE}(\sigma_1)\{t^n-(t-t_1)^n\} \\ & + g^{VE}(20+t_1)F^{VE}(\sigma_2)\{(t-t_1)^n-(t-t_2)^n\} \\ & + g^{VE}(20+t_2)F^{VE}(\sigma_3)(t-t_2)^n, \quad t_2<t \end{aligned} \tag{14}$$

$$\epsilon_{11}^{V}(t) = g^V(20+t_2)\Big[\{[\epsilon_{11}^{V}(t_2)]^{1/n} + [F^V(\sigma_3)]^{1/n}(t-t_2)\}^n - \epsilon_{11}^{V}(t_2)\Big] + \epsilon_{11}^{V}(t_2), \tag{15}$$

where

$$\epsilon_{11}^{V}(t_2) = g^V(20+t_1)\Big[\{[\epsilon_{11}^{V}(t_1)]^{1/n} + [F^V(\sigma_2)]^{1/n}(t_2-t_1)\}^n - \epsilon_{11}^{V}(t_1)\Big] + \epsilon_{11}^{V}(t_1),$$

$$\epsilon_{11}^{V}(t_1) = g^V(20)\{[F^V(\sigma_1)]^{1/n}t_1\}^n.$$

The predicted strains obtained by equations (14) and (15) are shown as long-dashed lines in Figs. 1–9. Equations (14) and (15) greatly improved the comparison with the data as shown in Fig. 1–9. Where the theory curves are the same as the other theory curves described later, only solid lines are shown.

The additional plastic strain produced by reloading to a higher stress than the previous stress was calculated as in the following example, considering the aging effect given by equation (11). For step-up stress changes $\sigma_1 \rightarrow \sigma_2$ ($\sigma^{*P} < \sigma_1 < \sigma_2$) at $t = t_1$, the new plastic strain $\Delta\epsilon_{11}^P$ was calculated as follows, using equations (2) and (3) with fixed yield limits

$$\Delta\epsilon_{11}^P = g^P(20+t_1)\{\epsilon_{11}^P(\sigma_2) - \epsilon_{11}^P(\sigma_1)\}. \tag{16}$$

The results are shown in the last column ("Prediction with Aging") of Table 2.

Revision (RSP) of (MSP) for Partial Unloading

From the comparisons of the theory with test data, shown in Figs. 1–9, substantial disagreements between theory and data were found for the cases of partial unloading as in period 4 of Fig. 5, period 6 of Fig. 6, and period 2 of Fig. 8, where the creep data increased at a reduced strain rate, but the predicted strain decreased. The viscous strain given by equation (15) always predicts a positive strain rate. Thus the disagreement was mainly due to the prediction of the viscoelastic strain by (MSP), equation (14), because equation (14) always predicts a decrease of ϵ^{VE} on partial unloading. So the (MSP) equation was revised (RSP) only for partial unloading cases using a closed form for stress changes. Both (MSP) and (RSP) predict the same result for full unloading. Among several modifications considered, the following (RSP) resulted in the best predictions. For example, modifying equation (14) including aging effects, for steps of partial unloading, $\sigma_1 > \sigma_2 > \sigma_3 > \sigma_4$, the revised superposition (RSP) yields,

$$\begin{aligned}\epsilon_{11}^{VE}(t) = & g(20)F^{VE}(\sigma_1)t^n - g(20)F^{VE}(\sigma_1-\sigma_2)(t-t_1)^n \\ & - g(20+t_1)F^{VE}(\sigma_1-\sigma_3)(t-t_2)^n \\ & - g(20+t_2)F^{VE}(\sigma_2-\sigma_4)(t-t_3)^n. \end{aligned} \tag{17}$$

In equation (17), a closed form $F(\sigma_1-\sigma_2)$ was used instead of an open form $\{F(\sigma_1)-F(\sigma_2)\}$ as in equation (14). Also the aging effect was approximated as $g(20)F(\sigma_1-\sigma_2)$ instead of $\{g(20)\ F(\sigma_1)-g(20+t_1)\ F(\sigma_2)\}$ as in equation (14). For a series of partial unloadings as in the foregoing example, $F(\sigma_1-\sigma_3)$ was used instead of $F(\sigma_2-\sigma_3)$ for the second step-down. That is, the creep recovery for all but the first step-down of a series of step-down stress changes was calculated on the basis of stress changes from one step before the previous step to the current stress as in $F(\sigma_2-\sigma_4)$ of equation (17). Since the recovery strain depends on the accumulated viscoelastic strain during the prior creep periods, the additional reduction of stress during the second step-down could cause not only recovery from the current stress change but additional recovery from the initial creep, partially due to nonlinearity of the viscoelastic strain. Equation (17) resulted in reasonably good predictions in most cases for a series of step-down stress changes as shown by solid lines in Figs. 5–9. For example, see the solid lines in periods 4–6 of Fig. 5 and periods 6–8 of Fig. 6.

Discussions on the Results of Analysis

As shown in Figs. 1–9 (solid lines), the prediction from the mathematical expressions employed satisfactorily described the experimental data. For some curves, agreement would become very good to excellent by a vertical shift, as in period 3 of Figs. 1, 5, and 7, and periods 1 and 2 of Fig. 3. Reloading after a long recovery period to the same stress as the initial stress level (periods 3 of Figs. 4 and 9) yielded very good predictions. For reloading to a lower stress, the prediction for period 3 of Fig. 2 was quite good. But the data for period 3 of Fig. 6 showed more initial "primary type" creep than the prediction. The data for period 3 of Fig. 3 showed a larger creep rate than the predictions. Reloading to a higher stress as in period 3 of Figs. 1, 5, and 7, yielded very good predictions if small vertical shifts were made.

For step-down stress changes and partial unloading and reloading as in Figs. 5–9, the revised superposition (RSP) equation (17) yielded quite reasonable predictions. But for period 7 of Fig. 7, equation (17) predicted a much larger creep recovery than the data, when $F^{VE}(\sigma_5-\sigma_7)$ was used for (RSP) and too small recovery when $F^{VE}(\sigma_6-\sigma_7)$ was used. The data seemed to lie between the two. The prediction of (RSP) using $F^{VE}(\sigma_{i-2}-\sigma_i)$ was satisfactory for periods 5–6 of Fig. 5 and periods 7–8 of Fig. 6, where the stress changes of several unloading steps were relatively small compared to the previous stress. However, the case of a small step-down stress following a large step-down was not well predicted by the (RSP), equation (17), as in period 7 of Fig. 7. A similar unloading occurred in periods 7 and 8, Fig. 9, with similar but not as pronounced a result.

The predicted plastic strain ϵ^P with aging (Table 2) in periods 3, Figs. 1, 5, and 7, and periods 5 and 6, Fig. 9, differed from the actual plastic strain data by +8.5, −0.04, +18.7, +62, and −9.4 percent, respectively. Considering the nature of plastic flow, these predictions are probably reasonable. The tensile stresses exceeded the yield point σ^{*P} or the prior stress level for the first three of the foregoing by 29.0, 34.5, and 34.5 MPa (4.2, 5, and 5 ksi), respectively. The largest stress occurred in period 3, Fig. 5.

In Fig. 9, the shearing stresses in period 5 exceeded the yield stress τ^* by only 6.76 MPa (0.98 ksi) and the step increase in stress in period 6 was 9.9 MPa (1.44 ksi). It may be that the smallness of the stress accounts in part for the 62 percent larger predicted strain than observed in period 5.

The reasonably close prediction to most of the data using equations (2) and (3) as a flow rule, suggests that the time-dependent creep strain during the previous periods of creep recovery did not affect the subsequent plastic strain significantly. The plastic strain and the viscous creep strain are usually considered to be controlled by physically equivalent mechanisms such as dislocation slip and glide at room temperature [15]. Since this may be partly right also at elevated temperature, there could exist some interactions between the two components ϵ^P and ϵ^V.

Conclusions

Analysis of creep data of 304 stainless steel at 593°C (1100°F) under pure tension and pure torsion for varying stress history, including reloadings, step-up, and step-down stress changes showed that a viscous-viscoelastic model with certain modifications predicted most of the features of the observed creep behavior reasonably well.

It was shown that the effect of aging must be included in predicting creep strains. A power function of aging time as a factor in each stress term produced reasonable results.

For recoverable time-dependent (viscoelastic) strain step increases were described by an open form for stress differences whereas steps of partial unloading were described by a closed form for stress differences.

Plastic (time-independent) strains were described reasonably well by a flow rule of form similar to that employed for nonrecoverable time-dependent (creep) strains.

Acknowledgments

This work was supported by the National Science Foundation under Grant No. ENG76-02519. The authors are grateful to R. M. Reed for assistance in experiments and Mrs. P. C. Capece and Ms. S. F. Mancino for typing the manuscript. The early experimental work on this project was supported and all material tested was supplied by the Oak Ridge National Laboratory of the U.S. Atomic Energy Commission.

References

1 Hult, J., ed., *Creep in Structures*, IUTAM Symposium, Gothenberg 1970, Springer-Verlag, 1972.

2 Workshop on Inelastic Constitutive Equations for Metals, Rennselaer Polytechnic Institute, Troy, N.Y., 1974.

3 Findley, W. N., Cho, U. W., and Ding, J. L., "Creep of Metals and Plastics Under Combined Stresses, A Review," *J. of Engineering Materials and Technology*, Vol. 101, 1979, pp. 365–368.

4 Findley, W. N., and Mark, R., "Multiaxial Creep Behavior of 304 Stainless Steel," Annual Report No. 1 (Brown University Report EMRL-55 Oct. 1972), No. 2. (EMRL-58, Nov. 1973), No. 3 (EMRL-62, Nov. 1974), No. 4 (EMRL-63, July 1975) to Oak Ridge National Laboratory.

5 Bhargava, R., Moteff, J., and Swindeman, R. W., "Correlation of the Microstructure with the Creep and Tensile Properties of AISI 304 Stainless Steel," ASME *Symposium on Structural Materials for Service at Elevated Temperatures in Nuclear Power Generation*, Doc. MPC-1, 1975, pp. 31–54.

6 Swindeman, R. W., Bhargava, R., Sikka, V. K., and Moteff, J., "Substructures Developed During Creep and Cyclic Tests of Type 304 Stainless

Steel (Heat 9T2796),"Oak Ridge National Laboratory, ORNL-5293, Sept. 1977.

7 Swindeman, R. W., "Correlation of Rupture Life, Creep Rate, and Microstrucure for Type 304 Stainless Steel," Oak Ridge National Laboratory, ORNL-5523, June 1979.

8 Cho, U. W., and Findley, W. N., "Creep and Creep Recovery of 304 Stainless Steel Under Combined Stress with a Representation by a Viscous-Viscoelastic Model," ASME JOURNAL OF APPLIED MECHANICS, Vol. 47, No. 4, Dec. 1980, pp. 755–761.

9 Cho, U. W., and Findley, W. N., "Creep and Creep Recovery of 304 Stainless Steel at Low Stresses with Effects of Aging on Creep and Plastic Strains," ASME JOURNAL OF APPLIED MECHANICS, Vol. 48, pp. 785–790.

10 Findley, W. N., and Gjelsvik, A., "A Biaxial Testing Machine for Plasticity, Creep, or Relaxation Under Variable Principal-Stress Ratios," *Proceedings, ASTM*, Vol. 62, 1962, pp. 1103–1118.

11 Findley, W. N., Lai, J. S., and Onaran, K., *Nonlinear Creep and Relaxation of Viscoelastic Materials, With an Introduction to Linear Viscoelasticity*, North Holland, Amsterdam, 1976.

12 Findley, W. N., and Lai, J. S., "A Modified Superposition Principle Applied to Creep of Nonlinear Viscoelastic Material Under Abrupt Changes in State of Combined Stress," *Transactions of the Society of Rheology*, Vol. 11, Part 3, 1967, pp. 361–380.

13 Michno, M. J., and Findley, W. N., "An Historical Perspective of Yield Surface Investigations for Metals," *International Journal of Nonlinear Mechanics*, Vol. 11, 1976, pp. 59–82.

14 Lai, J. S., and Findley, W. N., "Creep of 2618 Aluminum Under Step Stress Changes Predicted by a Viscous-Viscoelastic Model," ASME JOURNAL OF APPLIED MECHANICS, Vol. 47, No. 1, Mar. 1980, pp. 21–26.

15 Lagneborg, R., "Dislocation Mechanisms in Creep," *International Metallurgical Reviews*, Vol. 17, 1972, pp. 130–146.

A Thermoelastic-Viscoplastic Model With a Rate-Dependent Yield Strength

M. B. Rubin
Engineering Mechanics Department,
SRI International,
Menlo Park, Calif. 94025
Assoc. Mem. ASME

General nonlinear constitutive equations for a thermoelastic-viscoplastic material that exhibits a rate-dependent yield strength are developed by assuming that the yield function depends explicitly on the total strain rate and temperature rate. Following recent developments in continuum thermodynamics restrictions on the constitutive response functions are imposed to ensure that the moment of momentum and energy equations are identically satisfied and that various statements of the second law of thermodynamics are satisfied for all thermodynamical processes. A particular constitutive equation for a thermoelastic-viscoplastic material is proposed, and an analytical example is considered that examines the rate-dependent plastic response to a deformation history that includes segments of loading, unloading, and reloading, each occurring at varying strain rates.

Introduction

It is well known that many materials exhibit rate sensitivity in both their elastic and plastic response. However, some materials, such as titanium, are elastic-viscoplastic materials that exhibit less complicated behavior and are characterized by a strain-rate insensitive elastic response but a strain-rate sensitive plastic response [1]. Such elastic-viscoplastic materials also possess a rate-dependent yield strength.[1] Although previous constitutive models for elastic-viscoplastic materials include rate sensitivity in their plastic response they cannot model a rate-dependent yield strength. Therefore, the purpose of this paper is to develop a nonlinear constitutive model for a thermoelastic-viscoplastic material with a rate-dependent yield strength that includes the simplifications associated with rate-insensitive elastic response.

Situations often arise where it is essential to use a constitutive model that possesses a rate-dependent yield strength. More specifically, when the range of strain rate experienced by the material is large, the range of actual yield strength is also large and the yield strength cannot be adequately approximated by a constant value. However, if the range of strain rate experienced by the material is small, the common rate-independent elastic-plastic theories (e.g., Green and Naghdi [2, 3]) can be used even though they cannot model a rate-dependent yield strength. This is because the variation of the actual value of yield strength in such a situation is relatively small, so the value of yield strength in the rate-independent theories can be adequately approximated by the average value of the actual yield strength associated with that range of strain-rate [4, 5].

To contrast the developments of the present paper with previous developments, we recall some common constitutive models for rate-dependent plasticity. Malvern [6] considered the uniaxial deformation of a bar and introduced the overstress model for elastic-viscoplastic materials. This model admits the existence of a yield function and relates the rate of plastic strain to a function of "the excess of the instantaneous stress over the stress at the same strain in a static test." Within the context of the linearized theory, Perzyna [7] generalized the overstress model to include three-dimensional deformations. To summarize the generalization and to show that the overstress model does not possess a rate-dependent yield strength, we introduce a rate-independent yield function in the form[2]

$$F=\frac{f(\sigma_{ij},\epsilon_{ij}^{p})}{\kappa}-1, \tag{1}$$

where σ_{ij} is the Cauchy stress tensor, ϵ_{ij}^{p} is the plastic strain tensor, and κ is a hardening parameter. The total strain rate $\dot{\epsilon}_{ij}$ is assumed to be decomposed into an elastic part $\dot{\epsilon}_{ij}^{e}$ and a plastic part $\dot{\epsilon}_{ij}^{p}$. Constitutive equations for this material may then be specified in the form[3]

$$\dot{\epsilon}_{ij}=\dot{\epsilon}_{ij}^{e}+\dot{\epsilon}_{ij}^{p},\quad \dot{\epsilon}_{ij}^{e}=\frac{1}{2\mu}\dot{S}_{ij}+\frac{1-2\nu}{E}\dot{S}\delta_{ij}, \tag{2a,b}$$

[1] By yield strength, we mean the strength of the material at the transition point between elastic and plastic material response.

Contributed by the Applied Mechanics Division for publication in the JOURNAL OF APPLIED MECHANICS.

Discussion on this paper should be addressed to the Editorial Department, ASME, United Engineering Center, 345 East 47th Street, New York, N.Y. 10017, and will be accepted until two months after final publication of the paper itself in the JOURNAL OF APPLIED MECHANICS. Manuscript received by ASME Applied Mechanics Division, February, 1981; final revision, July 1981.

[2] For convenience, we have retained the notation used by Perzyna [7].

[3] The usual summation convention over repeated indices is used throughout the text.

$$\dot{\epsilon}^p_{ij} = \gamma < \Phi(F) > \frac{\partial f}{\partial \sigma_{ij}}, \quad \kappa = \hat{\kappa}(W_p), \quad \dot{W}_p = \sigma_{ij}\dot{\epsilon}^p_{ij}, \qquad (2c,d,e)$$

$$S = \frac{1}{3}\sigma_{mm}, \quad S_{ij} = \sigma_{ij} - S\delta_{ij}, \qquad (2f,g)$$

where μ is the shear modulus, E is Young's modulus, ν is Poisson's ratio, γ is a viscosity constant, and the symbol $< \Phi(F) >$ is defined by

$$< \Phi(F) > = \begin{cases} 0 & \text{when } F \leq 0 \\ \Phi(F) & \text{when } F > 0. \end{cases} \qquad (3)$$

The function $\Phi(F)$ characterizes the rate-dependent plastic response and requires a constitutive equation. In view of the equations (1) and (2) and the definition (3), we realize that when $F \leq 0$, the material exhibits rate-insensitive elastic response, and when $F > 0$, the material can exhibit rate-sensitive plastic response. More important, we note that the *overstress model does not possess a rate-dependent yield* strength since plastic yielding always initiates when the rate-independent yield function $F = 0$. This result is shown schematically by Fig. 1, which compares the constitutive response of the present model with that of the overstress model for loading histories of different total strain rates.

Here, it is important to clarify some confusion that exits in the literature. Figure 1.4, p. 112, in Cristescu [8] and Figures 18 and 19, p. 277, in Perzyna [7] suggest that the overstress model produces stress-strain curves more similar to the solid lines in our Fig. 1 than the broken lines. This, of course, cannot be accurate because we have just proved that the overstress model cannot model a rate-dependent yield strength. In fact, Malvern [6] states (p. 204) that; "The initial yield strain ϵ_y and yield stress $\sigma_y = E_0\,\epsilon_y$ have been considered as constant for all finite strain rates in the applications that have been made of the present theory." The correct response of the overstress model is shown in Figure 1 of reference [6].

Constitutive models that possess a rate-dependent yield strength have been developed for viscoelastic-plastic materials that exhibit rate sensitivity in both their elastic and plastic response. For example, linear constitutive equations for such materials were proposed by Naghdi and Murch [9] and nonlinear constitutive equations were proposed by Green and Naghdi [10]. Although these developments can model a material with a rate-dependent yield strength if the material is rate sensitive in both its elastic and plastic response, they cannot be simplified to describe a material that has rate-insensitive elastic response without losing the ability to model a rate-dependent yield strength. This is because the values of the arguments of the yield functions in these developments would be rate insensitive at the onset of yield from an elastic to a viscoplastic state.

Another constitutive model for rate-dependent materials was proposed by Bodner and Partom [11] and is based on the assumption that the rate of deformation tensor d_{ij} is separable into an elastic part d^e_{ij} and a plastic part d^p_{ij}. The plastic rate of deformation tensor d^p_{ij} is related to the stress through a flow rule of the form[4]

$$d^p_{ij} = \underline{d}^p_{ij} = \lambda \underline{\sigma}_{\theta\pi}, \qquad (4)$$

where σ_{ij} is the Cauchy stress and the bar indicates the deviatoric part of the tensors. Their development does not use a yield function to characterize loading from an elastic to a plastic state or unloading from a plastic to an elastic state. Instead, a constitutive equation for the function λ in (4) must be specified in such a way as to allow their model to simulate these elastic-plastic transitions. Although Bodner and Partom

[4] Here, we have retained the notation used by Bodner and Partom [11].

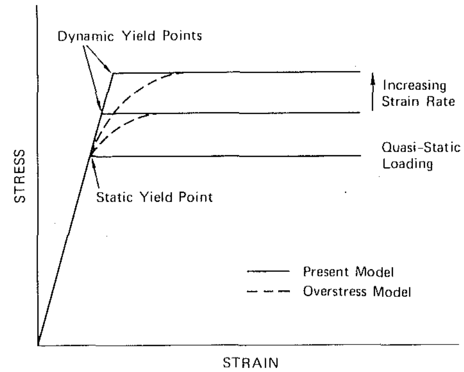

Fig. 1 Sketch of the constitutive response predicted by the present model and that predicted by the overstress model for loading histories of different total strain rates

[11] propose a constitutive equation for λ that allows their model to simulate a material with a rate-dependent yield strength, they specify λ to be a function that vanishes only asymptotically. This means that the material response is never truly elastic and that the values of the components of $\underline{\sigma}_{ij}$ will approach zero asymptotically with time.

In contrast to previous studies, we develop a nonlinear constitutive model for a thermoelastic-viscoplastic material with a rate-dependent yield strength by assuming that the yield function depends explicitly on the total strain rate and temperature rate. Because constitutive equations of all materials must be invariant under superposed rigid body *motions and must satisfy certain thermodynamic conditions*, we impose restrictions on our constitutive assumptions by using recent developments in continuum thermodynamics proposed by Green and Naghdi [12, 13]. After summarizing the basic equations and thermodynamic restrictions [12, 13], we develop general nonlinear rate-type constitutive equations for a thermoelastic-viscoplastic material with a rate-dependent yield strength. Next, we develop an explicit set of constitutive equations that satisfy all thermodynamic restrictions. Then an example of homogeneous, isothermal, uniaxial strain is considered to explore the response of this material to a deformation history that includes segments of loading, unloading, and reloading, each occurring at varying strain rates. Finally, we close with a few concluding comments.

Summary of the Basic Equations

Consider a finite body with material points X and identify the material point X with its position $\mathbf{X}$ in a fixed reference configuration. A motion of the body is defined by a sufficiently smooth vector function χ, which assigns position $\mathbf{x} = \chi(\mathbf{X}, t)$ to each material point $\mathbf{X}$ at each instant of time. In the procedure developed by Green and Naghdi [12], the usual balance laws for mass, linear momentum, moment of momentum and energy are supplemented by a balance law for entropy. Further, the moment of momentum and energy equations are assumed to be identities for all thermomechanical processes. For our present purpose, we need recall only the equations for the balance of entropy and the reduced form of the balance of energy, which may be referred to the reference configuration and represented, respectively, in the forms

$$\rho_0\dot{\eta} = \rho_0(s + \xi) - \mathrm{Div}\,\mathbf{P}, \qquad (5a)$$

$$-\rho_0(\dot{\psi} + \eta\dot{\theta}) + \mathbf{S}\bullet\dot{\mathbf{E}} - \rho_0\theta\xi - \mathbf{P}\bullet\mathbf{G} = 0, \qquad (5b)$$

where ρ_0 is the mass density in the reference configuration, η is the specific[5] entropy, s is the specific external rate of supply

[5] The term specific is used to denote that the quantity is measured per unit mass of the body.

of entropy, ξ is the specific internal rate of production of entropy, $\mathbf{P}$ is the entropy flux vector per unit area in the reference configuration, $\psi = \epsilon - \theta\eta$ is the specific Helmholtz free energy, ϵ is the specific internal energy, θ (> 0) is the absolute temperature, $\mathbf{S}$ is the symmetric Piola-Kirchhoff stress, $\mathbf{E} = (\mathbf{F}^T\mathbf{F} - \mathbf{I})/2$ is the Lagrangian strain, $\mathbf{F} = \partial\mathbf{x}/\partial\mathbf{X}$ is the deformation gradient, $\dot{\mathbf{E}}$ is the total strain rate at time t, where a superposed dot denotes material time differentiation holding $\mathbf{X}$ fixed, and $\mathbf{G} = \partial\theta/\partial\mathbf{X}$ is the temperature gradient with respect to the position $\mathbf{X}$. The divergence operator Div in (5a) is defined with respect to the position vector $\mathbf{X}$. Furthermore, we recall that the specific external rate of heat supply r and the heat flux vector $\mathbf{Q}$ per unit area of the reference configuration are related to s and $\mathbf{P}$ through the expressions

$$r = \theta s, \quad \mathbf{Q} = \theta\mathbf{P}. \tag{6a,b}$$

As in [12], the response functions for ϵ, η are assumed to include dependence on the set of variables $\dot{\mathbf{F}}$, $\dot{\theta}$, $\mathbf{G}$ and their higher space and time derivatives, and this set collectively is referred to as V. Further, let the quantities ϵ', η' denote the respective values of ϵ, η when the set V is set equal to zero in the response functions. Thus, for example,

$$\epsilon = \epsilon(\mathbf{F},\theta,V), \quad \epsilon' = \epsilon'(\mathbf{F},\theta) = \epsilon(\mathbf{F},\theta,0). \tag{7a,b}$$

It follows from [13] that a statement of the second law of thermodynamics may be expressed in the form

$$\rho_0 w^* = -\rho_0\theta(\dot{\eta} - \dot{\eta}') + \rho_0\theta\xi + \mathbf{P}\cdot\mathbf{G} \geq 0. \tag{8}$$

The inequality (8) is supplemented by two additional statements of the second law [12], which may be written as

$$-\mathbf{Q}\cdot\mathbf{G} \geq 0, \tag{9a}$$

$$\theta(t) - \theta(t_1) > 0 \text{ whenever } \epsilon(t) - \epsilon(t_1) > 0. \tag{9b}$$

The inequality (9a) is the classical heat conduction inequality and is adopted for all equilibrium processes, whereas the inequality (9b) is adopted when the continuum is in a state of rest and the temperature is spacially homogeneous. The time t_1 in (9b) is constant.

A Thermoelastic-Viscoplastic Model

In this section, we propose constitutive equations for a thermoelastic-viscoplastic material with a rate-dependent yield strength. To a certain extent, the nonlinear equations of rate-type proposed here follow previous developments for thermoelastic-plastic materials (see [14]); however, they differ from previous developments in that the yield function is assumed to depend explicitly on the total strain rate $\dot{\mathbf{E}}$ and temperature rate $\dot{\theta}$. It therefore is necessary to examine this new constitutive assumption within the context of the procedure and thermodynamic restrictions that were summarized in the preceding section.

At each point in the continuum, we admit the existence of a plastic strain specified by a symmetric second-order tensor $\mathbf{E}_p$, a measure of work-hardening specified by a positive scalar function κ, and a scalar-valued function[6] γ, called the yield function, which is assumed to depend on the variables[7]

$$\{\mathbf{E},\mathbf{E}_p,\theta,\kappa\}, \quad \{\dot{\mathbf{E}},\dot{\theta}\} \tag{10a,b}$$

and which at yield satisfies the equation

$$\gamma(\mathbf{E},\mathbf{E}_p,\theta,\kappa,\dot{\mathbf{E}},\dot{\theta}) = 0. \tag{11}$$

Further, the yield function γ is assumed to be continuously differentiable with respect to its arguments. For the constitutive model under discussion here, we assume that[8]

$$\mathbf{S} = \mathbf{S}(\mathbf{E},\mathbf{E}_p,\theta,\kappa), \tag{12a}$$

$$\mathbf{P} = \mathbf{P}(\mathbf{E},\mathbf{E}_p,\theta,\kappa,\mathbf{G}), \tag{12b}$$

$$\dot{\mathbf{E}}_p = \begin{cases} 0 & \text{during elastic response } (\gamma < 0), \\ 0 & \text{during unloading } (\gamma = 0 \text{ and } \hat{\gamma} < 0), \\ 0 & \text{during neutral loading } (\gamma = 0 \text{ and } \hat{\gamma} = 0), \\ \mu\mathbf{A}\hat{\gamma} & \text{during loading } (\gamma = 0 \text{ and } \hat{\gamma} > 0), \end{cases} \tag{13a}$$

$$\dot{\kappa} = \mathbf{M}\cdot\dot{\mathbf{E}}_p, \tag{13b}$$

where

$$\hat{\gamma} = \frac{\partial\gamma}{\partial\mathbf{E}}\cdot\dot{\mathbf{E}} + \frac{\partial\gamma}{\partial\theta}\dot{\theta} + \frac{\partial\gamma}{\partial\dot{\mathbf{E}}}\cdot\ddot{\mathbf{E}} + \frac{\partial\gamma}{\partial\dot{\theta}}\ddot{\theta}. \tag{14}$$

In the foregoing expressions μ, $\mathbf{A}$, and $\mathbf{M}$ are functions of the variables (10a) and (10b), with $\mathbf{A}$ and $\mathbf{M}$ being symmetric second-order tensors, and the quantities $\mathbf{E}$, $\mathbf{E}_p$, θ, κ, $\mathbf{G}$, $\mathbf{S}$, ψ, s, η, $\mathbf{P}$, γ, μ, $\mathbf{A}$, $\mathbf{M}$, ξ are unaltered under superposed rigid body motions. Response functions for the quantities ψ and η are assumed to take the same form as those for $\mathbf{S}$ in (12a). Taking the material time derivative of the yield criterion (11) and using the expressions (13) and (14), we may conclude that during loading, the quantity[9] μ must satisfy the equation

$$1 + \mu\mathbf{A}\cdot\left(\frac{\partial\gamma}{\partial\mathbf{E}_p} + \frac{\partial\gamma}{\partial\kappa}\mathbf{M}\right) = 0. \tag{15}$$

Furthermore, we can assume without loss in generality, that

$$\mu > 0. \tag{16}$$

The constitutive assumptions (12) and (13) must be supplemented by appropriate assumptions for the rate of supply of entropy ξ. For the thermoelastic-viscoplastic material under discussion, we suppose that ξ is prescribed by an equation of the form

$$\xi = \xi_1(\mathbf{E},\mathbf{E}_p,\theta,\kappa,\mathbf{G}) + \boldsymbol{\Sigma}(\mathbf{E},\mathbf{E}_p,\theta,\kappa,\mathbf{G},\dot{\mathbf{E}},\dot{\theta},\ddot{\mathbf{E}},\ddot{\theta})\cdot\dot{\mathbf{E}}_p \tag{17}$$

where $\boldsymbol{\Sigma}$ is a symmetric second-order tensor function of its arguments and is unaltered under superposed rigid body motions.

Following the procedure described in [12] restrictions on the constitutive assumptions may be obtained by demanding that the energy equation (5b) is an identity for all thermomechanical processes. Substitution of the constitutive assumptions into (5b) yields the equation

$$-\rho_0\left(\frac{\partial\psi}{\partial\theta} + \eta\right)\dot{\theta} + \left(\mathbf{S} - \rho_0\frac{\partial\psi}{\partial\mathbf{E}}\right)\cdot\dot{\mathbf{E}} - \rho_0\xi_1\theta - \mathbf{P}\cdot\mathbf{G}$$

$$-\rho_0\left(\theta\boldsymbol{\Sigma} + \frac{\partial\psi}{\partial\mathbf{E}_p} + \frac{\partial\psi}{\partial\kappa}\mathbf{M}\right)\cdot\dot{\mathbf{E}}_p = 0. \tag{18}$$

At any point in an arbitrary thermomechanical process, the values of the variables (10a,b) are arbitrary to the extent that $\gamma \leq 0$ and the constitutive equations (13a,b) have been satisfied. Hence for any fixed, but arbitrary, values of the variables (10a), we may vary the values of $\dot{\mathbf{E}}$ and $\dot{\theta}$ independently while maintaining the condition that $\dot{\mathbf{E}}_p = 0$. This is because either $\gamma < 0$ or $\gamma = 0$ and we may assume that not all components of $\partial\gamma/\partial\dot{\mathbf{E}}$ vanishes and thus may choose $\ddot{\mathbf{E}}$ so that $\hat{\gamma} < 0$ and $\dot{\mathbf{E}}_p = 0$. In either case, $\dot{\mathbf{E}}_p = 0$ and (18) reduces to

$$-\rho_0\left(\frac{\partial\psi}{\partial\theta} + \eta\right)\dot{\theta} + \left(\mathbf{S} - \rho_0\frac{\partial\psi}{\partial\mathbf{E}}\right)\cdot\dot{\mathbf{E}} - \rho_0\xi_1\theta - \mathbf{P}\cdot\mathbf{G} = 0. \tag{19}$$

It follows that we are free to specify the values of $\dot{\mathbf{E}}$ and $\dot{\theta}$

[6] The yield function γ should not be confused with the use of the same symbol in the Introduction.

[7] Here, it is convenient to use a strain-space formulation of plasticity instead of a stress-space formulation. For a discussion of the significance of formulating plasticity theory in strain-space, see Naghdi and Trapp [15].

[8] Explicit dependence of the response functions on the material point $\mathbf{X}$ can be included but it is suppressed for convenience.

[9] The function μ introduced in (13a) should not be confused with the use of the same symbol in the Introduction.

independently in equation (19). Since the coefficients of $\dot{\theta}$ and $\dot{\mathbf{E}}$ in (19) as well as the response functions ξ_l and $\mathbf{P}$ are independent of the rates $\dot{\theta}$, $\dot{\mathbf{E}}$, we may conclude that

$$\eta = -\frac{\partial \psi}{\partial \theta}, \quad \mathbf{S} = \rho_0 \frac{\partial \psi}{\partial \mathbf{E}}, \quad \rho_0 \xi_1 \theta = -\mathbf{P} \cdot \mathbf{G} \qquad (20a,b,c)$$

must hold for all possible values of the variables (10a) and the variable $\mathbf{G}$. Furthermore, the moment of momentum equation is automatically satisfied by the response function (20b) since ψ is a function of the symmetric tensor $\mathbf{E}$.

The restrictions (20) were derived for processes for which $\dot{\mathbf{E}}_p = 0$. However, at any point for which $\gamma = 0$, we may choose $\ddot{\mathbf{E}}$ so that $\dot{\mathbf{E}}_p = 0$ or $\dot{\mathbf{E}}_p \neq 0$ without affecting the values of the expressions (20), since (20) are independent of rates. It follows that the expressions (20) must hold for all thermomechanical processes. Hence, with the help of (13) and (20) we may conclude that during loading, the expression (18) reduces to

$$\left(\theta \boldsymbol{\Sigma} + \frac{\partial \psi}{\partial \mathbf{E}_p} + \frac{\partial \psi}{\partial \kappa} \mathbf{M}\right) \cdot \mathbf{A} = 0. \qquad (21)$$

If we now appeal to the inequality (8) and use (7), (13a), (17), (20), and (21), we obtain

$$-\mu \left(\frac{\partial \psi}{\partial \mathbf{E}_p} + \frac{\partial \psi}{\partial \kappa} \mathbf{M} \right) \cdot \mathbf{A} \hat{\gamma} \geq 0 \qquad (22)$$

whenever $\mu > 0$ and $\hat{\gamma} \geq 0$, so that

$$\left(\frac{\partial \psi}{\partial \mathbf{E}_p} + \frac{\partial \psi}{\partial \kappa} \mathbf{M} \right) \cdot \mathbf{A} \leq 0. \qquad (23)$$

Although further restrictions on constitutive equations are demanded by the inequalities (9a) and (9b), these cannot be exploited until explicit response functions are supplied.

It is interesting to note that the response functions ψ, η, $\mathbf{S}$, ξ_1 of the thermoelastic-viscoplastic material under discussion have the same form as those of a thermoelastic-plastic material (see [14]). The rate-dependent plastic response of this thermoelastic-viscoplastic material arises merely through the rate-dependence of the yield function γ and the expressions for the quantities $\dot{\mathbf{E}}_p$, $\dot{\kappa}$, and $\boldsymbol{\Sigma}$.

A Particular Constitutive Equation for a Thermoelastic-Viscoplastic Material

The development in the preceding section was intended to be general and therefore did not propose an explicit set of constitutive equations. In this section, we propose nonlinear constitutive equations for a thermoelastic-viscoplastic material and develop a set of response functions that satisfy all the constitutive restrictions demanded by the thermodynamical procedure of Green and Naghdi [12, 13].

For this discussion, it is convenient to refer all tensor quantities to a fixed set of Cartesian base vectors $\mathbf{e}_A$ ($A = 1, 2, 3$). For example, we let X_A be the coordinates of the material point $\mathbf{X}$ and let E^p_{AB} be the components of the plastic strain tensor $\mathbf{E}_p$. Recalling the constitutive restrictions (20) and (21), we note that once constitutive equations are provided for ψ, $\mathbf{P}$, γ, $\mathbf{A}$, $\mathbf{M}$, the response functions η, $\mathbf{S}$, and ξ are determined. Therefore, let us specify the Helmholtz free energy ψ and entropy flux P_A in the forms

$$\psi = \frac{1}{2} C_{ABCD}(E_{AB} - E^p_{AB})(E_{CD} - E^p_{CD}) \qquad (24a)$$

$$+ C_{AB}(E_{AB} - E^p_{AB}) - \theta D_{AB}(E_{AB} - E^p_{AB}) - D_1 \theta - \frac{1}{2} D_2 \theta^2,$$

$$P_A = -\frac{K_{AB} G_B}{\theta}, \qquad (24b)$$

where D_1 and D_2 are constants and the constant tensors

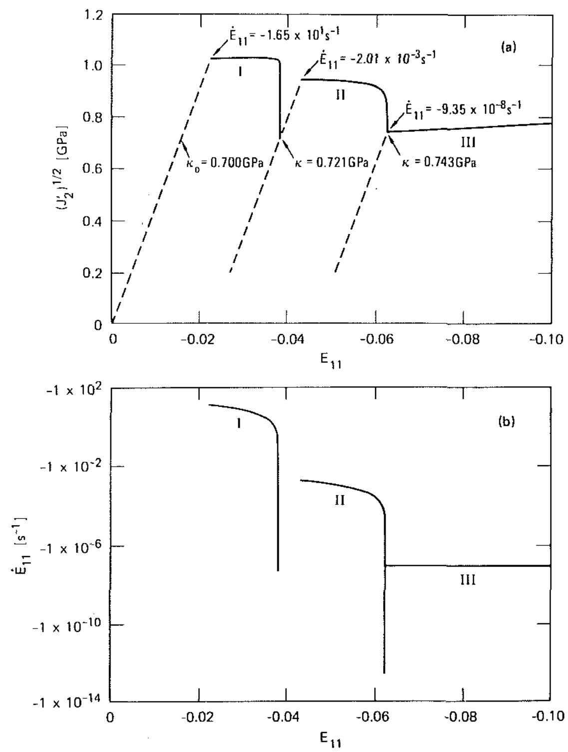

Fig. 2 (*a*) **Solution for the deformation described by equation (48) for the elastic segments (---) and the viscoplastic segments(-); (*b*) strain rates $\dot{E}_{11}$ corresponding to the viscoplastic segments.**

C_{ABCD}, C_{AB}, D_{AB}, K_{AB} have obvious symmetry properties. The specific nonlinear constitutive equations (24) were chosen mainly because their forms are similar to those of the usual constitutive equations for linear thermoelastic-plastic materials [2]. Next, we would like to propose a yield function that has a Von-Mises form. For simplicity, we will include dependence of the yield function on total strain rate $\dot{E}_{AB}$, but exclude dependence on temperature θ and temperature rate $\dot{\theta}$. Hence, we specify[10]

$$\gamma = J_2' - [\kappa + g(z)]^2 \qquad (25)$$

where J_2' is related to the deviatoric part τ_{AB} of the symmetric Piola-Kirchhoff tensor S_{AB} through the formulas

$$J_2' = \frac{1}{2} \tau_{AB} \tau_{AB}, \quad \tau_{AB} = S_{AB} - \frac{1}{3} S_{MM} \delta_{AB}, \qquad (26a,b)$$

and where the rate dependence of the yield function (25) is characterized by the nonnegative function $g(z)$, which is specified by

$$g = B \tanh z, \quad z = C\, ln\left(1 + \frac{1}{2} B_{ABCD} \dot{E}_{AB} \dot{E}_{CD}\right) \qquad (27a,b)$$

$$B \geq 0, \quad C \geq 0, \quad B_{ABCD} \dot{E}_{AB} \dot{E}_{CD} \geq 0 \qquad (27c,d,e)$$

with B and C being constants, B_{ABCD} being a constant tensor with obvious symmetry properties, and δ_{AB} being the Kronecker delta. In view of (11), the representation (25) and the assumption that κ is positive and $g(z)$ is nonnegative, we realize that during loading and in particular at the onset of yield

$$(J_2')^{1/2} = [\kappa + g(z)]. \qquad (28)$$

[10] The Von-Mises form of the yield function is generally written as a function of stress [see expression (25)] instead of strain as in (11). Since our basic developments utilize a strain space formulation of plasticity, it is necessary to represent the function (25) in the form (11) when determining the quantity $\hat{\gamma}$ that characterizes loading.

It follows from (27) and (28) that the material under discussion possesses a rate-dependent yield strength since a nonzero value of $\dot{E}_{AB}$ has the effect of instantaneously increasing the yield strength. Although the function $g(z)$ specified in (27) is chosen somewhat arbitrarily, it models the fact that at very high strain rates, the yield strength of some materials asymptotically approaches a finite limit ([7], Fig. 2, p. 248). The function $g(z)$ can, however, be determined experimentally and a procedure for doing this is outlined at the end of the next section.

For a complete description of the material under discussion, it is necessary to specify constitutive equations for the quantities A_{AB} and M_{AB} given in (13a) and (13b). Thus we take[11]

$$A_{AB}=\tau_{AB}, \quad M_{AB}=-\frac{\beta\tau_{AB}}{\mu\dfrac{\partial\gamma}{\partial\kappa}\tau_{MN}\tau_{MN}} \tag{29a,b}$$

where β is a constant that controls the amount of hardening.

Let us now assume that in the reference configuration, the material is homogeneous and isotropic and that

$$\theta=\theta_0, \quad S_{AB}=0, \quad E_{AB}=0, \quad E^p_{AB}=0, \quad \kappa=\kappa_0 \tag{30a,b,c,d,e}$$

where θ_0 and κ_0 are positive constants. It follows from (20b), (30), symmetry properties, and the condition of isotropy that

$$C_{ABCD}=C_1\delta_{AB}\delta_{CD}+C_2(\delta_{AC}\delta_{BD}+\delta_{AD}\delta_{BC}), \tag{31a}$$

$$C_{AB}=\theta_0 D\delta_{AB}, \quad D_{AB}=D\delta_{AB}, \quad K_{AB}=k\delta_{AB}, \tag{31b,c,d}$$

$$B_{ABCD}=B_1\delta_{AB}\delta_{CD}+B_2(\delta_{AC}\delta_{BD}+\delta_{AD}\delta_{BC}), \tag{31e}$$

where C_1, C_2, D, k, B_1 and B_2 are constants. Substituting (31) into (24) and using the constitutive restrictions (20), the response functions may be represented in the forms

$$\begin{aligned}\psi=\ &\frac{1}{2}C_1(E_{AA}-E^p_{AA})(E_{BB}-E^p_{BB})\\ &+C_2(E_{AB}-E^p_{AB})(E_{AB}-E^p_{AB})\\ &-(\theta-\theta_0)D(E_{AA}-E^p_{AA})-D_1\theta-\frac{1}{2}D_2\theta^2,\end{aligned} \tag{32a}$$

$$\begin{aligned}\epsilon=\ &\frac{1}{2}C_1(E_{AA}-E^p_{AA})(E_{BB}-E^p_{BB})\\ &+C_2(E_{AB}-E^p_{AB})(E_{AB}-E^p_{AB})\\ &+\theta_0 D(E_{AA}-E^p_{AA})+\frac{1}{2}D_2\theta^2,\end{aligned} \tag{32b}$$

$$\eta=D_1+D_2\theta+D(E_{AA}-E^p_{AA}), \tag{32c}$$

$$\begin{aligned}S_{AB}=\ &\rho_0[C_1(E_{MM}-E^p_{MM})\delta_{AB}\\ &+2C_2(E_{AB}-E^p_{AB})-(\theta-\theta_0)D\delta_{AB}],\end{aligned} \tag{32d}$$

$$P_A=-\frac{kG_A}{\theta}, \quad \xi_1=\frac{kG_AG_A}{\rho_0\theta^2}. \tag{32e, f}$$

Furthermore, it follows from (13–15), (21), (25), (26), (29), and (32) that

$$\tau_{AB}=2\rho_0C_2[(E_{AB}-E^p_{AB})-\frac{1}{3}(E_{MM}-E^p_{MM})\delta_{AB}], \tag{33a}$$

$$\mu=\frac{(1-\beta)}{2\rho_0C_2\tau_{AB}\tau_{AB}}, \tag{33b}$$

$$\hat{\gamma}=2\rho_0C_2\tau_{AB}\dot{E}_{AB}-2[\kappa+g(z)]\dot{g}, \tag{33c}$$

$$\left.\begin{aligned}&\dot{E}^p_{AB}=0, &(34a)\\ &\dot{\kappa}=0, &(34b)\\ &\Sigma_{AB}\dot{E}^p_{AB}=0, &(34c)\end{aligned}\right\}\text{during elastic response, unloading, or neutral loading}$$

$$\left.\begin{aligned}&\dot{E}^p_{AB}=\frac{(1-\beta)\tau_{AB}}{2\rho_0C_2\tau_{MN}\tau_{MN}}\hat{\gamma}, &(35a)\\ &\dot{\kappa}=\frac{\beta}{2[\kappa+g(z)]}\hat{\gamma}, &(35b)\\ &\Sigma_{AB}\dot{E}^p_{AB}=\frac{(1-\beta)}{2\rho_0{}^2C_2\theta}\hat{\gamma} &(35c)\end{aligned}\right\}\text{during loading}$$

and from (27b), (27e), and (31e) that

$$z=C\,ln\left(1+\frac{1}{2}B_1\dot{E}_{AA}\dot{E}_{BB}+B_2\dot{E}_{AB}\dot{E}_{AB}\right) \tag{36a}$$

$$B_1+\frac{2}{3}B_2\geq 0, \quad B_2\geq 0. \tag{36b,c}$$

Now by comparing the response of the material defined by (32d) with that of a linear thermoelastic solid[12] (see [16], p. 359), the constants C_1, C_2 and D can be identified. It follows that

$$\rho_0C_1=\frac{\nu\mathrm{E}}{(1+\nu)(1-2\nu)}, \quad \rho_0C_2=\frac{\mathrm{E}}{2(1+\nu)}, \quad \rho_0D=\frac{\mathrm{E}\alpha}{(1-2\nu)} \tag{37a,b,c}$$

where E is Young's modulus, ν is Poisson's ratio, and α is the thermal coefficient of linear expansion.

Once the constants

$$\{\mathrm{E}, \nu, \kappa_0, \beta, B, B_1, B_2, C, \theta_0, \alpha, k, D_1, D_2\} \tag{38}$$

are specified, the constitutive nature of the material under discussion will be known. The constants (38) cannot, however, be chosen totally arbitrarily. In particular, we recall the restrictions (27c,d) and (36b,c) as well as the usual conditions

$$\mathrm{E}>0, \quad -1<\nu<\frac{1}{2}, \tag{39a,b}$$

which arise by making physical assumptions about the response of a linearly elastic solid during simple tension, simple shear, and hydrostatic compression. Additional restrictions on the constants (38) may be deduced by imposing the thermodynamic conditions (9a), (9b), and (23). With the help of (6b), (29a), (32), (33b), (37), and (39), the condition (23) is automatically satisfied and the inequalities (9a), (9b), and (16) reduce to

$$k\geq 0, \quad D_2>0, \quad \beta<1. \tag{40a,b,c}$$

Finally, we make the usual assumption for work-hardening materials that $\dot{\kappa}$ is non-negative and deduce from (35b) and the fact that κ is positive and g is non-negative that

[11] By using appropriate expressions for τ_{AB}, we can rewrite the expressions A_{AB} and M_{AB} in terms of the variables (10a,b).

[12] Recall that in the linear theory, there is no distinction between the Cauchy stress and the symmetric Piola-Kirchhoff stress **S**.

$$\beta \geq 0. \tag{41}$$

With the help of the expressions (7), (8), (17), (32), and (35) and the restrictions (39) and (40*a*,*c*), it is interesting to note that during loading

$$w^* > 0, \quad \xi > 0. \tag{42a,b}$$

The conditions (42*a*,*b*) are consistent with the notion that plastic deformation is a dissipative process.

An Example of a Uniaxial Strain Process

In this section, we consider a uniaxial strain process in which a bar is compressed[13] axially but not allowed to deform laterally. Furthermore, we require the process to be homogeneous and isothermal. For such a process, we specify

$$x_1 = a(t)X_1, \quad x_2 = X_2, \quad x_3 = X_3, \quad \theta = \theta_0, \quad (43a,b,c,d)$$

where a is a function of time only, θ_0 is the constant temperture, and where the vectors $\mathbf{x}$ and $\mathbf{X}$ are referred to the same set of fixed Cartesian base vectors. Although this process may be impossible to produce experimentally, it allows us to analytically examine some of the important features of the thermoelastic-viscoplastic constitutive model described in the preceding section. Now with the help of (25), (32–37), and (43), we may deduce the results

$$\mathrm{E}_{11} = \frac{1}{2}(a^2 - 1), \tag{44a}$$

$$\tau_{11} = -2\tau_{22} = -2\tau_{33} = 2\rho_0 C_2 \left[\frac{2}{3}\mathrm{E}_{11} - \mathrm{E}^p_{11}\right], \tag{44b}$$

$$\mathrm{E}^p_{22} = \mathrm{E}^p_{33} = -\frac{1}{2}\mathrm{E}^p_{11}, \tag{44c}$$

$$\gamma = \frac{3}{4}\tau^2_{11} - [\kappa + g(z)]^2, \tag{44d}$$

$$\hat{\gamma} = 2\rho_0 C_2 \tau_{11}\dot{E}_{11} - 2[\kappa + g(z)]\dot{g}, \tag{44e}$$

$$\dot{E}^p_{11} = \frac{(1-\beta)}{3\rho_0 C_2 \tau_{11}}\hat{\gamma}, \quad \dot{\kappa} = \frac{\beta}{2[\kappa + g(z)]}\hat{\gamma} \text{ during loading}, \tag{44f,g}$$

$$z = C\, ln[1 + B_3 \dot{E}^2_{11}], \quad B_3 = \frac{1}{2}B_1 + B_2 > 0, \tag{44h,i}$$

where B_3 is a constant and where we have identified the reference configuration as the initial configuration and have used the conditions (30). The remaining components of E_{AB}, τ_{AB} and E^p_{AB} all vanish. Since κ is positive and $g(z)$ is nonnegative, it follows from (11), (44*d*), and (44*e*) that during loading τ_{11} is nonvanishing so we may write

$$\tau_{11} = \pm\left(\frac{4}{3}\right)^{1/2}[\kappa + g(z)], \tag{45a}$$

$$\hat{\gamma} = [\kappa + g(z)]\left[\pm 2\rho_0 C_2\left(\frac{4}{3}\right)^{1/2}\dot{E}_{11} - 2\dot{g}\right], \tag{45b}$$

$$\hat{\gamma} = -\tau_{11}[-2\rho_0 C_2 \dot{E}_{11} \pm (3)^{1/2}\dot{g}]. \tag{45c}$$

With the help of (45*b*) and (45*c*), the equations (44*f*) and (44*g*) may be reduced to the forms

$$\dot{E}^p_{11} = -\frac{(1-\beta)}{3\rho_0 C_2}[-2\rho_0 C_2 \dot{E}_{11} \pm (3)^{1/2}\dot{g}], \tag{46a}$$

$$\dot{\kappa} = \pm\left(\frac{\rho_0 C_2 \beta}{1-\beta}\right)(3)^{1/2}\dot{E}^p_{11}, \tag{46b}$$

where the plus sign is used in the expressions (45) and (46) if τ_{11} is positive during loading and the minus sign is used if τ_{11} is negative during loading.

It is now apparent that the equations (46*a*) and (46*b*) may be integrated and the quantities S_{AB}, E^p_{AB}, and κ determined analytically for arbitrary specifications of $a(t)$ in (43*a*) and the non-negative function $g(z)$ in (25). Of course, for the balance laws to be satisfied for an arbitrary specification of the homogeneous, isothermal process defined by (43), the specific body force and specific external rate of entropy supply must be specified appropriately. Keeping this in mind, we consider an example that examines the constitutive response of our thermoelastic-viscoplastic model to a deformation history that includes segments of loading, unloading, and reloading, each occurring at varying strain rates.

For the purposes of this example, we specify the material properties in a somewhat arbitrary manner and take[14]

$$\mathrm{E} = 120\text{ GPa}, \quad \nu = 0.4, \quad \kappa_0 = 0.7\text{ GPa}, \quad \beta = 0.02,$$
$$B = 0.35\text{ GPa}, \quad B_3 = 1\times 10^{12}s^{-2}, \quad C = 5\times 10^{-2}, \tag{47}$$

Furthermore, the function $a(t)$ in (43) is specified in the form

$$a(t) = 1 - a_1(1 - e^{-a_2 t}) + a_3(1 - e^{-a_4 t})$$
$$- a_5(1 - e^{-a_6 t}) + a_7(1 - e^{-a_8 t}) - a_9 t \tag{48}$$

where

$$a_1 = 0.04, \quad a_2 = 1000s^{-1}, \quad a_3 = 0.0145, \quad a_4 = 10s^{-1},$$
$$a_5 = 0.04, \quad a_6 = 0.1s^{-1}, \quad a_7 = 0.0145, \quad a_8 = 1\times 10^{-3}s^{-1},$$
$$a_9 = 1\times 10^{-7}s^{-1} \tag{49}$$

The solutions for the elastic segments of this example are obtained by merely using the expressions (37), (44), (47), and (48) with E^p_{AB} being constant, whereas the solutions for the viscoplastic segments are obtained by using the expressions (27*a*), (37), (44), (47), and (48) as well as the equations (46) (utilizing the minus signs). In addition, the yield point associated with each viscoplastic segment is determined by calculating the time at which the value of the yield function γ changes from being negative to being zero. The transition point between viscoplastic loading ($\gamma = 0$ and $\hat{\gamma} > 0$) and elastic unloading ($\gamma < 0$) is called neutral loading and is determined by calculating the time (during each viscoplastic segment) at which $\gamma = 0$ and $\hat{\gamma} = 0$. The solution of this example is shown in Fig. 2(*a*) where the quantity $(J_2')^{1/2}$ is plotted verses strain E_{11}. Also indicated in Fig. 2(*a*) are the strain rates $\dot{E}_{11}$ at the yield points, the initial value of κ and the value of κ at the end of each viscoplastic loading segment of the process. The elastic segments are denoted by dashed lines while the viscoplastic segments I, II, and III are denoted by solid lines. Since this deformation is occurring at varying strain rate, we have also plotted in Fig. 2(*b*) the strain rate $\dot{E}_{11}$ versus strain E_{11} for the viscoplastic loading segments I, II, and III. For this example, it can be shown that the transition point between viscoplastic loading and elastic unloading can be determined by requiring $\gamma = 0$ and $\dot{E}_{11} = 0$ instead of $\gamma = 0$ and $\hat{\gamma} = 0$. The extent to which we have satisfied the condition $\dot{E}_{11} = 0$ at this transition point is represented by the end points of the viscoplastic segments shown in Fig. 2(*b*).

This example clearly exhibits the fact that the value of $(J_2')^{1/2}$ can exceed the value of κ during viscoplastic loading at high strain rates. In this example, the magnitude of the strain rate in the viscoplastic segments monotonically decreases with increase in strain. Therefore, during viscoplastic loading, the value of κ is increasing whereas the value of $g(z)$ is decreasing. Since equation (28) must be satisfied during viscoplastic loading, we realize that these effects complete with each other. In this regard, we point out that near the ends of the viscoplastic segments I and II in Fig. 2(*a*) strain rate effects dominate and the curves have steep slopes. The shapes of

[13] This process should not be confused with a standard compression test, which maintains uniaxial stress instead of uniaxial strain.

[14] Since we are mainly interested in examining the mechanical response of the model and are not solving the balance laws, no specification is made for the quantities ρ_0, θ_0, α, k, D_1, and D_2.

these transition regions (from high strain rate to low strain rate) are very similar to the shape of the experimentally determined transition region reported by Bodner and Partom ([11], Fig. 4, p. 388) for uniaxial stress tests. Furthermore, we note from equation (28) and the form of $g(z)$ given by (27) that when the material is loaded quasi-statically ($\dot{E}_{11} \simeq 0$ and $g(z) \simeq 0$) from an elastic state to a viscoplastic state yield occurs when the value of $(J_2')^{1/2}$ equal the current value of the hardening parameter. This fact is also exhibited by the yield point of the viscoplastic loading segment III shown in Fig. 2(*a*).

Since strain-rate effects dominate in the transition regions described in the foregoing, the quantitative characteristics of this transition are controlled to a large extent by our choice of the function $g(z)$ in (27). In this regard, we would like to briefly discuss how experimental data may be used to determine the constitutive constants and functions that characterize the mechanical response of the thermoelastic-viscoplastic model described in this paper. Apart from the usual determination of the material constants E and ν, we need to determine the initial value of the hardening parameter κ_0; the constant β, which controls the amount of hardening; as well as the function $g(z)$, which characterizes the rate-dependent yield strength of the material. From a single uniaxial stress experiment conducted under quasi-static loading conditions, it is possible to determine the value of κ_0 by measuring the yield strength and the value of β by measuring the slope of the stress-strain curve in the viscoplastic segment. To determine the function $g(z)$, it is necessary to conduct a series of experiments at various strain rates. The function $g(z)$ may then be determined by using equation (28) (with $\kappa = \kappa_0$) and plotting the measured values of $(J_2')^{1/2}$ at yield against the imposed strain rates.

Conclusions

A nonlinear constitutive model for a thermoelastic-viscoplastic material with a rate-dependent yield strength is developed using recent advances in continuum thermodynamics. In contrast with other constitutive models for materials with rate-sensitive plastic response, the model developed in this paper incorporates the simplifications associated with rate-insensitive elastic response without losing the ability to model a rate-dependent yield strength.

References

1 Maiden, C. J., and Green, S. J., "Compressive Strain-Rate Tests on Six Selected Materials at Strain Rates from 10^{-3} to 10^4 In/In/Sec," ASME Journal of Applied Mechanics, Vol. 33, Sept. 1966, pp. 496-504.

2 Green, A. E., and Naghdi, P. M., "A General Theory of an Elastic-Plastic Continuum," *Archive for Rational Mechanics and Analysis*, Vol. 18, No. 4, 1965, pp. 251-281.

3 Green, A. E., and Naghdi, P. M., "A Thermodynamic Development of Elastic-Plastic Continua," *Proceedings of the IUTAM Symposium on Irreversible Aspects of Continuum Mechanics and Transfer of Physical Characteristics in Moving Fluids*, Springer-Verlag, 1966, pp. 117-131.

4 Taylor, Sir G. I., "The Use of Flat-Ended Projectiles for Determining Dynamic Yield Stress, I. Theoretical Considerations," *Proceedings of the Royal Society of London*, Series A, Vol. 194, No. 1038, 1948, pp. 289-299.

5 Wilkins, M. L., and Guinan, M. W., "Impact of Cylinders on a Rigid Boundary," *Journal of Applied Physics*, Vol. 44, No. 3, Mar 1973, pp. 1200-1206.

6 Malvern, L. E., "The Propagation of Longitudinal Waves of Plastic Deformation in a Bar of Material Exhibiting a Strain-Rate Effect," ASME Journal of Applied Mechanics, Vol. 18, June 1951, pp. 203-208.

7 Perzyna, P., "Fundamental Problems in Viscoplasticity," in *Advances in Applied Mechanics*, Vol. 9, Academic Press, 1966, pp. 243-277.

8 Cristescu, N., *Dynamic Plasticity*, North-Holland, Amsterdam, 1967.

9 Naghdi, P. M., and Murch, S. A., "On the Mechanical Behavior of Viscoelastic/Plastic Solids," ASME Journal of Applied Mechanics, Vol. 30, Sept. 1963, pp. 321-328.

10 Green, A. E., and Naghdi, P. M., "A Class of Viscoelastic-Plastic Media," *Acta Mechanica*, Vol. IV/3, 1967, pp. 288-295.

11 Bodner, S. R., and Partom, Y., "Constitutive Equations for Elastic Viscoplastic Strain-Hardening Materials," ASME Journal of Applied Mechanics, Vol. 42, June 1975, pp. 385-389.

12 Green, A. E., and Naghdi, P. M., "On Thermodynamics and the Nature of the Second Law," *Proceedings of the Royal Society of London*, Series A, Vol. 357, 1977, pp. 253-270.

13 Green, A. E., and Naghdi, P. M., "The Second Law of Thermodynamics and Cyclic Processes," ASME Journal of Applied Mechanics, Vol. 45, Sept. 1978, pp. 487-492.

14 Green, A. E., and Naghdi, P. M., "On Thermodynamic Restrictions in the Theory of Elastic-Plastic Materials," *Acta Mechanica*, Vol. 30, 1978, pp. 157-162.

15 Naghdi, P. M., and Trapp, J. A., "The Significance of Formulating Plasticity Theory with Reference to Loading Surfaces in Strain Space," *International Journal of Engineering Science*, Vol. 13, 1975, pp. 785-797.

16 Sokolnikoff, I. S., *Mathematical Theory of Elasticity*, McGraw-Hill, New York, 1956.

An Integral Equation Approach to the Inclusion Problem of Elastoplasticity

W. C. Johnson
NRC Postdoctoral Research Associate,
National Bureau of Standards,
A153 Materials,
Washington, D.C. 20234

J. K. Lee
Associate Professor,
Department of Metallurgical Engineering,
Michigan Technological University,
Houghton, Mich. 49931

An integral equation approach is derived for the calculation of the elastoplastic strain field associated with a transformed inclusion of constant stress-free transformation strain and for an inhomogeneity when the far stress field remains elastic. The assumptions of a coherent precipitate and the deformation theory of plasticity are employed although any yield condition and flow rule can be chosen. The complexity of the integral equation is such that an iterative solution scheme is necessary. The technique is applied to a spherical precipitate in a uniform elastic stress field where associated stress and strain fields and plastic zone are calculated. The nature of the plastic relaxation process compares qualitatively with two-dimensional plane stress behavior. Extension of this technique to the nonaxisymmetric problem is also examined.

1 Introduction

The elastoplastic deformation of the matrix surrounding misfitting precipitates can lead to substantial decreases in the energy of the system and profound changes in the associated stress fields. These changes in turn can cause substantial modification in a number of physical and mechanical properties of the material. Solutions to inclusion problems in elastoplasticity are usually complex, especially for the three-dimensional problem. If radial symmetry exists, then relatively simple expressions can be obtained for the stress, strain, and the strain energy associated with a misfitting spherical precipitate [1, 2]. However, most cases do not exhibit radial symmetry and recourse must often be made to plane stress or plane strain assumptions.

A number of approximations have been employed to model the stress distribution in the vicinity of an ellipsoidal inclusion. The simplest approaches, such as those due to Shibata and Ono [3] and Tanaka and Mori [4] treat the stress field as a superposition of an inhomogeneity term and a plastic deformation term when an ellipsoid of revolution is subjected to a uniform stress field. Although this approach can be used successfully in work-hardening theories, such a formulation might be a poor approximation since it is based on the superposition of stress fields. More often, when information is needed on the development of a plastic zone in the vicinity of a precipitate, recourse is made to the two-dimensional plane stress case. Here several analytical solutions exist for rigid cylindrical inclusions embedded in matrices exhibiting Ramberg-Osgood type strain hardening [5] and ideal plasticity [4]. Argon, Im, and Safoglu [6] compare the analytical approximations with a finite-element

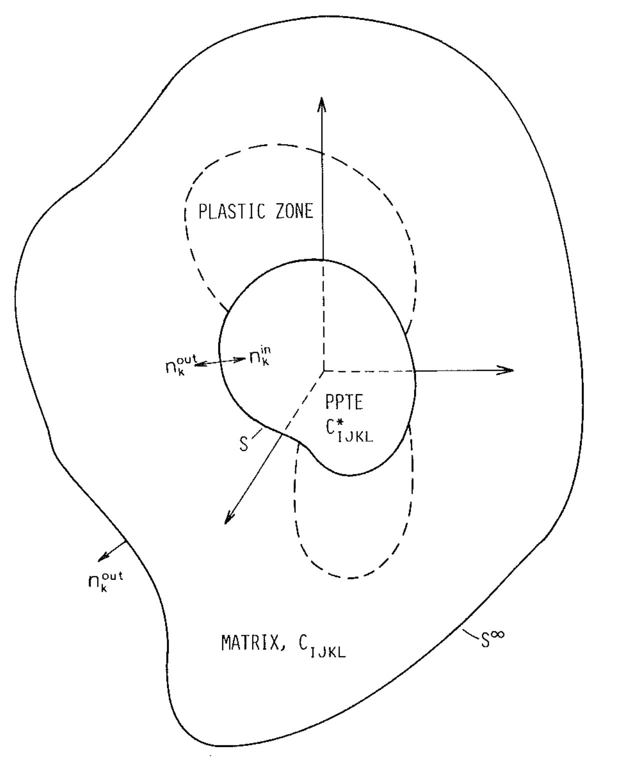

Fig. 1 Schematic representation of a precipitate and associated plastic zone. Notation employed in development of the elastoplastic integral equations is also shown.

approach and use the results to predict cavity nucleation at rigid spherical precipitates. When the cylindrical inclusion is considered to be a cavity, series approximations to the displacement and stress are also obtainable using stress function and perturbation methods [7, 8] and energy methods

Contributed by the Applied Mechanics Division for publication in the JOURNAL OF APPLIED MECHANICS.

Discussion on this paper should be addressed to the Editorial Department, ASME, United Engineering Center, 345 East 47th Street, New York, N.Y. 10017, and will be accepted until two months after final publication of the paper itself in the JOURNAL OF APPLIED MECHANICS. Manuscript received by ASME Applied Mechanics Division, September, 1981; final revision, January, 1982.

[9]. The techniques of plane stress plasticity, however, are not readily extendable to the three-dimensional problem.

In this study, we formulate an integral approach to the inclusion problem of elastoplasticity. Two independent integral equations are derived. The first concerns the displacement field associated with a precipitate possessing a constant stress-free transformation strain. The second integral equation defines the displacement for an inhomogeneity problem for an applied stress field that is constant and is less than the yield stress. Since the resulting integral equations are quite complex, an iterative solution scheme is employed. The technique is illustrated by application to the case of a relatively hard precipitate in a uniform stress field.

2 Development of Elastoplastic Integral Equations

In dealing with the elastoplastic inclusion problem, we assume that, for simplicity, the inclusion remains elastic and thus plastic deformation occurs only in the matrix adjacent to the inclusion. Furthermore, the plastic relaxation is assumed to be independent of strain rate and stress orientation. The inclusion-matrix interface is taken as coherent, and deformation theory is assumed as is infinitesimal continuum theory. The displacement, u_k, and total strain, ϵ_{kl}, are related by

$$\epsilon_{kl}(\vec{x}\,') = \frac{1}{2}(u_{k,l}(\vec{x}\,') + u_{l,k}(\vec{x}\,')). \tag{1}$$

The comma denotes differentiation with respect to x_k'. For deformation-type plastic behavior, the total strain is equal to the sum of the elastic, ϵ_{ij}^e, and plastic, ϵ_{ij}^p, strains, i.e.,

$$\epsilon_{kl}(\vec{x}\,') = \epsilon_{kl}^e(\vec{x}\,') + \epsilon_{kl}^p(\vec{x}\,'). \tag{2}$$

For an elastoplastic system to maintain static equilibrium, the equations of equilibrium must be satisfied identically at every point. Making reference to Fig. 1 depicting the geometry of the problem and the notation employed, the equations of equilibrium can be expressed as

$$C_{ijkl}^*[\epsilon_{kl}(\vec{x}\,') - \epsilon_{kl}^p(\vec{x}\,')]_{,j} = 0 \quad \text{if } \vec{x}\,' \text{ in precipitate} \tag{3}$$

$$C_{ijkl}[\epsilon_{kl}(\vec{x}\,') - \epsilon_{kl}^p(\vec{x}\,')]_{,j} = 0 \quad \text{if } \vec{x}\,' \text{ in matrix} \tag{4}$$

where C_{ijkl} and C_{ijkl}^* are the elastic constants of the matrix and precipitate phases, respectively. Equations (3) and (4) can be combined into one equation as [10, 11]

$$C_{ijkl}u_{k,lj}(\vec{x}\,') = [C_{ijkl} - C_{ijkl}(\vec{x}\,')]u_{k,lj}(\vec{x}\,') + C_{ijkl}(\vec{x}\,')\epsilon_{kl,j}^p(\vec{x}\,') \tag{5}$$

where

$$C_{ijkl}(\vec{x}\,') = C_{ijkl} \qquad \text{if } \vec{x}\,' \text{ in matrix}$$
$$C_{ijkl}(\vec{x}\,') = C_{ijkl}^* \qquad \text{if } \vec{x}\,' \text{ in precipitate.}$$

We can define the operator

$$D_{li} = C_{ijkl}\partial x_j' \partial x_k' \tag{6}$$

from which the elastic Green's function, $G_{im}(\vec{x} - \vec{x}\,')$ can be defined as

$$D_{li}G_{im}(\vec{x} - \vec{x}\,') + \delta_{lm}\delta(\vec{x} - \vec{x}\,') = 0 \tag{7}$$

where δ_{lm} is the Kronecker delta function and $\delta(\vec{x} - \vec{x}\,')$ is the Dirac delta function. A solution for the displacement can be obtained by multiplying equation (5) by $G_{im}(\vec{x} - \vec{x}\,')$ and equation (7) by $u_l(\vec{x}\,')$ and then subtracting equation (7) from equation (5). Integrating the resultant expression over all space with respect to $\vec{x}\,'$, the following integral equation is obtained for the displacement

$$\begin{aligned} u_m(\vec{x}) \;&=\; \iiint_\infty [G_{ml}(\vec{x} - \vec{x}\,')D_{li}u_i(\vec{x}\,') \\ &-\; u_l(\vec{x}\,')D_{li}G_{im}(\vec{x} - \vec{x}\,')]dV(\vec{x}\,') \\ &+\; \iiint_\infty [C_{ijkl}(\vec{x}\,') - C_{ijkl}]G_{ml}(\vec{x} - \vec{x}\,')u_{i,jk}(\vec{x}\,')dV(\vec{x}\,') \\ &-\; \iiint_\infty C_{ijkl}(\vec{x}\,')\epsilon_{ij,k}^p(\vec{x}\,')G_{ml}(\vec{x} - \vec{x}\,')dV(\vec{x}\,'). \end{aligned} \tag{8}$$

Equation (8) can now be manipulated in the same manner as for the case of an elastic system [11] by involving continuity of displacement and traction at the precipitate-matrix interface. Equation (8) allows for plastic relaxation in both precipitate and matrix phases; however, it shall now be assumed that plastic relaxation is restricted to the matrix. Under this condition, continuity of displacement requires

$$\hat{\hat{u}}_i(\vec{x}\,') = \hat{u}_i(\vec{x}\,') \tag{9}$$

where $\hat{\hat{u}}_i$ is the displacement on the precipitate side and $\hat{u}_i$ is the displacement on the matrix side of the precipitate-matrix interface.

For the transformation problem with a constant stress-free transformation strain $\epsilon_{ij}^{T^*}$, continuity of traction necessitates

$$[C_{ijkl}^*\hat{\hat{u}}_{k,l}^c(\vec{x}\,') - \sigma_{ij}^{T^*}]n_j^{\text{out}} = [C_{ijkl}\hat{u}_{k,l}^c(\vec{x}\,') - C_{ijkl}\epsilon_{kl}^p(\vec{x}\,')]n_j^{\text{out}}. \tag{10}$$

The left and right-hand sides of equation (10) are the tractions on the precipitate and matrix sides of the precipitate-matrix interface, respectively. The stress-free transformation stress is $\sigma_{ij}^{T^*}$ and is determined by $\sigma_{ij}^{T^*} = C_{ijkl}^*\epsilon_{kl}^{T^*}$. The superscript c on the displacement implies a measure of the constrained displacement; i.e., the displacement is referred to the system in its initial state before the stress-free transformation strain is applied. For the inhomogeneity problem, continuity of traction can be written

$$C_{ijkl}^*\hat{\hat{u}}_{i,j}(\vec{x}\,')n_k^{\text{out}} = [C_{ijkl}\hat{u}_{i,j}(\vec{x}\,') - C_{ijkl}\epsilon_{ij}^p(\vec{x}\,')]n_k^{\text{out}} \tag{11}$$

where the displacement referred to for the inhomogeneity problem is the *total* displacement and is still measured with respect to the position of the system before the boundary conditions are applied.

Use of the divergence theorem and equations (8)–(10) yields the following integral equation for the displacement field with an imposed transformation strain [11]

$$\begin{aligned} u_m^c(\vec{x}) \;&=\; \iiint_V \sigma_{kl}^{T^*}G_{ml,k}(\vec{x} - \vec{x}\,')dV(\vec{x}\,') \\ &-\; \Delta C_{ijkl}\iiint_V G_{ml,k}(\vec{x} - \vec{x}\,')u_{i,j}^c(\vec{x}\,')dV(\vec{x}\,') \\ &+\; C_{ijkl}\iiint_M G_{ml,k}(\vec{x} - \vec{x}\,')\epsilon_{ij}^p(\vec{x}\,')dV(\vec{x}\,') \end{aligned} \tag{12}$$

where $\Delta C_{ijkl} = C_{ijkl}^* - C_{ijkl}$ and the integral over the matrix reduces to an integral over the plastic zone. Equation (12) is the governing equation for the displacement associated with an arbitrarily shaped precipitate possessing an eigenstrain $\epsilon_{ij}^{T^*}$ in which the matrix phase is able to relax plastically. If no plastic relaxation in the system is allowed, the integral over the matrix is eliminated and equation (12) becomes equivalent to an integral equation [11] for the displacement field associated with a misfitting precipitate in an elastic medium.

Likewise, an integral equation for the displacement associated with the inhomogeneity problem can be obtained from equations (8), (9), and (11)

$$\begin{aligned} u_m(\vec{x}) \;&=\; u_m^a(\vec{x}) - \Delta C_{ijkl}\iiint_V u_{i,j}(\vec{x}\,')G_{ml,k}(\vec{x} - \vec{x}\,')dV(\vec{x}\,') \\ &+\; C_{ijkl}\iiint_M \epsilon_{ij}^p(\vec{x}\,')G_{ml,k}(\vec{x} - \vec{x}\,')dV(\vec{x}\,') \end{aligned} \tag{13}$$

where $u_m^a(\vec{x})$ is the applied displacement field and again the integral over the matrix is performed only over the plastic zone.

3 Numerical Results

Equations (12) and (13) are actually differential-integral equations in the displacement, u_m. Furthermore, the bounds on the volume integral over the matrix are complicated functions of the strains and displacements. Such difficulties seem to preclude any attempt at achieving analytical solutions

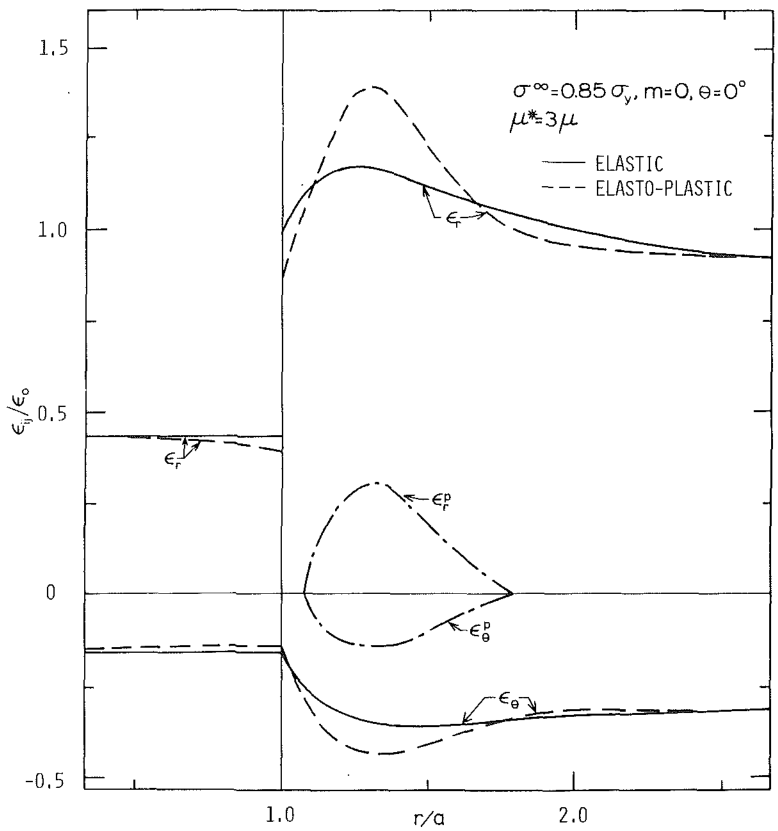

Fig. 2 The strains normalized to the strain at yielding are plotted as a function of radial distance from the inclusion center for θ = 0 deg and ideal plastic behavior. The far stress field is taken as 85 percent of the yield stress, the elastic strains are given by the solid lines and the elastoplastic strains by the broken lines.

to the displacements field. Of the several approaches available for the numerical solution of integral equations [12–14], one of the most straightforward is the iterative technique. Iteration to the final displacement field requires that an initial estimate be made of the displacements, total strains, and plastic strains of sufficient accuracy to ensure convergence. This assumes, of course, that the integral equation is expressed in a form that does converge for the specific problem of interest.

When invoking the iteration scheme, an approximation is first made to the elastoplastic displacement field by equating it with the elastic displacements. The displacement field then allows numerical calculation of the distortion (displacement gradient) and plastic strains, which can be substituted into the integrands of the volume integrals appearing on the right-hand sides of the integral equations. The integration can be performed numerically and a new estimate of the displacement obtained. The preceding process is simply repeated until the displacement field converges to a unique solution.

As derived, the elastoplastic integral equations are general since no restrictions are placed on the stress-strain relations nor is a specific yield criterion or flow rule defined. For computational purposes, we employ von Mises' yield condition and the associated Prandtl-Reuss flow rule for deformation theory, i.e., yielding takes place when the equivalent stress, σ_e, is equal to the yield stress in uniaxial tension, σ_y, or $\sigma_e = \sqrt{3S_{ij}S_{ij}/2} = \sigma_y$ where S_{ij} is the deviatoric stress tensor. For deformation theory, the Prandtl-Reuss relations can be written as

$$\epsilon_{ij}^p = \frac{3}{2}\,\frac{\epsilon_p}{\sigma_e}\,S_{ij} \tag{14}$$

where ϵ_p is a measure of the effective plastic strain and is defined by $\epsilon_p = \sqrt{2\epsilon_{ij}^p\epsilon_{ij}^p/3}$. ϵ_p is directly related to the plastic strain for a uniaxial tension test. In this study we restrict our considerations to linear strain-hardening behavior.

In an effort to examine the formulation of the elastoplastic integral equations, the choice of solution technique, the rapidity of convergence, and the accuracy of solution, the integral equation for the transformation problem is first applied to a spherical precipitate possessing a purely dilational stress-free transformation strain for which analytical solutions exist [1, 2]. The radially symmetric displacement field evident in this problem necessitates computation of only one displacement component. Using a standard five-point formula for numerical differentiation and a six-point Simpson-type numerical integration routine, it is found that the accuracy of the numerical results is surprisingly good. In all cases the displacement is found to lie within 1 percent of the exact analytical solution [16]. The tangential strains, being determined directly from the displacements, also fall within the same tolerances. Deviation of the radial strain from analytical results is less than 1 percent for distances greater than about 1.5 precipitate radii increasing to about 10 percent near the precipitate-matrix interface. Since the computed displacements are quite accurate near the precipitate, error in the radial strains is almost certainly due to the calculation of numerical derivatives especially in this region where the displacement field is changing rapidly and there exists a natural discontinuity in the slope of the displacement at the precipitate-matrix interface. The rate of convergence seems to be slower as the precipitate phase becomes softer. This general trend is accentuated as the inhomogeneity of the system becomes more pronounced. When the elastic constants of the precipitate are much less than those of the matrix, the rate of convergence is very slow requiring many iterations before the analytical results are

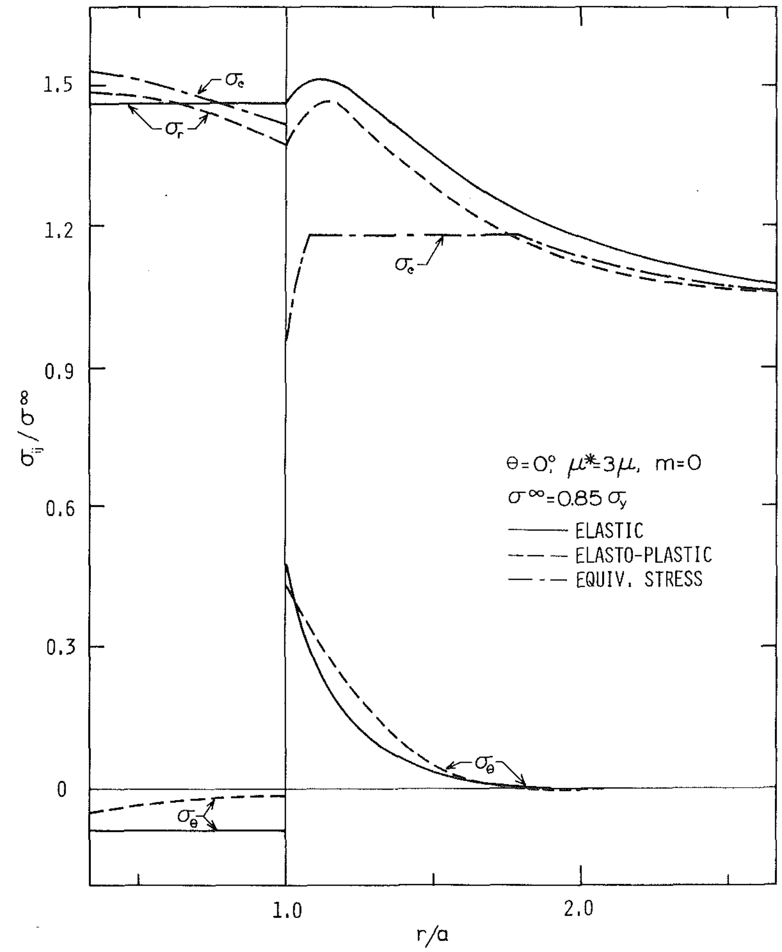

Fig. 3 The stress normalized to the far stress field is plotted as a function of radial distance from the center of the inclusion for $\theta = 0$ deg and ideal plastic behavior. The solid lines depict the elastic case and the broken lines the elastoplastic case. The stresses depicted here correspond to the strains given by Fig. 2.

achieved. Such behavior is a function of the form taken by the integral equation and may indicate that employment of the elastic solution for a first-guess approximation is a poor one.

For a spherical precipitate immersed in a uniform stress field, a system is chosen in which precipitate and matrix possess identical Poisson's ratios ($\nu = 1/3$) but the precipitate has a shear modulus three times that of the matrix; $\mu^* = 3\mu$. Linear strain hardening is employed for ideal plastic behavior with the hardening coefficient $m = 0$. The yield stress is taken as $\sigma_y = 10^{-3}\mu$ and a far stress field corresponding to uniaxial tension is chosen in the elastic range of $\sigma^\infty = 0.85\sigma_y$ and is applied in the x_3 direction.

Although the geometry of the axisymmetric system is such that calculation of the displacements in one quadrant only is required, two components of the displacement exist as portrayed in Fig. 2. This necessitates in the determination of the displacement component in the direction of the applied stress as well as in any direction perpendicular to the applied stress. For the cases examined in this study, the volume integration is performed over the quarter space defined by $x_3 \geq 0$ and $x_2 \geq 0$; the contribution of the plastic strains within the region $x_2 \leq 0$ being incorporated into the integrand by setting $x_2 = -x_2$.

Figure 2 illustrates the behavior of the strain field as a function of distance, measured in terms of the precipitate radius, for the direction $\theta = 0$ where θ is measured from the x_3-axis. The strains are normalized to the strain at yielding, ϵ_0, and are portrayed in spherical coordinates. The solid lines depict the strain field for pure elastic behavior while the broken lines correspond to the elastoplastic case. The equally

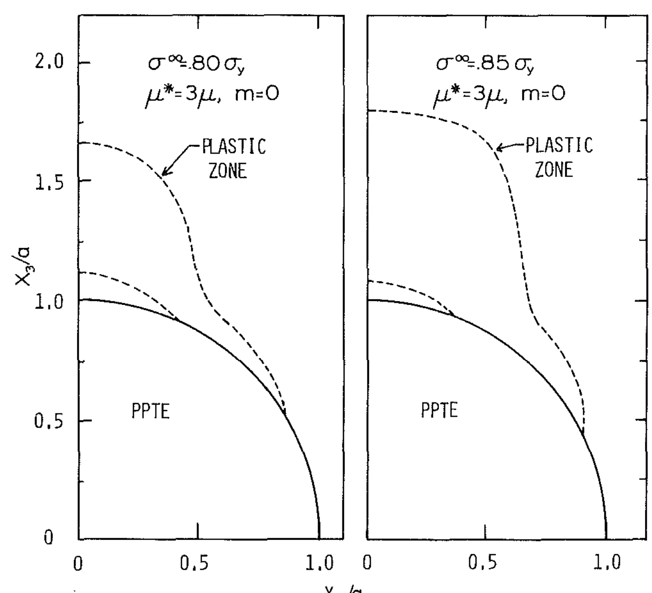

Fig. 4 The geometry of the plastic zone for a relatively hard precipitate in which $\mu^* = 3\mu$. The figures show one quadrant of the plane $x_2 = 0$. The solid line represents the precipitate-matrix boundary and the broken line the extent of plastic relaxation. The representation on the left is for $\sigma^\infty = 0.80\,\sigma_y$ and the one on the right for $\sigma^\infty = 0.85\,\sigma_y$.

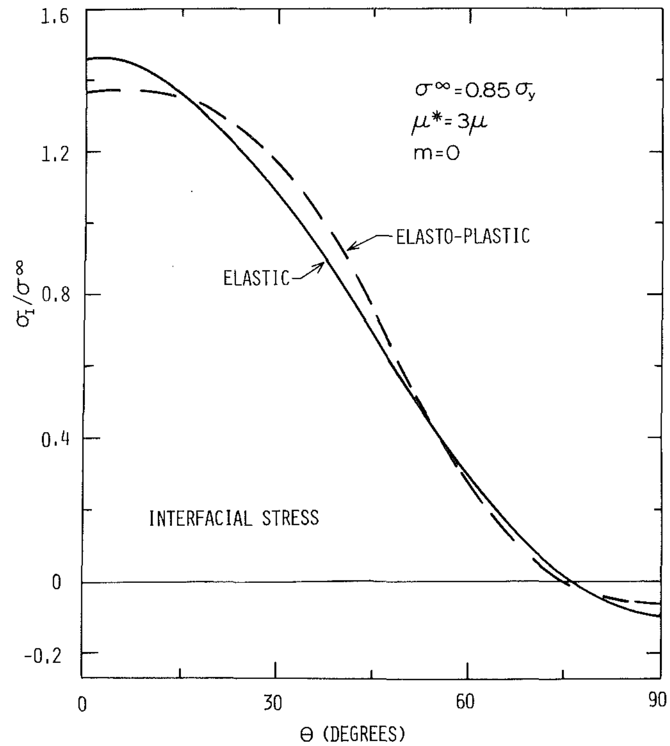

Fig. 5 The interfacial stress is normalized to the far stress field and is plotted as a function of theta. The solid line is for the elastic behavior when $\sigma^\infty = 0.85\,\sigma_y$.

spaced broken lines represent the total strain state on plastic relaxation while the dotted-dashed lines depict the plastic strains. The behavior observed is most interesting in that plastic flow does not initiate at the precipitate-matrix interface along the $\theta = 0$ direction. Instead there is an elastic region extending from the precipitate out to a distance of approximately $1.07a$, where a is the precipitate radius. Upon yielding, the extent of plastic relaxation increases rapidly reaching a peak value at about $r = 1.3a$ before decreasing gradually to become purely elastic at $r = 1.78a$. The total strains take the same form as the plastic strains reaching peak values at about $r = 1.3a$ before tapering off and approaching the strains encountered in the pure elastic solution. One very significant manifestation of the plastic relaxation in the vicinity of the precipitate is the reduction in the strain field encountered, as compared with the pure elastic case, when the matrix resumes elastic behavior. The decrease in strains in this region, corresponding to the attainment of the far stress field at a much more rapid rate, signifies a decrease in the perturbation of the applied stress field and a decrease in the energy of the system associated with the presence of the inhomogeneity as compared with the elastic solution. This change in the elastic strain field is as high as 7 or 8 percent at distances as far as $r = 2a$. As expected for ideal plastic behavior, the elastic field within the plastic zone is also reduced with respect to the elastic system as can be verified by subtracting the plastic strains from the total strains.

A small change in the strain field of the precipitate is also observed at the onset of plastic relaxation. The strain field is no longer constant, decreasing very gradually as the precipitate-matrix interface is approached. It also obtains a strain at the center of the inclusion slightly greater than the pure elastic case. Such a reduction in the precipitate strain field would be expected from the energetics of the system. Since it is more difficult for the far stress field to make a hard inclusion conform to the applied strain field of the matrix, the tendency for the system would be to decrease the distortion associated with the precipitate while incorporating it into the matrix phase. One must exercise discretion when evaluating strain fields in the immediate vicinity of the interface. As observed in the study of the transformation problem, the necessity of calculating numerical derivatives may lead to errors as large as 10 percent near the precipitate-matrix interface. However, these errors are usually encountered in the matrix phase while behavior in the precipitate is observed to be fairly gradual. Furthermore, and most importantly, it is shown later that continuity of traction calculations are fairly reasonable across the precipitate-matrix interface indicating that the strain calculations are reasonably acceptable.

As an illustration of the behavior of the stress field surrounding a relatively hard inhomogeneity immersed in a uniform strain field, we have plotted the stresses, normalized to the stress at infinity, as a function of the radial distance for the case corresponding to the strains depicted in Fig. 2. Figure 3 portrays the stress field for $\theta = 0$. For comparative purposes, the equivalent stress as calculated from the plastic results is also included as the dashed line of unequal length. In the matrix phase, the radial stress for the plastic solution is consistently less than that obtained when plastic relaxation is prohibited, especially in the direction defined by $\theta = 0$. In the precipitate, the radial stress achieves values slightly greater than the elastic case in the center of the sphere while decreasing significantly below the elastic solution as the interface is approached.

The tangential stress, σ_θ, is also observed to decrease substantially within the precipitate phase. Unexpected behavior is observed in the tangential stress exterior to the inclusion however, where σ_θ for the elastoplastic solution is greater than that of the elastic case. Such a stress field is not in contradiction with Fig. 2 where the elastic strains for the plastic solution are shown to lie below the strains for the pure elastic case in this region, but can be clarified by reference to the stress-strain relations where $\sigma_{ij} = \lambda\epsilon^e_{kk}\delta_{ij} + 2\mu\epsilon^e_{ij}$. For the elastoplastic solution the dilatation is a larger, positive number than for the elastic case while the tangential strain, ϵ^e_θ, is a smaller (in magnitude) negative number. Hence, when the two terms are added, the results depicted in Fig. 3 follow naturally.

The equivalent stress for the plastically relaxed case is also portrayed in Fig. 3. Since ideal plasticity dictates that flow occurs when the equivalent stress is equal to the yield stress and that no work hardening takes place, the equivalent stress should be equal to the yield stress in the plastic zone. This is precisely the situation realized in Fig. 3.

The stress and strain fields depicted by Figs. 2 and 3 might be better grasped with reference to the geometry of the plastic zone as a whole. One quadrant of the plastic zone which is symmetrically related to the other three quadrants is illustrated in Fig. 4. For comparative purposes, the plastic zone corresponding to the identical system only with a far stress field of $\sigma^\infty = 0.80\sigma_y$ is also shown at the left. The solid line represents the precipitate-matrix interface while the broken line depicts the boundary between the plastic zone and elastic behavior in the matrix phase. The majority of the plastic relaxation takes place in the direction of the applied stress field. What is interesting to observe is the presence of an elastic region completely surrounded by a plastic zone situated on the precipitate-matrix interface extending from zero to almost 20 deg for the case $\sigma^\infty = 0.85\sigma_y$. Apparently, this behavior is not unique to the three-dimensional problem. Argon et al. [6] have modeled the spread of the plastic zone for the two-dimensional problem of a rigid cylinder subjected to a far stress field that is of shear character, by finite-element techniques. Although the grid network employed is rather coarse, they observe the nucleation of a plastic region that is removed from the interface in the directions of the maximum tensile stress. As the far shear stress is increased, a new plastic region is formed in the direction of the applied shear stress. These distinct plastic zones merge leaving regions of elastic behavior surrounded by a plastic zone in the maximum tensile directions and situated on the precipitate-matrix interface. The boundary conditions invoked by Argon et al. [6] are fundamentally different from ours, yet it is interesting to note that similar behavior is observed in the spread of the plastic zone.

For the case of an applied tensile stress, direct application of von Mises's yield criterion to the elastic solution indicates that distinct plastic regions form in the direction of the applied stress away from the interface and at the interface in roughly the direction of the maximum applied shear stress. As the far tensile stress is increased, these regions overlap, leaving behind the elastic cap depicted in Fig. 4. Although we have applied our technique only to the cases of $\sigma^\infty/\sigma_y = 0.85$ and 0.80, it appears that the overlap of the distinct plastic regions occurs, for $\mu^* = 3\mu$, when the far stress field is about $\sigma^\infty \cong 0.79\sigma_y$.

The existence of the elastic cap at the precipitate-matrix interface is possibly understood on physical grounds by considering two points. The first concern is that the system desires to decrease the effective presence of the strong inhomogeneity by shielding its disturbance from as much of the matrix as possible while specifically attempting to decrease the stress and strain field of the precipitate in order to achieve a lower total energy to the system. At the same time, a continuity of displacement and traction must be maintained at the precipitate-matrix interface—the traction continuity necessitating an equivalence of radial stresses across the interface. Hence, if radial stresses in the matrix at the interface are sufficient to cause plastic relaxation, then the stresses within the precipitate must be correspondingly larger, which would have the tendency to raise the energy of the system. Consequently, the problem may be circumvented by maintaining an elastic buffer zone between the plastic region and the precipitate. This same behavior is observed for the elastic case and a hard precipitate where Fig. 2 also exhibits a maximum value in the radial elastic strain rather than a monotonic decrease from the precipitate-matrix interface. The peak behavior of the radial elastic strain was also noticed in the work of Moschovidis and Mura [17], who studied the elastic stress field associated with inhomogeneities through an equivalent inclusion method.

Of important concern in some material behavior is the development of large interfacial stresses associated with a relatively hard inclusion subjected to a far stress field. Although we have been concerned only with the incipient stages of plastic relaxation, certain trends in the interfacial stress have begun to manifest themselves. In Fig. 5 the interfacial stress normalized to the applied tensile stress is plotted as a function of orientation angle, θ. We retain the same system with $\sigma^\infty = 0.85\sigma_y$, $\mu^* = 3\mu$ and $m = 0$. The solid line depicts the interfacial stress for the purely elastic condition with the broken line representing the elastoplastic case. The trend observed is that on plastic relaxation the interfacial stress decreases for low angles of $\theta (\theta < 15$ deg) and increases for the higher values of θ (15 deg $< \theta < 55$ deg) maintaining a fairly flat value for θ less than about 15 deg. Huang [5], in his study of rigid cylindrical inclusions in an incompressible Ramberg-Osgood strain-hardening material subjected to an applied shear stress, finds that a maximum interfacial stress develops about 12 deg from the direction of the principal tensile axis. Orr and Brown [18] find for the same type of problem a maximum in the shear stress developing at about an angle of 17 deg from the principal tensile axis for very large distant strain levels. In our work we see what may be the initial stages of the shift in the maximum interfacial stress.

With the substantial error that may arise in calculation of the strains from the numerical derivatives of the displacements, some question may arise as to the validity of the solution in the region of the precipitate-matrix interface. In an attempt to determine the magnitude of the errors that may be occurring, the tractions are calculated on the interface in both precipitate and matrix phases. These results indicate that the continuity of traction is reasonable along the entire precipitate-matrix interface. The radial stresses are within 3 or 4 percent for $\theta \leq 20$ deg rising to about 20 percent at $\theta \simeq 40$ deg. The agreement between tractions in precipitate and matrix phases then improves greatly until θ approaches 90 deg where larger divergences begin to occur (although the magnitude of the radial stress has become much smaller). The tangential stresses usually fall within 15–20 percent of one another for the smaller values of θ (where the magnitude of the tangential stress is small) while becoming quite similar for values of θ exceeding 45 deg. Since the difference in these values is not too much greater than the error occurring from the derivatives in the transformation problem, it is felt that the representation of the stress and strain field is reasonable for the results obtained.

The effectiveness of the integral equation approach to the inclusion problem of plasticity is determined by the ability to handle the volume integral over the plastic zone. Clearly if the plastic zone becomes too large, performing the volume integral becomes unreasonable at least in the manner that we have approached the problem. Such difficulties become all important when nonaxisymmetric problems are considered. For these cases, the volume integral over the plastic zone must still be calculated, but the determination of the displacement must be accomplished over some three-dimensional region. This would require large increases in the computation time per iteration of the solution. Hence, it appears that the integral equation approach to plasticity problems of a nonaxisymmetric nature is straightforward in principle but not necessarily in application.

For axisymmetric systems, however, the need to determine displacements over a planar region makes the integral equation approach attractive so long as the plastic zone does not become too large. If the problem defined in the displacements can be reformulated in the distortions, then the difficulty associated with the calculation of numerical derivatives may be avoided and the uncertainty in the immediate vicinity of the interface may be somewhat alleviated. Although the integral equation procedure is employed with the intent of arriving at solutions to the three-dimensional inclusion problem, it may be most applicable to the two-dimensional problem, especially the plane stress case. This is because the integration need be performed only over a planar region with the displacements being calculated over a planar region. In this manner, reformulation of the displacement problem in terms of the distortion should not greatly increase the computer time necessary to iterate to a stable solution.

4 Summary

In this study we have derived an integrodifferential equation for the solution of the displacement field associated with either a transformed inclusion or inhomogeneity when the matrix phase is allowed to relax plastically. When the technique is applied to a misfitting spherical precipitate using an iterative solution scheme, the results are found to be in good agreement with analytical solutions. The integral equation is then applied to a relatively hard precipitate in a uniform stress field. On the basis of the results obtained from the transformation problem and continuity of traction calculations, we feel our solution to the inhomogeneity problem is reasonable. General trends in the behavior of the plastic zone size are similar to those observed for the two-dimensional plane stress case including the formation of an elastic cap in the direction of the maximum tensile stress.

Acknowledgments

This work was supported by the Division of Materials Research of the National Science Foundation under Grant DMR79-01693 for whose support it is gratefully acknowledged. The authors are indebted to Prof. D. M. Barnett of Stanford for valuable suggestions during the course of this work.

References

1 Lee, J. K., Earmme, Y. Y., Aaronson, H. I., and Russell, K. C., "Plastic Relaxation of the Transformation Strain Energy of a Misfitting Spherical Precipitate: Ideal Plastic Behavior," *Met. Trans.*, Vol. 11A, 1980, pp. 1837–1847.

2 Earmme, Y. Y., Johnson, W. C., and Lee, J. K., "Plastic Relaxation of the Transformation Strain Energy of a Misfitting Spherical Precipitate: Linear and Power-Law Strain Hardening," *Met. Trans.*, Vol. 12A, No. 8, 1981.

3 Shibata, M., and Ono, K., "Internal Stresses Due to an Oblate Spheroidal Inclusion: Misfit, Inhomogeneity and Plastic Deformation Effects," *Acta Met.*, Vol. 26, 1978, pp. 921–932.

4 Tanaka, K., and Mori, T., "The Hardening of Crystals by Non-Deforming Particles and Fibres," *Acta Met.*, Vol. 18, 1970, pp. 931–941.

5 Huang, W. C., "Theoretical Study of Stress Concentration at Circular Holes and Inclusions in Strain Hardening Materials," *Int. J. Solid Structure*, Vol. 8, 1972, pp. 149–192.

6 Argon, A. S., Im, J., and Safoglu, R., "Cavity Formation From Inclusions in Ductile Fracture," *Met. Trans.*, Vol. 6A, 1975, pp. 825–837.

7 Tuba, I. S., "A Method of Elastic-Plastic Plane Stress and Strain Analysis," *J. Strain Anal.*, Vol. 1, 1966, pp. 115–120.

8 Tuba, I. S., "An Analytic Method for Elastic-Plastic Solution," *Int. J. Solid Structure*, Vol. 3, 1967, pp. 543–564.

9 Schlack, A. L., "Elastic Stability of Pierced Square Plates," *Exp. Mech.*, Vol. 4, 1964, pp. 167–172.

10 Chen, F. C., and Young, K., "Inclusions of Arbitrary Shape in an Elastic Medium," *J. Math. Phys.*, Vol. 18, 1977, pp. 1412–1416.

11 Johnson, W. C., Earmme, Y. Y., and Lee, J. K., "Approximation of the Strain Field Associated With an Inhomogeneous Precipitate: Theory," ASME Journal of Applied Mechanics, Vol. 47, 1980, pp. 775–780.

12 Irving, J., and Mullineux, N., *Mathematics in Physics and Engineering*, Chapter 12, Academic Press, New York, 1959.

13 Lovitt, W. V., *Linear Integral Equations*, Dover, New York, 1950.

14 Atkinson, K. E., *A Survey of Numerical Methods for the Solution of Fredholm Integral Equations of the Second Kind*, Society for Industrial and Applied Mechanics, Philadelphia, 1976.

15 Mendelson, A., *Plasticity: Theory and Application*, MacMillan, New York, 1968.

16 Details of numerical results are listed in W. C. Johnson's Ph.D. thesis "The Elasto-Plastic Behavior of Inclusions," Michigan Technological University, Houghton, Michigan, 1980.

17 Moschovidis, Z. A., and Mura, T., "Two-Ellipsoidal Inhomogeneities by the Equivalent Inclusion Method," ASME Journal of Applied Mechanics, Vol. 42, 1975, pp. 847–852.

18 Orr, J., and Brown, D. K., Dept. of Mech. Eng., Report, University of Glasgow, 1973.

Bounds on the Transverse Effective Conductivity of Computer-Generated Fiber Composites

J. J. McCoy
Professor,
Department of Civil Engineering,
The Catholic University of America,
Washington, D.C. 20064
Mem. ASME

Using trial functions that are motivated by single-body calculations, we have derived bounds on the effective transverse thermal conductivity of a fiber composite. These bounds incorporate both fiber area fraction information and some information of the configurational statistics. Simplified expressions for the bounds are obtained for the limits of widely differing conductivity values for the constitutent phases, and of a dilute suspension. The bounds are made specific for a given computer-generated fiber composite and these specific bounds are compared with the best available bounds that require area fraction information alone. The conclusions reached are that configuration statistics are significant for effective property calculations for moderately dense composites for component conductivity values that differ by some one to two orders of magnitude, or greater. Further, the bounds based on the single-body calculation are reasonably close for component conductivity values that differ by some two orders of magnitude, or less.

Introduction

In constructing prediction models for the effective properties of a suspension of an inclusion phase randomly dispersed throughout a matrix, the engineer or scientist must address two problems of some difficulty. Both problems arise because the effective properties are dependent on complicated multiple particle interactions. One of the problems is a problem in analysis; it is to develop solution algorithms capable of incorporating the multiple particle interactions. The second problem is a problem in description; it is to prescribe the statistics of the microstructure that are required by the algorithms developed, if they are to be applied to a specific suspension. Clearly, logical priority should be given the problem in analysis and the literature of effective property prediction modeling is consistent with this. With a number of methods of analysis available, it is now appropriate to consider the description problem and its impact on the goals of the engineer or scientist; e.g., improved designs of composite materials or the development of inverse algorithms by which some aspect of the microstructure geometry is inferred from a bulk property measurement.

We can distinguish between effective property prediction models which are direct, in the sense that the goal is to predict a numerical value for an effective property measure, from models intended to place upper and lower bounds on permissible numerical values of the measure. Direct models can be obtained in limiting situations; e.g., a weakly inhomogeneous limit or a dilute suspension limit and their extensions (see reference [1] for a discussion). Such models are perturbative in their nature and their utility in discussing real suspensions is qualitative. For example, the importance of inclusion shape on an effective property measure can be demonstrated by a dilute suspension calculation. Nonperturbative direct models can be derived based on "self-consistent" calculations. These models have been severely criticized in the literature and the domain of the validity, if any, is a subject of some controversy. From the perspective of our studies this controversy is largely academic. Central to the application of a self-consistent calculation of an effective property measure is an assumption that the effective property is independent of refined information of the microstructure geometry. Thus, in a sense our interest is limited, by definition, to that class of microstructures for which self-consistent calculations fail. Nonperturbative direct models that are based on "exact" calculations are also available, for an ingenious and precisely described geometry, the concentric sphere assemblage, or its two-dimensional counterpart, the concentric cylinder assemblage [2, 3]. While the rigor of these last calculations, for the specified microstructures for which they are derived, is not a subject of controversy, their applicability to more general microstructures requires an assumption as to the lack of importance of differences in microstructure geometry. Thus, from the perspective of our studies, this use of calculations based on precisely defined microstructures suffer the same limitation as do self-consistent calculations.

Contributed by the Applied Mechanics Division for publication in the JOURNAL OF APPLIED MECHANICS.

Discussion on this paper should be addressed to the Editorial Department, ASME, United Engineering Center, 345 East 47th Street, New York, N.Y. 10017, and will be accepted until two months after final publication of the paper itself in the JOURNAL OF APPLIED MECHANICS. Manuscript received by ASME Applied Mechanics Division, October, 1981; final revision, December, 1981.

Finally, we can envision a direct model based on a numerical solution to the microstructure field problem, for a given random suspension. A direct numerical approach is well within the capability of available computers. A numerical derivation of a direct effective property prediction model would serve to extend the models based on the composite sphere and composite cylinder assemblage to other microstructure geometries. Completely unanswered, however, is the question of relating a direct prediction model obtained for a given microstructure geometry model to the effective property of a given physical specimen, if the microstructure model is not a point-by-point simulation of the actual microstructure.

Bounding the permissible values of an effective property measure provides an approach which enables the introduction of limited information of the microstructure geometry, in a systematic fashion, while retaining a formulism that is mathematically rigorous. Presumably, as more information is incorporated into a given bound pair the smaller will be their spread. That is, the spread of a bound pair is a measure of the geometric information not incorporated in their determination. Any single bound pair can be interpreted to apply to a class of suspensions, the class being defined by the geometric information that is incorporated in its derivation. Thus, bounds that are based on volume fraction information alone are applicable to all suspensions with the prescribed volume fraction. Viewed in this light, widely separated bounds are widely separated because the class of suspensions to which they apply is very broad. This may be very disconcerting to an analyst with an interest in predicting an effective property; it should, on the other hand, be a very welcome event for a designer interested in exploiting the bounds, by judiciously controlling more refined microstructure geometry than that on which the bounds are based.

In our studies our goal is to develop rigorous bounds that incorporate more detailed information of the microstructure geometry than that contained in volume fraction information. With this accomplished we wish to reduce, or specify the bounds for a given suspension that we can "manufacture" in a digital computer. Of course any given suspension would exist as manufactured and, consequently, it would, in principle, be possible for us to directly calculate an effective property measure for it. As noted previously, however, such a calculation would apply only to it. By restricting our calculation to bounds, a given suspension is representative of a class of suspensions, a class that is defined by the geometric measures that are identified by the bounds.

In the specific study reported, herein, we consider a two-dimensional calculation and bound the transverse effective thermal conductivity of a fiber composite consisting of oriented, infinitely long, equisized, circular fibers dispersed randomly in an infinite matrix. It is well known [1, 2, 4] that by a simple redefinition of terms, the resulting expressions can be directly interpreted to provide bounds on a variety of effective property measures.

The outline of the paper is as follows. In the next section we provide a brief review of the bounding approach to predicting effective property measures. This is followed, in the third section, by a development of bounds that require information of the microstructure geometry that is more detailed than volume fraction information. A discussion of the newly derived bounds, including a comparison with bounds requiring only volume fraction information is given in the fourth section. It is in that section that we discuss the computer-generated composites and present the numerical results obtained for these.

Bounds on Effective Property Measures

All bounds on an effective property measure of a heterogeneous material are based on a definition of the measure in terms of an averaged energy stored in the material. Thus, the effective thermal conductivity makes reference to a specimen, comprised to the heterogeneous material, which is large enough to be representative of a collection of like manufactured specimens. The specimen is envisioned to be forced, at the boundary surfaces, in a manner that would result in homogeneous, i.e., constant heat flux, $\mathbf{q}(\mathbf{x})$, and temperature gradient, $\mathbf{T}(\mathbf{x})$, fields if applied to a similarly shaped specimen but comprised of a homogeneous material. The effective thermal conductivity is defined by equating the averaged thermal energy stored in a homogeneous, effective material specimen to that stored in the given, heterogeneous material specimen.

Reducing the definition to mathematical formulas, we have

$$\frac{1}{2}\mathbf{q}_0\cdot\mathbf{T}_0=\frac{1}{2V}\int\mathbf{q}(\mathbf{x})\cdot\mathbf{T}(\mathbf{x})d\mathbf{x}, \tag{1}$$

where $\mathbf{q}_0$ and $\mathbf{T}_0$ denote the constant heat flux and temperature gradient fields in the homogeneous, effective material specimen and $\mathbf{q}(\mathbf{x})$ and $\mathbf{T}(\mathbf{x})$ denote the spatially varying fields in the heterogeneous material specimen. The volume integral is over the extent of the specimen. Based on equation (1), we can write two expressions for computational definitions of k^*, the effective thermal conductivity.

$$\frac{1}{2}k^*\mathbf{T}_0\cdot\mathbf{T}_0=\frac{1}{2V}\int k(\mathbf{x})\mathbf{T}(\mathbf{x})\cdot\mathbf{T}/\mathbf{x})\,d\mathbf{x}, \tag{2a}$$

and

$$\frac{\mathbf{q}_0\cdot\mathbf{q}_0}{2k^*}=\frac{1}{2V}\int\frac{\mathbf{q}(\mathbf{x})\cdot\mathbf{q}(\mathbf{x})}{k(\mathbf{x})}d\mathbf{x}. \tag{2b}$$

Here, $k(\mathbf{x})$ is the spatially varing conductivity for the heterogeneous material specimen.

The bounds on k^* are obtained by making use of two, complementary variational formulations of the heat conduction problem. Thus, the actual temperature gradient field in the specimen is the member of a class of precisely prescribed vector fields, which minimizes the right-hand side of equation (2a). The class of trial fields are described as vector fields that are derived from scalar potentials which, in turn, are required to satisfy prescribed temperature conditions applied at the boundary of the specimen. In the context of the thought experiment in which k^* is to be determined, the foregoing requirement on the boundary condition to be satisfied by an appropriate trial function can be translated into a condition that the spatial average of the trial function must equal the temperature gradient in the homogeneous, effective material specimen; i.e., $\mathbf{T}_0$ [2]. On introducing $\mathbf{T}_T(\mathbf{x})$ to denote a generic member of the allowable class of vector fields, i.e., to denote a trial function, the variational formulation leads to an upper bound on k^*, i.e.

$$k^*\mathbf{T}_0\cdot\mathbf{T}_0\leq\frac{1}{V}\int k(\mathbf{x})\mathbf{T}_T(\mathbf{x})\cdot\mathbf{T}_T(\mathbf{x})d\mathbf{x}. \tag{3a}$$

The lower bound makes use of a complementary variational principle. The actual heat flux in the specimen is the member of a class of precisely prescribed vector fields that minimizes the right-hand side of equation (2b). The class of trial functions is now described as vector fields that are derived from vector potentials, and that satisfy prescribed heat flux conditions applied at the boundary of the specimen. The boundary condition to be satisfied, in the context of the present problem, is translated into a condition that the spatial average of the trial function must equal the heat flux in the homogeneous, effective material specimen, i.e., $\mathbf{q}_0$ [2]. On introducing $\mathbf{q}_T(x)$ to denote a trial function, the variational principle leads to the lower bound,

$$\frac{\mathbf{q}_0 \cdot \mathbf{q}_0}{k^*} \leq \frac{1}{V} \int \frac{q_T(\mathbf{x}) \cdot q_T(\mathbf{x})}{k(\mathbf{x})} d\mathbf{x}. \quad (3b)$$

The most elementary, or classical bounds follow immediately from equations (3*a*) and (3*b*) on noting that the constant $\mathbf{T}_0$ and $\mathbf{q}_0$ fields are appropriate trial functions for equations (3*a*), (3*b*), respectively. Thus we write

$$\frac{1}{\left\langle \frac{1}{k} \right\rangle} \leq k^* \leq \langle k \rangle, \quad (4a)$$

where the angular brackets are used to denote a spatial average taken over the specimen. It has been noted by a number of researchers, e.g., [4], that the law of mixtures, equating the effective property measure to a spatial average of the heterogeneous property measure, actually provides a rigorous upper bound to the effective property measure. Further, it is well appreciated, for heterogeneous materials that are described as suspensions of an inclusion phase dispersed throughout a matrix phase, that the nature of the geometric information in $\langle k \rangle$ and in $\langle 1/k \rangle$ is the relative amount of the two phases, i.e., volume fraction information.

Improved bounds can be obtained by choosing trial functions that more nearly reproduce the actual temperature gradient and heat flux fields. This is accomplished by approximately solving for the temperature gradient and heat flux fields. For the bounds to remain rigorous, it is of course necessary that the trial functions satisfy exactly the conditions dictated by the variational principle on which the bound is founded. A hierarchy of improved bounds can be obtained by using trial functions motivated by perturbation calculations [5]. These reported studies on improved bounds accept a statistical interpretation of the problem; an interpretation that replaces the spatial averages in eqaution (2*a*) and (2*b*) by statistical, or ensemble averages. Notice that, for the conditions stated in the definition of k^*, all the fields involved are to be statistically homogeneous in the limit of an unboundedly large specimen size, as observed on a length scale determined by variations in $k(\mathbf{x})$. The equation of a spatial average with an ensemble average amounts, then, to an ergodic hypothesis, the validity of which requires the specimen geometry to be representative. The hierarchy of bounds obtained as outlined collects additional information of $k(\mathbf{x})$ in the form of multipoint correlation functions. First-order bounds [6, 7], the classical bounds are referred to as zero-order, require, in addition to $\langle k \rangle$ and $\langle 1/k \rangle$, three-point correlation functions of the form $\langle k'(x_1)\ k'(x_2)\ k'(x_3) \rangle$ and $\langle k'(x_1)\ k'(x_2)/k(x_3) \rangle$, where $k'(x) = k(x) - \langle k \rangle$, for their evaluation. Second-order bounds require still further information in the form of four and five-point correlation functions [8]. For two-phase suspensions, the higher-order correlation functions are dependent on more refined information of the microstructure geometry, such as inclusion shape information or size distribution information. An interesting problem is to determine the relationship between these analytical measures and recognizable geometrical descriptions, a task that has been discussed by several researchers. (See, for example, [1] for a summary discussion.)

An alternative to using perturbation calculations to motivate trial functions, would be to consider the other limiting situation for which we can approximately solve for the effective property measure of a suspension, namely the dilute suspension limit. To first order the calculation requires the solution of a single-body problem. Although extensions to higher order can be envisioned (in the solutions to two-body calculations, then, three-body calculations, etc.,) the computational difficulties are expected to be significant. It is this alternate approach that we consider in the remainder of this paper. We note, here, that while the approach may seem to be natural, the author is familiar with only reference [9] as a published report of a similar calculation.

Effective Property Bounds Based on Single-Body Calculations

We consider a continuous fiber-reinforced composite and calculate bounds for the effective thermal conductivity measured transverse to the fiber direction. The bounds are based on trial functions that are motivated by solutions to single-body formulations. Thus, an appropriate trial function for the upper bound is

$$\mathbf{T}_T(\mathbf{x}) = \frac{T_0}{1-\alpha c} \left[\mathbf{e}_1 + \alpha \sum_{i=1} \mathbf{t}(\mathbf{x} - x_i) \right]_1 \quad (5)$$

where

$$\alpha = \frac{k_F - 1}{k_F + 1} \quad (6)$$

and

$$\mathbf{t}(\mathbf{x} - x_i) = \frac{\cos 2\theta_i \mathbf{e}_1 + \sin 2\theta_i \mathbf{e}_2}{r_i^2}; \; r_i > 1,$$
$$= -\mathbf{e}_1; \; r_i < 1. \quad (7)$$

In these expressions, $\mathbf{T}_0 = T_0 \mathbf{e}_1$ is the constant temperature gradient field in the homogeneous, effective medium, $\mathbf{e}_1$ being a distinguished direction in the plane transverse to the fiber direction; c is the area fraction of the inclusion, or fiber, phase; and k_F is the normalized fiber conductivity taken relative to the matrix conductivity, which is set equal to unity. The fibers are assumed to be circular in cross section and are to be equisized. We normalize transverse dimensions relative to the fiber radius, which is set equal to unity. The fibers are located by transverse position vectors, $\mathbf{x}_i$; the $\mathbf{r}_i = \mathbf{x} - x_i$ locate the fiber centers relative to the generic field point $\mathbf{x}$; and θ_i is the angle made by $\mathbf{r}_i$ and the distinguished direction, $\mathbf{e}_1$. The summation is over all the fibers, taken to be infinite in number in an appropriate limit.

That $\mathbf{T}_T(\mathbf{x})$ is derived from a scalar potential, i.e., that $\nabla x \mathbf{T}_T = 0$ for all $\mathbf{x}$, is readily demonstrated by a direct computation. As noted in the last section, it is also necessary to demonstrate that the average of $\mathbf{T}_T(\mathbf{x})$ is equal to $T_0 \mathbf{e}_1$ before accepting $\mathbf{T}_T(\mathbf{x})$ as a trial function. To do so requires specification of the average of interest. Depending on one's perspective of the problem, an average can be interpreted as a spatial average taken over the field point coordinate, $\mathbf{x}$, or a statistical average, the precise nature of which depends on different but equivalent definitions of the underlying stochastic process. For example, we can envision a specimen in which the locations of the individual fibers are precisely given, relative to a fixed origin, and a stochastic process in which the field point location, relative to this fixed origin, is random. The averaging is over the locations of the field point. This stochastic interpretation closely mirrors the deterministic interpretations; operationally the two interpretations lead to the same integration.

Alternately, we can envision an experiment in which the location of the field point, relative to a fixed origin is precisely given, but the locations of the fibers, relative to the fixed origin, are random. The averaging is over the locations of the fibers, or, over an ensemble of specimens. The equivalence of the two stochastic processes can be argued in the limit of an infinite number of unboundedly large, statistically identical specimens. We can envision still a third experiment in which the "fixed" origin is chosen to coincide with the location of a reference fiber and the stochastic process is defined by locating the field point, relative to this reference, randomly and also locating all other fibers, relative to this reference, randomly. Again the equivalence of this process with those outlined can be argued in the limit described.

Depending on the calculation to be performed, it is sometimes convenient to change our interpretation of the underlying process. For averaging $\mathbf{T}_T(\mathbf{x})$ it is convenient to consider a statistical average taken over the locations of the fibers. Operationally this requires multiplying the *r.h.s.* of equation (5) by a joint probability density function of the $\mathbf{x}_i$ coordinates and integrating the result over a $2N$ (N is the number of fibers, taken to be infinite in the limit) dimension configuration space. Because of the relatively slow rate of decay of $\mathbf{t}(\mathbf{r}_i)$ with increasing r_i, i.e., r_i^{-2}, we encounter a convergence difficulty in accomplishing the configuration space integration in the infinite domain limit. Further, due to the angular dependence of the numerator in equation (7), the nature of the convergence difficulty is not a logarithmic divergence, as a minus two decay rate might indicate; the difficulty is, instead, a conditional convergence. That is, while a finite limit can be achieved, the value of the limit depends on the precise manner of taking the limit; the value of the limit depends on the "shape" of infinity. The appearance of conditionally convergent integrals in effective property measure calculations, and the need to "renormalize" the calculations to remove the convergence problem have been the subjects of a fair number of recent papers [10-13]. It is, therefore, not necessary to consider this point in detail here. We simply note that conditionally convergent integrals are encountered in accomplishing the averages required on both sides of the inequalities that provide bounds on k^*, e.g., equation ($3a$), and that a mathematically acceptable renormalization is to be consistent in the manner of accomplishing the required integrations. That is, for example, the infinite domain integrations over $\mathbf{r}_i$ are to be accomplished first by integrating over θ_i followed by an integration over r_i wherever they are encountered. Following this operational rule, the average of $\mathbf{T}_T(x)$ calculates to $T_0\mathbf{e}_1$ for isotropic statistics.

We are now ready to calculate the average of $k(\mathbf{x})$ $\mathbf{T}_T(\mathbf{x})\cdot\mathbf{T}_T(\mathbf{x})$. It is convenient, here, to consider a statistical average taken over the random location of the field point, x. The following expression can be written,

$$\langle k(\mathbf{x})\mathbf{T}_T(\mathbf{x})\cdot\mathbf{T}_T(\mathbf{x})\rangle = (1-c)\langle\mathbf{T}_T(\mathbf{x})\cdot\mathbf{T}_T(\mathbf{x})\rangle_M + k_F c\langle\mathbf{T}_T(\mathbf{x})\cdot\mathbf{T}_T(\mathbf{x})\rangle_F) \qquad (8)$$

where the indicated averages on the *r.h.s.* are conditional averages, given that the field point is located in the matrix (M) or a fiber (F), and $(1-c)$ and c are the probabilities that the field point is located in the matrix and a fiber, respectively. These can, of course, be equated to area fractions. On substituting equations (5)-(7) into equation (8), and making use of equation ($3a$), the following equation is obtained for the upper bound of k^*, k_U^*.

$$(1-\alpha c)^2 k_U^* = F_U(\mathcal{C}, k_F), \qquad (9)$$

where the *r.h.s.* depends on the configuration statistics ($\mathcal{C}$) and on k_F according to

$$F_U(\mathcal{C}, k_F) = 1 - c + 4k_F c/(k_F+1)^2$$
$$+\alpha^2\left\{(1-c)\left[\left\langle\left(\sum_{i=1}\frac{\cos 2\theta_i}{r_i^2}\right)^2\right\rangle_M + \left\langle\left(\sum_{i=1}\frac{\sin 2\theta_i}{r_i^2}\right)^2\right\rangle_M\right]\right.$$
$$\left.+k_F c\left[\left\langle\left(\sum_{i=2}\frac{\cos 2\theta_i}{r_i^2}\right)^2\right\rangle_F + \left\langle\left(\sum_{i=2}\frac{\sin 2\theta_i}{r_i^2}\right)^2\right\rangle_F\right]\right\}. \qquad (10)$$

The conditional averages for the field point located in the matrix contains contributions from all fibers; the conditional averages for the field located in a fiber contains contributions from all fibers except the one within which the field point is located, the fiber denoted by $i = 1$.

In our numerical investigation of the bounds, presented in the next section, it is convenient to directly evaluate the conditional averages required by $F_U(\mathcal{C},k_F)$, as indicated by equation (10). Perhaps a more easily interpreted expression for $F_U(\mathcal{C},k_F)$, however, is in terms of integrations taken over certain conditional probability densities. We write

$$F_U(\mathcal{C},k_F) = (1-c)\left[1+\alpha^2\int\int\frac{P_{1M}(r)}{r^4}d\mathbf{r}\right] + \frac{4k_F}{(k_F+1)^2}c$$
$$+\alpha^2(1-c)\left[\int\int\frac{P_{2M}(r)}{r^4}d\mathbf{r}\right.$$
$$\left.+(1-c)\int\int\int\frac{(2\cos^2\theta-1)P_M(r,s,\theta)}{r^2s^2}drdsd\theta\right]$$
$$+\alpha^2 k_F c\left[\int\int\frac{P_{2I}(r)}{r^4}d\mathbf{r}\right.$$
$$\left.+c\int\int\int\frac{(2\cos^2\theta-1)P_I(r,s,\theta)}{r^2s^2}drdsd\theta\right], \qquad (11)$$

where the following conditional probability measures have been introduced.

$P_{1M}(r)$ *Conditional probability density on the location of* the nearest fiber to the origin, given the origin is in the matrix.

$P_{2M}(r)$ $(P_{2I}(r))$ Conditional probability density on the location of any fiber other than the fiber nearest the origin given in the origin is in the matrix (a fiber).

$P_M(r,s,\theta)$ $(P_I(r,s,\theta))$ Conditional probability density that the exterior vertices of a triangle formed by two lines of lengths r and s and included angle θ, locate the centers of two distinct fibers given the interior vertex lies in the matrix (a third fiber).

The two-dimensional integrations are over the transverse plane of the composite; the three-dimensional integrations are over the indicated coordinates. The probability densities are normalized and we have restricted the statistics of the suspension to be isotropic. It is clear from these probability density functions that the bounds given by equations (9), (10), or (11) require up to three-body information of the relative positions of the fibers.

A lower bound to k^* can be obtained using the trial function

$$\mathbf{q}_T(\mathbf{x}) = \frac{Q_0}{1+\alpha c}\left[\mathbf{e}_1 + \sum_{i=1}\mathbf{q}(\mathbf{x}-\mathbf{x}_i)\right], \qquad (12)$$

where $\mathbf{q}(\mathbf{x}-\mathbf{x}_i)$ differs from $\mathbf{t}(\mathbf{x}-\mathbf{x}_i)$ only in the sign of $\mathbf{e}_1$ for points such that $r_i < 1$. It is not difficult to demonstrate that $\nabla\cdot\mathbf{q}_T = 0$ and that the average of $\mathbf{q}_T(x)$ equals $Q_0\mathbf{e}_1$. The difference in the sign of $\mathbf{e}_1$ that distinguishes the two trial functions arises in satisfying the proper continuity conditions at the interface $r_i = 1$, for the separated single-body solutions. Using equation (12), we next calculate the average of $\mathbf{q}_T(x)\cdot\mathbf{q}_T(x)/k(x)$ *in exactly the same fashion* as indicated by equation (8). The following expression is obtained for the lower bound, $k_L{}^*$.

$$\frac{k_L^*}{(1+\alpha c)^2} = \frac{1}{F_L(\mathcal{C},k_F)}, \qquad (13)$$

where

$$F_L(\mathcal{C},k_F) = (1-c) + 4k_F c/(k_F+1)^2$$
$$+\alpha^2\left\{(1-c)\left[\left\langle\left(\sum_{i=1}\frac{\cos 2\theta_i}{r_i^2}\right)^2\right\rangle_M + \left\langle\left(\sum_{i=1}\frac{\sin 2\theta_i}{r_i^2}\right)^2\right\rangle_M\right]\right.$$
$$\left.+\frac{c}{k_F}\left[\left\langle\left(\sum_{i=2}\frac{\cos^2\theta_i}{r_i^2}\right)^2\right\rangle_F + \left\langle\left(\sum_{i=2}\frac{\sin 2\theta_i}{r_i^2}\right)^2\right\rangle_F\right]\right\}. \qquad (14)$$

Thus, $F_L(\mathcal{C}, k_F)$ is obtained from $F_U(\mathcal{C}, k_F)$ on replacing k_F

by $1/k_F$ in the last term of the defining equation. The configurational statistics required for $F_L(\mathcal{C}, k_F)$ are identical as those required for $F_U(\mathcal{C}, k_F)$.

In the next section we turn to a discussion of the derived bounds. We consider reduced expressions for them in limiting situations, their numerical evaluation for a computer simulation of a fiber composite, and compare them with previously presented bounds that incorporate less information of the microstructure geometry.

Discussion of the Bounds

We consider certain limiting expressions for the bounds. The limit $k_F \to 0$ corresponds to a suspension of nonconducting holes in a matrix of finite conductivity. For fixed c, the upper bound reduces, in this limit, to

$$(1+c)^2 k_U^* = \left[1 + \left\langle \left(\sum_{i=1} \frac{\cos 2\theta_i}{r_i^2} \right)^2 \right\rangle_M + \left\langle \left(\sum_{i=1} \frac{\sin 2\theta_i}{r_i^2} \right)^2 \right\rangle_M \right](1-c), \tag{15}$$

while the lower bound approaches zero as

$$\frac{k_L^*}{(1-c)^2} = \frac{(k_F/c)}{\left\langle \left(\sum_{i=2} \frac{\cos 2\theta_i}{r_i^2} \right)^2 \right\rangle_F + \left\langle \left(\sum_{i=2} \frac{\sin 2\theta_i}{r_i^2} \right)^2 \right\rangle_F}. \tag{16}$$

The loss of the lower bound for a suspension consisting of a void phase dispersed throughout a matrix is sometimes used as evidence of the weakness of the bounding approach to the effective property prediction problem. This loss, however, is actually a result of the fact that the bounds are rigorous and incorporate all aspects of the underlying physics exactly. The lower bound must vanish in the limit of $k_F \to 0$ since the bound does not incorporate sufficient geometric information to explicity exclude suspensions in which the void phase, i.e., the holes, form connected surfaces that separate the matrix phase into unconnected regions.[1] Such a suspension, which is more properly viewed as a suspension of unconnected inclusions of finite conductivity dispersed throughout a matrix of zero conductivity, will have an effective conductivity that is zero.

Similarly, we can consider the limit of $k_F \to \infty$. Because of the normalization of the problem, the limit of $k_F \to \infty$ can be interpreted as a suspension of fibers of finite conductivity dispersed through a matrix of zero conductivity. For fixed c, the upper bound increases without bound, in this limit, as

$$(1-c)^2 k_U{}^* = k_F c \left[\left\langle \left(\sum_{i=2} \frac{\cos 2\theta_i}{r_i^2} \right)^2 \right\rangle_F + \left\langle \left(\sum_{i=2} \frac{\sin 2\theta_i}{r_i^2} \right)^2 \right\rangle_F \right], \tag{17}$$

and the lower bound reduces to

$$\frac{k_L^*}{(1+c)^2} = \frac{1}{(1-c)\left[1 + \left\langle \left(\sum_{i=1} \frac{\cos 2\theta_i}{r_i^2} \right)^2 \right\rangle_M + \left\langle \left(\sum_{i=1} \frac{\sin 2\theta_i}{r_i^2} \right)^2 \right\rangle_M \right]}. \tag{18}$$

The upper bound corresponds to a geometry in which the high conductivity fibers form connected surfaces that may separate the zero conductivity matrix into unconnected regions. The fact that it increases without bound, in the limit, is due to the normalization of k^*, with respect to the matrix conductivity which is zero in the limit. The lower bound corresponds to a geometry in which the high conductivity fibers are isolated, separated by the zero conductivity matrix. The fact that it remains finite in the limit is, again, due to the normalization chosen.

As a general conclusion, then, for suspensions in which the conductivities of the two phases differ widely, effective conductivity values near to the upper bound are appropriate for geometries for which the higher conductivity phase forms connected surfaces. In this situation, the effective conductivity value is properly scaled using the higher conductivity value. Effective conductivity values near to the lower bound are appropriate for geometries for which the lower conductivity phase forms connected surfaces that separate the matrix into unconnected regions. In this situation, the effective conductivity value is properly scaled using the lower conductivity value.

Another limit of interest is the dilute suspension, or small c, limit. We refer to equations (11) and (14) and consider the simplifications to be introduced in F_U and F_L, for $c << 1$. Consider first the terms containing the conditional probabilities P_{2M}, P_{2I}, P_M, and P_I. These can all be neglected in the limit provided we introduce a restriction that precludes any clustering of fibers into groupings of two or more. More precisely, the requirement is that the distance separating a fiber from its neighbor is to be scaled by $c^{-1/2}$, in the limit. The two functions, F_L and F_U, minus the neglected terms are identical and the only remaining term containing configurational information is the indicated integral over the conditional probability P_{1M}. Moreover, it is not difficult to conclude that the dependence of this integral on the relative positioning of the fibers vanishes to lowest order in c, in the small c limit, subject to the same restriction introduced in the foregoing. Thus, we are justified in evaluating this integral for a specified configuration, say, the fibers are located at the intersection of a square grid. Specifically, then, we consider the average of r^{-4} for a stochastic experiment in which r is the distance from a fixed origin to a point that is randomly and uniformly positioned through the region that is exterior to a circle of unit radius and interior to a square of $\sqrt{\pi/c}$ sides, both centered at the origin. By direct calculation, this average, to lowest order in c, is equal to c. Thus, in the small c limit

$$F_U(\mathcal{C}, k_F) = F_L(\mathcal{C}, k_F) = 1 + 0(c^2) \tag{19}$$

and the bounds coincide in the limit to

$$k^* = 1 + 2\alpha c. \tag{20}$$

The coincidence of the bounds in the small concentration limit for suspensions in which there is no clustering is to be expected since the trial functions on which the bounds are based are a sum of exact solutions to the single body problem.

There is no contradiction in the loss of one of the bounds in the limits of $k_F \to 0$ or $k_F \to \infty$, and the coincidence of the

[1] It might appear at first that the condition that two inclusions touch would place strong restrictions on the probability density defined on the relative positions of the inclusion, and that knowledge of the two-particle probability density should enable us to distinguish particles that join to form closed surfaces. It must be remembered, however, that the two-particle probability density required of the bounds refers to all combinations of inclusion pairs. Thus, even if the inclusions were joined to form connected surfaces, the overwhelming preponderance of pairs would not touch.

Table 1 Evaluated measures of microstucture geometry for computer-generated fiber composites

c	0.05	0.10	0.20	0.30	0.10 (Rect.)
p_M	4.99×10^{-2}	9.05×10^{-2}	1.52×10^{-1}	1.3×10^{-1}	8.67×10^{-2}
p_F	7.78×10^{-4}	2.85×10^{-3}	9.56×10^{-3}	1.8×10^{-2}	3.27×10^{-6}
$\langle 1/r_1{}^4 \rangle_M$	4.94×10^{-2}	9.22×10^{-2}	1.77×10^{-1}	2.55×10^{-1}	9.75×10^{-2}

Table 2 Upper and lower bounds for computer-generated fiber composites and comparison with Hashin-Shtrikman bounds ($k_F = 100$)

Table 2[(a)]—Upper bound

c	0.05	0.10	0.20	0.30	0.10 (Rect.)
k_U^*	1.19	1.55	2.90	5.15	1.21
k_{UH}^*	3.56	6.26	12.10	18.61	6.26

Table 2[(b)]—Lower bound

c	0.05	0.10	0.20	0.30	0.10 (Rect.)
k_L^*	1.10	1.18	1.49	2.00	1.22
k_{LH}^*	1.10	1.22	1.50	1.83	1.22

bounds in the limit of small c. The first set of limits explicitly assumed that c remained an order one term, and the second limit assumed that k_F remained an order one term. The limit, for example, in which $k_F \to \infty$ and $c \to 0$ such that $k_F c$ remains finite would need to be considered separately.

We next turn to a comparison of the bounds given by equations (9), (10), (13), and (14) with bounds that are based on area fraction information alone. The simplest of these bounds is given by equation (4a) but we eschew any detailed discussion of these in favor of improved bounds, which we take from Hashin [2]. The bounds are one of a class of bounds that are most commonly referred to as Hashin-Shtrikman bounds. The text by Christensen [3] discusses the Hashin-Shtrikman bounds in detail. For the specific application of interest to us, the Hashin-Shtrikman bounds are

$$k_{UH}^* = \frac{[2+(k_F-1)c]k_F}{[2k_F-(k_F-1)c]}, \tag{21a}$$

and

$$k_{LH}^* = \frac{1+\alpha c}{1-\alpha c}. \tag{21b}$$

We can consider the behavior of these bounds in the same limits as in the foregoing. Similar conclusions are reached for the limits of $k_F \to \infty$ and $k_F \to 0$. The small c limit is of special interest, however, and we write, to order c,

$$k_{UH}^* = 1 + \frac{k_F^2-1}{2k_F}c \tag{22a}$$

and

$$k_{LH}^* = 1 + 2\alpha c \tag{22b}$$

Thus, the bounds no longer coincide even in this limit. This simply mirrors the facts that the Hashin-Shtrikman bounds do not make use of an exact single-body calculation in the small c limit and that they do not explicitly exlcude any fiber clustering, which was necessary to obtain equation (20). The fact that the lower Hashin-Shtrikman bound does reduce to equation (20) would be expected by one familar with the relationship between the Hashin-Shtrikman lower bound and an exact calculation of k^* for a suspension that is modeled by a concentric cylinder assemblage [2, 3].

Referring to equations (10) and (14) the measures of the mcrostructure geometry required by the bounds are the area fraction of the fibers and the two parameters,

$$p_M = (1-c)\left[\left\langle\left(\sum_{i=1}\frac{\cos 2\theta_i}{r_i{}^2}\right)^2\right\rangle_M + \left\langle\left(\sum_{i=1}\frac{\sin 2\theta_i}{r_i{}^2}\right)^2\right\rangle_M\right], \tag{23a}$$

and

$$p_F = c\left[\left\langle\left(\sum_{i=2}\frac{\cos 2\theta_i}{r_i{}^2}\right)^2\right\rangle_F + \left\langle\left(\sum_{i=2}\frac{\sin 2\theta_i}{r_i{}^2}\right)^2\right\rangle_F\right]. \tag{23b}$$

These parameters are functionals of probability densities defined on the relative positions of the fibers taken two and three at a time. We are interested in the possibility of measuring these parameters for a given fiber composite cross section and in some indication of the importance of these parameters in determining the value of the effective thermal conductivity. Thus, we undertook a numerical study in which we calculated p_M and p_F for computer-generated fiber composites, evaluated the bounds for the calculated values of p_M and p_F and prescribed values of k_F, and compared the resulting bounds with those given by Hashin, equation (21a) and (21b). We next consider this numerical study.

The computer-generated composites were constructed according to the following description. One thousand circles of equal radius were located, at random, within a rectangular region of unit dimension. The size of the circles were determined by the condition that the area fraction of the 1000 circles equaled the prescribed area fraction of the total cross section. The circles were positioned one at a time, with the only constraint placed on the location of any one circle being that any location in the square is equally likely, provided the circle does not overlap with previously located circles. In the event of an overlap, the last positioned circle was removed and a new one positioned as if the overlap has not occurred. An ensemble of 100 cross sections was generated for each area fraction of interest. The only test applied to determine the degreee to which the generated ensembles were representative, was a test of uniformity. Thus, each of the 100 cross sections were further subdivided into 25 subsections and the variance of the number of circles located in the subsections was calculated to be approximately equal to 3. This number, being more than an order of magnitude less than the mean number of circles (40), was deemed to be sufficiently small to accept the ensemble of cross sections as reasonable. The values of p_M and p_F were calculated for the ensemble of cross sections according to the following program. First two subensembles of field point locations were obtained for each of the 100 cross sections by randomly positioning the field points in the unit square and noting if the points so located were in the matrix or in the fiber. All of the 100 subensemble of field points located in the matrix were used to calculate p_M and all of the subensemble of field points located in the fiber were used to calculate p_F, according to the expressions in equation (23*a*) and (23*b*). Of course, the absolute size of the circles were scaled to be of unit radius before applying these formulas.

The calculated values of p_M and p_F are summarized in Table 1 for area fractions of 5, 10, 20, and 30 percent. Area fractions greater than 30 percent are difficult to obtain because of the large number of failures obtained in positioning nonoverlapping circles in constructing the media. Also shown in the figure are the calculated values for $\langle 1/r_1{}^4 \rangle_M$, r_i being the distance from a field point located in a matrix to the nearest inclusion. As discussed previously, the value of this average should be c in the small c limit. Finally shown in the figure are the values of p_M and p_F for a 10 percent concentration of circles for a cross section in which the circles are located at the intersections of a square grid. It was clear from the calculations that it is reasonable to determine values for p_M and p_F for a given cross section. Further, the comparison of the calculated average for $\langle 1/r_1{}^4 \rangle_M$ and the value of c leads to a degree of confidence in the calculated values.

With the calculated values of p_M and p_F, it is a straightforward calculation to obtain bounds, for any prescribed value for k_F. In Tables (2*a*) and (2*b*) are summarized calculated values for the upper and lower bounds for the four concentrations for a k_F value of 100 (times the value of the matrix). In the tables we include both the bounds containing p_M and p_F information and the bounds of Hashin, which depend only on area fraction information. An alternate presentation of these same results is given in graphical form in Fig. 1.

It is clear that the upper bound containing p_M and p_F information lies totally within the Hashin bounds, a heartening result. The fact that the lower bound values are, in some instances, slightly below the Hashin-Shtrikman bound (in the third significant figure) is thought to be a result of numerical inaccuracy. It is also clear that for a $k_F = 100$, incorporation of two and three fiber-positioning information does result in a considerable narrowing of the bounds. Finally, it can be noted that the newly calculated bounds lie much nearer to the Hashin lower bound than it does to the Hashin upper bound. This is consistent with the appreciated fact, already commented on, that suspensions for which the lower conductivity phase forms connected regions, isolating the higher conducting phase, have lower effective conductivity values. The manner of generating our composities would appear to preclude any possibility of the fibers forming closed contours, hence, we should expect the newly constructed bounds to be nearer the Hashin lower bound. Finally we can note that the upper bound value for the 10 percent concentration for the circles positioned on a rectangular grid is measurably lower than for the randomly positioned circles. This result might also be expected since the retangular grid might be thought of as a "well-separated" composite, as compared to the randomly positioned case, which might be thought of as a "well-mixed" composite. This distinction is discussed by McCoy and Beran [12] in which a conclusion consistent with that reached here was drawn. The fact that the upper bound value for the rectangular grid is actually a slight amount less than the lower bound value (in the third significant figure) is thought to be an insignificant numerical inaccuracy.

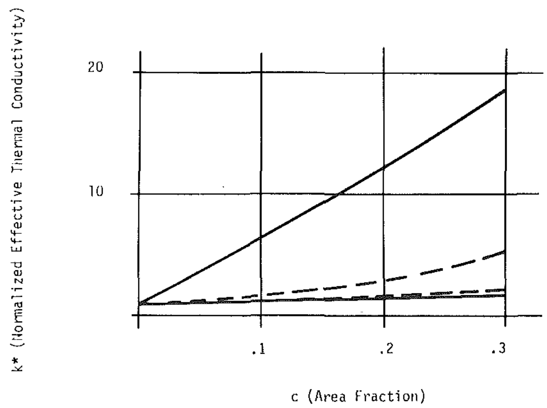

Fig. 1 Upper and lower bounds for computer-generated fiber composites (k_F = 100). Solid line are the Hashin-Shtrikman bounds; dashed lines are bounds that incorporate information of fiber positions.

Summary

In summary, the effort reported in this paper consists of two parts. The first is the derivation of a new pair of bounds on the transverse effective conductivity of a fiber composite. The newly derived bounds explicitly incorporate some configuration statistics, in the form of precisely described functionals of joint probability functions on the locations of the fibers. The second part is the evaluation of the newly derived bounds for a computer-generated model of a fiber composite.

As noted in the Introduction, an alternate approach, once the computer-generated model was constructed, would be to exactly calculate the transverse effective conductivity. We ignored this approach for two reasons. First, the exactly calculated value would apply only to the specific computer model for which it was calculated. Any change in any measure of the configurational statistics would affect an exactly calculated effective property, and, in a manner that is not precisely known. The bounds, on the other hand, apply to a class of composites; the class is defined by the configurational statistics required by the bounds. The second reason is related to the first. The motivation of the studies of which the present one is an example, is to identify numerical measures of the microstructure geometry, which can significantly effect an effective property value. The bounding approach enables one to accomplish this by systematically incorporating more and more refined information of the microstructure geometry, within the framework of an exact formulism. In the present study, for example, the measures denoted by p_M and p_F were identified. Further, we showed that p_M and p_F are easily determined for a given microstructure geometry and that the incorporation of the information in p_M and p_F results in a significant reduction in bound pair separation.

Identifying significant numerical measures of the microstructure geometry, from the perspective of their influence on effective property values, is not an end to itself. A later step is to relate the identified numerical measures either to the "manufacturing process" for constructing the composite or to an alternate, more intuitive, description of the microstructure geometry. Only then will it be possible to exploit variations in the configurational statistics of a composite material in the search for improved designs. We plan to continue the study reported, herein, by constructing computer-generated models according to different prescriptions and in measuring the changes in p_M and p_F.

Acknowledgment

This material is based on work supported by the National Science Foundation under Grant No. ENG 7820613. The author expresses his appreciation of Dr. Clifford J. Astill of the National Science Foundation for his continuing support of statistical studies of the mechanics of composite materials. The computer programming was carried out by John McPhillips. Finally, the author acknowledges numerous discussions with Dr. Louis Fishman, on problems arising in statistical physics and in the modeling of random microstructures. These discussions have had a significant impact on the reported study.

References

1 McCoy, J. J., "Macroscopic Response of Continue with Random Microstructures," *Mechanics Today (Vol. 6)*, Nemat-Nasser, S., ed., Pergamon Press, 1981, pp. 1-40.

2 Hashin, Z., *Theory of Fiber Reinforced Materials*, NASA Report Contract NAS1-8818, Langley Research Center, Hampton, Va., 1970.

3 Christensen, R. M., *Mechanics of Composite Materials*, Wiley, New York, 1979.

4 Beran, M. J., *Statistical Continuum Theories*, Wiley, 1968.

5 A substantial number of references to this approach are discussed in reference [1].

6 Beran, M., "Use of a Variational Approach to Determine Bounds for the Effective Permittivity of a Random Medium," *Il Nuovo Cimento*, Vol. 38, 1965, pp. 771-782.

7 McCoy, J. J., "A New Set of Bounds for the Effective Permittivity of a Random Medium," *Il Nuovo Cimento*, Vol. 57, 1968, pp. 139-153.

8 Elsayed, M. A., "Bounds for Effective Thermal, Electrical and Magnetic Properties of Heterogeneous Materials Using High Order Statistical Information," *J. Math. Phys.*, Vol. 15, 1974, pp. 2001-2015.

9 Weissberg, H. L., and S. Prager, "The Viscosity of Concentrated Suspensions," *Trans. Soc. of Rheology*, Vol. 9, No. 1, 1965, pp. 321-338.

10 Batchelor, G. K., and J. T. Green, "The Determination of the Bulk Stress in a Suspension of Spherical Particles to Order c^2," *J. Fluid Mech.*, Vol. 56, 1972, pp. 401-427.

11 Jeffrey, D. J., "Conduction Through a Random Suspension of Spheres," *Proc. R. Soc. London*, Series A, Vol. 335, 1973, pp. 355-367.

12 McCoy, J. J., and M. J. Beran, "On the Effective Thermal Conductivity of a Random Suspension of Spheres," *Int. J. Eng. Sci.*, Vol. 14, 1976, pp. 7-18.

13 McCoy, J. J.. "On the Calculation of Bulk Properties of Heterogeneous Materials," *Q. Appl. Math.*, Vol. 37, No. 2, 1979, pp. 137-149.

Plasticity Analysis of Fibrous Composites

G. J. Dvorak
Professor and Chairman,
Department of Civil Engineering,
University of Utah,
Salt Lake City, Utah 84112

Y. A. Bahei-El-Din
Lecturer,
Division of Structures,
Department of Civil Engineering,
Cairo University, Giza, Egypt

The elastic-plastic behavior of composites consisting of aligned, continuous elastic filaments and an elastic-plastic matrix is described in terms of constituent properties, their volume fractions, and mutual constraints between the phases indicated by the geometry of the microstructure. The composite is modeled as a continuum reinforced by cylindrical fibers of vanishingly small diameter which occupy a finite volume fraction of the aggregate. In this way, the essential axial constraint of the phases is retained. Furthermore, the local stress and strain fields are uniform. Elastic moduli, yield conditions, hardening rules, and overall instantaneous compliances, as well as instantaneous stress concentration factors are derived. Specific results are obtained for the case of a Mises-type matrix which obeys the Prager-Ziegler kinematic hardening rule. Any multiaxial mechanical load may be applied. Comparisons are made between the present results and certain other theories.

1 Introduction

Metal-matrix composites reinforced by continuous elastic fibers may experience an appreciable amount of elastic-plastic deformation which is caused by plastic flow of the matrix. Although the fibers strengthen the matrix substantially, and are the principal source of the high composite stiffness, their presence has a relatively small effect on the overall stress level that causes the onset of plastic yielding.

For example, in our recent experimental study of the boron-aluminum system [1], it was found that the initial yield stress of annealed unidirectional and laminated plates was approximately equal to 20–25 percent of their ultimate strength. This and other examples, as well as theoretical calculations described in references [2, 3] suggest that elastic-plastic deformation is at least as common in structural applications of metal-matrix composites as the elastic deformation, because the plastic range occupies the major portion of the total strength range. To take advantage of the high strength and stiffness of the metal-matrix composite materials, it is necessary to admit working loads that exceed their elastic limits.

However, the existence of an extensive plastic deformation range does not imply that metal-matrix composites may experience large plastic strains before failure. In most cases the failure strain of the composite will be of the same order of magnitude as that of the elastic fiber. As pointed out in [4], the failure strains of the fibers used in actual material systems vary from $\epsilon_u^f \doteq 0.005$ for the FP fiber, to $\epsilon_u^f \doteq 0.014$ for certain graphite fibers (T − 50). For the boron fiber, $\epsilon_u^f \doteq 0.009$. These magnitudes indicate that the deformation of metal-matrix composite materials, is limited to the range of small strains. When compared with the initial yield strain of as-fabricated aluminum matrices, which is approximately equal to 0.001, the fiber failure strains suggest once again that elastic-plastic deformation will dominate the response of the composite.

Under these circumstances, plasticity analysis of metal-matrix composite materials must emphasize accuracy in the small strain region. This requires that the theory be based on a micromechanical model that allows for the derivation of the overall response from the properties of the constituents and from their mutual constraints which are indicated by the geometry of the microstructure. Furthermore, it is probably obvious that the theory cannot admit certain assumptions that are often accepted in plasticity or in large strain theories, such as rigid-plastic behavior of the phases, inextensibility of the fiber, or plastic incompressibility of the composite medium.

Formulation of constitutive relations for elastic-plastic composite materials has been impeded by the lack of reasonably simple solutions which would describe, at least approximately, the local plastic deformation of the matrix in the vicinity of the fiber. Progress has been made only in special cases, e.g., in axisymmetric deformation of elastic, perfectly plastic matrices reinforced by circular, cylindrical elastic fibers, subjected to mechanical loads and uniform thermal changes [5–7].

Attempts to model elastic-plastic deformation of fibrous composites under more general loading conditions, and for a wider range of constituent properties, have relied on numerical solutions of the local problem [8–10] obtained for a specific loading path, usually for uniaxial tension transverse to the fiber direction. Results of these studies cannot be used to construct general constitutive relations. However, they illustrate the complexity of the local fields and indicate the need for simpler microstructural models.

Contributed by the Applied Mechanics Division for publication in the JOURNAL OF APPLIED MECHANICS.

Discussion on this paper should be addressed to the Editorial Department, ASME, United Engineering Center, 345 East 47th Street, New York, N.Y. 10017, and will be accepted until two months after final publication of the paper itself in the JOURNAL OF APPLIED MECHANICS. Manuscript received by ASME Applied Mechanics Division, July, 1981; final revision, October, 1981.

This paper presents constitutive relations for elastic-plastic deformation of fibrous composites in the small strain range. The development is based on a specific material model, described in Section 4, which simplifies the geometry of the microstructure, but admits, in general, any constitutive relations for the constituent phases. The model permits construction of yield conditions, hardening rules, and flow rules for the composite aggregate in terms of local properties and volume fractions of the phases. Response to any mechanical as well as thermal loading path can be obtained. However, for reasons mentioned in Section 6.1, we limit our attention to mechanical loads. Certain applications of the theory are discussed. A more extensive description of specific results is presented in related papers [2, 4, 11, 12].

2 Notation

We shall use a notation which is formally similar, but not identical to that introduced by Hill [13, 14]. In the present work, except as noted, six-dimensional vectors are identified by lowercase, boldface Greek letters, e.g., $\boldsymbol{\sigma}$, $\boldsymbol{\epsilon}$; 3×3 matrices are denoted by lowercase, boldface Latin letters, e.g., $\mathbf{a}$, $\mathbf{c}$; 6×6 matrices are denoted by uppercase, lightface, Latin italicized letters, e.g., A, B, L, M, and A^{-1} denotes the inverse of A, defined when it exists, to satisfy

$$AA^{-1}=I=A^{-1}A,$$

where I is a 6×6 unit matrix. We shall also write $\mathbf{a}^{-1}$ for the inverse of $\mathbf{a}$, defined, when it exist, to satisfy,

$$\mathbf{a}\mathbf{a}^{-1}=\mathbf{I}=\mathbf{a}^{-1}\mathbf{a}$$

where $\mathbf{I}$ is a 3×3 unit matrix. Scalars are denoted by lowercase, lightface Latin and Greek letters.

To describe the elastic properties of a transversely isotropic medium we shall use the symbols E_A, G_A, ν_A, E_T, G_T, ν_T for the axial and transverse Young's and shear moduli, and Poisson's ratios. In addition, we shall also use related Hill's constants defined as follows [15]

$$k=-E_TG_T/[E_T-4G_T+4\nu_A{}^2G_TE_T/E_A]$$

$$l=2k\nu_A, \quad n=E_A+l^2/k, \quad m=G_T, \quad p=G_A. \tag{1}$$

Other useful connections are:

$$E_T = 2(1+\nu_T)G_T=4km/(k+tm)$$

$$\nu_T = (k-tm)/(k+tm),$$

where $t = 1 + (4k\nu_A{}^2)/E_A$.

For an isotropic solid, equation (1) can be simplified with the following equalities:

$$l=k-m, \quad n=k+m, \quad m=p,$$

$$E=E_A=E_T, \quad G=G_A=G_T, \quad \nu=\nu_A=\nu_T \tag{1a}$$

Phase moduli will have an index r, e.g., k_r, E_A^r, such that $r=f, m$, for fiber, and matrix, respectively.

3 Governing Equations

A representative volume V of a binary composite contains a large number of aligned cylindrical inclusions embedded in a continuous matrix and is typical of the microstructure on average. The spatial arrangement of the inclusions in the transverse plane is such that the composite can be regarded as homogeneous and transversely isotropic under uniform macroscopic elastic strains. Let $d\bar{\boldsymbol{\sigma}}$ and $d\bar{\boldsymbol{\epsilon}}$ denote the uniform, overall stress and strain increments applied to V; and $d\boldsymbol{\sigma}_f$, $d\boldsymbol{\sigma}_m$, $d\boldsymbol{\epsilon}_f$, $d\boldsymbol{\epsilon}_m$ the volume averages of the stress and strain increments in the fiber and matrix, respectively. The volume fractions of the phases are $c_f = V_f/V$, $c_m = V_m/V$, such that $c_f + c_m = 1$.

The local and overall increments are related by:

$$d\bar{\boldsymbol{\sigma}}=c_f\, d\boldsymbol{\sigma}_f+c_m\, d\boldsymbol{\sigma}_m; \quad d\bar{\boldsymbol{\epsilon}}=c_f\, d\boldsymbol{\epsilon}_f+c_m\, d\boldsymbol{\epsilon}_m. \tag{2}$$

The consituent properties in the elastic and plastic range are defined as:

$$d\boldsymbol{\sigma}_r=L_r\, d\boldsymbol{\epsilon}_r, \quad d\boldsymbol{\epsilon}_r=M_r\, d\boldsymbol{\sigma}_r, \quad (r=f, m). \tag{3}$$

The matrices L_r, M_r, describe the instantaneous local moduli and compliances; $M_r = L_r{}^{-1}$, if the inverse exists.

The local averages are assumed to be related to the overall quantities in a unique way [13]:

$$d\boldsymbol{\sigma}_r=B_r\, d\bar{\boldsymbol{\sigma}}, \quad d\boldsymbol{\epsilon}_r=A_r\, d\bar{\boldsymbol{\epsilon}}, \tag{4}$$

where B_r, A_r, are the instantaneous stress and strain concentration factors. For consistency with (2), these factors must satisfy:

$$c_f\, B_f+c_m\, B_m=I, \quad c_f\, A_f+c_m\, A_m = I. \tag{5}$$

Finally, the macroscopic response of the composite in V at each instant of plastic loading follows from (2), (3), and (4), as

$$d\bar{\boldsymbol{\sigma}}=L\, d\bar{\boldsymbol{\epsilon}}, \quad d\bar{\boldsymbol{\epsilon}}=M\, d\bar{\boldsymbol{\sigma}} \tag{6}$$

where the overall instantaneous moduli L and compliances M are

$$L=\Sigma\, c_rL_rA_r, \quad M=\Sigma c_rM_rB_r, \quad (r=f, m) \tag{7}$$

providing that $M_r = L_r{}^{-1}$ exists. It can be shown that for elastic and stable elastic-plastic materials, the matrices L_r, M_r, L, and M have diagonal symmetry [14, 16].

When the constituent properties (3) are specified, the overall moduli L or compliances M in the plastic range can be found from (7) and (4), providing that the concentration factors A_r or B_r are known for at least one constituent [13]. In this way, the description of the overall response of the composite medium is reduced to evaluation of the concentration factors, which must be found from the solution of an inclusion problem.

4 Elastic Behavior

Consider again the representative volume V of a binary composite that contains a large number of aligned cylindrical inclusions or fibers embedded in a continuous matrix. Both the inclusions and the matrix may be transversely isotropic in their respective elastic deformation ranges; the axis of symmetry of each phase is parallel to the fiber axis. To simplify the elastic-plastic solution of the inclusion problem, we assume that each of the cylindrical fibers has a vanishing diameter, and that the fibers occupy a finite volume fraction of the composite. In this way we retain the micromechanical character of the model, and the essential axial constraint of the phases. Furthermore, the local stress and strain fields in the constituents will be uniform. The assumption affects interaction of the phases in the transverse plane, and thus the overall behavior of the composite aggregate. These effects, which are relatively small, are discussed in Section 6.2.

The overall elastic properties of the composite aggregate can now be evaluated with the procedure outlined in Section 3. Coordinates x_i ($i = 1, 2, 3$) are associated with the representative volume V, such that x_3 is in the fiber direction, and x_1, x_2 are in the transverse plane. The constraints between the fiber and matrix phases implied by the material model lead to the following form of (2):

$$d\bar{\sigma}_{ij}=d\sigma^f_{ij}=d\sigma^m_{ij} \quad \text{for } ij \neq 33 \tag{8}$$

$$d\bar{\sigma}_{33}=c_f\, d\sigma^f_{33}+c_m\, d\sigma^m_{33} \tag{9}$$

$$d\bar{\epsilon}_{ij}=c_f d\epsilon^f_{ij}+c_m d\epsilon^m_{ij} \quad \text{for } ij \neq 33 \tag{10}$$

$$d\bar{\epsilon}_{33}=d\epsilon^f_{33}=d\epsilon^m_{33} \tag{11}$$

Let the overall stress and strain increment vectors be defined as

$$d\bar{\sigma} = [d\bar{\sigma}_{11}\ d\bar{\sigma}_{22}\ d\bar{\sigma}_{33}\ d\bar{\sigma}_{12}\ d\bar{\sigma}_{13}\ d\bar{\sigma}_{23}]^T$$

$$d\bar{\epsilon} = [d\bar{\epsilon}_{11}\ d\bar{\epsilon}_{22}\ d\bar{\epsilon}_{33}\ 2d\bar{\epsilon}_{12}\ 2d\bar{\epsilon}_{13}\ 2d\bar{\epsilon}_{23}]^T, \qquad (12)$$

with analogous forms for the phase increments $d\boldsymbol{\sigma}_r$, $d\boldsymbol{\epsilon}_r$, $r=f$, m. These vectors can be introduced into (6) together with the matrices L and M, which are:

$$L = \left[\begin{array}{ccc|ccc} k+m & k-m & l & & & \\ k-m & k+m & l & & \mathbf{0} & \\ l & l & n & & & \\ \hline & & & m & 0 & 0 \\ & \mathbf{0} & & 0 & p & 0 \\ & & & 0 & 0 & p \end{array}\right], \quad M=L^{-1}; \qquad (13)$$

and also into (3) with analogous expressions for L_r, M_r, providing that the inverses of L and L_r exist.

The unknown overall moduli in (13) can be evaluated from (7), using the concentration factors A_r and B_r in (4). The concentration factors for the phase r are obtained from solutions of inclusion problems for the fiber and matrix. For the present composite model, with phase constraints given by (8)–(11), the individual coefficients in A_r and B_r can be found from solutions of equations (3)–(5), and (8)–(11), for subsequent single, nonzero entries in the overall stress and strain increments (12). In the case of elastic deformation of the phases we attach an additional subscript e, i.e., B_{me}, etc., to denote elastic concentration factors. The results are:

$$A_{re} = \left[\begin{array}{c|c} \mathbf{a}_r' & \mathbf{0} \\ \hline \mathbf{0} & \mathbf{a}_r'' \end{array}\right], \quad B_{re} = \left[\begin{array}{c|c} \mathbf{b}_r' & \mathbf{0} \\ \hline \mathbf{0} & \mathbf{I} \end{array}\right] \qquad (14)$$

where

$$\mathbf{a}_r' = 1/2 \begin{bmatrix} (k/k_r+m/m_r) & (k/k_r-m/m_r) & (l-l_r)/k_r \\ (k/k_r-m/m_r) & (k/k_r+m/m_r) & (l-l_r)/k_r \\ 0 & 0 & 2 \end{bmatrix}$$

$$\mathbf{a}_r'' = \begin{bmatrix} m/m_r & 0 & 0 \\ 0 & p/p_r & 0 \\ 0 & 0 & p/p_r \end{bmatrix},$$

$$\mathbf{b}_r' = \frac{1}{E_c} \begin{bmatrix} E_c & 0 & 0 \\ 0 & E_c & 0 \\ (1-c_r)a_r & (1-c_r)a_r & E_A^r \end{bmatrix}$$

$r=f$, m;

$$E_c = c_f E_A^f + c_m E_A^m; \quad a_f = (\nu_A^f E_A^m - \nu_A^m E_A^f) = -a_m, \qquad (15)$$

and $\mathbf{I}$ is a 3×3 identity matrix.

The concentration factors A_{re}, B_{re}, and equations (7) and (13) yield the following values of the overall moduli:

$$k = (c_f/k_f + c_m/k_m)^{-1}$$

$$l = (c_m k_f l_m + c_f k_m l_f)/(c_f k_m + c_m k_f)$$

$$n = c_m n_m + c_f n_f - [c_f c_m (l_f - l_m)^2/(c_f k_m + c_m k_f)]$$

$$m = (c_f/m_f + c_m/m_m)^{-1}$$

$$p = (c_f/p_f + c_m/p_m)^{-1}. \qquad (16)$$

When the geometry of the microstructure of a fibrous composite is specified only in terms of the volume fractions of the phases, the overall elastic moduli can be bracketed by rigorous bounds [15, 17, 18]. The results (16) obtained with the composite model will be now compared with the bounds.

We note that the moduli k, l, and n satisfy the universal connections [15]:

$$\frac{k-k_f}{l-l_f} = \frac{k-k_m}{l-l_m} = \frac{l-c_f l_f - c_m l_m}{n-c_f n_f - c_m n_m}. \qquad (17)$$

The exact lower bound k_L on the modulus k was obtained in [15, 17] as:

$$k_L = [c_1/(k_1+m_2) + c_2/(k_2+m_2)]^{-1} - m_2, \qquad (18)$$

with phases numbered so that $m_1 \geq m_2$. It is seen that $k < k_L$. Since l and n in (16) are related to k by (17), these moduli will also be lower than their respective lower bounds. The same is true for the lower bounds on p and m [18]:

$$p_L = p_2[c_2 p_2 + (1+c_1)p_1]/[c_2 p_1 + (1+c_1)p_2] > p$$

$$m_L = m_2[(c_2 - b_2 c_2)m_2$$

$$+ (c_1 + b_2 c_2)m_1]/[c_2 b_2 m_1 + (1 - c_2 b_2)m_2] > p$$

with phases numbered so that $p_1 > p_2$, and $(m_1 - m_2)(k_1 - k_2) \geq 0$; $b_2 = (k_2 + 2m_2)/[2(k_2 + m_2)]$.

As one might expect, the simplifications required for tractable solutions of elastic-plastic inclusion problems render the model inaccurate in the elastic range. However, in actual composite systems, e.g., in the $B-Al$ system at low and moderate fiber concentrations ($c_f \leq 0.5$), the moduli (16) differ only slightly from the lower bounds [19].

Correct values of elastic strains can be obtained with the composite model if the elastic moduli of the matrix are adjusted in such a way that the composite moduli (16) are within the bounds. The adjustment requires a choice of admissible values of overall moduli (denoted by a prime) k' (or n', or l'), m', and p', which are within the bounds. Possible choices are the self-consistent estimates [20]. These can be substituted for the overall moduli in (16) and the equations solved for the appropriate matrix moduli. The adjusted matrix moduli then are:

$$k_m' = c_m k' k_f (k_f - c_f k')$$

$$m_m' = c_m m' m_f (m_f - c_f m')$$

$$p_m' = c_m p' p_f (p_f - c_f p'). \qquad (19)$$

When these adjusted matrix moduli are used in (16) and (17), the composite model yields correct values of overall elastic strains.

The elastic thermal expansion coefficients α and β of the composite medium can be found from the universal connection [7]:

$$\frac{k-k_f}{l-l_f} = \frac{k\alpha + l\beta - \Sigma c_r(k_r\alpha_r + l_r\beta_r)}{l\alpha + n\beta - \Sigma c_r(l_r\alpha_r + n_r\beta_r)}, \qquad (20)^{1}$$

and equation (17).

The coefficients α_r, β_r, and α, β, in (20) describe, respectively, the thermal expansion in the transverse plane, and in the longitudinal direction. Specifically, for an isotropic material with a linear thermal expansion coefficient $\bar{\alpha}$: $\alpha_r = 2\bar{\alpha}$, $\beta_r = \bar{\alpha}$.

[1] Equation (20) is the corrected form of equation (39) in reference [7].

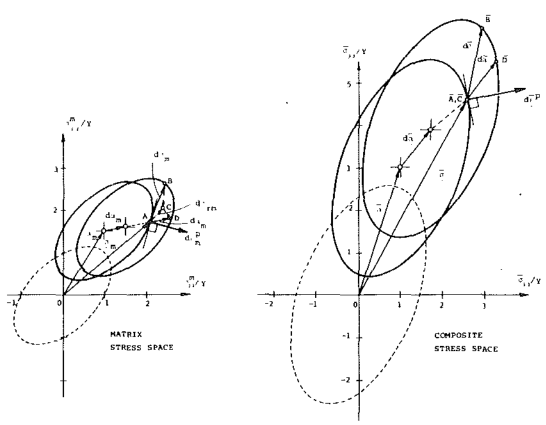

Fig. 1 Kinematic hardening in matrix and composite stress spaces

5 Elastic-Plastic Behavior

5.1 The Yield Surface. We assume that the fibers are elastic until failure, whereas the matrix obeys a yield condition $f(\sigma_m) = 0$. Then, for a stress-free composite material, the initial yield condition in the overall stress space is, according to (4),

$$f(B_{me}\bar{\sigma}) = 0. \tag{21}$$

In the present composite model the local stress fields are uniform; the stress concentration factor B_{me} is given by (14). The overall yield condition (21) can be constructed for any given form of $f(\sigma_m) = 0$.

For example, in the case of a Mises-type matrix, (21) becomes:

$$f = \bar{\sigma}^T \left[\begin{array}{c|c} (\mathbf{b}_m')^T \mathbf{c} \mathbf{b}'_m & \mathbf{0} \\ \hline \mathbf{0} & 3\mathbf{I} \end{array} \right] \bar{\sigma} - Y^2 = 0, \tag{22}$$

where $\mathbf{c}$ is a symmetric 3×3 matrix such that $c_{11} = c_{22} = c_{33} = 1$, and $c_{12} = c_{13} = c_{23} = -½$; Y is the tension yield stress of the matrix; $\mathbf{b}_m'$ and $\mathbf{I}$ are given in (14). Here and in the sequel we will assume that a Mises-type matrix is elastically isotropic, with equations (1a) applied to its elastic moduli.

Next we consider the motion and possible distortion of the yield surface in the overall stress space during plastic deformation of the model composite aggregate. In general, there are two factors that determine the position and shape of the overall yield surface after a plastic load increment. One is the interaction between the phases, which leads to constraint hardening. Another is phase hardening, due to local work hardening of the plastically deforming phases. The constraint hardening of a fibrous composite material with a nonhardening matrix was studied earlier [6, 7], for the special case of axisymmetric deformation. We recall that in the axisymmetric case the yield surface had experienced pure translation in the overall stress plane, and that the motion of the center of the surface was determined by two vectors, one in the $\bar{\sigma}_{33}$ direction and one in the direction of transverse hydrostatic stress $(\bar{\sigma}_{11} + \bar{\sigma}_{22})/2$. Each of these translation vectors corresponded to a specific constraint between the elastic fiber and the plastically deforming matrix.

The constraint hardening of the present composite model can be regarded as a special case of the earlier results. The model prescribes only a single, axial constraint between the phases, specified by equations (9) and (11). This constraint can cause axial residual normal stress components σ_{33}^r ($r = f$, m), to exist in the elastic fiber and in the plastically deformed matrix. When the residual stress σ_{33}^m is accounted for in the yield condition (21), it will appear there as a translation factor causing motion of the original yield surface in the direction $\bar{\sigma}_{33}$.

In addition to constraint hardening, the composite may exhibit phase-hardening effects which originate in the matrix. Since most actual metal-matrix composite systems have aluminum matrices, and these harden kinematically at small plastic strains [21, 22], we shall direct our attention to the particular case of a kinematically hardening matrix. Certain results for a composite with a nonhardening matrix will follow from this development.

Consider an isotropic elastic-plastic matrix with kinematic hardening such that if the initial yield surface is given by the condition $f(\sigma_m) = 0$, then any subsequent matrix yield surface is

$$f(\sigma_m - \alpha_m) = 0. \tag{23}$$

In analogy with (22), the overall yield surface for the present composite model will be

$$f(\bar{\sigma} - \bar{\alpha}) = 0, \tag{24}$$

where $\bar{\alpha}$ is an unknown translation vector which contains both constraint and local hardening contributions. To determine the magnitude of $d\bar{\alpha}$ corresponding to a plastic loading increment $d\bar{\sigma}$, we apply a loading/unloading sequence $\pm d\bar{\sigma}$ in the overall stress space. The corresponding matrix stress increment is, as in (4),

$$d\sigma_m = B_m d\bar{\sigma}, \tag{25}$$

where B_m is an instantaneous stress concentration factor which will be determined in Section 5.3. In the case of elastic unloading $B_m = B_{me}$ (14). At the end of the loading path $\pm d\bar{\sigma}$, the residual stress in the matrix will be:

$$d\sigma_{rm} = (B_m - B_{me}) d\bar{\sigma}. \tag{26}$$

This is illustrated in Fig. 1 which shows the $\sigma_{11}\sigma_{33}$-plane section of the overall and local yield surfaces; $\bar{A}\bar{B}\bar{C}$ is the overall loading path, ABC is the local response.

During the loading part of the applied sequence the two surfaces will experience translations $d\bar{\alpha}$ and $d\alpha_m$, respectively, which are related by

$$B_{me} d\bar{\alpha} = d\alpha_m - d\sigma_{rm}. \tag{27}$$

These magnitudes correspond to vectors $\bar{C}\bar{D}$ and CD in Fig. 1. From (26) and (27):

$$d\bar{\alpha} = B_{me}^{-1} d\alpha_m - (B_{me}^{-1} B_m - I) d\bar{\sigma}. \tag{28}$$

As an example of kinematic hardening of the matrix we consider Prager's hardening rule with Ziegler's modification [23] and a matrix of the Mises type. The hardening rule is based on the assumption that the local translation is of the form

$$d\alpha_m = d\mu_m (\sigma_m - \alpha_m). \tag{29}$$

Here, $d\mu_m$ is a scalar multiplier that can be found from the equation of consistency $df = 0$, which, in conjunction with (23) gives

$$(\partial f / \partial \sigma_m)^T (d\sigma_m - d\alpha_m) = \mathbf{0}. \tag{30}$$

From (29) and (30):

$$d\mu_m = [(\partial f / \partial \sigma_m)^T d\sigma_\omega] / [(\partial f / \partial \sigma_m)^T (\sigma_m - \alpha_m)]. \tag{31}$$

For a Mises-type matrix, equation (23) becomes

$$f(\sigma_m - \alpha_m) \equiv (\sigma_m - \alpha_m)^T C (\sigma_m - \alpha_m) - Y^2 = 0, \tag{32}$$

where

$$C = \left[\begin{array}{c|c} \mathbf{c} & \mathbf{0} \\ \hline \mathbf{0} & 3\mathbf{I} \end{array} \right],$$

with $\mathbf{c}$ as in (22). One can find that

$$(\partial f/\partial \sigma_m) = 2C(\sigma_m - \alpha_m),$$

and

$$(\partial f/\partial \sigma_m)^T(\partial f/\partial \sigma_m) = 4(\sigma_m - \alpha_m)^T CC(\sigma_m - \alpha_m). \tag{33}$$

Hence (31) can be written in the final form

$$d\mu_m = (1/Y^2)(\sigma_m - \alpha_m)^T C \; d\sigma_m, \tag{34}$$

and substituted into (29). This permits evaluation of $d\bar{\alpha}$ from (28) and completes the formulation of the overall hardening rule for the composite aggregate with elastic fibers and a kinematically hardening elastic-plastic matrix.

Specific results obtained with this formulation from (28) are:

$$\begin{aligned} d\bar{\alpha}_{ij} &= d\alpha_{ij}^m \quad \text{for } ij \neq 33; \\ d\bar{\alpha}_{33} &= (c_f a_f/E_c)(d\alpha_{11}^m + d\alpha_{22}^m) + (E_c/E_m)\, d\alpha_{33}^m \\ &+ (1/E_m)(c_f a_m - E_c B_{31}^m) d\bar{\sigma}_{11} \\ &+ (1/E_m)(c_f a_m - E_c B_{32}^m) d\bar{\sigma}_{22} \\ &+ (1/E_m)(E_m - E_c B_{33}^m) d\bar{\sigma}_{33} \\ &- (E_c/E_m)(B_{34}^m d\bar{\sigma}_{12} \\ &+ B_{35}^m d\bar{\sigma}_{13} + B_{36}^m d\bar{\sigma}_{23}). \end{aligned}$$

$$d\lambda_m = \frac{(\sigma_m - \alpha_m)^T C \; d\sigma_m}{3H_m\{Y^2 + 3[(\sigma_{12}{}^m - \alpha_{12}{}^m)^2 + (\sigma_{13}{}^m - \alpha_{13}{}^m)^2 + (\sigma_{23}{}^m - \alpha_{23}{}^m)^2]\}} \tag{40}$$

Here, B_{ij}^m are coefficients of the instantaneous matrix stress-concentration factor B_m (25), which will be determined from the matrix flow rule in Section 5.3. The coefficients a_f, a_m, E_c were introduced in (15). The matrix is now regarded as elastically isotropic, with connections (1a) applied to the moduli.

These results permit the evaluation of the current yield surface at the end of each loading step. This can be done using equation (24), or the more explicit form (22) with $\bar{\sigma}$ replaced by $(\bar{\sigma} - \bar{\alpha})$.

We observe that the first two terms in (35) represent a contribution to $d\bar{\alpha}_{33}$ from the hardening of the matrix, whereas the remaining terms are caused by constraint hardening. If the matrix material does not harden, the composite exhibits only constraint hardening. The hardening rule of the aggregate is then obtained by prescribing $d\alpha_m = \mathbf{0}$ in (23), (28), and (35). One recovers only a single nonvanishing vector $d\bar{\alpha}_{33}$ which determines the translation of the center of the overall yield surface. This, of course, is the consequence of the constraints (9) and (11) specified by the material model.

5.2 Overall Strains. The composite strains at each stage of the loading program can be determined from the volume averages of strain increments in the phases, equation (2). If the fiber remains elastic until failure, the strain increment in the fiber is

$$d\epsilon_f = M_{fe} d\sigma_f = M_{fe} B_f d\bar{\sigma}, \tag{36}$$

where the elastic compliance matrix M_{fe} is obtained by substitution of appropriate fiber moduli into (13). B_f is the instantaneous stress concentration factor of the fiber which will be found in the sequel.

The matrix material is elastic-plastic, and, if it is stable, then its plastic strain increment is normal to the yield surface. This implies that

$$d\epsilon_m = d\epsilon_m^e + d\epsilon_m^p = M_{me} B_m d\bar{\sigma} + d\lambda_m (\partial f/\partial \sigma_m). \tag{37}$$

B_m represents the instantaneous matrix stress concentration factor; $d\lambda_m$ is a scalar multiplier; the elastic compliance matrix M_{me} of the matrix material follows again from (13), with connections (1a).

To determine the scalar $d\lambda_m$, it is necessary to specify a flow rule associated with the Ziegler's modification of Prager's hardening rule. Then, $d\lambda_m$ is obtained in analogy with equation (2.9) in [23] as

$$d\lambda_m = \frac{(\partial f/\partial \sigma_m)^T d\sigma_m}{H_m (\partial f/\partial \sigma)^T (\partial f/\partial \sigma)}, \tag{38}$$

where the matrix hardening parameter H_m can be expressed in terms of stress and deviation strain invariants $d\hat{\sigma}_m = (3/2\, d\sigma_{ij}^m d\sigma_{ij}^m)^{1/2}$, $d\hat{\epsilon}_m^p = (2/3\, de_{ij}^{mp} de_{ij}^{mp})^{1/2}$ as:

$$d\hat{\sigma}_m = H_m d\hat{\epsilon}_m^p. \tag{39}$$

In the case of a Mises-type matrix, equation (23), the form (38) becomes

A more convenient formulation of equations (37)–(40) is obtained with the following notation. Let the vector η be defined as

$$\eta = [\eta_1 \eta_2 \eta_3 \eta_4 \eta_5 \eta_6]^T = 2qC(\sigma_m - \alpha_m); \tag{41}$$

with the scalar q given by

$$q = \frac{[-(\sigma_{11}{}^m - \alpha_{11}{}^m) - (\sigma_{22}{}^m - \alpha_{22}{}^m) + 2(\sigma_{33}{}^m - \alpha_{33}{}^m]}{6\{Y^2 + 3[(\sigma_{12}{}^m - \alpha_{12}{}^m)^2 + (\sigma_{13}{}^m - \alpha_{13}{}^m)^2 + (\sigma_{23}{}^m - \alpha_{23}{}^m)^2]\}} \tag{42}$$

and with C taken from (32).

Then,

$$\begin{aligned} d\lambda_m &= (q\eta^T B_m / H_m \eta_3) d\bar{\sigma}, \\ (\partial f/\partial \sigma_m) &= \eta/q. \end{aligned} \tag{43}$$

The overall strain increment $d\bar{\epsilon}$ follows from (10), (36), (37), and (43):

$$\begin{aligned} d\bar{\epsilon} &= c_f d\epsilon_f + c_m d\epsilon_m \\ &= [c_f M_{fe} B_f + c_m (M_{me} + \eta\eta^T / H_m \eta_3) B_m] d\bar{\sigma} \end{aligned} \tag{44}$$

This is the overall constitutive equation of the elastic-plastic fibrous composite material. The factors in the square brackets depend only on the current stress state. The stress concentration factors B_m and B_f remain to be determined.

5.3 Instantaneous Concentration Factors. We now proceed to evaluate the instantaneous stress concentration factors B_f and B_m. As in the elastic case, we utilize the constraint equation

$$d\bar{\epsilon}_{33} = d\epsilon_{33}^f = d\epsilon_{33}^m \tag{11}$$

and the equilibrium conditions

$$d\bar{\sigma}_{ij} = d\sigma_{ij}^f = d\sigma_{ij}^m, \quad (ij \neq 33) \tag{8}$$

with

$$d\bar{\sigma}_{33} = c_f d\sigma_{33}^f + c_m d\sigma_{33}^m \tag{9}$$

Using (37) and (43) we find the plastic, axial strain increment in the matrix as

$$\begin{aligned} d\epsilon_{33}^{mp} &= d\lambda_m (\partial f/\partial \sigma_{33}^m) \\ &= d\lambda_m [-(\sigma_{11}^m - \alpha_{11}^m) - (\sigma_{22}^m - \alpha_{22}^m) \\ &+ 2(\sigma_{33}^m - \alpha_{33}^m)] \\ &= (\eta^T / H_m) d\sigma_m. \end{aligned} \tag{45}$$

The total axial strain increment in the matrix follows from (37) and (45) as:

$$\begin{aligned} d\epsilon_{33}^m &= (\eta_1/H_m - \nu_m/E_m) d\sigma_{11}^m + (\eta_2/H_m - \nu_m/E_m) d\sigma_{22}^m \\ &+ (\eta_3/H_m - 1/E_m) d\sigma_{33}^m \\ &+ (\eta_4 d\sigma_{12}^m + \eta_5 d\sigma_{13}^m + \eta_6 d\sigma_{23}^m)/H_m. \end{aligned} \tag{46}$$

The axial strain increment in the elastic fiber is:

$$\begin{aligned} d\sigma_{33}^f &= -(\nu_A^f/E_A^f) d\sigma_{11}^f \\ &- (\nu_A^f/E_A^f) d\sigma_{22}^f + (1/E_A^f) d\sigma_{33}^f. \end{aligned} \tag{47}$$

The constituent strain increments (46) and (47) can now be substituted into (11), and the local stress increments in the resulting equation, with the exception of $d\sigma_{33}^m$, can be expressed in terms of the overall stress increments with the help of (8) and (9). This procedure leads to the evaluation of the sress concentration factor B_m in

$$d\sigma_m = B_m d\bar{\sigma}. \tag{25}$$

The result is:

$$B_m = \left[\begin{array}{ccc|ccc} 1 & 0 & 0 & 0 & 0 & 0 \\ 0 & 1 & 0 & 0 & 0 & 0 \\ B_{31}^m & B_{32}^m & B_{33}^m & B_{34}^m & B_{35}^m & B_{36}^m \\ \hline & \mathbf{0} & & & \mathbf{I} & \end{array}\right], \tag{48}$$

where

$$\begin{aligned} B_{31}^m &= (c_f/h)(H_m a_m - E_A^f E_m \eta_1) \\ B_{32}^m &= (c_f/h)(H_m a_m - E_A^f E_m \eta_2) \\ B_{33}^m &= H_m E_m / h \\ B_{34}^m &= -(c_f/h)(E_A^f E_m \eta_4) \\ B_{35}^m &= -(c_f/h)(E_A^f E_m \eta_5) \\ B_{36}^m &= -(c_f/h)(E_A^f E_m \eta_6) \end{aligned} \tag{48a}$$

and

$$h = H_m E_c + c_f E_A^f E_m \eta_3.$$

In the absence of phase hardening in the matrix, i.e., for $H_m = 0$ one can derive B_{ij}^m directly from the equation of consistency for the matrix [24]. The results are:

$$\begin{aligned} &[B_{31}^m \; B_{32}^m \; B_{33}^m \; B_{34}^m \; B_{35}^m \; B_{36}^m] \\ &= [-s_{11}^m \;\; -s_{22}^m \;\; 0 \;\; -2\sigma_{12}^m \;\; -2\sigma_{13}^m \;\; -2\sigma_{23}^m]/s_{33}^m \end{aligned} \tag{48b}$$

where:

$$\begin{aligned} s_{11}^m &= (2\sigma_{11}^m - \sigma_{22}^m - \sigma_{33}^m)/3 \\ s_{22}^m &= (2\sigma_{22}^m - \sigma_{33}^m - \sigma_{11}^m)/3 \\ s_{33}^m &= (2\sigma_{33}^m - \sigma_{11}^m - \sigma_{22}^m)/3 \end{aligned}$$

The instantaneous fiber stress-concentration factor B_f follows from (5) and (47) as

$$B_f = (I - c_m B_m)/c_f. \tag{49}$$

5.4 Overall Compliance. The evaluation of the stress concentration factors (48) and (49) makes it possible to write the overall constitutive equation (44) in an explicit form. With reference to (6), (44), and (49)

$$d\bar{\epsilon} = M d\bar{\sigma} \tag{6}$$

where:

$$M = M_{fe} + c_m[(M_{me} - M_{fe}) + \eta\eta^T/(H_m \eta_3)]B_m. \tag{50}$$

We recall that M_{me} and M_{fe} are given by (13), η by (41) and (42), H_m by (39), and B_m by (48). After substitution from these equations into equation (50) one obtains the following expressions for the coefficients of M:

$$\begin{aligned} M_{11} &= (c_m/E_m + c_f/E_T^f) - s a_m B_{31}^m \\ &\quad + s\eta_1 (c_f a_m - E_c B_{31}^m)/(c_f \eta_3) \\ M_{12} &= -(c_m \nu_m/E_m + c_f \nu_T^f/E_T^f) \\ &\quad - s a_m B_{31}^m + s\eta_2 (c_f a_m - E_c B_{31}^m)/(c_f \eta_3) \\ M_{13} &= -\nu_A^f/E_A^f - [c_m/(c_f E_A^f)] B_{31}^m \\ M_{14} &= s\eta_4 (c_f a_m - E_c B_{31}^m)/(c_f \eta_3) \\ M_{15} &= \eta_5 M_{14}/\eta_4, \quad M_{16} = \eta_6 M_{14}/\eta_4 \\ M_{22} &= (c_m/E_m + c_f/E_T^f) - s a_m B_{32}^m \\ &\quad + s\eta_2 (c_f a_m - E_c B_{32}^m)/(c_f \eta_3) \\ M_{23} &= -\nu_A^f/E_A^f - [c_m/(c_f E_A^f)] B_{32}^m \\ M_{24} &= s\eta_4 (c_f a_m - E_c B_{32}^m)/(c_f \eta_3) \\ M_{25} &= \eta_5 M_{24}/\eta_4, \quad M_{26} = \eta_6 M_{24}/\eta_4 \\ M_{33} &= (1 - c_m B_{33}^m)/(c_f E_A^f) \\ M_{34} &= s\eta_4 (E_m - E_c B_{33}^m)/(c_f \eta_3) \\ M_{35} &= \eta_5 M_{34}/\eta_4, \quad M_{36} = \eta_6 M_{34}/\eta_4 \\ M_{44} &= (c_m/G_m + c_f/G_A^f) - s\eta_4 E_c B_{34}^m/(c_f \eta_3) \\ M_{45} &= -s\eta_5 E_c B_{34}^m/(c_f \eta_3) \\ M_{46} &= \eta_6 M_{45}/\eta_5 \\ M_{55} &= (c_m/G_m + c_f/G_A^f) - s\eta_5 E_c B_{35}^m/(c_f \eta_3) \\ M_{56} &= -s\eta_6 E_c B_{35}^m/(c_f \eta_3) \\ M_{66} &= (c_m/G_m + c_f/G_T^f) - s\eta_6 E_c B_{36}^m/(c_f \eta_3), \end{aligned}$$

where:

$$s = c_m/(E_m E_A^f)$$

$$E_c = c_m E_m + c_f E_A^f$$

$$a_m = \nu_m E_A^f - \nu_A^f E_m,$$

and the various axial and transverse moduli are given by (1).

Although (50), as written, is not applicable when the matrix does not harden, i.e., $H_m = 0$, it is possible to evaluate the overall compliances for this particular case [24]. The result can be obtained by substituting the B_{ij}^m values from (48b) into the preceding expressions for M_{ij}. However, for certain loading directions, e.g., for pure shear, many coefficients of M are unbounded. Therefore, the behavior of fibrous composites with perfectly plastic matrices should be described in terms of the overall stiffness matrix L, as in [7]. The analysis of this special case for general mechanical loading is beyond the scope of the present paper.

6 Comparison with Related Results

6.1 Axisymmetric Deformation. The elastic-plastic response of fibrous composites to axisymmetric mechanical loads and to uniform thermal changes has been described in references [6] and [7]. The models used in these studies included the composite cylinder model as well as variants of the self-consistent scheme. The model results were compared with finite element analyses of composite cylinder and regular, fiber array representations of the composite aggregate, and also with selected experimental results [25]. These comparisons indicated that the composite cylinder model [6], as well as certain modified self-consistent schemes [7] give very accurate predictions of both overall behavior and local stresses during axisymmetric deformation of fibrous composites.

Therefore, it is of interest to examine the response of the present composite model in the axisymmetric loading case. The initial yield surface equation (22), can be expressed in the following equivalent form:

$$\bar{k}_{11}(\bar{\sigma}_{11}^2 + \bar{\sigma}_{22}^2) + \bar{k}_{33}\bar{\sigma}_{33}^2 + 2\bar{k}_{12}\bar{\sigma}_{11}\bar{\sigma}_{22} + 2\bar{k}_{13}\bar{\sigma}_{11}\bar{\sigma}_{33} + 2\bar{k}_{23}\bar{\sigma}_{22}\bar{\sigma}_{33} + 3(\bar{\sigma}_{12}^2 + \bar{\sigma}_{13}^2 + \bar{\sigma}_{23}^2) - Y^2 = 0, \quad (51)$$

where:

$$\bar{k}_{11} = d^2 - d + 1, \quad \bar{k}_{12} = \bar{k}_{11} - 3/2$$
$$\bar{k}_{13} = \bar{k}_{23} = g(d - 1/2), \quad \bar{k}_{33} = g^2,$$

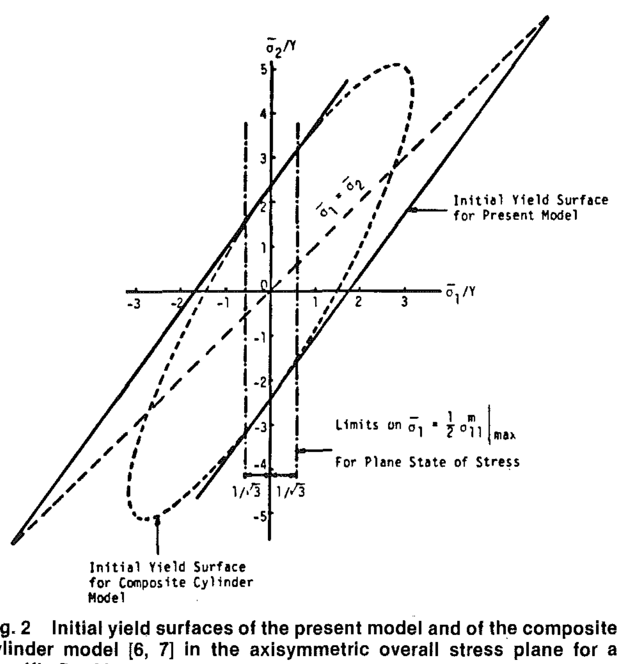

Fig. 2 Initial yield surfaces of the present model and of the composite cylinder model [6, 7] in the axisymmetric overall stress plane for a specific $B-Al$ system

and (15):

$$d = c_f a_m / E_c, \quad g = E_m / E_c. \quad (51a)$$

Let the axisymmetric stresses be denoted as

$$\bar{\sigma}_1 = (\bar{\sigma}_{11} + \bar{\sigma}_{22})/2, \quad \bar{\sigma}_2 = \bar{\sigma}_{33} \quad (52)$$

Then, the initial yield surface (51) in the axisymmetric stress plane (52) becomes:

$$[(1-2d)\,\bar{\sigma}_1 - g\bar{\sigma}_2]^2 = Y^2. \quad (53)$$

To illustrate the differences between the bilinear form (53), and the elliptical, initial yield surface for a composite cylinder model in the $\bar{\sigma}_1\bar{\sigma}_2$-plane, we plot the respective results in Fig. 2 for a specific $B-Al$ system. It is clear that the yield surfaces almost coincide at low values of $\bar{\sigma}_1/Y$, and particularly so in the case of plane stress loading of the lamina, where the composite model limits the transverse hydrostatic stress $\bar{\sigma}_1$ to $|\bar{\sigma}_1/Y| \leq 1/\sqrt{3}$. On the other hand, relatively poor agreement is obtained in the presence of high hydrostatic stress.

This observation is significant in evaluation of the suitability of the present composite model for thermoplastic analysis of fibrous composites. We recall that when, in the absence of mechanical loading, a uniform thermal change is applied to a fibrous composite with isotropic phases, the initial yield surface experiences a translation in the direction $\bar{\sigma}_1 = \bar{\sigma}_2$, until it intersects the origin of stress coordinates [3, 2, 25]. This translation affects both yield surfaces in Fig. 2; its magnitude, which is indepedent of the choice of the model, is given by equation (16) in Reference [3], or by (41) in [7]. It is obvious that the thermal change needed for initial yielding in the composite cylinder model will be considerably smaller than that predicted by the present composite model. Also, one may easily construct thermal loading sequences in which the two models will produce entirely different predictions of overall thermal strains. The case of cyclic thermal loading is a particularly useful example of practical significance.

However, it appears likely that the present composite model will give adequate predictions of overall strains under loading conditions that are characterized by large, monotonic, thermal changes. We derive this expectation from the results obtained with the unmodified self-consistent model (Fig. 7 in [7]), which is similar in its axisymmetric response to the model used in the present paper: Note the similarity between Fig. 2 here, and Fig. 2 in [7]. Unfortunately, the unmodified self-consistent model predicted entirely erroneous microstresses after large, monotonic, thermal changes (c.f., Table 1 in [7]). A similar difficulty may be encountered in analogous applications of the present composite model. In view of these qualifications we feel that, in its present form, the composite model is not entirely suitable for thermal analysis.

6.2 Transverse Tension. The elastic-plastic deformation of a unidirectional lamina in simple tension applied in the direction perpendicular to the fiber has been studied by several authors who used finite element analysis of regular fiber arrays. The results obtained by Needleman [9] for rigid circular fibers in a matrix exhibiting isotropic hardening, are the most suitable for comparison with those obtained with the present model. It was found that at low-fiber volume concentrations the present composite model predicted flow stress levels similar to those obtained by Needleman. At higher fiber volume fractions the model underestimated the flow stress.

6.3 Hill's Anisotropic Yield Criterion. In recent years, the anisotropic yield criterion proposed in 1948 by Hill [26] has been applied by several authors to elastic-plastic analysis of fibrous composites. The criterion, which was designed to account for anisotropic behavior of metals, rather than fibrous composite materials, implies that the superposition of the hydrostatic stress does not influence yielding, and that there is no Bauschinger effect.

It is well known that neither of these implications are valid in the case of fibrous composites. For example, it has been shown that the compressibility of fibrous composites is of the same order of magnitude in the elastic and plastic deformation modes [6]. In view of the extensive plastic deformation range of these materials, assumptions that neglect hydrostatic stress effects on overall plastic yielding appear to be entirely unjustified. Additional results supporting this view were presented by Lin et al. [27]. This aspect of the theory is especially significant in the case of thermal loading, where the assumption of overall plastic incompressibility would lead to the erroneous conclusion that no plastic yielding may take place due to differential dilatation of the phases. This can be seen from Fig. 2 and the discussion in Section 6.1. In a plastically incompressible material the yield surface in the axisymmetric $\bar{\sigma}_1 \bar{\sigma}_2$ -plane must consist of two linear branches parallel to the hydrostatic direction $\bar{\sigma}_1 = \bar{\sigma}_2$. We recall that this is also the direction of the thermal loading path in binary composites with elastically isotropic phases.

One can find from (51) that under a hydrostatic stress state $\bar{\sigma}_{11} = \bar{\sigma}_{22} = \bar{\sigma}_{33} = \bar{\sigma}_0$, the composite model indicates the onset of yielding at

$$\sigma_0 = \pm Y/(g+2d-1).$$

The absence of the Bauschinger effect, i.e., of kinematic hardening in the Hill's anisotropic yield criterion excludes consideration of constraint hardening, and also of kinematic phase hardening in the matrix. Of course, constraint hardening is an essential feature of plastic behavior of metal-matrix fibrous composites, which had been well established, both theoretically and experimentally, even in the early studies of the subject [28, 29]. It must be accounted for in any serious attempt to develop a realistic theory.

6.4 Invariant Form of the Yield Condition. As pointed out by Hill [5], and by Mulhern, Rogers, and Spencer [30], the yield function f, equation (22), for a transversely isotropic material must be invariant under rigid body rotations about the fiber axis x_3, and also under the transformation $x_3' = -x_3$. Therefore, the yield function can be expressed in terms of the transversely isotropic invariants of $\bar{\sigma}_{ij}$. The yield condition (22) can be rewritten in terms of four of these invariants. The result is:

$$f = \mathbf{J}^T \begin{bmatrix} (1-2d)^2 & -g(1-2d) & 0 & 0 \\ -g(1-2d) & g^2 & 0 & 0 \\ 0 & 0 & 3 & 0 \\ 0 & 0 & 0 & 3 \end{bmatrix} \mathbf{J} - Y^2 = 0,$$

where

$$\mathbf{J} = [J_1 \;\; J_2 \;\; J_3 \;\; J_4]^T,$$

and

$$J_1 = \tfrac{1}{2}(\bar{\sigma}_{11} + \bar{\sigma}_{22}), \quad J_2 = \bar{\sigma}_{33},$$
$$J_3 = (\bar{\sigma}_{13}^2 + \bar{\sigma}_{23}^2)^{1/2}, \quad J_4 = [\tfrac{1}{4}(\bar{\sigma}_{11} - \bar{\sigma}_{22})^2 + \bar{\sigma}_{12}^2]^{1/2},$$

with constants d and g given by (51a).

7 Discussion

The present material model, by virtue of the assumption that the fibers have a vanishingly small diameter, offers certain advantages which are essential in the development of plasticity theories of fibrous materials. The most important feature, of course, is the existence of uniform strain fields in the phases. As a result, one can derive analytical expressions for overall compliance of the aggregate in terms of the local properties and volume fractions of the phases. Indeed, the model can be utilized well beyond the scope of the results presented herein. Obvious extensions may be made to composites with matrices following other hardening rules, as well as to aggregates reinforced with plastically extensible fibers, and thus into the finite deformation range. Further modifications can account for time-dependent behavior of the phases.

Of course, these advantages must be balanced against other considerations, such as the accuracy of the overall response predicted by the model. As noted in Section 4, the model underestimates elastic moduli of the aggregate, but only in a minor way and, in any event, this defect can be rectified as indicated by equation (19). Of greater concern is the behavior in the plastic range, namely the low-constraint hardening rates in the transverse direction at high fiber concentrations (c.f., Section 6.2), and the shape of the overall yield surface in the axisymmetric plane, Fig. 2. These aspects of the model predictions indicate that applications of the theory should prefer materials with low to moderate fiber densities, and stress states with low isotropic components. Applications to thermal loading problems require further theoretical work.

However, the tendency of the model to overestimate the magnitudes of overall plastic strains is not necessarily inconvenient in applications to composite structures in which one seeks to determine maximum deflections or permanent strains. Also, as pointed out in [4], plastic deformation of the matrix generally leads to greater stress concentration in the fibers. Therefore, the model will often overestimate the fiber stresses, and thus provides an additional margin of safety in strength calculations. The requirement of low-applied isotropic stresses does not affect applications of the model to laminated plates, which are of major practical interest.

The model would not be suitable for problems involving metal forming, where one might desire to determine upper bounds on instantaneous moduli. The use of the self-consistent model, which generally overestimates the overall moduli and initial yield stresses, and underestimates plastic strains would be indicated in such instances, which are not very likely to arise in metals reinforced by brittle fibers.

From the physical standpoint, the assumption of a vanishing diameter fiber appears to be more acceptable in materials reinforced by very thin fibers, such as the FP, or graphite (T-50) fibers, which have diameters equal to 20, and 1.25 μm, respectively. These are of the same order of magnitude or less than the aluminum matrix grain size. In contrast, the boron or SiC filaments have diameters of about 140 μm, and usually form monolayers in laminated structures. A different modeling procedure may be indicated in certain applications of these materials.

8. Acknowledgments

This work has been supported by a grant from the U. S. Army Research Office. Mr. C. J. Wung made certain calcultions used herein.

References

1 Dvorak, G. J., and Johnson, W. S., "Fatigue of Metal Matrix Composites," *International Journal of Fracture,* Vol. 16, 1980, pp. 585–607.

2 Bahei-El-Din, Y. A., and Dvorak, G. J., "Plastic Yielding at a Circular Hole in a Laminated FP-Al Plate," in *Modern Developments in Composite Materials and Structures,* J. R. Vinson, ed., ASME 1979, pp. 123–147.

3 Dvorak, G. J., Rao, M. S. M., and Tarn, J. Q., "Generalized Initial Yield Surfaces for Unidirectional Composites," ASME Journal of Applied Mechanics, Vol. 41, No. 1, Mar. 1974, pp. 249–253.

4 Bahei-El-Din, Y. A., and Dvorak, G. J., "Plastic Deformation of a Laminated Plate with a Hole," ASME Journal of Applied Mechanics, Vol. 47, No. 4, 1980, pp. 827–832.

5 Hill, R., "Theory of Mechanical Properties of Fiber-Strengthened Materials: II: Inelastic Behavior," *Journal of the Mechanics and Physics of Solids,* Vol. 12, 1964, pp. 213–218.

6 Dvorak, G. J., and Rao, M. S. M., "Axisymmetric Plasticity Theory of

Fibrous Composites," *International Journal of Engineering Science,* Vol. 14, 1976, pp. 361–373.

7 Dvorak, G. J., and Bahei-El-Din, Y. A., "Elastic-Plastic Behavior of Fibrous Composites," *Journal of the Mechanics and Physics of Solids,* Vol. 27, 1979, pp. 51–72. Also, Erratum, Vol. 29, 1981, p. 267.

8 Huang, W. C., "Plastic Behavior of Some Composite Materials," *Journal of Composite Materials,* Vol. 5, 1971, pp. 320–338.

9 Needleman, A., Ph.D. Dissertation, Harvard University, 1970.

10 Huang, W. C., "Theoretical Study of Stress Concentrations at Circular Holes and Inclusions in Strain Hardening Materials," *International Journal of Solids and Structures,* Vol. 8, 1972, pp. 149–192.

11 Bahei-El-Din, Y. A., Dvorak, G. J., and Utku, S., "Finite Element Analysis of Elastic-Plastic Fibrous Composite Structures," *Computers and Structures,* Vol. 13, 1981, pp. 321–330.

12 Bahei-El-Din, Y. A., and Dvorak, G. J., "Plasticity Analysis of Laminated Composite Plates," Submitted for publication.

13 Hill, R., "Elastic Properties of Reinforced Solids: Some Theoretical Principles," *Journal of the Mechanics of Physics of Solids,* Vol. 11, 1963, pp. 357–372.

14 Hill, R., "Continuum Micromechanics of Elastoplastic Polycrystals," *Journal of the Mechanics and Physics of Solids,* Vol. 13, 1965, pp. 89–101.

15 Hill, R., "Theory of Mechanical Properties of Fiber-Strengthened Materials: I: Elastic Behavior," *Journal of the Mechanics and Physics of Solids,* Vol. 12, 1964, pp. 199–212.

16 Hill, R., "The Essential Structure of Constitutive Laws for Metal Composites and Polycrystals," *Journal of the Mechanics and Physics of Solids,* Vol. 15, 1967, pp. 79–95.

17 Hashin, Z., and Rosen, B. W., "The Elastic Moduli of Fiber-Reinforced Materials," ASME Journal of Applied Mechanics, Vol. 31, 1964, pp. 223–232.

18 Hashin, Z., "On Elastic Behavior of Fiber Reinforced Materials of Arbitrary Transverse Phase Geometry," *Journal of the Mechanics and Physics of Solids,* Vol. 13, 1965, pp. 119–134.

19 Bahei-El-Din, Y. A., Ph.D. Dissertation, Duke University, 1979.

20 Hill, R., "Theory of Mechanical Properties of Fiber-Strengthened Materials — III, Self-Consistent Model," *Journal of the Mechanics and Physics of Solids,* Vol. 13, 1965, pp. 189–198.

21 Phillips, A., and Ricciutti, M., "Fundamental Experiments in Plasticity and Creep of Aluminum," *International Journal of Solids and Structures,* Vol. 12, 1976, pp. 159–171.

22 Phillips, A., and Moon, H., "An Experimental Investigation Covering Yield Surfaces and Loading Surfaces," *Acta Mechanica,* Vol. 27, 1977, pp. 91–102.

23 Ziegler, H., "A Modification of Prager's Hardening Rule," *Quarterly of Applied Mathematics,* Vol. 17, 1959, pp. 55–65.

24 Dvorak, G. J., and Bahei-El-Din, Y. A., "Plasticity of Composite Laminates," *Proc. Research Workshop on Mechanics of Composite Materials,* G. J. Dvorak, ed., Duke University, Oct. 1978, pp. 32–54.

25 Dvorak, G. J., and Rao, M. S. M., "Thermal Stresses in Heat-Treated Fibrous Composites," ASME Journal of Applied Mechanics, Vol. 43, 1976, pp. 619–624.

26 Hill, R., "A Theory of the Yielding and Plastic Flow of Anisotropic Metals," *Proc. Royal Society,* London, Vol. A193, 1948, pp. 281–297.

27 Lin, T. H., Salinas, D., and Ito, Y. M., "Effects of Hydrostatic Stress on the Yielding of Cold Rolled Metals and Fiber-Reinforced Composites," *Journal of Composite Materials,* Vol. 6, 1972, pp. 409–413.

28 Baker, A. A., and Cratchley, D., "Stress-Strain Behavior and Toughness of a Fiber-Reinforced Metal," *Applied Materials Research,* Vol. 5, 1966, pp. 92–103.

29 Fedor, R. J., and Ebert, L. J., "A Study of the Effects of Prestrain on the Tensile Properties of Filamentary Composites," *Journal of Engineering Materials and Technology,* Vol. 95, 19793, pp. 69–75.

30 Mulhern, J. F., Rogers, T. G., and Spencer, A. J. M., "A Continuum Model for Fiber-Reinforced Plastic Materials," *Proc. Royal Soc. London,* Vol. A301, 1967, pp. 473–492.

Rotational Sliding of Rubber: Second-Order Stresses, Seizure, and Buckling

A. N. Gent

R. L. Henry
Assoc. Mem. ASME

Institute of Polymer Science,
The University of Akron,
Akron, Ohio 44325

Measurements are described of the frictional torque required to make a flat-ended rubber cylinder, bonded at one end to a flat metal plate, rotate about the cylinder axis when the other end is pressed against a flat Plexiglas surface. The contact pressure is found to increase on rotation, by an amount proportional to the square of the torsional deformation of the cylinder. The frictional torque then tends toward extremely large values (seizure) when the imposed compression approaches a critical level of about 20 percent, as predicted by theory. The rubber cylinder then transforms to a nonuniform state of deformation in which parts of the curved surfaces are drawn into contact with the Plexiglas surface. Sliding continues in this torsionally buckled state, at relatively low pressures and torques.

1 Introduction

When elastic materials are placed in a state of simple shear, the theory of large elastic deformations predicts that inwardly directed normal stresses, approximately proportional to the square of the amount of shear, will be required in order to maintain the sheared surfaces at a constant separation [1]. This effect has been studied for rubber by Rivlin and Saunders [2], and Gent and Rivlin [3], and shown to be in good quantitative agreement with the predictions of the theory. Thus, when a block of a highly elastic material is subjected to forces tending to make it slide against a rigid frictional substrate while its compressive deformation is maintained constant, normal forces will be generated, pressing the block more firmly against the substrate. When the compressive deformation exceeds a critical amount of the order of 10 percent, sliding is predicted to become impossible because the shear-generated normal stresses will increase the frictional resistance to sliding in such a way that it always exceeds the imposed shear force [4]. The critical amount of compression e_c at which frictional seizure occurs is predicted to be [4]

$$e_c = 1/12\mu^2 \tag{1}$$

for the leading and trailing edges of a sheared block, where μ is the coefficient of friction, and

$$e_c = (C_1 + C_2)/12\mu^2 C_2 \tag{2}$$

for the side surfaces of the block, where C_1, C_2 denote the two elastic constants in the Mooney form of strain-energy function [5]. The shear modulus G is given by $2(C_1 + C_2)$ and Young's modulus E by $6(C_1 + C_2)$ [5]. For a neo-Hookean material, $C_2 = 0$ [1], and equation (2) then predicts that e_c is infinitely large, i.e., that the side regions of the block will undergo sliding at any degree of compression. Although rubbery solids do not follow the Mooney form of strain-

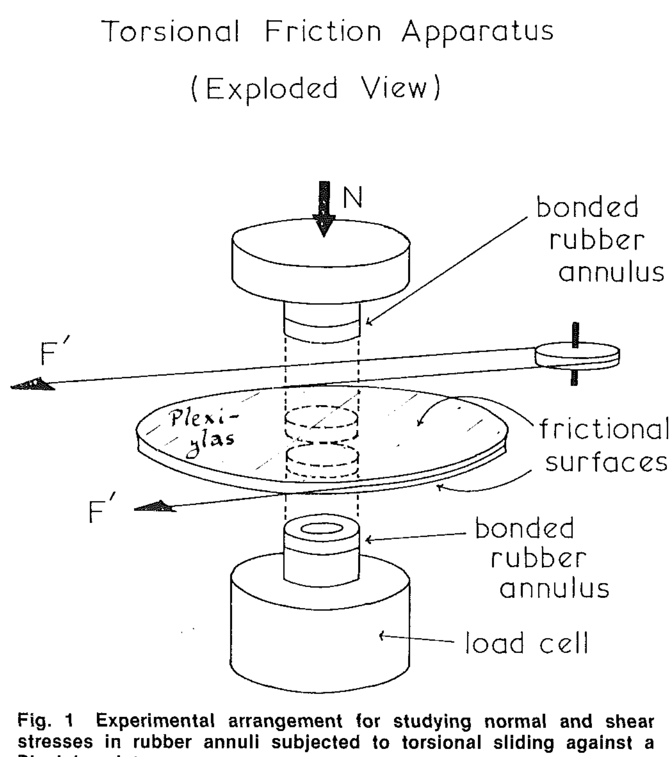

Fig. 1 Experimental arrangement for studying normal and shear stresses in rubber annuli subjected to torsional sliding against a Plexiglas plate

Contributed by the Applied Mechanics Division for publication in the JOURNAL OF APPLIED MECHANICS.

Discussion on this paper should be addressed to the Editorial Department, ASME, United Engineering Center, 345 East 47th Street, New York, N.Y. 10017, and will be accepted until two months after final publication of the paper itself in the JOURNAL OF APPLIED MECHANICS. Manuscript received by ASME Applied Mechanics Division, November, 1981; final revision, January, 1982.

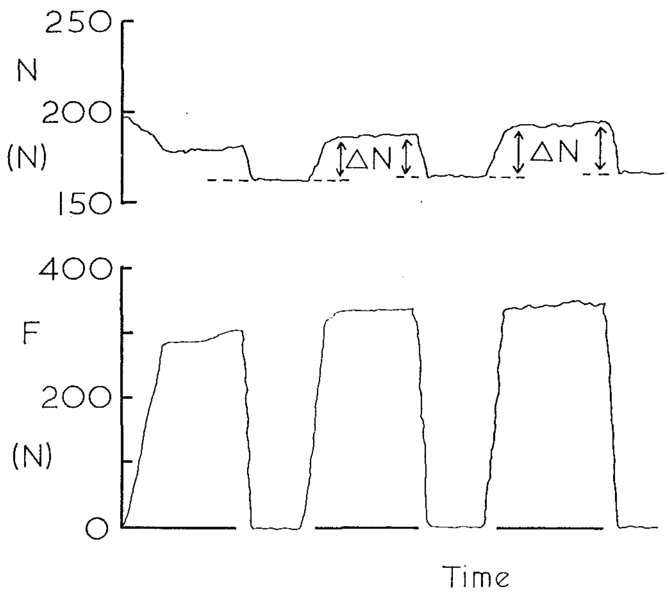

Fig. 2 Representative relations for the compressive force N and effective shear force F as rotational sliding is imposed repeatedly. Initial compressive force: 200 N.

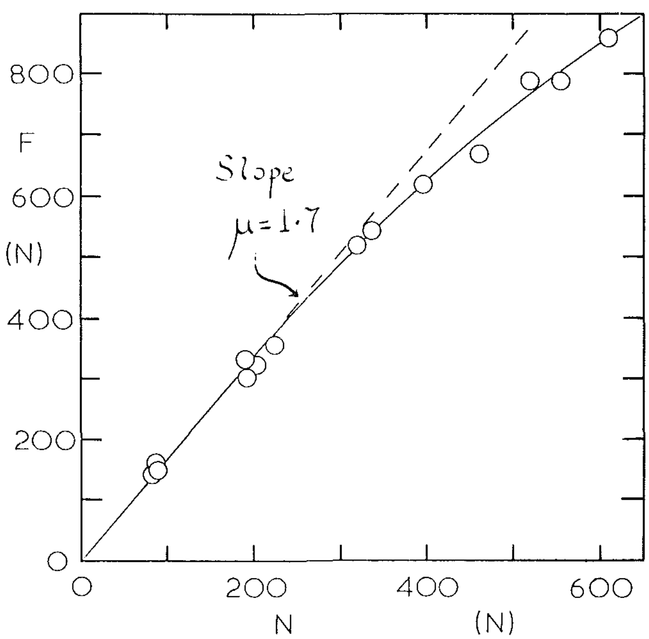

Fig. 3 Mean sliding force F versus mean total compressive force N for unfilled natural rubber annuli sliding against a Plexiglas plate

energy function accurately, their elastic behavior can be represented approximately in this way, with C_2 generally of the same order of magnitude as C_1 [5]. If C_2 is put equal to C_1, then equation (2) predicts that e_c, for the side edges of a sheared block, is about twice as large as for the front and rear edges.

Measurements of the interfacial stresses set up at the front and rear edges of sliding blocks are somewhat difficult to carry out. We have therefore examined the sliding of a cylindrical rubber annulus, pressed against a frictional surface and rotated about its axis. The distribution of stresses in rubber annuli under compression and torsion are given elsewhere [6]. When the annulus is thin-walled and compressed only to a small degree, then the stresses conform closely to those developed at the side edges of a sheared block, as would be expected. The critical amount of compression e_c at which frictional seizure occurs is predicted to be given by equation (2).

In the following sections of the paper, experimental measurements of interfacial stresses for cylindrical rubber annuli are compared with the theoretical predictions. In the final section some observations are presented of the rotational behavior of an annulus subjected to a compressive deformation greater than that at which frictional seizure is expected.

2 Experimental Details

Cylindrical rubber annuli were prepared as described in the Appendix. Each annulus was bonded on one face to a metal plate, used for securing it in the test fixture. Two identical annuli were pressed against opposite faces of a Plexiglas plate, as shown schematically in Fig. 1. The amount of compression was held constant and the compressive force N was monitored continuously during the experiment by means of a strain-gauge load cell and indicating recorder. While the annuli were compressed against the Plexiglas plate, it was slowly rotated between them at a rate of about 5 deg /min by means of the cable and pulley arrangement shown in Fig. 1. The cables employed to rotate it were also connected to a load cell, so that the rotational forces F' could be continuously monitored during the rotation. Equivalent frictional forces F acting at the mean radius $\bar{r}$ of the rubber annuli were calculated from the measured forces F' using the scaling factor $r_s/\bar{r}$, where r_s denotes the radius of the Plexiglas plate, about 170 mm

Typical dimensions of the rubber annuli were: external diameter 62.5 mm; internal diameter, 37.8 mm; height 11.9 mm. Experiments were also carried out with annuli of about three times this height, 38.5 mm, with similar results.

3 Experimental Results

(*a*) Typical Measurements. Some representative results are shown in Fig. 2. The compressive force N pressing each annulus against the Plexiglas plate and the effective shear force F acting at each interface are plotted in Fig. 2 against the elapsed time. When rotation of the Plexiglas plate began, the imposed shear force gradually built up to a limiting value at which interfacial sliding started. Simultaneously, the compressive force decreased somewhat, probably as a result of the rubber annuli spreading outward on the Plexiglas surface and thus partially relieving the compressive stresses set up initially. When the rotation was halted temporarily, and the applied shear force removed, the compressive force N was found to decrease simultaneously. When rotation was resumed, the compressive force increased by an amount denoted ΔN in Fig. 2. Values of ΔN were determined in this way by applying the rotational sliding force F repeatedly. Similar experiments were carried out for a wide range of values of the initial compressive force.

(*b*) Coefficient of Sliding Friction μ and Shear Modulus *G*. The effective force F at which sliding took place is represented by the plateau values in the lower part of Fig. 2. The corresponding compressive force N is represented by the plateau values in the upper part of the figure, where the equilibrium rest value of N, denoted N_0, is augmented by ΔN. The ratio $F/(N_0+\Delta N)$ then affords a measure of the coefficient of sliding friction μ. When values of F and $N_0+\Delta N$ were determined in this way for a wide range of initial conditions, they were found to be approximately proportional to each other (Fig. 3) and yielded values for μ of 1.7 and 1.8 for an unfilled natural rubber material A and a carbon-black-filled SBR material B, respectively. These values are representative of those reported for rubbery materials sliding over smooth rigid substrates [7].

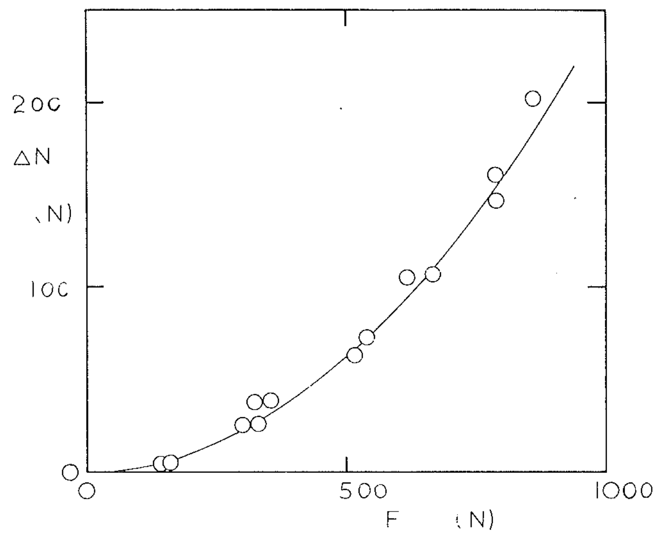

Fig. 4 Increase ΔN in the compressive force N versus mean sliding force F for unfilled natural rubber annuli sliding against a Plexiglas plate

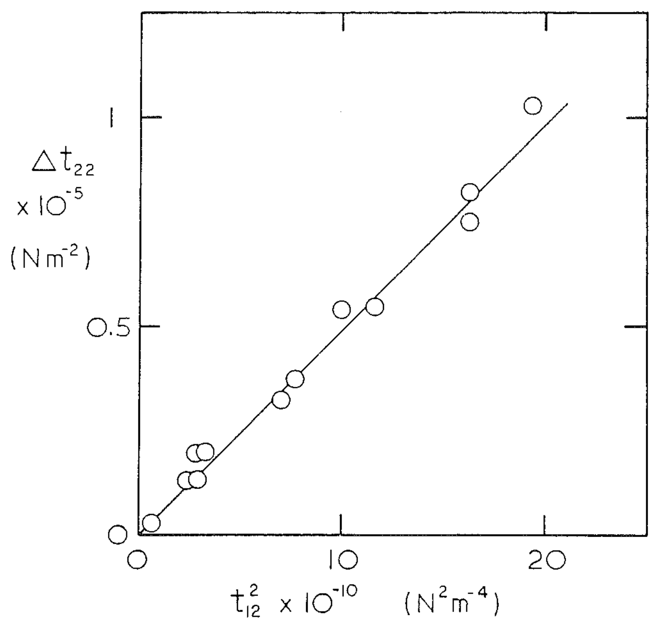

Fig. 5 Increase Δt_{22} in the mean compressive stress t_{22} versus $t_{12}{}^2$ for unfilled natural rubber annuli sliding against a Plexiglas plate

When the applied shear force F was removed, the Plexiglas disk rotated back through a few degrees as the rubber annulus recovered from its twisted state. By comparing the sliding force F with the recoverable rotation, the shear modulus G of the rubber was determined. Values of 0.56 MPa and 3.2 MPa were obtained in this way for materials A and B, respectively. They are consistent with the measured indentation hardnesses of each compound, namely 45 and 72 Shore A degrees [8].

(*c*) Increase ΔN in the Compressive Force. As shown in Fig. 4, the increase ΔN in the compressive force required to maintain the rubber annuli at a fixed degree of compression when they were subjected to a sliding (shearing) force F was found to increase sharply as the original compression, and hence the force F required to cause sliding, was increased. The value of ΔN was found to be approximately proportional to F^2, as the theory of large elastic deformations suggests. This is illustrated in Fig. 5, where the experimental results shown in Fig. 4 are replotted as the increase Δt_{22} in the mean normal stress t_{22} versus the square of the mean applied shear stress, $t_{12}{}^2$. They are seen to be described reasonably well by a direct

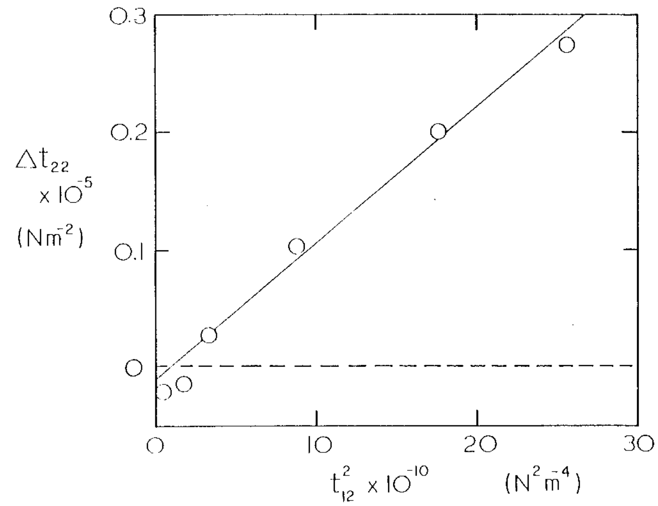

Fig. 6 Increase Δt_{22} in the mean compressive stress versus $t_{12}{}^2$ for carbon-black-filled SBR annuli sliding against a Plexiglas plate

Table 1 Experimentally determined values of the shear modulus G, second-order normal stress Δt_{22}, and calculated values of C_2/C_1

G (MPa)	$\Delta t_{22}/t_{12}{}^2$ (MPa)$^{-1}$	C_2/C_1
unfilled natural rubber annuli		($\mu = 1.7$)
0.57	0.50	0.39
carbon-black-filled SBR annuli		($\mu = 1.8$)
3.2	0.13	0.68
Bonded annuli of unfilled natural rubber		
0.56	0.42	0.31

proportionality in this representation. Similar results were obtained for annuli of the carbon-black-filled material B (Fig. 6), although the values of ΔN and Δt_{22} were considerably smaller in this case.

Values of the slopes of the linear relations shown in Fig. 5 and 6 are given in Table 1. Corresponding values of the ratio C_2/C_1 of the elastic coefficients were calculated from them by means of theory of large elastic deformations [1], specialized to the case of a material obeying the Mooney strain-energy function, for which

$$\Delta t_{22}/t_{12}{}^2 = C_2/2(C_1 + C_2)^2.$$

This relation applies to the side regions of a block subjected to a homogeneous shear deformation because it is based on the assumption that these surfaces are stress-free, i.e., $t_{33} = 0$. These conditions are assumed to hold for the sliding annuli used in the present experiments.

Values of the ratio C_2/C_1 obtained in this way are given in the final column of Table 1. They are seen to be quite comparable to those obtained by direct measurement of the nonlinear elastic behavior of rubbery materials [5], generally ranging between 0.2–1.5. Thus, the second-order normal stresses set up in sliding seem to arise from shear deformation of the sliding block and the values can be calculated on this basis. This conclusion was corroborated by studying the additional compressive forces ΔN generated by twisting two soft rubber annuli that were bonded to the central plate in Fig. 1, and were therefore unable to slide. The results, given on the last line of Table 1, are in good agreement with measurements carried out on the same annuli during sliding, given on the first line of Table 1. Thus, although a thin sliding annulus is not strictly subjected to a homogeneous shear deformation, nevertheless the deformation is sufficiently similar to allow

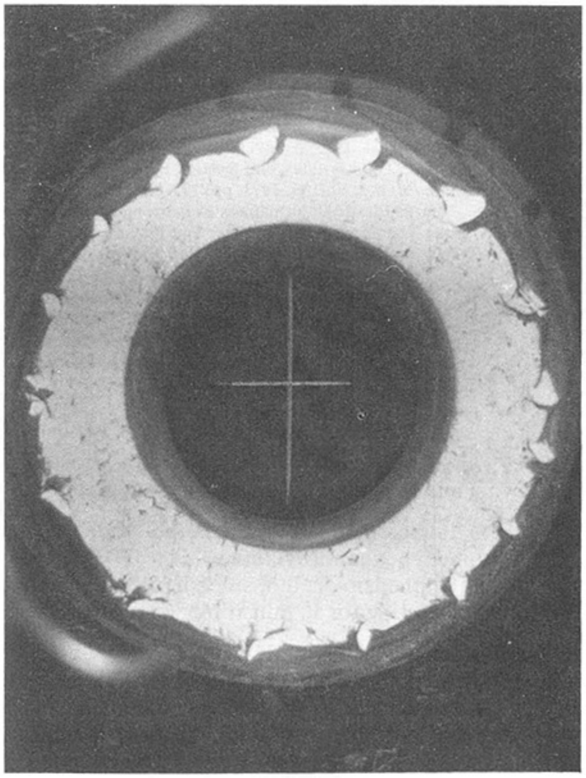

Fig. 7 Photograph of the contact surface (in white) for a short rubber annulus subjected to torsional sliding under a nominal compressive stress of 0.65 MPa. Annulus dimensions: length, 3.05 mm; outer diameter, 25.4 mm; and inner diameter, 15.9 mm.

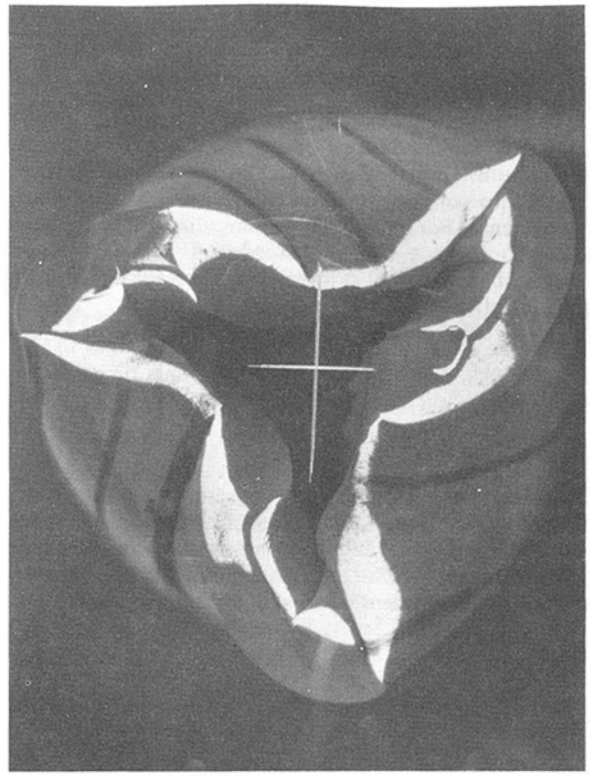

Fig. 8 Photograph of the contact surface (in white) for a relatively tall rubber annulus subjected to torsional sliding under a nominal compressive stress of 0.26 MPa. Annulus dimensions: length, 9.52 mm; outer diameter, 25.4 mm; and inner diameter, 15.9 mm.

the normal stresses generated on sliding to be evaluated on this assumption.

(*d*) **Frictional Seizure and Buckling.** Critical amounts of compression at which sliding becomes theoretically prohibited can be calculated from equation (2) for the two rubbery materials employed in the preceding experiments. The values obtained for e_c were 0.12 and 0.062 for the unfilled natural rubber and the carbon-black-filled SBR material, respectively, corresponding to initial compressive forces N_0 of 400 N and 1200 N. As the initial compressive loads were raised toward these levels in the sliding experiments, the measured increase ΔN in the compressive force generated by frictional shear forces was found to increase dramatically (Fig. 4), becoming comparable in magnitude to the original value N_0. Simultaneously, the frictional shear force increased correspondingly. Eventually, at values of N_0 quite close to the theoretically predicted critical values, i.e., 400 and 1200 N, continuous sliding of the rubber over the Plexiglas surface ceased and the annulus underwent severe distortion, causing its flat surface to be no longer in uniform contact with the Plexiglas. Subsequently, sliding took place with the rubber surface distorted in characteristic ways, depending on the dimensions of the annulus.

An example of the distorted contact surface for a relatively short rubber annulus is shown in Fig. 7. Parts of the cylindrical outer surface of the annulus have been dragged into contact with the Plexiglas plate at a number of points around the circumference, forming a series of rather regular cusps. These cusps completely transform the state of strain of the rubber so that it is no longer subjected to a uniform shear deformation. In consequence, the large second-order compressive stresses generated by frictional shearing are alleviated and sliding proceeds with this distorted contact surface under compressive loads greatly exceeding the predicted limiting value.

Similar effects were noted for tall annuli, having heights comparable to, or greater than the width of the contact band. In these cases the distortion that set in at the critical amount of compression was found to affect the entire contact surface, rather than its outer edge, and to take the form of a small number of lobes generated by buckling of the walls of the annulus. An example is shown in Fig. 8.

For both short and tall annuli, the same general behavior was observed. When the amount of compression exceeded the theoretically predicted value, normal sliding ceased, to be replaced by sliding over a markedly distorted contact surface with parts of the original flat contact surface lifted out of contact and parts of the original cylindrical surface dragged into contact. The reason for this distortion, whatever its detailed form, is to overcome the frictional seizure that occurs in a homogeneously sheared body as a consequence of second-order stresses.

4 Conclusions

The following conclusions were obtained.

1 Thin cylindrical rubber annuli, bonded at one end to a flat metal plate and pressed at the other end against a Plexiglas plate rotating about the cylinder axis, develop additional contact pressures due to shear deformation of the rubber under frictional stresses.

2 These additional pressures are approximately proportional to the square of the frictional stresses. They can be calculated by means of the theory of large elastic deformation.

3 The additional pressures are smaller for rubber of higher elastic modulus, as the theory suggests.

4 Frictional "seizure" is encountered at a critical amount of compression, when the additional pressures generated by

shear of the rubber become so large that normal sliding is impossible. The rubber annulus then buckles in characteristic ways, and slides with a distorted contact surface.

5 The shape of the contact surface after buckling depends on the original dimensions of the annulus. For a relatively short annulus, portions of the cylindrical outer surface are dragged into contact, forming a series of cusps around the circumference. For a relatively tall annulus, the entire annulus buckles to form a two or three-lobed figure, again with portions of the original cylindrical surfaces dragged into the sliding interface.

6 Similar effects are expected at the side edges of sliding rubber blocks, and at even smaller amounts of compression for the leading and trailing edges.

Acknowledgments

This work was supported by a research grant from the Engineering Division of the National Science Foundation (NSF-ENG-75-16982) and by a research grant-in-aid from Cabot Corporation. The authors are also indebted to Mr. R. L. Paden for experimental assistance.

References

1 Rivlin, R. S., "Large Elastic Deformations of Isotropic Materials. Part 4. Further Development of the General Theory," *Philosophical Transactions of the Royal Society (London)*, Series A, Vol. 241, 1948, pp. 379–397.

2 Rivlin, R. S., and Saunders, D. W., "Large Elastic Deformations of Isotropic Materials. Part 7. Experiments on the Deformation of Rubber," *Philosophical Transactions of the Royal Society (London)*, Series A, Vol. 243, 1951, pp. 251–288.

3 Gent, A. N., and Rivlin, R. S., "Experiments on the Mechanics of Rubber. Part 2. The Torsion, Inflation, and Extension of a Tube," *Proceedings of the Physical Society (London)*, Part B, Vol. 65, 1952, pp. 487–501.

4 Gent, A. N., "Friction and Wear of Highly-Elastic Solids," *Wear*, Vol. 29, 1974, pp. 111–116; Vol. 31, 1975, p. 189.

5 Treloar, L. R. G., "The Elasticity and Related Properties of Rubbers," *Reports on Progress in Physics*, Vol. 36, 1973, pp. 755–826.

6 Rivlin, R. S., "Large Elastic Deformations of Isotropic Materials. Part 6. Further Results in the Theory of Torsion, Shear and Flexure," *Philosophical Transactions of the Royal Society (London)*, Series A, Vol. 242, 1949, pp. 173–195.

7 Schallamach, A., "Recent Advances in Knowledge of Rubber Friction and Tyre Wear," *Rubber Chemistry and Technology*, Vol. 41, 1968, pp. 209–244.

8 Gent, A. N., "Science of Rubbers," *Polymer Science and Materials*, Tobolsky, A. V., and Mark, H. F., Eds., Wiley, New York, 1971, Chapter 13.

APPENDIX

Rubber annuli were prepared by a molding process using the following mix formulations in parts by weight:

A Natural rubber (SMR-5L), 100; zinc oxide, 5; stearic acid, 2; phenyl-β-naphthylamine, 1; N-cyclohexyl-2-benzothiazole sulphenamide, 0.6; sulphur, 2.5. Vulcanization was effected by heating for 50 min at 145°C.

B Styrene-butadiene copolymer (25:75, FRS-1502, Firestone Tire & Rubber Company), 100; zinc oxide, 5; stearic acid, 2; phenyl-β-naphthylamine, 1; N-cyclohexyl-2-benziothiazole sulphenamide, 1; sulphur, 2; N220 carbon black (Vulcan 6, Cabot Corporation) 54. Vulcanization was effected by heating for 60 min at 150° C.

G. M. L. Gladwell
Chairman and Professor,
Solid Mechanics Division,
Faculty of Engineering,
University of Waterloo,
Waterloo, Ontario, Canada W2L 3GL

V. I. Fabrikant
Department of Mechanical Engineering,
Concordia University,
Montreal, Quebec, Canada H3G 1MB

The Interaction Between a System of Circular Punches on an Elastic Half Space

Galin derived an expression for the pressure produced under a rigid circular punch by the application of a concentrated load at another point of the half space. This result is used to derive approximate relationships among the forces, moments, and indentations for a system of punches on an elastic half space. The results are compared with a number of earlier approximate solutions.

Introduction

Collins [1] discussed the interaction between two identical flat-ended rigid punches of circular cross section, each indenting an isotropic elastic half space by an equal amount ϵ. He set up the problem as an infinite set of Fredholm integral equations which he solved by an iteration technique; this is valid when the distance between the punches is large compared to the radii of the punches. Panasyuk and Andreikiv [2] derived virtually the same result by using the method derived by Galin [3] and which is described in the following. Andreikiv and Dubetskii [4] considered the interaction between four punches by a method of successive approximation. A similar method is used by Buzko and Prosenko [5] for the interaction between two punches on a half space that has a Young's modulus $E = E_0 z^\nu$ $(0 \leq \nu < 1)$. Marzitsin and Popov [6] applied the method of orthogonal polynomials to this problem.

In all these papers an attempt is made to find the stress distributions under the punches. If it is then required to find the total forces applied by the punches, these stress distributions are integrated over the punch contact regions. In this paper we show that it is possible to find good approximations to the total applied forces directly, without first finding the stress distributions.

Theory

Consider a single rigid flat-ended punch of radius a in frictionless contact with a transversely isotropic elastic half space $z \geq 0$ with planes of isotropy parallel to $z = 0$. If the normal displacement under the punch is (Gladwell [7], p. 88)

$$w(x,y) = w_0 + \alpha_y x - \alpha_x y, \tag{1}$$

then the normal pressure exerted by the punch is

$$p(x,y) = \frac{1}{\pi^2 H} \frac{w_0 + 2\alpha_y x - 2\alpha_x y}{(a^2 - x^2 - y^2)^{1/2}}, \tag{2}$$

where H is an elastic constant which reduces to $H = (1-\nu)/(2\pi\mu)$ when the half space is an isotropic medium with shear modulus μ and Poisson's ratio ν, (see [7], p. 581).

Now suppose that a unit-concentrated normal load is applied to the surface of the half space at a point (x_0, y_0) outside the circle $x^2 + y^2 \leq a^2$. This load will produce an additional contact pressure under the punch. This additional pressure, which is such that, together with the concentrated load, it produces no additional normal displacement under the punch, was found by Galin [3]; it is

$$p_e(x,y) = -\frac{(x_0^2 + y_0^2 - a^2)^{1/2}}{\pi^2 (a^2 - x^2 - y^2)^{1/2} \{(x-x_0)^2 + (y-y_0)^2\}}. \tag{3}$$

Equations (2) and (3) give the only fundamental results used in this paper. Equation (3) was derived by Galin for an isotropic elastic half space, but clearly holds when the medium is transversely isotropic.

Figure 1 shows punches j and k of a set of N punches. Punch k occupies the circle S_k of radius a_k; its center (x_k, y_k) has polar coordinates (b_{jk}, ϕ_{jk}) relative to punch j. Equations (2) and (3) show that if the displacement under punch j is

$$w(x,y) = w_j + \alpha_{jy}(x-x_j) - \alpha_{jx}(y-y_j), \quad (x,y)\epsilon S_j, \tag{4}$$

then the normal pressure under punch j is

$$p_j(x,y) = \frac{1}{\pi^2 \{a_j^2 - (x-x_j)^2 - (y-y_j)^2\}^{1/2}} \left\{ \frac{w_j + 2\alpha_{jy}(x-x_j) - 2\alpha_{jx}(y-y_j)}{H} - \sum_{k=1}^{N}{}' \iint_{S_k} \frac{p_k(x_0,y_0)\{(x_0-x_j)^2 + (y_0-y_j)^2 - a_j^2\}^{1/2}}{(x-x_0)^2 + (y-y_0)^2} \right\} dxdy, \tag{5}$$

where the prime on the summation indicates that $k \neq j$.

Now transform to polar coordinates as shown in Fig. 1; then

$$x - x_j = r\cos\phi, \quad y - y_j = r\sin\phi, \tag{6}$$

$$x_0 - x_j = r_0\cos\phi_0, \quad y_0 - y_j = r_0\sin\phi_0, \tag{7}$$

and equation (5) becomes

Contributed by the Applied Mechanics Division for publication in the JOURNAL OF APPLIED MECHANICS.

Discussion on this paper should be addressed to the Editorial Department, ASME, United Engineering Center, 345 East 47th Street, New York, N.Y. 10017, and will be accepted until two months after final publication of the paper itself in the JOURNAL OF APPLIED MECHANICS. Manuscript received by ASME Applied Mechanics Division, June, 1981.

$$p_j(r,\phi) = \frac{1}{\pi^2(a_j^2 - r^2)^{1/2}}\left[\frac{w_j + 2\alpha_{jy} r\cos\phi - 2\alpha_{jx} r\sin\phi}{H}\right.$$

$$\left. - \sum_{k=}^{N}{}' \iint_{S_k} \frac{p_k(r_0,\phi_0)(r_0^2 - a_j^2)^{1/2} r_0 dr_0 d\phi_0}{r^2 + r_0^2 - 2rr_0\cos(\phi - \phi_0)}\right]. \quad (8)$$

We now integrate this expression over the circle S_j and use the integrals

$$\int_0^{2\pi} \frac{d\phi}{r^2 + r_0^2 - 2rr_0\cos(\phi - \phi_0)} = \frac{2\pi}{r_0^2 - r^2}, \quad r_0 > r, \quad (9)$$

$$\int_0^{a_j} \frac{rdr}{(r_0^2 - r^2)(a_j^2 - r^2)^{1/2}} = \frac{1}{(r_0^2 - a_j^2)^{1/2}} \sin^{-1}\left(\frac{a_j}{r_0}\right), \quad r_0 > a_j, \quad (10)$$

to obtain

$$P_j = \frac{2a_j w_j}{\pi H} - \frac{2}{\pi}\sum_{k=1}^{N}{}' \iint_{S_k} p_k(r_0,\phi_0)\sin^{-1}\left(\frac{a_j}{r_0}\right) r_0 dr_0 d\phi_0. \quad (11)$$

This equation is exact, within the assumption of classical elasticity theory. If we now assume that a_j/b_{jk} is small we may take

$$\sin^{-1}\left(\frac{a_j}{r_0}\right) \simeq \sin^{-1}\left(\frac{a_j}{b_{jk}}\right), \quad (12)$$

and obtain

$$P_j = \frac{2a_j w_j}{\pi H} - \frac{2}{\pi}\sum_{k=1}^{N}{}' P_k \sin^{-1}\left(\frac{a_j}{b_{jk}}\right) \quad (13)$$

The punch j applies a moment with components

$$M_{jx} = -\iint_{S_j} (y - y_j)p_j(x,y) \quad dxdy$$
$$= -\int_0^{2\pi}\int_0^{a_j} r^2 p_j(r,\phi)\sin\phi dr d\phi, \quad (14)$$
$$M_{jy} = \iint_{S_j} (x - x_j)p_j(x,y) \quad dxdy$$
$$= \int_0^{2\pi}\int_0^{a_j} r^2 p_j(r,\phi)\cos\phi dr d\phi, \quad (15)$$

so that

$$M_j = M_{jx} + iM_{jy} = i\int_0^{2\pi}\int_0^{a_j} r^2 e^{i\phi} p_j(r,\phi) dr d\phi. \quad (16)$$

Thus, if we multiply equation (8) by $re^{i\phi}$ and integrate over S_j we find

$$M_j = \frac{4a_j^3\alpha_j}{3\pi H} - \frac{2i}{\pi}\sum_{k=1}^{N}{}'$$
$$\iint_{S_k}\left\{r_0\sin^{-1}\left(\frac{a_j}{r_0}\right) - \frac{a_j}{r_0}(r_0^2 - a_j^2)^{1/2}\right\}\cdot$$
$$\cdot p_k(r_0,\phi_0)\, e^{i\phi_0} r_0 dr_0 d\phi_0, \quad (17)$$

where $\alpha_j = \alpha_{jx} + i\alpha_{jy}$. In deriving this we used the result

$$\int_0^{2\pi} \frac{e^{i\phi}d\phi}{r^2 + r_0^2 - 2rr_0\cos(\phi - \phi_0)} = \frac{2\pi e^{i\phi_0}}{r_0^2 - r^2}\cdot\frac{r}{r_0}, \quad r_0 > r, \quad (18)$$

and

$$\int_0^{a_j} \frac{r^3 dr}{(r_0^2 - r^2)(a_j^2 - r^2)^{1/2}} = \frac{r_0}{(r_0^2 - a_j)^{1/2}}\{r_0\sin^{-1}\left(\frac{a_j}{r_0}\right)$$
$$- \frac{a_j}{r_0}(r_0^2 - a_j)^{1/2}\}, \quad (19)$$

when $r_0 > a_j$.

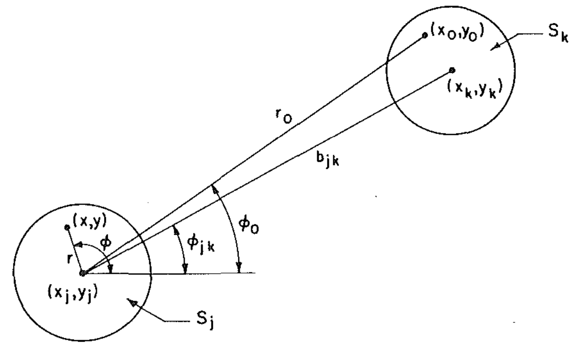

Fig. 1 The geometry of the punch configuration

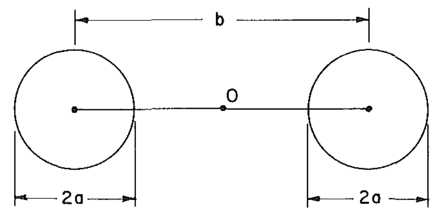

Fig. 2 *Collins' two-punch problem*

Again equation (19) is exact within classical elasticity theory. If a_j/b_{kj} is small we may take

$$e^{i\phi_0}\{r_0\sin^{-1}\left(\frac{a_j}{r_0}\right) - \frac{a_j}{r_0}(r_0^2 - a_j^2)^{1/2}\} \simeq e^{i\phi_{jk}}$$
$$\{b_{jk}\sin^{-1}\left(\frac{a_j}{b_{jk}}\right) - \frac{a_j}{b_{jk}}(b_{jk}^2 - a_j^2)^{1/2}\},$$
$$\simeq \frac{2}{3} b_{jk}\left(\frac{a_j}{b_{jk}}\right)^3 e^{i\phi_{jk}}, \quad (20)$$

so that

$$M_j = \frac{4a_j^3}{3\pi}\left\{\frac{\alpha_j}{H} - i\sum_{k=1}^{N}{}' \frac{e^{i\phi_{jk}}}{b_{jk}^2} P_k\right\}. \quad (21)$$

This formula may be rewritten

$$M_j = \frac{4a_j^3\alpha_j}{3\pi H} - \frac{4}{3\pi}\sum_{k=1}^{N}{}'\left(\frac{a_j}{b_{jk}}\right)^3 M_{jk} \quad (22)$$

where $M_{jk} \equiv i\, b_{jk}\, e^{i\phi_{jk}}\, P_k$ is the moment of P_k about the center of the jth punch. A study of the errors made by using the replacements (12) and (20) shows that they are of the same order as that incurred by proceeding to (21). Equations (13) and (22) are the main results of this paper.

Applications

For Collins' problem of two identical punches of radius a, distance b, as shown in Fig. 2 apart along the x-axis, equation (13) gives

$$P \doteq \frac{2aw_0}{\pi H} - \frac{2}{\pi}\sin^{-1}\left(\frac{a}{b}\right)P, \quad (23)$$

so that if

$$P_0 = \frac{2aw_0}{\pi H}, \quad \epsilon = \frac{a}{b}, \quad (24)$$

then

$$\frac{P}{P_0} = \frac{1}{1 + \dfrac{2}{\pi}\sin^{-1}\epsilon}. \quad (25)$$

When expanded in powers of ϵ this gives

$$\frac{P}{P_0} = 1 - \frac{2\epsilon}{\pi} + \frac{4\epsilon^2}{\pi^2} - \frac{8\epsilon^3}{\pi^3}\left(1 + \frac{\pi^2}{24}\right) + 0(\epsilon^4). \quad (26)$$

This differs from Collins' result

$$\frac{P}{P_0} = 1 - \frac{2\epsilon}{\pi} + \frac{4\epsilon^2}{\pi^2} - \frac{8\epsilon^3}{\pi^3}\left(1 + \frac{\pi^2}{12}\right) + 0(\epsilon^4), \quad (27)$$

only in the fourth term. In their approximate solution Panasyuk and Andreikiv [2] obtained a stress distribution

$$p(r,\phi) = \frac{Hw_0}{\pi^2(a^2-r^2)^{1/2}}\left\{1 - \frac{2\epsilon}{\pi}\left(1 + \frac{2r\cos\phi}{h} + \frac{3r^2\cos^2\phi}{h^2} - \frac{r^2\sin^2\phi}{h^2}\right) + \frac{4\epsilon^2}{\pi^2}\left(1 + \frac{2r\cos\phi}{h}\right) + \frac{8\epsilon^3}{\pi^3}\left(\frac{\pi^2}{12} - 1\right) + 0(\epsilon^4)\right\} \quad (28)$$

and, on integration, this agrees with Collins' result (27).

For the configuration of Fig. 2, the angles are $\phi_{12} = 0$, $\phi_{21} = \pi$. Therefore, if the punches are not allowed to tilt, then the moment applied by punch 1 is

$$M_1 = M_{1x} + iM_{1y} = -\frac{4a^3 iP}{3\pi b^3} = -\frac{4i}{3\pi}a\epsilon^2 P \quad (29)$$

so that

$$M_{1x} = 0, \quad M_{1y} = -\frac{4a\epsilon^2}{3\pi}\left\{1 - \frac{2\epsilon}{\pi} + 0(\epsilon^2)\right\}P_0. \quad (30)$$

This agrees with the result found by integrating (28). If, on the other hand, no moments are applied, then the rotation of punch 1 is

$$\alpha_1 = \alpha_{1x} + i\alpha_{1y} = \frac{HiP}{b^2} = \frac{Hi}{b^2}\left\{1 - \frac{2\epsilon}{\pi} + 0(\epsilon^2)\right\}P_0 \quad (31)$$

so that

$$\alpha_{1x} = 0, \quad \alpha_{1y} = \frac{HP_0}{b^2}\left\{1 - \frac{2\epsilon}{\pi} + 0(\epsilon^2)\right\}. \quad (32)$$

If the punches in Fig. 2 are subjected to different forces P_1, P_2, then equation (13) yields

$$w_1 = \frac{\pi H}{2a}\left\{P_1 + \frac{2}{\pi}(\sin^{-1}\epsilon)P_2\right\}. \quad (33)$$

This may be contrasted with the approximate result obtained by Marzitsin and Popov [5] (equation (1.16)), namely

$$w_1 = \frac{\pi H}{2a}\left\{P_1 + 4\left(\epsilon + \frac{1}{3}\epsilon^3 + \frac{2}{5}\epsilon^5 + \ldots\right)P_2\right\}. \quad (34)$$

This not only contradicts (33), but is also clearly unrealistic; even for $\epsilon = 1/4$, the multiplier of P_2 will be greater than unity, whereas the multiplier in equation (33) is (correctly) always less than unity.

Figure 3 shows a configuration of $(N+1)$ punches, one central punch of radius a_0, normal force P_0, and displacement w_0, and N ($=8$) identical peripheral punches of radii a, with forces P, and displacement w, situated equidistantly on a circle of radius b. Equation (13) applied to the central punch yields

$$P_0 = \frac{2a_0 w_0}{\pi H} - \frac{2N}{\pi}P\sin^{-1}\frac{a_0}{b}, \quad (35)$$

so that

$$w_0 = \frac{\pi H}{2a_0}\left(P_0 + \frac{2NP}{\pi}\sin^{-1}\frac{a_0}{b}\right). \quad (36)$$

On the other hand, equation (13) applied to a peripheral punch yields

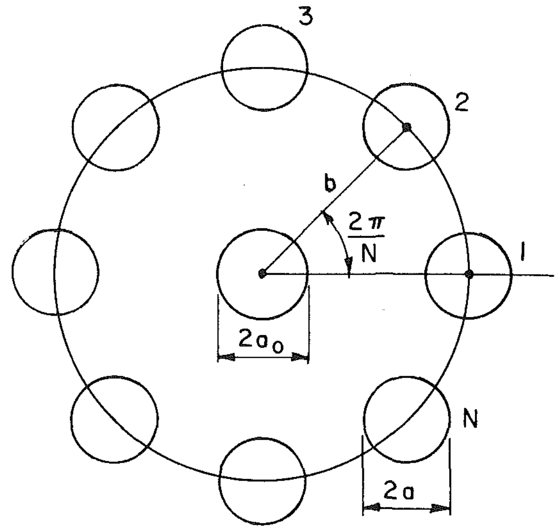

Fig. 3 N equal punches circling a central punch

$$P = \frac{2aw}{\pi H} - \frac{2}{\pi}P_0\sin^{-1}\left(\frac{a}{b}\right) - \frac{2}{\pi}SP, \quad (37)$$

where

$$S = \sum_{K=1}^{N-1}\sin^{-1}\left(\frac{a}{2b\sin\left(\frac{k\pi}{N}\right)}\right). \quad (38)$$

In the particular case of four punches at the corners of a square of side h and *no* central punch, we have $N = 4$, $b = \sqrt{2}h/2$, so that

$$w = \frac{\pi HP}{2a}\left(1 + \frac{2}{\pi}\sin^{-1}\left(\frac{\epsilon}{\sqrt{2}}\right) + \frac{4}{\pi}\sin^{-1}\epsilon\right), \quad \epsilon = \frac{a}{h}. \quad (39)$$

This does *not* agree with the expression

$$w = \frac{\pi HP}{2a}(1 - 2.586\epsilon - 1.0976\epsilon^3 + 12.22\epsilon^4) \quad (40)$$

obtained by Andreikiv and Dubetskii [4], but their formula contradicts common sense – w decreases as ϵ increases! The expression in equation (39), on the other hand, increases with ϵ.

The peripheral punches of Fig. 3 will all tilt inward, and, according to equation (22), the tilt of punch 1 will be

$$\alpha_1 = \frac{H}{b^2}ie^{i\pi}P_0 + \frac{HP}{b^2}\sum_{k=2}^{N}\frac{ie^{i[\frac{\pi}{2} + \frac{(k-1)\pi}{N}]}}{[2\sin\frac{(k-1)\pi}{N}]^2}. \quad (41)$$

In particular, when N is even ($=2M$) the tilt α_{1x} of punch 1 is zero and

$$\alpha_{1y} = -\frac{H}{b^2}\left\{P_0 + \frac{P}{2}\left[\frac{1}{2} + \sum_{k=1}^{M-1}\mathrm{cosec}\left(\frac{k\pi}{2M}\right)\right]\right\}. \quad (42)$$

A final application of equations (34), is the determination of the ratio P/P_0 which yields equal displacements $w = w_0$. The required ratio is

$$\frac{P}{P_0} = \frac{\frac{a}{a_0} - \frac{2}{\pi}\sin^{-1}\left(\frac{a}{b}\right)}{1 + \frac{2}{\pi}S - \left(\frac{a}{a_0}\right)\frac{2N}{\pi}\sin^{-1}\left(\frac{a_0}{b}\right)}. \quad (43)$$

Figure 4 shows values of this ratio for three values of $\epsilon_0 = a_0/a$. Results are displayed only for $\epsilon \equiv a/b < \sin(\pi/N)/2$;

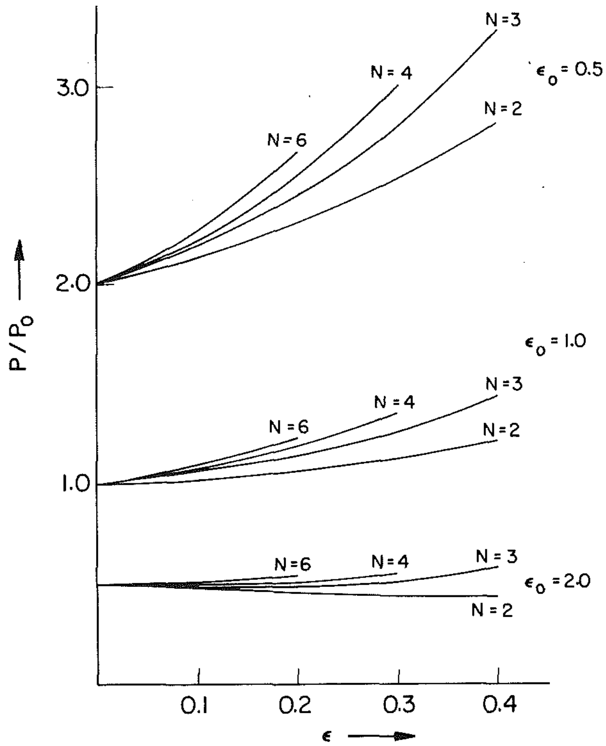

Fig. 4 The ratio P/P_0 which yields $w = w_0$

this inequality must be satisfied if the peripheral punches are to be sufficiently separated for the approximations used to be valid.

Conclusions

Formulas (13) and (22) yield approximate relations between forces, moments, displacements, and rotations for a set of punches on an elastic half space. These relations agree well with previous analyses derived, for instance, by Collins [1] and Panasyuk and Andreikiv [2]. On the other hand, they provide credible replacements for other formulas (equations (34) and (40)) which do not exhibit the behavior expected of them.

The results presented in Fig. 4, though maybe not of immediate practical interest, illustrate how the basic formulas may be used.

References

1 Collins, W. D., "Some Coplanar Punch and Crack Problems in Three-Dimensional Elasticity," *Proc. Roy. Soc.*, Series A, Vol. 274, 1963, pp. 507–528.

2 Panasyuk, V. V., and Andreikiv, A. E., "A Limiting Equilibrium Problem for an Infinite Brittle Solid With a Crack," *Soviet Applied Mechanics*, Vol. 6, 1973, pp. 589–592.

3 Galin, L. A., *Contact Problems in the Theory of Elasticity*, (in Russian) Gostekhizdat, Moscow, 1953. English Translation, Sneddon, I.N., North Carolina State College, Department of Mathematics, Raleigh, N.C., 1961, p. 169.

4 Andreikiv, A. E., and Dubetskii, S. A., "Pressure Exerted by a System of Four Stamps on an Elastic Half-Space," *Soviet Applied Mechanics*, Vol. 9, 1973, pp. 569–660.

5 Buzko, A. N., and Protsenko, V. S., "Pressure Under a System of Circular Stamps Acting on an Elastic Half-Space with $E = E_0 z^\nu$ $(0 \le z < 1)$," *Dokl. Akad. Nauk. UkrSSR*, Series A, No. 3, 1974, pp. 246–248.

6 Marzitsin, P. M., and Popov, G. Ya., "Three-Dimensional Contact Problem with Two Circular Contact Sections," *Soviet Applied Mechanics*, Vol. 11, 1976, pp. 923–928.

7 Gladwell, G. M. L., *Contact Problems in the Classical Theory of Elasticity*, Sijthoff and Noordhoff, Alphen aan den Rijn, The Netherlands, 1980.

M. D. Bryant
Department of Mechanical and Aerospace Engineering,
North Carolina State University,
Raleigh, N.C. 27650
Assoc. Mem. ASME

L. M. Keer
Northwestern University,
The Technological Institute,
Evanston, Ill. 60201
Mem. ASME

Rough Contact Between Elastically and Geometrically Identical Curved Bodies

Surface and subsurface stresses and displacements are obtained when two geometrically and elastically identical rough bodies are pressed together by normal and tangential loads. The theories of Cattaneo and Mindlin, who introduce zones of slip and stick within an elliptical contact area, are used. Von Mises yield criterion and maximum principle tensile stresses are used as failure criteria to assess potential failure due to shear or brittle fracture.

Introduction

This paper considers the state of stress when two identical rough bodies are pressed together, first by normal and then by tangential loads (see Fig. 1(*a*). The dimensions of the contact are considered to be sufficiently small compared with those of the body that the assumptions of Hertz [1] are considered valid.

The problem of determining the stress field throughout a body, normally loaded by Hertzian stresses and tangentially loaded by stresses proportional to the normal Hertzian stresses, was solved by Hamilton and Goodman [2] for a circular region of contact. Using their solution for the total field, Hamilton and Goodman calculated the second deviatoric stress invariant, J_2, in an attempt to determine the location and amount of plastic yielding present in the body; they also determined the location and magnitude of important tensile stresses acting near the region of contact as an aid in predicting the onset of surface cracking.

Chen [3] and Dahan and Zarka [4] have solved for the stress field in a perfectly smooth, transversely isotropic half space in contact with an elastic spherical indenter under normal loading. In both papers results are plotted for several transversely isotropic materials to show the effect of the anisotropy on the indentation of an elastic half space. Equations were obtained by Keer and Mowry [5] for the stress field created by a circular sliding contact on transversely isotropic rough spheres.

This paper extends the work of Hamilton and Goodman to the general case of an elliptical contact, first studied by Hertz [1]. In addition, zones of slip and stick will be included, where both the stick zone displacements and the tangential stresses are oriented along the major or minor axis of the ellipse of contact. The boundary conditions on $z = 0$ for this problem are:

Contributed by the Applied Mechanics Division for publication in the JOURNAL OF APPLIED MECHANICS.

Discussion on this paper should be addressed to the Editorial Department, ASME, United Engineering Center, 345 East 47th Street, New York, N.Y., 10017, and will be accepted until two months after final publication of the paper itself in the JOURNAL OF APPLIED MECHANICS. Manuscript received by ASME Applied Mechanic Division, August 1981.

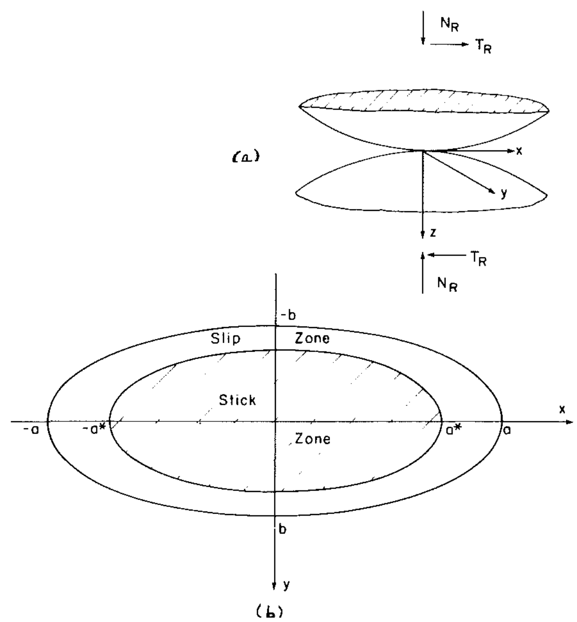

Fig. 1 Rough contact between two identical curved bodies. Figure 1(*a*) shows the loading and overall geometry; Fig. 1(*b*) depicts the geometry of the contact region.

$$\sigma_z = \begin{cases} -P_0 N(x,y;a,e) = -P_0\sqrt{1-\dfrac{x^2}{a^2}-\dfrac{y^2}{a^2(1-e^2)}} \\ \quad \text{for } (x,y) \in E^0 \\ 0 \qquad \text{for } (x,y) \notin E^0 \end{cases} \tag{1}$$

$$\left.\begin{aligned} \tau_{xz} &= p\, T(x,y) = pf\sigma_z \\ \tau_{yz} &= q\, T(x,y) = qf\sigma_z \end{aligned}\right\} \text{ for } (x,y) \in E^0 - E^* \tag{2}$$

$$\left.\begin{aligned} u &= U_x = pU \\ v &= U_y = qU \end{aligned}\right\} \text{ for } (x,y) \in E^* \tag{3}$$

where $p = \cos\delta$; $q = \sin\delta$; δ is the directional angle of tangential force application, measured clockwise from the positive x-axis; f is the coefficient of friction acting on the contact region; $e^2 = 1 - (b/a)^2$, where a and b are the lengths of the major and minor axes of the contact ellipse E^0 (the major axis is oriented along the x-axis); (u,v,w) are Cartesian displacements; and U is the constant stick displacement, acting over the entire zone of stick E^* (see Fig. 1(*b*)). As discovered by Cattaneo [6] and Mindlin [7], E^* is an ellipse of major axis a^* interior to and concentric with E^0 also having eccentricity e; however, it was found that special conditions must be placed on δ to make the proposed boundary conditions consistent.

Method of Analysis

In [8], Lure obtains the solution for the frictionless, elliptical Hertzian contact problem in terms of elliptical coordinates (ρ,ζ,ν) and the displacement potentials (equation 5.2.2, p. 256):

$$u^z = -\frac{1}{4\pi\mu}\left[z\frac{\partial\omega}{\partial x} + (1-2\eta)\frac{\partial\omega_1}{\partial x}\right]$$

$$v^z = -\frac{1}{4\pi\mu}\left[z\frac{\partial\omega}{\partial y} + (1-2\eta)\frac{\partial\omega_1}{\partial y}\right] \tag{4}$$

$$w^z = \frac{1-\eta}{2\pi\mu}\omega - \frac{1}{4\pi\mu}z\frac{\partial\omega}{\partial z}.$$

Here, η is Poisson's ratio, μ is the shear modulus, and $\omega_1 = \partial\omega/\partial z$, where

$$\omega(x,y,z) = P_0\pi a(1-e^2)^{1/2}\int_\rho^\infty \frac{dt}{[(t^2-1)(t^2-e^2)]^{1/2}} \times\left\{1 - \frac{x^2}{a^2t^2} - \frac{y^2}{a^2(t^2-e^2)} - \frac{z^2}{a^2(t^2-1)}\right\} \tag{5}$$

and (ρ,ζ,ν) are determined as roots of

$$\frac{x^2}{a^2R^2} + \frac{y^2}{a^2(R^2-e^2)} + \frac{z^2}{a^2(R^2-1)} - 1 = 0$$

and where $0 \le \nu^2 \le e^2 \le \zeta^2 \le 1 \le \rho^2 < \infty$; $e^2 = 1 - (b/a)^2$; a and b are the major and minor axes of the elliptical contact region E^0; and P_0 is the maximum Hertzian contact stress.

As in [8], for normal contact, the elliptical contact parameters P_0, a, and e can be related to the bulk contact parameters N_R, R_x, and R_y through the following:

$$\frac{R_y}{R_x} = \frac{(1-e^2)[K(e)-E(e)]}{E(e)-(1-e^2)K(e)}$$

$$a = \left[\frac{3}{2}\frac{N_RR_xD(e)(1-\eta)}{\pi\mu}\right]^{1/3}$$

$$P_0 = \frac{3N_R}{2\pi a^2(1-e^2)^{1/2}} = \frac{3N_R}{2\pi ab}$$

where R_x and R_y are the radii of curvature of the contacting bodies along the x and y directions, respectively; $K(e)$ and $E(e)$ are the complete elliptic integrals of the first and second kind; N_R is the resultant normal stress; and $D(e) = [K(e) - E(e)]/e^2$.

The displacements and stresses are:

Normal Load—z-Direction.

$$u^z = \frac{P_0(1-e^2)^{1/2}}{2\mu}\frac{x}{a}\{2z(1-\eta)\psi_1(\rho) - (1-2\eta)aI_{11}\}$$

$$v^z = \frac{P_0(1-e^2)^{1/2}}{2\mu}\frac{y}{a}\{2z(1-\eta)\psi_2(\rho) - (1-2\eta)aI_{12}\} \tag{6a}$$

$$w^z = \frac{P_0(1-e^2)^{1/2}}{2\mu}\{(1-\eta)[aF(\phi,e) - \frac{x^2}{a}\psi_1(\rho) - \frac{y^2}{a}\psi_2(\rho)] + \eta z\Psi(\rho,x,y,z)\}$$

$$\sigma_x^z = P_0(1-e^2)^{1/2}\left\{-2\eta\Psi(\rho,x,y,z) + 2(1-\eta)\frac{z}{a}\psi_1(\rho) + (1-2\eta)\left[\frac{x^2}{a^2}I_8 - I_{11}\right] - \frac{x^2z}{a^3}\frac{\Delta(\rho)}{\rho^3\Theta(\rho,\zeta,\nu)}\right\}$$

$$\sigma_y^z = P_0(1-e^2)^{1/2}\left\{-2\eta\Psi(\rho,x,y,z) + 2(1-\eta)\frac{z}{a}\psi_2(\rho) + (1-2\eta)\left[\frac{y^2}{a^2}I_3 - I_{12}\right] - \frac{y^2z}{a^3}\frac{\rho\Delta(\rho)}{(\rho^2-e^2)^2\Theta(\rho,\zeta,\nu)}\right\}$$

$$\sigma_z^z = -P_0(1-e^2)^{1/2}\frac{\rho(\rho^2-e^2)^{1/2}[Z(\zeta,\nu;e)]^3}{\Theta(\rho,\zeta,\nu)} \tag{6b}$$

$$\tau_{xy}^z = P_0(1-e^2)^{1/2}\frac{xy}{a^2}\left\{(1-2\eta)I_4 - \frac{z\Delta(\rho)}{a\rho(\rho^2-e^2)\Theta(\rho,\zeta,\nu)}\right\}$$

$$\tau_{xz}^z = -P_0(1-e^2)^{1/2}\frac{x}{a}\frac{[Z(\zeta,\nu;e)]^2\Delta(\rho)}{\rho\Theta(\rho,\zeta,\nu)}$$

$$\tau_{yz}^z = -P_0(1-e^2)^{1/2}\frac{y}{a}\frac{\rho[Z(\zeta,\nu;e)]^2\Delta(\rho)}{(\rho^2-e^2)\Theta(\rho,\zeta,\nu)}.$$

The functions $F(\phi,e)$; I_j, $j = 1,12$; $\Psi(\rho,x,y,z)$; $\psi_1(\rho)$; $\psi_2(\rho)$; $Z(\zeta,\nu;e)$; $\Theta(\rho,\zeta,\nu)$; and $\Delta(\rho)$ are defined in the Appendix.

The solution to the problem in which the contact shearing stresses are proportional to the normal Hertzian contact stresses can be found using the potential solution of Boussinesq and Cerruti found in Love [9]:

$$u = \frac{1}{2\pi\mu}\frac{\partial^2F}{\partial z^2} + \frac{\lambda}{4\pi\mu(\lambda+\mu)}\frac{\partial}{\partial x}\left(\frac{\partial F}{\partial x} + \frac{\partial H}{\partial y}\right) - \frac{z}{4\pi\mu}\frac{\partial^2}{\partial x\partial z}\left(\frac{\partial F}{\partial x} + \frac{\partial H}{\partial y}\right)$$

$$v = \frac{1}{2\pi\mu}\frac{\partial^2H}{\partial z^2} + \frac{\lambda}{4\pi\mu(\lambda+\mu)}\frac{\partial}{\partial y}\left(\frac{\partial F}{\partial x} + \frac{\partial H}{\partial y}\right) - \frac{z}{4\pi\mu}\frac{\partial^2}{\partial y\partial z}\left(\frac{\partial F}{\partial x} + \frac{\partial H}{\partial y}\right)$$

$$w = \frac{1}{4\pi(\lambda+\mu)}\frac{\partial}{\partial z}\left(\frac{\partial F}{\partial x} + \frac{\partial H}{\partial y}\right) - \frac{z}{4\pi\mu}\frac{\partial^2}{\partial z^2}\left(\frac{\partial F}{\partial x} + \frac{\partial H}{\partial y}\right); \tag{7}$$

$$F = pf\left\{-z\int_z^\infty \omega(x,y,s)\,ds + \int_z^\infty s\omega(x,y,s)\,ds\right\}$$

$$H = qf\left\{-z\int_z^\infty \omega(x,y,s)\,ds + \int_z^\infty s\omega(x,y,s)\,ds\right\} \tag{8}$$

where (u,v,w) are the Cartesian displacements; f is the coefficient of friction between contact indenter and half space; F and H are the components of the tangential traction T, in the x and y directions, respectively; and λ and μ are Lamé's constants.

The Cartesian displacements and stresses corresponding to these tangential traction components in the x and y directions, respectively, are:

Tangential Load—x-Direction.

$$u^x = \frac{P_0(1-e^2)^{1/2}}{2\mu}\Big\{a(1-\eta)F(\phi,e) + \Big[(1-\eta)\frac{z^2}{a} + a\eta - \frac{x^2}{a}\Big]\psi_1(\rho) - \frac{y^2}{a}\psi_2(\rho) - z\Psi(\rho,x,y,z) - zI_{11} + \frac{x^2z}{a^2}I_8 + \eta\Big[\frac{3x^2}{a}I_9 + \frac{y^2}{a}I_2 + 2zI_{11} - \frac{2x^2}{a^2}zI_8\Big]\Big\}$$

$$v^x = \frac{P_0(1-e^2)^{1/2}}{2\mu}\frac{xy}{a}\Big\{(1-2\eta)\frac{z}{a}I_4 + 2\eta I_2\Big\} \tag{9a}$$

$$w^x = \frac{P_0(1-e^2)^{1/2}}{2\mu}x\Big\{(1-2\eta)I_{11} + 2\eta\frac{z}{a}\psi_1(\rho)\Big\}$$

$$\sigma_x^x = P_0(1-e^2)^{1/2}\frac{x}{a}\Big\{-2(1+\eta)\psi_1(\rho) + 6\eta I_9 + (1-2\eta)\Big[3\frac{z}{a}I_8 + \frac{x^2}{a^2}I_{10}\Big] - \frac{x^2}{a^2}\frac{(\rho^2-1)\Delta(\rho)}{\rho^5\Theta(\rho,\zeta,\nu)}\Big\}$$

$$\sigma_y^x = P_0(1-e^2)^{1/2}\frac{x}{a}\Big\{-2\eta\psi_1(\rho) + 2\eta I_2 + (1-2\eta)\Big[\frac{z}{a}I_4 + \frac{y^2}{a^2}I_6\Big] - \frac{y^2}{a^2}\frac{(\rho^2-1)\Delta(\rho)}{\rho(\rho^2-e^2)^2\Theta(\rho,\zeta,\nu)}\Big\}$$

$$\sigma_z^x = -P_0(1-e^2)^{1/2}\frac{x}{a}\frac{[Z(\rho,\nu;e)]^2\Delta(\rho)}{\rho\Theta(\rho,\zeta,\nu)} \tag{9b}$$

$$\tau_{xy}^x = P_0(1-e^2)^{1/2}\frac{y}{a}\Big\{-\psi_2(\rho) + 2\eta I_2 + (1-2\eta)\Big[\frac{z}{a}I_4 + \frac{x^2}{a^2}I_7\Big] - \frac{x^2}{a^2} \times \frac{(\rho^2-1)\Delta(\rho)}{\rho^3(\rho^2-e^2)\Theta(\rho,\zeta,\nu)}\Big\}$$

$$\tau_{xz}^x = P_0(1-e^2)^{1/2}\Big\{\frac{z}{a}\Big[\psi_1(\rho) - \frac{x^2}{a^2}\frac{\Delta(\rho)}{\rho^3\Theta(\rho,\zeta,\nu)}\Big] - \Psi(\rho,x,y,z)\Big\}$$

$$\tau_{yz}^x = -P_0(1-e^2)^{1/2}\frac{xyz}{a^3}\frac{\Delta(\rho)}{\rho(\rho^2-e^2)\Theta(\rho,\zeta,\nu)}$$

Tangential Load—y-Direction.

$$u^y = \frac{P_0(1-e^2)^{1/2}}{2\mu}\frac{xy}{a}\Big\{(1-2\eta)\frac{z}{a}I_4 + 2\eta I_2\Big\}$$

$$v^y = \frac{P_0(1-e^2)^{1/2}}{2\mu}\Big\{a(1-\eta)F(\phi,e) - \frac{x^2}{a}\psi_1(\rho) + \Big[(1-\eta)\frac{z^2}{a} + a\eta(1-e^2) - \frac{y^2}{a}\Big]\psi_2(\rho) - z\Psi(\rho,x,y,z) - zI_{12} + z\frac{y^2}{a^2}I_3 + \eta\Big[\frac{x^2}{a}I_2 + \frac{3y^2}{a}I_1 + 2zI_{12} - 2\frac{y^2z}{a^2}I_3\Big]\Big\} \tag{10a}$$

$$w^y = \frac{P_0(1-e^2)^{1/2}}{2\mu}y\Big\{(1-2\eta)I_{12} + 2\eta\frac{z}{a}\psi_2(\rho)\Big\}$$

$$\sigma_x^y = P_0(1-e^2)^{1/2}\frac{y}{a}\Big\{-2\eta\psi_2(\rho) + 2\eta I_2 + (1-2\eta)\Big[\frac{z}{a}I_4 + \frac{x^2}{a^2}I_7\Big] - \frac{x^2}{a^2}\frac{\rho(\rho^2-1)\Delta(\rho)}{(\rho^2-e^2)\Theta(\rho,\zeta,\nu)}\Big\}$$

$$\sigma_y^y = P_0(1-e^2)^{1/2}\frac{y}{a}\Big\{-2(1+\eta)\psi_2(\rho) + 6\eta I_1 + (1-2\eta)\Big[3\frac{z}{a}I_3 + \frac{y^2}{a^2}I_5\Big] - \frac{y^2}{a^2}\frac{\rho(\rho^2-1)\Delta(\rho)}{(\rho^2-e^2)^3\Theta(\rho,\zeta,\nu)}\Big\}$$

$$\sigma_z^y = -P_0(1-e^2)^{1/2}\frac{y}{a}\frac{\rho\Delta(\rho)[Z(\zeta,\nu;e)]^2}{(\rho^2-e^2)\Theta(\rho,\zeta,\nu)} \tag{10b}$$

$$\tau_{xy}^y = P_0(1-e^2)^{1/2}\frac{x}{a}\Big\{-\psi_1(\rho) + 2\eta I_2 + (1-2\eta)\Big[\frac{z}{a}I_4 + \frac{y^2}{a^2}I_6\Big] - \frac{y^2}{a^2}\frac{(\rho^2-1)\Delta(\rho)}{\rho(\rho^2-e^2)^2\Theta(\rho,\zeta,\nu)}\Big\}$$

$$\tau_{xz}^y = -P_0(1-e^2)^{1/2}\frac{xyz}{a^3}\frac{\Delta(\rho)}{\rho(\rho^2-e^2)\Theta(\rho,\zeta,\nu)}$$

$$\tau_{yz}^y = P_0(1-e^2)^{1/2}\Big\{-\Psi(\rho,x,y,z) + \frac{z}{a}\Big[\psi_2(\rho) - \frac{y^2}{a^2}\frac{\rho\Delta(\rho)}{(\rho^2-e^2)^2\Theta(\rho,\zeta,\nu)}\Big]\Big\}.$$

For all stresses and displacements presented, the superscripts refer to the direction of the contact tractions producing them. Also, all terms containing the factor $1/\Theta(\rho,\zeta,\nu)$ vanish as ρ and ζ both tend to one.

Using the results of Cattaneo [6], the aforementioned formulas can be extended to the case where an elliptical region E^* of stick, having eccentricity, e, and being interior and concentric to the contact region E^0, has a constant displacement U in either the x or y direction. For this problem involving slip and stick, Cattaneo determined the resulting components X and Y of tangential traction acting over the entire contact region:

$$X = \begin{cases} pfP_0N(x,y;a,e) & \text{for } (x,y)\ \epsilon\ (E^0-E^*) \\ pfP_0[N(x,y;a,e) - X_0N(x,y;a^*,e)] & \text{for } (x,y)\ E^* \end{cases} \tag{11a}$$

$$Y = \begin{cases} qfP_0N(x,y;a,e) & \text{for } (x,y)\ \epsilon\ (E^0-E^*) \\ qfP_0[\mathrm{N}(\mathrm{x},y;a,e) - Y_0N(x,y;a^*,e)] & \text{for } (x,y)\ E^* \end{cases} \tag{11b}$$

where

$$X_0 = \Big[1 - \frac{2\mu U_x}{a(1-e^2)^{1/2}pfP_0\mathcal{G}(e,\eta)}\Big]^{1/2};$$

$$Y_0 = \Big[1 - \frac{2\mu U_y}{a(1-e^2)^{1/2}qfP_0\mathcal{H}(e,\eta)}\Big]^{1/2};$$

$\mathcal{G}(e,\eta) = (1-\eta)K(e) + \eta[K(e) - E(e)]/e^2$, $\mathcal{H}(e,\eta) = K(e) - \eta[K(e) - E(e)]/e^2$, $K(e)$, and $E(e)$ are the complete elliptic integrals of the first and second kind; a^* is the major axis of the ellipse E^*; and U_x and U_y are the surface displacements in the x and y directions.

From [6], a^* can be related to a using either

$$a^*/a = X_0 \quad \text{or} \quad a^*/a = Y_0.$$

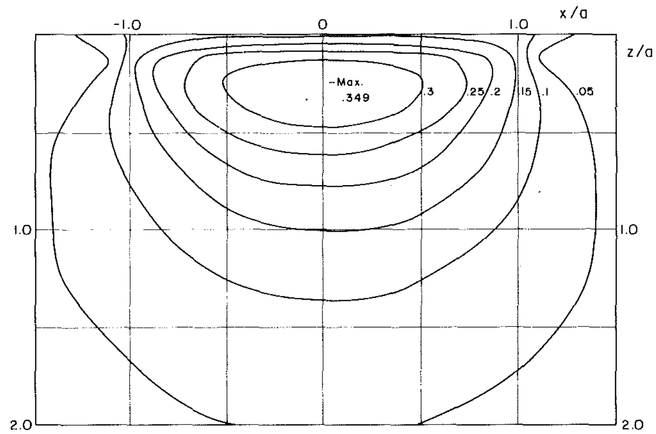

Fig. 2(a)

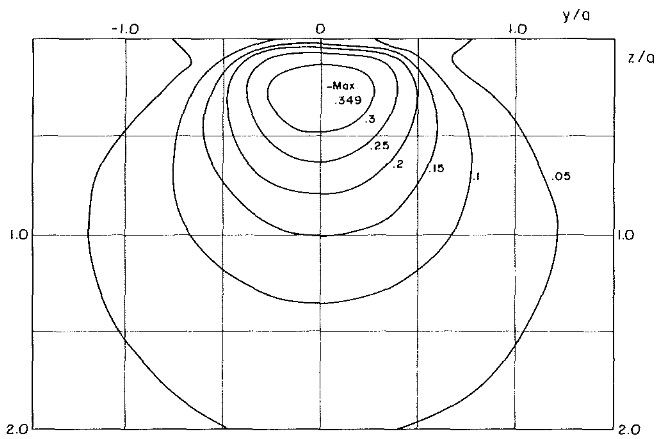

Fig. 2(b)

Fig. 2 Contours of $(J_2)^{1/2}/P_0$ beneath the contact zone for $f = a^* = 0$, and for $b/a = 0.4$. Figure 2(a) is directed along $y = 0$ while Fig. 2(b) is directed along $x = 0$.

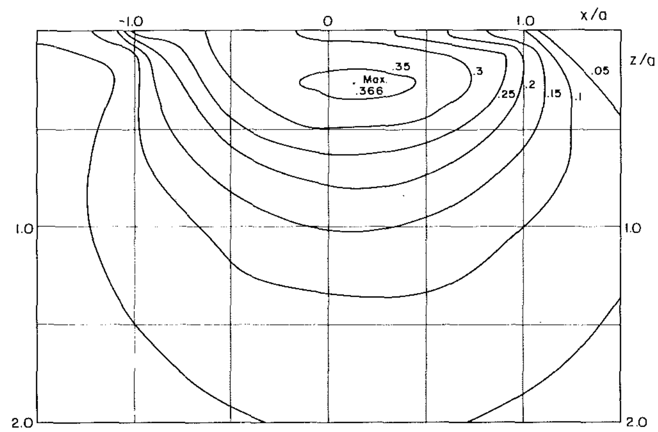

Fig. 3(a)

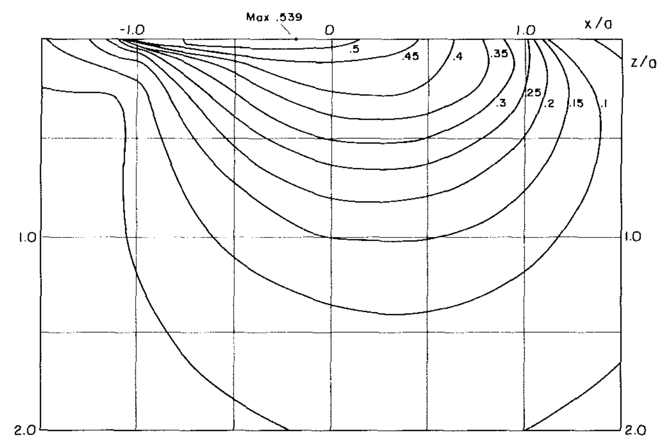

Fig. 3(b)

Fig. 3 Contours of $(J_2)^{1/2}/P_0$ on $y = 0$ beneath the contact zone (having $a^* = 0$ and $b/a = 0.4$) for x-directed tangential tractions. In Fig. 3(a), $f = 0.25$; in Fig. 3(b), $f = 0.5$.

For consistency, $qU_x/\mathcal{G}(e,\eta) = pU_y/\mathcal{K}(e,\eta)$; hence, the only cases for which the resultant surface displacements and the resultant tangential traction are codirectional are when $e = 0$, or when δ is either 0 deg or 90 deg (since $U_x = pU$, $U_y = qU$).

For the cases of slip-stick in which δ is either 0 deg or 90 deg, equation (11*a*) and (11*b*) imply that the solution due to the resultant tractions of a normally loaded Hertzian contact with regions of slip and stick can be obtained by superposing three solutions: the solution for the normal Hertzian contact over the region E^0, equation (6); the solution for shearing tractions arising from Coulomb friction and proportional to the normal Hertzian load, taken over the region E^0, equation (9) and (10); and the negative of the solution for shearing tractions, proportional to a fictitious normal Hertzian load having maximum contact stress $P_0(pX_0 + qY_0)$, and taken over the region E^*. The resultant stress tensor and displacement vector can be written as

$$\tau_R = \tau_z^0 + (p\tau_x^0 + q\tau_y^0) - (p\tau_x^* + q\tau_y^*)$$

$$\mathbf{U}_R = \mathbf{U}_z^0 + (p\mathbf{U}_x^0 + q\mathbf{U}_y^0) - (p\mathbf{U}_x^* + q\mathbf{U}_y^*)$$

where the τ and $\mathbf{U}$ notations refer to stress tensor and displacement vector; the subscripts R, x, y, and z refer to solutions for the resultant, the x-directed, the y-directed, and the z-directed tractions; and the superscripts 0 and * refer to the regions E^0 and E^*.

Results and Discussion

As in [2], questions of mechanical failure will be approached by calculating the von Mises yield parameter

$$J_2 = \tau_{xy}^2 + \tau_{xz}^2 + \tau_{yz}^2 + \frac{1}{6}[(\sigma_x - \sigma_y)^2 + (\sigma_x - \sigma_z)^2 + (\sigma_y - \sigma_z)^2],$$

useful in predicting plastic flow and in determining regions of residual stress and cracking; and by calculating the largest principal tensile stress σ_p, useful in predicting cracking of brittle materials. The length of the major axis a was chosen to be the unit distance, while the maximum Hertzian stress P_0 was chosen to be the unit stress. For the following, Poisson's ratio $\eta = 0.3$; when calculating surface displacements U_x or U_y within the region of stick E^*, the shear modulus $= 11.5 \times 10^6$ psi and $P_0 = 200{,}000$ psi.

In Figs. 2–4, lines of constant $(J_2)^{1/2}/P_0$ are plotted beneath the contact region along the planes $x = 0$ and $y = 0$ of the stressed half space. For these figures, $b/a = 0.4$ and $a^*/a = 0$. In Figs. 2(*a*) and 2(*b*) where $f = 0$, $(J_2)^{1/2}/P_0$ is exhibited along the planes $y = 0$ and $x = 0$, respectively. Comparison between Figs. 2(*a*) and 2(*b*) reveals an expansion of the contours directed parallel to the major axis (x-axis) and a contraction of the contours directed parallel to the minor axis (y-axis). This expansion and contraction is especially noticeable if compared to the $f = 0$ contour for circular contact given in [2]. Figure 2 also displays a subsurface maximum of J_2 located beneath the contact center, similar to [2]. In fact, the depth of the maximum J_2 value in Fig. 2 can be shown approximately equal to that in [2] if the square root of the contact area is used as the unit of length for both cases (the circular contact and the elliptical contact would then possess equivalent resultant traction and equivalent contact area).

Figures 3(*a*), (*b*), 4(*a*), and (*b*) contain $(J_2)^{1/2}/P_0$ contour plots oriented along the planes $y = 0$ and $x = 0$, respectively,

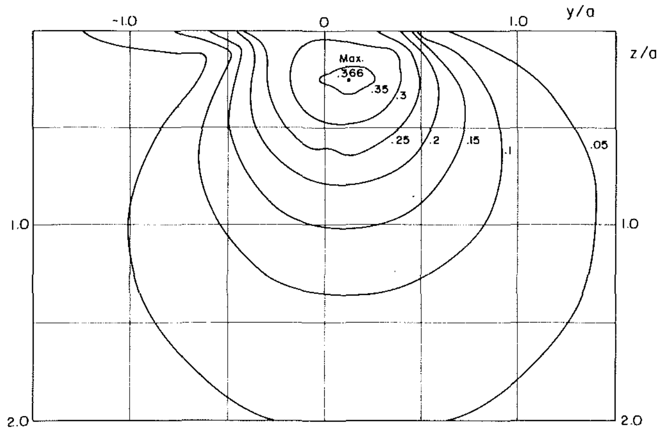

Fig. 4(a)

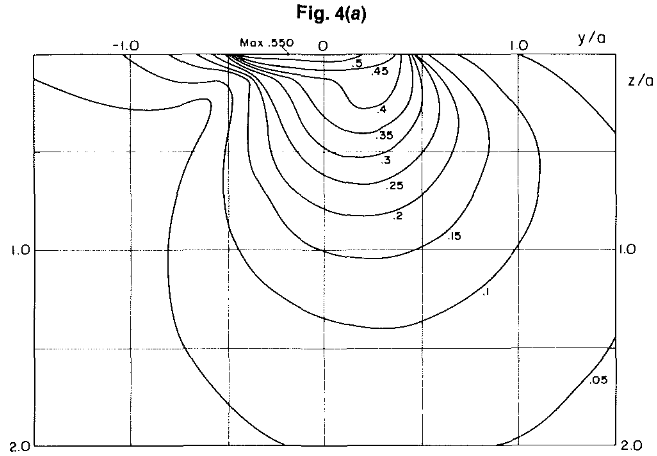

Fig. 4(b)

Fig. 4 Contours of $(J_2)^{1/2}/P_0$ on $x = 0$ beneath the contact zone (having $a^* = 0$ and $b/a = 0.4$) for y-directed tangential tractions. In Fig. 4(a), $f = 0.25$; in Fig. 4(b), $f = 0.5$.

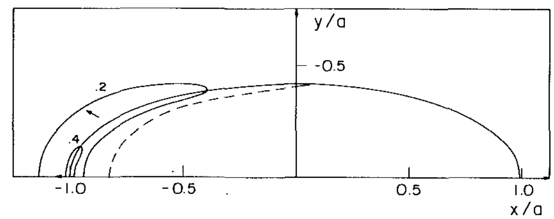

Fig. 5(a)

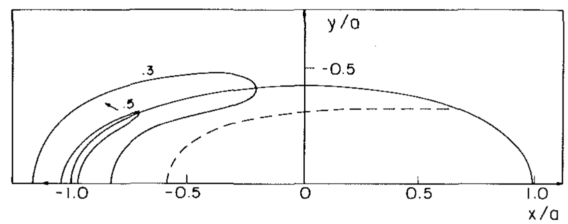

Fig. 5(b)

Fig. 5 Contours of the largest principal tensile stress σ_p/P_0 inside and near the contact zone (having $a^* = 0$ and $b/a = 0.4$) for x-directed tangential tractions. In Fig. 5(a), $f = 0.25$; in Fig. 5(b), $f = 0.5$. Both Figs. 5(a) and 5(b) are symmetric about the x-axis.

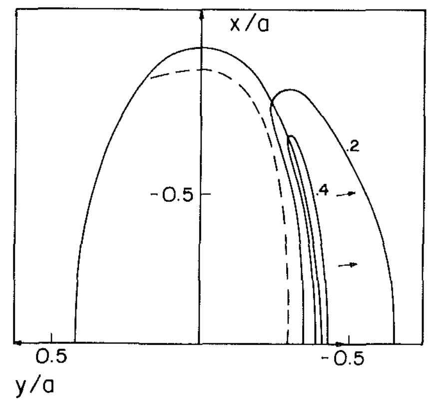

Fig. 6(a)

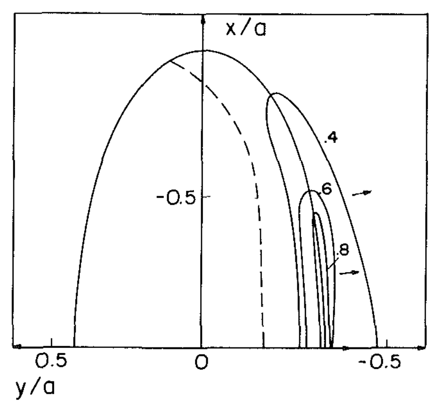

Fig. 6(b)

Fig. 6 Contours of the largest principal tensile stress σ_p/P_0 inside and near the contact zone (having $a^* = 0$ and $b/a = 0.4$) for y-directed tangential tractions. In Fig. 6(a), $f = 0.25$; in Fig. 6(b), $f = 0.5$. Both Figs. 6(a) and 6(b) are symmetric about the y-axis.

corresponding to nonzero tangential tractions directed along the major and minor axes of the contact ellipse. For the "a" figures, $f = 0.25$, while for the "b" figures $f = 0.5$. As in Figs. 2(a) and 2(b), an elongation along the major axis and a contraction along the minor axis can be observed if Figs. 3 and 4 are compared to their counterparts in [2]. Comparison between Figs. 2–4 shows that as f increases, the maximum value of J_2 increases and its location moves closer toward the half-space surface; when $f = 0.5$, the maximum J_2 value lies on the half-space surface. This phenomenon was also observed in [2] for circular contacts.

Figures 5(a), (b), 6(a), and (b) contain lines of constant maximum principal tensile stress σ_p/P_0 existing on $z = 0$ inside and near the contact zone.[1] Figures 5(a) and (b) correspond to x-directed tangential tractions having $f = 0.25$ and 0.5, respectively; while Figs. 6(a) and (b) correspond to y-directed tangential tractions having $f = 0.25$ and 0.5, respectively.[2] Since Figs. 5(a) and (b) were found to be symmetric about the x-axis and Figs. 6(a) and (b) symmetric about the y-axis, only half of each figure is shown. The arrows in Figs. 5 and 6 shows the orientation of the stress σ_p, the dotted lines bound regions of compression from tension, and the elliptical contours represent boundaries of the contact ellipse.

Inspection of Figs. 5 and 6 shows that the maximum value of σ_p/P_0 is located at $x/a = -1$, $y = 0$ for x-directed tangential tractions, and $y/a = -0.4$, $x = 0$ for y-directed tangential tractions. Furthermore, this maximum σ_p is always oriented along a line parallel to the direction of the tangential traction; i.e., the largest σ_p will coincide with the largest σ_x for Fig. 5 and the largest σ_y for Fig. 6. Finally, this maximum increases in magnitude with increasing frictional coefficient f. These findings are consistent with [2] for circular contact.

[1] Subsurface values of σ_p/P_0 were found to be small in comparison to values at $z = 0$.

[2] σ_p/P_0 plots for $f = 0$ yielded elliptical contours concentric to and larger than the contact ellipse E^0. The maximum value of σ_p is located at $y = z = 0$, $x = \pm a$.

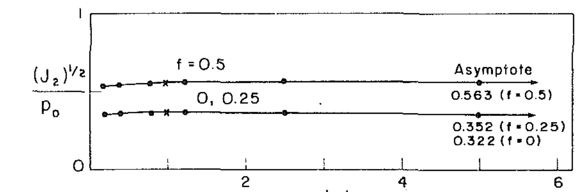

Fig. 7 Maximum $(J_2)^{1/2}/P_0$ versus b/a for $a^* = 0$ and for $f = 0, 0.25$, and 0.5. The asymptotes and the values at $b/a = 1$ were taken from [2].

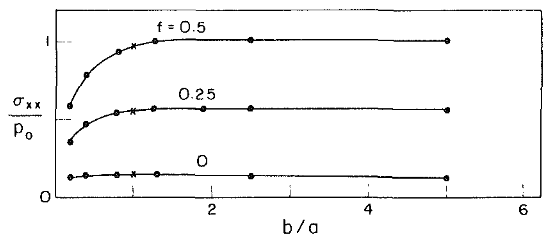

Fig. 8 Maximum σ_p/P_0 versus b/a for $a^* = 0$ and for $f = 0, 0.25$, and 0.5. Note that these maximum values coincide with $\sigma_x\Big|_{\substack{x=-a\\ y=z=0}}$, and that values at $b/a = 1$ were taken from [2].

Figures 7 and 8 are plots of b/a versus the maximum value of $(J_2)^{1/2}/P_0$ or σ_p/P_0, respectively, for $f = 0$, 0.25, and 0.5. For these figures, it is assumed that the tangential traction (if any) is oriented along the major axis (x-axis). Values of $b/a \geq 1$, corresponding to the minor axis being longer than the major axis, were obtained by using cases in which the tangential tractions were y-directed and $b/a \leq 1$; the major axis then became b and the minor axis a. The asymptotes and the points at $b/a = 1$ were taken from [2]. Finally, note that in Fig. 8, $\sigma_p = \sigma_x\Big|_{\substack{x=-a\\ y=z=0}}$.

Figures 7 and 8 show for $b/a \geq 1$ essentially constant values of $(J_2)^{1/2}/P_0$ and σ_p/P_0, given f. For $b/a \leq 1$, $(J_2)^{1/2}/P_0$ remains constant, while σ_p/P_0 decreases, especially for larger values of f.

Cases corresponding to Figs. 2–8 in which $a^*/a = 0.25$ were also calculated. In general, values of $(J_2)^{1/2}/P_0$ and σ_p/P_0 were reduced by less than 5 percent, the largest reductions occurring inside or near the zone of stick. Also, the constant surface displacements U_x/a or U_y/a within the zone of stick E^* were found to be of order 10^{-3}.

Conclusions

The following important conclusions are listed:

1 Damage parameters σ_p and $J_2{}^{1/2}$ are essentially constant for most values of b/a and increase with increasing f. Hence values of σ_p and $J_2{}^{1/2}$ derived from line contact may be used in place of or as bounds to values of σ_p and $J_2{}^{1/2}$ derived from elliptical contact, given the same f.

2 The qualitative findings of [2] for circular contact may be valid for elliptical contact, excepting the relative locus of $J_2{}^{1/2}$ maximums for larger f.

3 Tangential tractions oriented along the minor axis of the elliptical contact (for $b/a < 1$) produce a larger maximal tensile stress σ_p than tangential tractions oriented along the major axis; minor axis loading may be more dangerous than major axis loading.

4 A small zone of stick acts weakly as a stress reducer.

Acknowledgments

Support for this research by the U. S. Army Research Office under Grant DAAG 29-78-0199 is gratefully acknowledged. The authors are indebted to many helpful discussions with Professor H. S. Cheng, coprincipal investigator on this project during the course of this research.

References

1 Hertz, H., "Über die Berührung fester elastischer Korper," *J. f. d. Reine u. Angewandte Math.*, Vol. 92, 1882, pp. 156–171.

2 Hamilton, G. M., and Goodman, L. E., "The Stress Field Created by a Circular Sliding Contact," ASME Journal of Applied Mechanics, Vol. 33, 1966, pp. 371–376.

3 Chen, W. T., "Stresses in Some Anisotropic Bodies Due to Indentation and Sliding," *Int. J. Solids Structures*, Vol. 5, 1969, pp. 191–214.

4 Dahan, M., and Zarka, J., "Elastic Contact Between a Sphere and a Semi-Infinite Transversely Isotropic Body," *Int. J. Solids Structures*, Vol. 13, 1977, pp. 229–238.

5 Keer, L. M., and Mowry, D. B., "The Stress Field Created by a Circular Sliding Contact on Transversely Isotropic Spheres," *Int. J. Solids Structures*, Vol. 15, 1979, pp. 33–39.

6 Cattaneo, C., "Sul contatto di due corpi elastici: distribuzione locale degli storzi," *Rendiconti dell Accademia nazionale dei Lincei*, Vol 27, Series *b*, 1938, pp. 342–348, 434–436, and 474–478.

7 Mindlin, R. D., "Compliance of Elastic Bodies in Contact," ASME Journal of Applied Mechanics, Vol. 15, 1949, pp. 259–268.

8 Lure, A. I., *Three Dimensional Problems of the Theory of Elasticity*, Interscience Publishers, 1964, pp. 286–313.

9 Love, A. E. H., *A Treatise on the Mathematical Theory of Elasticity*, Dover, New York, 1944.

APPENDIX

Unless stated otherwise, assume $0 \leq \nu^2 \leq e^2 \leq \zeta^2 \leq 1 \leq \rho^2 < \infty$ throughout the Appendix. Also, note that

$$\frac{z/a}{\chi_0}, \frac{z/a}{\chi_1}, \text{ and } \frac{z/a}{\chi_2} \text{ all tend to } \frac{1}{\rho}\sqrt{\frac{\rho^2-1}{\rho^2-e^2}}$$

as ζ tends to 1. ($z = 0$ but outside of contact zone.)

$$\psi_1(\rho) = \begin{cases} \dfrac{1}{2}\left[\phi - \dfrac{\sqrt{\rho^2-1}}{\rho^2}\right]; & e^2 = 0 \\ \dfrac{1}{e^2}\left[F(\phi,e) - E(\phi,e)\right]; & 0 < e^2 \end{cases}$$

$$\psi_2(\rho) = \begin{cases} \dfrac{1}{2}\left[\phi - \dfrac{\sqrt{\rho^2-1}}{\rho^2}\right]; & e^2 = 0 \\ \dfrac{1}{e^2(1-e^2)}\left[E(\phi,e) - (1-e^2)F(\phi,e)\right] & \\ \quad - \dfrac{1}{1-e^2}\,\dfrac{1}{\rho}\sqrt{\dfrac{\rho^2-1}{\rho^2-e^2}}; & 0 < e^2 < 1 \\ \dfrac{1}{2}\left[\dfrac{\rho}{\rho^2-1} + \log\sqrt{\dfrac{\rho-1}{\rho+1}}\right]; & e^2 = \zeta^2 = 1 < \rho^2 \end{cases}$$

$$\Psi(\rho,x,y,z) = \begin{cases} \dfrac{-zE(\phi,e)}{a(1-e^2)} + \dfrac{1}{(1-e^2)}\,\dfrac{Z(\zeta,\nu;e)\sqrt{\rho^2-e^2}}{\rho}; & \\ e^2 < 1 & \\ \dfrac{z}{2a}\left[\dfrac{\rho}{\rho^2-1} + \log\sqrt{\dfrac{\rho-1}{\rho+1}}\right]; & e^2 = \zeta^2 = 1 < \rho^2 \end{cases}$$

$$I_1 = \begin{cases} \dfrac{1}{8}\left[\phi - \dfrac{\sqrt{\rho^2-1}}{\rho^4}(\rho^2-2)\right]; & e^2 = 0 \\ \dfrac{1}{3e^2}\left\{2\psi_2(\rho) - \dfrac{1}{1-e^2}\left[E(\phi,e) - \dfrac{e^2}{\rho}\sqrt{\dfrac{\rho^2-1}{\rho^2-e^2}}\right]\right. & \\ \quad \left. + \dfrac{\rho\Delta(\rho)}{(\rho^2-e^2)^2}\right\}; & 0 < e^2 < 1 \\ \dfrac{1}{2}\left[\dfrac{\rho}{\rho^2-1} + \log\sqrt{\dfrac{\rho-1}{\rho+1}}\right]; & e^2 = \zeta^2 = 1 < \rho^2 \end{cases}$$

$$I_2 = \begin{cases} \dfrac{1}{8}\left[\phi - \dfrac{\sqrt{\rho^2-1}}{\rho^4}(\rho^2-2)\right]; & e^2=0 \\ \dfrac{1}{e^2}\psi_1(\rho) - \dfrac{(1-e^2)}{e^2}\psi_2(\rho); & 0<e^2 \end{cases}$$

$$I_3 = \begin{cases} \left(\dfrac{a}{r}\right)^4 \{\Gamma_1(\rho,r)-\Gamma_2(\rho,r)\}; & e^2=0, r^2>0 \\ \dfrac{1}{2C}\left[\Phi_1(\rho,x,y;e)+\dfrac{B}{2}\mathcal{S}(\rho,x,y;e)\right]; & e^2>0, y\neq 0 \\ \dfrac{1}{3B}\left\{-\dfrac{2}{B}\Phi_3(\rho,x;e)+\dfrac{\chi_1(\rho,x;e)}{(\rho^2-e^2)^2}\right\}; & y=0, x^2\neq a^2e^2 \\ \dfrac{1}{4(\rho^2-e^2)^2}; & y=0, x^2=a^2e^2 \end{cases}$$

$$I_4 = \begin{cases} \left(\dfrac{a}{r}\right)^4 \{\Gamma_1(\rho,r)-\Gamma_2(\rho,r)\}; & e^2=0, r^2>0 \\ \dfrac{1}{4\rho^4}; & e^2=r^2=0 \\ \dfrac{1}{2e^2}[J_{14}-J_{24}] \end{cases}$$

$$I_5 = \begin{cases} \dfrac{z}{a}\left(\dfrac{a}{r}\right)^6 \{\Gamma_1(\rho,r)-2\Gamma_2(\rho,r)+\Gamma_3(\rho,r)\}; \\ \quad e^2=0, r^2>0 \\ \dfrac{1}{2}[J_{15}+e^2J_{25}] \end{cases}$$

$$I_6 = \begin{cases} \dfrac{z}{a}\left(\dfrac{a}{r}\right)^6 [\Gamma_1(\rho,r)-2\Gamma_2(\rho,r)+\Gamma_3(\rho,r)]; \\ \quad e^2=0, r^2>0 \\ \dfrac{1}{2}J_{15} \end{cases}$$

$$I_7 = \begin{cases} \dfrac{z}{a}\left(\dfrac{a}{r}\right)^6 \{\Gamma_1(\rho,r)-2\Gamma_2(\rho,r)+\Gamma_3(\rho,r)\}; \\ \quad e^2=0, r^2>0 \\ \dfrac{z}{6a\rho^6}; \quad e^2=r^2=0 \\ \dfrac{z}{a}\left[\dfrac{1}{\mathcal{B}\mathcal{D}^2}\left\{\mathcal{A}-\dfrac{\mathcal{A}\rho^2-2\mathcal{B}+\mathcal{A}^2}{\chi_0(\rho,x,y;e)}\right\}+\dfrac{\mathcal{L}_0(\rho,x,y)}{2\mathcal{B}}\right]; \\ \quad e^2>0, x^2>0 \\ \dfrac{z}{3\mathcal{A}a}\left\{\dfrac{8}{\mathcal{A}^2}-\left[\dfrac{8\rho^2}{\mathcal{A}^2}+\dfrac{4}{\mathcal{A}}-\dfrac{1}{\rho^2}\right]\dfrac{1}{\chi_2(\rho,y;e)}\right\}; \\ \quad x=0, \mathcal{A}<0 \end{cases}$$

$$I_8 = \begin{cases} \left(\dfrac{a}{r}\right)^4 \{\Gamma_1(\rho,r)-\Gamma_2(\rho,r)\}; & e^2=0, r^2>0 \\ \dfrac{1}{4\rho^4}; & e^2=r^2=0 \\ \dfrac{1}{2\mathcal{B}}\left\{\Phi_2(\rho,x,y;e)-\dfrac{\mathcal{A}}{2}\mathcal{L}_0(\rho,x,y)\right\}; & e^2>0, x^2>0 \\ \dfrac{1}{3\mathcal{A}}\left\{-\dfrac{2}{\mathcal{A}}\Phi_4(\rho,y;e)+\dfrac{\chi_2(\rho,y;e)}{\rho^4}\right\}; & x=0, \mathcal{A}<0 \end{cases}$$

$$I_9 = \begin{cases} \dfrac{1}{8}\left[\phi-\dfrac{\sqrt{\rho^2-1}}{\rho^4}(\rho^2-2)\right]; & e^2=0 \\ \dfrac{1}{3e^2}\left[(e^2-2)\psi_1(\rho)-\dfrac{\Delta(\rho)}{\rho^3}+F(\phi,e)\right] \end{cases}$$

$$I_{10} = I_7 - e^2 J_{110}$$

$$I_{11} = \begin{cases} \left(\dfrac{a}{r}\right)^2 \Gamma_2(\rho,r); & e^2=0, r^2>0 \\ \dfrac{1}{2\rho^2}; & e^2=r^2=0 \\ \dfrac{1}{2e^2}\left\{\dfrac{C}{e^2}J_{14}-\left(\dfrac{\mathcal{B}}{e^2}+\dfrac{\mathcal{A}}{2}\right)J_{24}-\Phi_2(\rho,x,y;e)\right\} \end{cases}$$

$$I_{12} = \begin{cases} \left(\dfrac{a}{r}\right)^2 \Gamma_2(\rho,r); & e^2=0, r^2>0 \\ \dfrac{1}{2\rho^2}; & e^2=r^2=0 \\ \dfrac{1}{2e^2}\left\{\dfrac{\mathcal{B}}{e^2}J_{24}+\left(\dfrac{B}{2}-\dfrac{C}{e^2}\right)J_{14}+\Phi_1(\rho,x,y;e)\right\} \end{cases}$$

$$J_{14} = \begin{cases} -\mathcal{S}(\rho,x,y;e); & e^2>0, y\neq 0 \\ \dfrac{2}{B}\Phi_3(\rho,x;e); & y=0, x^2\neq a^2e^2 \\ \dfrac{1}{\rho^2-e^2}; & y=0, x^2=a^2e^2 \end{cases}$$

$$J_{24} = \begin{cases} \mathcal{L}_0(\rho,x,y); & e^2>0, x^2>0 \\ \dfrac{2}{\mathcal{A}}\Phi_4(\rho,y;e); & x=0, \mathcal{A}<0 \end{cases}$$

$$J_{15} = \begin{cases} \dfrac{z}{a}\left\{-\dfrac{2[B(\rho^2-e^2)-2C+B^2]}{CD^2\chi_0(\rho,x,y;e)}+\dfrac{2B}{CD^2} \right. \\ \left. -\dfrac{1}{C}\mathcal{S}(\rho,x,y;e)\right\}; \quad e^2>0, y\neq 0 \\ \dfrac{2z}{Ba}\left\{\dfrac{8}{3B^2}-\dfrac{1}{3}\left[\dfrac{8(\rho^2-e^2)}{B^2}+\dfrac{4}{B}-\dfrac{1}{(\rho^2-e^2)}\right] \right. \\ \left. \quad \times\dfrac{1}{\chi_1(\rho,x;e)}\right\}; \quad y=0, x^2\neq a^2e^2 \\ \dfrac{z/a}{3(\rho^2-e^2)^3}; \quad y=0, x^2=a^2e^2 \end{cases}$$

$$J_{25} = \begin{cases} \dfrac{z}{a}\left\{-\dfrac{3B^2-8C}{C^2D^2}+\dfrac{1}{C\chi_0(\rho,x,y;e)}\left[\dfrac{1}{(\rho^2-e^2)} \right.\right. \\ \left. +\dfrac{(3B^2-8C)(\rho^2-e^2)+(3B^2-10C)B}{CD^2}\right] \\ \left. \quad +\dfrac{3B}{2C^2}\mathcal{S}(\rho,x,y;e)\right\}; \quad e^2>0, y\neq 0 \\ \dfrac{2z}{5aB}\left\{\left[\dfrac{1}{(\rho^2-e^2)^2}-\dfrac{2}{B(\rho^2-e^2)}+\dfrac{8}{B^2} \right.\right. \\ \left.\left. +\dfrac{16(\rho^2-e^2)}{B^3}\right]\dfrac{1}{\chi_1(\rho,x;e)}-\dfrac{16}{B^3}\right\}; \quad y=0, x^2\neq a^2e^2 \\ \dfrac{z/a}{4(\rho^2-e^2)^4}; \quad y=0, x^2=a^2e^2 \end{cases}$$

$$J_{110} = \begin{cases} \dfrac{z}{2a\mathcal{B}^2}\left\{\dfrac{\mathcal{B}}{\rho^2\chi_0(\rho,x,y;e)} - \dfrac{3\mathcal{A}^2-8\mathcal{B}}{\mathfrak{D}^2} \right. \\ \quad + \dfrac{(3\mathcal{A}^2-8\mathcal{B})\rho^2+(3\mathcal{A}^2-10\mathcal{B})\mathcal{A}}{\mathfrak{D}^2\chi_0(\rho,x,y;e)} \\ \quad \left. - \dfrac{3}{2}\mathcal{A}\mathcal{L}_0(\rho,x,y)\right\}; \quad e^2>0,\, x^2>0 \\ \dfrac{z}{5a\mathcal{A}}\left\{\dfrac{1}{\chi_2(\rho,y;e)}\left[\dfrac{16\rho^2}{\mathcal{A}^3}+\dfrac{8}{\mathcal{A}^2}-\dfrac{2}{\mathcal{A}\rho^2}+\dfrac{1}{\rho^4}\right] \right. \\ \quad \left. -\dfrac{16}{\mathcal{A}^3}\right\}; \quad x=0,\, \mathcal{A}<0 \\ \text{bounded;} \quad e^2=0 \end{cases}$$

$$\phi = \arcsin(1/\rho)$$

$$F(\phi,e) = \int_0^\phi \frac{d\xi}{(1-e^2\sin^2\xi)^{1/2}}$$

$$E(\phi,e) = \int_0^\phi (1-e^2\sin^2\xi)^{1/2}\, d\xi$$

$$\Theta(\rho,\zeta,\nu) = (\rho^2-\zeta^2)(\rho^2-\nu^2)$$

$$\Delta(\rho) = \sqrt{(\rho^2-1)(\rho^2-e^2)}$$

$$Z(\zeta,\nu;e) = \begin{cases} \sqrt{\dfrac{(1-\zeta^2)(1-\nu^2)}{1-e^2}} \\ \sqrt{1-\nu^2}, \quad e^2=\zeta^2=1 \end{cases}$$

$$\mathcal{A} = -\left[e^2+\frac{x^2}{a^2}+\frac{y^2}{a^2}\right]$$

$$\mathcal{B} = e^2\frac{x^2}{a^2}$$

$$B = e^2 - \frac{x^2}{a^2} - \frac{y^2}{a^2}$$

$$C = -e^2\frac{y^2}{a^2}$$

$$D = \sqrt{B^2-4C}$$

$$\mathfrak{D} = \sqrt{\mathcal{A}^2-4\mathcal{B}}$$

$$r^2 = x^2+y^2$$

$$\mathcal{S}(\rho,x,y;e) = \frac{1}{\sqrt{-C}}\left\{\arcsin\frac{B(\rho^2-e^2)+2C}{(\rho^2-e^2)D} - \arcsin\frac{B}{D}\right\}$$

$$\Phi_1(\rho,x,y;e) = \frac{\chi_0(\rho,x,y;e)}{\rho^2-e^2}-1$$

$$\Phi_2(\rho,x,y;e) = \frac{\chi_0(\rho,x,y;e)}{\rho^2}-1$$

$$\Phi_3(\rho,x;e) = \frac{\chi_1(\rho,x;e)}{(\rho^2-e^2)}-1$$

$$\Phi_4(\rho,y;e) = \frac{\chi_2(\rho,y;e)}{\rho^2}-1$$

$$\chi_0(\rho,x,y;e) = \sqrt{\rho^4+\mathcal{A}\rho^2+\mathcal{B}}$$

$$\chi_1(\rho,x;e) = \sqrt{(\rho^2-e^2)\left(\rho^2-\frac{x^2}{a^2}\right)}$$

$$\chi_2(\rho,y;e) = \rho\sqrt{\rho^2-e^2-\frac{y^2}{a^2}}$$

$$\Gamma_1(\rho,r) = 1-\sqrt{1-\left(\frac{r}{a\rho}\right)^2}$$

$$\Gamma_2(\rho,r) = \frac{1}{3}\left\{1-\left[1-\left(\frac{r}{a\rho}\right)^2\right]^{3/2}\right\}$$

$$\Gamma_3(\rho,r) = \frac{1}{5}\left\{1-\left[1-\left(\frac{r}{a\rho}\right)^2\right]^{5/2}\right\}$$

$$\mathcal{L}_0(\rho,x,y) = \begin{cases} \dfrac{1}{\sqrt{\mathcal{B}}}\log\dfrac{2\sqrt{\mathcal{B}}\chi_0(\rho,x,y)+2\mathcal{B}+\rho^2\mathcal{A}}{\rho^2(2\sqrt{\mathcal{B}}+\mathcal{A})} \\ \dfrac{1}{e^2}\log\dfrac{\rho^2-e^2}{\rho^2}; \quad y=0,\, x^2=a^2e^2>0 \end{cases}$$

H. C. Yang[1]
Y. T. Chou
Department of Metallurgy
and Materials Engineering,
Lehigh University,
Bethlehem, Pa. 18015

The ⟨111⟩ Elliptic Inclusion in an Anisotropic Solid of Cubic Symmetry

This paper deals with a generalized plane problem in which a uniform stress-free strain transformation takes place in the region of an elliptic cyclinder (the inclusion) oriented in the ⟨111⟩ direction in an anisotropic solid of cubic symmetry. Closed-form solutions for the elastic fields and the strain energies are presented. The perturbation of an otherwise uniform stress field due to a ⟨111⟩ elliptic inhomogeneity is also treated including two extreme cases, elliptic cavities and rigid inhomogeneities.

1 Introduction

A simple method of treating the generalized plane problems of elastic inclusions in an anisotropic solid was recently presented by the authors [1]. The method is based on the anisotropic elasticity theory for line defects [2] and the point force method for inclusions [3, 4]. In general, it is difficult to obtain closed-form solutions for the elastic fields; the difficulty hinges on the solution of a sextic equation, which, except for the presence of symmetry elements, cannot be obtained analytically.

For the elastic field of an elliptic inclusion in an infinite medium with a (or a set of) two-fold rotation axis, closed-form solutions have been obtained and reported [1, 5, 6]. Typical examples in this class are the ⟨100⟩ and ⟨110⟩ elliptic inclusions in a cubic crystal. By a ⟨100⟩ (or ⟨110⟩) inclusion, we mean that the axis of the cylinder is parallel to the ⟨100⟩ (or ⟨110⟩) direction of a cubic lattice.

Another equally important case in the cubic system is the ⟨111⟩ inclusion of which the axis is parallel to a three-fold rotation axis. Since the solution for a ⟨111⟩ line force is known [7], it is possible to treat the ⟨111⟩ inclusion using the line force results. The detailed formulation will be presented in Section 2. It is worth noting that for this class of plane problems the elastic field cannot be separated into plane strain and antiplane strain parts. The three displacement components (and six stress components) have to be solved simultaneously. This class of elastic systems has not previously been analyzed.

In Section 3 we shall summarize the results for the transformation problem in which the inclusion tends to undergo a stress-free strain transformation. Because the resulting stress field is uniform inside the inclusion, the analysis can be extended to the inhomogeneity problem in which a uniform stress field in the matrix is perturbed by the presence of a second phase. For the purpose of illustration, two extreme cases concerning elliptic cavities and rigid inhomogeneities will be treated in detail. These are presented in Sections 4 and 5.

2 General Formulation

Consider an infinite anisotropic medium of cubic symmetry which contains an elliptic inclusion described by $x_1{}^2/a^2 + x_2{}^2/b^2 = 1$, where x_1 and x_2 are coordinates of a right-handed cartesian coordinate system x_i ($i = 1, 2, 3$). To specify a ⟨111⟩ elliptic inclusion, the x_1, x_2, and x_3 axes are oriented in $[11\bar{2}]$, $[\bar{1}10]$, and $[111]$ directions, respectively. The elastic constants associated with this coordinate system (the ⟨111⟩ elastic system) are given by

$$C_{MN} = \begin{bmatrix} C_{11} & C_{12} & C_{13} & 0 & C_{15} & 0 \\ & C_{11} & C_{13} & 0 & -C_{15} & 0 \\ & & C_{33} & 0 & 0 & 0 \\ & & & C_{44} & 0 & -C_{15} \\ & & & & C_{44} & 0 \\ & & & & & C_{66} \end{bmatrix} \tag{1}$$

where the C_{MN} ($MN = 1, 2, \ldots, 6$) are related to the standard elastic constants C_{11}^0, C_{12}^0, and C_{44}^0 of the cubic medium by

$$\begin{aligned} C_{11} &= C_{11}^0 - \frac{1}{2}H & C_{33} &= C_{11}^0 - \frac{2}{3}H \\ C_{12} &= C_{12}^0 + \frac{1}{6}H & C_{44} &= C_{44}^0 + \frac{1}{3}H \\ C_{13} &= C_{12}^0 + \frac{1}{3}H & C_{66} &= C_{44}^0 + \frac{1}{6}H \\ C_{15} &= -\frac{\sqrt{2}}{6}H & H &= C_{11}^0 - C_{12}^0 - 2\,C_{44}^0 \end{aligned} \tag{2}$$

[1] Presently at Burns and Roe, Inc., Woodbury, N. Y. 11797.

Contributed by the Applied Mechanics Division for publication in the JOURNAL OF APPLIED MECHANICS.

Discussion on this paper should be addressed to the Editorial Department, ASME, United Engineering Center, 345 East 47th Street, New York, N. Y. 10017, and will be accepted until two months after final publication of the paper itself in the JOURNAL OF APPLIED MECHANICS. Manuscript received by ASME Applied Mechanics Division, September, 1981; final revision, December, 1981.

In this case, the stress and strain tensors are related by

$$\begin{aligned}
\mathbf{p}_{11} &= C_{11}\, e_{11} + C_{12}\, e_{22} + 2\, C_{15}\, e_{13} \\
\mathbf{p}_{22} &= C_{12}\, e_{11} + C_{11}\, e_{22} - 2\, C_{15}\, e_{13} \\
\mathbf{p}_{33} &= C_{13}\, (e_{11} + e_{22}) \\
\mathbf{p}_{23} &= 2\, C_{44}\, e_{23} - 2\, C_{15}\, e_{13} \\
\mathbf{p}_{13} &= C_{15}\, (e_{11} - e_{22}) + 2\, C_{44}\, e_{13} \\
\mathbf{p}_{12} &= -2\, C_{15}\, e_{13} + 2\, C_{66}\, e_{12}
\end{aligned} \tag{3}$$

For generalized plane strain problems, and in particular for the ⟨111⟩ elastic system, it is convenient to use the reduced elastic compliances defined by the relation

$$S_{MN} = s_{MN} - \frac{s_{M3}\, s_{N3}}{s_{33}} \tag{4}$$

where s_{MN} are the elastic compliances. The stress and strain tensors of the ⟨111⟩ system are then related by

$$\begin{aligned}
e_{11} &= S_{11}\mathbf{p}_{11} + S_{12}\, \mathbf{p}_{22} + S_{15}\, \mathbf{p}_{13} \\
e_{22} &= S_{12}\, \mathbf{p}_{11} + S_{11}\, \mathbf{p}_{22} - S_{15}\, \mathbf{p}_{13} \\
e_{23} &= \frac{1}{2} S_{44}\, \mathbf{p}_{23} - S_{15}\, \mathbf{p}_{12} \\
e_{13} &= \frac{1}{2} [S_{15}(\mathbf{p}_{11} - \mathbf{p}_{22}) + S_{44}\, p_{13}] \\
e_{12} &= -S_{15}\, \mathbf{p}_{23} + (S_{11} - S_{12})\, \mathbf{p}_{12}
\end{aligned} \tag{5}$$

with $e_{33} = 0$. Expressions for S_{MN} in (5) in terms of the standard elastic constants (C^0_{11}, C^0_{12}, and C^0_{44}) are given in reference [8].

To analyze the ⟨111⟩ inclusion problem by the line force method, it is necessary to solve the elastic fields of a ⟨111⟩ line force. This has been done in reference [7]. The displacement field of a line force F_m ($m = 1,2,3$), acting at a point y along the x_3 axis, can be written in a modified form as

$$\begin{aligned}
u_1 &= \Re\left\{ \sum_{l=1}^{3} [(S_{11}\, \mu^2{}_{(l)} + S_{12}) - \beta\, S_{15}\, \mu_{(l)}] d_{(l)m} F_m \ln z_{(l)} \right\} \\
u_2 &= \Re\left\{ \sum_{l=1}^{3} [(S_{12}\, \mu_{(l)} + S_{11}/\mu_{(l)}) + \beta\, S_{15}] d_{(l)m}\, F_m \ln z_{(l)} \right\} \\
u_3 &= \Re\left\{ \sum_{l=1}^{3} [S_{15}(\mu^2_{(l)} - 1) - \beta\, S_{44}\, \mu_{(l)}] d_{(l)m}\, F_m \ln z_{(l)} \right\}
\end{aligned} \tag{6}$$

where $\Re$ stands for the real part of a complex function. The complex coefficients, $\mu_{(l)}$ ($l = 1,2,3$), are the three roots with positive imaginary parts of the sextic equation (see equation (23) in reference [7]) with

$$\begin{aligned}
\mu_{(1)} &= i\frac{(R+1)^{1/3} + (R-1)^{1/3}}{(R+1)^{1/3} - (R-1)^{1/3}} \\
\mu_{(2)} &= \frac{\mu_{(1)} - \sqrt{3}}{1 + \mu_{(1)}\sqrt{3}} \\
\mu_{(3)} &= \frac{\mu_{(1)} + \sqrt{3}}{1 - \mu_{(1)}\sqrt{3}}
\end{aligned} \tag{7}$$

and

$$R = \left[\frac{S_{11}\, S_{44}}{S_{11}\, S_{44} - S^2_{15}} \right]^{1/2} \tag{8}$$

The functions $d_{(l)m}$ are defined as

$$\begin{aligned}
d_{(l)1} &= \frac{1}{6\pi i(1 + \mu^2_{(l)})} \left[\frac{16\, \mu_{(l)}}{1 - 3\, \mu^2_{(l)}} + \left(\frac{S_{12}}{S_{11}} - 5 \right) i R \right] \\
d_{(l)2} &= \frac{1}{6\pi i(1 + \mu^2_{(l)})} \left[\mu_{(l)} \left(1 + \frac{S_{12}}{S_{11}} \right) i R + 2 \right] \\
d_{(l)3} &= \frac{S_{15}\, \mu_{(l)}\, (\mu^2_{(l)} - 3)}{6\pi i(1 + \mu^2_{(l)})\, S_{11}}
\end{aligned} \tag{9}$$

and β is given by

$$\beta = \frac{S_{11}(1 + \mu^2_{(l)})^2}{S_{15}\, \mu_{(l)}\, (\mu^2_{(l)} - 3)} = \frac{S_{15}\, \mu_{(l)}\, (\mu^2_{(l)} - 3)}{S_{44}(1 + \mu^2_{(l)})} \tag{10}$$

The complex functions $z_{(l)}$ are defined by

$$\begin{aligned}
z_{(l)} &= (x_1 + \mu_{(l)} x_2) - (y_1 + \mu_{(l)} y_2) \\
&= \frac{1}{2} [(x + \bar{x} - i\, \mu_{(l)}\, x + i\, \mu_{(l)}\, \bar{x}) - (y + \bar{y} - i\, \mu_{(l)}\, y + i\, \mu_{(l)}\, \bar{y})]
\end{aligned} \tag{11}$$

where the complex variables $x = x_1 + i\, x_2$ (with its conjugate $\bar{x} = x_1 - i\, x_2$) and $y = y_1 + i\, y_2$ (with its conjugate $\bar{y} = y_1 - i\, y_2$).

In equations (6) and in the subsequent equations, summation convention for tensor components is adopted, i.e., summation is understood to be carried out over repeated subscripts. However, subscripts not used for tensor characteristics are enclosed in parentheses. In this case, summation will be written explicitly as shown in (6).

From equations (3) and (6), the stress components produced by a ⟨111⟩ line force at a point y can be given by

$$\begin{aligned}
\mathbf{p}_{11} &= \Re\left\{ \sum_{l=1}^{3} \mu^2_{(l)}\, d_{(l)m} F_m \frac{1}{z_{(l)}} \right\} \\
\mathbf{p}_{22} &= \Re\left\{ \sum_{l=1}^{3} d_{(l)m} F_m \frac{1}{z_{(l)}} \right\} \\
\mathbf{p}_{33} &= -\frac{s^0_{12} + \delta/3}{s^0_{11} - 2\,\delta/3} (\mathbf{p}_{11} + \mathbf{p}_{22}) \\
\mathbf{p}_{23} &= \Re\left\{ \sum_{l=1}^{3} \beta\, d_{(l)m} F_m \frac{1}{z_{(l)}} \right\} \\
\mathbf{p}_{13} &= -\Re\left\{ \sum_{l=1}^{3} \beta\, \mu_{(l)}\, d_{(l)m}\, F_m \frac{1}{z_{(l)}} \right\} \\
\mathbf{p}_{12} &= -\Re\left\{ \sum_{l=1}^{3} \mu_{(l)}\, d_{(l)m}\, F_m \frac{1}{z_{(l)}} \right\}
\end{aligned} \tag{12}$$

where s^0_{MN} ($MN = 1,2,\ldots 6$) are the standard elastic compliances and

$$\delta = s^0_{11} - s^0_{12} - \frac{1}{2} s^0_{44} \tag{13}$$

2.1 The Transformation Problem. It is appropriate at this stage to review Eshelby's approach to a stress-free strain transformation taking place in an inclusion. His concept comprises a set of hypothetical operations. The inclusion is thought to be cut out of the matrix and allowed to achieve a uniform stress-free strain E^0_{ij}. A traction $-T_i = P^0_{ij}\, n_j$ is applied to the surface of the inclusion, S (n_j are the direction cosines of the outward normal at a surface element dS). This produces a strain $-E^0_{ij}$ in the inclusion and restores it to its original form. The inclusion is then put back into the hole of the matrix and rejoined with the material across the cut. At this time, the matrix is unstressed and there is a uniform stress $-P^0_{ij}$ in the inclusion. The applied surface traction $-T_i$ remains in the medium as a layer of body force spread over the interface S, given by

$$dF_i = -P^0_{ij}\, n_j\, dS \tag{14}$$

Finally this layer of body force is removed by applying equal but opposite line forces on S. Now both the matrix and the inclusion are in an elastic state which can be determined by the strain transformation that has taken place in the inclusion and by the elastic fields produced by the line forces on S.

Thus, in considering a transformation problem, it is essential to determine the total contribution of the line force F_m on S. For this purpose it is useful to introduce the following integrals:

$$g_{(l)}(x) = \frac{1}{2}\oint_s \frac{d_{(l)m}\, F_m}{z_{(l)}}\, dS \tag{15a}$$

and

$$g_{(3+l)}(x) = \frac{S_{15}\,\mu_{(l)}\,(\mu^2_{(l)}-3)}{S_{44}(1+\mu^2_{(l)})}\, g_{(l)}(x) = \beta\, g_{(l)}(x) \tag{15b}$$

and, in terms of Eshelby's hypothetical stress field P^0_{ij}, we have

$$F_m\, dS = -\frac{1}{2}\left[(P^0_{2m} + i\,P^0_{1m})\,dy + (P^0_{2m} - i\,P^0_{1m})\,d\bar{y}\right] \tag{16}$$

As shown in reference [1], the integral in equation (15a) can be simplified by mapping the elliptic contour to a unit circle in the X frame, using the transformation

$$x = \frac{1}{2}\left[(a+b)X + (a-b)\bar{X}\right] \tag{17}$$

From equations (15a), (16), and (17) we obtain

$$g_{(l)}(x) = -\frac{1}{2}\, d_{(l)m}\left[(P^0_{2m} + i\,P^0_{1m})\,I_{(l)} + (P^0_{2m} - i\,P^0_{1m})\,J_{(l)}\right] \tag{18}$$

where P^0_{ij} are related to E^0_{ij} by equation (3). If $|X| > 1$, i.e., for the matrix, $I_{(l)}$ and $J_{(l)}$ are given by

$$I_{(l)} = \frac{\pi i[(1+e) - (1-e)/\Gamma_{(l)}]}{(1 - ie\mu_{(l)})} \times \left\{ \frac{(X + \Gamma_{(l)}\bar{X}) - [(X+\Gamma_{(l)}\bar{X})^2 - 4\Gamma_{(l)}]^{1/2}}{2[(X+\Gamma_{(l)}\bar{X})^2 - 4\Gamma_{(l)}]^{1/2}} \right\} \tag{19a}$$

$$J_{(l)} = \frac{\pi i[(1-e) - (1+e)/\Gamma_{(l)}]}{(1 - ie\mu_{(l)})} \times \left\{ \frac{(X + \Gamma_{(l)}\bar{X}) - [(X+\Gamma_{(l)}\bar{X})^2 - 4\Gamma_{(l)}]^{1/2}}{2[(X+\Gamma_{(l)}\bar{X})^2 - 4\Gamma_{(l)}]^{1/2}} \right\} \tag{19b}$$

where

$$e = b/a \tag{20}$$

and

$$\Gamma_{(l)} = \frac{1 + ie\,\mu_{(l)}}{1 - ie\,\mu_{(l)}}, \quad |\Gamma_{(l)}| < 1 \tag{21}$$

If $|X| < 1$, i.e., for the inclusion, we have

$$I_{(l)} = \frac{-\pi i\,(1+e)}{1 - ie\,\mu_{(l)}} \tag{22a}$$

$$J_{(l)} = \frac{-\pi i\,(1-e)}{1 - ie\,\mu_{(l)}} \tag{22b}$$

The elastic fields of the system can thus be expressed by the following equations:

$$\begin{aligned} u_1 &= 2\Re\left\{ \sum_{l=1}^{3} \int \left[(S_{11}\,\mu^2_{(l)} + S_{12})\,g_{(l)}(x) - S_{15}\,\mu_{(l)}\,g_{(3+l)}(x)\right] dz_{(l)} \right\} \\ u_2 &= 2\Re\left\{ \sum_{l=1}^{3} \int \left[(S_{11}/\mu_{(l)} + S_{12}\,\mu_{(l)})\,g_{(l)}(x) + S_{15}\,g_{(3+l)}(x)\right] dz_{(l)} \right\} \\ u_3 &= 2\Re\left\{ \sum_{l=1}^{3} \int \left[S_{15}(\mu^2_{(l)} - 1)\,g_{(l)}(x) - S_{44}\,\mu_{(l)}\,g_{(3+l)}(x)\right] dz_{(l)} \right\} \end{aligned} \tag{23}$$

and

$$\begin{aligned} \mathbf{p}_{11} &= 2\Re\left\{ \sum_{l=1}^{3} \mu^2_{(l)}\, g_{(l)}(x) \right\} \\ \mathbf{p}_{22} &= 2\Re\left\{ \sum_{l=1}^{3} g_{(l)}(x) \right\} \\ \mathbf{p}_{23} &= 2\Re\left\{ \sum_{l=1}^{3} g_{(3+l)}(x) \right\} \\ \mathbf{p}_{13} &= -2\Re\left\{ \sum_{l=1}^{3} \mu_{(l)}\, g_{(3+l)}(x) \right\} \\ \mathbf{p}_{12} &= -2\Re\left\{ \sum_{l=1}^{3} \mu_{(l)}\, g_{(l)}(x) \right\} \end{aligned} \tag{24}$$

The elastic displacements and stresses in the matrix are given by (23) and (24) with $I_{(l)}$ and $J_{(l)}$ given by (19). Equations (23) and (24) with $I_{(l)}$ and $J_{(l)}$ given by (22) provide the constrained field U^c_i and P^c_{ij} in the inclusion (U^c_i are also the equilibrium displacements of the inclusion). The actual elastic stresses in the inclusion are given by $P_{ij} = P^c_{ij} - P^0_{ij}$ and are uniform. However, they are not continuous across the boundary surface S. To assure a perfect bond at the interface, the surface tractions across S are required to be continuous. If the boundary stresses of the matrix are denoted by $\mathbf{p}^b_{ij}$, it is required that

$$\mathbf{p}^b_{ij} n_j = P_{ij}\, n_j = (P^3_{ij} - P^0_{ij})\, n_j, \text{ across } S \tag{25}$$

An important consideration in the inclusion problem is the evaluation of the strain energy of the system. A detailed discussion has been presented by Eshelby [4]. For an elliptic inclusion the strain energy per unit height is found to be

$$W = -\frac{1}{2}\,\pi ab\, P_{ij}\, E^0_{ij} \tag{26}$$

2.2 The Inhomogeneity Problem. A useful conclusion obtained from the transformation problem is that the stress field produced by the uniform strain field E^0_{ij} is also uniform in the inclusion. This result permits an extension of the analysis to the inhomogeneity problem.

Consider that an elliptic inhomogeneity, with elastic constants C'_{MN} (not necessarily restricted to the form of matrix (1)) that differ from the C_{MN} of the matrix, perturbs an otherwise uniform stress field which results from the constant surface tractions $P^A_{ij}\, n_j$ applied at infinity. According to Eshelby [3], the elastic state of the system can be solved by introducing an equivalent inclusion, with the same elastic constants C_{MN} as the matrix, which tends to undergo a stress-free transformation. If P^A_{ij} produces E^A_{ij} in the matrix in the absence of the inhomogeneity, the free deformations E^0_{ij} of the equivalent inclusion can be determined from the expressions,

$$P_{ij}=C_{ijkl}(E^c_{kl}-E^0_{kl})$$
$$=C'_{ijkl}(E^c_{kl}+E^A_{kl})-P^A_{ij} \quad (27)^1$$

With the help of equations (22) and (24), E^0_{kl} can be obtained in terms of P^A_{ij}. The perturbation fields are thus given by equations (23) and (24) in the same manner as a transformed inclusion. The increase of elastic strain energy due to the presence of the elliptic inhomogeneity is simply

$$\Delta W=\frac{1}{2}\pi ab\, P^A_{ij}\, E^0_{ij} \quad (28)$$

per unit height of the medium [1, 4].

3 Results of the Transformed Elliptic Inclusions

For an elliptic inclusion tending to undergo a uniform deformation E^0_{ij}, equations (24), (15), and (18) give the constrained stresses P^c_{ij} inside the inclusion. From the relation $P_{ij} = P^c_{ij} - P^0_{ij}$, the actual elastic stresses in the inclusion are found to be

$$P_{11}=\frac{-R}{2S_{11}Q}[e(1+R\,e)(E^0_{11}+E^0_{22})+2(R+e)E^0_{11} - 4(S_{15}/S_{44})\,R\,E^0_{13}] \quad (29a)$$

$$P_{22}=\frac{-R\,e}{2S_{11}Q}[(1+R\,e)(E^0_{11}+E^0_{22})+2e(R+e)E^0_{22} + 4(S_{15}/S_{44})R\,e\,E^0_{13}] \quad (29b)$$

$$P_{23}=\frac{-2R\,e}{S_{44}Q}\,[(1+2R\,e+e^2)\,E^0_{23}+(S_{15}/S_{11})R\,e\,E^0_{12}] \quad (29c)$$

$$P_{13}=\frac{R}{S_{44}Q}[R\,(S_{15}/S_{11})(E^0_{11}-e^2E^0_{22}) - 2(R+2e+R\,e^2)E^0_{13}] \quad (29d)$$

$$P_{12}=\frac{-R\,e}{S_{11}Q}\,[2(S_{15}/S_{44})\,R\,e\,E^0_{23}+(1+R\,e)\,E^0_{12}] \quad (29e)$$

where

$$Q=1+3\,R\,e+3\,e^2+R\,e^3 \quad (30)$$

It is noted that when isotropy is approached ($S_{15} = 0, R = 1$), the plane strain components (E^0_{11}, E^0_{22}, E^0_{12}) and antiplane strain components (E^0_{23}, E^0_{13}) are no longer mixed in equations (29) and can be treated separately as expected.

The stresses in the matrix are determined by equations (24) with $g_{(l)}(x)$ determined by (18) and (19). However, the boundary stressses $\mathbf{p}^b_{ij}$ are of particular interest. Referring to local axes taken in the outward normal (n) and counterclockwise tangential (t) directions on the boundary surface S, the angle φ between n and the major axis a is defined by

$$\sin\varphi=\frac{x_2}{(e^4{x_1}^2+{x_2}^2)^{1/2}}\,,\quad \cos\varphi=\frac{e^2x_1}{(e^4{x_1}^2+{x_2}^2)^{1/2}} \quad (31)$$

To satisfy the continuity of surface traction across S, given by equation (25), $\mathbf{p}^b_{nn}$, $\mathbf{p}^b_{tn}$, and $\mathbf{p}^b_{3n}$ must be equal to P_{nn}, P_{tn}, and P_{3n}, respectively. It can be shown that

$$\mathbf{p}^b_{nn}=P_{nn}=\frac{-R}{S_{11}Q}\Big\{\frac{1}{2}[e(1+R\,e)\,(E^0_1+E^0_{22}) + (R+e)\,(E^0_{11}+e^2E^0_{22})-2R\,(S_{15}/S_{44})(1-e^2)E^0_{13}] + \Big[\frac{1}{2}\,(R+e)\,(E^0_{11}-e^2E^0_{22})-R\,(S_{15}/S_{44})(1+e^2)E^0_{13}\Big]\cos2\varphi + e[2(S_{15}/S_{44})R\,e\,E^0_{13}+(1+R\,e)E^0_{12}]\sin2\varphi\Big\} \quad (32a)$$

$$\mathbf{p}^b_{tn}=P_{tn}=\frac{-R}{S_{11}Q}\Big\{e[2(S_{15}/S_{44})R\,e\,E^0_{23}+(1+R\,e)E^0_{12}]\cos2\varphi - \frac{1}{2}[(R+e)\,(E^0_{11}-e^2E^0_{22})-2R\,(S_{15}/S_{44})(1+e^2)E^0_{13}]\sin2\varphi\Big\} \quad (32b)$$

$$\mathbf{p}^b_{3n}=P_{3n}=\frac{R}{S_{44}Q}\Big\{[R\,(S_{15}/S_{11})(E^0_{11}-e^2\,E^0_{22}) - 2(R+2e+Re^2)E^0_{13}]\cos\varphi - 2e[(1+2R\,e+e^2)E^0_{23}+(S_{15}/S_{44})R\,e\,E^0_{12}]\sin\varphi\Big\} \quad (32c)$$

Equation (32) provides a check for the boundary conditions. On the other hand, there is a jump across S for the stress components $\mathbf{p}^b_{tt}$, $\mathbf{p}^b_{3t}$ and P_{tt}, P_{3t}. It is found that

$$\mathbf{p}^b_{tt}-P_{tt}=\frac{R^2}{S_{11}Q^*}\Big\{\sin^2\varphi\,E^0_{11}+\cos^2\varphi\,E^0_{22}-\sin2\varphi\,E^0_{12} + 2(S_{15}/S_{44})\sin\varphi(\sin^2\varphi-3\cos^2\varphi)\,(\cos\varphi\,E^0_{23}-\sin\varphi\,E^0_{13})\Big\} \quad (33a)$$

$$P_{tt}=\frac{-R}{S_{11}Q}\Big\{\frac{1}{2}[e(1+R\,e)\,(E^0_{11}+E^0_{22})+(R+e)\,(E^0_{11}+e^2\,E^0_{22}) - 2R\,(S_{15}/S_{44})(1-e^2)E^0_{13}]-\frac{1}{2}[(R+e)\,(E^0_{11}-e^2\,E^0_{22}) - 2R\,(S_{15}/S_{44})(1+e^2)\,E^0_{13}]\cos2\varphi - e[2(S_{15}/S_{44})\,R\,e\,E^0_{23}+(1+R\,e)\,E^0_{12}]\sin2\varphi\Big\} \quad (33b)$$

$$\mathbf{p}^b_{3t}-P_{3t}=\frac{R^2}{S_{44}Q^*}\Big\{2[\cos\varphi\,E^0_{23}-\sin\varphi\,E^0_{13}] + (S_{15}/S_{11})\sin\varphi(\sin^2\varphi-3\cos^2\varphi)\,[\sin^2\varphi\,E^0_{11} + \cos^2\varphi E^0_{22}-\sin2\varphi\,E^0_{12}]\Big\} \quad (33c)$$

$$P_{3t}=\frac{-R}{S_{44}Q}\Big\{2e[(1+2R\,e+e^2)E^0_{23} + (S_{15}/S_{11})R\,e\,E^0_{12}]\cos\varphi+[R\,(S_{15}/S_{11})(E^0_{11}-e^2E^0_{22}) - 2(R+2e+R\,e^2)E^0_{13}]\sin\varphi\Big\} \quad (33d)$$

where

$$Q^*=\sin^2\varphi(\sin^2\varphi-3\cos^2\varphi)^2+R^2\cos^2\varphi(3\sin^2\varphi-\cos^2\varphi)^2 \quad (34)$$

Equations (33) are useful in the discussion of the stress contentration around an elliptic inhomogeneity.

The equilibrium configuration of the inclusion is also of interest. The constrained strains in the inclusion can be obtained from equations (29), (3), and the relation $E^c_{ij} = E_{ij} + E^0_{ij}$. It is found that

$$E^c_{11}=\frac{-e}{2Q}\Big\{R_1(1+R\,e)\,(E^0_{11}+E^0_{22}) - 2(2R+3e+R\,e^2)E^0_{11}+2e[R_1(R+e)-(1+R\,e)]E^0_{22} + 4R\,(S_{15}/S_{44})(2+R_1\,e)E^0_{13}\Big\} \quad (35a)$$

[2] The fourth-order tensor C_{ijkl} ($i,j,k,l=1,2,3$) is used here to replace C_{MN}($M,N=1,2,\ldots 6$) with 1 replaced by the pair of subscripts 11, 2 by 22, 3 by 33, 4 by 23, 5 by 31, and 6 by 12.

$$E_{22}^c = \frac{-1}{2Q}\Big\{R_1\, e(1+R\,e)\,(E_{11}^0+E_{22}^0) + 2[R_1(R+e)-(1+R\,e)]E_{11}^0 - 2(1+3R\,e+2e^2)E_{22}^0 - 4R\,(S_{15}/S_{44})(R_1+2e)\,E_{13}^0\Big\} \tag{35b}$$

$$E_{23}^c = \frac{1}{Q}\Big\{(1+2R\,e+e^2)E_{23}^0 + (S_{15}/S_{11})R\,e\,E_{12}^0\Big\} \tag{35c}$$

$$E_{13}^c = \frac{-e}{2Q}\Big\{R\,(S_{15}/S_{11})(E_{11}^0 - e^2\,E_{22}^0) - 2(R+2e+R\,e^2)E_{13}^0\Big\} \tag{35d}$$

$$E_{12}^c = \frac{1}{Q}(1+R_1\,e+e^2)[2(S_{15}/S_{44})R\,e\,E_{23}^0 + (1+R\,e)E_{12}^0] \tag{35e}$$

where

$$R_1 = R\left(1+\frac{S_{12}}{S_{11}}\right) \tag{36}$$

The constrained displacements U_i^c cannot be obtained directly from (35), but from equations (23), (18), and (22)

$$U_1^c = E_{11}^c\, x_1 + (E_{12}^c+\omega)x_2 \tag{37a}$$

$$U_2^c = (E_{12}^c-\omega)x_1 + E_{22}^c\, x_2 \tag{37b}$$

$$U_3^c = 2E_{13}^c\, x_1 + 2E_{23}^c\, x_2 \tag{37c}$$

where

$$\omega = \frac{1-e^2}{Q}[2(S_{15}/S_{44})R\,e\,E_{23}^0 + (1+R\,e)\;E_{12}^0] \tag{38}$$

It is seen that both E_{23}^0 and E_{12}^0 will produce a rigid body rotation which vanishes for a circular inclusion ($e = 1$).

The strain energy per unit height of the medium can be calculated from equation (26) with P_{ij} given by (29). For the principal strains $E_{11}^0 \neq 0$, $E_{22}^0 \neq 0$, we have

$$W_I = \pi ab\left(\frac{R}{4S_{11}Q}\right)[e(1+R\,e)\,(E_{11}^0+E_{22}^0)^2 + 2(R+e)\,({E_{11}^0}^2 + e^2\,{E_{22}^0}^2)] \tag{39}$$

For pure shear strain $E_{12}^0 \neq 0$,

$$W_{II} = \pi ab\left(\frac{R\,e}{S_{11}Q}\right)(1+R\,e)\;{E_{12}^0}^2 \tag{40}$$

and for antiplane shear strain $E_{23}^0 \neq 0$, $E_{13}^0 \neq 0$,

$$W_{III} = \pi ab\left(\frac{2R}{S_{44}Q}\right)[e(1+2R\,e+e^2){E_{23}^0}^2 + (R+2e+R\,e^2){E_{13}^0}^2] \tag{41}$$

On approaching isotropy, W_I and W_{II} agree with those reported by Jaswon and Bhargava [9], and W_{III} reduces to the previous result for a cubic symmetric medium [1], which also represents the solutions for an isotropic medium.

For a general deformation inclusion, $E_{ij}^0 \neq 0$ (except for $E_{33}^0 = 0$), the strain energy per unit height of the system is given by

$$W = W_I + W_{II} + W_{III} + \pi ab\left(\frac{2S_{15}R^2}{S_{11}S_{44}Q}\right)[2e^2\,E_{23}^0\,E_{12}^0 - (E_{11}^0 - e^2\,E_{22}^0)\,E_{13}^0] \tag{42}$$

The additional terms in equation (42) represent the interaction between E_{23}^0 and E_{12}^0, and between E_{11}^0, E_{22}^0, and E_{13}^0. When isotropy is approached ($S_{15} = 0$), the interaction terms vanish as expected.

4 The Elliptic Cavity and Slit Crack

As outlined in Section 2, the analysis of the transformation problem for an elliptic inclusion can be extended to the inhomogeneity problem in which a uniform applied stress field is perturbed by the presence of an inhomogeneity. In this section, we present an extreme case in which the inhomogeneity is an elliptic cavity ($C'_{ijkl} = 0$). The other extreme case of a rigid elliptic inhomogeneity ($C'_{ijkl} = \infty$) will be discussed in Section 5.

Consider that an elliptic cavity perturbs an otherwise uniform stress field in the matrix produced by a constant surface traction $T_i = P^A_{ij}\,n_j$ ($n_3 = 0$) at infinity. By introducing an equivalent inclusion with stress-free deformations E_{ij}^0, equations (27), with $C'_{ijkl} = 0$, lead to

$$P_{ij} = -P_{ij}^A \tag{43}$$

where P_{ij} are the elastic stresses in the equivalent inclusion, and the stresses in the cavity are $P_{ij} + P_{ij}^A = 0$, which satisfy the condition that no stresses appear in a cavity. By equations (29) and (43) the stress-free deformations of the equivalent inclusion are found to be:

$$E_{11}^0 = S_{11}\left[\left(1+\frac{2e}{R}\right)P_{11}^A - P_{22}^A\right] + S_{15}\,P_{13}^A \tag{44a}$$

$$E_{22}^0 = -S_{11}\left[P_{11}^A - \left(1+\frac{2}{Re}\right)P_{22}^A\right] - S_{15}\,P_{13}^A \tag{44b}$$

$$E_{23}^0 = \frac{1}{2}S_{44}\left(1+\frac{1}{Re}\right)P_{23}^A - S_{15}\,P_{12}^A \tag{44c}$$

$$E_{13}^0 = \frac{1}{2}S_{15}(P_{11}^A - P_{22}^A) + \frac{1}{2}S_{44}\left(1+\frac{e}{R}\right)P_{13}^A \tag{44d}$$

$$E_{12}^0 = -S_{15}\,P_{23}^A + S_{11}\left(2+\frac{1}{Re}+\frac{e}{R}\right)P_{12}^A \tag{44e}$$

The stress distribution in the matrix is given by $\mathbf{p}_{ij} + P_{ij}^A$, where $\mathbf{p}_{ij}$ are obtained from equations (24), (18), and (19), with P_{ij}^0 related to E_{ij}^0 by equations (44) and (3). However, explicit expressions are not presented here. It will suffice to report the stresses at the edge of the elliptic cavity in view of their importance in fracture processes. By equations (32) and (43) it is easy to see that $\mathbf{p}_{nn}^b + P_{nn}^A = 0$, $\mathbf{p}_{tn}^b + P_{tn}^A = 0$, and $\mathbf{p}_{3n}^b + P_{3n}^A = 0$, as required for the traction free on the surface of the cavity. On the other hand, we have

$$\begin{aligned}\mathbf{p}_{tt}^b + P_{tt}^A = \frac{-1}{Q^*}\Big\{&[R^2\cos 2\varphi + (1-R^2)\sin^2\varphi(1+2\cos 2\varphi)]\\ &\times(P_{11}^A - P_{22}^A) - 2R\left[e\sin^2\varphi\,P_{11}^A + \frac{1}{e}\;\cos^2\varphi\,P_{22}^A\right]\\ &-(S_{15}/S_{11})R\sin 2\varphi\left[R - \frac{1}{2}\left(R+\frac{1}{e}\right)(1+2\cos 2\varphi)\right]P_{23}^A\\ &+R\,(S_{15}/S_{11})[R\cos 2\varphi - (R+e)\;\sin^2\varphi(1+2\cos 2\varphi)]P_{13}^A\\ &+\sin 2\varphi\left[R\left(\frac{1}{e}+2R+e\right) + (1-R^2)(1+2\cos 2\varphi)\right]P_{12}^A\Big\}\end{aligned} \tag{45a}$$

and

$$\begin{aligned}\mathbf{p}_{3t}^b + P_{3t}^A = \frac{-1}{Q^*}\Big\{&(S_{15}/S_{44})R\sin\varphi\Big\langle R[1\\ &-\cos\varphi(1+2\cos 2\varphi)](P_{11}^A - P_{22}^A)\\ &-2(1+2\cos 2\varphi)\left[e\sin^2\varphi\,P_{11}^A + \frac{1}{e}\cos^2\varphi\,P_{22}^A\right]\Big\rangle\\ &-\cos\varphi\left[R\left(\frac{1}{e}+R\right) + 2(1-R^2)\sin^2\varphi(1+2\cos 2\varphi)\right]P_{23}^A\\ &+\sin\varphi[R\,(R+e) + (1-R^2)\cos 2\varphi(1+2\cos 2\varphi)]P_{13}^A\end{aligned}$$

$$+ 2(S_{15}/S_{44})R\cos\varphi\left[R - \left(\frac{1}{e} + 2R + e\right)\right.$$

$$\left.\times \sin^2\varphi(1 + 2\cos 2\varphi)\right]P_{12}^A\Big\} \tag{45b}$$

It is noted that all stress components P_{ij}^A will produce both $\mathbf{p}_{tt}^b + P_{tt}^A$ and $\mathbf{p}_{3t}^b + P_{3t}^A$ at the edge of the cavity and the anisotropy effect is strongly related to the factor R. On approaching isotropy, equation (45) reduces to

$$\mathbf{p}_{tt}^b + P_{tt}^A = (2e\sin^2\varphi - \cos 2\varphi)P_{11}^A + \left(\frac{2}{e}\cos^2\varphi + \cos 2\varphi\right)P_{22}^A - \frac{(1+e)^2}{e}\sin 2\varphi\, P_{12}^A \tag{46a}$$

$$\mathbf{p}_{3t}^b + P_{3t}^A = (1+e)\left[\frac{\cos\varphi}{e}P_{23}^A - \sin\varphi\, P_{13}^A\right] \tag{46b}$$

Equation (46a) can be shown to be in agreement with the result of Pöschl [10, 11] given in elliptical coordinates. Equation (46b) is the same as that reported in the previous work [5] for the antiplane strain inclusion problem.

The extreme case of an elongated ellipse (crack) can be obtained by letting $e \to 0$. Retaining only the terms of order $1/e$ in equations (45), one finds

$$\mathbf{p}_{tt}^b + P_{tt}^A = \frac{R\cos\varphi}{eQ^*}[2(\cos\varphi\, P_{22}^A - \sin\varphi\, P_{12}^A) - (S_{15}/S_{11})\sin\varphi(1 + 2\cos 2\varphi)\, P_{23}^A] \tag{47a}$$

$$\mathbf{p}_{3t}^b + P_{3t}^A = \frac{R\cos\varphi}{eQ^*}[2(S_{15}/S_{44})\sin\varphi(1 + 2\cos 2\varphi) \times (\sin\varphi\, P_{12}^A - \cos\varphi\, P_{22}^A) + P_{23}^A] \tag{47b}$$

Clearly, P_{11}^A and P_{13}^A have no contribution to the stress magnification effect on an elongated cavity. As $e \to 0$

$$\left.\frac{\cos\varphi}{e}\right|_{\substack{e=0\\ \varphi=\pi/2}} = \frac{x_1}{(a^2 - x_1^2)^{1/2}}, \quad |x_1| < a \tag{48}$$

The elongated cavity then becomes a slit crack, and equations (47a) and (47b) approach

$$\mathbf{p}_{11}^b = \frac{R\,x_1}{(a^2 - x_1^2)^{1/2}}\left[\frac{S_{15}}{S_{11}}P_{23}^A - 2P_{12}^A\right] \tag{49a}$$

$$\mathbf{p}_{13}^b = \frac{R\,x_1}{(a^2 - x_1^2)^{1/2}}\left[P_{23}^A - \frac{2S_{15}}{S_{44}}P_{12}^A\right] \tag{49b}$$

with singular points at $x_1 = \pm a$. When referred to the local coordinates (r, θ) at the crack tip ($x_1 = a + r\cos\theta$, $x_2 = r\sin\theta$), equations (49a) and (49b) can be further simplified to

$$\mathbf{p}_{11}^b = R\left(\frac{a}{2r}\right)^{1/2}\left[\frac{S_{15}}{S_{11}}P_{23}^A - 2P_{12}^A\right] \tag{50a}$$

$$\mathbf{p}_{13}^b = R\left(\frac{a}{2r}\right)^{1/2}\left[P_{23}^A - \frac{2S_{15}}{S_{44}}P_{12}^A\right] \tag{50b}$$

It should be noted that the stress magnifications discussed here are based on the stress field along the boundary and are different from the stress intensity factor defined in fracture mechanics.

With the stress and strain fields known, it is a simple matter to calculate the elastic energy of the cavity. The increase of elastic energy per unit height of the system can be obtained from equation (28) with E_{ij}^0 given by (44). For biaxial tensile loading $P_{11}^A \neq 0$, $P_{22}^A \neq 0$,

$$\Delta W_I = \pi ab\left(\frac{S_{11}}{2R}\right)\left[(R + 2e)\,{P_{11}^A}^2 + \left(\frac{2}{e} + R\right){P_{22}^A}^2 - 2R\,P_{11}^A\,P_{22}^A\right] \tag{51a}$$

for transverse shear loading $P_{12}^A \neq 0$,

$$\Delta W_{II} = \pi ab\left(\frac{S_{11}}{R}\right)\left(\frac{1}{e} + 2R + e\right){P_{12}^A}^2 \tag{51b}$$

and for longitudinal shear loading $P_{13}^A \neq 0$, $P_{23}^A \neq 0$,

$$\Delta W_{III} = \pi ab\left(\frac{S_{44}}{2R}\right)\left[\left(\frac{1}{e} + R\right){P_{23}^A}^2 + (R + e)\,{P_{13}^A}^2\right] \tag{51c}$$

In the general case, the increase of the strain energy is given by

$$\Delta W = \Delta W_I + \Delta W_{II} + \Delta W_{III} + \pi ab\,S_{15}[(P_{11}^A - P_{22}^A)P_{13}^A - 2\,P_{23}^A\,P_{12}^A] \tag{52}$$

The additional terms in equation (52) represent the interaction energy between P_{12}^A and P_{23}^A, and between P_{11}^A, P_{22}^A, and P_{13}^A. It is noted that the interaction energy vanishes in an isotropic medium ($S_{15} = 0$) or for a slit crack ($e = 0$).

When isotropy is approached, equations (51) reduce to the results of Sih and Liebowitz [12]. For the special case of a slip crack ($e = 0$), equation (52) reduces to

$$\Delta W = \frac{\pi a^2}{2R}[2S_{11}({P_{22}^A}^2 + {P_{12}^A}^2) + S_{44}\,{P_{23}^A}^2] \tag{53}$$

which agrees with the expression reported by Yang and Chou [13], using the equivalence of a double-ended dislocation pileup to a slit crack.

5 The Rigid Elliptic Inhomogeneity

The perturbation of an otherwise uniform stress field P_{ij}^A due to a rigid elliptic inhomogeneity can be treated in a similar manner by introducing an equivalent inclusion with stress-free deformations E_{ij}^0. In this case $C'_{ijkl} = \infty$. Equation (27) then reduces to

$$E_{ij}^c = -E_{ij}^A \tag{54}$$

which implies that there are no strains in the inhomogeneity. The stress-free deformations E_{ij}^0 can be obtained by solving (54) with E_{ij}^c given by (35). The results obtained are

$$E_{11}^0 = \frac{1}{4 - {R_1}^2}\left\{\left[R_1 R - 2\left(\frac{R}{e} + 2\right)\right]E_{11}^A - [R_1(R + 2e) - 2\,Re]E_{22}^A\right\} - 2\frac{R\,S_{15}}{e\,S_{44}}E_{13}^A \tag{55a}$$

$$E_{22}^0 = \frac{-1}{4 - {R_1}^2}\left\{\left[R_1\left(\frac{2}{e} + R\right) - \frac{2R}{e}\right]E_{11}^A - [R_1 R - 2(2 + Re)]E_{22}^A\right\} + 2\frac{R\,S_{15}}{e\,S_{44}}E_{13}^A \tag{55b}$$

$$E_{23}^0 = -(1 + Re)\,E_{23}^A + \left(\frac{Re}{1 + R_1\,e + e^2}\right)\frac{S_{15}}{S_{11}}E_{12}^A \tag{55c}$$

$$E_{13}^0 = \frac{1}{4 - {R_1}^2}\left(\frac{R\,S_{15}}{2\,S_{11}}\right)[R_1(E_{11}^A - E_{22}^A) - \frac{2}{e}(E_{11}^A - e^2\,E_{22}^A)] - \left(1 + \frac{R}{e}\right)E_{13}^A \tag{55d}$$

$$E_{12}^0 = 2\,Re\left(\frac{S_{15}}{S_{44}}\right)E_{23}^A - \left(\frac{1 + 2R\,e + e^2}{1 + R_1\,e + e^2}\right)E_{12}^A \tag{55e}$$

The stresses inside the rigid inhomogeneity can be obtained from equations (27), (54), and (3). They are

$$
\begin{aligned}
&P_{11}+P_{11}^{A}=C_{11}\,E_{11}^{0}+C_{12}\,E_{22}^{0}+2\,C_{15}\,E_{13}^{0}\\
&P_{22}+P_{22}^{A}=C_{12}\,E_{11}^{0}+C_{11}\,E_{22}^{0}-2\,C_{15}\,E_{13}^{0}\\
&P_{33}+P_{33}^{A}=C_{15}(E_{11}^{0}+E_{22}^{0})\\
&P_{23}+P_{23}^{A}=2\,C_{44}\,E_{23}^{0}-2\,C_{15}\,E_{12}^{0}\\
&P_{13}+P_{13}^{A}=C_{15}\,(E_{11}^{0}-E_{22}^{0})+2\,C_{44}\,E_{13}^{0}\\
&P_{12}+P_{12}^{A}=-2C_{15}\,E_{23}^{0}+2C_{66}\,E_{12}^{0}
\end{aligned}
\tag{56}
$$

The rigid body displacements of the inhomogeneity are given by $U_i^c + U_i^A$, with U_i^c given by (37) and U_i^A corresponding to E_{ij}^A. More explicity,

$$
\begin{aligned}
&U_1^c+U_1^A=\omega x_2\\
&U_2^c+U_2^A=-\omega x_1\\
&U_3^c+U_3{}^A=0
\end{aligned}
\tag{57}
$$

and

$$
\begin{aligned}
\omega&=\frac{-(1-e^2)}{1+R_1\,e+e^2}\,E_{12}^{A}\\
&=\frac{1-e^2}{1+R_1\,e+e^2}\,[S_{15}\,P_{23}^{A}-(S_{11}-S_{12})\,P_{12}^{A}]
\end{aligned}
\tag{58}
$$

It is clear that the rigid body rotation ω depends only on the applied strain component E_{12}^A, which is a function of P_{23}^A and P_{12}^A. There is no rotation for a circular inhomogeneity ($e = 1$) or for the stress condition when $P_{12}^A = P_{23}^A\,S_{15}/(S_{11}-S_{12})$. On approaching isotropy, equation (58) reduces to equation (12) of reference [6], and the contribution of P_{23}^A vanishes. For the limiting case of a rigid line reinforcement

$$
\omega=-E_{12}^{A}=S_{15}\,P_{23}^{A}-(S_{11}-S_{12})\,P_{12}^{A}
\tag{59}
$$

The stresses in the matrix are equal to $\mathbf{p}_{ij} + P_{ij}^A$, in which $\mathbf{p}_{ij}$ are given by (24) and E_{ij}^0 given by (55). Explicit expressions of the stresses at the boundary of the matrix and the inhomogeneity can be obtained from equations (32), (33), and (55). For the purpose of illustration, we may examine a special case of an elongated rigid reinforcement ($e << 1$).

From equations (55), retaining only the terms of order $1/e$, we have

$$
E_{11}^{0}=\frac{-2\,R}{e}\left[\frac{1}{4-R_1{}^2}\,E_{11}^{A}+\frac{S_{15}}{S_{44}}E_{13}^{A}\right]
\tag{60a}
$$

$$
E_{22}^{0}=\frac{-2\,R}{e}\left[\frac{1}{4-R_1{}^2}\left(\frac{S_{12}}{S_{11}}\right)E_{11}^{A}-\frac{S_{15}}{S_{44}}E_{13}^{A}\right]
\tag{60b}
$$

$$
E_{13}^{0}=\frac{-R}{e}\left[\frac{1}{4-R_1{}^2}\left(\frac{S_{15}}{S_{11}}\right)E_{11}^{A}+E_{13}^{A}\right]
\tag{60c}
$$

$$
E_{23}^{0}=E_{12}^{0}=0
\tag{60d}
$$

in which E_{11}^A and E_{13}^A are related to the applied stresses by (5). Using the relations (32), (33), and (60), it can be shown that for $e << 1$,

$$
\mathbf{p}_{nn}^{b}=P_{nn}=\frac{R}{e\,S_{11}(4-R_1{}^2)}(1+\cos 2\varphi)\,E_{11}^{A}
\tag{61a}
$$

$$
\mathbf{p}_{tn}^{b}=P_{tn}=\frac{-R}{e\,S_{11}(4-R_1{}^2)}\sin 2\varphi\,E_{11}^{A}
\tag{61b}
$$

$$
\mathbf{p}_{3n}=P_{3n}=\frac{2\,R}{e\,S_{44}}\cos\varphi\,E_{13}^{A}
\tag{61c}
$$

The discontinuous stress components $\mathbf{p}_{tt}^b$, $\mathbf{p}_{3t}^b$, and P_{tt}, P_{3t} are given by

$$
\begin{aligned}
\mathbf{p}_{tt}^{b}-P_{tt}=\frac{-2\,R^3}{e\,S_{11}\,Q^*}\Bigg\{&\frac{1}{4-R_1{}^2}\left[\sin^2 2\varphi+\frac{S_{12}}{S_{11}}\cos^2\varphi\right.\\
&\left.-\frac{\sin^2\varphi}{R^2}(1+2\cos 2\varphi)\right]E_{11}^{A}-\frac{S_{15}}{S_{44}}[\cos^2 2\varphi-\sin^2\varphi]E_{13}^{A}\Bigg\}
\end{aligned}
\tag{62a}
$$

$$
P_{tt}=\frac{2R}{e\,S_{11}(4-R_1{}^2)}\sin^2\rho\,E_{11}^{A}
\tag{62b}
$$

$$
\begin{aligned}
\mathbf{p}_{3t}^{b}-P_{3t}=\frac{2\,R^3\sin\varphi}{e\,S_{44}\,Q^*}\Bigg\{&\frac{S_{15}}{S_{11}(4-R_1{}^2)}\\
&\times\left[1+(1+2\cos 2\varphi)\left(\sin^2\varphi+\frac{S_{12}}{S_{11}}\cos^2\varphi\right)\right]E_{11}^{A}\\
&+\left[1+\left(1-\frac{1}{R^2}\right)(\sin^2\varphi-3\cos^2\varphi)\cos 2\varphi\right]E_{13}^{A}\Bigg\}
\end{aligned}
\tag{62c}
$$

$$
P_{3t}=\frac{-2\,R}{e\,S_{44}}\sin\varphi\,E_{13}^{A}
\tag{62d}
$$

In the limiting case of line inhomogeneity ($e \to 0$), $\varphi \to 0, \pi$ at the ends of the major axis ($x_1 = \pm a$, $x_2 = 0$), and $\varphi \to \pm \pi/2$ at all other boundary points ($|x_1| < a$, $x_2 = 0$). Therefore, along the boundary of a rigid line inhomogeneity $\mathbf{p}_{ij}^b = 0$. On the other hand, significant stress magnification occurs at the end points of the line reinforcement, given by

$$
\mathbf{p}_{nn}^{b}=P_{nn}=\frac{2\,R}{e\,S_{11}(4-R_1{}^2)}\,E_{11}^{A}
\tag{63a}
$$

$$
\mathbf{p}_{3n}^{b}=P_{3n}=\frac{\pm\,2\,R}{e\,S_{44}}\,E_{13}^{A}
\tag{63b}
$$

$$
\mathbf{p}_{tt}^{b}=\frac{-2\,R}{e\,S_{11}}\left[\frac{S_{12}}{S_{11}(4-R_1{}^2)}\,E_{11}^{A}+\frac{S_{15}}{S_{44}}\,E_{13}^{A}\right]
\tag{63c}
$$

$$
\mathbf{p}_{tn}^{b}=P_{tn}=P_{tt}=\mathbf{p}_{3t}^{b}=p_{3t}=0
\tag{63d}
$$

The "+" sign in (63b) corresponds to the point $x_1 = a$, $x_2 = 0$, and the "−" sign to the point $x_1 = -a$, $x_2 = 0$. Equations (63c) reduce to those given in Jaswon and Bhargava [9] when isotropy is approached. Equation (63b) leads to the same isotropic solutions for the antiplane strain problem. It is noted that significant magnification depends only on the applied strain components E_{11}^A and E_{13}^A, which are functions of the applied stresses P_{11}^A, P_{22}^A, and P_{13}^A.

The increase in elastic energy per unit height of the system due to the presence of a rigid elliptic inhomogeneity can be calculated from equation (28) with E_{ij}^0 of (55). For biaxial tensile loading ($P_{11}^A, \neq 0, P_{22}^A \neq 0$),

$$
\begin{aligned}
\Delta W_I=\pi ab\Bigg\{&\frac{1}{4-R_1{}^2}\Bigg\langle\frac{1}{2}R_1R(S_{11}-S_{12})(P_{11}^{A}-P_{22}^{A})^2\\
&-2[S_{11}(P_{11}^{A}{}^2+P_{22}^{A}{}^2)+S_{12}(2+Re)P_{11}^{A}\,P_{22}^{A}]\\
&-\frac{R}{S_{11}}[e(S_{12}^2\,P_{11}^{A}{}^2+S_{11}{}^2\,P_{22}^{A}{}^2)+\frac{1}{e}\,(S_{11}\,P_{11}^{A}+S_{12}\,P_{22}^{A})^2]\Bigg\rangle\\
&-\frac{R\,S_{15}{}^2}{2\,e\,S_{44}}\,(P_{11}^{A}-P_{22}^{A})^2\Bigg\}
\end{aligned}
\tag{64}
$$

For transverse shear loading ($P_{12}^A \neq 0$),

$$\Delta W_{II} = -\pi ab \left[\frac{1+2\,R\,e+e^2}{1+R_1\,e+e^2}\,(S_{11}-S_{12}) + 2\left(\frac{R^2-1}{R}\right) e\,S_{11}\right] P_{12}^{A\,2} \tag{65}$$

And for longitudinal shear loading ($P_{23}^A \neq 0$, $P_{13}^A \neq 0$),

$$\Delta W_{III} = -\pi ab\, S_{44} \left\{ \left[\frac{(R^2-1)e}{R\,(1+R_1\,e+e^2)} + \frac{1}{2}(1+R\,e)\right] P_{23}^{A\,2} + \left[\frac{(R^2-1)(1-R_1\,e+e^2)}{R\,e\,(4-R_1{}^2)} + \frac{1}{2}\left(\frac{R}{e}+1\right)\right] P_{13}^{A\,2} \right\} \tag{66}$$

For an arbitrary external loading condition ($P_{ij}^A \neq 0$), the increase of elastic energy is

$$\Delta W = \Delta W_I + \Delta W_{II} + \Delta W_{III} + \pi ab\, S_{15} \left\{ \frac{1}{e(4-R_1{}^2)} \times \Big\langle (2\,R_1 - R)\,(e^2\,P_{11}^A - P_{22}^A) - R\,(P_{11}^A - e^2\,P_{22}^A) + [R_1\,R(R_1+2\,e) - (5\,R+4\,e+R\,e^2)](P_{11}^A - P_{22}^A) \Big\rangle P_{13}^A + 2\left(\frac{1+2\,R\,e+e^2}{1+R_1\,e+e^2} + R\,e\right) P_{23}^A\,P_{12}^A \right\} \tag{67}$$

The additional terms in equation (67) represent the interaction energy between P_{11}^A, P_{22}^A, and P_{13}^A, and between P_{12}^A and P_{23}^A. On approaching isotropy, the interaction energy in (67) vanishes, and ΔW_I, ΔW_{II}, and ΔW_{III} reduce to the expressions given by Yang and Chou [5, 6].

The increase of strain energy due to the presence of a rigid line inhomogeneity ($e = 0$) is given as

$$\Delta W = -\pi\, a^2\, R \left[\frac{1}{S_{11}(4-R_1{}^2)}\, E_{11}^{A\,2} + \frac{2}{S_{44}}\, E_{13}^{A\,2}\right] \tag{68}$$

It is noted that ΔW depends only on E_{11}^A and E_{13}^A, i.e., it is independent of the applied stresses P_{12}^A and P_{23}^A. As can be seen from the relations (5), the interaction energy between P_{11}^A, P_{22}^A, and P_{13}^A still exists for a rigid line inhomogeneity.

By comparing the results of this section with those obtained in Section 4, the following conclusions are valid. For a ⟨111⟩ slit crack, both the stress magnification and the increase of elastic energy depend only on the applied stress components P_{12}^A, P_{22}^A, and P_{23}^A; there is no interaction energy between these three stress components. For a ⟨111⟩ rigid line inhomogeneity, both the stress magnification and the increase in elastic energy depend on the applied strain components E_{11}^A and E_{13}^A (consequently on P_{11}^A, P_{22}^A, and P_{13}^A), and there is interaction energy between P_{11}^A, P_{22}^A, and P_{13}^A. In addition, the rigid body rotation of an elliptic rigid inhomogeneity depends only on the applied strain E_{12}^A, which is a function of P_{12}^A and P_{23}^A.

Acknowledgment

This work was supported by the National Science Foundation under Grant No. DMR-7915799.

References

1 Yang, H. C., and Chou, Y. T., "Generalized Plane Problems of Elastic Inclusions in Anisotropic Solids," ASME JOURNAL OF APPLIED MECHANICS, Vol. 43, 1976, pp. 424–430.

2 Eshelby, J. D., Read, W. T., and Shockley, W., "Anisotropic Elasticity With Applications to Dislocation Theory," *Acta Metallurgica*, Vol. 1, 1953, pp. 251–259.

3 Eshelby, J. D., "The Determination of the Elastic Field of an Ellipsoidal Inclusion, and Related Problems," *Proceedings of the Royal Society*, Vol. 241, Series A, 1957, pp. 376–396.

4 Eshelby, J. D., "Elastic Inclusions and Inhomogeneities," *Progress in Solid Mechanics*, Sneedon, I. N., and Hill, R., eds., North Holland Publishing Company, Vol. 2, 1961, pp. 89–140.

5 Yang, H. C., and Chou, Y. T., "Antiplane Strain Problems of an Elastic Inclusion in an Anisotropic Solid," ASME JOURNAL OF APPLIED MECHANICS, Vol. 44, 1977, pp. 437–441.

6 Yang, H. C., and Chou, Y. T., "On Rigid Elliptic Inclusions in Orthotropic Solids," ASME JOURNAL OF APPLIED MECHANICS, Vol. 45, 1978, pp. 683–685.

7 Yang, H. C., and Chou, Y. T., "The ⟨111⟩ Line Force in a Cubic Crystal," *Journal of Applied Physics*, Vol. 50, 1979, pp. 773–776, 6570.

8 Chou, Y. T., and Mitchell, T. E., "Stress and Dilatation Fields of the ⟨111⟩ Dislocation in Cubic Crystals," *Journal of Applied Physics*, Vol. 38, 1967, pp. 1533–1540.

9 Jaswon, M. A., and Bhargava, R. D., "Two-Dimensional Elastic Inclusion Problems," *Proceedings of the Cambridge Philosophical Society*, Vol. 57, 1961, pp. 669–680.

10 Pöschl, Th., "Üben eine partikuläre Losung des biharmonischen Problems für den Aussenraum der Ellipse," *Mathematische Zeitschrift*, Vol. 17, 1921, pp. 89–96.

11 Taylor, G. I., "Faults in a Material with Yields to Shear Stress While Retaining Its Volume Elasticity," *Proceedings of the Royal Society*, Vol. 145, Series A, 1934, pp. 1–18.

12 Sih, G. C., and Liebowitz, H., "Mathematical Theories of Brittle Fracture," in *Fracture—an Advanced Treastie*, Liebowitz, H., ed., Academic Press, New York, Vol. II, 1968, pp. 67–190.

13 Yang, H. C., and Chou, Y. T., "Strain Energy of ⟨111⟩ Slit Cracks in Cubic Crystals," *Materials Science and Engineering*, Vol. 17, 1975, pp. 57–62.

Maria Comninou
Department of Civil Engineering,
University of Michigan,
Ann Arbor, Mich. 48109
Mem. ASME

J. R. Barber
Department of Mechanical Engineering
& Applied Mechanics,
University of Michigan,
Ann Arbor, Mich. 48109

John Dundurs
Department of Civil Engineering,
Northwestern University,
Evanston, Ill. 60201
Fellow, ASME

Disturbance at a Frictional Interface Caused by a Plane Elastic Pulse

We consider a plane pulse striking the frictional interface between two elastic solids which are held together by compressive applied tractions and sheared. The pulse causes a disturbance involving separation or slip between the bodies, which propagates along the interface at supersonic speed. The extent of these zones is determined using a convenient graphical representation and the interface tractions are given in closed form. It is found that the results change qualitatively when the coefficient of friction exceeds a critical value.

Introduction

The interface between two bodies in unbonded elastic contact exhibits an asymmetric behavior with respect to tensile and compressive tractions, the latter being physically admissible while the former are not. Such an interface is described as "unilateral" in contrast to the "bilateral" bonded interface which can transmit normal tractions of either sign.

The interaction of a plane elastic wave with a unilateral interface has been discussed in a number of recent papers [1-3]. The results can be obtained in closed form if the angle of incidence of the wave front is such that the disturbance propagates along the interface at a speed that is supersonic with respect to the materials of both bodies (i.e., if none of the reflected or refracted waves become surface waves). For this case, solutions have been given for an incident P or SV wave of harmonic form both with and without friction at the interface [1, 2] and the results for the frictionless interface were extended to a wave of arbitrary form in [3]. The work of Miller and Tran aimed at developing approximate methods for treating more general friction laws may also be noted [4].

In this paper we consider the problem of a wave of arbitrary form incident on an interface with Coulomb friction. We assume that the static and kinetic coefficients of friction are equal. In general, we anticipate the development of regions of slip and separation at the interface and a major part of the problem is to determine the extents of these regions from the controlling inequalities which are:

(*a*) The gap must be non-negative – i.e., there is no interpenetration of material.

(*b*) Normal tractions must be compressive.

(*c*) Tangential tractions must not exceed the limiting value at which slip occurs.

(*d*) Relative slip must be in the direction opposed by the tangential tractions – i.e., negative work is done by these tractions during slip.

A simple method will be developed for determining these regions and the normal and tangential tractions at the interface. It will be shown that the behavior of the interface changes qualitatively when the coefficient of friction exceeds a certain value that depends on the elastic constants.

Formulation and Method of Solution

We consider two half spaces of different materials pressed together and sheared by tractions p^∞, q^∞ applied at infinity as shown in Fig. 1. We require $|q^\infty| < fp^\infty$ to rule out the possibility of catastrophic slip. Now suppose that a plane elastic stress pulse with velocity c_0 strikes the interface at an angle of incidence θ_0. The disturbance due to the incident pulse will propagate along the interface with velocity

$$v = c_0/\sin\theta_0 \qquad (1)$$

and we restrict attention to the case where v is supersonic with respect to both half spaces. The disturbance will therefore be stationary with respect to the dimensionless moving coordinate

$$\eta = k_0(x_1 \sin\theta_0 - c_0 t) \qquad (2)$$

where the wave number k_0 can here be regarded as the reciprocal of a characteristic length for the pulse.

Following the notation of the previous papers we denote the velocity of propagation of P and SV waves in the lower body by c_L, c_T, respectively, and use bars to distinguish the corresponding quantities for the upper body. The angles of reflection and refraction θ_i ($i=1, 2, 3, 4$) are illustrated in Fig. 1 and are related by the equation

$$\frac{\sin\theta_0}{c_0} = \frac{\sin\theta_1}{c_L} = \frac{\sin\theta_2}{c_T} = \frac{\sin\theta_3}{\bar{c}_L} = \frac{\sin\theta_4}{\bar{c}_T} \qquad (3)$$

Contributed by the Applied Mechanics Division for publication in the JOURNAL OF APPLIED MECHANICS.

Discussion on this paper should be addressed to the Editorial Department, ASME, United Engineering Center, 345 East 47th Street, New York, N.Y. 10017, and will be accepted until two months after final publication of the paper itself in the JOURNAL OF APPLIED MECHANICS. Manuscript received by ASME Applied Mechanics Division, August 1981; final revision, October, 1981.

The Bilateral Solution. We first consider the bilateral problem in which the incident pulse strikes a *bonded* interface. The solution of this problem is algebraically tedious but routine and will not be given here. Derivations for the related case of a harmonic wave can be found in most books on elastic waves – e.g., [5, 6] and the case of an incident pulse of arbitrary form can be treated in the same way or by superposition using Fourier integrals.

For the supersonic case treated here, all the reflected and refracted pulses in the bilateral solution have the same wave form as the incident pulse and hence the tractions transmitted by the interface can be written in the form

$$\sigma_{22} = -p\infty + \mathcal{A}F(\eta) \equiv N_0(\eta) \tag{4}$$

$$\sigma_{12} = q\infty + \mathcal{B}F(\eta) \equiv S_0(\eta) \tag{5}$$

where $F(\eta)$ is determined by the shape of the pulse [3] and $\mathcal{A}$, $\mathcal{B}$ are constants depending on the material properties and angle of incidence.

The Corrective Solution. The values of N_0, S_0 calculated for the bilateral problem may violate the physical conditions given in the Introduction in some region, in which case the bilateral and unilateral solutions will differ, separation or slip regions occurring in the latter. Note however that these regions do not necessarily coincide with the regions of violation in the bilateral solution.

To treat this case, we develop a corrective solution which is superposed on the bilateral solution to give the unilateral solution.

In the frictionless case [3], such a solution was obtained from results for a moving dislocation at the interface. The same method could be used here, but it proves to be algebraically more efficient to use the results for a force pair moving along the interface.

We first consider the lower body alone, with a tangential force Q and a normal (tensile) force P acting at a point O moving to the right at supersonic velocity v over the surface as shown in Fig. 2.

The solution is given by Eringen and Suhubi [7] as follows

$$\frac{\partial u_1}{\partial \eta} = \{-m_2(1+m_2^2)Q - (1+2m_1m_2-m_2^2)P\}\frac{\delta(\eta)}{\mu R} \tag{6}$$

$$\frac{\partial u_2}{\partial \eta} = \{(1+2m_1m_2-m_2^2)Q - m_1(1+m_2^2)P\}\frac{\delta(\eta)}{\mu R} \tag{7}$$

where u_1 and u_2 are the surface displacements, $\delta(\eta)$ is the Dirac delta function and

$$m_1 = \left(\frac{v^2}{{c_L}^2}-1\right)^{1/2} = \cot\theta_1, \tag{8}$$

$$m_2 = \left(\frac{v^2}{{c_T}^2}-1\right)^{1/2} = \cot\theta_2, \tag{9}$$

$$R = (1-m_2^2)^2 + 4m_1m_2 \tag{10}$$

We now apply equal and opposite forces to the upper body (see Fig. 2) producing

$$\frac{\partial \bar{u}_1}{\partial \eta} = \{\bar{m}_2(1+\bar{m}_2^2)Q - (1+2\bar{m}_1\bar{m}_2-\bar{m}_2^2)P\}\frac{\delta(\eta)}{\bar{\mu}\bar{R}} \tag{11}$$

$$\frac{\partial \bar{u}_2}{\partial \eta} = \{(1+2\bar{m}_1\bar{m}_2-\bar{m}_2^2)Q + \bar{m}_1(1+\bar{m}_2^2)P\}\frac{\delta(\eta)}{\bar{\mu}\bar{R}} \tag{12}$$

where

$$\bar{m}_1 = \cot\theta_3, \quad \bar{m}_2 = \cot\theta_4, \quad \bar{R} = (1-\bar{m}_2^2)^2 + 4\bar{m}_1\bar{m}_2 \tag{13}$$

The force pair generates a gap

$$g(\eta) = \bar{u}_2 - u_2 \tag{14}$$

and a tangential shift

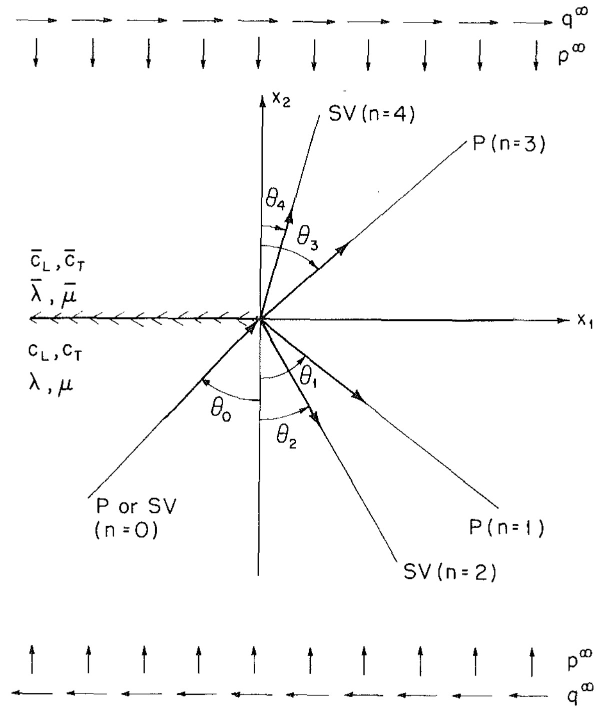

Fig. 1 Incident ($n = 0$), reflected ($n = 1, 2$), and refracted ($n = 3, 4$) waves

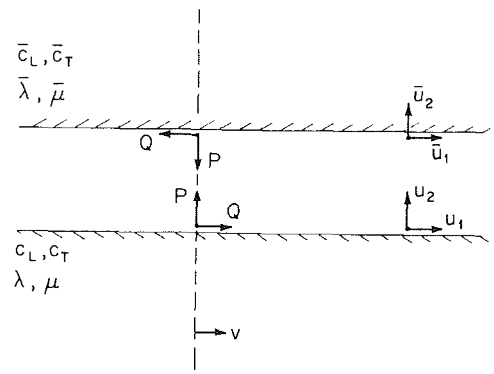

Fig. 2 Force pair moving at the interface with speed v. The two bodies are shown separated for clarity.

$$h(\eta) = \bar{u}_1 - u_1 \tag{15}$$

Note that a positive value of $\dot{h}$ corresponds to the upper body slipping to the right over the lower body.

Substituting from (6), (7), (11), (12) into (14) and (15), we have

$$\frac{\partial g}{\partial \eta} = \frac{\sin\theta_1}{\mu}(\lambda_2 P - \lambda_1 Q)\delta(\eta) \tag{16}$$

$$\frac{\partial h}{\partial \eta} = \frac{\sin\theta_1}{\mu}(\lambda_3 Q + \lambda_1 P)\delta(\eta) \tag{17}$$

where

$$\lambda_1 = \frac{\mu}{\sin\theta_1}\left[\frac{1+2m_1m_2-m_2^2}{\mu R} - \frac{1+2\bar{m}_1\bar{m}_2-\bar{m}_2^2}{\bar{\mu}\bar{R}}\right], \tag{18}$$

$$\lambda_2 = \frac{\mu}{\sin\theta_1}\left[\frac{m_1(1+m_2^2)}{\mu R} + \frac{\bar{m}_1(1+\bar{m}_2^2)}{\bar{\mu}\bar{R}}\right], \tag{19}$$

$$\lambda_3 = \frac{\mu}{\sin\theta_1}\left[\frac{m_2(1+m_2^2)}{\mu R} + \frac{\bar{m}_2(1+\bar{m}_2^2)}{\bar{\mu}\bar{R}}\right] \tag{20}$$

The dimensionless coefficients λ_1, λ_2, λ_3 also arise in the solution for an incident harmonic wave [2]. We note that λ_2, $\lambda_3 > 0$, but λ_1 may be of either sign, and vanishes for identical materials.

Equations (16) and (17) can also be cast in terms of the gap-opening velocity and slip velocity using equation (2). Thus,

$$\dot{g}(\eta)=\frac{\partial g}{\partial \eta}\frac{\partial \eta}{\partial t}=-\frac{k_0 c_0 \sin\theta_1}{\mu}(\lambda_2 P-\lambda_1 Q)\delta(\eta), \tag{21}$$

$$\dot{h}(\eta)=-\frac{k_0 c_0 \sin\theta_1}{\mu}(\lambda_3 Q+\lambda_1 P)\delta(\eta) \tag{22}$$

The delta functions in these equations show that the force system produces a purely local effect. Hence, with a more general distribution of tractions $S_1(\eta)$, $N_1(\eta)$ at the interface, $\dot{g}$, $\dot{h}$ will depend only on the local tractions of the corrective solution.

Boundary Conditions

In the unilateral solution, the interface may contain regions of stick, slip, or separation, in each of which two boundary conditions must be imposed. In addition, one or more *inequalities must be satisfied corresponding to the physical* conditions listed in the Introduction. We first consider the equality conditions.

The solution is obtained by superposing the bilateral and corrective solutions and hence the total tangential and normal tractions are

$$S(\eta)=S_0(\eta)+S_1(\eta) \tag{23}$$

$$N(\eta)=N_0(\eta)+N_1(\eta) \tag{24}$$

The bilateral solution by definition involves no slip or separation and hence the unilateral values of $\dot{g}$, $\dot{h}$ are identical with those of the corrective solution.

Equalities.

Stick. In stick zones, we have $\dot{h}=0$, $\dot{g}=0$ and hence from equations (21) and (22), $S_1=0$, $N_1=0$. In other words, the bilateral tractions are unchanged

$$S=S_0, \quad N=N_0 \tag{25}$$

Slip. In slip zones, we must have $g=0$ and hence $\dot{g}=0$,

$$\lambda_2 N_1-\lambda_1 S_1=0 \tag{26}$$

from equation (21).

The second boundary condition is

$$S=-fN sgn\dot{h} \tag{27}$$

since N must be negative. We define *conforming* slip as that for which $\lambda_1\dot{h}>0$ and hence

$$S_0+S_1=-f(N_0+N_1)sgn\lambda_1 \tag{28}$$

Solving (26) and (28) for S_1, N_1, we find

$$S_1=-\frac{\lambda_2(S_0+fN_0 sgn\lambda_1)}{\lambda_2+|\lambda_1|f} \tag{29}$$

$$N_1=-\frac{\lambda_1(S_0+fN_0 sgn\lambda_1)}{\lambda_2+|\lambda_1|f} \tag{30}$$

and hence the slip velocity is

$$\dot{h}=\frac{c_L(\lambda_1^2+\lambda_2\lambda_3)(S_0+fN_0 sgn\lambda_1)}{\mu(\lambda_2+|\lambda_1|f)} \tag{31}$$

from equation (22).

The total tractions are

$$S=S_0+S_1=\frac{f sgn\lambda_1(\lambda_1 S_0-\lambda_2 N_0)}{\lambda_2+|\lambda_1|f} \tag{32}$$

$$N=N_0+N_1=-\frac{\lambda_1 S_0-\lambda_2 N_0}{\lambda_2+|\lambda_1|f} \tag{33}$$

In *nonconforming* slip $\lambda_1\dot{h}<0$, giving a change of sign in equation (27). A similar process gives

$$S=-\frac{f sgn\lambda_1(\lambda_1 S_0-\lambda_2 N_0)}{\lambda_2-|\lambda_1|f} \tag{34}$$

$$N=-\frac{\lambda_1 S_0-\lambda_2 N_0}{\lambda_2-|\lambda_1|f} \tag{35}$$

$$\dot{h}=\frac{c_L(\lambda_1^2+\lambda_2\lambda_3)(S_0-fN_0 sgn\lambda_1)}{\mu(\lambda_2-|\lambda_1|f)} \tag{36}$$

Separation. In separation zones, the tractions S, N are zero and hence from (23) and (24)

$$S_1=-S_0, \quad N_1=-N_0 \tag{37}$$

It follows from equations (21), (22) that

$$\dot{g}=\frac{c_L}{\mu}(\lambda_2 N_0-\lambda_1 S_0) \tag{38}$$

$$\dot{h}=\frac{c_L}{\mu}(\lambda_3 S_0+\lambda_1 N_0) \tag{39}$$

Inequalities. The physical conditions leading to inequalities serve to determine the extents of the various zones.

Stick. *In stick zones, we require that the normal tractions* be nontensile and the shear tractions do not exceed the value at slip, i.e.,

$$N\le 0, \tag{40}$$

$$|S|\le -fN \tag{41}$$

The condition (41) includes (40) and we have already shown that in stick zones the bilateral tractions are unchanged. Hence stick is possible if and only if

$$-fN_0\ge S_0\ge fN_0 \tag{42}$$

Conforming Slip. In conforming slip we still require nontensile normal tractions and hence

$$\lambda_1 S_0-\lambda_2 N_0\ge 0 \tag{43}$$

since

$$\lambda_2+|\lambda_1|f>0 \tag{44}$$

It is convenient to define the ratio

$$\hat{f}=\frac{\lambda_2}{|\lambda_1|} \tag{45}$$

in terms of which (43) can be written

$$S_0 sgn\lambda_1\ge \hat{f}N_0 \tag{46}$$

Furthermore, the definition of conforming slip requires $\lambda_1\dot{h}>0$ and hence from (31), (44),

$$S_0 sgn\lambda_1>-fN_0 \tag{47}$$

since

$$\lambda_1^2+\lambda_2\lambda_3>0 \tag{48}$$

Notice that both conditions (46) and (47) must be satisfied in a conforming slip zone. Clearly (46) is the stronger if $N_0>0$ and (47) if $N_0<0$, since $f, \hat{f}>0$.

Nonconforming Slip. In nonconforming slip, the expressions (34)–(36) for S, N, and $\dot{h}$ all involve the multiplier $(\lambda_2-|\lambda_1|f)$ which can be of either sign. We therefore consider the two cases separately.

(*a*) $f<\hat{f}$

If $f<\hat{f}$ (i.e., $\lambda_2>|\lambda_1|f$), condition (40) gives

$$S_0 sgn\lambda_1\ge \hat{f}N_0 \tag{49}$$

as in conforming slip, but we now need $\lambda_1\dot{h}<0$ which implies

$$S_0 sgn\,\lambda_1<fN_0 \tag{50}$$

using (36).

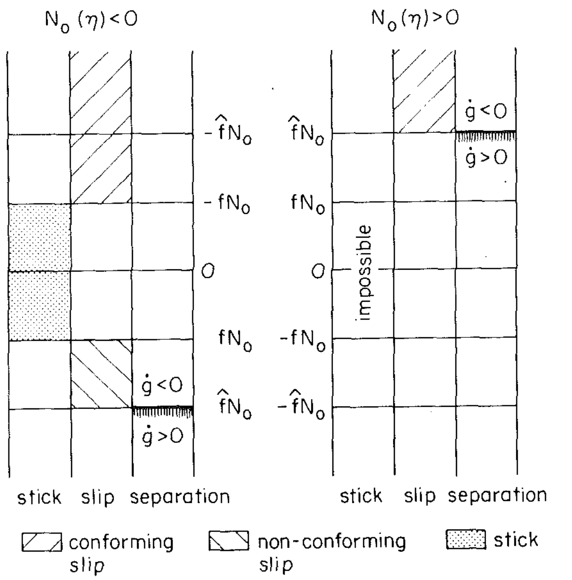

Fig. 3 Permissible ranges of $S_0(\eta)\, sgn\lambda_1$ for stick, slip, or gap for $f<\hat{f}$

Combining (49) and (50) we have

$$fN_0 > S_0 sgn\lambda_1 \geq \hat{f}N_0 \tag{51}$$

and hence nonconforming slip is only possible if $N_0 \leq 0$, since $f<\hat{f}$.

(*b*) $f>\hat{f}$

Applying similar arguments to the case $f>\hat{f}$, we find

$$fN_0 < S_0 sgn\lambda_1 \leq \hat{f}N_0 \tag{52}$$

Once again, nonconforming slip is only possible for $N_0 \leq 0$.

Separation. In the separation zone, we require that the gap $g \geq 0$. The equality conditions give an expression for $\dot{g}$ only, and hence we cannot deduce unique conditions on S_0, N_0 to be satisfied throughout the separation zone.

However it may be possible to determine the point at which separation starts, since the crack must then have a positive opening velocity ($\dot{g} \geq 0$) and hence a negative slope ($dg/d\eta \leq 0$). From equation (38) this implies

$$S_0 sgn\lambda_1 \leq \hat{f}N_0 \tag{53}$$

At the other end of the zone where the gap is closing we must have

$$S_0 sgn\lambda_1 \geq \hat{f}N_0 \tag{54}$$

If one of these two points can be determined uniquely, the other can always be found from the condition

$$\int_L \frac{dg}{d\eta}\, d\eta = 0 \tag{55}$$

where L is the extent of the separation zone.

Graphical Representation. The inequality conditions developed in the foregoing are all expressed in terms of the relationship between $S_0(\eta) sgn\lambda_1$ and $N_0(\eta)$ and can conveniently be summarized graphically.

(*a*) $f<\hat{f}$

We first consider the case $f<\hat{f}$ illustrated in Fig. 3. The diagrams show the ranges of the function $S_0 sgn\lambda_1$ for which stick, conforming, or nonconforming slip or gap are permitted. For example, stick is permitted only in the range

$$fN_0 \leq S_0 sgn\lambda_1 \leq -fN_0 \quad \text{for} \quad N_0 < 0 \tag{56}$$

These states cover all possible values of $S_0 sgn\lambda_1$ and are mutually exclusive, so we can uniquely define the state at any given point on the interface. The procedure is best explained through an example. When the bilateral problem is solved, we find N_0 as a function of η and hence plot the boundaries $\pm fN_0$, $\pm\hat{f}N_0$ as shown in Fig. 4. Notice that N_0 must tend to $-p\infty$ away from the pulse, but otherwise the shape chosen has no particular significance except as constrained by (4) and (5).

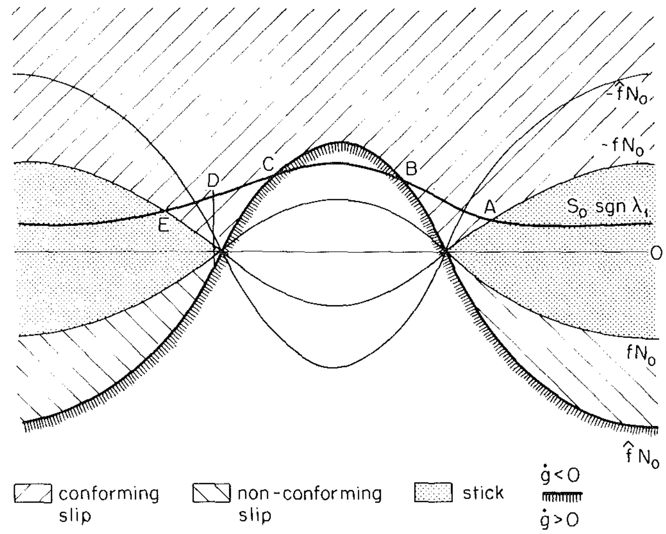

Fig. 4 Graphical determination of slip and separation zones for a typical example, $f<\hat{f}$

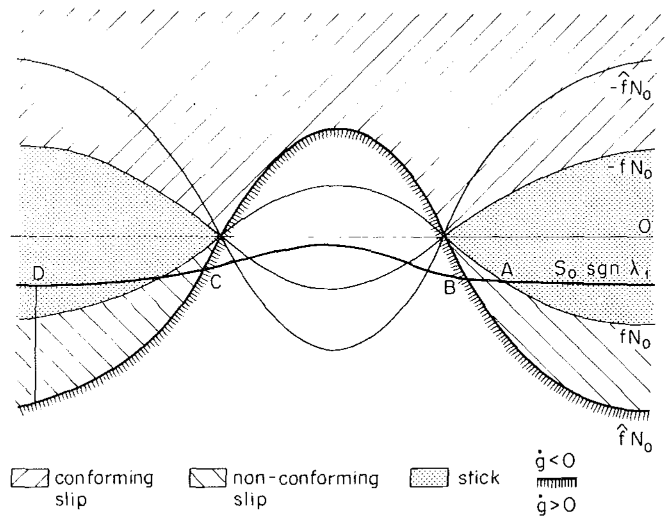

Fig. 5 Second example for $f<\hat{f}$ exhibiting a transition from separation to stick at D

We next plot the value of $S_0 sgn\lambda_1$ on the same graph. Away from the pulse, this function tends to $q\infty\, sgn\lambda_1$ which must be between $\pm fN_0$. To the right of point A in Fig. 4, the interface must stick, while between A and B only conforming slip is possible. To the left of B, a separation zone is developed. The gap increases from B to C where $S_0 sgn\lambda_1$ is below the line $\hat{f}N_0$ and then starts to shrink. The closure point, D, is found from the condition that the gap there is zero. Thus, we choose D such that the algebraic sum of the areas between the lines $S_0 sgn\lambda_1$ and $\hat{f}N_0$ is zero. The location of D shows that in this case the interface passes from separation to conforming slip at the closure point and the interface sticks again at E.

A second example is illustrated in Fig. 5. There, nonconforming slip is developed in AB and the closure point D lies in the stick zone, indicating a direct transition from separation to stick. Note, however, that a direct transition from stick to separation is not possible.

It is clear from these examples that the controlling inequalities enable the arrangement of zones at the interface

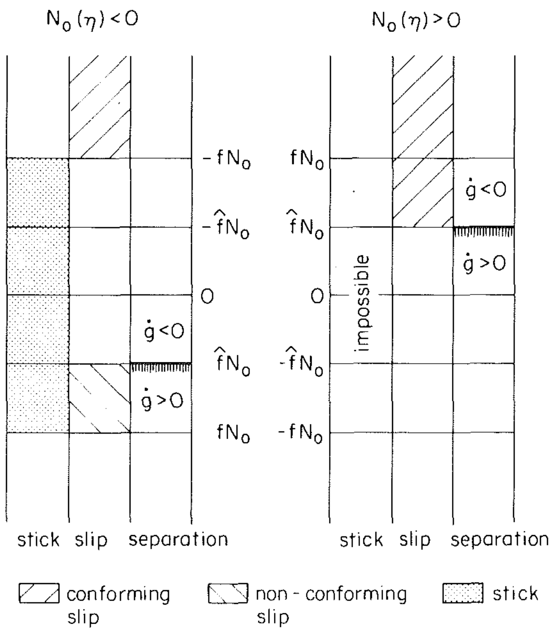

Fig. 6 Permissible ranges of $S_0(\eta)\, sgn\lambda_1$ for stick, slip, or gap, $f > \hat{f}$

to be determined simply and uniquely once the bilateral solution is known. The appropriate tractions and displacement velocities at the interface can then be written down using equations (23)-(39).

(*b*) $f > \hat{f}$

Corresponding results for the case $f > \hat{f}$ are shown in Figs. 6 and 7. From Fig. 6, we note that the ranges defined by the inequalities are not now mutually exclusive: three ranges overlap in $\hat{f}N_0 \geq S_0 sgn\lambda_1 \geq fN_0$ (which only exists for $N_0 < 0$). This suggests that certain problems may not have unique solutions. For the example shown in Fig. 7, stick must occur to the right of A, but the conditions in AB could be stick, nonconforming slip, or separation. Furthermore, no inconsistency arises in the regions to the left of B, whichever of these states is assumed.

We notice from equation (38) that the gap will start to open with a nonzero velocity unless the separation zone starts at A where $S_0 sgn\lambda_1 = \hat{f}N_0$. The condition that the gap opens smoothly can therefore be used to impose uniqueness on the problem and it has the effect of permitting only separation in the overlapping range.

We note, however, that no physical principles are violated by a velocity jump at the transition to separation, and indeed a jump in tangential velocity is implied by the expression for $\dot{h}$, (39), whatever conditions are assumed between A and B (for $f < \hat{f}$, continuity of both $\dot{g}$ and $\dot{h}$ is automatically satisfied at the transitions from stick to slip and slip to separation if the incident pulse has no step changes). An alternative hypothesis is that stick, once established continues until the inequalities make it inadmissible, i.e., that the transition from stick to separation occurs at B in Fig. 7.

A second paradoxical result for the case $f > \hat{f}$ is illustrated by the example in Fig. 8. If $q\infty$ lies in the range $-fp\infty < q\infty < -\hat{f}p\infty$, it is possible that a gap opened by the pulse never closes, since $S_0 sgn\lambda_1$ need never pass above the line $\hat{f}N_0$. The solids will then be separated to infinity on the left and are "unzipped" by the pulse, despite the presence of the compressive traction $p\infty$. This peculiar result can be traced back to the results for the moving force pair, equations (21) and (22). If P and Q are positive there is a limiting ratio of Q/P equal to $\hat{f}$ which, if exceeded, causes the force pair to leave a gap behind it, although the normal component P is tensile.

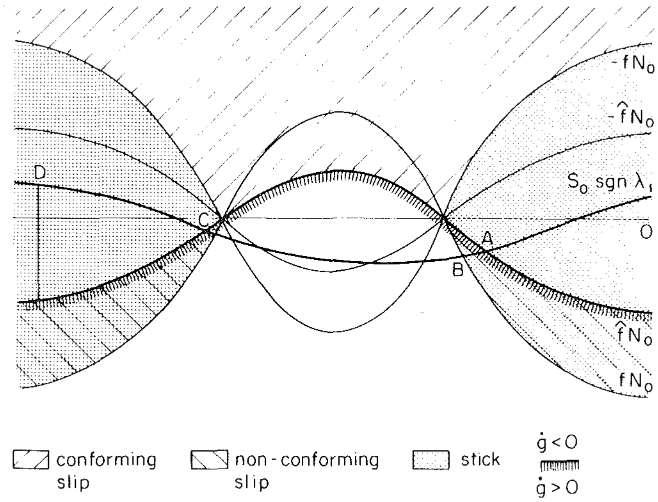

Fig. 7 Determination of slip and separation zones for $f > \hat{f}$

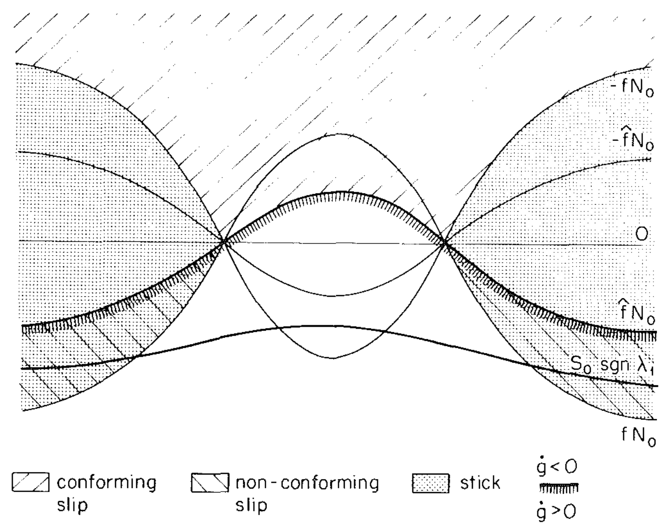

Fig. 8 Example for $f > \hat{f}$ in which the gap cannot close

In view of these various results, it is relevant to ask whether the condition $f > \hat{f}$ corresponds to any realistic combination of material properties. For similar materials, λ_1 is zero and hence $\hat{f}$ is infinite. Values of $\hat{f}$ that might be exceeded by a realistic coefficient of friction, can be obtained by choosing materials with significantly differing elastic moduli and an angle of incidence such that the largest of θ_i is close to $\pi/2$.

Acknowledgment

Support by the National Science Foundation under the grant CME 8019281 awarded to one of the authors (MC) is gratefully acknowledged.

References

1 Comninou, M., and Dundurs, J., "Reflexion and Refraction of Elastic Waves in Presence of Separation," *Proc. Roy. Soc.*, Vol. A356, 1977, pp. 509-528.

2 Comninou, M., and Dundurs, J., "Interaction of Elastic Waves With a Unilateral Interface," *Proc. Roy. Soc.*, Vol. A368, 1979, pp. 141-154.

3 Dundurs, J., and Comninou, M., "Interface Separation Caused by a Plane Elastic Wave of Arbitrary Form," *Wave Motion*, Vol. 1, 1979, pp. 17-23.

4 Miller, R. K., and Tran, H. T., "Reflection, Refraction and Absorption of Elastic Waves at a Frictional Interface: P and SV Motion," ASME Journal of Applied Mechanics, Vol. 48, 1981, pp. 155-160.

5 Achenbach, J. D., *Wave Propagation in Elastic Solids*, North Holland, Amsterdam, 1973.

6 Ewing, W. M., Jardetzky, W. S., and Press, F., *Elastic Waves in Layered Media*, McGraw-Hill, New York, 1957.

7 Eringen, A. C., and Suhubi, E. S., *Elastodynamics*, Academic Press, New York, Vol. II., 1957, p. 582.

P. Burgers
Assistant Professor,
Department of Mechanical Engineering
and Applied Mechanics,
University of Pennsylvania,
Philadelphia, Pa. 19104
Assoc. Mem. ASME

J. P. Dempsey
Assistant Professor,
Department of Civil and Environmental
Engineering,
Clarkson College of Technology,
Potsdam, N.Y. 13676
Assoc. Mem. ASME

Two Analytical Solutions for Dynamic Crack Bifurcation in Antiplane Strain

A semi-infinite crack is subjected to constant magnitude, dynamic antiplane loading at time $t = 0$. At the same instant the crack is assumed to bifurcate and propagate normal to its original plane or to propagate without branching. For constant crack-tip velocities the stresses and particle velocity are functions of r/t and θ only, which allows Chaplygin's transformaton and conformal mapping to be used to obtain two Riemann-Hilbert problems which can be solved analytically. Expressions for the elastodynamic Mode III stress-intensity factors are then computed as functions of the crack-tip velocity and some conclusions concerning crack initiation are drawn.

1 Introduction

Crack bifurcation is observed frequently in brittle materials. It is therefcre of interest to analyze the situation when a single crack divides into two cracks. Eventually we would like to be able to formulate a criterion for bifurcation so that these events could be reliably predicted. Since the general Mode I problem is extremely difficult, two cases in antiplane strain for which the complete solution for the relevant stress component can be found, will be presented. These solutions will solve some of the difficulties found in attempting the Mode I analysis, and will open the way for the solution of some more relevant problems. They will also serve as good check cases for numerical calculations.

2 Description of Problem

The problem to be considered is as follows: initially in a stress-free, infinite, linear-elastic, isotropic full space, there is a straight, semi-infinite sharp crack parallel to the x-axis with the origin of the coordinate system at the crack tip as in Fig. 1. At time $t = 0$, a uniform stress, $\sigma_{\theta z} = \tau_0$, is applied to the faces of the semi-infinite crack (from now on referred to as the original crack), where τ_0 is a constant. At the same instant, two cracks propagate out of the original crack tip, each with crack tip velocity, v, making an angle $\pm\kappa\pi$ with the x-axis. In [1] a method was proposed to solve this problem and although the problem for arbitrary values of κ is not solved here, we use the notation in [1] so that connection can be made with the results presented there.

With the polar coordinate system as in Fig. 1, the governng equilibrium equation is

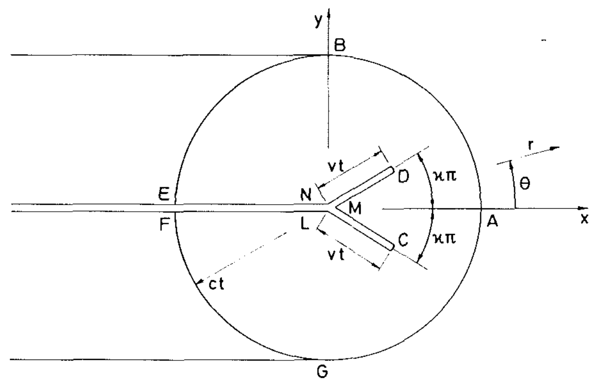

Fig. 1 Bifurcation of a semi-infinite crack subjected to dynamic loading in antiplane strain

$$\frac{\partial^2 w}{\partial r^2} + \frac{1}{r}\frac{\partial w}{\partial r} + \frac{1}{r^2}\frac{\partial^2 w}{\partial \theta^2} = \frac{1}{c^2}\frac{\partial^2 w}{\partial t^2}, \qquad (2.1)$$

where w is the displacement in the z direction and c is the shear wave velocity for the material. For ease of reference the same labels for important geometrical points in the problem are used as in [1].

The boundary conditions for loading case a are

$$\sigma_{\theta z} = \tau_0 H(t), \quad \theta = \pm\pi, \quad r > 0, \qquad (2.2)$$

$$\sigma_{\theta z} = 0, \quad \theta = \pm\kappa\pi, \quad 0 < r < vt, \qquad (2.3)$$

where $H(t)$ is the Heaviside step function. Two plane waves and a cylindrical wave are generated by this loading as shown in Fig. 1. Outside the wavefronts, $w = 0$ and in the region behind the plane waves, but outside the cylindrical wave, the particle velocity is $\dot{w} = \pm c\tau_0/\mu$ for $y \gtrless 0$. The jump conditions across the cylindrical wave front are

$$[\sigma_{rz}] + c\rho[\dot{w}] = 0, \qquad (2.4)$$

$$[\dot{w}] + c[\partial w/\partial r] = 0, \qquad (2.5)$$

Contributed by the Applied Mechanics Division for publication in the JOURNAL OF APPLIED MECHANICS.

Discussion on this paper should be addressed to the Editorial Department, ASME, United Engineering Center, 345 East 47th Street, New York, N.Y. 10017, and will be accepted until two months after final publication of the paper itself in the JOURNAL OF APPLIED MECHANICS. Manuscript received by ASME Applied Mechanics Division, July, 1981.

where ρ is the mass density of the material. To first order in stresses and particle velocity, the conditions immediately behind the wavefronts are the same as those for the problem where no bifurçaton cracks are present. This implies that stresses and velocities are continuous across the cylindrical wave front, i.e.

$$\dot{w}=0 \quad \text{on} \quad r=ct, \quad -\frac{\pi}{2} \le \theta < \frac{\pi}{2}, \tag{2.6}$$

$$\dot{w}=c\tau_0/\mu \quad \text{on} \quad r=ct, \quad \frac{\pi}{2} < \theta \le \pi, \tag{2.7}$$

$$\dot{w}=-c\tau_0/\mu \quad \text{on} \quad r=ct, \quad -\pi \le \theta < -\frac{\pi}{2}. \tag{2.8}$$

The problem is obviously antisymmetric about the x-axis with respect to displacements, so that only the upper half plane need be considered.

From the jump conditions, we also conclude

$$\frac{\partial \dot{w}}{\partial \theta}=0 \quad \text{on} \quad r=ct. \tag{2.9}$$

On the original crack faces

$$\sigma_{\theta z}=\tau_0 H(t), \quad \theta=\pi, \quad r>0, \tag{2.10}$$

which implies

$$\frac{\partial \dot{w}}{\partial \theta}=0, \quad \theta=\pi, \quad r>0. \tag{2.11}$$

Similarly, for traction-free surfaces of the bifurcation cracks,

$$\frac{\partial \dot{w}}{\partial \theta}=0, \quad \theta=\kappa\pi, \quad r>0. \tag{2.12}$$

Note, however, that in the final solution the actual traction conditions must be met, not just the conditions on the time derivative of tractions since any constant tractions on the crack surface will satisfy the condition that time derivatives of tractions be zero.

Following [1], we note that the problem can be written in terms of the two variables, θ and $s = r/t$, since the particle velocity is self-similar. Hence, use of Chaplygin's transformation (see [1] for details) maps the physical plane into a semi-infinite strip in the γ-plane as shown in Fig. 2, where

$$\gamma=\beta+i\theta = \cosh^{-1}(c/s)+i\theta. \tag{2.13}$$

The equilibrium equations transform into Laplace's equation for $\dot{w}$ in terms of independent variables β and θ. This implies

$$\dot{w}=\mathrm{Re}\, G(\gamma), \tag{2.14}$$

where G is an analytic function of γ.

The solutions for the particular cases $\kappa = 1/2, 0$ will now be given. In these cases the stress $\sigma_{\theta z}$ along the crack line ahead of the crack tip can be worked out explicitly, which is unusual in dynamics. We consider first the case $\kappa = 1/2$.

3 Solution for $\kappa = 1/2$

Following [1], the strip is conformally mapped into the upper half plane in the ζ-plane as in Fig. 3, where $\zeta = \xi + i\eta$. In this case

$$\xi_M=v/c, \quad \xi_N=v/c, \quad \xi_B\to\infty, \quad \xi_D=0, \tag{3.1}$$

and the points A and E have been mapped into the points -1 and $+1$, respectively. The conformal mapping gives

$$\zeta^2=1-(1-v^2/c^2)\tanh^2(\gamma-i\pi) \tag{3.2}$$

Equating $F(\zeta)$ to $G(\gamma)$, we have $\dot{w} = \mathrm{Re}\, F(\zeta)$, where $F(\zeta)$ is an analytic function in ζ. The boundary conditions on the real axis in the upper half ζ-plane become

$$-\infty<\xi\le-\xi_M: \quad \dot{w}=0 \qquad \to \frac{\partial \dot{w}}{\partial \xi}=0, \tag{3.3}$$

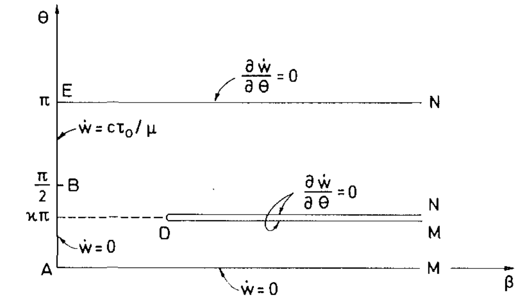

Fig. 2 The $\gamma = \beta + i\theta$ plane

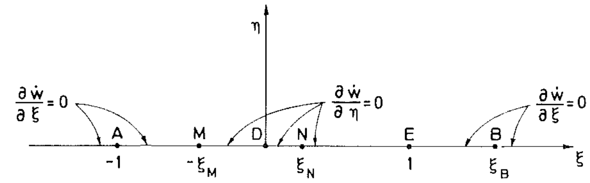

Fig. 3 The $\zeta = \xi + i\eta$ plane

$$-\xi_M<\xi<1: \quad \dot{\sigma}_{\theta z}=0 \qquad \to \frac{\partial \dot{w}}{\partial \eta}=0, \tag{3.4}$$

$$1<\xi<\xi_B: \quad \dot{w}=\frac{c\tau_0}{\mu}, \qquad \frac{\partial \dot{w}}{\partial \theta}=0 \to \frac{\partial \dot{w}}{\partial \xi}=0, \tag{3.5}$$

$$\xi_B<\xi<\infty: \quad \dot{w}=0, \qquad \frac{\partial \dot{w}}{\partial \theta}=0 \to \frac{\partial \dot{w}}{\partial \xi}=0. \tag{3.6}$$

These boundary conditions together with $\dot{w} = \mathrm{Re}\, F(\zeta)$ pose a standard Riemann-Hilbert problem in the ζ-plane once the definition of $F(\zeta)$ is extended to the lower half ζ-plane. The most suitable way to do this is to require for ζ in the lower half ζ-plane that $F'(\zeta) = -\overline{F'(\bar{\zeta})}$, where the bar denotes complex conjugate (see Muskhelishvili [2] chapter 13 for a discussion of a similar analytic continuation in the plane-strain half-plane problem). This implies that the boundary conditions in equations (3.3), (3.5)–(3.6) are satisfied automatically. The problem is then to find the analytic function $F'(\zeta)$ such that for $\zeta = \xi$, $-\xi_M < \xi < 1$, $F'^{+}(\zeta) = F'^{-}(\zeta)$ where superscript $+$ or $-$ means the limit of the function as $\zeta \to \xi + i0$ or $\zeta \to \xi - i0$, respectively.

The Riemann-Hilbert problem is not completely specified however until the behavior of $F'(\zeta)$ at all singular points and as $\zeta \to \infty$ is specified. This can be done by requiring that when $F'(\zeta)$ is integrated to give $F(\zeta)$, Re $F(\zeta)$ satisfies the conditions on the ξ-axis and that at the crack tip, the time derivative of stresses have the appropriate singularity. An asymptotic analysis of the deformation fields about a dynamically propagating crack tip, similar to that given by Freund and Clifton [3] reveals that terms like $\dot{\sigma}_{\theta z}$ must be singular as distance from the crack tip to the power $-3/2$.

The solution to the Riemann-Hilbert problem is of the form

$$F'(\zeta) = (\zeta-1)^{-1/2}(\zeta+v/c)^{-1/2}\zeta^{-n}, \tag{3.7}$$

where n is an integer. Any combination of terms that satisfies the conditions given in the foregoing must in general appear in the solution. When $n = 0$, the conditions on $\dot{w}$ can be met, but $\dot{\sigma}_{\theta z}$ is only square-root singular at the crack tip. To obtain the correct singularity at the crack tip, there must be a term with $n = 2$. To meet the conditions on $\dot{w}$ with this term, a term with $n = 1$ must also be included. The appropriate form for $F'(\zeta)$ is

$$F'(\zeta)=i(\zeta-1)^{-1/2}(\zeta+v/c)^{-1/2}(A+B/\zeta+C/\zeta^2). \tag{3.8}$$

The expression for $F'(\zeta)$ given in equation (3.31) of [1] for

$\kappa = 1/2$ agrees with equation (3.8) only if $B = C = 0$. However, B and C must be nonzero to obtain the necessary singularities in the particle velocity and the time derivative of stress. For this reason the results obtained in [1] for $\kappa = 1/2$ are incorrect. Finally, note that terms involving ζ^n for $n \geq 1$ or $n \leq -3$ cannot be admitted in equation (3.8) without either violating the boundary conditions or introducing inadmissible singularities.

Integrating equation (3.8) with respect to ζ, we obtain

$$F(\zeta) = iA\, ln[(\zeta-1)^{1/2} + (\zeta+v/c)^{1/2}]^2$$
$$+ iC(c/v)(\zeta-1)^{1/2}(\zeta+v/c)^{1/2}\zeta^{-1}$$
$$- i[2vB-(c-v)C](c/v)^{1/2}(2v)^{-1}$$
$$\sin^{-1}\left[\frac{2v/c+(1-v/c)\zeta}{(1+v/c)\zeta}\right] + D, \tag{3.9}$$

where D = constant. The term involving inverse sine gives rise to a logarithmic singularity in $\dot{w}$ as $r \rightarrow vt$. Therefore we require

$$B = C(c-v)/2v. \tag{3.10}$$

Matching the condition $\dot{w} = c\tau_0/\mu$ for $1 < \xi < \xi_B$ requires

$$A = c\tau_0/\mu\pi, \quad D = c\tau_0/\mu. \tag{3.11}$$

To determine the stress-intensity factor we must work from $\dot{\sigma}_{\theta z}$. In general,

$$\frac{\partial \dot{w}}{\partial \theta} = \text{Re}\left[F'(\zeta)\,\frac{d\zeta}{d\gamma}\,\frac{\partial \gamma}{\partial \theta}\right], \tag{3.12}$$

so that

$$\frac{\partial \dot{w}}{\partial \theta} = Im\left\{\frac{(\zeta-v/c)(\zeta+v/c)^{1/2}(1+\zeta)^{1/2}}{\zeta(1-v^2/c^2)^{1/2}}\left[\frac{c\tau_0}{\mu\pi}\right.\right.$$
$$\left.\left. + C\left(\frac{(\zeta+v/c)-(v/c)(\zeta-1)}{2(v/c)\zeta^2}\right)\right]\right\} \tag{3.13}$$

For $\theta = \pi/2$ and $r > vt$, we find

$$\zeta = i\left(\frac{s^2-v^2}{c^2-s^2}\right)^{1/2}, \tag{3.14}$$

and that

$$\dot{\sigma}^a_{\theta z} = \frac{\mu}{r}\,\frac{\partial \dot{w}}{\partial \theta}$$
$$= \left(\frac{c-v}{2v}\right)^{1/2}\left[\frac{\tau_0}{\pi(t-r/c)^{1/2}(r/v-t)^{1/2}}\right.$$
$$\left. -\mu C\left(\frac{c+v}{2v^2}\right)\frac{(t-r/c)^{1/2}}{(r/v-t)^{3/2}}\right] \tag{3.15}$$

where the superscript a on $\sigma_{\theta z}$ indicates loading case a.

Integrating with respect to time from $t' = r/c$ to $t' = t$ we obtain

$$\sigma^a_{\theta z}(r > vt, \theta = \pi/2) =$$
$$-\mu C(c/v+1)v^{-1}2^{-1/2}(c/v-1)^{1/2}\left(\frac{t-r/c}{r/v-t}\right)^{1/2}$$
$$+ 2^{-1/2}(c/v-1)^{1/2}[2(\tau_0/\pi)$$
$$+ \mu C(c/v+1)v^{-1}]\tan^{-1}\left(\frac{t-r/c}{r/v-t}\right)^{1/2}. \tag{3.16}$$

We note that as $r \rightarrow vt$

$$\tan^{-1}\left(\frac{t-r/c}{r/v-t}\right)^{1/2} \simeq \frac{\pi}{2} - \left(\frac{r/v-t}{t-r/c}\right)^{1/2} + \ldots\ldots \tag{3.17}$$

From the asymptotic analysis of the deformation field about a dynamically propagating crack tip, we see that it is terms like $(r-vt)^n$ where n is an integer such that $n \geq 0$ which causes crack-face tractions to exist. In this case, the only term of this form is the constant term and for zero crack-face tractions we require

$$\mu C(c/v+1)v^{-1} = -2\tau_0/\pi. \tag{3.18}$$

The stress $\sigma_{\theta z}$ then has the very simple form

$$\sigma^a_{\theta z}(r > vt, \theta = \pi/2) = \frac{\tau_0}{\pi}2^{1/2}(1-v/c)^{1/2}\left(\frac{ct-r}{r-vt}\right)^{1/2}. \tag{3.19}$$

The stress-intensity factor for $\kappa = 1/2$ is

$$K^a_{\text{III}} = \lim_{r\rightarrow vt}(2\pi)^{1/2}(r-vt)^{1/2}\sigma_{\theta z}(r > vt, \theta = \pi/2)$$
$$= 2\pi^{-1/2}\tau_0(ct)^{1/2}(1-v/c) \tag{3.20}$$

We now consider loading on both the original and the bifurcation crack faces (case b). The boundary conditions are given by equation (2.2) and

$$\sigma_{\theta z} = -\tau_0 H(t), \quad \theta = \pi/2, \quad 0 < r < vt, \tag{3.21}$$

where the negative sign ensures that the loading on $\theta = \pi/2$ and $\theta = \pi$ has the same sense. In the limit as $r \rightarrow vt$, the constant term in equation (3.16) must now equal $-\tau_0$. The stress-intensity factor for $\kappa = 1/2$ for case b is

$$K^b_{\text{III}} = 2\pi^{-1/2}\tau_0(ct)^{1/2}[(1-v/c)$$
$$+ 2^{1/2}(v/c)^{1/2}(1-v/c)^{1/2}]. \tag{3.22}$$

By superposition, the stress-intensity factor for $\kappa = 1/2$ and the loading on the new crack faces only (case c) is [from equations (3.20) and (3.22)]

$$K^c_{\text{III}} = 2(2/\pi)^{1/2}\tau_0(ct)^{1/2}(v/c)^{1/2}(1-v/c)^{1/2}. \tag{3.23}$$

4 Solution for $\kappa = 0$

We now consider the case when the crack propagates straight ahead without bifurcating. The stress-intensity factor for this problem is incorrectly given in [1]. In the mapping from the γ- to the ζ-plane

$$\xi_M = 0, \quad \xi_N = v/c, \quad \xi_B = c/v, \quad \xi_D = 0, \quad \xi_A = -1, \quad \xi_E = 1, \tag{4.1}$$

so that

$$\zeta = \frac{1+(v/c)\cosh(\gamma - i\pi)}{(v/c)+\cosh(\gamma - i\pi)}. \tag{4.2}$$

The boundary conditions in the ζ-plane are the same as for the case $\kappa = 1/2$ with the foregoing values of ξ_M, ξ_N and ξ_B. The solution to the Riemann-Hilbert problem is

$$F'(\zeta) = \frac{i(A+B/\zeta)}{(\zeta-c/v)}\,\frac{(c/v)^{1/2}(c/v-1)^{1/2}}{\zeta^{1/2}(\zeta-1)^{1/2}}. \tag{4.3}$$

Note the extra term C/ζ^2 that appeared in equation (3.8) does not appear here as it would cause the stresses at the crack tip to be more than square-root singular. Integrating, we obtain

$$F(\zeta) = -i(A+Bv/c)\,ln\left\{\frac{[\zeta^{1/2}(1-v/c)^{1/2}+(\zeta-1)^{1/2}]^2}{[(1-v/c)^{1/2}+1]^2(\zeta-c/v)}\right\}$$
$$- i2(1-v/c)^{1/2}B(\zeta-1)^{1/2}\zeta^{-1/2}. \tag{4.4}$$

Satisfying the condition on $\dot{w}$ on the ξ-axis for $1 < \xi < \xi_B$, gives

$$A + Bv/c = -c\tau_0/\mu\pi. \tag{4.5}$$

To determine the stress-intensity factor we need to find $\dot{\sigma}_{\theta z}$. The relation in equation (3.12) gives

$$\frac{\partial \dot{w}}{\partial \theta} = Im\left\{\frac{(A+B/\zeta)(\zeta-v/c)(1+\zeta)^{1/2}}{(v/c)(1+v/c)^{1/2}(\zeta-c/v)\zeta^{1/2}}\right\}. \tag{4.6}$$

For $\theta = 0$ and $r > vt$, we find

$$\zeta = -\left(\frac{1-v/s}{c/s-v/c}\right), \tag{4.7}$$

and that

$$\dot{\sigma}^a_{\theta z} = \mu B(1-v^2/c^2)\,\frac{(ct-r)^{1/2}}{(r-vt)^{3/2}}$$

$$-\mu(A+Bv/c)\,\frac{(ct-r)^{1/2}}{ct\,(r-vt)^{1/2}}. \tag{4.8}$$

Integrating with respect to time from $t' = r/c$ to $t' = t$ we obtain

$$\sigma^a_{\theta z}(r>vt,\theta=0) = \mu B 2v^{-1}(1-v^2/c^2)\left(\frac{ct-r}{r-vt}\right)^{1/2}$$

$$-\mu 2(vc)^{-1/2}(A+Bc/v)\tan^{-1}\left(\frac{t-r/c}{r/v-t}\right)^{1/2}$$

$$+\mu 2c^{-1}(A+Bv/c)\tan^{-1}\left(\frac{ct-r}{r-vt}\right)^{1/2}. \tag{4.9}$$

For zero loads on the crack faces that have extended out from the original crack tip, we require, using the discussion after equation (3.17),

$$-\mu 2(vc)^{-1/2}(A+Bc/v)\,\pi/2$$

$$+\mu 2c^{-1}(A+Bv/c)\,\pi/2 = 0. \tag{4.10}$$

Using equations (4.5) and (4.10) we have

$$A+Bc/v = -(v/c)^{1/2}c\tau_0/\mu\pi,$$

$$B = (\tau_0/\mu\pi)\,v(1-(v/c)^{1/2})/(1-v^2/c^2). \tag{4.11}$$

Then

$$\sigma^a_{\theta z}(r>vt,\theta=0) =$$

$$2\frac{\tau_0}{\pi}\left\{(1-(v/c)^{1/2})\left(\frac{ct-r}{r-vt}\right)^{1/2} - \tan^{-1}\left(\frac{ct-r}{r-vt}\right)^{1/2}\right.$$

$$\left.+\tan^{-1}\left(\frac{t-r/c}{r/v-t}\right)^{1/2}\right\}. \tag{4.12}$$

To obtain an independent check on equation (4.12), the same problem was also solved by means of Fourier transform techniques. By using the one-sided Laplace transform on time and the Fourier transform on the spatial coordinate $\bar{x} = x - vt$, in conjunction with an application of the Weiner-Hopf technique, the transformed stress was obtained. The inverse transform was evaluated by means of the Cagniard-de Hoop method and the solution obtained verified equation (4.12).

The stress-intensity factor for $\kappa = 0$ is

$$K^a_{\rm III} = \lim_{r\to vt}(2\pi)^{1/2}(r-vt)^{1/2}\sigma_{\theta z}(r>vt,\theta=0)$$

$$= 2(2/\pi)^{1/2}\tau_0(ct)^{1/2}(1-(v/c)^{1/2})(1-v/c)^{1/2}. \tag{4.13}$$

It should be noted that the solution for the stress-intensity factor for the bifurcated cracks, in the limit as $\kappa \to 0$, is expected from consideration of energy flux into the crack-tip regions, to be $2^{-1/2}$ times the value given in equation (4.13) for crack propagation with no bifurcation.

To treat loading on the propagating crack faces as well as on the original crack faces (case b), we specify the boundary conditions given by equation (2.2) and

$$\sigma_{\theta z} = -\tau_0 H(t),\theta=0, \quad 0<r<vt. \tag{4.14}$$

In this case we require that the right-hand side of equation (4.10) be $-\tau_0$, so that

$$A+Bc/v=0, \quad B=(\tau_0/\mu\pi)\,v/(1-v^2/c^2). \tag{4.15}$$

Then

$$\sigma^b_{\theta z}(r>vt,\,\theta=0) = 2\frac{\tau_0}{\pi}\left\{\left(\frac{ct-r}{r-vt}\right)^{1/2}\right.$$

$$\left.-\tan^{-1}\left(\frac{ct-r}{r-vt}\right)^{1/2}\right\}, \tag{4.16}$$

and

$$K^b_{\rm III} = 2(2/\pi)^{1/2}\tau_0(ct)^{1/2}(1-v/c)^{1/2}. \tag{4.17}$$

By superposition, for $\kappa=0$ and loading on only the crack faces that have propagated out from the original crack tip (case c)

$$\sigma^c_{\theta z}(r>vt,\,\theta=0) = 2\frac{\tau_0}{\pi}\left\{(v/c)^{1/2}\left(\frac{ct-r}{r-vt}\right)^{1/2}\right.$$

$$\left.-\tan^{-1}\left(\frac{t-r/c}{r/v-t}\right)^{1/2}\right\}, \tag{4.18}$$

and

$$K^c_{\rm III} = 2(2/\pi)^{1/2}\tau_0(ct)^{1/2}(v/c)^{1/2}(1-v/c)^{1/2}. \tag{4.19}$$

The problem of the bifurcation of a stationary crack in Mode III when $0 < \kappa < 1/2$ was considered by Achenbach [1]. The inversion of the conformal mapping for $\kappa \neq 0$, 1/2 does not appear to be possible. This would preclude obtaining any further analytical results for $\kappa \neq 0$, 1/2 using the method described in the foregoing since it would not be possible then to determine the behavior of ζ ahead of the crack tip (that is on $\theta = \kappa\pi$, $r > vt$). The correct choice of $F'(\zeta)$ could not be made then and the integration of $\dot{\sigma}_{\theta z}$ would not be possible.

The stress-intensity factors obtained in this paper for $\kappa = 1/2$, 0 differ significantly from those obtained in [1]. These analytical results suggest that the expression derived therein for the stress-intensity factor is not correct for any κ.

5 Conclusions

Due to the type of loading considered it is not physically reasonable to expect that the foregoing results model the bifurcation of a rapidly propagating crack properly. This is not a feature only of the preceding solutions but of any model in which the resulting problem can be described as self-similar.

However a reason why a crack might bifurcate can be found in the foregoing results. For $v/c > 1/9$, $K^{a,b}_{\rm III}$ ($\kappa = 1/2$) is greater than $K^{a,b}_{\rm III}$ ($\kappa=0$, no bifurcation). Therefore if the original crack begins to propagate as modeled in the foregoing, it would be expected to do so as a bifurcated crack if the speed of the crack tips was greater than $v/c = 1/9$. It would be tempting to claim that the preceding conclusions apply for an initially rapidly propagating crack which suddenly stops and bifurcates, but obviously this can not be proven here.

An alternative point of view is to consider the crack-tip region for short times and compare the total energy flux into this region for the two cases. For short times, the energy flux into the crack-tip region for $\kappa = 1/2$ (including the contribution of both crack tips in this calculation) is greater than that for $\kappa = 0$ for all values of v/c. This again indicates that bifurcation at initiation with $\kappa > 0$ is the more favorable situation. Obviously, this can only apply to the initiation event and says nothing about continued propagation. In fact, for the type of loading considered, it would be surprising if the crack tips continued at the same velocity at which they initiated.

Finally, it is pointed out that for $v \to 0$, the stress-intensity factors for the bifurcation case when $\kappa\to 0$ and $\kappa=1/2$ are equal. Whether this is true for arbitrary values of κ can not be shown here. However if it is, it will have interesting implications concerning fracture of brittle materials at low velocities. Also, it is noted that K_{III}^{c} ($\kappa = 1/2$) equals K_{III}^{c} ($\kappa = 0$, no bifurcation).

Acknowledgment

The authors would like to thank Professors J. D. Achenbach and L. B. Freund for reading a first draft of the paper. The first author (P.B.) was supported for part of the time during this work by the National Science Foundation (Solid Mechanics Program) through grant CME-8018404. The second author (J.P.D.) acknowledges support from the Air Force Office of Scientific Research under grant AFOSR 73-3589 to Northwestern University.

References

1 Achenbach, J. D., "Bifurcation of a Running Crack in Antiplane Strain," *Int. J. Solids Structures,* Vol. 11, 1975, pp. 1301–1314.

2 Muskhelishvili, N. I., *Singular Integral Equations,* translated by Radok, J. R. M., Noordhoff, 1946.

3 Freund, L. B., and Clifton, R. J., "On the Uniqueness of Plane Elastodynamic Solutions for Running Cracks," *J. Elasticity,* Vol. 4, No. 4, 1974, pp. 293–299.

Dynamic Propagation of a Kinked or Bifurcated Crack in Antiplane Strain

P. Burgers
Assistant Professor,
Department of Mechanical Engineering and Applied Mechanics,
University of Pennsylvania,
Philadelphia, Pa. 19104

An initially unloaded, semi-infinite, stationary crack is assumed to kink or bifurcate at time $t=0$ and the new crack tip(s) propagate out along a straight line at a constant velocity v_{CT}. A Green's function, consisting of a dislocation whose Burgers vector is growing linearly with time, that is suddenly emitted from the tip of a stress-free semi-infinite crack and propagates out along the kinked crack line at constant velocity u, is used to form a Cauchy singular integral equation. This equation is solved using standard numerical techniques and the stress-intensity factor is obtained as a function of crack-tip speed v_{CT} and kink angle δ. The bifurcation case is treated in a similar manner. Finally, some conclusions concerning crack initiation and propagation are drawn.

1 Introduction

The problems that have been solved involving dynamic propagation of cracks are restricted mainly to geometries in which the line of crack propagation is straight. Techniques have now been developed to take into account time-dependent loading and arbitrary variations in crack-tip velocity for a semi-infinite crack in an infinite, isotropic, linear-elastic body. The work in antiplane strain has been extensively reviewed by Achenbach [1] who, with his co-workers, has made many contributions in this area. In a series of papers [2–5], Freund has essentially solved the general problem in mode I. This area has been reviewed in [6] by him.

When a crack is initiated by impact loading in brittle materials, such as glass, the crack is frequently observed to propagate into the body and then bifurcate into two branches. Under suitably high loading, these branches will again bifurcate, repeating the pattern. Experimental observations [7–9] have shown that the included angle of the branches of the bifurcated crack is approximately 25–40 deg, and the decrease in velocity of the bifurcated crack tips from the crack-tip velocity just prior to bifurcation is in the region of 10 percent.

The problem of a rapidly propagating crack in plane strain that suddenly bifurcates is too difficult to solve at present. To reduce the problem to a tractable level, the antiplane-strain (mode III) problem is considered, and the simpler problem of an initially stationary, semi-infinite crack in a stress-free, isotropic, linear-elastic, infinite body is solved. This problem was considered in [10] and two particular cases in [11], where the self-similar nature of the solution allowed the problem to be represented as a particular Riemann-Hilbert problem that could be solved analytically. In [24], Aboudi has used a finite difference scheme to solve the skew crack problem discussed in the following.

Contributed by the Applied Mechanics Division for publication in the JOURNAL OF APPLIED MECHANICS.

Discussion on this paper should be addressed to the Editorial Department, ASME, United Engineering Center, 345 East 47th Street, New York, N.Y. 10017, and will be accepted until two month after final publication of the paper itself in the JOURNAL OF APPLIED MECHANICS. Manuscript received by ASME Applied Mechanics Division, August, 1981; final revision, December, 1981.

2 Problem Definition

We consider a stationary, semi-infinite, straight crack in an initially stress-free, isotropic, full space. At time $t=0$, a single crack (for the kinked crack case) or two cracks (for the bifurcated crack case) start propagating out from the original crack tip at an angle δ or angles $\pm\delta$ to the original crack line with constant crack-tip velocity(ies) v_{CT}. Also, at time $t=0$ the loads are applied. The loading cases considered are: (1) constant tractions on the original crack faces suddenly applied at $t=0$ with traction-free crack faces for the kinked (or bifurcated) crack, and (2) uniform tractions appearing on the kinked (or bifurcated) crack faces with zero tractions on the original crack faces. The geometry and stress wavefront pattern for the bifurcated crack and loading case (1) is shown in Fig. 1.

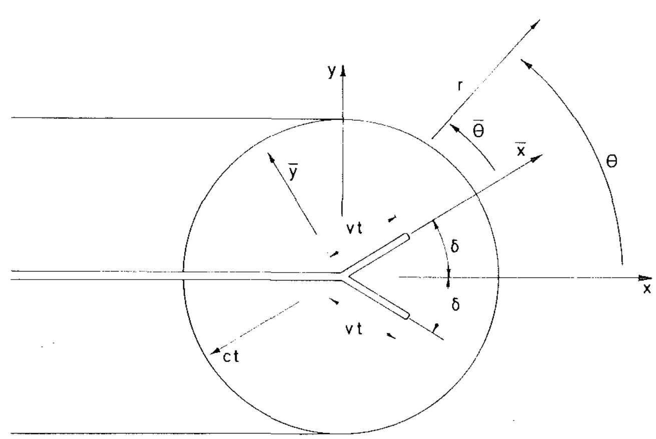

Fig. 1 Geometry and stress-wave pattern for the bifurcation of a semi-infinite crack subjected to step-function loading on the original crack

For both geometries, loading, due to a stress wave of constant magnitude whose wavefront is parallel to the original crack, which strikes the original crack at time $t=0$, can be constructed by superimposing the result of loading case (1) with $\cos\delta \times$ the result of the loading case (2). This case (3) was considered by Achenbach and Varatharajulu [12] for the kinked crack case where the same method was used as in [10].

Loading by a planar stress wave of constant magnitude, whose wavefront makes an angle α with the original crack line, is also considered for the kinked crack case. Again the problem with this loading, case (4), can be solved by using two simpler loadings, although this will not be done explicitly here. The case when $\delta=0$ has been solved analytically by Achenbach [13] and Kostrov [14].

3 Method of Solution

The method of solution follows that which was used by Burgers and Freund [15, 16] (in [16] an error in [15] is corrected). Only the kinked case will be described in detail as the bifurcation case can be obtained with only minor modifications. For the types of loading and geometry changes considered, we note that the stresses and particle velocity are self-similar, i.e., they are functions of r/t and θ only. A Green's function is constructed that also has this property and with this result, a Cauchy singular integral equation is formulated.

Consider a screw dislocation (Fig. 2a), with a discontinuity in displacement in the $\bar{y}(=y)$-direction (out-of-plane direction) along the line $\theta=\delta$ and Burgers vector (displacement discontinuity) growing linearly with time. The dislocation appears at time $t=0$ at the origin of an isotropic, linear-elastic full space (no crack present), with one end propagating out from the origin along the $\bar{x}$-axis ($\theta=\delta$) at constant velocity u and the other end fixed at the origin. The $\bar{z}$-axis is perpendicular to the line $\theta = \delta$ and the only nonzero displacement is w in the y-direction. The initial conditions are

$$w=0 \ \text{ for } \ t<0. \tag{3.1}$$

Since the problem is antisymmetric in displacement about the $\bar{x}$-axis only the half plane $\bar{z}\geq 0$ need be considered. The boundary conditions for this half plane are

$$w(\bar{x})=\Delta t H(ut-\bar{x})-\Delta t H(-\bar{x}), \quad \bar{z}=0 \tag{3.2}$$

where H is the Heaviside step function, and Δ is a magnitude factor required for dimensional consistency. Zero initial conditions are used for this and all the problems that follow. The Cagniard-de Hoop technique for inverting Laplace transforms is used in solving the foregoing problem and the relevant stresses are

$$\sigma^D_{\bar{x}\bar{y}}(r/t,\ \bar{\theta};\ u)=-\frac{\mu\Delta}{\pi} Im\int_b^{t/r} \frac{(2d+\lambda)\lambda}{(\lambda+d)^2}\ \frac{\partial\lambda}{\partial\left(\dfrac{\tau}{r}\right)}\ d(\tau/r), \tag{3.3}$$

$$\sigma^D_{\bar{z}\bar{y}}(r/t,\ \bar{\theta};\ u)=-\frac{\mu\Delta}{\pi} Im\int_b^{t/r} \frac{(2d+\lambda)\beta(\lambda)}{(\lambda+d)^2}\ \frac{\partial\lambda}{\partial\left(\dfrac{\tau}{r}\right)}\ d(\tau/r), \tag{3.4}$$

and

$$\lambda=-\tau/r\cos\bar{\theta}+i|\sin\bar{\theta}|(\tau^2/r^2-b^2)^{1/2},\ \ \beta(\lambda)=(b^2-\lambda^2)^{1/2} \tag{3.5}$$

where $r^2=(\bar{x}^2+\bar{z}^2)$, $\tan\bar{\theta}=\bar{z}/\bar{x}$, $b=1/c$, μ is the shear modulus, c is the shear wave speed of the material, and $d=1/u$. The branch cut for β is taken along the Re (λ) axis from $\lambda\rightarrow-\infty$ to $\lambda=-b$ and $\lambda=b$ to $\lambda\rightarrow\infty$. Superscript D will always be used to refer to this dislocation problem. Note that along any radial line, constant magnitude stress levels propagate out from the origin with velocity $v=r/t$ and that the stresses $\sigma^D_{\bar{x}\bar{y}}$, $\sigma^D_{\bar{z}\bar{y}}$ have a single pole at $r/t=u$, $\bar{\theta}=0$.

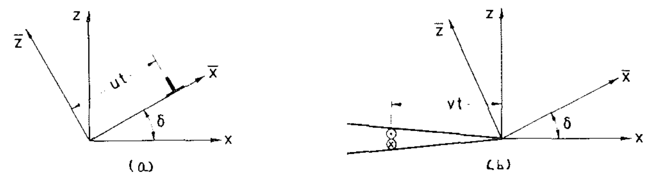

Fig. 2(a) **Geometry for a dislocation, suddenly appearing at the origin and propagating along the $\bar{x}$-axis at constant velocity u; (b) point loads propagating out along the original crack faces at constant velocity v**

Instead of thinking of the dislocation appearing in an infinite body with no crack, we consider the original semi-infinite crack to be present with exactly the correct tractions appearing on the crack faces so that no relative displacements occur between the crack faces of the semi-infinite crack. These tractions are given by the stresses for the foregoing problem evaluated along $\bar{\theta}=(\pi-\delta)$.

To create traction-free crack surfaces, the negative of these tractions must be applied to the faces of the original semi-infinite crack. This can be done by using the superposition described by Freund [3]. For this superposition the solution to point forces that propagate out along the faces of the semi-infinite crack at a constant velocity v is required. The point forces start at the origin at time $t=0$ and their magnitude grows linearly with time (see Fig. 2(b)). This problem is antisymmetric in displacement and therefore only the half plane $z\geq 0$ need be considered. The boundary conditions are

$$\sigma_{zy}(x<0)=\mu\tilde{\Delta}t\ \delta(vt+x), \quad z=0, \tag{3.6}$$

$$w(x>0)=0, \quad z=0, \tag{3.7}$$

where $\tilde{\Delta}$ is an amplitude factor used for dimensional consistency. The relevant stress components are

$$\sigma^{PL}_{xy}(r/t,\theta;v)=$$
$$\frac{\mu\tilde{\Delta}}{\pi}\ \omega^2 Im\int_b^{t/r} \beta_+(\lambda)\ \frac{\partial}{\partial\omega}\left[\frac{1}{\beta_+(\omega)}\ \frac{1}{(\lambda-\omega)}\right] \frac{\partial\lambda}{\partial\left(\dfrac{\tau}{r}\right)}\ d(\tau/r), \tag{3.8}$$

$$\sigma^{PL}_{zy}(r/t,\theta;v)=-\frac{\mu\tilde{\Delta}}{\pi}\ \omega^2$$
$$Im\int_b^{t/r} \frac{\lambda}{\beta_-(\lambda)}\ \frac{\partial}{\partial\omega}\left[\frac{1}{\beta_+(\omega)}\ \frac{1}{(\lambda-\omega)}\right] \frac{\partial\lambda}{\partial\left(\dfrac{\tau}{r}\right)}\ d(\tau/r), \tag{3.9}$$

and

$$\beta_+(\lambda)=(b+\lambda)^{1/2}, \quad \beta_-(\lambda)=(b-\lambda)^{1/2}$$

where λ is defined as in equation (3.5) with $\bar{\theta}$ replaced by θ and $r^2=(x^2+z^2)$, $\tan\theta=z/x$, and $\omega=1/v$. Superscript PL will always be used to refer to the point load problem. The negative of the stresses due to the dislocation along the original crack line is superimposed with the stresses due to the point force problem over all velocities v, from zero to c. When the result of the superposition is added to the dislocation problem, the solution to a screw dislocation, whose Burgers vector grows linearly with time, and which appears at time $t=0$ at the tip of a semi-infinite crack and propagates at constant velocity u along the line $\theta=\delta$, is obtained. This result will be used as the Green's function required to solve the Cauchy singular integral equation. The stresses due to the superposition are given by

$$\sigma^{\text{Sup}}_{\alpha y}(r/t,\theta;u)$$
$$=\int_0^c \frac{1}{\mu\tilde{\Delta}}\ \sigma^{PL}_{\alpha y}(r/t,\theta;v)\sigma^D_{\alpha y}((r/t)'=v,\theta'=\pi;u) \quad dv \tag{3.10}$$

(where $\alpha = x$ or z), and therefore the stresses to be used as the Green's function are

$$\sigma^G_{\bar{\alpha}\bar{y}}(r/t,\bar{\theta};u) = \sigma^D_{\bar{\alpha}\bar{y}}(r/t,\bar{\theta};u) - \sigma^{\text{Sup}}_{\bar{\alpha}\bar{y}}(r/t,\bar{\theta};u). \tag{3.11}$$

Note that the superposition is most easily performed in the x-z coordinate system but that the stresses for the Green's function are required in the $\bar{x}$-$\bar{z}$ coordinate system. Care must be taken when evaluating $\sigma^D_{\bar{z}\bar{y}}$ and $\sigma^D_{\bar{x}\bar{y}}$ along $\bar{\theta}=0$ as discussed for a similar situation in [16]. It should be pointed out also that $\sigma^G(r/t,\theta)$ is square-root singular with respect to r/t at the tip of the semi-infinite crack, and that the faces of the semi-infinite crack are traction free.

Using the superposition of the screw dislocations over their speed of propagation, u, the stress at any point in the body for an arbitrary distribution $F(u)$ of such dislocations, each propagating with velocity u, can be found. The $\sigma_{\bar{z}\bar{y}}$ stress can be evaluated along $\theta = \delta$ and equated to the negative of the tractions across this line due to loading case (1) being applied to a semi-infinite crack (with no kinked or bifurcation cracks present) or to the applied stresses in loading case (2). The other loading cases can be treated in a similar manner. In this way, a Cauchy singular integral equation is obtained; for example, in case (1)

$$-\sigma^{\text{Loads}}_{\bar{z}\bar{y}}(r/t,\bar{\theta}=0) = \int_0^{v_{CT}} \frac{1}{\Delta}\, \sigma^G_{\bar{z}\bar{y}}(r/t,\bar{\theta}=0;u)F(u)\,du. \tag{3.12}$$

The numerical solution of Cauchy singular integral equations is now fairly routine after the initial work by Erdogan and co-workers [17, 18] (in the solid mechanics field). Numerous investigations of the static problem equivalent to the one described in the foregoing have been considered, and Lo [19] has listed many of these references. From [15, 16] it is known that $F(u)=0\ [(v_{CT}-u)^{1/2}]$ as $u \to v_{CT}$. As $u \to 0$ the stresses are known to have a maximum singularity (square root) with respect to r/t at the original crack tip. This singularity will occur only when the loading on the kinked (or bifurcated) crack faces is square-root singular. Otherwise the stresses at the crack tip will be less than square-root singular. Since the Green's function is already square-root singular at the original crack tip and if the form [15, 16, 19, 20]

$$F(u) = \frac{g(u)}{u^{1/2}(v_{CT}-u)^{1/2}}, \tag{3.13}$$

where $g(u)$ is a bounded function, is assumed the condition

$$g(u=0)=0 \tag{3.14}$$

must be imposed. This technique of handling the behavior at $u=0$ has been used numerically in [19, 20]. Muskhelishvili [21] uses a similar method for the plane-strain problem of a punch applied to a half space.

The dynamic stress-intensity factor is given by

$$K_{\text{III}} = \lim_{r \to v_{CT}t} (2\pi)^{1/2}(r-v_{CT}t)^{1/2}\sigma_{\bar{z}\bar{y}}(r/t,\bar{\theta}=0) = (2\pi)^{1/2}(1-v_{CT}^2/c^2)g(v_{CT})t^{1/2}/v_{CT}{}^{1/2} \tag{3.15}$$

For the bifurcated crack case, the solution to a dislocation propagating along $\theta = -\delta$ is also required. Let $\underset{\sim}{\sigma}^{D1}$ ($\underset{\sim}{\sigma}^{D2}$) be the solution for a dislocation, whose Burgers vector is growing linearly with time, and which suddenly appears at the origin and propagates along $\theta = \delta$ ($\theta = -\delta$) at constant velocity u ($\underset{\sim}{\sigma}^{D1}$ is the same as $\underset{\sim}{\sigma}^D$ in equations (3.3–4) and the same applies for $\underset{\sim}{\sigma}^{D2}$ if the $\bar{x}$-axis lined up with $\theta=-\delta$ instead of $\theta=\delta$). The stresses due to the superposition are

$$\sigma^{\text{Sup}}_{zy}(r/t,\theta;u) = 2\int_0^c \frac{1}{\mu\tilde{\Delta}}\,\sigma^{PL}_{zy}(r/t,\theta;v)\,\sigma^{D1}_{zy}((r/t)'=v;\theta'=\pi;u)\,dv, \tag{3.16}$$

$$\sigma^{\text{Sup}}_{xy}(r/t,\theta;u)=0, \tag{3.17}$$

and the stresses for the Green's function are then

$$\sigma^G_{\bar{\alpha}\bar{y}}(r/t,\bar{\theta};u) = \sigma^{D1}_{\bar{\alpha}\bar{y}}(r/t,\bar{\theta};u) + \sigma^{D2}_{\bar{\alpha}\bar{y}}(r/t,\bar{\theta};u) - \sigma^{\text{Sup}}_{\bar{\alpha}\bar{y}}(r/t;\bar{\theta};u). \tag{3.18}$$

obviously, very little extra work is required to calculate the bifurcation case once the kinked crack case has been solved. Since the displacements are antisymmetric about the x-axis, only the half plane $z \geq 0$ need be considered; that is, only one integral equation is required.

4 Numerical Procedure and Results

The superposition calculation and the evaluation of $\underset{\sim}{\sigma}^D$ and $\underset{\sim}{\sigma}^{PL}$ were performed numerically. Gaussian integration was used (see [22] for computer programs used). To obtain sufficient accuracy when the point where the stresses had to be evaluated was close to the original crack tip, the integrations for $\underset{\sim}{\sigma}^D$, $\underset{\sim}{\sigma}^{PL}$ were performed as follows: if $r/t < 0.1c$, the range of integration was split up into ranges from r/t to $r/t+0.1c$ and $r/t+0.1c$ to c; otherwise a single range from r/t to c was used. For the superposition where the range of v was from 0 to c, two ranges were used; 0 to $0.1c$ and $0.1c$ to c. In each range the appropriate end conditions were used. From convergence tests, 25 integration points were found to give satisfactory results.

The Cauchy singular integral equation was solved using either the method given in [17] with the modification to obtain the stress-intensity factor given by Krenk [23] or by the method suggested in [20]. Either method gave sufficiently accurate results using 11 collocation points. However care had to be taken when the modified method in [20] was used for $v_{CT} < 0.1c$.

For loading case (1) the boundary and initial conditions are the same as for the point load problem with equation (3.6) replaced by

$$\sigma^{\text{Loads}}_{zy}(x<0,\ z=0) = \tau_0 H(t). \tag{4.1}$$

The relevant stresses are

$$\sigma^{\text{Loads}}_{zy}(r/t,\theta) = -\frac{\tau_0}{\pi b^{1/2}}\, Im\int_b^{t/r} \frac{\beta_+(\lambda)}{\lambda}\,\frac{\partial\lambda}{\partial\left(\frac{\tau}{r}\right)}\,d(\tau/r) + \tau_0 H(t-bz)H(-x), \tag{4.2}$$

and

$$\sigma^{\text{Loads}}_{xy}(r/t,\theta) = \frac{\tau_0}{\pi b^{1/2}}\, Im\int_b^{t/r} \frac{1}{\beta_-(\lambda)}\,\frac{\partial\lambda}{\partial\left(\frac{\tau}{r}\right)}\,d(\tau/r). \tag{4.3}$$

For case (2)

$$\sigma^{\text{Loads}}_{\bar{z}\bar{y}}(r/t,\ \bar{\theta}=0) = \tau_0 H(vt-\bar{x}). \tag{4.4}$$

The stress-intensity factor for loading cases (1–3) for $0 \leq \delta \leq \pi/2$ and $v_{CT}/c = 0.1,\ 0.3,\ 0.5,\ 0.7$, are shown in Fig. 3 for the kinked crack and in Fig. 4 for the bifurcated crack. To check the accuracy of the program the results for the bifurcated crack with $\delta = 0,\ \pi/2$ with loading case (1) were compared with the analytical results in [11] and were found to be within 2 percent. For $v_{CT} < 0.1c$, the number of integration points has to be increased before sufficiently accurate results can be obtained.

For all graphs the stress-intensity factor has been normalized with respect to the longitudinal wave speed of the material, c_L. A Poisson's ratio of $\nu=0.25$ was used which gives $c=c_L/\sqrt{3}$. The results were not normalized with respect to c since this work was used to gain experience before attempting the Mode I problem. To obtain the more usual normalization with respect to c, the results need only be multiplied by $3^{1/4}$.

The near coincidence of the results for loading case (2) and velocities $v_{CT}=0.3c$ and $0.7c$ can probably be explained as follows. The stress-intensity factor depends very strongly on $\sigma_{\bar{z}\bar{y}}^{\text{Loads}}$ *along the kinked crack line near the crack tip.* For loading case (2) $\sigma_{\bar{z}\bar{y}}^{\text{Loads}}$ near the crack tip is the same for all values of δ, which would explain why the change in K_{III} is small over the whole range of δ. As the velocity of the kinked crack increases from zero, the total force due to the loading gets greater, causing a tendency for K_{III} to increase as v_{CT} increases. However, as v_{CT} approaches c, the ability of the crack tip to act as an energy sink diminishes. This can be seen by looking at the asymptotic field about the crack as $v_{CT}\rightarrow c$ and observing that the square-root singular term in stresses is invalid when $v_{CT}=c$. That is, when $v_{CT}=c$, the stress-intensity factor will be zero. Therefore, it is reasonable to assume K_{III} will decrease as $v_{CT}\rightarrow c$ for v_{CT} close enough to c. The trade off in these two effects is believed to be the reason for the near coincidence in K_{III} for $v_{CT}=0.3c$ and $0.7c$ for loading case (2), together with the observation of the dependence of K_{III} on δ through $\sigma_{\bar{z}\bar{y}}^{\text{Loads}}$.

Loading case (4) can be considered as the sum of two problems. One part is a plane stress wave of constant magnitude that propagates in an infinite body. The direction of propagation of this wave is $\theta=\pi/2+\alpha$, where is α considered only for $0\leq\alpha\leq\pi/2$. At time $t=0$ the wave reaches the origin. The second part consists of the stress field due to loading the faces of a semi-infinite crack so that when the two parts are added together, the stress field for the reflection and diffraction of a plane stress wave by a semi-infinite crack is obtained. The stress due to this field along $\theta=\delta$ is used as $\sigma_{\bar{z}\bar{y}}^{\text{Loads}}(\bar{r}/t,\bar{\theta}=0)$.

The boundary conditions for the second part are

$$\sigma_{zy}(x<0)=-\tau_0\cos\alpha H(ct+\sin\alpha x)H(t),z=0, \tag{4.5}$$

$$w(x>0)=0,\ z=0. \tag{4.6}$$

The stress field due to both parts is given by

$$\sigma_{zy}^{\text{Loads}}(r/t,\theta>0)$$

$$=\frac{\tau_0\cos\alpha}{\pi b^{1/2}(1+\sin\alpha)^{1/2}}Im\int_b^{t/r}\frac{\beta_+(\lambda)}{\lambda-b\sin\alpha}\frac{\partial\lambda}{\partial\left(\frac{\tau}{r}\right)}H(\tau-br)d(\tau/r)$$

$$-\tau_0\cos\alpha H(t-b\ z\cos\alpha+bx\sin\alpha)\left[H\left(\frac{-x}{r}-\sin\alpha\right)-1\right],$$

and (4.7)

$$\sigma_{xy}^{\text{Loads}}(r/t,\theta>0)$$

$$=\frac{-\tau_0\cos\alpha}{\pi b^{1/2}(1+\sin\alpha)^{1/2}}$$

$$Im\int_b^{t/r}\frac{\lambda}{\beta_-(\lambda)(\lambda-b\sin\alpha)}\frac{\partial\lambda}{\partial\left(\frac{\tau}{r}\right)}H(\tau-br)d(\tau/r)$$

$$-\tau_0\sin\alpha H(t-b\cos\alpha z+b\sin\alpha x)\left[H\left(\frac{-x}{r}-\sin\alpha\right)-1\right]. \tag{4.8}$$

The stress-intensity factors for loading case (4) and the kinked crack case are shown in Fig. 5 for $v_{CT}/c=0.1$ and 0.5, $\alpha=0$, $\pi/8$, $\pi/4$, $3\pi/8$, and $\pi/2$ and $0<\delta<\pi/2$.

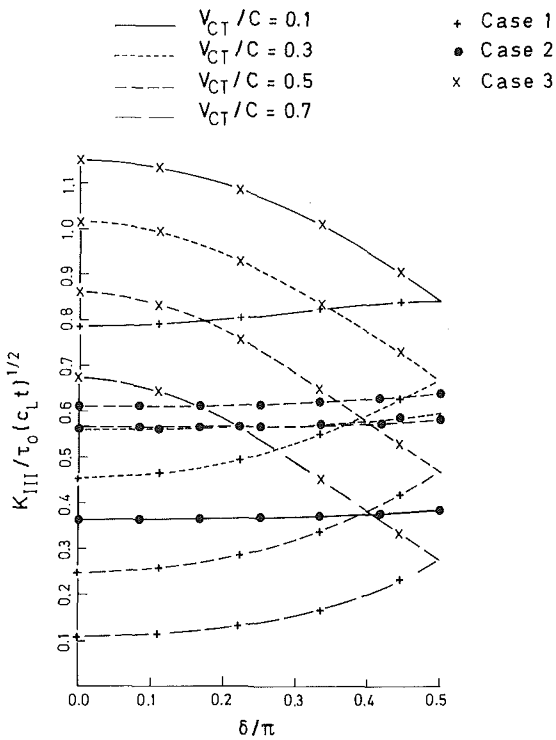

Fig. 3 Stress-intensity factor K_{III} for the kinked crack versus δ/π for $v_{CT}/c=0.1, 0.3, 0.5, 0.7$, and loading cases 1-3

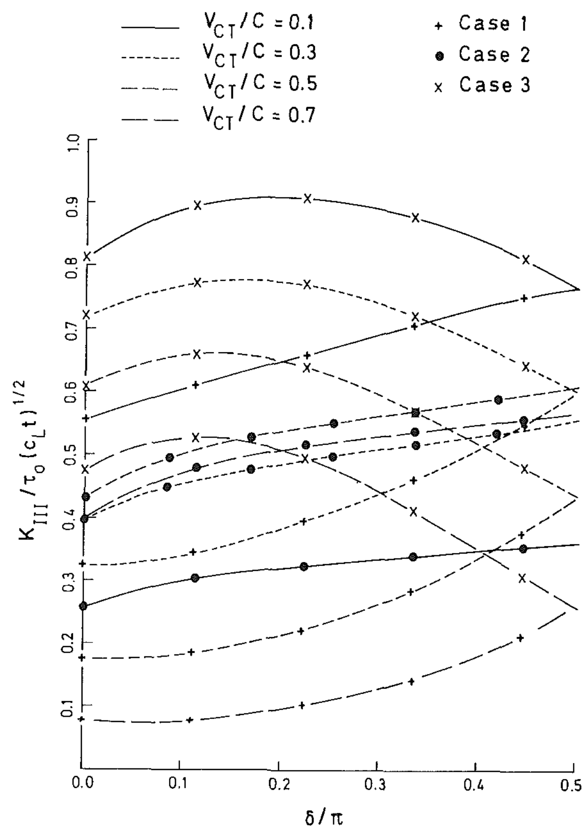

Fig. 4 Stress-intensity factor K_{III} for the bifurcated crack versus δ/π for $v_{CT}/c=0.1, 0.3, 0.5, 0.7$, and loading cases 1-3

5 Conclusions

The results in Fig. 4 for loading case (1) are plotted in a different format in Fig. 6, i.e., holding δ fixed, K_{III} is plotted against v_{CT}/c. Although it could not be shown analytically for arbitrary δ, it was shown in [11] that as $v_{CT} \rightarrow 0$, for $\delta = 0$, $\pi/2$, K_{III} (for the bifurcated crack case) was equal for the loading case (1). If the numerical results are extrapolated back from $v_{CT} = 0.1c$ to $v_{CT} = 0$, they strongly suggest that K_{III} $(\delta, v_{CT} \rightarrow 0)$ is a constant for loading case (1) for arbitrary $\delta \leq \pi/2$ and $v_{CT} \rightarrow 0$. Figure 6 has been plotted enforcing K_{III} $(\delta; v_{CT} = 0) = K_{III}$ $(\delta = 0, \pi/2; v_{CT} = 0) = 0.865\ \tau_0\ (c_L t)^{1/2}$.

With this assumption it is clear that for any velocity at which the bifurcation crack tips initiate, K_{III} is larger for larger δ. This implies that if a critical stress-intensity factor is used as a fracture initiation criterion for loading case (1), the bifurcation cracks will immediately propagate out of plane. The stress-intensity factors are also monotonically decreasing functions of v_{CT} for this loading case. However, since K_{III} behaves as $t^{1/2}$ for these problems it is not possible to consider the behavior of continued crack growth for a fracture criterion of the form dynamic energy-release rate equal a constant.

From Fig. 4, it is seen that, for stress-wave loading case (3) with the bifurcation geometry, there is a peak in $K_{III}/(\tau_0 t^{1/2})$ occurring, for each bifurcation crack speed, in the range $\delta = \pi/8$–$\delta = \pi/4$. This would imply bifurcation will occur with δ in this range, if, again, critical stress-intensity factor is used as an initiation of crack growth criterion. Also, since for $v_{CT}/c \rightarrow 0$ K_{III} for loading case (2) is zero, and if the foregoing assumption is used for K_{III} as $v_{CT}/c \rightarrow 0$ with loading case (1), K_{III} $(\delta, v_{CT}/c \rightarrow 0) = 0.865$ $\tau_0 (c_L t)^{1/2}$ for loading case (3) as well. From Fig. 4 it can be seen that only for crack-tip velocities near $v_{CT}/c = 0.1$, is K_{III} greater than the stress-intensity factor for $v_{CT}/c = 0$. We can therefore conclude that, at initiation, the original crack, if it bifurcates as modeled in the foregoing, will do so with δ approximately in the range $\pi/8$–$\pi/4$ and with v_{CT}/c small; that is v_{CT}/c is greater than zero and approximately equal to 0.1.

It is interesting to note that in [16], it was concluded that for initiation of a Mode I problem, the crack-tip speed must be also in this range. The reasons for this are completely different however.

The behavior of K_{III} for the kinked crack, under loading case (3) which corresponds to the stress-wave loading considered in [12] when the original stress wave is parallel to the semi-infinite crack, is very different to that given in [12]. Although it was not pointed out in [11], the problems in [10] mentioned in [11] also apply directly to [12]. Unfortunately, due to the lack of symmetry in the kinked crack case, no analytical results can be obtained for $\delta \neq 0$. However, since the numerical results were shown to be correct for the bifurcation case for $\delta = 0$, $\pi/2$ and the same program with only minor modifications was used for the kinked crack case, the results for this case are considered to be of the same accuracy. It is also noted that the results follow the trend one might expect physically from considering the static case as δ is increased. The results of Aboudi [24] who considered the skew crack case with loading case (3) and $\delta = \pi/4$ also do not agree with [12].

In the stress-wave loading case (3) K_{III} decreases as δ increases and therefore we would expect the crack to propagate straight ahead. If the crack had kinked along $\theta = -\delta$ instead of along $\theta = \delta$ the stress-intensity factor for the former case would be the same as for the latter case, provided $0 \leq \delta \leq \pi/2$. In Fig. 5, the effect of different values of α is shown. For fixed α and v_{CT}, $K_{III}/(\tau_0 t^{1/2})$ has a maximum at increasing values of δ for α increasing. This implies that the crack will tend to kink for sufficiently large values of α and in fact for $\alpha = \pi/2$ the kink angle δ would most likely be $\pi/2$. This follows intuition obtained from the static case in that the stress-intensity factor is close to a maximum along the line which has the largest tractions acting across it.

It has already been pointed out that these models cannot be used to model problems where the dynamic energy release rate is assumed to be constant. However, it is frequently observed

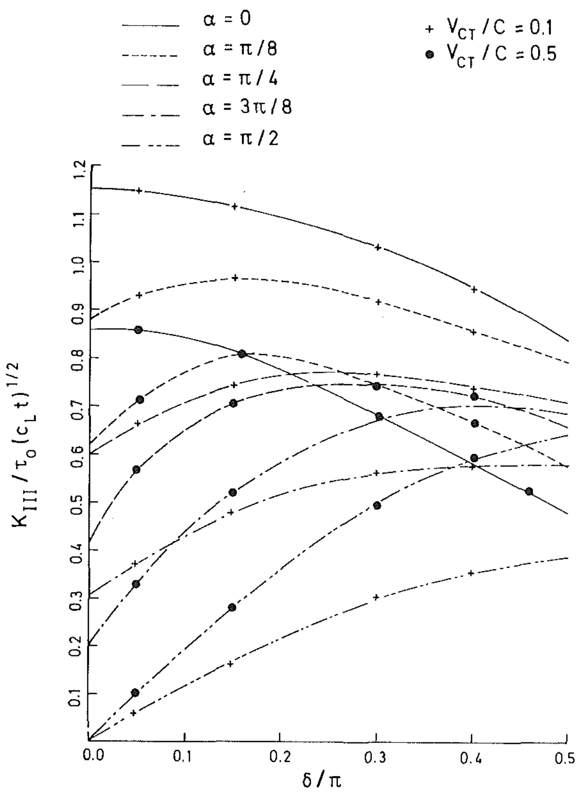

Fig. 5 Stress-intensity factor K_{III} for the kinked crack versus δ/π for $\alpha/\pi = 0$, 1/8, 1/4, 3/8, 1/2, and $v_{CT}/c = 0.1$, 0.5 for loading case 4

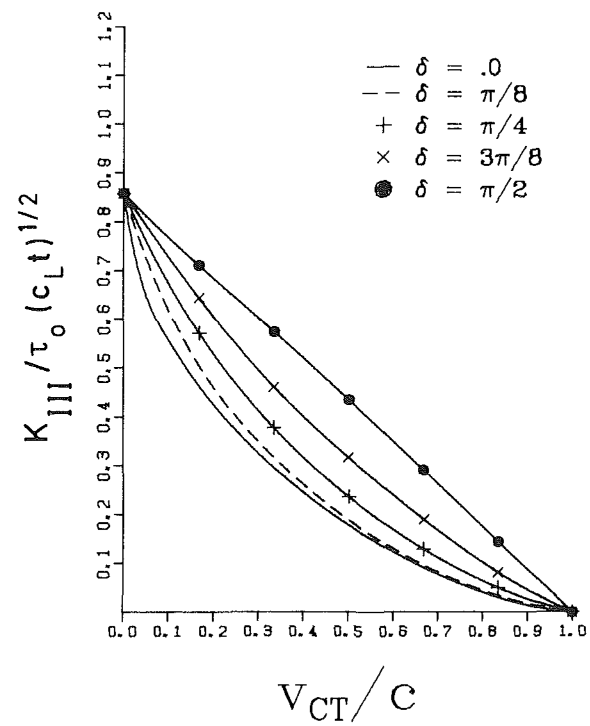

Fig. 6 Stress-intensity factor K_{III} for bifurcated crack versus v_{CT}/c for different δ and loading case 1

that cracks propagate at a constant velocity which is significantly less than the shear wave speed. This might indicate that a linear elastic model does not account for the dissipative effects occurring in the fracture process zone. Therefore, a fracture criterion such as constant dynamic energy release rate, when this quantity is calculated only from a linear elastic analysis, may in fact not be a reasonable fracture criterion if the material is not extremely brittle.

Although it is not immediately obvious from Fig. 4, the stress-intensity factor for loading case (1) has a minimum, which for the higher crack-tip velocities, is not at $\delta=0$. The effect is very slight but increases for increasing v_{CT}. For $v_{CT}/c=0.3$, the minimum appears to be at $\delta=0$ whereas for $v_{CT}/c=0.7$ it is approximately at $\delta=5$ deg and is about 5 percent less than K_{III} ($\delta=0$, $v_{CT}/c=0.7$). For $v_{CT}/c=0.5$ the minimum appears to be around $\delta \simeq 5$ deg and the effect is only about 2 percent. The calculations have been shown to be within 2 percent accuracy for two particular choices of δ but the preceding feature is so small that it is not certain that this feature is not at least in part numerical inaccuracy. In plotting all the other graphs the effect was ignored since at the scale plotted it could barely have been seen.

Acknowledgment

The author would like to thank Professors J. P. Dempsey, L. B. Freund, and J. D. Achenbach for many useful discussions during the course of this work. The research support of the National Science Foundation through grant CME-8018404 is gratefully acknowledged.

References

1 Achenbach, J. D., "Dynamic Effects in Brittle Fracture," *Mechanics Today*, Vol. 1, Nemat-Nasser, S., ed., Pergamon, New York, Chapter 1, 1974, pp. 1-57.

2 Freund, L. B., "Crack Propagation in an Elastic Solid Subjected to General Loading - 1. Constant Rate of Extension," *J. Mech. Phys. Solids*, Vol. 20, 1972, pp. 129-140.

3 Freund, L. B., "Crack Propagation in an Elastic Solid Subjected to General Loading - 2. Non-uniform Rate of Extension," *J. Mech. Phys. Solids*, Vol. 20, 1972, pp. 141-152.

4 Freund, L. B., "Crack Propagation in an Elastic Solid Subjected to General Loading - 3. Stress Wave Loading," *J. Mech. Phys. Solids*, Vol. 21, 1973, pp. 47-61.

5 Freund, L. B., "Crack Propagation in an Elastic Solid Subjected to General Loading - 4. Obliquely Incident Stress Pulse, *J. Mech. Phys. Solids*, Vol. 22, 1974, pp. 137-146.

6 Freund, L. B., "The Analysis of Elastodynamic Crack Tip Stress Fields," *Mechanics Today*, Vol. 3, Nemat-Nasser, S., ed., Pergamon, New York, Chapter 2, 1976.

7 Congleton, J., "Practical Applications of Crack-branching Measurements," *Dynamic Crack Propagation*, Sih, G. C., ed., Noordhoff, Leyden, 1974.

8 Kobayashi, A. S., Wade, B. G., Bradley, W. B., and Chiu, S. T., "Crack Branching in Homalite-100 Sheets," *Eng. Frac. Mech.*, Vol. 6, 1974, pp. 81-92.

9 Kalthof, J. F., "On the Propagation Direction of Bifurcated Cracks," *Dynamic Crack Propagation*, Sih, G. C., ed., Noordhoff, Leyden, 1974.

10 Achenbach, J. D., "Bifurcation of a Running Crack in Antiplane Strain," *Int. J. Solids Structures*, Vol. 11, 1975, pp. 1301-1314.

11 Burgers, P., and Dempsey, J. P., "Two Analytical Solutions for Dynamic Crack Bifurcation in Antiplane Strain," accepted by ASME Journal of Applied Mechanics, for publication, 1981.

12 Achenbach, J. D., and Varatharajulu, V. K., "Skew Crack Propagation at the Diffraction of a Transient Stress Wave," *Quart. Appl. Math.*, Vol. 32, No. 2, 1974, pp. 123-135.

13 Achenbach, J. D., "Extension of a Crack by a Shear Wave," *ZAMP*, Vol. 21, 1970, pp. 887-900.

14 Kostrov, B. V., "Unsteady Propagation of Longitudinal Shear Cracks," *PMM*, Vol. 30, (English translation), 1966, pp. 1241-1248.

15 Burgers, P., and Freund, L. B., "Dynamic Growth of an Edge Crack in a Half Space," *Int. J. Solids Structures*, Vol. 16, 1980, pp. 265-274.

16 Burgers, P., and Freund, L. B., "An Addendum to the Paper: Dynamic Growth of an Edge Crack in a Half Space," *Int. J. Solids Structures*, Vol. 17, 1981, pp. 721-727.

17 Erdogan, F., and Gupta, G. D., "On the Numerical Solution of Singular Integral Equations," *Quart. Appl. Math.*, Vol. 30, 1972, pp. 525-534.

18 Erdogan, F., Gupta, G. D., and Cook, T. S., "Numerical Solution of Singular Integral Equations," *Mechanics of Fracture*, Sih, G. C., ed., Noordhoff, Leyden, Netherlands, 1973, pp. 368-425.

19 Lo, K. K., "Analysis of Branched Cracks," ASME Journal of Applied Mechanics, Vol. 45, 1978, pp. 797-802.

20 Ioakimidis, N. I., and Theocaris, P. S., "The Modified Lobatto-Chebyshev Method Applied to the Numerical Evaluation of Stress Intensity Factors in Cracks With a Corner Point," *Rev. Roum. Sci. Tech. -Mec. Appl.*, Vol. 25, No. 2, 1980, pp. 151-159.

21 Muskhelishvili, N. I., *Singular Integral Equations*, Translated by Radok, J.R.M., Noordhoff, Leyden, 1946.

22 Stroud, A. H., and Secrest, D., *Gaussian Quadrature Formulas*, Prentice-Hall, Englewood Cliffs, N.J.

23 Krenk, S., "A Note on the Use of the Interpolation Polynomial for Solutions of Singular Integral Equations," Lehigh University, Report IFSM-73-48, Aug. 1973.

24 Aboudi, J., "The Dynamic Stresses Induced by the Propagation of Skew Cracks," *Com. Meth. Appl. Mech. and Eng.*, Vol. 15, 1978, pp. 181-199.

K. J. Chang
Assistant Professor of Engineering Mechanics,
Senior Research Investigator in Rock Mechanics
and Explosives Research Center,
University of Missouri-Rolla,
Rolla, Mo. 65401
Assoc. Mem. ASME

A Further Examination on the Application of the Strain Energy Density Theory to the Angled Crack Problem

The strain energy density theory (the S-theory) has been examined. Two points that may lead to confusion have been discussed when the S-theory is employed in the study of the angled crack problem. Predictions for the biaxial tension configuration based on the S-theory compared with one based on the maximum strain criterion are presented. Use of the ratio of core region radius as a material parameter in the S-theory is also questioned.

Introduction

Explanation for the failure of solids containing cracks has been an interesting and challenging subject for investigators in the field of fracture mechanics. In 1963, Erdogan and Sih [1] pioneered the study of the initial crack extension of a brittle plate containing a centrally located, small inclined crack under uniform uniaxial tension. This study, which was later referred to as "the angled crack problem" by Williams and Ewing [2], has since been extensively investigated by researchers in the field of fracture mechanics.

The configuration of the angled crack problem is shown in Fig. 1. In this problem, an isotropic, homogeneous, linearly elastic plate containing a small, inclined, traction-free sharp crack or elliptic crack, in its center, is subjected to a uniformly distributed edge load. The load at which new crack surfaces are created, or the fracture strength, and the direction of the initial crack extension are subjects of interest. The inclined "crack angle," β, an independent variable in the study, is measured positive clockwise from the main loading axis, 0-0′, to the major axis of the elliptic crack (the x-axis); the "fracture angle," θ_0, a result of interest in the study, is measured positive counterclockwise from the major axis of the elliptic crack to the direction of the initial crack extension. The ratio of the two perpendicular edge loads (λ) may be either positive or negative.

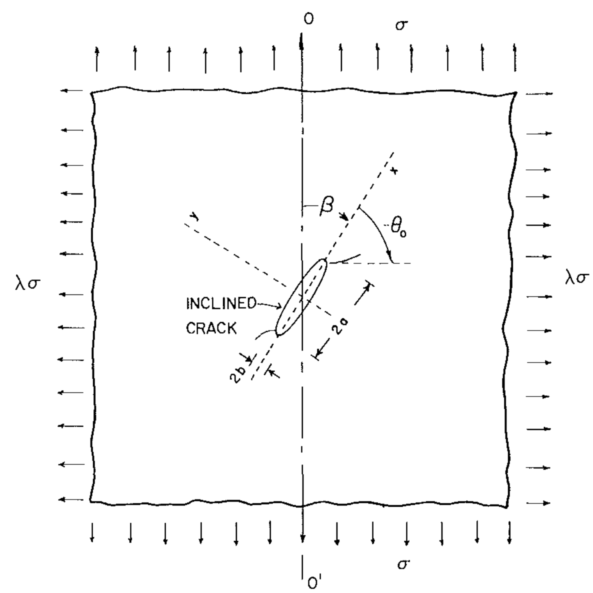

Fig. 1 The configuration of the angled crack problem

Both experimental and theoretical work abound on this subject. Experimental work [1–13] include tests on various materials such as PMMA, glass, and toluene swollen polyurethane under uniaxial tension, uniaxial compression and pure shear edge stresses. Some of the experimental work [10, 11] applied loads on plates containing an elliptic crack (the elliptic model) and others [1–9, 13] loaded plates with a sharp slit crack (the slit model). Theoretical work [1–39] include various criteria and approaches proposed to the study of the problem. Among proposed theoretical approaches only the strain energy density theory (the S-theory) proposed by Sih [16–22] and the modified maximum stress criterion and the maximum strain criterion by Chang [35, 36] have been employed to study both elliptic and slit model versions of the problem, utilizing exact stress solutions.

The subject of the present work is to examine the application of the S-theory to the study of the angled crack problem. Detailed calculations have been carried out and analyzed using exact stress solutions. It is noted that some problems may arise in many of loading configurations when the S-theory is employed to predict the fracture angles (θ_0 in Fig. 1). Discussion of these problems will be presented first. The correlation between existing experimental data and analytical results based on the S-theory for some particular

Contributed by the Applied Mechanics Division for publication in the JOURNAL OF APPLIED MECHANICS.

Discussion on this paper should be addressed to the Editorial Department, ASME, United Engineering Center, 345 East 47th Street, New York, N.Y. 10017, and will be accepted until two months after final publication of the paper itself in the JOURNAL OF APPLIED MECHANICS. Manuscript received by ASME Applied Mechanics Division, July, 1981; final revision, October, 1981.

loading configurations will be presented next. Finally, predictions for biaxial tension conditions, utilizing the S-theory, will be presented and compared with the corresponding predictions of the maximum strain criterion.

The Strain Energy Density Theory and the Maximum Strain Criterion

When applied to the angled crack problem, the strain energy density theory by Sih [16–22] may be stated as follows:

a Crack extension starts from the location of the maximum surface tension, point M in Fig. 2(a), along a ray $\theta = \theta_0$, at which the strain energy density factor, $S(\theta)$, of the stress elements on a circular arc (the core region) of (small) radius r_0 from point M, reaches a stationary (relative minimum) value.

b Fracture is imminent when the relative minimum strain energy density factor, $S(\theta_0)$, at the distance r_0 from point M, reaches a critical critical value, S_c, Here θ_0 is such that:

$$\frac{\partial S}{\partial \theta}\Big|_{\theta=\theta_0} = 0 \qquad (1a)$$

and

$$\frac{\partial^2 S}{\partial \theta^2}\Big|_{\theta=\theta_0} > 0 \qquad (1b)$$

are satisfied. The core region radius, r_0, and the critical strain energy density factor, S_c, are assumed to be material constants; the strain energy density factor, S, is defined by Sih [21] as

$$S = r_0\left(\frac{dW}{dA}\right) = \frac{r_0}{16\mu}\left[(1+\kappa)(\sigma_{11}^2+\sigma_{22}^2) - 2(3-\kappa)\sigma_{11}\sigma_{22} + 8\sigma_{12}^2\right] \qquad (2)$$

where κ is defined to be 3-4ν for plane strain and $(3-\nu)/(1+\nu)$ for plane stress, μ is the shear modulus, and ν is Poisson's ratio.

On the other hand, the maximum strain criterion proposed by Chang [36] for this problem may be stated as follows:

a Crack extension starts from the location of the maximum surface tangential strain, point M in Fig. 2(a), along a ray $\theta = \theta_0$, at which the circumferential strain, ϵ_θ, of the macro-elements on a circular arc of a (small) radius r_0 from Point M, reaches a maximum value (absolute maximum) with respect to θ.

b Fracture is imminent when the maximum strain, $\epsilon_\theta(\theta_0)$, at the distance r_0 from Point M, reaches a critical value, ϵ_T. Both r_0 and ϵ_T are assumed to be material parameters.

Referring to Figs. 1 and 2, where the plate is loaded under uniform stresses σ and $\lambda\sigma$, it is noted that the location of the maximum tangential strain along the traction-free crack surface is in fact coincident with that of the maximum tangential stress. Thus, the starting points of crack extension, M, and the arc of the core region proposed in the foregoing two criteria are the same.

In the present analyses, all stress components are calculated based on the exact elastic stress solutions of an infinitive plate under the loading configuration shown in Fig. 1. Expressed in elliptic coordinates, shown in Fig. 2(b), these solutions, which can be obtained by employing Muskhelishvili's [40] complex potentials, have been expressed in references [34–36], and will not be repeated in the present work. The corresponding strain components may be enumerated by use of Hooke's Law once the stresses are calculated. For the slit model, $\xi_0 = 0.0$ is used.

All numerical values for the fracture measures, $S(\theta)$ and $\epsilon_\theta(\theta)$, are obtained by using a unit applied stress, $\sigma = +1$ for tensile and $\sigma = -1$ for compressive cases. This simplification does not affect the predictions utilizing the foregoing two criteria because the values of $S(\theta)$ and $\epsilon_\theta(\theta)$ are directly proportional to σ^2 and σ, respectively. The material constants used are $E = 2(1+\nu)\mu = 4.5 \times 10^5$ psi, which represents the elastic modulus of PMMA [41], where ν may vary between 0.0–0.5, and μ varies accordingly.

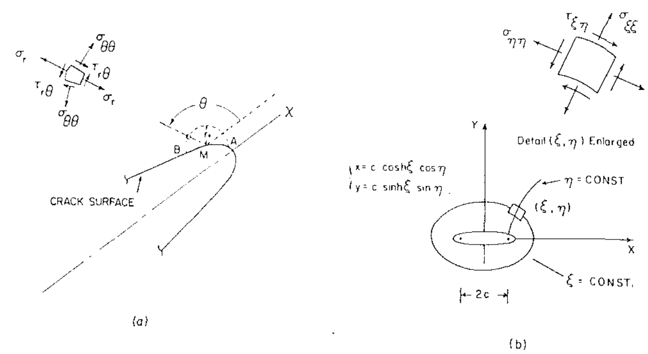

Fig. 2 (a) The care region and its stress element; (b) the elliptic coorrdinates and the stress element

For a slit model, the center of the core region, point M in Fig. 2, is chosen at the tip of the crack because of its stress singularity nature. For an elliptic model, along the crack surface, $\xi = \xi_0$, the location of the maximum surface tension, (ξ_0, η_M), i.e., point M in Fig. 2, is calculated numerically to the accuracy of η_M within $\pm 3 \times 10^{-6}$ rad using the exact stress solutions.

Dilemmas Arising From the Application of the S-Theory

Two dilemmas that can lead to uncertainty arise when the S-theory is employed to predict the fracture angle (θ_0) for the angled crack problem. These dilemmas are discussed in this section.

A **Ambiguity in the Choice of the Relative Minimum $S(\theta)$.** The S-theory would be clear if there were only one relative minimum value of $S(\theta)$ along the arc of the core region for all loading configurations. However, calculations reveal that there exist two or more relative minimum values of $S(\theta)$ along the arc of the core region for most loading configurations. This implies that one more restriction is required to help determine which of these relative minima governs the occurrence of crack extension.

The aforementioned situation has been discussed by Swedlow [39]. In reference [39], Swedlow has pointed out that, for many loading configurations, the choice of the global, i.e., the smallest, relative minimum of $S(\theta)$, which corresponds to a global relative maximum of potential energy, leads to a wrong prediction on the fracture angle, θ_0. Alternatively, it seems to be reasonable to assume that the largest of the relative minima of $S(\theta)$ governs the crack extension. Because, as defined in equation (2), S is proportional to the square of the externally applied stress, σ; thus, as σ increases, the value of $S(\theta)$ along the core region increases accordingly, and the largest relative minimum $S(\theta)$ will always reach its critical value, S_{cr}, first, which leaves no chance for other relative minima to reach S_{cr}. However, if this assumption is followed, the S-theory will also lead to wrong prediction on the fracture angle under certain loading configurations.

In reference [39], Swedlow has further suggested that the S-theory be used in conjunction with a corollary that the critical minimum $S(\theta)$ must be associated with a tensile hoop stress, $\sigma_\theta > 0$. This corollary is confirmed for most loading configurations; however, there still are cases that do not follow its

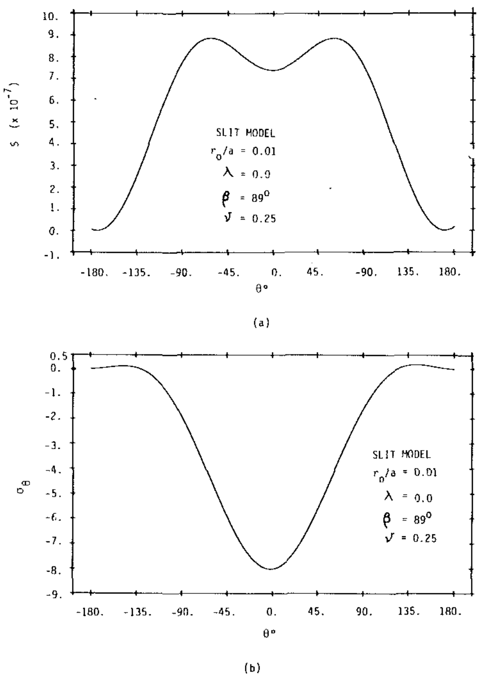

Fig. 3 Analytical results for S and σ_θ along the arc of the core region as functions of θ for the uniaxial compressive case with b/a = 0.0, r_0/a = 0.01, ν = 0.25, and β = 89 deg. (*a*) Strain-energy-density factor, S, and (*b*) tangential stress, σ_θ.

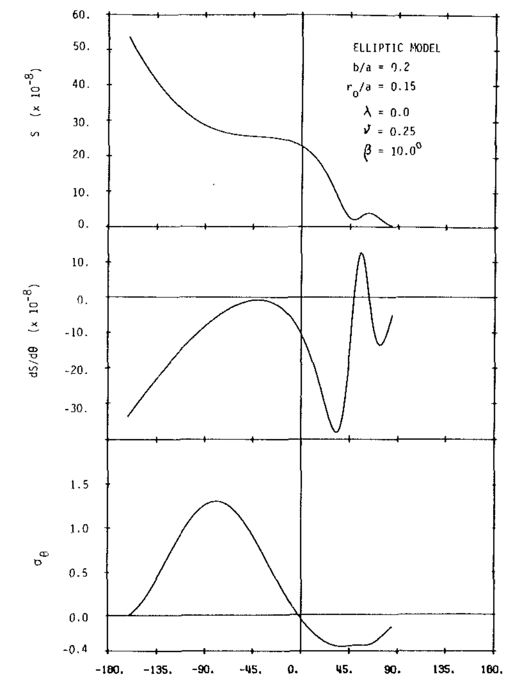

Fig. 4 Analytical results for S, $dS/d\theta$, and σ_θ along the arc of the core region as functions of θ for the uniaxial tensile case with b/a = 0.2, r_0/a = 0.15, ν = 0.25, and β = 10 deg

statements exactly. Figures 3 and 4 show the analytical results for two particular cases for which use of Swedlow's [39] corollary will lead to no conclusive predictions for the fracture angle, θ_0.

Figure 3 shows the $S-\theta$ and $\sigma_\theta-\theta$ curves for a slit model under uniaxial compressive load with $r_0/a = 0.01$, $\nu = 0.25$, and $\beta = 89$ deg. It is seen that three relative minima for $S(\theta)$ exist, and two of them are associated with a tensile hoop stress. Figure 4 shows the $S-\theta$, $dS/d\theta-\theta$, and $\sigma_\theta-\theta$ curves for an elliptic model under uniaxial tension, with $b/a = 0.2$, $r_0/a = 0.15$, $\nu = 0.25$, and $\beta = 10$ deg. It is seen that for these loading configurations there exist only one relative minimum of $S(\theta)$ which corresponds to a compressive hoop stress as shown. It is clear that the corollary proposed by Swedlow [39] does not lead to a definite conclusion on the fracture angle prediction for these particular loading configurations.

***B* Nonexistence of the Relative Minimum $S(\theta)$ Along the Arc of the Core Region.** There are cases when the values of $S(\theta)$ along the arc of the core region possess no relative minimum for all θ values in the θ domain. In such cases, the S-theory leads to no conclusion to the fracture angle prediction. Such a problem does not exist if the maximum strain, ϵ_θ, is employed to govern the fracture occurrence.

Two typical cases that possess such a dilemma when the S-theory is employed are hereby discussed. Figures 5 and 6 represent the $S-\theta$, $dS/d\theta-\theta$, and/or $d^2S/d\theta^2-\theta$ curves along the core regions for the biaxial tension cases of an elliptic model with $b/a = 0.1$, $\lambda = 8$, and $r_0/a = 0.01$, and a slit model with $\lambda = 0.25$ and $r_0/a = 0.01$, respectively. In Fig. 5 it shows that for β angle between 72–84 deg, the first derivative, $dS/d\theta$, remain positive throughout the θ domains. This reveals that there exists no relative minimum $S(\theta)$ for these particular configurations. Such a phenomenon can also be observed, although in different form, for the slit model shown in Fig. 6. In Fig. 6, it is seen that when β equals 0, 1, and 2 deg, the second derivative in the neighborhood of the peak of each curve, which is the only location that satisfies $dS/d\theta = 0$, are clearly negative indicating no possible shallow

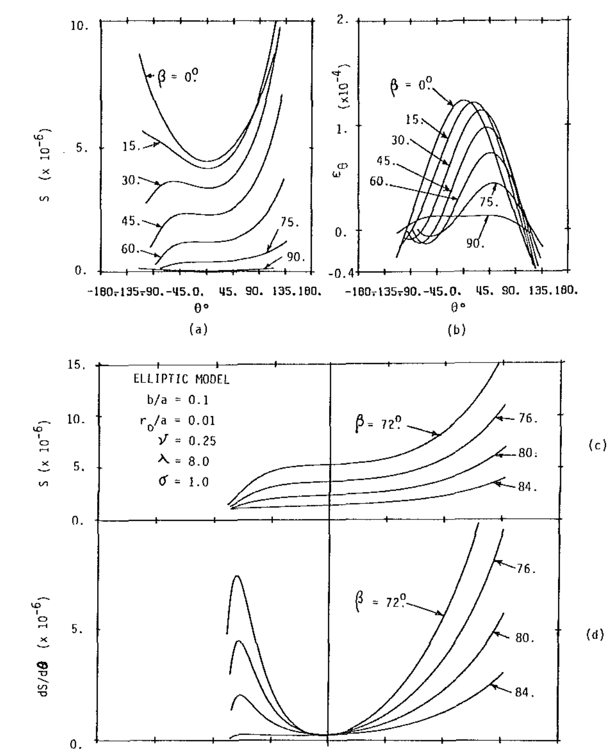

Fig. 5 Analytical results for S, ϵ_θ, and $dS/d\theta$ along the arc of core region as functions of θ for the biaxial tension case with b/a = 0.1, r_0/a = 0.01, λ = 8.0, and ν = 0.25. (*a*) Strain-energy-density factor, S, for 0 deg ≤ β ≤ 90 deg; (*b*) tangential strain, ϵ_θ, for 0 deg ≤ β ≤ 90 deg; (*c*) strain-energy-density factor, S, for β = 72, 76, 80, and 84 deg; (*d*) first derivative, $dS/d\theta$, for β = 72, 76, 80, and 84 deg.

unseenable relative minimum to exist. In obtaining Figs. 5 and 6 all calculations are based on exact stress solutions and chain rule of differentiation, the numerical differentiation formula has not been used.

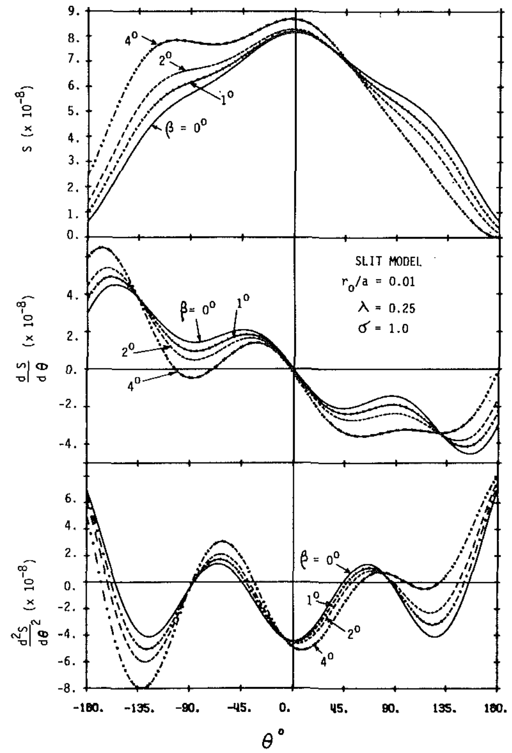

Fig. 6 Analytical results for S, $dS/d\theta$, and $d^2S/d\theta^2$ along the arc of core region as functions of θ, for the biaxial tension case with $b/a = 0.0$, $r_0/a = 0.01$, $\lambda = 0.25$, and $\nu = 0.25$

Figures 7(a) and (b) show the $S-\theta$ and $\epsilon_\theta-\theta$ curves for a biaxially loaded elliptic model with $b/a = 0.1$, $r_0/a = 0.01$, $\sigma = 1$, and $\lambda = -2.0$. It reveals that the shape of the $S(\theta)$ curve changes irregularly as β varies from 0–90 deg, and the first dilemma discussed in the foregoing occurs when β is close to 41 and 86 deg. On the other hand, the shape of the $\epsilon_\theta(\theta)$ curves, as shown in Figs. 5(b) and 7(b) has a regular trend with distinctive absolute maxima as β varies.

In Figs. 5 and 7, it is noted that the θ domain of the presented curves do not cover the entire region of $(-\pi, \pi)$. This is expected because of the definition of the core region for an elliptic model, as can be illustrated in Fig. 2(a).

It is further noted that the fracture angle predictions presented in Fig. 16 of reference [21] have no values for θ_0, when β is small, for cases such as $r_0/a = 0.03$, 0.05, and 0.1. It is believed that this phenomenon is mainly caused by the aforementioned dilemmas.

In the presentation that follows, curves representing predictions based on the S-theory will be cut off if there is no relative minimum $S(\theta)$ or if the relative minimum causes a discontinuity in the $\theta_0-\beta$ prediction, or the prediction will be shown by a dotted line if a compensatory decision, choosing a relative minimum $S(\theta)$ other than the largest, will keep the $\theta_0-\beta$ prediction a smooth curve.

Predictions of Experimental Data

Despite the foregoing two dilemmas, the S-theory can still predict results comparable to those of the experimental data [21, 22] if one is flexible in choosing the relative minimum $S(\theta)$, and sometimes ignores the transition β range where the corresponding relative minimum $S(\theta)$ disappears.

Sih and coworkers [16–22] have applied S-theory to the uniaxial tension case of the slit model [22] and the uniaxial compression case of the elliptic model [21], and the resulting predictions have been compared with existing experimental data. However, no such exercise has been undertaken for other loading configurations where data are available, such as

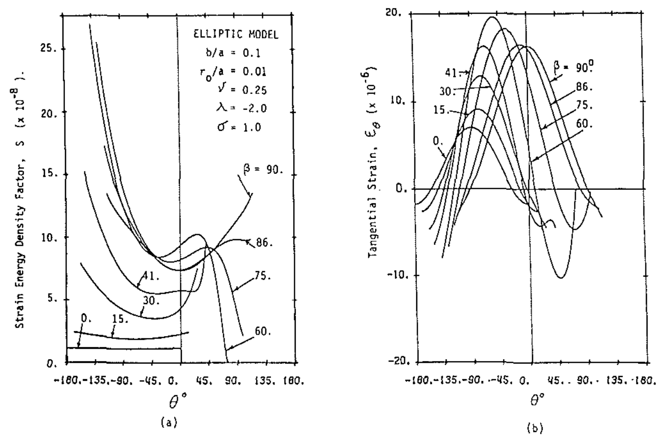

Fig. 7 Analytical results for S and ϵ_θ along the arc of the core region as functions of θ, for the biaxial loading case with $b/a = 0.1$, $r_0/a = 0.01$, $\nu = 0.25$, $\lambda = -2$, and $\sigma = 1$. (a) Strain-energy-density factor, S; and (b) tangential strain, ϵ_θ.

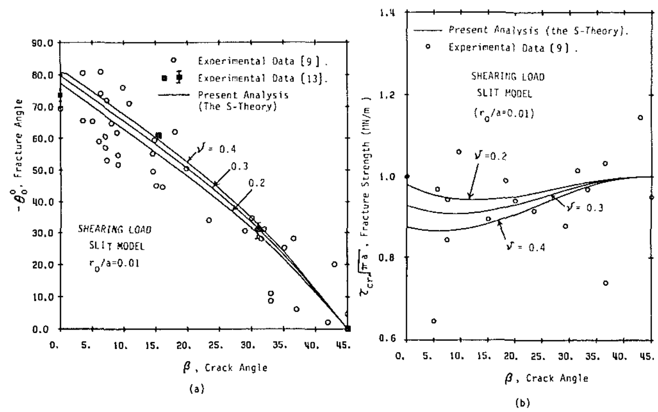

Fig. 8 Theoretical predictions for the shear loading case of the slit model compared with existing experimental data. (a) Fracture angle; and (b) fracture strength.

the slit model under shearing stress [9, 13] and the elliptic model under uniaxial tension [11]. In this section, results of such a study are presented and discussed.

***A* The Slit Model Under Inplane Shear.** Experiments of this particular case have been performed by Ewing and Williams [9], and Liu [13]. Analyses of the fracture angle for the case of inplane shear employing the S-theory have been discussed by Sih and MacDonald [17] and Sih [18]. However, only reference [18] has presented a quantitative prediction for the case of "Mode II Crack Extension" using a singular-term eigenfunction stress solution. For prediction of the general inplane shear case with varying β angle, analysis on the case of $\lambda = -1$ with 45 deg $\leq \beta \leq$ 90 deg, which has been shown [34] to be identical to the inplane shear case, is employed in the present study. Reasonable agreement between S-theory predictions and experimental data [9, 13] are obtained for both the fracture angle and the fracture strength, as shown in Figs. 8(a) and 8(b), respectively. In obtaining predictions given in Figs. 8(a) and 8(b), $b/a = 0.0$, $r_0/a = 0.01$, and $\nu = 0.20$, 0.30, and 0.40, have been used and no compensatory decision had to be made.

***B* The Elliptic Model Under Uniaxial Tension.** Wu, et al. [11] have presented experimental data for this particular case using PMMA plates ($\nu \simeq 0.35$) containing an elliptic crack of $b/a = 0.2$. Figures 9(a) and 9(b) show the predictions based on S-theory for the fracture angle, θ_0, and the strength, σ_{cr}, as functions of β, together with the experimental data of reference [11]. In Figs. 9(a) and 9(b), $b/a = 0.2$ and $r_0/a = 0.15$, and $\nu = 0.2$, 0.25, 0.3, 0.35, and 0.4 have been used.

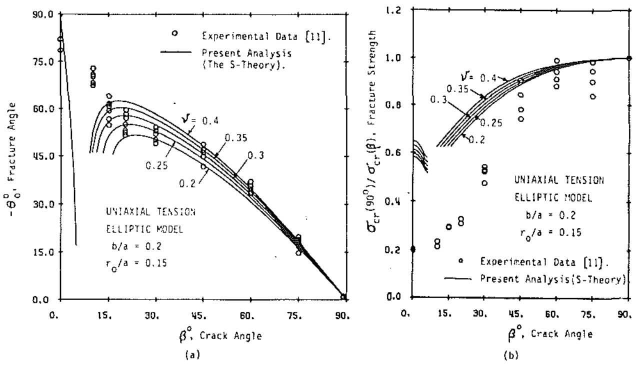

Fig. 9 Theoretical predictions for the uniaxial tension case of the elliptic model compared with existing experimental data. (*a*) Fracture angle; and (*b*) fracture strength.

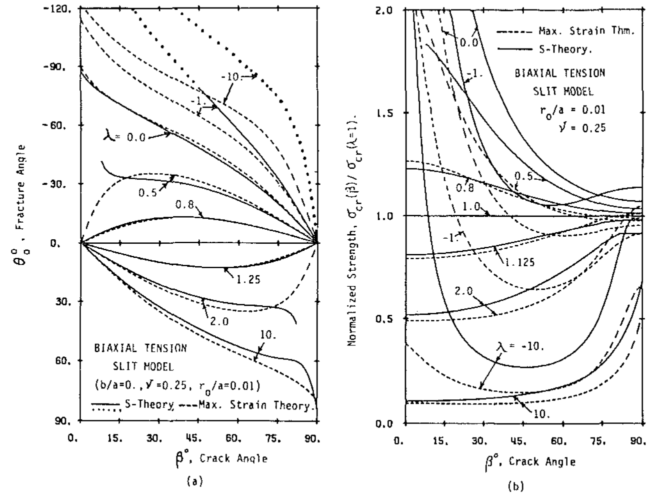

Fig. 10 Theoretical results employing both the S-theory and the maximum strain criterion for biaxial tension cases of the slit model with r_0/a = 0.01, ν = 0.25, and λ from −10 to +10. (*a*) Fracture angle; and (*b*) fracture strength

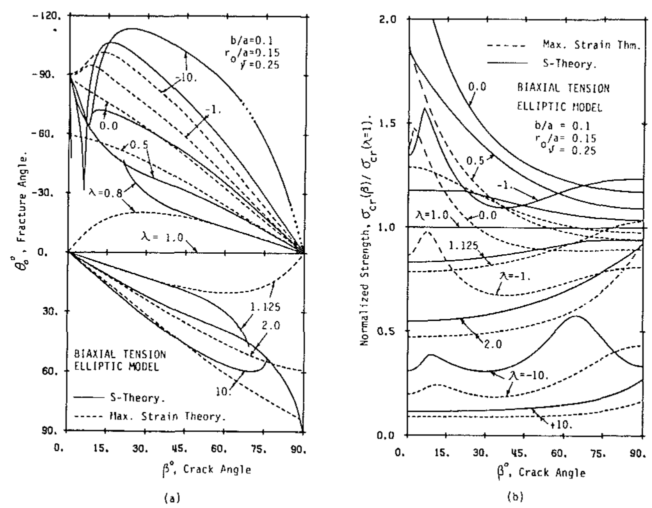

Fig. 11 Theoretical results employing both the *S*-theory and the maximum strain criterion for biaxial tension cases of the elliptic model with *b/a* = 0.1, r_0a = 0.15, ν = 0.25, and λ from −10 to +10. (*a*) Fracture angle; and (*b*) fracture strength.

For small angles of β between 6–15 deg, no curves are presented because of the dilemmas mentioned in the foregoing. It is seen that when r_0/a is chosen as 0.15, *S*-theory provides a fair correlation with respect to Wu et al.'s [11] experimental data on $\theta_0 - \beta$ variations for $\beta \geq 15$ deg. However, the corresponding strength predictions are not close to the experimental data.

***C* Justification of the Ratio of Core Region Radius, r_0/a, as a Material Parameter.** In reference [22], Sih has used $r_0/a = 0.005$ and 0.02 to obtain predictions on θ_0 versus β which agree well with the experimental data obtained by Williams and Ewing [2]. In the present work, it has been shown that $r_0/a = 0.01$ in Fig. 8 and $r_0/a = 0.15$ in Fig. 9 have to be used to provide reasonable predictions to the experimental data obtained by Ewing and Williams [9] and Wu et al. [11], respectively. In references [2, 9, 11], all tests use the same material, PMMA, but in order to obtain reasonable predictions of the fracture angle for all cases, the *S*-theory has to choose r_0/a of magnitudes (from 0.005–0.15) that differ considerably from each other. This implies that the ratio of core region radius, r_0/a, can hardly be justified as a material parameter in the *S*-theory.

Biaxial Tension Configuration

Application of the *S*-theory under biaxial loading conditions has not been discussed in the literature. The present section compares *S*-theory predictions under biaxial tension with those based on the maximum strain criterion proposed by Chang [36].

Fracture angle prediction under uniaxial loading is very much sensitive to the values chosen for the core region radius, r_0/a, when the *S*-theory is applied to the elliptic model, as illustrated by Sih in Figs. 16 and 21 of reference [21], but not so sensitive when applied to the slit model (see Fig. 14 of reference [21]). A similar tendency is also true when it is applied to biaxial loading cases.

Figures 10(*a*) and 10(*b*) show, respectively, the fracture angle and the fracture strength predictions based on both the *S*-theory and the maximum strain criterion for a slit model under biaxial tension. To obtain *S*-theory predictions shown in Figs. 10(*a*) and (*b*), we have restricted that $\theta_0 \leq 0$ for cases $\lambda = 0, 0.5, 0.8, -1$, and -10 and that $\theta_0 \geq 0$ for cases $\lambda = 1.25, 2.0$, and 10, to avoid the first dilemma. It is seen that for a slit model under biaxial tension, fracture angle predictions based on the two theories are pretty close when λ is negative; and their fracture strength predictions have similar trends although their values differ significantly.

For the case of $\lambda = 1$, the same stress is applied in all directions at the edge of the plate; therefore, the stress state in terms of (ξ, η) is the same for all values of β, i.e., independent of β, thus the fracture angle as well as the fracture strength must be the same for all values of β, as shown in Figs. 10(*a*) and (*b*). In Fig. 10(*b*), the strength values have been divided by the strength values obtained for the case of $\lambda = 1$.

In obtaining predictions for an elliptic model under biaxial tension utilizing the *S*-theory, we found a strong sensitivity to the r_0/a value. In the following discussion, $b/a = 0.1$ and $\nu = 0.25$ are considered. Figures 11(*a*) and 11(*b*) show the predictions based on the *S*-theory as well as the maximum strain criterion using $r_0/a = 0.15$. It is seen that with such a relatively large r_0/a ratio, the *S*-theory predicts fracture angles that are comparable to and fracture strength that has similar trends to the corresponding predictions obtained by the maximum strain criterion. However, if $r_0/a = 0.01$ is used, the fracture angles predicted by the *S*-theory for λ = 0.5, 0.8, 1.25, 2.0, and 10.0 are all close to 0 deg or otherwise indeterminate; such a tendency can be seen by examing the $S - \theta$ curves for the case of $\lambda = 8$ shown in Fig. 5(*a*). This is quite different from predictions obtained by other criteria [34–36].

Concluding Remarks

In the present work, the *S*-theory has been examined. Two dilemmas have been discussed. The *S*-theory is very sensitive to the r_0/a ratio when applied to an elliptic model of the problem, but not so sensitive when applied to the slit model. The justification of the core region radius (r_0) to be a material parameter in the *S*-theory is questioned. The *S*-theory provides predictions that are comparable to those obtained by other existing criteria when applied to the slit model and to the elliptic model with relatively large $r_0/a(\simeq 0.15)$ values, but not when applied to the elliptic model with small $r_0/a(\simeq 0.01)$ values.

From the present theoretical results and from references [16, 24-26], it is noted that although the predictions based on various criteria [1-36] are close to one another in the uniaxial loading cases of the problem, their predictions for biaxial loading ($\lambda \neq 0$) differ substantially. Therefore, more experimental data for biaxial loading is needed to help identify the most realistic criteria.

References

1 Erdogan, F., and Sih, G. C., "On the Crack Extension in Plates Under Plane Loading and Transverse Shear," ASME *Journal of Basic Engineering*, Vol. 85, 1963, pp. 519-525.

2 Williams, J. G., and Ewing, P. D., "Fracture Under Complex Stress The Angled Crack Problems," *International Journal of Fracture*, Vol. 8, 1972, pp. 441-446.

3 Brace, W. F., and Bombolakis, E. G., "A Note on Brittle Crack Growth in Compression," *Journal of Geophysical Research*, Vol. 68, 1963, pp. 3709-3713.

4 Hoek, E., and Bieniawski, Z. T., "Brittle Fracture Propagation in Rock Under Compression," *International Journal of Fracture*, Vol. 1, 1965, pp. 137-155.

5 Pook, L. P., "The Effect of Crack Angle on Fracture Toughness," *Engineering Fracture Mechanics*, Vol. 3, 1971, pp. 205-218.

6 Shah, R. C., "Fracture Under Combined Modes in 4340 Steel," presented at the *7th National Symposium on Fracture Mechanics*, University of Maryland, Aug. 27-29, 1973, the Boeing Co., Seattle, Wash.

7 Marcus, H. L., Ho, C. L., and Frandsen, J. D., "Mixed Mode Crack Extension in Aluminum Alloy," *Proc. of 10th Annual Meeting, Society of Engineering Science*, Raleigh, N.C., Nov. 5-7, 1973.

8 Panasyuk, V. V., Berezhnitsky, L. T., and Kovichik, S. Ye, "Propagation of an Arbitrarily Oriented Rectilinear Crack During Extension of a Plate," NASA Technical Translation F-402, Dec. 1965.

9 Ewing, P. D. and Williams, J. G., "The Fracture of Spherical Shells Under Pressure and Circular Tubes with Angled Cracks in Torsion," *International Journal of Fracture*, Vol. 10, 1974, pp. 537-544.

10 Cotterell, B., "Brittle Fracture in Compression," *International Journal of Fracture*, Vol. 8, 1972, pp. 195-208.

11 Wu, H. C., Yao, R. F., and Yip, M. C., "Experimental Investigation of the Applied Elliptic Notch Problem in Tension," ASME Journal of Applied Mechanics, Vol. 44, 1977, pp. 455-461.

12 Palaniswamy, K., and Knauss, W. G., "On the Problem of Crack Extension in Brittle Solids Under General Loading," *Mechanics Today*, Nemat-Nasser, S., ed., Vol. 4, 1976, pp. 87-148.

13 Liu, A. F., "Crack Growth and Failure of Aluminum Plate Under In-Plane Shear," *AIAA Journal*, Vol. 12, 1974, pp. 180-185.

14 McClintock, F. A., "Discussion on 'The Crack Extension in Plates Under Plane Loading and Transverse Shear' by Erdogan, F. and Sih, G. C.," ASME *Journal of Basic Engineering*, Vol. 85, 1963, pp. 525-527.

15 Finnie, I., and Saith, A., "A Note on the Angled Crack Problem and the Directional Stability of Cracks," *International Journal of Fracture*, Vol. 9, 1973, pp. 484-468.

16 Effis, J., and Subramonian, N., "The Inclined Crack Under Biaxial Loading," *Engineering Fracture Mechanics*, Vol. 10, 1978, pp. 43-67.

17 Sih, G. C., and MacDonald, B., "Fracture Mechanics Applied to Engineering Problems—Strain Energy Density Factor Criterion," *Engineering Fracture Mechanics*, Vol. 6, 1974, pp. 361-386.

18 Sih, G. C., "Introductory Chapter: A Special Theory of Crack Propagation," in *Methods of Analysis and Solutions to Crack Problems*, Sih, G. C., ed., Noordhoof International, 1973, pp. 17-45.

19 Sih, G. C., "Some Basic Problems in Fracture Mechanics and New Concepts," *Engineering Fracture Mechanics*, Vol. 5, 1973, pp. 365-377.

20 Sih, G. C., "Strain-Energy-Density Factor Applied to Mixed Mode Crack Problems," *International Journal of Fracture*, Vol. 10, 1974, pp. 305-321.

21 Kipp, M. E., and Sih, G. C., "The Strain-Energy-Density Failure Criterion Applied to Notched Elastic Solids," *International Journal of Solids and Structure*, Vol. 11, 1975, pp. 153-173.

22 Sih, G. C., and Kipp, M. E., "Discussion on 'Fracture Under Complex Stress—The Angled Crack Problem,' by Williams, J. G. and Ewing, P. D.," *International Journal of Fracture*, Vol. 10, 1974, pp. 261-265.

23 Hsu, Y. C., and Forman, R. G., "Fracture Angle and Strain-Energy-Density-Factor for a Crack at Hole at an Arbitrary Angle," *Engineering Fracture Mechanics*, Vol. 7, 1975, pp. 743-750.

24 Finnie, I., and Weiss, H. D., "Some Observations on Sih's Strain Energy Density Approach for Fracture Prediction," *International Journal of Fracture*, Vol. 10, 1974, pp. 136-137.

25 Coughlan, J., and Barr, B. I. G., "Fracture Path Predictions," Report, Department of Civil Engineering and Building, Glamorgan Polytechnic, U.K., 1974.

26 Wu, C. H., "Maximum-Energy-Release-Rate Criterion Applied to a Tension-Compression Specimen with Crack," *Journal of Elasticity*, Vol. 8, 1978, pp. 235-257.

27 Wang, T. C., "Fracture Criteria for Combined Mode Cracks," *Fourth International Conference on Fracture*, June 1977, Waterloo, Canada. In *Advances in Research on the Strength and Fracture of Materials*, Taplin, D. M. R., ed., Vol. 4, 1977, pp. 135-154.

28 Lindsey, G. H., "Some Observation on Fracture Under Combined Loading," *Progress in Flaw Growth and Fracture Toughness Testing*, ASTM STP 536, American Society for Testing and Materials, 1973, pp. 22-31.

29 Labourdette, R. and Pellas, J., "A New Approach to the Three-Dimensional Crack Growth Problem," *International Journal of Fracture*, Vol. 14, 1978, pp. R121-124.

30 Tirosh, J., "Incipient Fracture Angle, Fracture Loci, and Critical Stress for Mixed Mode Loading," *Engineering Fracture Mechanics*, Vol. 9, 1977, pp. 607-616.

31 Tirosh, J. and Catz, E., "Mixed Mode Fracture Angle and Fracture Locus of Materials Subjected to Compressive Loading," *Engineering Fracture Mechanics*, Vol. 14, 1981, pp. 27-38.

32 Hussain, M. A., Pu, S. L., Underwood, J., "Strain Energy Release Rate for a Crack Under Combined Mode I and Mode II," *Fracture Analysis, Proceedings of the 1973 National Symposium on Fracture Mechanics, Part II*, ASTM, STP 560, 1974, pp. 2-28.

33 Wu, H. C., and Chang, K. J., "Angled Elliptic Notch Problem in Compression and Tension," ASME Journal of Applied Mechanics, Vol. 45, 1978, pp. 258-262.

34 Chang, K. J., and Wu, H. C., "Angled Elliptic Notch Problem Under Biaxial Loading," ASME Journal of Applied Mechanics, Vol. 47, 1980, pp. 57-63.

35 Chang, K. J., "Further Studies of the Maximum Stress Criterion on the Angled Crack Problem," *Engineering Fracture Mechanics*, Vol. 14, pp. 125-247.

36 Chang, K. J., "On the Maximum Strain Criterion—A New Approach to the Angled Crack Problem," *Engineering Fracture Mechanics*, Vol. 14, 1981, pp. 107-124.

37 Ingraffea, A. R., Heuze, F. E., Ko, H. Y., and Gerstle, K., "An Analysis of Discrete Fracture Propagation in Rock Loaded in Compression," *Proceedings, 18th Symposium on Rock Mechanics*, Keystone, Colo., 1977, pp. 2A4-1-2A4-7.

38 Ingraffea, A. R., "On Discrete Fracture Propagation in Rock Loaded in Compression," Proceedings, *First International Conference on Numerical Methods in Fracture Mechanics*, Swansea, 1978, pp. 235-248.

39 Sweldlow, J. L., "Criteria for Growth of the Angled Crack," *Cracks and Fracture, ASTM STP 601, American Society for Testing and Materials*, 1976, pp. 506-521.

40 Muskhelishvili, N. I., "Some Basic Problems of the Mathematical Theory of Elasticity," Noordhoof, Groningen, 1953.

41 Plexiglas Design and Fabrication Data PL-229 K. Rohm and Haas, Co., Philadelphia, Pa., 1971.

Unconventional Internal Cracks Part 2: Method of Generating Simple Cracks

C. H. Wu
Professor,
Department of Materials Engineering,
University of Illinois at Chicago Circle,
Box 4348,
Chicago, Ill. 60680
Mem. ASME

The meaning of the word crack is extended to include holes with cusps of vanishing cusp angle. A crack is said to be simple if the associated elasticity problem has a closed-form solution. Many classes of simple cracks are constructed and solved in this two-part paper. In particular, a method of constructing very sharp cusps is described. These cusps possess not only a zero slope (zero cusp angle) but a vanishing curvature as well. In fact, a crack may be constructed in such a way that the first N derivatives are all zero.

1 Introduction

As in Part 1 [1] of this two-part paper, the conventionally implied meaning of the word crack is extended to include holes with cusps. Moreover, a crack is said to be simple if the associated elasticity problem can be explicitly solved to yield a closed-form solution. The premise of this two-part paper is that any simple crack, however unconventional in appearance it may be, is a relevant one in that its explicit solution may be useful in many of the fracture-mechanics related parametric studies.

The several classes of cracks discussed in Part 1 were constructed by the method of successive mappings by rational functions. This procedure will be described in detail in Section 2. The outcome of the procedure is a composite mapping function which is again rational; the idea behind the procedure is, of course, to exploit the nice properties of rational functions. With the objective of constructing simple cracks in mind, however, the family of suitable component rational functions is rather small. It includes the mappings of straight cracks, circles, ellipses, hypocycloids, hypotrochoidal holes, and perhaps a few other cases. Furthermore, when the number of poles of a composite function is greater than two, even the nice properties of the composite rational function become unwieldy. This leads to our device of a second procedure which will also be described in Section 2. In this latter procedure, a product of the former is expanded with respect to one or several of its small parameters and the first few terms are retained. The result is very often a polynomial, the simplest of all rational functions. This polynomial, considered as an offspring of its paternal function, is obviously not a new simple mapping if the pertinent parameters are restricted to remain small. If, however, the offspring polynomial remains holomorphic for much wider ranges of its parameters, then it is possible for the offspring to grow out of resemblance to its paternal figure. In this way, a simple or nonsimple rational function may be used to generate many more simple mappings. Several cases will be discussed in this paper. In all these cases the new simple mappings are derivatives of "thin" approximations of certain other simple mappings. This observation leads to a third procedure which will enable us to directly give birth to new simple mappings. A class of cracks constructed by this procedure is presented in Section 4. The cusps associated with these cracks can be made very, very sharp in the sense that the cusp boundary is almost the same as a straight line.

Several classes of the aforementioned mappings have hypocycloids as their limits beyond which the mappings cease to be holomorphic. For this reason, hypocycloidal cracks are first discussed in Section 3. These cracks have been discussed in [2, 3] and, in view of their simplicity in the context of complex formulation, may have been the subject of investigation of other researcher. The several asymptotic interpretations of the exact solution appear to be new and useful.

All the simple mappings discussed here are of the general form specified by (21) of [1]. For brevity, we shall use (1-n) to denote equation (n) of [1]. Moreover, most of the symbols defined in Part 1 are not redefined in Part 2.

We are indebted to a reviewer of Part 1 [1] for bringing to our attention some closely related results reported in [3–6]. These authors are in complete agreement with us in stressing the relevance of the roles of cuspidal holes in fracture mechanics. In particular, the maximum-stress criterion [7][1] was applied to hypocycloidal cracks in [3], and a general discussion on the geometric properties of cuspidal contours was given in [6]. They did not seem to place any particular emphasis on generating more exact solutions and the crack solutions included in this two-part paper appear not to have been studied before.

2 Unconventional Cracks by Simple Mappings

Let z $(=x_1+ix_2)$ be the physical complex plane and ζ $(=\xi+i\eta)$ an auxiliary complex plane. Suppose that C[z;**p**] is a

Contributed by the Applied Mechanics Division for Publication in the JOURNAL OF APPLIED MECHANICS.

Discussion on this paper should be addressed to the Editorial Department ASME, United Engineering Center, 345 East 47th Street, New York, N.Y. 10017, and will be accepted until two months after final publication of the paper itself in the JOURNAL OF APPLIED MECHANICS. Manuscript received by ASME Applied Mechanics Division, August, 1981.

[1] While the maximum-stress criterion is generally credited to the authors of [7], neither the criterion nor the reference was mentioned in [3].

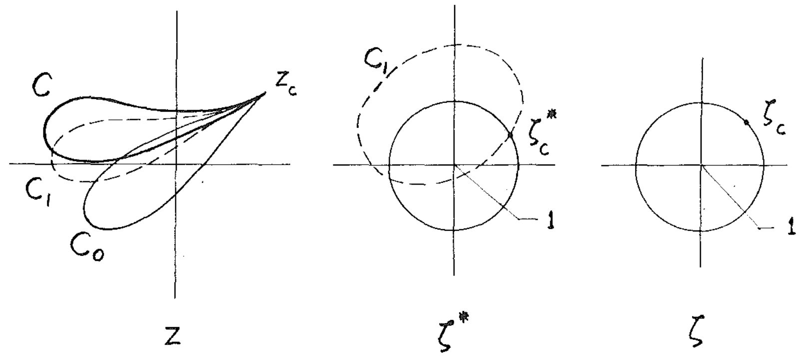

Fig. 1 Successive mappings

crack in the z-plane, depending on a set of parameters $\mathbf{p}$. The crack is assumed to be the image of the unit circle $|\zeta|=1$ under the transformation

$$z=M(\zeta)=M(\zeta;\mathbf{p}). \tag{1}$$

The objective of this section is to describe a procedure via which many, many simple mappings $M(\zeta)$ may be generated. As a matter of our definition, a mapping is said to be simple if the elasticity problem associated with the crack has an explicit and exact solution.

Our procedure begins with the introduction of another auxiliary complex $\zeta^*\ (=\xi^*+i\eta^*)$-plane. Also, the description may be best understood by referring to Fig. 1. Let $C_0[z;\mathbf{p}]$ be a crack in the z-plane that may be mapped onto the unit circle $|\zeta^*|=1$ by the inverse of

$$z=m^*(\zeta^*)=m^*(\zeta^*;\mathbf{p})\quad(|\zeta^*|\geq 1), \tag{2}$$

where $\mathbf{p}$ is a set of parameters. The image in the ζ^*-plane of a cusp-tip located at $z=z_c$ is denoted by $\zeta^*=\zeta_c^*$. In the ζ^*-plane, a second contour/crack $C_1[\zeta^*;\mathbf{p}]$, depending on several or all of the parameters, is drawn to intersect the unit circle $|\zeta^*|=1$ at ζ_c^*. The image of $C_1[\zeta^*;\mathbf{p}]$ in the z-plane under the mapping (2) is a new crack $C_1[z;\mathbf{p}]$ which retains the cusp characteristics at $z=z_c$. If we assume that $C_1[\zeta^*;\mathbf{p}]$ may be mapped onto the unit circle $|\zeta|=1$ by the inverse of

$$\zeta^*=m(\zeta)=m(\zeta;\mathbf{p})\quad(|\zeta|\geq 1), \tag{3}$$

then $C_1[z;\mathbf{p}]$ is just the image of $|\zeta|=1$ under the mapping

$$z=F(\zeta)=F(\zeta;\mathbf{p})=m^*(m(\zeta;\mathbf{p});\mathbf{p}). \tag{4}$$

A rather general restriction on the choices of $m^*(\zeta^*)$ and $m(\zeta)$ is that $F(\zeta)$ must not lead to a self-intersecting crack periphery. The new mapping function $F(\zeta)$ is a hybrid of $m^*(\zeta^*)$ and $m(\zeta)$. If it is already simple in the sense described, then a new class of simple cracks has been successfully invented. The problems presented in [1] are of this nature.

The nature of candidates suitable for the roles of $m^*(\zeta^*)$ and $m(\zeta)$ is limited, but the number of possible combinations is still quite substantial. Let us restrict our choices of $m^*(\zeta^*)$ and $m(\zeta)$ to rational functions. Then the composite mapping $F(\zeta)$ is also rational. In general, $F(\zeta)$ has poles of different orders at many locations and hence is not simple. However, it is very often possible to generate simple mapping functions from $F(\zeta;\mathbf{p})$ by retaining only the first few terms of a Taylor's expansion of $F(\zeta;\mathbf{p})$ in one or several of its parameters. These "offsprings" of F are, of course, approximate versions of F if the appropriate parameters are restricted to remain in their appropriately small ranges. On the other hand, since we have no particular interest in $F(\zeta;\mathbf{p})$ to begin with, the restrictions on the smallness of the parameters may be lifted so that the offsprings themselves may be considered as new classes of simple mappings.

Consider, for example, a function $F(\zeta;p_1,p_2)$ depending on two parameters where $0\leq p_1<1$. The elasticity solution associated with the crack C_F generated by F is denoted by $S_F(z;p_1,p_2)$. The function $M(\zeta)$ defined by

$$M(\zeta;p_1,p_2)=F(\zeta;0,p_2)+p_1\frac{\partial}{\partial p_1}F(\zeta;0,p_2) \tag{5}$$

is an approximation of F for $p_1<<1$. The associated approximate solution is just

$$S_M(z;p_1,p_2)=S_F(z;0,p_2)+p_1\frac{\partial}{\partial p_1}S_F(z;0,p_2) \tag{6}$$

which is, once again, valid for $p_1<<1$ as far as the crack C_F is concerned. The function $M(\zeta;p_1,p_2)$, however, may itself be considered as an independent mapping with a crack C_M in the z-plane as its image. The *exact* elasticity solution associated with C_M is just $S_M(z;p_1,p_2)$! Of course, nothing would have been gained if p_1 were to remain small. It happens very often that $M(\zeta)$ remains holomorphic for

$$0\leq p_1\leq p_1^*(p_2)\quad\text{and}\quad p_1^*>>0. \tag{7}$$

In this range, the crack C_M bears very little resemblance to the crack C_F. We have thus enlarged the family of cracks defined by F with very, very little effort. Even if F is not simple, the function M may turn out to be simple and the solution S_M may be directly determined.

3 Hypocycloidal Cracks

We begin with the mapping function

$$z=M(\zeta)=\frac{nR_0}{1+n}\left(\zeta+\frac{1}{n}\frac{1}{\zeta^n}\right)(|\zeta|>1) \tag{8}$$

which maps a hypocycloid with $n+1$ cusps onto the unit circle $|\zeta|=1$. The cusps are located at

$$z=z_c=R_0\zeta_c=R_0\exp\frac{2k\pi}{n+1}i\quad(k=0,1,\ldots,n). \tag{9}$$

The few important geometric properties are:

radius of the circumscribed circle $=R_0$

radius of the inscribed circle $=r_0=\dfrac{n-1}{n+1}R_0$,

perimeter of a hypocycloid $=\dfrac{8n}{n-1}r_0=\dfrac{8n}{n+1}R_0$,

$$\text{area enclosed by a hypocycloid}=\frac{n^2-n+2}{(n+1)^2}\pi R_0^2. \tag{10}$$

Since $M(\zeta)$ has a pole of order n at $\zeta=\zeta_0=0$, the function Ω_H defined by (1-34) involves n unknown constants. These constants may be determined by examining the properties of $\omega(\zeta)$ defined by (1-35). The stress-intensity factors at $z=R_0$ ($\zeta=1$) and the flaw energy U are:

$$K_1=\frac{2\sqrt{n\pi R_0}}{n+1}\left\{\frac{3n^2-3n+2}{2(n^2-n+2)}\sigma_{22}\right.$$

$$- \frac{n^2-n-2}{2(n^2-n+2)}\sigma_{11}\Big\}(n>1) \tag{11}$$

$$K_2 = \frac{2\sqrt{n\pi R_0}}{n+1}\,\frac{2n}{n^2-n+2}\,\sigma_{12}(n\geq 1), \tag{12}$$

$$K_3 = \frac{2\sqrt{n\pi R_0}}{n+1}\,\sigma_{32}(n\geq 1), \tag{13}$$

$$U = \frac{\pi}{2}(\kappa+1)R_0^2\Big\{\frac{n}{8(n+1)}(\sigma_{11}^2+\sigma_{22}^2+2\sigma_{11}\sigma_{22})$$

$$+\frac{n^4}{4(n+1)^2(n^2-n+2)}(\sigma_{11}^2+\sigma_{22}^2-2\sigma_{11}\sigma_{22}+4\sigma_{12}^2)\Big\}$$

$$+\pi\frac{n^2R_0^2}{(n+1)^2}(\sigma_{31}^2+\sigma_{32}^2)\quad (n\neq 1,3), \tag{14}$$

and the term

$$\frac{1}{2}\left(\frac{3}{4}\right)^3\left[\frac{1}{4}(\sigma_{11}^2+\sigma_{22}^2-2\sigma_{11}\sigma_{22})-\sigma_{12}^2\right] \tag{15}$$

should be added to (14) for $n=3$.

For the special case $\sigma_{11}=\sigma_{22}=\sigma$ and $\sigma_{12}=\sigma_{13}=\sigma_{23}=0$, the preceding results reduce to

$$K_1 = \frac{2\sqrt{n\pi R_0}}{n+1}\sigma,\quad K_2=K_3=0, \tag{16}$$

$$U = \frac{\pi}{4}(K+1)R_0^2\frac{n}{n+1}\sigma^2\quad (n\geq 1). \tag{17}$$

It is seen that

$$K_1 = \frac{2}{\sqrt{n}}\sqrt{\pi R_0}\,\sigma\quad \text{as}\quad n\to\infty \tag{18}$$

which is in complete agreement with the asymptotic expression obtained by Westmann for a pressurized star crack [8][2].

For n sufficiently large, a hypocycloidal hole may be interpreted as a circular hole of radius r_0, the radius of the inscribed circle, with $n+1$ equally spaced radial cracks of length c and circumferential spacing $2b$. It follows from (10) that

$$c = R_0 - r_0 = \frac{2}{n-1}r_0,\quad b = \frac{\pi r_0}{n+1}, \tag{19}$$

and hence

$$\delta \equiv \frac{b}{b+c} = \left[1+\frac{2}{\pi}\,\frac{n+1}{n-1}\right]^{-1} = \frac{\pi}{2+\pi}\quad \text{as}\quad n\to\infty. \tag{20}$$

The problem of an infinite row of normal edge cracks of crack length c and spacing $2b$ was solved by Benthem and Koiter [9]. Their formula may be applied to deduce a very accurate estimate for the current problem provided that the remote tension in their formula is replaced by the hoop tension

$$\sigma_H = \sigma\left[1+\left(\frac{r_o}{R_0}\right)^2\right] = 2\sigma\frac{n^2+1}{(n+1)^2} \tag{21}$$

Using the explicit formula given in [9], we obtain

$$K_1 = \sigma_H\sqrt{\pi c}\,\delta^{1/2} f(\delta) = 1.468\sqrt{\pi c}\,\sigma\left(\frac{c}{b}=\frac{2}{\pi}\right) \tag{22}$$ [3]

for $\delta = \pi/2+\pi$, i.e., $n\to\infty$. In terms of c, (18) becomes

$$K_1 = \sqrt{2}\sqrt{\pi c}\,\sigma\quad (n\to\infty). \tag{23}$$

The close agreement between (22) and (23) leads us to believe that (18) may be used to approximate (22) by interpreting n as the noninteger root of (20). The result is

[2] In our notation Westmann's result is $K_1 = (\sqrt{2/n+1})\sqrt{\pi R_0}\,\sigma$. His result, however, was normalized by the factor K_1 (line crack) $= \sqrt{2}\sqrt{\pi R_0}\,\sigma$.

[3] $f(\delta)$ is given by equation (3.149) of [9].

$$K_1 = \sigma_H\sqrt{\pi c}\,\delta K = \sigma_H\sqrt{\pi c}\,\delta\,\frac{1}{2}\left[\left(1+\frac{c}{b}\right)\left(1+\frac{2b}{\pi c}\right)\right]^{1/2} \tag{24}$$

where K was plotted in [9]. Equation (24) is only about 5 percent off for $0.3 < c/b < 1.0$. Alternatively, we may express n in terms of r_0 and c, and write

$$K_1 = \left(\frac{c+2r_0}{c+r_0}\right)^{1/2}\sqrt{\pi c}\,\sigma\quad \text{(many short radial cracks).} \tag{25}$$

4 Symmetric Variations of a Straight Crack

We begin with the crack-to-circle and ellipse-to-circle transformations

$$z = m^*(\zeta^*) = m^*(\zeta^*;a,\delta) = \frac{(1-\delta^2)a}{2}\left(\zeta^*+\frac{1}{\zeta^*}+\frac{\delta}{1-\delta}\right) \tag{26}$$

$$\zeta^* = m(\zeta) = m(\zeta;\delta,\lambda) = \frac{1}{1-\delta}\left[\frac{1+\lambda}{2}\left(\zeta+\frac{1-\lambda}{1+\lambda}\,\frac{1}{\zeta}\right)-\delta\right] \tag{27}$$

where $0 \leq \delta < 1$ and $\lambda^2 \geq 1-\delta$. Equation (26) maps the crack $-\tfrac{1}{2}(2-\delta-3\delta^2)a < z < \tfrac{1}{2}(2+\delta-\delta^2)a$ onto the circle $|\zeta^*|=1$, while (27) maps the ellipse

$$\left[\left(\xi^*+\frac{\delta}{1-\delta}\right)\Big/\frac{1}{1-\delta}\right]^2 + \left[\eta^*\Big/\frac{\lambda}{1-\delta}\right]^2 = 1 \tag{28}$$

onto the unit circle $|\zeta|=1$. The composite mapping $F(\zeta)$ is

$$F(\zeta) = F(\zeta;a,\delta,\lambda) = m^*(m(\zeta;\delta,\lambda);a,\delta). \tag{29}$$

This mapping is already simple in the sense described and the associated class of problems was solved in [1]. However, it may still be used to generate new and simpler mappings.

4.1 Symmetric Airfoil Cracks (Special case of (29) studied in [1]).

$$M(\zeta;a,\delta) = F(\zeta;a,\delta,1) = \frac{1-\delta^2)a}{2}$$

$$\left[\frac{\zeta}{1-\delta}+\frac{1-\delta}{\zeta-\delta}\right](0\leq\delta<1) \tag{30}$$

The solution is given by (1–65)-(1-69). In particular,

$$\Omega_H(\zeta) = \frac{(1+\delta)a}{2}\left[W_1\zeta-\bar{w}_1\frac{1}{\zeta}+\frac{\Omega_{11}/M_1}{\zeta-\delta},\right] \tag{31}$$

where

$$\frac{\Omega_{11}}{M_1} = \frac{(1-\delta^2)^2}{1+2\delta-\delta^2}\left[\frac{\delta^2}{2}(\sigma_{11}-\sigma_{22})\right.$$

$$\left.-\frac{1}{4}(\sigma_{11}+\sigma_{22})\right] - i\delta^2(1-\delta)^2\sigma_{12}. \tag{32}$$

4.2 Derivatives of Thin Airfoil Cracks.

$$M(\zeta;a,\delta) = F(\zeta;a,0,1)+\delta\frac{\partial}{\partial\delta}F(\zeta;a,0,1)$$

$$= \frac{a}{2}\left[(1+\delta)\zeta+\frac{1-\delta}{\zeta}+\frac{\delta}{\zeta^2}\right]\quad (0\leq\delta<1) \tag{33}$$

This is clearly an approximation of (30) for small values of δ. However, (33) is holomorphic for all values of δ in the range specified. Thus it defines a new class of simple mappings which is not merely a special case of (30). The exact solution associated with (33) is just the first two terms of the Taylor expansion of (31). It follows that

$$\Omega_H(\zeta) = \frac{a(1+\delta)}{2}\left[W_1\zeta-\bar{w}_1\frac{1}{\zeta}\right.$$

$$\left.-\frac{1-\delta}{1+\delta}\,\frac{W_1}{\zeta}-\frac{\delta}{1+\delta}\,\frac{W_1}{\zeta^2}\right] \tag{34}$$

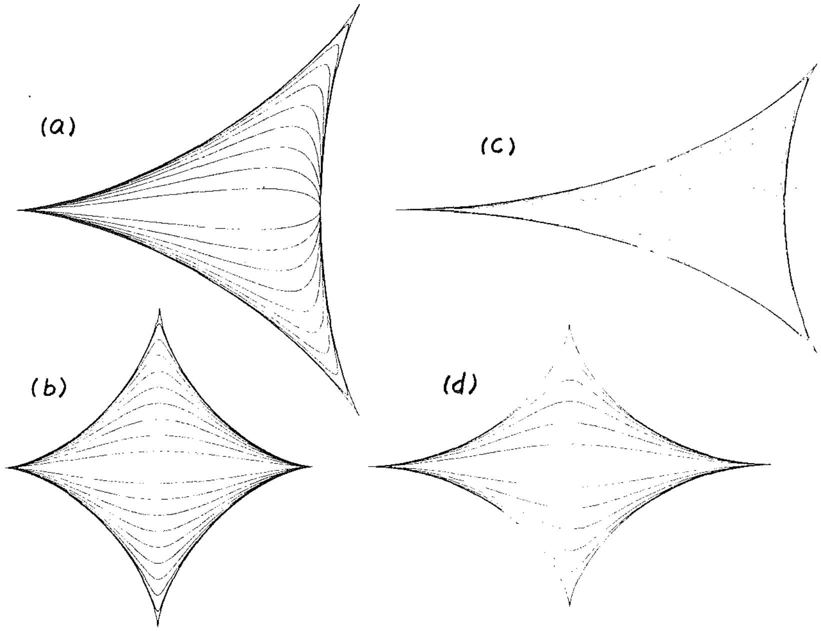

Fig. 2 Symmetric variations of a straight crack: (a) derivatives of thin airfoil cracks ($0.1 \le \delta \le 1.0$ at 0.1); (b) derivatives of thin lip-shaped cracks ($0.1 \le \lambda - 1 \le 2.0$ at 0.1); (c) one-tip cracks defined by (63) ($0.1 \le \epsilon \le 1/3$ at 0.005); (d) two-tip cracks defined by (72) ($0.1 \le \epsilon \le 2/3$ at 0.1)

All the relevant physical quantities may now be computed by the formulas given in [1]. We have

$$(K_1, K_2, K_3) = \sqrt{\pi a}\,\frac{1+\delta}{(1+2\delta)^{1/2}}(\sigma_{22}, \sigma_{12}, \sigma_{32}), \tag{35}$$

$$U = \frac{\pi}{2}(\kappa+1)\frac{a^2(1+\delta)^2}{4}\left\{\left[\frac{3}{8} + \frac{5-2\delta-\delta^2}{8(1+\delta)^2}\right]\sigma_{22}^2 + \left[\frac{3}{8} + \frac{7\delta^2-2\delta-3}{8(1+\delta)^2}\right]\sigma_{11}^2 + \left[\frac{3\delta^2-2\delta+1}{4(1+\delta)^2} - \frac{1}{4}\right]\sigma_{11}\sigma_{22} + \sigma_{12}^2\right\} + \pi\frac{a^2(1+\delta)}{2}(\sigma_{32}^2 + \delta\sigma_{31}^2). \tag{36}$$

The crack periphery defined by (33) has the parametric representation

$$\begin{cases} x_1/a = \cos\phi + \dfrac{\delta}{2}\cos 2\phi \\ x_2/a = \delta\sin\phi(1-\cos\phi) \end{cases} \qquad (0 \le \phi \le 2\pi, 0 \le \delta < 1) \tag{37}$$

which reduces to

$$\frac{x_2}{a} = \pm\delta\left(1 - \frac{x_1}{a}\right)^{3/2}\left(1 + \frac{x_1}{a}\right)^{1/2} \quad \text{for } \delta << 1. \tag{38}$$

For $\delta = 1$, (33) reduces to (8), a hypocycloid with three cusps. The complete set of cracks is given in Fig. 2*a*. It is noted that for $0 < 1 - \delta << 1$ the crack may be viewed as a curvilinear triangle with a short corner crack.

4.3 Symmetric Lip-Shaped Cracks (Special case of (29) studied in [1]).

$$M(\zeta; a, \lambda) = F(\zeta; a, 0, \lambda) \quad (\lambda \ge 1) \tag{41}$$

The exact solution is given by (1-79) – (1-85).

4.4 Derivatives of Thin Lip-Shaped Cracks.

$$M(\zeta; a, \lambda) = F(\zeta; a, 0, 1) + (\lambda - 1)\frac{\partial}{\partial\lambda}F(\zeta; a, 0, 1)$$

$$= \frac{a}{2}\left[\frac{\lambda+1}{2}\zeta + \frac{2-\lambda}{\zeta} + \frac{\lambda-1}{2}\frac{1}{\zeta^3}\right] \quad (1 \le \lambda \le 2). \tag{42}$$

This is obviously an approximation of (41) for small values of $\lambda - 1$. It is, however, holomorphic for $1 \le \lambda \le 2$ and hence defines a new class of simple mappings. The exact solution associated with (42) is just the first two terms of the Taylor expansion of the exact solution associated with (41). The result is

$$\Omega_H(\zeta) = \frac{\lambda+1}{4}a\left[W_1\zeta - \frac{\bar{w}_1}{\zeta} - \frac{\Omega_{10}}{\zeta} - \frac{\Omega_{30}}{\zeta^3}\right] \tag{43}$$

where

$$\Omega_{10} = \frac{(\lambda-1)^2}{4\lambda}\bar{w}_1 + \frac{\lambda^2-1}{4\lambda}w_1 + \frac{2\lambda(2-\lambda)}{\lambda+1}W_1,$$

$$\Omega_{30} = \frac{\lambda-1}{\lambda+1}W_1; \tag{44}$$

and

$$K_1 = \frac{\lambda+1}{2}\left[\frac{\pi a}{2\lambda-1}\right]^{1/2}\left[\frac{10\lambda-\lambda^2-1}{4(\lambda+1)}\sigma_{22} - \frac{3(\lambda-1)^2}{4(\lambda+1)}\sigma_{11}\right], \tag{45}$$

$$K_2 = \frac{\lambda+1}{2}\left[\frac{2\lambda-1}{\pi a}\right]^{1/2}\frac{\lambda+1}{2\lambda}\sigma_{12}, \tag{46}$$

$$K_3 = \frac{\lambda+1}{2}\left[\frac{\pi a}{2\lambda-1}\right]^{1/2}\sigma_{32}, \tag{47}$$

$$U = \frac{\pi}{64}(\kappa+1)a^2\left\{\left[\frac{3}{4}(3-\lambda)(\lambda+1)^2 + (\lambda-1)^3 + 2\right]\sigma_{22}^2 + \left[\frac{1}{4}(5\lambda-7)(\lambda+1)^2 + (\lambda-1)^3 + 2\right]\sigma_{11}^2 + \left[4 + 2(\lambda-1)^3 - \frac{1}{2}(\lambda+1)^3\right]\sigma_{11}\sigma_{22} + \frac{1}{\lambda}(\lambda+1)^3\sigma_{12}^2\right\} + \frac{\pi a^2}{16}(\lambda+1)\left[3(\lambda-1)\sigma_{31}^2 + (5-\lambda)\sigma_{32}^2\right]. \tag{48}$$

The crack periphery associated with (42) has the parametric representation

$$\left\{\begin{aligned}\frac{x_1}{a} &= \cos\phi[1-(\lambda-1)\sin^2\phi] \\ \frac{x_2}{a} &= (\lambda-1)\sin^3\phi\end{aligned}\right. \qquad (0\le\phi\le 2\pi,\ 1\le\lambda\le 2)\ , \quad (49)$$

which reduces to

$$\frac{x_2}{a} = \pm(\lambda-1)\left[1-\left(\frac{x_1}{a}\right)^2\right]^{3/2} \quad \text{for} \quad 0<\lambda-1<<1. \quad (50)$$

For $\lambda=2$, (42) reduces to (8) which maps a hypocycloid with four cusps onto the unit circle $|\zeta|=1$. The complete set of cracks is given in Fig. 2(b). It is noted that for $2-\lambda<<1$ the crack may be viewed as a curvilinear square with two short corner cracks.

4.5 Cracks with Very Sharp Cusps. The classes of cracks defined by (33) and (42) may be considered as generalizations of the thin cracks defined by (38) and (50), respectively. It is obvious from the latter two equations that the first derivatives vanish at the cusp tip (zero cusp angle). This is termed by Berezhnitskii as a cusp of first-order tangency in [6] in which a method of constructing cracks with two nth-order tangency cusps is described. Our objective here is to further generalize the descriptions of (33) and (42) to include cusps of nth-order tangency. Our method is different from that of [6] and our results for the two-cusp version are different from those given in [6]. This is due to the fact that the order of tangency of the cusps does not dictate the shape of the crack in the large. For convenience, we shall treat the one-tip and two-tip cases separately.

4.5(a) One-Tip Variations. Let $2a$ be the "length" of a crack and let ϵ be a measure of the gap sustained by the upper and lower surfaces of the crack. Our objective is to find a simple mapping $M(\zeta;a,\epsilon,N)$ for a class one-tip cracks such that as $\epsilon\to 0$ the crack periphery is defined by

$$\frac{x_2}{a} = \pm\epsilon\left(1+\frac{x_1}{a}\right)^{1/2}\left(1-\frac{x_1}{a}\right)^{N-1/2} \quad (N\ge 2). \quad (51)$$

It is clear that the first $N-1$ derivatives of (51) vanish at $x_1=a$. Following (33), we write

$$M(\zeta;a,\epsilon,N) = \frac{a}{2}\left[\zeta+\frac{1}{\zeta}+\epsilon f(\zeta;N)\right] \quad (52)$$

where

$$f(\zeta;N) = 2\left[A_0\zeta - \sum_{n=1}^{N} A_n\zeta^{-n}\right], \quad (53)$$

and A_n $(n=0,1,\ldots,N)$ are real constants to be determined. Setting $\zeta=e^{i\phi}$ in (52) we find

$$\frac{x_1}{a} = \cos\phi + 0(\epsilon), \quad \frac{x_2}{a} = \epsilon\left[A_0\sin\phi + \sum_{n=1}^{N} A_n\sin n\phi\right]. \quad (54)$$

It follows from the foregoing and (51) that, as $\epsilon\to 0$,

$$A_0\sin\phi + \sum_{n=1}^{\mathrm{N}} A_n\sin n\phi = \sin\phi(1-\cos\phi)^{N-1}. \quad (55)$$

Since $\sin n\phi/\sin\phi$ is a polynomial of $\cos\phi$ of degree $n-1$, the preceding equation yields N algebraic equations for the $N+1$ constants A_n. One way of obtaining these equations is to examine the Taylor expansion of (55) at $\phi=0$, and the results are

$$A_0 + \sum_{n=1}^{N} n^{2m-1}A_n = 0 \quad (m=1,2,\ldots,N-1), \quad (56)$$

$$A_0 + \sum_{n=1}^{N} n^{2N-1}A_n = (-1/2)^{N-1}(2N-1)!. \quad (56)$$

The remaining equation is the normalizing condition

$$M(1)-M(-1) = 2a, \quad (57)$$

i.e.,

$$A_0 = \sum_{\text{odd}} A_n. \quad (58)$$

The determinants involved in solving (56) are of the Vandermonde type [10] and hence the constants may be explicitly determined. They are

$$A_n = \frac{1}{n}(1/2)^{N-1}(2N-1)!\prod_{\substack{k=1\\k\ne n}}^{N}(n^2-k^2)^{-1}. \quad (59)$$

For $n=1$, however, (59) is to be interpreted as A_0+A_1.

It remains to be shown that $\zeta=1$ is always a root of $M'(\zeta)=0$ which may be written as

$$\zeta^{N-1}(\zeta^2-1)+2\epsilon\left(A_0\zeta^{N+1}+\sum_{n=1}^{N} nA_n\zeta^{N-n}\right)=0 \quad (60)$$

The first of (56) implies that the ϵ-term of (60) vanishes at $\zeta=1$. More specifically, we may define C_n by the expressions

$$c_1 = A_1, \quad c_n = nA_n + c_{n-1},$$

$$C_N = NA_N + C_{N-1} = -A_0. \quad (61)$$

Then (60) becomes

$$(\zeta-1)\left[\left(1+2\epsilon A_0\right)\left(\zeta^N+\zeta^{N-1}\right) + 2\epsilon\sum_{m=1}^{N-1}\left(C_m+A_0\right)\zeta^{N-m-1}\right]=0 \quad (62)$$

We have thus completed the construction of a simple polynomial mapping. It is clear that $M(\zeta)$ is holomorphic for ϵ sufficiently small. The range of ϵ must be determined by the other roots of (62). For $N=3$, the mapping is

$$M(\zeta;a,\epsilon,3) = \frac{a}{2}\left[\left(1+\frac{3}{2}\epsilon\right)\zeta+(1-\epsilon)\frac{1}{\zeta} + \frac{2\epsilon}{\zeta^2}-\frac{\epsilon}{2}\frac{1}{\zeta^3}-2\epsilon\right], \quad (63)$$

and the crack periphery is given by

$$\left\{\begin{aligned}\frac{x_1}{a} &= \cos\phi+\epsilon\sin^2\phi(\cos\phi-2)\ , \\ \frac{x_2}{a} &= \epsilon\sin\phi(1-\cos\phi)^2\ .\end{aligned}\right. \quad (64)$$

It is found that (63) remains holomorphic for $0\le\epsilon\le 1/3$ and for $\epsilon=1/3$ the crack assumes the shape of an elongated three-cusp hypocycloid. The complete set of configurations is given in Fig. 2(c). In view of the length of the paper, the simple solution associated with (63) is not included here.

4.5(b) Two-Tip Variations. The objective now is to find a simple mapping $M(\zeta;a,\epsilon,N)$ for a class of doubly symmetric cracks such that as $\epsilon\to 0$ the crack periphery is given by

$$\frac{x_2}{a} = \pm\epsilon\left[1-\left(\frac{x_1}{a}\right)^2\right]^{(2N-1)/2} \quad (N\geq 2) \tag{64}$$

where N is an integer. Following (42), we write

$$M(\zeta;a,\epsilon,N) = \frac{a}{2}\left[\zeta+\frac{1}{\zeta}+\epsilon f(\zeta;N)\right] \tag{65}$$

where

$$f(\zeta;N) = 2\left[A_0\zeta - \sum_{n=1}^{N} A_n \zeta^{-(2n-1)}\right]. \tag{66}$$

The real constants A_n $(n=0,1,\ldots,N)$ must satisfy the conditions

$$A_0 + \sum_{n=1}^{N}(2n-1)^{2m-1}A_n = 0 \quad (m=1,2,\ldots,N-1), \tag{67}$$

$$A_0 + \sum_{n=1}^{N}(2n-1)^{2N-1}A_n = (-1)^{N-1}(2N-1)! \tag{68}$$

$$A_0 = \sum_{n=1}^{N} A_n. \tag{69}$$

The solution is

$$A_n = \frac{1}{2n-1}(2N-1)!\prod_{\substack{k=1\\k\neq n}}^{N}[(2n-1)^2-(2k-1)^2]^{-1}. \tag{70}$$

Once again (70) is to be interpreted as A_0+A_1 for $n=1$.

The vanishing of $M'(\zeta)$ implies

$$\zeta^{2(N-1)}(\zeta^2-1)+2\epsilon\left[A_0\zeta^{2N}+\sum_{n=1}^{N}(2n-1)A_n\zeta^{2(N-n)}\right]=0 \tag{71}$$

where the ϵ-term evaluated at $\zeta^2=1$ is just (67). It follows that $\zeta=\pm 1$ are two of the roots. We give the explicit results for $N=3$. It is

$$M(\zeta;a,\epsilon,3) = \frac{a}{2}\left[\left(1+\frac{3}{8}\epsilon\right)\zeta+\left(1-\frac{7}{8}\epsilon\right)\frac{1}{\zeta} \right.$$
$$\left. \frac{5}{8}\epsilon\frac{1}{\zeta^3}-\frac{\epsilon}{8}\frac{1}{\zeta^5}\right] \tag{72}$$

and

$$\begin{cases} \dfrac{x_1}{a} = \cos\phi - \epsilon\dfrac{3}{2}\cos\phi\sin^2\phi\left(1-\dfrac{2}{3}\cos^2\phi\right), \\[2ex] \dfrac{y_1}{a} = \epsilon\sin^5\phi. \end{cases} \tag{73}$$

This mapping remains holomorphic for $0 \leq \epsilon \leq 2/3$ and the limit is a flattened four-cusp hypocycloid. The complete set of configurations is given in Fig. 2(d). Once again, the simple exact solution is not included here.

5 Remarks

The idea behind the procedures outlined in Section 2 is very straightforward. However, the fact that the simple polynomial function can be used to generate so many relevant unconventional cracks is somewhat unexpected. Of particular importance is the class of corrugated cracks and holes with or without internal contact. These configurations are natural candidates for studying compressive loads in that the associated contact problems can be solved in closed forms. This is so because the complication generated by the configuration is removed by the fact that the mapping is simple. Moreover, the characteristics of the contact zones are the same as those of the Hertz problem. In other words, a contact zone is simply characterized by two constants, a contact-zone size, and a "resultant" contact force. The contact of a figure-eight hole will be presented in a forthcoming paper.

The contact near a cusp, however, may not turn out to be so simple. This speculation stems from the fact that near a cusp of Nth order tangency the periphery is defined by

$$y = |x|^{N+½} \quad (N\geq 1) \tag{74}$$

in which $x=y=0$ is the cusp tip. The standard Hertz body is simply the parabola

$$y=x^2. \tag{75}$$

The most puzzling case is perhaps given by $N=1$ for which the radius of curvature at $x=y=0$ is zero.

References

1 Wu, C. H., "Unconventional Internal Cracks Part 1. Symmetric Variations of a Straight Crack," ASME, Journal of Applied Mechanics, Vol. 49, Mar. 1982, pp. 62–68.

2 England, A. H., *Complex Variable Methods in Elasticity*, Wiley-Interscience, 1971.

3 Panasyuk, V. V., and Berezhnitskii, L. T., "Limit Equilibrium of Plates With Sharp Stress Raisers," *Soviet Material Science*, Vol. 1, No. 4, 1965, pp. 293–301.

4 Berezhnitskii, L. T., and Sadivskii, V. M., "Stress Distribution Near Elastic Inclusions with Cuspidal Points on the Outline," *Soviet Material Science*, Vol. 12, No. 3, 1976, pp. 261–265.

5 Berezhnitskii, L. T., and Sadivskii, V. M., "Theory of Sharp-Pointed Stress Concentrations in Anisotropic Plates," *Soviet Material Science*, Vol. 13, No. 3, 1977, pp. 303–311.

6 Berezhnitskii, L. T., "Theory of Cuspidal Defects with Different Types of Angular Cuspidal Points," *Soviet Material Science*, Vol. 13, No. 4, 1977, pp. 414–420.

7 Erdogan, F., and Sih, G. E., "On the Crack Extension in Plates Under Plane Loading and Transverse Shear," ASME *Journal of Basic Engineering*, Vol. 85, 1963, pp. 519–527.

8 Westman, R. A., "Pressurized Star Crack," *J. Math. Phys.*, Vol. 43, 1964, pp. 191–198.

9 Benthem, J. P., and Koiter, W. T., "Asymptotic Approximations to Crack Problems," *Mechanics of Fracture* 1, G. C. Sih, editor, Noordhoff, 1973.

10 Kurosh, A., *Higher Algebra*, Mir Publishers, Moscow, 1972.

S. Mukherjee
Associate Professor.
Mem. ASME

M. A. Morjaria
Research Associate.
Assoc. Mem. ASME

F. C. Moon
Professor.
Mem. ASME

Department of Theoretical and
Applied Mechanics,
Cornell University,
Ithaca, N.Y. 14853

Eddy Current Flows Around Cracks in Thin Plates for Nondestructive Testing

The boundary element method is used to calculate the induced electric current flow around cracks in thin conducting plates. A low frequency approximation leads to a Poisson equation for the current density potential or stream function. A kernel is used which produces the correct singularity at the crack tip. The boundary condition on the crack, derived from Faraday's law, requires the line integral of the current density around the crack to be zero. Numerical results for induced currents due to a circular induction coil are given. These results show that hot spots, due to Joule heating, can occur at the tips of the crack. Comparison of numerical results with infrared scanning experiments of eddy currents in a cracked plate are given. It is hoped that the numerical method presented here will provide a tool to simulate both new and conventional nondestructive eddy current testing techniques.

Introduction

Induced electric currents are generated in conductors by time varying magnetic fields. When the source of the field is outside the body, the induced currents must flow in closed paths, hence the designation "eddy currents." In most problems eddy currents are unwanted since they are a source of heat and energy loss and in some applications can create dynamic forces and magnetic pressures. A few applications, such as magnetic forming and levitation, have exploited the dynamic force producing capability of eddy currents. A third interest in eddy currents is their potential for nondestructive testing. The presence of flaws or cracks interrupt the natural flow of electric current, and the detection of the change of electron flow can give a clue to the presence of flaws in solid conductors. In fact, a dynamic electromagnetic force tends to open up a crack, and, if it is of sufficient magnitude, can cause a crack to grow and lead to fracture [1]. This matter can be of great concern in the design of fusion reactors.

The calculation of eddy currents in conductors is generally carried out by either using a magnetic or an electric potential. A comparison of the two methods is given by Carpenter [2]. The electric field or current density potential has the advantage that it need be calculated only in the conductor, whereas the magnetic potential must be solved both inside and outside the conductor. The latter method, therefore, poses potential problems for numerical methods.

Numerical methods must generally be used for the solution of eddy current problems in conductors of complex shape. The finite element method (FEM) and the discrete circuit element have been used for some years for the solution of these problems. Recently, the boundary element method (BEM) (also called the boundary integral equation method) has been applied to problems in electromagnetics. Wu et al. [3] and Ancelle et al. [4] have addressed magnetostatic problems by the BEM while Trowbridge [5] has considered magnetostatic problems and eddy current problems by the magnetic potential approach. Very recently, Salon and Schneider [6] have solved problems of eddy current flow in long prismatic conductors by the BEM based on an electric potential approach. The boundary element method has the important advantage that only the boundary of a body (rather than the entire domain) needs to be discretized in a numerical solution procedure – thus effectively reducing the dimension of a problem by one. However, a full matrix must be treated in the BEM whereas the FEM requires operations on sparse matrices.

The direct boundary element approach [3–6] uses a singular solution of a differential equation in an infinite domain as a kernel in the corresponding integral equation. This direct approach can be used in simply connected as well as multiply connected domains. However, if a cutout in a conducting plate is a crack, numerical difficulties might arise from discrete modeling of the crack boundary. This difficulty can be overcome if modified kernels are used so that the new kernels are the singular solutions of the governing differential equations for an infinite region with a crack already present in it. This technique has been recently developed for two-dimensional harmonic and biharmonic operators in connection with study of stresses near crack tips in bodies undergoing inelastic deformation [7–9]. Use of these modified kernels allows the proper boundary conditions to be satisfied exactly over the entire crack surface and discretization of the crack surface is no longer necessary in a numerical solution procedure. The method is thus perfectly suited to the study of two-dimensional problems of eddy current flow in cracked bodies.

Contributed by the Applied Mechanics Division for publication in the JOURNAL OF APPLIED MECHANICS.

Discussion on this paper should be addressed to the Editorial Department, ASME, United Engineering Center, 345 East 47th Street, New York, N.Y. 10017, and will be accepted until two months after final publication of the paper itself in the JOURNAL OF APPLIED MECHANICS. Manuscript received by ASME Applied Mechanics Division, March, 1981; final revision, October, 1981.

The purpose of this paper is the study of eddy currents in thin cracked plates with a view toward detection of cracks or flaws by nondestructive testing. An analytical formulation using an electric potential is first presented for the determination of eddy currents in a thin flat conducting plate with a line crack present in it. The applied magnetic field is assumed to be harmonic in time but can have an arbitrary spatial distribution inside the plate. This results in Poisson's equation for the electric potential. A boundary element formulation is next presented using modified kernels for the Laplacian operator in two dimensions.

Numerical results are given for eddy currents in a center-cracked square plate with the applied field being that due to a circular coil. Stream lines are given for various positions of the coil relative to the crack. The induced temperature at any point in the plate is proportional to the square of the density of the induced current at that point. Calculated induced temperature profiles are presented for various coil positions. An eddy current intensity factor, analogous to a stress intensity factor, is defined at a crack tip. Finally, experimental results are presented for an infrared isotherm of induced eddy currents in a cracked aluminum plate.

Governing Differential Equations

A thin, flat uniform plate made of a conducting material is considered in this paper (Fig. 1). The plate boundary can be arbitrary, its thickness is h, and the conductivity of the plate material is σ. The plate has a line crack of length $c = 2a$ present in it. The crack can have arbitrary orientation relative to the outside boundary of the plate. The coordinate system used is shown in Fig. 1. The origin of coordinates lies at the center of the crack in the midsurface of the plate.

Consider a current density $\mathbf{J}$, which is induced in the plate by an oscillatory magnetic field $\mathbf{B}^\circ$ outside the plate. The current distribution is assumed to be uniform across the plate thickness and oscillatory in nature. The skin depth, which is inversely proportional to the square root of the frequency, is assumed to be large compared to the plate thickness. Under these assumptions no bending occurs in the plate.

According to Ohm's law

$$\mathbf{J} = \sigma \mathbf{E} \tag{1}$$

where $\mathbf{E}$ is the electric field (the Hall effect or magnetoresistive terms are neglected in Ohm's law).

For low frequency currents, the continuity condition is

$$\nabla \cdot \mathbf{J} = 0 \tag{2}$$

where ∇ is the gradient operator in two dimensions. Thus, a stream function (or electric potential) $\psi(x_1, x_2)$ can be defined such that

$$\mathbf{J} = \nabla \times (\psi \mathbf{k}) = -\mathbf{k} \times \nabla \psi \tag{3}$$

so that

$$J_1 = \frac{\partial \psi}{\partial x_2}, \quad J_2 = -\frac{\partial \psi}{\partial x_1}.$$

Using Faraday's law of induction

$$\nabla \times \mathbf{E} = -\frac{\partial \mathbf{B}}{\partial t} \tag{4}$$

with $\mathbf{B}$ the total magnetic field inside the plate and t time, the governing differential equation for the stream function is

$$\nabla^2 \psi = \sigma \frac{\partial B_3}{\partial t} = \sigma \frac{\partial}{\partial t} (B_3^\circ + B_3^1) \tag{5}$$

In the foregoing, B_3^1 is the self magnetic field inside the plate due to the current $\mathbf{J}$. In general, this field can be obtained from the Biot-Savart law as an integral, over the plate, of a kernel times the stream function ψ. Equation (5) would then become an integro-differential equation for the stream

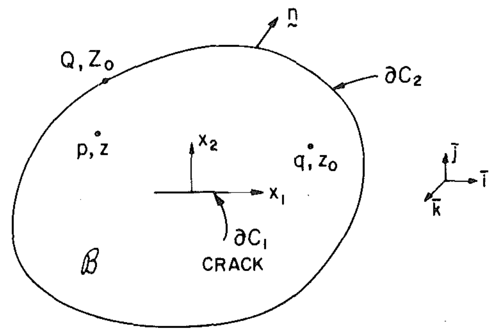

Fig. 1 Cracked plate

function [10]. If, however, the applied field is sinusoidal and the resulting skin depth is greater than 10 times the plate thickness, the self field term can be neglected relative to the applied field $\mathbf{B}^\circ$ [11]. Under this assumption, and with $B_3^\circ = \hat{B}_3^\circ e^{i\omega t}$ (where $i = \sqrt{-1}$ and ω is the oscillation frequency), the spatial part of the stream function ψ satisfies the equation

$$\nabla^2 \psi = i\omega\sigma \hat{B}_3^\circ = f(x_1, x_2) \tag{6}$$

which is a two-dimensional Poisson's equation with a prescribed nonhomogeneous term. For simplicity, the same notation is used in the following for the amplitudes of the various oscillatory functions, as has been used so far for the functions themselves.

Eddy current distributions using a similar electric potential approach have been obtained by Salon and Schneider [6]. Their formulation is valid for the determination of currents in long prismatic conductors and results in a Helmholtz equation for the stream function ψ. Thus, the work of Schneider and Salon is analogous to plane strain problems in mechanics, while the present paper addresses conductors in the shape of thin plates. This is analogous to plane stress.

The current must be tangential to the boundary of the plate at a point on it. Thus, for a point on either the crack boundary ∂C_1 or on the outside boundary ∂C_2 (Fig. 1)

$$\mathbf{J} \cdot \mathbf{n} = \frac{d\psi}{ds} = 0 \tag{7}$$

where $\mathbf{n}$ is an unit normal to the boundary at a point on it and s is the distance measured along a boundary in the anticlockwise sense. Thus, if ψ is a constant a_1 on ∂C_1 and another constant a_2 on ∂C_2, equation (7) is satisfied. One of these constants can be set to zero without loss of generality and the other one is determined by the auxiliary condition

$$\oint_{\partial C_1} \mathbf{J} \cdot \mathbf{t} \, ds = 0 \tag{8}$$

where $\mathbf{t}$ is an unit tangent to ∂C_1 at a point on it. Physically, this equation implies that the net flux flowing through the crack is zero.

The boundary conditions on ψ, in this formulation, are therefore

$$\psi = 0 \text{ on the crack boundary } \partial C_1 \tag{9}$$

$$\frac{d\psi}{ds} = 0 \text{ on the outside boundary } \partial C_2 \tag{10}$$

$$\oint_{\partial C_1} \frac{d\psi}{dn} \, ds = 0 \tag{11}$$

Equations (9)–(11) together with the field equation (6) constitute a well-posed problem.

It should be noted that this formulation assumes that no current flows across the crack or crack tip. This formulation leads to a current density singularity at the crack tip, as does analogous formulations for the stress at a crack tip.

Physically it is suspected that there is a finite resistance or current leakage across the crack tip which would relieve the singularity in actual conductors. However this is not considered in this paper. Instead we will characterize the current at the crack tip by a current density intensity factor analogous to that in fracture mechanics.

Boundary Element Formulation

Integral Equations. An integral equation formulation for Poisson's equation (6) can be written as (Fig. 1)

$$2\pi\psi(p) = \oint_{\partial C_2} K(p,Q)G(Q)\, ds_Q + \int_A K(p,q)f(q)\,dA_q \tag{12}$$

The function G, a source strength function on the outside boundary, must be determined from the boundary condition on it, equation (10). The points p (or P) and q (or Q) are source and field points, respectively, with capital letters denoting points on the boundary of the body and lowercase letters denoting points inside the body. The area of the body B is denoted by A.

The kernel $K(p, q)$, for a simply connected region, is normally chosen to be a singular solution of Laplace's equation in appropriate dimensions, e.g.,

$$K = ln r_{pq} = Re[\hat{\phi}(z, z_0)] \text{ with } \hat{\phi}(z, z_0) = ln(z - z_0)$$

Here r_{pq} is the distance between a source point p and a field point q, Re denotes the real part of the complex argument, and z and z_0 are the source and field points, respectively, in complex notation.

In this problem, however, the kernel must be chosen such that it vanishes on the crack boundary ∂C_1. This is achieved by augmenting $\hat{\phi}$ with a second piece $\phi *$ which equals the negative of $\hat{\phi}$ when the source point z lies on ∂C_1 (Fig. 1). Furthermore, $\phi *$ must satisfy Laplace's equation and be regular inside the body B. For an elliptical cutout ∂C_1, $\phi *$ is derived by making use of the mapping function

$$z = \omega(\xi) = \frac{1}{\xi} + m\xi \tag{13}$$

which transforms the region on and outside an ellipse in the z plane to a region on and inside an unit circle in the ξ plane. The parameter m equals $(a-b)/(a+b)$ (with $(a+b)=2$) in terms of the semimajor and minor axies, a and b, respectively, of the ellipse. For the line crack in this problem, a is taken to be equal to 2 and b is zero. Thus, m equals 1. Using this value of m, the augmented function ϕ is determined as [7]

$$\phi(z,\bar{z},z_0) = ln(1 - r_i/\xi) - ln(1 - r_i\bar{\xi}) \tag{14}$$

where

$$r_i = \frac{z_0 \pm \sqrt{z_0^2 - 4}}{2}, \ |r_i| \le 1; \ \xi = \frac{z \pm \sqrt{z^2 - 4}}{2}, \ |\xi| \le 1$$

and the kernel K in equation (12) is

$$K(p,q) = Re[\phi(z,\bar{z},z_0)] \tag{15}$$

A superposed bar denotes, as usual, the complex conjugate of a complex quantity.

Use of K from equation (15) in equation (12) satisfies equation (9). It has been proved in reference [7] that this formulation also satisfies the integral condition (11) on the crack surface. Thus, the proper boundary conditions on the crack surface are satisfied in an implicit manner and discretization of the crack boundary is not necessary in a numerical solution procedure.

The remaining boundary condition (10) on the outside surface is satisfied by using a differentiated version of (12) and taking the limit as p inside B approaches a point P on ∂C_2. Defining

$$H_1 = Re\left(\frac{\partial\phi}{\partial x_2}\right), \ H_2 = -Re\left(\frac{\partial\phi}{\partial x_1}\right) \tag{16}$$

and

$$\frac{dK}{ds} = Re\left[\frac{d\phi}{ds}\right] = H_i n_i \ (i \text{ summed over } 1, 2)$$

where n_i are the components of the unit outward normal to ∂C_2 at some point on it, the boundary condition (10) becomes

$$0 = \oint_{\partial C_2} H_i(P,Q)n_i(P)G(Q)\, ds_Q + \int_A H_i(P,q)n_i(P)f(q)\,dA_q \tag{17}$$

Equation (17) is valid for a point P on ∂C_2 where it is locally smooth. The current components J_1 and J_2 at a point p inside the body are obtained from equations like (12) with the kernel K replaced by $H_1(p,Q)$ and $H_2(p,Q)$, respectively. Care must be taken to include the appropriate residues in the formula for J_j when p approaches a boundary point P [7].

Discretization of Equations and Solutions Strategy. The outer boundary of the body, ∂C_2, is divided into N_2 straight boundary elements using N_b ($N_b = N_2$) boundary nodes and the interior of the body, A, is divided into n_i triangular internal elements. A discretized version of equation (17) is

$$0 = \Sigma_{N_2} \int_{\Delta s_i} H_i(P_M,Q)n_i(P_M)G(Q)\, ds_Q + \Sigma_{n_i} \int_{\Delta A_i} H_i(P_M,q)n_i(P_M)f(q)\, dA_q \tag{18}$$

where P_M is the point P where it coincides with a node M at a center of a boundary segment on ∂C_2 and Δs_i and ΔA_i are boundary and internal elements, respectively.

A simple numerical scheme is used in which the source strengths G are assumed to be piecewise uniform on each boundary segment with their values to be determined at the nodes that lie at the centers of each segment. The integrals of H_i on boundary elements are evaluated analytically for the singular and by Gaussian quadrature for the regular portions. Nonsingular area integrals of known integrands over triangular internal cells are evaluated by Gaussian quadrature. Evaluation of singular area integrals require special care [12].

Substitution of the piecewise uniform source strengths into equation (18) and carrying out of the necessary integrations leads to an algebraic system of the type

$$\{0\} = [A]\{G\} + \{d\} \tag{19}$$

where the vector $\{G\}$ contains the unknown source strengths on ∂C_2.

Equation (12) for the stream function ψ and analogous equations for the current components J_i are discretized in similar fashion.

The solution strategy is as follows. The matrix $[A]$ and vector $\{d\}$ in equation (19) are first evaluated by using the appropriate expressions for the kernels and the prescribed function f in equation (6). Equation (19) is solved for the vector $\{G\}$. This value of $\{G\}$ is now used in a discretized version of equation (12) to obtain the values of the stream funciton ψ at any point p. Finally, the current vector at any point is obtained from equations analogous to (12).

Numerical Results

Field Due to a Circular Induction Coil. A center-cracked square plate with a circular induction coil placed above it is shown in Fig. 2. The square plate is of side L with a center crack of length $c = 2a$. The coordinate system is shown in Figs. 1 and 2. The coil is of radius a_0 with its center at the point (x_1°, x_2°, h_0). The induced field $\mathbf{B}^\circ$ at a point $q(x_1, x_2)$ in the plate, from the Biot-Savart law, is

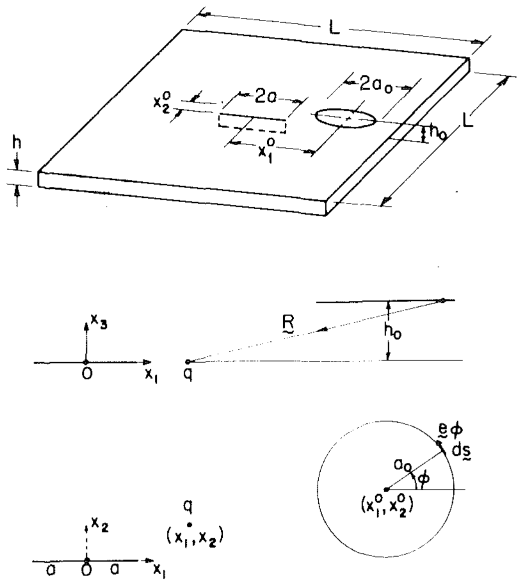

Fig. 2 Diagram showing coil and cracked plate geometry

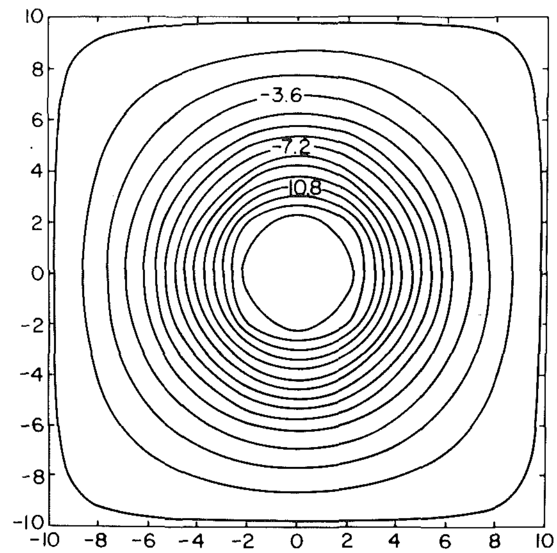

Fig. 3 Stream lines for induced currents in an uncracked square plate by a circular coil. $\hat{L}=20$, $\hat{a}_0=4$, $\hat{x}_1^0=\hat{x}_2^0=0$, $\hat{h}_0=1$.

$$\mathbf{B}^\circ = \frac{\mu_0 I}{4\pi}\oint_{\text{coil}} \frac{d\mathbf{s}\times\mathbf{R}}{R^3} \tag{20}$$

where μ_0 is the permeability of vacuum, I is the current in the coil, $d\mathbf{s}$ a length element along the coil ($d\mathbf{s}=\mathbf{e}_\phi a_0 d\phi$) and

$$-\mathbf{R}=(x_1^\circ - x_1 + a_0\cos\phi)\,\mathbf{i} + (x_2^\circ - x_2 + a_0\sin\phi)\,\mathbf{j} + h_0\mathbf{k}$$

with $R=|\mathbf{R}|$.

Thus, the function $f(x_1, x_2)$ in equation (6) is

$$f(x_1,x_2)=\frac{i\omega\sigma\mu_0 I}{c4\pi}\oint_{\text{coil}}\frac{c\mathbf{k}\cdot(d\mathbf{s}\times\mathbf{R})}{R^3} \tag{21}$$

The dimensionless line integral $\mathcal{G}$ can be written as

$$\oint_{\text{coil}}\frac{\mathbf{k}\cdot(d\mathbf{s}\times\mathbf{R})c}{R^3}=\int_0^{2\pi}$$

$$\frac{c\{a_0[(x_1^0-x_1)\cos\phi+(x_2^0-x_2)\sin\phi]+a_0^2\}\,d\phi}{[(x_1^0-x_1)^2+(x_2^0-x_2)^2+2a_0[(x_1^0-x_1)\cos\phi+(x_2^0-x_2)\sin\phi]+a_0^2+h_0^2]^{3/2}}$$

This integral is evaluated by Gaussian integration in the numerical calculations (6 Gauss points between 0–$\pi/2$).

Nondimensional Equations. Equation (6), with $f(x_1,x_2)$ defined by equation (21), can be nondimensionalized to the form

$$\hat{\nabla}^2\hat{\psi}(\hat{x}_1,\hat{x}_2)=\mathcal{G} \tag{22}$$

where

$$\hat{\psi}=\frac{64\psi c}{iIR},\quad \hat{x}_i=4x_i/c,\quad \hat{x}_i^0=4x_i^0/c$$

$$(i=1,2),\ \hat{L}=4L/c,\ \hat{a}_0=4a_0/c,\ \hat{h}_0=4h_0/c$$

$$\hat{\nabla}^2=\frac{\partial^2}{\partial\hat{x}_1^2}+\frac{\partial^2}{\partial\hat{x}_2^2},\ R=\frac{16c^2}{2\pi\delta^2}$$

and the skin depth

$$\delta=\sqrt{\frac{2}{\omega\sigma\mu_0}}$$

Further, the dimensionless current density is

$$\hat{J}=\frac{16Jc^2}{iIR}$$

Geometrical Parameters and Boundary Mesh. The values of the geometrical parameters, used in the numerical calculations, are

$$\hat{L}=20,\ \hat{a}_0=4 \text{ and } 1,\ \hat{h}_0=1,$$

$$\hat{x}_1^0=0,1,2,3,4,5,\text{ and }6,\ \hat{x}_2=0$$

The dimensionless crack length here is 4. The results for any crack length c can be determined from the preceding equations.

A typical boundary element mesh for the problem is shown in Fig. 3 of [12]. Only the upper half of the plate is modeled due to symmetry. Nonsingular integrals are evaluated by Gaussian quadrature with 6 Gauss points on a boundary segment and 7 Gauss points in an internal cell. A 4×4 grid is used for the evaluation of singular area integrals (see [12]).

The uniform field problem is analogous to the Saint Venant problem of torsion of long prismatic bars with end couples. The computer program used here has been verified by solving torsion problems in the absence of cracks [13] and the logic for inclusion of the crack has been verified by solving Mode III crack problems [7].

The boundary integral algorithm was also applied to a plate with a notch cut instead of a crack. The results were compared with an analysis using a finite element method [11], and the agreement was very good.

Eddy Current and Temperature Lines. Eddy current stream lines (constant $\hat{\psi}$ lines) are shown in Figs. 3–4 for a coil of radius 4. Figure 3 shows the lines in a plate without a crack in it, and Fig. 4 shows how the stream lines are affected by the crack for different coil positions. The crowding of stream lines near the crack tip leads to large gradients of $\hat{\psi}$ (and therefore large induced currents) in this region. The local temperature is proportional to the square of the current density ($\hat{\mathbf{J}}\cdot\hat{\mathbf{J}}$) and this leads to a hot spot at the crack tip. This is shown in Fig. 5 which shows lines of constant induced temperature. The contour lines go off scale as one approaches the crack tip. The behavior of the singularity at the crack tip is discussed later in the section entitled "Eddy Current Intensity Factor."

Temperature Scans. A matter of considerable interest in this approach to nondestructive testing is the existence of hot spots due to the presence of a crack. Figure 6 shows calculated temperature profiles along a line slightly above the crack

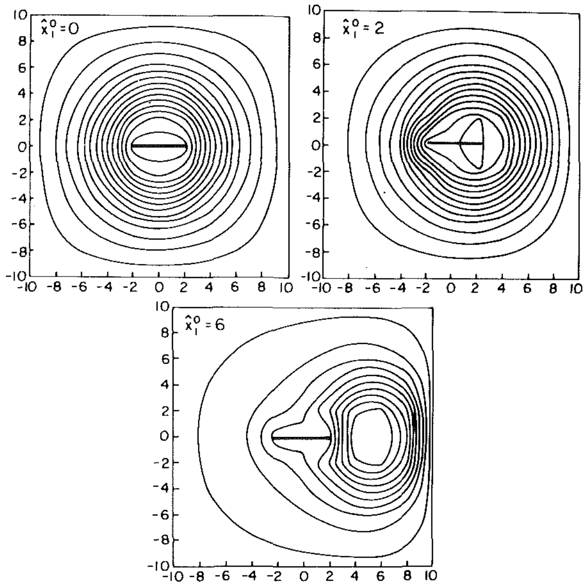

Fig. 4 Stream lines for induced currents in a cracked square plate by a circular coil for various coil positions. $\hat{L} = 20, \hat{a}_0 = 4, \hat{x}_2^0 = 0, \hat{h}_0 = 1$.

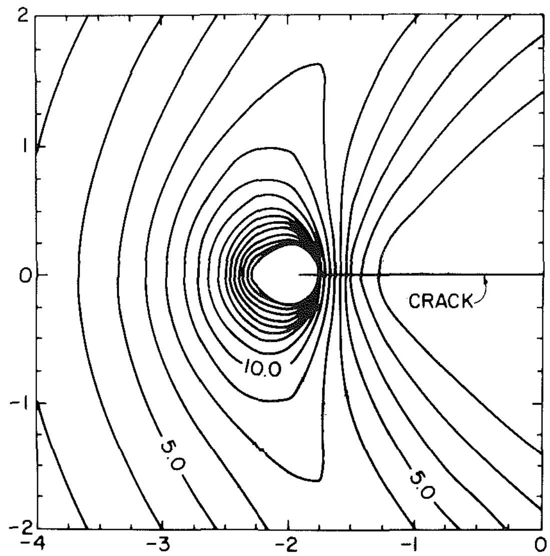

Fig. 5 Induced temperature or eddy current density square lines for induced currents in a cracked plate by a circular coil. $\hat{a}_0 = 4, \hat{x}_1^0 = 2, \hat{x}_2^0 = 0, \hat{h}_0 = 1$.

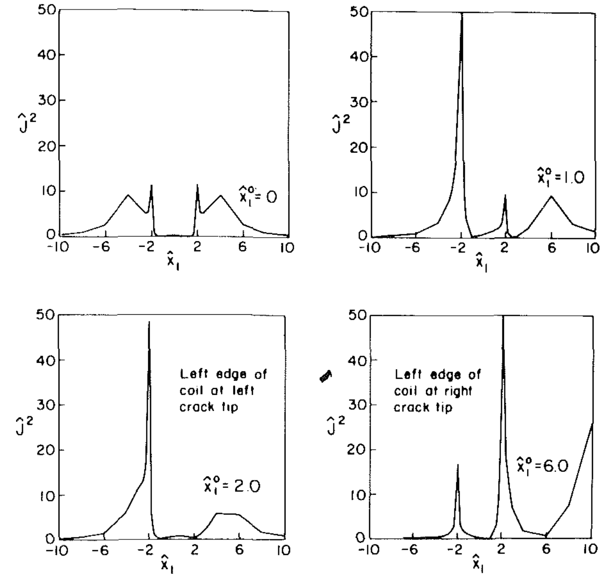

Fig. 6 Plots of induced temperature or eddy current density squared along a line slightly above the crack ($\hat{x}_2 = 0.05$) for various coil positions. $\hat{a}_0 = 4, \hat{x}_2^0 = 0, \hat{h}_0 = 1$.

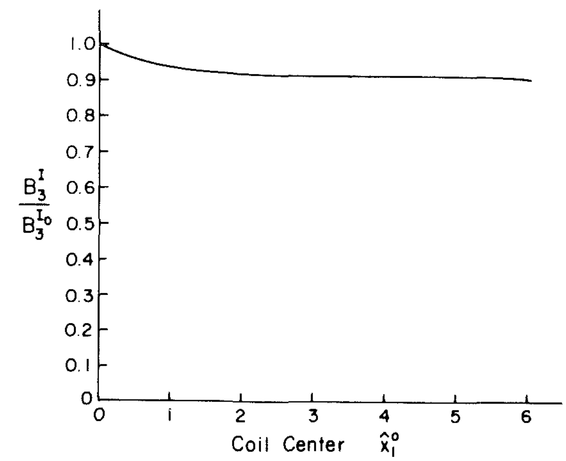

Fig. 7 Self induced field at the center of the induction coil as a function of coil position. $\hat{a}_0 = 4, \hat{x}_2^0 = 0, \hat{h}_0 = 1$.

($\hat{x}_2 = 0.05$) for different coil positions ($\hat{x} = 0$, 1, 2, and 6). The coil radius here is 4 (equal to the crack length). Hot spots are seen near the crack tips. The strongest hot spots arise when an edge of the coil is near a crack tip. These temperatures are much higher than other moderate hot spots elsewhere in the plate. A discussion of experimental results is given in the next section.

Self Induced Field at Center of Coil. One method of electromagnetic nondestructive testing uses one or more passive sensing coils together with an active induction coil [14]. The purpose of the sensing coils is to measure the self induced field (back e.m.f.) and to try to observe changes in back e.m.f. due to the presence of cracks. With this in view, the self induced field was calculated at the center of the induction coil for various coil positions. The method used is the Biot-Savart Law which gives the induced field B_3^I as

$$B_3^I = \frac{\mu_0 h}{4\pi} \int_{\text{plate}} \mathbf{k} \cdot \frac{(\mathbf{J} \times \mathbf{R})}{R^3} dA \tag{23}$$

where now the induced current density in the plate must be used. The integral must be evaluated over the plate with dA an area element in the plate. The current density is assumed to be piecewise uniform over each internal cell in this approximate calculation, with the value determined at the centroid (x_1^c, x_2^c) of the cell. Thus, in this case

$$\mathbf{R} = (x_1^0 - x_1^c)\mathbf{i} + (x_2^0 - x_2^c)\mathbf{j} + h_0 \mathbf{k}$$

and

$$B_3^I = \frac{\mu_0 h}{4\pi} \sum_{i=1}^{n_i} \frac{\Delta A_i [J_1(x_2^0 - x_2^c) - J_2(x_1^0 - x_1^c)]}{R^3} \tag{24}$$

where ΔA_i is the area of the ith triangular element.

A plot of normalized B_3^I with respect to coil position $\hat{x}_1^0$ is shown in Fig. 7. The values are normalized with respect to B_3^I when the coil center is directly above the crack center (i.e., $x_1^0 = x_2^0 = 0$). It is seen that in this example the position of the coil relative to the crack causes little variation in the induced field at the coil center. The variation of B_3^I with $\hat{x}_2^0$ has not been calculated. From these calculations, it appears that for low frequencies the back e.m.f. method may not be useful for detection of cracks and that the temperature scan approach appears to be much more promising for nondestructive testing in this case.

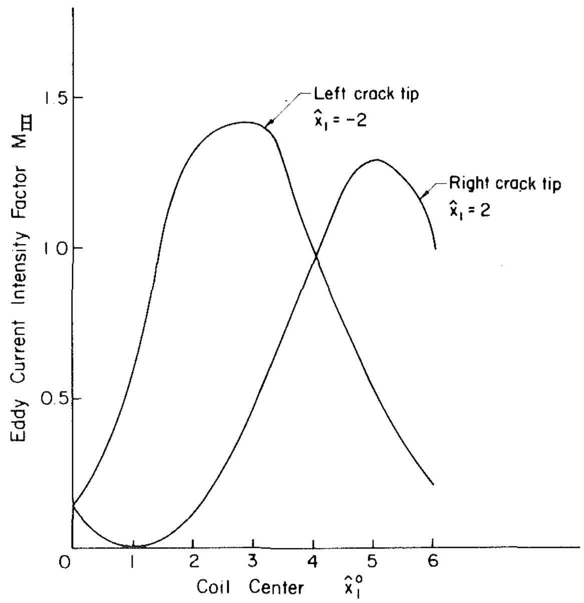

Fig. 8 Eddy current intensity factor at crack tips as functions of coil position. $\hat{a}_0 = 4, \hat{x}_2^0 = 0, \hat{h}_0 = 1$.

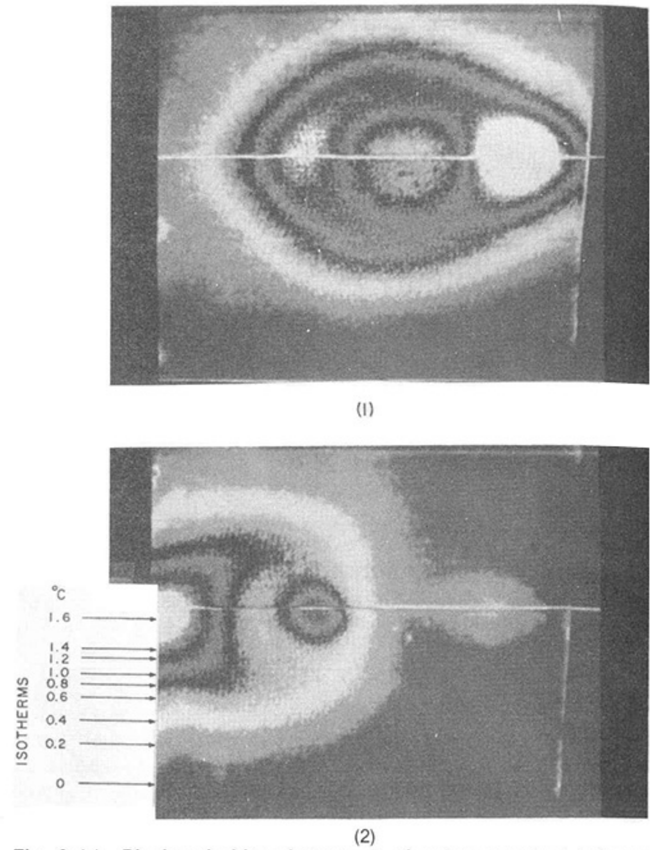

Fig. 9 (*a*) Black-and-white photograph of color quantized infrared isotherms of induced eddy currents in a cracked aluminum plate

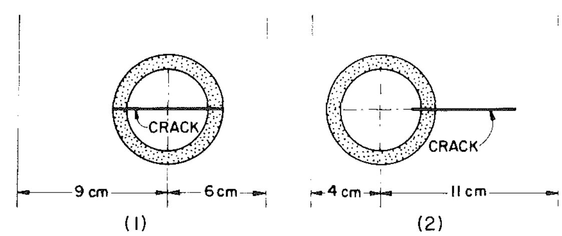

Fig. 9 (*b*) Crack and coil geometries for the photographs shown in Fig. 9 (*a*)

Fig. 9

Eddy Current Intensity Factor. It is well known from linear elastic fracture mechanics that stress components exhibit a square root singularity near a crack tip. It is therefore expected that the components of the current vector, in this problem, should display similar behavior near a crack tip. This, in fact, is the case, and the eddy current density squared is inversely proportional to the distance r from the crack tip (see Fig. 11 in [12]).

An eddy current intensity factor M_{III}, analogous to the stress intensity factor for Mode III, is defined here as

$$\hat{J}_2 = M_{III} \frac{c}{r} \tag{25}$$

A plot of M_{III} at the two crack tips, as functions of coil position, is shown in Fig. 8. The eddy current intensity factor is seen to peak when an edge of the coil is near a crack tip. At low frequencies, displacement currents are expected to have little effect on current singularity at a crack tip.

Computing Times. All the computing reported in this paper was carried out on an IBM 370/168 computer at Cornell University. A typical computing time for stream lines in a cracked plate was a fixed coil position is 100 c.p.u. sec.

Experimental Results

Infrared Experiments. Conventional eddy current nondestructive techniques use a small induction coil and search coils to induce eddy currents near the surface of solids and to measure the back e.m.f. generated by these currents [14]. To detect a flaw or a crack, the coils must be moved over the surface near the flaw in order to measure a change in voltage in the search coil. Recently a new method has been proposed using infrared scanning technology [11]. This method is based on the fact that eddy currents create heat and that this small temperature change can be detected using an infrared sensitive device.

In the present experiments an aluminum plate 15 cm × 30 cm, 0.51 mm thick, had a crack placed in its center, parallel to the 15 cm width. The crack was created by scoring a line in the aluminum with a sharp edge and flexing the plate until fatigue produced a through crack in the plate. The length of the crack was 6 cm. One tip of the crack was 3 cm from one edge of the plate and the other was 6 cm from the other edge [see Fig. 9(*b*)].

The induction coil was wound from 10 turns of copper wire on a 5.1-cm coil form so that the mean diameter of the coil was about 5.7 cm, slightly smaller than the crack length. The width of the coil was 1.3 cm and the coil face was placed 6.4 mm from the plane of the cracked plate.

Pulsed electric currents of the order of 9.3 KA peak current and 3.2 msec. duration were used with a rise time to peak of about 0.7 msec. The sensitivity of the infrared system was 0.1–0.2°C. If an infrared scan is made of the plate immediately after the firing of the current pulse, heat conduction may be neglected, and the measured rise in temperature is proportional to the integral of J^2 over time. (See e.g. [11].)

The infrared system used for these experiments is a UTI Corp. Spectrotherm infrared scanning system. Radiation from different points in the plane of focus is detected by a photoconductive crystal. A two-dimensional scan is obtained by two sets of rotating mirrors. The output can be displayed either on a grey scale tube or the voltage can be color quantized into 10 colors. Figure 9(*a*) shows a black-and-white photograph of two color-quantized infrared scans. Each photograph is obtained from a single firing of the current pulse. The scan time for this infrared system is about 1 sec. Other systems exist with scan times of the order of 1/16 sec. Each of the scans represent J^2 "isotherms" for different induction coil positions. The top photograph corresponds to a coil position centered at the middle of the crack. The bottom photograph corresponds to an induction coil position centered to the left of the crack with the coil center 4 cm from the left edge of the plate [Fig. 9(*b*)]. These photographs show that a "hot" spot forms at the tip of the crack due to the current flowing around the crack. (The white line shows the vertical position of the crack.) In Fig. 9(*a*) a right crack tip shows up as circular isotherms. When the coil position is moved to the left the left crack tip shows up as a hot spot, which appears as circular isotherms. The hot spot on the left edge is due to increase of current density near the edge. Needless to say, the color photographs are more dramatic. But the experiments show the same qualitative behavior as the numerical results in Figs. 5, 6, 10 and 11.

Self field effects are present in these experiments since the skin depth here is not very large compared to sample thickness. As mentioned before, self field effects have been ignored in the calculations presented earlier in this paper. Thus, the idea here is to show qualitative agreement between theory and experiment. Also, finite element calculations including self field effects predict hot spots at crack tips [11].

Further experimental work must be done to establish the practical use of this technique, especially regarding below-surface cracks that do not penetrate the solid. The results do indicate the potential for such a technique. It is a visual method whose features change qualitatively as well as quantitatively when a crack interupts the flow of induced currents.

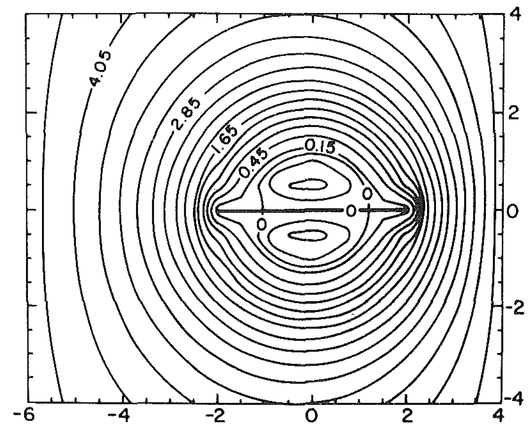

Fig. 10 Calculated stream lines for induced currents in a cracked square plate by a circular coil for the experimental situation [Fig. 9 (a); part (1)] with $\hat{a}_0 = 1.91, \hat{x}_1^0 = 0, \hat{h}_0 = 0.85$.

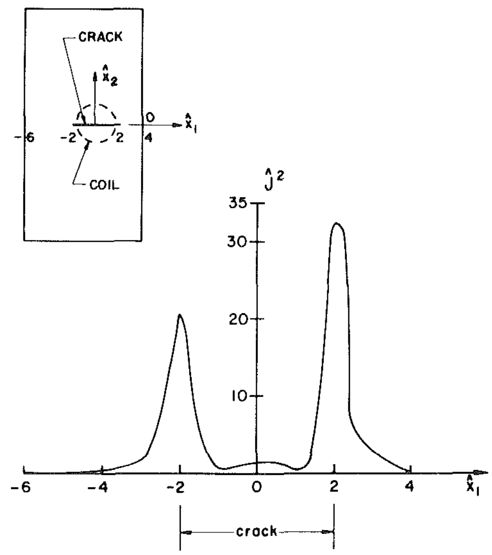

Fig. 11 Calculated induced temperature (or eddy current density squared) along a line slightly above the crack ($\hat{x}_2 = 0.05$) for the experimental situation [Fig. 9 (a); part (1)] with $\hat{a}_0 = 1.91, \hat{x}_1^0 = \hat{x}_2^0 = 0, \hat{h}_0 = 0.85$.

Acknowledgments

This research was supported by the Office of Naval Research, Washington, D.C. under Contract Number N00014-79-C-0224, Task number NR064-621 with Cornell University. The assistance of Mr. K. Hara with the infrared experiments is acknowledged.

References

1 Yagawa, G., Masuda, M., Horie, T. and Ando, Y., "Dynamic Fracture of Cracked Beam Under Electromagnetic Force." *Proceedings of International Conference on Analytical and Experimental Fracture Mechanics*, Sih, G. C., and Mirabile, M., eds., Sijthoff and Noordhoff, 1981, pp 757–769.

2 Carpenter, C. J., "Comparison of Alternative Formulations of Three-Dimensional Magnetic Field and Eddy Current Problems at Power Frequencies," *Proceedings of the IEE*, Vol. 124, No. 11, Nov. 1977, pp. 66–74.

3 Wu, Y. S., Rizzo, F. J., Shippy, D. J., and Wagner, J. A., "An Advanced Boundary Integral Equation Method for Two-Dimensional Electromagnetic Field Problems," *Electric Machines and Electromechanics*, Vol. 1, 1977, pp. 301–313.

4 Ancelle, B., and Sabonnadiere, J. C., "Numerical Solution of 3D Magnetic Field Problems using Boundary Integral Equations," *IEEE Transactions on Magnetics, Proceedings of INTERMAG*, Sept. 1980.

5 Trowbridge, C. W., "Applications of Integral Equation Methods for the Numerical Solution of Magnetostatic and Eddy Current Problems," Report No. RL-76-071, Rutherford Laboratory, Chilton, Didcot, England, June 1976.

6 Salon, S. J., and Schneider, J. M., "A Comparison of Boundary Integral and Finite Element Formulations of the Eddy Current Problem," *IEEE Paper 80 SM 526-4*, 1980.

7 Mukherjee, S., and Morjaria, M., "Boundary Element Analysis of Time-Dependent Inelastic Deformation of Cracked Plates Loaded in Anti-plane Shear." *International Journal of Solids and Structures*, Vol. 17, No. 8, Aug. 1981, pp. 753–763.

8 Mukherjee, S., and Morjaria, M., "A Boundary Element Formulation for Planar, Time-dependent Inelastic Deformation of Plates with Cutouts," *International Journal of Solids and Structures*, Vol. 17, No. 1, Jan. 1981, pp. 115–126.

9 Morjaria, M., and Mukherjee, S., "Numerical Analysis of Planar Time-Dependent Inelastic Deformation of Plates with Cracks by the Boundary Element Method," *International Journal of Solids and Structures*, Vol. 17, No. 1, Jan. 1981, pp. 127–143.

10 Moon, F. C., "Problems in Magneto-Solid Mechanics," Chapter 5 in *Mechanics Today*, Vol. 4, Nemat-Nasser, S., ed., Pergamon Press, Oxford, 1978, pp. 307–390.

11 Yuan, K. Y., Moon, F. C., and Abel, J. F., "Numerical Solutions for Coupled Magnetomechanics," Department of Structural Engineering Report Number 80-5, Departments of Structural Engineering and Theoretical and Applied Mechanics, Cornell University, February 1, 1980. See also, "Magnetic Forces in Plates Using Finite Elements," *Proceedings of the Third Engineering Mechanics Division Speciality Conference*, ASCE, Austin, Texas, September 1979, pp. 730–733.

12 Mukherjee, S., Morjaria, M. A., and Moon, F. C., "Eddy Current Flows Around Cracks in Thin Plates for Nondestructive Testing." Report for ONR Contract N00014-79-C-0224. Departments of Theoretical and Applied Mechanics and Structural Engineering, Cornell University, Ithaca, N.Y., Mar. 1981.

13 Mukherjee, S., and Morjaria, M., "Comparison of Boundary Element and Finite Element Methods in the Inelastic Torsion of Prismatic Shafts," *International Journal for Numerical Methods in Engineering*, Vol. 17, No. 10, Oct. 1981, pp. 1576–1588.

14 Libby, H. L., *Introduction to Electromagnetic Nondestructive Test Methods*. Wiley-Interscience, New York, 1971.

J. N. Reddy
Professor.
Mem. ASME

W. C. Chao
Graduate Research Assistant.

Department of Engineering Science and Mechanics,
Virginia Polytechnic Institute and State University,
Blacksburg, Va. 24061

Nonlinear Oscillations of Laminated, Anisotropic, Rectangular Plates

A finite-element analysis of the equations governing the large-amplitude, free, flexural oscillations of laminated, anisotropic, rectangular plates is presented. The equations account for transverse shear strains as well as large rotations. Numerical results of nonlinear fundamental frequencies are presented for rectangular plates of both angle-ply and cross-ply constructions. The effects of amplitude, boundary conditions, transverse shear, aspect ratio, orientation of layers, and materials anisotrophy on natural frequencies are investigated. The present finite element results agree with other approximate solutions available in the literature.

Introduction

The determination of natural frequencies is of fundamental importance in the design of many structural components, including turbine blades, compressor blades, aircraft propeller blades, and helicopter rotor blades. It is necessary that the natural frequencies of vibration be determined accurately in order to obtain a design that results in virtually resonant-free structural components. An accurate determination of stresses and natural frequencies depends largely on the theory used to model a given structure. The theory should accurately describe the kinematics, nonlinear material behavior, and boundary and loading conditions. In the case of composite plates and shells, the inclusion of transverse shear strains is very important because the natural frequencies calculated using the classical (thin-plate or thin-shell) theory are higher than those obtained using a theory that accounts for the transverse shear strains. Further, when the amplitudes of vibration are large compared to the thickness, the interaction between the inplane modes and normal modes must be considered.

The first generalization of the Reissner-Mindlin thick-plate theory for homogeneous, isotropic plates to arbitrarily laminated anisotropic plates is due to Yang, Norris, and Stavsky [1]. Whitney and Pagano [2] presented closed-form solutions to the theory when applied to certain cross-ply and angle-ply rectangular plates. A generalization of the von Karman nonlinear plate theory (see Herrmann [3]) for isotropic plates to include the effects of transverse shear and rotatory inertia in the theories of orthotropic plates was due to Medwadowski [4], and anisotropic plates was due to Ebcioglu [5].

A review of the literature on the geometrically nonlinear oscillations of continuous media reveals that two fundamental approaches have been followed. The first is the true free oscillation problem, in which the displacement modes are assumed and the nonlinear partial differential equations are reduced to ordinary differential equations in time (a single differential equation when the transverse shear and rotatory inertia are omitted). The second approach assumed a priori that the deflection time function is sinusoidal. The first approach has been employed by most of the previous works (see [6–19]) and the second approach was used in [20].

Geometrically nonlinear oscillations of single-layer orthotropic plates was considered by Ambartsumyan [6], and Hassert and Nowinski [7]. Using the Galerkin method, Nowinski [8, 9] analyzed rectilinearly orthotropic plates of circular and triangular planforms. In [6–9] the effects of transverse shear deformation and rotatory inertia were not considered. The dynamic analog of Berger's equation of motion, including the effects of the transverse shear and rotary inertia, was presented by Wu and Vinson [10, 11] for isotropic and specially orthotropic plates (also, see Sathyamoorthy [12, 13]). Mayberry and Bert [14] presented the results of both experimental and theoretical investigation of a single-layer specially orthotropic rectangular plate with all four edges clamped. The theoretical investigation did not consider the effect of transverse shear deformation and rotatory inertia. Using the Galerkin and Runge-Kutta methods, Prabhakara and Chia [15] and Sathyamoorthy and Chia [16] analyzed orthotropic and anisotropic rectangular plates.

Compared to the literature cited in the foregoing for single-layer orthotropic plates, the literature on the geometrically nonlinear oscillations of multilayer anisotropic plates is limited. Whitney and Leissa [17] presented a dynamic analog of the von Karman nonlinear plate theory for layered composite plates. In this paper the transverse shear deformation and rotatory inertia were neglected, and no numerical results were presented. An extension of their earlier works [10, 11] to deal with nonlinear vibration of symmetrically stacked

Contributed by the Applied Mechanics Division for publication in the JOURNAL OF APPLIED MECHANICS.

Discussion on this paper should be addressed to the Editorial Department, ASME, United Engineering Center, 345 East 47th Street, New York, N.Y. 10017, and will be accepted until two months after final publication of the paper itself in the JOURNAL OF APPLIED MECHANICS. Manuscript received by ASME Applied Mechanics Division, June, 1981; final revision, October, 1981.

laminated composite plates was presented by Wu and Vinson [18]. In symmetrically stacked (with respect to the midplane) laminated plates, the bending-stretching coupling terms vanish and the equations become relatively simpler. The analysis of unsymmetrically laminated, simply supported, angle-ply plates was due to Bennett [19]. Using the thin-plate theory of layered composite plates and the Galerkin method, Bert [20] investigated the nonlinear vibration of a rectangular plate arbitrarily laminated of anisotropic material. A multimode (two-term) solution for nonlinear vibration of unsymmetric all-clamped and all-simply supported angle-ply and cross-ply laminated plates was reported by Chandra and Basava Raju [21, 22]. Chandra [23] used a one-term Galerkin approximation of the dynamic von Karman plate equations and the perturbation technique for the resulting ordinary equation in time to investigate the large-amplitude vibration of a cross-ply plate which is simply supported at two opposite edges and clamped at the other two edges. Chia and Prabhakara [24] presented an analytical investigation of the nonlinear, free flexural vibrations of unsymmetric cross-ply and angle-ply plates with all-clamped and all-simply supported edges. The normal and tangential boundary forces in the plane of the plate were assumed to be zero. In [17, 19–24], the effects of shear deformation and rotatory inertia were neglected, and special goemetries and plate constructions were considered. Recently, the effect of transverse shear and rotatory inertia on large-amplitude free vibration of anisotropic skew plates was reported by Sathyamoorthy and Chia [25, 26]. These papers used a single-modal analysis, in which the boundary conditions and any geometrical requirements are satisfied by the assumed mode shapes.

A review of the literature indicates that no finite-element analyses of geometrically nonlinear oscillations of layered composite plates are available. The preliminary works of the authors [27, 28], in which it was assumed that the stiffness matrix is independent of the time functions – an assumption not valid in general – are the only ones known to the authors. The present paper investigates the two traditional approaches (assumed displacement-mode shape approach, and assumed time function approach) using the finite-element method. For the first time, an agreement between the present finite-element approximate results and other approximate results (see [21–24]) of nonlinear frequencies of layered anisotropic composite plates is found.

Equations of Motion

The displacement assumptions of the shear deformable theory (see Whitney and Pagano [2]) and the nonlinear strain-displacement relations of the von Karman theory (see Whitney and Leissa [17]) are used in the formulation of the equations of motion. It should be pointed out that the theory does not account for delamination between layers and large strains. It is assumed that the stresses normal to the middle surface of the plate are negligible when compared to the inplane stresses. The plate under consideration is composed of a finite number of orthotropic layers of uniform thickness having principal axes of elasticity that are oriented arbitrarily with respect to the plate axes. The plate x and y coordinates are taken in the midplane of the plate with z-axis normal to the midplane. Under these assumptions, the equations governing a layered composite plate are identical to those of an ordinary plate with the exception of the plate constitutive equations. Here a brief review of the pertinent equations is given. For additional details, the reader is referred to [2, 17, 27].

Like in the Reissner-Mindlin thick-plate theory, the displacement field in a layered composite plate is assumed to be of the form,

$$\begin{aligned} u_1(x,y,z,t) &= u(x,y,t) + z\psi_x(x,y,t), \\ u_2(x,y,z,t) &= v(x,y,t) + z\psi_y(x,y,t), \\ u_3(x,y,z,t) &= w(x,y,t). \end{aligned} \tag{1}$$

Here t is the time, u_1, u_2, u_3 are the displacements in x, y, z directions, respectively, u, v, w are the associated midplane displacements, and ψ_x and ψ_y are the slopes in the xz and yz planes due to bending only. It is clear that the transverse shear strains (γ_{xz} and γ_{yz}) are constant through the thickness. To allow for linear distribution of the transverse shear strains, one must add higher-order terms in z (see [29]) to the displacements in (1). However, this in turn increases the number of dependent variable and hence the computational effort.

The equations of motion are the same as those governing an ordinary plate (with transverse shear strains, rotatory inertia terms, and nonlinear terms included). The plate constitutive equations are given by

$$\begin{Bmatrix} N_i \\ M_i \end{Bmatrix} = \begin{bmatrix} A_{ij} & B_{ij} \\ B_{ji} & D_{ij} \end{bmatrix} \begin{Bmatrix} \epsilon_j^0 \\ K_j \end{Bmatrix},$$

$$\begin{Bmatrix} Q_2 \\ Q_1 \end{Bmatrix} = \begin{bmatrix} A_{44} & A_{45} \\ A_{45} & A_{55} \end{bmatrix} \begin{Bmatrix} \epsilon_4 \\ \epsilon_5 \end{Bmatrix}. \tag{2}$$

The A_{ij}, B_{ij}, D_{ij} $(i,j=1,2,6)$, and A_{ij} $(i,j=4,5)$ are the

Nomenclature

A_{ij},B_{ij},D_{ij} = extensional, flexural-extensional, and flexural stiffnesses $(i,j=1,2,6)$
a,b = plate planform dimensions of x,y directions, respectively
E_1,E_2 = layer elastic moduli in directions along fibers and normal to them, respectively
G_{12},G_{13},G_{23} = layer inplane and thickness shear moduli
h = total thickness of the plate
I = rotatory inertia coefficient per unit midplane area of layer
k_i = shear correction coefficients associated with the yz and xz planes, respectively $(i=4,5)$
M_i,N_i = stress couple and stress resultant, respectively $(i=1,2,6)$
P = laminate normal inertia coefficient per unit midplane area
Q_i = shear stress resultant $(i=1,2)$
Q_{ij} = plane-stress reduced stiffness coefficients $(i,j=1,2,6)$
R = laminate rotatory-normal coupling inertia coefficient per unit midplane area
u,v,w = displacement components in x,y,z directions, respectively
U_i,V_i,W_i = nodal values of displacements u, v, w $(i=1,2,\ldots,n)$
x,y,z = position coordinates in cartesian system
$\{\Delta\}$ = column vector of generalized nodal displacements
ϵ_i = strain components $(i=1,2,\ldots,6)$
θ_m = orientation of mth layer $(m=1,2,\ldots,L)$
$\rho^{(m)}$ = density of mth layer $(l=1,2,\ldots L)$
σ_i = stress components $(i=1,2,\ldots,6)$
ϕ_i = finite-element interpolation functions $(i=1,2,\ldots,n)$
ψ_x,ψ_y = bending slope (rotation) functions
ω = natural frequency of free vibration
ω_L,ω_{NL} = linear and nonlinear fundamental frequencies, respectively

respective inplane, bending-inplane coupling, bending or twisting, and thickness-shear stiffness, respectively:

$$(A_{ij}, B_{ij}, D_{ij}) = \sum_m \int_{z_m}^{z_{m+1}} Q_{ij}^{(m)} (1,z,z^2)\, dz, (i,j=1,2,6)$$

$$A_{ij} = \sum_m \int_{z_m}^{z_{m+1}} k_i k_j Q_{ij}^{(m)}\, dz, \quad (i,j=4,5) \tag{3}$$

where $Q_{ij}^{(m)}$ are the stiffness coefficients of the mth layer in the plate coordinates, k_i are the shear correction coefficients, and z_m denotes the distance from the midplane to the lower bottom surface of the mth layer.

Finite-Element Formulation

Toward constructing the finite element model of the equations of motion, first we write a variational (i.e., virtual-work) form of the governing equations (see [27])

$$0 = \int_R \{ \delta u_{,x} N_1 + \delta u_{,y} N_6 + \delta u (P u_{,tt} + R\psi_{x,tt}) + \cdots$$

$$+ \cdots + \frac{\partial \delta w}{\partial x}\frac{\partial w}{\partial x} N_1 + \left(\frac{\partial \delta w}{\partial y}\frac{\partial w}{\partial x} + \frac{\partial \delta w}{\partial w}\frac{\partial w}{\partial y} \right) N_6 + \frac{\partial \delta w}{\partial y}\frac{\partial w}{\partial y} N_2$$

$$+ \cdots \} dxdy + \text{work done by applied forces (if any)}, \tag{4}$$

wherein the stress and moment resultants (N_i, M_i, Q_i) are given in terms of A's, B's, D's, and the displacement gradients. Due to the presence of the nonlinear terms (in N's and M's), the resulting stiffnesses are nonlinear and unsymmetric. To see this, consider the terms

$$\delta u_{,x} N_1 = \underline{\delta u_{,x}} \{ A_{11} [u_{,x} + \underline{\tfrac{1}{2}(w_{,x})^2}] + \cdots + B_{16}\psi_{x,y} \} \tag{5}$$

$$\delta(w_{,x}) w_{,x} N_1 = \underline{\delta w_{,x} w_{,x}} \{ A_{11} [u_{,x} + \tfrac{1}{2}(w_{,x})^2] + \cdots + B_{16}\psi_{y,y} \} \tag{6}$$

Note that the underlined terms are nonlinear and not the same when δu and δw are interchanged. The underlined term in (5) contributes to the stiffness coefficients in location (1), (3) wherein the underlined terms in (6) contributes to location (3), (1). In the finite-element analysis of the nonlinear von Karman equations, most investigators linearize the equations before taking the variation:

$$\frac{1}{2}(w_{,x})^2 \equiv P_x w_{,x}, \quad P_x = \frac{1}{2} w_{,x}, \tag{7}$$

where P_x is kept constant during the variation. Although the procedure yields a symmetric stiffness matrix, it is mathematically incorrect. The linearization must be carried only after the variational formulation is completed. We now return to the finite-element formulation.

Over a typical finite element R^e, the generalized displacements are assumed to be of the form,

$$u \simeq U(x,y)\tau_1(t), \quad U = \sum_i^n U_i \phi_i$$

$$v \simeq V(x,y)\tau_2(t), \quad V = \sum_i^n V_i \phi_i$$

$$w \simeq W(x,y)\tau_3(t), \quad W = \sum_i^n W_i \phi_i$$

$$\psi_x \simeq X(x,y)\tau_4(t), \quad X = \sum_i^n X_i \phi_i$$

$$\psi_y \simeq Y(x,y)\tau_5(t), \quad Y = \sum_i^i Y_i \phi_i \tag{8}$$

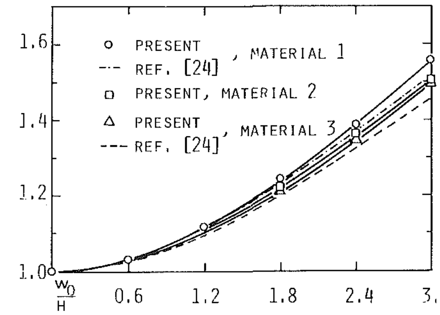

Fig. 1 Effect of elastic properties on the ratio of nonlinear to linear fundamental frequencies of two-layer (0 deg/90 deg) simply supported (*BC*6) square plate ($b/h = 1000$)

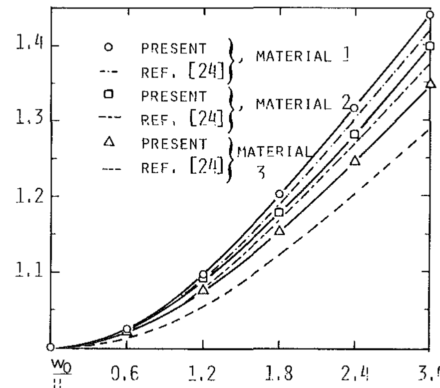

Fig. 2 Effect of elastic properties on the ratio of nonlinear to linear fundamental frequencies of two-layer (0 deg/90 deg) clamped (*BC*2) square plate ($a/h = 1000$)

where ϕ_i are the finite interpolation functions, U_i is the nodal value of U at node i, and τ_i ($i=1,2,\ldots,5$) are the time functions whose specific form is to be determined. Substituting (8) into the variational form (4), we get

$$[M]\{\ddot{\tau}\Delta\} + [K(\tau,\Delta)]\{\Delta\} = \{0\} \tag{9}$$

where $\{\Delta\} = \{U_i, V_i, W_i, X_i, Y_i\}^T$ is the column vector of the nodal values of the generalized displacements, $[K]$ is the stiffness matrix, and $[M]$ is the mass matrix (see the Appendix for the details). An examination of the stiffness matrix shows that the amplitudes of various generalized displacements are coupled and that the usual eigenvalue problem of the linear theory is not present in the nonlinear theory.

When the effects of transverse shear and rotatory inertia are not considered, equation (9) can be reduced to a "Duffing-type" equation (see [10, 11]). In [27, 28] it was assumed that $\tau_1 = \tau_2 = \ldots = \tau_5 = \cos\omega t$ and then only the first term in the expansion of $\cos\omega t$ was retained in the stiffness matrix. Clearly, this is equivalent to assuming that $[K] = [\hat{K}(\Delta)]\tau$ is a linear function of τ, where $[\hat{K}(\Delta)]$ is the nonlinear stiffness matrix in the nonlinear static bending analysis (see [27]). Although this assumption cannot be justified on physical or mathematical grounds, the results obtained in [28] are apparently in good agreement with the results of Rao, et al. [30], Mei [31], Chu and Herrmann [32], Wah [33], Yamaki [34], and Kanaka Raju, and Hinton [35] for isotropic plates (without the inclusion of shear deformation and rotatory inertia).

In the present study, we considered equation (9) in its actual form and assumed that (see Sandman and Walker [36])

$$\tau_1 = \tau_2 = \tau_3^2 = \tau_4^2 = \tau_5^2 = \sin^2\omega t. \tag{10}$$

After substituting the time functions (10) into (9), the equation element equations were integrated over the half period π/ω. The resulting equation is a standard eigenvalue equation:

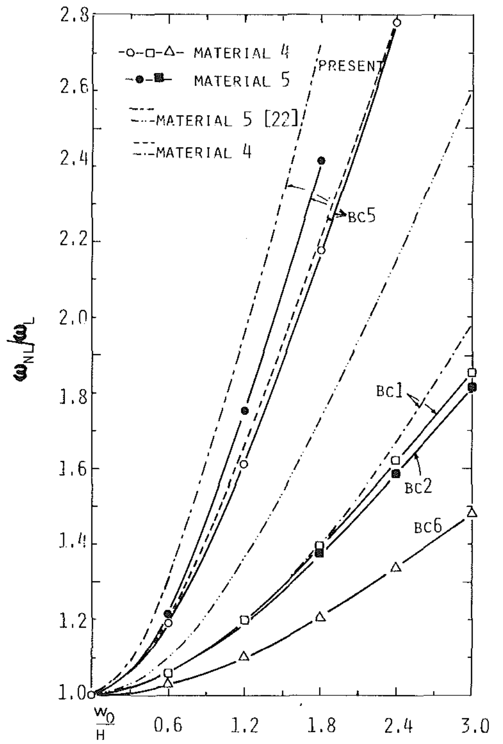

Fig. 3 Effect of elastic properties and boundary conditions on the ratio of nonlinear to linear fundamental frequencies of two-layer (0 deg/90 deg) square plates ($a/h = 1000$)

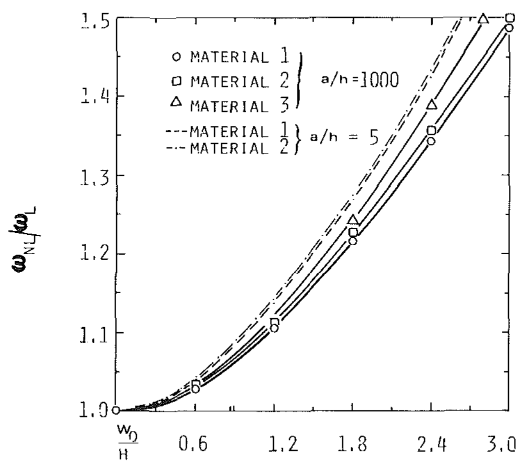

Fig. 4 Effect of plate thickness on the ratio of nonlinear to linear fundamental frequencies of two-layer (0 deg/90 deg) square plates (*BC*6)

$$([M] - \omega^2[\bar{K}(\Delta)])\{\Delta\} = \{0\}. \tag{11}$$

Element equations (11) are assembled in the usual manner and the boundary conditions of the problem at hand are imposed before solving the eigenvalue problem. The computational procedure consists of direct iteration, in which the global stiffness is updated using the eigenvector from the previous iteration. The iteration begins with the linear eigenvalue problem (so that we obtain the linear frequencies), and terminates when the nonlinear frequencies obtained during two consecutive iterations differ by some small number (say, 10^{-3}).

Numerical Results

The numerical results presented in the following were obtained using the nine-node quadratic element on an IBM 3032 computer. The element was already tested in the

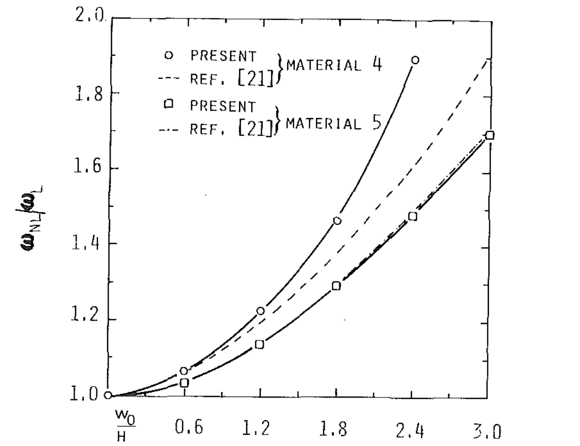

Fig. 5 Effect of elastic properties on the ratio of nonlinear to linear fundamental frequencies of two-layer angle-ply (45 deg/ − 45 deg) square plates ($a/h = 1000$, *BC*4)

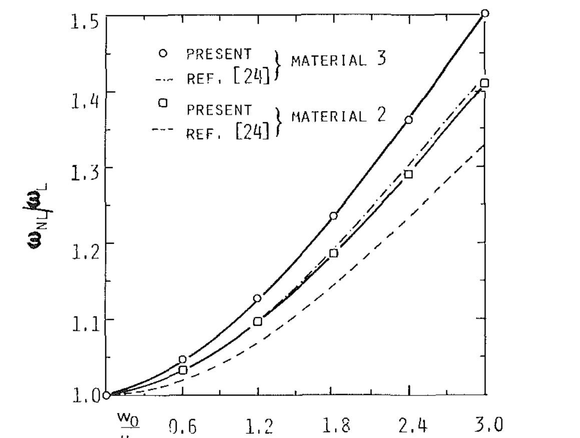

Fig. 6 Effect of elastic properties on the ratio of nonlinear to linear fundamental frequencies of two-layer angle-play (45 deg/ − 45 deg) square plates ($a/h = 1000$, *BC*6)

nonlinear bending of layered composite plates (see [27]). Only one quadrant of the plate was modeled in all of the cases reported here. The following boundary conditions were considered:

- *BC*1: Transverse deflection, tangential rotation, and inplane displacement parallel to the edge are zero on the boundary.
- *BC*2: Transverse deflection and both rotations are zero on the boundary.
- *BC*3: Transverse deflection and normal rotation are zero on the boundary.
- *BC*4: Transverse deflection and tangential rotations are specified to be zero on the boundary; the symmetry boundary conditions are:

$$\text{at } x = 0: \quad v = \psi_x = 0; \text{ at } y = 0: \quad u = \psi_y = 0$$

- *BC*5: The transverse deflection, inplane displacements normal to the boundary, and tangential rotations are specified to be zero at the boundary.
- *BC*6: Same as *BC*5, except that no inplane displacements are specified on the boundary.

The symmetry boundary conditions for *BC*1, *BC*2, *BC*3, *BC*5, and *BC*6 are:

at $x=0$: $u=\psi_x=0$; at $y=0$: $v=\psi_y=0$.

The following material properties were used in the analysis ($G_{12}=G_{23}=G_{13}$):

Material 1: $E_1/E_2=40$, $G_{12}/E_2=0.5$, $\nu_{12}=0.25$

Material 2: $E_1/E_2=10$, $G_{12}/E_2=1/3$, $\nu_{12}=0.30$

Material 3: $E_1/E_2=3$, $G_{12}/E_2=0.5$, $\nu_{12}=0.25$

Material 4: $E_1=7.07\times10^6$ psi, $E_2=3.58\times10^6$ psi, $G_{12}=1.41\times10^6$ psi, $\nu_{12}=0.3$

Material 5: $E_1=36.4\times10^6$ psi, $E_2=4.79\times10^6$ psi, $G_{12}=1.96\times10^6$ psi, $\nu_{12}=0.3$

These particular material properties were selected in order to compare the present solutions with those available in the literature.

First, numerical results of cross-ply plates are discussed. Figure 1 shows the plot of nonlinear to linear fundamental frequencies versus the amplitude-to-thickness ratio for two-layer (0 deg/90 deg) square plates ($a/h=1000$) of Materials 1, 2, and 3, and subjected to boundary conditions described in *BC*6. The figure compares the present finite element results with the Fourier series solutions of Chia and Prabhakara [24]. The results are in fair agreement with each other (considering the fact that the scale used is large). The difference between the two solutions increase with the amplitude-to-thickness ratio, and degree of material orthotropy. This is also observed in the case of clamped (*BC*2) square plates (0 deg/90 deg) from Fig. 2. The results obtained for *BC*3 were almost identical to those obtained for *BC*2.

Figure 3 shows similar results (i.e., ω_{NL}/ω_L versus w_0/h) for square plates (0 deg/90 deg) of Materials 4 and 5, and subjected to various boundary conditions. The present results are compared with the Galerkin/perturbation solution of Chandra and Raju [22], who investigated the influence of movable and immovable inplane boundary conditions. The present results agree with those of Chandra and Raju [22] for plates of Material 4 ($E_1/E_2\approx2$) subjected to boundary conditions *BC*1 and *BC*5. However, the present results for plates of Materials 5 ($E_1/E_2\approx7.6$) subjected to the same boundary conditions differ considerably from those of Chandra and Raju [22]. Note that the difference is more for larger ratios of E_1-E_2. It appears that Chandra and Raju [22] do not include the coupling terms in the nonlinear part of the von Karman theory (see Bennett [19]). It should also be pointed out that the present finite-element results are higher compared to those of Chia and Prabhakara [24] and lower compared to the results of Chandra and Raju [22].

The effect of thickness on the ratio of nonlinear to linear frequencies was also investigated. Figure 4 shows plots of ω_{NL}/ω_L versus w_0/h for square plates (0 deg/90 deg, *BC*6) of various materials and two different ratios of side-to-thickness: $a/h=1000$, and 10. For Material 3 (Glass-Epoxy) the thickness effect was found to be negligible and therefore not plotted. Since the thickness shear deformation has a pronounced effect on linear fundamental frequency, one can conclude from Fig. 4 that the thickness shear deformation has relatively less pronounced effect on nonlinear fundamental frequencies.

Next, numerical results of angle-ply plates are presented. Figure 5 shows plots of ω_{NL}/ω_L versus w_0/h for thin ($a/h=1000$) square plates (45 deg/-45 deg) of Materials 4 and 5 subjected to boundary conditions in *BC*4. The present results are compared with the Galerkin/perturbation results of Chandra and Raju [21]. Again, the present results for Material 4 agree more closely with those of Chandra and Raju [21], while they differ considerably for Material 5.

Finally, Fig. 6 shows similar results for square plates (45 deg/-45 deg) of Materials 2 and 3, and subjected to boundary conditions in *BC*6. In this case the results were obtained by employing the following time functions:

$$\tau=\mu=\lambda=\sin\omega t \tag{14}$$

The present results are compared with the double Fourier series solutions of Chia and Prabhakara [24]. The results agree with each other (within 5 percent) with the present results being higher. The finite-element results obtained by using the time functions in equation (10) for the same problem were found to be quite larger when compared to the results of Chia and Prabhakara [24]. This discrepancy can be explained as follows. In their analysis, Chia and Prabhakara [24] do not have the coupling terms (B_{ij}) in the nonlinear expressions. As a result, the time functions in (14) are more suitable for the problem. However, the coupling terms are not zero in the nonlinear expressions of the present formulation [in fact, they are relatively large for the two-layer (45 deg/-45 deg) case], and the nonlinearity influenced our results obtained by using the time functions in equation (10).

Summary and Conclusions

A finite-element analysis of the shear deformable theory that also takes into account the nonlinear strain-displacement relations (in the von Karman sense) of layered composite plates is presented for the nonlinear oscillations of rectangular laminated plates. Numerical results of nonlinear to linear frequencies are presented showing the effect of large amplitudes, boundary conditions, thickness shear deformation, orientation of layers, and material orthotropy. The present finite-element solutions are compared with other approximate solutions available in the literature. The agreement is found to be very good. It is also observed that the shear deformation has less pronounced effect on the nonlinear frequencies.

Two areas of further research deserve attention. First, a more general approach for the selection of the time functions τ_i is necessary. For nonhomogeneous plates, it is logical to expect that the wave speeds in x and y directions would not be the same (i.e., $\tau_1\neq\tau_2$). Second, for an accurate prediction of higher modes, a more refined theory of laminated plates is necessary.

Acknowledgments

The results reported in the paper were obtained during an investigation supported by the Structural Mechanics program of the Air Force Office of Scientific Research (Grant AFOSR-81-0142) and the Structures Research Section of the NASA (Lewis Grant NAG. 3-208). The support is gratefully acknowledged. The authors wish to thank Dr. W. C. Bert of the University of Oklahoma for his constructive comments on an earlier version of the paper. It is a pleasure to acknowledge the skillful typing of Mrs. Vanessa McCoy.

References

1 Yang, P. C., Norris, C. H., and Stavsky, Y., "Elastic Wave Propagation in Heterogeneous Plates," *International Journal of Solids and Structures*, Vol. 2, 1966, pp. 665-684.

2 Whitney, J. M., and Pagano, N. J., "Shear Deformation in Heterogeneous Anisotropic Plates," ASME JOURNAL OF APPLIED MECHANICS, Vol. 37, 1970, pp. 1031-1036.

3 Herrmann, G., "Influence of Large Amplitudes on Flexural Motions of Elastic Plates," National Advisory Committee for Aeronautics, Technical Note 3578, Washington, D. C., May 1955.

4 Medwadowski, S. J., "A Refined Theory of Elastic, Orthotropic Plates," ASME JOURNAL OF APPLIED MECHANICS, Vol. 25, 1958, pp. 437-443.

5 Ebcioglu, I. K., "A Large Deflection Theory of Anisotropic Plates," *Ingenieur-Archiv*, Vol. 33, 1964, pp. 396-403.

6 Ambartsumyan, S. A., *Theory of Anisotropic Plates* (English translation), Technomic, Stamford, Conn., 1970.

7 Hassert, J. E., and Nowinski, J. L., "Nonlinear Transverse Vibration of a Flat Rectangular Orthotropic Plate Supported by Stiff Ribs," *Proceedings of*

5th International Symposium on Space Technology and Science, Tokyo, 1962, pp. 561–570.
8 Nowinski, J. L., "Nonlinear Vibrations of Elastic Circular Plates Exhibiting Rectilinear Orthotropy," *Zeitschrift fur Angewandte Methematik and Physik*, Vol. 14, 1963, pp. 112–124.
9 Nowinski, J. L., and Ismail, I. A., "Large Oscillations of an Anisotropic Triangular Plate," *Journal of the Franklin Institute*, Vol. 280, 1965, pp. 417–424.
10 Wu, C. I., and Vinson, J. R., "Influences of Large Amplitudes, Transverse Shear Deformation, and Rotary Inertia on Lateral Vibrations of Transversely Isotropic Plates," ASME JOURNAL OF APPLIED MECHANICS, Vol. 36, 1969, pp. 254–460.
11 Wu, C. I., and Vinson, J. R., "On the Nonlinear Oscillations of Plates Composed of Composite Materials," *Journal of Composite Materials*, Vol. 3, 1969, pp. 548–561.
12 Sathyamoorthy, M., "Vibration of Plates Considering Shear and Rotary Inertia," *AIAA Journal*, Vol. 16, 1978, pp. 285–286.
13 Sathyamoorthy, M., "Vibration of Skew Plates at Large Amplitudes Including Shear and Rotary Inertia Effects," *International Journal of Solids and Structures*, Vol. 14, 1978, pp. 869–880.
14 Mayberry, B. L., and Bert, C. W., "Experimental Investigation of Nonlinear Vibrations of Laminated Anisotropic Panels," *Shock and Vibration Bulletin*, Vol. 39, Part 3, 1969, pp. 191–199.
15 Prabhakara, M. K., and Chia, C. Y., "Nonlinear Flexural Vibrations of Orthtropic Rectangular Plates," *Journal of Sound and Vibration*, Vol. 52, 1977, pp. 511–518.
16 Sathyamoorthy, M., and Chia, C. Y., "Non-Linear Vibration of Anisotropic Rectangular Plates Including Shear and Rotatory Inertia," *Fibre Science and Technology*, Vol. 13, 1980, pp. 337–361.
17 Whitney, J. M., and Leissa, A. W., "Analysis of Heterogeneous Anisotropic Plates," ASME JOURNAL OF APPLIED MECHANICS, Vol. 36, pp. 261–266, 1969.
18 Wu, C. I., and Vinson, J. R., "Nonlinear Oscillations of Laminated Specially Orthotropic Plates with Clamped and Simply Supported Edges," *Journal of the Acoustical Society of America*, Vol. 49, 1971, pp. 1561–1567.
19 Bennett, J. A., "Nonlinear Vibration of Simply Supported Angle Ply Laminated Plates," *AIAA Journal*, Vol. 9, No. 10, 1971, pp. 1697–1700.
20 Bert, C. W., "Nonlinear Vibration of a Rectangular Plate Arbitrarily Laminated of Anisotropic Material," ASME JOURNAL OF APPLIED MECHANICS, Vol. 40, 1973, pp. 452–458.
21 Chandra, R., and Basava Raju, B., "Large Deflection Vibration of Angle Ply Laminated Plates," *Journal of Sound and Vibration*, Vol. 40, 1975, pp. 393–408.
22 Chandra, R., and Basava Raju, B., "Large Amplitude Flexural Vibration of Cross-Ply Laminated Composite Plates," *Fibre Science and Technology*, Vol. 8, 1975, pp. 243–263.
23 Chandra, R., "Large Deflection Vibration of Cross-Ply Laminated Plates with Certain Edge Conditions," *Journal of Sound and Vibration*, Vol. 47, No. 4, 1976, pp. 509–514.
24 Chia, C. Y., and Prabhakara, M. K., "A General Mode Approach to Nonlinear Flexural Vibrations of Laminated Rectangular Plates," ASME JOURNAL OF APPLIED MECHANICS, Vol. 45, No. 3, 1978, pp. 623–628.
25 Sathyamoorthy, M., and Chia, C. Y., "Effect of Transverse Shear and Rotary Inertia on Large Vibration of Anisotropic Skew Plates, Part 1—Theory," ASME JOURNAL OF APPLIED MECHANICS, Vol. 47, 1980, pp. 128–132.
26 Sathyamoorthy, M., and Chia, C. Y., "Effect of Transverse Shear and Rotary Inertia on Large Vibration of Anisotropic Skew Plates, Part 2—Numerical Results," ASME JOURNAL OF APPLIED MECHANICS, Vol. 47, 1980, pp. 133–138.
27 Reddy, J. N., and Chao, W. C., "Large Deflection and Large Amplitude Free Vibrations of Laminated Composite-Material Plates," *Computers and Structures*, Vol. 13, No. 2, 1981, pp. 341–347.
28 Reddy, J. N., "Nonlinear Vibration of Layered Composite Plates Including Transverse Shear and Rotatory Inertia," ASME 8th Vibration Conference, Hartford, Conn., ASME Paper No. 81-DET-144.
29 Lo, K. H., Christensen, R. M., and Wu, E. M., "A Higher-Order Theory of Plate Deformation, Part 2: Laminated Plates," ASME JOURNAL OF APPLIED MECHANICS, Vol. 44, 1977, pp. 669–676.
30 Rao, G. V., Raju, I. S., Kanaka Raju, K., "A Finite Element Formulation for Large Amplitude Flexural Vibrations of Thin Rectangular Plates," *Computers and Structures*, Vol. 6, 1976, pp. 163–167.
31 Mei, C., "Finite Element Displacement Method for Large Amplitude Free Flexural Vibrations of Beams and Plates," *Computers and Structures*, Vol. 3, 1973, pp. 163–174.
32 Chu, H. N., and Herrmann, G., "Influence of Large Amplitudes on Free Flexural Vibrations of Rectangular Elastic Plates," ASME JOURNAL OF APPLIED MECHANICS, Vol. 23, 1956, pp. 532–540.
33 Wah, T., "Large Amplitude Flexural Vibration of Rectangular Plates," *International Journal of Mechanical Sciences*, Vol. 5, 1963, pp. 425–438.
34 Yamaki, N., "Influence of Large Amplitudes on Flexural Vibrations of Elastic Plates," *Zeitschrift fur angewandte Mathematik and Mechanik*, Vol. 41, 1967, pp. 501–510.
35 Kanaka Raju, K. and Hinton, E., "Nonlinear Vibrations of Thick Plates Using Mindlin Plate Elements," *International Journal for Numerical Methods in Engineering*, Vol. 15, 1980, pp. 249–257.
36 Sandman, B. E., and Walker, H. S., "An Experimental Observation in Large Amplitude Plate Vibrations," ASME JOURNAL OF APPLIED MECHANICS, Vol. 40, 1973, pp. 633–634.

APPENDIX

Elements of Stiffness and Mass Matrices

Stiffness Matrix:

$$[K] = \begin{bmatrix} [K^{11}] & \tau[K^{12}] & \lambda^2[K^{13}] & \mu[K^{14}] & \mu[K^{15}] \\ \tau[K^{21}] & \tau[K^{22}] & \lambda^2[K^{23}] & \mu[K^{24}] & \mu[K^{25}] \\ \lambda\tau[K^{31}] & \lambda\tau[K^{32}] & (\lambda[K_1^{33}] + \lambda^3[K_2^{33}]) & (\mu[K_1^{34}] + \mu\lambda[K_2^{34}]) & (\mu[K_1^{35}] + \mu\lambda[K_2^{35}]) \\ \tau[K^{41}] & \tau[K^{42}] & (\lambda[K_1^{43}] + \lambda^2[K_2^{43}]) & \mu[K^{44}] & \mu[K^{45}] \\ \tau[K^{51}] & \tau[K^{52}] & (\lambda[K_1^{53}] + \lambda^2[K_2^{53}]) & \mu[K^{54}] & \mu[K^{55}] \end{bmatrix}$$

Mass Matrix:

$$[M] = \begin{bmatrix} P[S] & [0] & [0] & R[S] & [0] \\ [0] & P[S] & [0] & [0] & R[S] \\ [0] & [0] & P[S] & [0] & [0] \\ R[S] & [0] & [0] & I[S] & [0] \\ [0] & R[S] & [0] & [0] & I[S] \end{bmatrix}$$

The matrix coefficients $K_{ij}^{\alpha\beta}$ are given by

$$[K^{11}] = A_{11}[S^{xx}] + A_{16}([S^{xy}] + [S^{xy}]^T) + A_{66}[S^{yy}],$$

$$[K^{12}] = A_{12}[S^{xy}] + A_{16}[S^{xx}] + A_{26}[S^{yy}] + A_{66}[S^{xy}]^T = [K^{21}]^T,$$

$$[K^{13}] = A_{11}[R_x^{xx}] + A_{16}[R_y^{xy}] + A_{12}([R_x^{xy}] + [R_x^{xy}]^T + [R_y^{xx}]) + A_{26}[R_y^{yy}] + A_{66}([R_y^{xy}]^T + [R_x^{yy}]) = \frac{1}{2}[K^{31}]^T,$$

$$[K^{14}] = B_{11}[S^{xx}] + B_{16}([S^{xy}] + [S^{xy}]^T, + B_{66}[S^{yy}] = [K^{41}]^T,$$

$$[K^{15}] = B_{12}[S^{xy}] + B_{16}[S^{xx}] + B_{26}[S^{yy}] + B_{66}[S^{xy}]^T = [K^{51}]^T$$

$$[K^{22}] = A_{22}[S^{yy}] + A_{26}([S^{xy}]^T + [S^{xy}]) + A_{66}[S^{xx}],$$

$$[K^{23}] = A_{12}[R_x^{xy}]^T + A_{22}[R_y^{yy}] + A_{26}([R_y^{xy}]^T + [R_y^{xy}] + [R_x^{yy}]) + A_{16}[R_x^{xx}] + A_{66}([R_x^{xy}]^T + [R_y^{xx}]) = \frac{1}{2}[K^{32}]^T$$

$$\bar{K}^{24}] = B_{12}[S^{xy}]^T + B_{26}[S^{yy}] + B_{16}[S^{xx}] + B_{66}[S^{xy}] = [K^{42}]^T,$$

$$[K^{25}] = B_{22}[S^{yy}] + B_{26}([S^{xy}] + [S^{xy}]^T) + B_{66}[S^{xx}] = [K^{52}]^T$$

$$[K_1^{33}] = A_{55}[S^{xx}] + A_{45}([S^{xy}] + [S^{xy}]^T) + A_{44}[S^{yy}],$$

$$[K_2^{33}] = \frac{1}{2}\int_{Re}\left[\bar{N}_1 \frac{\partial\phi_i}{\partial x}\frac{\partial\phi_j}{\partial x} + \bar{N}_6\left(\frac{\partial\phi_i}{\partial x}\frac{\partial\phi_j}{\partial y} + \frac{\partial\phi_i}{\partial y}\frac{\partial\phi_j}{\partial x}\right)\right.$$

$$+\bar{N}_2 \frac{\partial \phi_i}{\partial y} \frac{\partial \phi_j}{\partial y}\Big] dxdy,$$

$$[K_1^{34}] = A_{55}[S^{x0}] + A_{45}[S^{y0}] = [K_1^{43}]^T,$$

$$[K_2^{34}] = B_{11}[R_x^{xx}] + B_{16}([R_x^{xy}] + [R_x^{xy}]^T + [R_y^{xx}]) + B_{12}[R_y^{xy}]^T + B_{26}[R_y^{yy}] + B_{66}([R_x^{yy}] + [R_y^{xy}]) = 2[K_2^{43}]^T,$$

$$[K_1^{35}] = A_{45}[S^{x0}] + A_{44}[S^{y0}] = [K_1^{53}]^T,$$

$$[K_2^{35}] = B_{12}[R_x^{xy}] + B_{16}[R_x^{xx}] + B_{22}[R_y^{yy}] + B_{26}([R_y^{xy}]^T + = 2\bar{K}_2^{53}]^T$$

$$[R_x^{yy}] + [R_y^{xy}]) + B_{66}([R_x^{xy}]^T + [R_y^{xx}]) = 2[K_2^{53}]^T$$

$$[K^{44}] = D_{11}[S^{xx}] + D_{16}[S^{xy}] + [S^{xy}]^T) + D_{66}[S^{yy}] + A_{55}[S],$$

$$[K^{45}] = D_{12}[S^{xy}] + D_{16}[S^{xx}] + D_{26}[S^{yy}] + D_{66}[S^{xy}]^T + + A_{45}[S] = [K^{54}]^T,$$

$$[K^{55}] = D_{26}([S^{xy}] + [S^{xy}]^T) + D_{66}[S^{xx}] + D_{22}[S^{yy}] + + A_{44}[S]$$

and

$$S_{ij}^{\xi\eta} = \int_{Re} \frac{\partial \phi_i}{\partial \xi} \frac{\partial \phi_j}{\partial \eta} dxdy;\ \xi,\eta = 0,x,y;\ S_{ij}^{00} \equiv S_{ij},$$

$$R_{\zeta}^{\xi\eta} = \int_{Re} \frac{1}{2}\left(\frac{\partial \zeta_j}{\partial \zeta}\right) \frac{\partial \phi_i}{\partial \xi} \frac{\partial \phi_j}{\partial \eta} dxdy,\ \zeta,\xi,u = 0,x,y,$$

$$\bar{N}_1 = A_{11}\left(\frac{\partial w}{\partial x}\right)^2 + A_{12}\left(\frac{\partial w}{\partial y}\right)^2 + 2A_{16}\frac{\partial w}{\partial x}\frac{\partial y}{\partial y},$$

$$\bar{N}_2 = A_{12}\left(\frac{\partial w}{\partial w}\right)^2 + A_{22}\left(\frac{\partial w}{\partial y}\right)^2 + 2A_{26}\frac{\partial w}{\partial x}\frac{\partial w}{\partial y},$$

$$\bar{N}_6 = A_{16}\left(\frac{\partial w}{\partial x}\right)^2 + A_{26}\left(\frac{\partial w}{\partial y}\right)^2 + 2A_{66}\frac{\partial w}{\partial x}\frac{\partial w}{\partial y}.$$

J. N. Reddy
Professor,
Department of Engineering
Science and Mechanics,
Virginia Polytechnic Institute
and State University,
Blacksburg, Va. 24061

On the Solutions to Forced Motions of Rectangular Composite Plates

For two different lamination schemes, under appropriate boundary conditions and sinusoidal distribution of the transverse load, the exact form of the spatial variation of the solution is obtained, and the problem is reduced to the solution of a system of ordinary differential equations in time, which are integrated numerically using Newmark's direct integration method. Numerical results for deflections and stresses are presented showing the effect of plate side-to-thickness ratio, aspect ratio, material orthotropy, and lamination scheme. The results presented herein should be of interest to composite-structure designers, and to experimentalists and numerical analysts in verifying their results.

Introduction

With the increased application of composites in high performance aircraft, studies involving the assessment of the transient response of laminated composite plates are receiving attention of composite-structure designers. The linear elastic transient response of isotropic plates has been investigated by several researchers. Reismann and his colleagues [1-3] analyzed a simply supported, rectangular, isotropic plate subjected to a suddenly applied, uniformly distributed load over a rectangular area. Exact solution was obtained using (classical) three-dimensional elasticity theory, and classical and improved plate theories. Hinton and his associates [4-7] presented transient finite-element analysis of thick and thin isotropic plates. The element is based on the Reissner-Mindlin thick-plate theory for homogeneous, isotropic plates. Excellent agreement of the finite-element solutions with the analytical solutions of Reismann and Lee [1] was obtained. Recently, Akay [8] presented large deflection transient response of isotropic plates using a mixed finite element. All of these studies were confined to homogeneous, isotropic plates.

Layered composite plates exhibit, in general, coupling between the inplane displacements and the transverse displacement and shear rotations. Consequently, the response of composite plates is sensitive to the lamination scheme. Also, due to the low transverse shear moduli relative to the inplane Young's moduli, the transverse shear deformation effects are more pronounced in composites than in isotropic plates. Moon [9, 10] has investigated the response of infinite laminated plates subjected to transverse impact loads at the center of the plate. Chow [11] has employed the Laplace transform technique to investigate the dynamic response of orthotropic laminated plates, and Wang, Chou, and Rose [12] applied the method of characteristics to unsymmetrical orthotropic laminated plates. In a series of papers Sun and his colleagues [13-16] have employed the classical method of separation of variables combined with the Mindlin-Goodman [17] procedure for treating time-dependent boundary conditions and/or dynamic external loadings. However, these papers were confined to plates under cylindrical bending.

The purpose of the present analysis is to present the exact forms of the spatial variation of the solution for two different lamination schemes of rectangular plates, under appropriate boundary conditions and sinusoidal distribution of the transverse load, and to reduce the problem to one of finding a numerical solution to a system of ordinary differential equations in time. Then the differential equations are integrated numerically using Newmark's direct integration method. The results, although limited to a special class of problems, should be of interest to experimentalists and numerical analysts in verifying their data.

Governing Equations

Here we briefly review the equations governing the heterogeneous laminated plate theory originated by Yang, Norris, and Stavsky [18] (also see Whitney and Pagano [19]). The theory is a generalization of the Reissner-Mindlin thick-plate theory for homogeneous, isotropic plates to arbitrarily laminated anisotropic plates and therefore includes shear deformation and rotary inertia effects. However, the theory does not account for delamination (i.e., layers are assumed to be perfectly bonded together).

Consider a plate laminated of a finite number of homogeneous, uniform-thickness, orthotropic layers with the material axes of each layer being arbitrarily oriented with respect to the midplane of the plate. Let us select a Cartesian rectangular coordinate system such that the x-y plane coincides with the midplane of the plate. The displacement field in the plate is assumed to be of the form,

$$\begin{aligned} u_1(x,y,z,t) &= u(x,y,t) + z\psi_x(x,y,t), \\ u_2(x,y,z,t) &= v(x,y,t) + z\psi_y(x,y,t), \\ u_3(x,y,z,t) &= w(x,y,t). \end{aligned} \tag{1}$$

Here t is the time; u_1, u_2, u_3 are the displacements in x, y, z

Contributed by the Applied Mechanics Division for publication in the JOURNAL OF APPLIED MECHANICS.

Discussion on this paper should be addressed to the Editorial Department, ASME, United Engineering Center, 345 East 47th Street, New York, N.Y. 10017, and will be accepted until two months after final publication of the paper itself in the JOURNAL OF APPLIED MECHANICS. Manuscript received by ASME Applied Mechanics Division, September 1981; final revision, December, 1981.

directions, respectively; u, v, w are the associated midplane displacements; and ψ_x and ψ_y are the slopes in the xz and yz planes due to bending only.

Neglecting the body moments and surface shearing forces, we write the equations of motion in the presence of applied transverse forces, q, as

$$
\begin{aligned}
N_{1,x}+N_{6,y}&=Pu_{,tt}+R\psi_{x,tt}\\
N_{6,x}+N_{2,y}&=Pv_{,tt}+R\psi_{y,tt}\\
Q_{1,x}+Q_{2,y}&=Pw_{,tt}+q(x,y,t)\\
M_{1,x}+M_{6,y}-Q_1&=I\psi_{x,tt}+Ru_{,tt}\\
M_{6,x}+M_{2,y}-Q_2&=I\psi_{y,tt}+Rv_{,tt}
\end{aligned}
\tag{2}
$$

where P, R, and I are the normal, coupled normal-rotary, and rotary inertia coefficients,

$$
\begin{aligned}
(P,R,I)&=\int_{-h/2}^{h/2}(1,z,z^2)\rho dz\\
&=\sum_m\int_{z_m}^{z_{m+1}}(1,z,z^2)\rho^{(m)}dz
\end{aligned}
\tag{3}
$$

$\rho^{(m)}$ being the material density of the mth layer, and N_i, Q_i, and M_i are the stress and moment resultants.

The laminate constitutive equations can be expressed in the form:

$$
\begin{Bmatrix} N_i\\ M_i\end{Bmatrix}=\begin{bmatrix}A_{ij} & B_{ij}\\ B_{ji} & D_{ij}\end{bmatrix}\begin{Bmatrix}\epsilon_j^0\\ K_j\end{Bmatrix},
\qquad
\begin{Bmatrix} Q_2\\ Q_1\end{Bmatrix}=\begin{bmatrix}\bar{A}_{44} & \bar{A}_{45}\\ \bar{A}_{45} & \bar{A}_{55}\end{bmatrix}\begin{Bmatrix}\epsilon_4\\ \epsilon_5\end{Bmatrix}
\tag{4}
$$

where

$$
\epsilon_1^0=\frac{\partial u}{\partial x},\ \epsilon_2^0=\frac{\partial v}{\partial y},\ \epsilon_6^0=\frac{\partial u}{\partial y}+\frac{\partial v}{\partial x},
$$

$$
\epsilon_5=\psi_x+\frac{\partial w}{\partial x},\ \epsilon_4=\psi_y+\frac{\partial w}{\partial y},
$$

$$
K_1=\frac{\partial \psi_x}{\partial x},\ K_2=\frac{\partial \psi_y}{\partial y}, K_6=\frac{\partial \psi_x}{\partial y}+\frac{\partial \psi_y}{\partial x}.
\tag{5}
$$

The A_{ij}, B_{ij}, D_{ij} $(i,j=1,2,6)$, and $\bar{A}_{ij}\,(i,j=4,5)$ are the respective inplane, bending-inplane coupling, bending or twisting, and thickness-shear stiffnesses, respectively:

$$
(A_{ij},B_{ij},D_{ij})=\sum_m\int_{z_m}^{z_{m+1}}Q_{ij}^{(m)}(1,z,z^2)\,dz,
$$

$$
\bar{A}_{ij}=\sum_m\int_{z_m}^{z_{m+1}}k_ik_jQ_{ij}^{(m)}\,dz.
\tag{6}
$$

Here z_m denotes the distance from the midplane to the lower surface of the mth layer, and k_i are the shear correction coefficients.

Equations (2) and (4) can be conveniently expressed in the operator form as follows:

$$
[L]\{\delta\}=\{f\}+[M]\{\ddot{\delta}\}
\tag{7}
$$

where $\{\delta\}=\{u,v,w,\psi_x,\psi_y\}^T$, superposed dots indicate differentiation with respect to time, and $[L]$ and $[M]$ are matrices given in Appendix 1.

Exact Form of the Spatial Variation of the Solution

The boundary initial-value problem associated with the forced motion of layered anisotropic composite plates involves solving the operator equation (7) subjected to a given set of boundary and initial conditions. It is not possible to construct exact solutions to equation (7) when the plate is of arbitrary geometry, constructed of arbitrarily oriented layers, and subjected to an arbitrary loading or boundary condition. However, an exact form of the spatial variation of the solution to equation (7) can be developed for two different lamination schemes and associated boundary conditions, when the plate is of rectangular geometry and subjected to sinusoidally distributed (with respect to x and y; arbitrary with respect to time) transverse loading. We begin with a set of boundary conditions and a solution form that satisfies the boundary conditions, and then determine the lamination scheme and loading that would satisfy the operator equation (7). It turns out that there are two sets of boundary conditions and two lamination schemes for which the exact form of the spatial variation of the solution can be constructed [20].

1 Cross-Ply Plates. Consider the following boundary conditions (for any $t>0$):

$$
\begin{aligned}
x=0,a:&\ v=w=\psi_y=0;\ N_1=M_1=0\\
y=0,b:&\ u=w=\psi_x=0;\ N_2=M_2=0.
\end{aligned}
\tag{8}
$$

The following form of the solution satisfies the boundary conditions in equation (8),

$$
u=\sum_{m,n}U_{mn}(t)\,\phi_1(x,y),\ v=\sum_{m,n}V_{mn}(t)\,\phi_2(x,y)
$$

$$
w=\sum_{m,n}W_{mn}(t)\,\phi_3(x,y)
\tag{9}
$$

$$
\psi_x=\sum_{m,n}X_{mn}(t)\,\phi_1(x,y),\ \psi_y=\sum_{m,n}Y_{mn}(t)\,\phi_2(x,y)
$$

where

$$
\phi_1=\cos\alpha x\ \sin\beta y,\ \phi_2=\sin\alpha x\ \cos\beta y,\ \phi_3=\sin\alpha x\ \sin\beta y,
$$

$$
\alpha=m\pi/a,\ \beta=n\pi/b.
\tag{10}
$$

Substituting equation (9) into equation (7), we find that solution to equation (7) exists when the transverse loading q is of the form

$$
q(x,y,t)=\sum_{m,n}Q_{mn}(t)\,\phi_3(x,y)
\tag{11}
$$

and the lamination scheme is such that (which corresponds to cross-ply lamination scheme),

$$
A_{16}=A_{26}=A_{45}=B_{16}=B_{26}=D_{16}=D_{26}=0.
\tag{12}
$$

Under these conditions, equation (7) becomes,

$$
[M]\{\ddot{\Delta}\}+[C]\{\Delta\}=\{F\}
\tag{13}
$$

where $\{\Delta\}=\{U_{mn},V_{mn},W_{mn},X_{mn},Y_{mn}\}^T$, $\{F\}=\{0,\ 0,\ Q_{mn},\ 0,\ 0\}$, and the elements of the coefficient matrix $[C]$ are given in Appendix 1.

2 Angle-Ply Plates. Next, we consider the following boundary conditions,

$$
\begin{aligned}
x=0,a:&\ u=w=\psi_y=0;\ N_6=M_1=0,\\
y=0,b:&\ v=w=\psi_x=0;\ N_6=M_2=0.
\end{aligned}
\tag{14}
$$

The following displacement functions satisfy the boundary conditions in equation (14):

$$
u=\sum_{m,n}U_{mn}(t)\,\phi_2(x,y),\ v=\sum_{m,n}V_{mn}(t)\,\phi_1(x,y),
$$

$$
w=\sum_{m,n}W_{mn}(t)\,\phi_3(x,y),\ h\psi_x=\sum_{m,n}X_{mn}\phi_1(x,y),
$$

$$
h\psi_y=\sum_{m,n}Y_{mn}\phi_2(x,y)
\tag{15}
$$

After substituting equation (15) into equation (7), we find once again that solution exists when q is given by equation (11), and the lamination scheme is such that (which corresponds to antisymmetric angle-ply scheme)

$$A_{16} = A_{26} = A_{45} = B_{11} = B_{12} = D_{16} = D_{26} = 0. \quad (16)$$

Then equation (7) takes the form

$$[M]\{\ddot{\Delta}\} + [K]\{\Delta\} = \{F\}, \quad (17)$$

wherein the coefficients of the matrix $[K]$ are listed in Appendix 1.

Thus for a given $\alpha = m\pi/a$ and $\beta = n\pi/b$, one needs to integrate the 5 by 5 matrix differential equations (13) and (17) for the vector $\{\Delta\}$ of the generalized displacements. A discussion of the numerical integration of these equations is given next.

Numerical Integration of Equations (13) and (17)

To integrate equations (13) and (17), Newmark's direct integration technique [21] is employed. In the Newmark direct integration method the first time derivative $\{\dot{\Delta}\}$ and the solution $\{\Delta\}$ are approximated at $(n+1)$ time step (i.e., at time $t = t_{n+1} \equiv (n+1)\Delta t$) by the following expressions:

$$\{\dot{\Delta}\}_{n+1} = \{\dot{\Delta}\}_n + [(1-\alpha)\{\ddot{\Delta}\}_n + \alpha\{\ddot{\Delta}\}_{n+1}]\Delta t,$$

$$\{\Delta\}_{n+1} = \{\Delta\}_n + \{\dot{\Delta}\}_n \Delta t + \left[\left(\frac{1}{2} - \beta\right)\{\ddot{\Delta}\}_n + \beta\{\ddot{\Delta}\}_{n+1}\right](\Delta t)^2 \quad (18)$$

where α and β are parameters that control the accuracy and stability of the scheme, and the subscript n indicates that the solution is evaluated at nth time step (i.e., at time, $t = t_n$). The choice $\alpha = 1/2$ and $\beta = 1/4$ is known to give an unconditionally stable scheme (in linear problems).

Rearranging, for example, equations (17) and (18), we arrive at

$$[\hat{K}]\{\Delta\}_{n+1} = \{\hat{F}\}_{n,n+1} \quad (19)$$

where

$$[\hat{K}] = [K] + a_0[M], \quad \{\hat{F}\} = \{F\}_{n+1} + [M](a_0\{\Delta\}_n + a_1\{\dot{\Delta}\}_n + a_2\{\ddot{\Delta}\}_n),$$

$$a_0 = 1/(\beta\Delta t^2), \quad a_1 = a_0\Delta t, \quad a_2 = \frac{1}{2\beta} - 1. \quad (20)$$

Once the solution $\{\Delta\}$ is known at $t_{n+1} = (n+1)\Delta t$, the first and second derivatives (velocity and accelerations) of $\{\Delta\}$ at t_{n+1} can be computed from (rearranging the expressions in equation (18)),

$$\{\ddot{\Delta}\}_{n+1} = a_0(\{\Delta\}_{n+1} - \{\Delta\}_n) - a_1\{\dot{\Delta}\}_n - a_2\{\ddot{\Delta}\}_n$$

$$\{\dot{\Delta}\}_{n+1} = \{\dot{\Delta}\}_n + a_3\{\ddot{\Delta}\}_n + a_4\{\ddot{\Delta}\}_{n+1} \quad (21)$$

where $a_3 = (1-\alpha)\Delta t$, and $a_4 = \alpha\Delta t$.

For a given set of initial conditions $\{\Delta\}_0$, $\{\dot{\Delta}\}_0$, and $\{\ddot{\Delta}\}_0$, one can solve equation (19) repeatedly, marching in time, for the generalized displacements and their time derivatives at any time $t > 0$. Although the spatial part of the solution is exact, error is introduced into the equation via the numerical integration in time. In the next section numerical results are presented for a number of illustrative examples.

Numerical Results

In all of the numerical examples presented herein, zero initial conditions were assumed. All of the computations were carried in double precision on an IBM 3032 computer.

The following data (in dimensional form) were used in all of the computations (except in parametric studies, where a and h are varied):

$$a = b = 25\text{cm},\ h = 5\text{cm}(a/b = 1,\ a/h = 5),$$

$$\rho = 8 \times 10^{-6}\,\text{Nsec}^2/\text{cm}^4, E_2 = 2.1 \times 10^6\,\text{N/cm}^2. \quad (22)$$

The values of α and β in the Newmark integration scheme are taken to be 0.5 and 0.25, respectively (which correspond to constant-average acceleration method). The selection of the time step was guided by the following estimate of the time step for *conditionally stable* time integration schemes:

$$(\Delta t)^2 \leq a^2[\rho(1-\nu^2)/E] \Big/ \left\{2 + (1-\nu)\frac{\pi}{12}\left[1 + 1.5\left(\frac{a}{h}\right)^2\right]\right\} \quad (23)$$

Estimate in equation (23) is a modification of the estimate given by Leech [22] for classical plate theory to thick-plate theory (see Tsui and Tong [23]). For $\nu = 0.3$ and $a/h = 5$, 10, and 1000 the estimate yields,

$\frac{a}{h} \rightarrow$	5	10	1000	
$\Delta t\ (\mu\text{sec}) \rightarrow$	9.46	4.9	0.05.	(24)

The effect of the time step on the accuracy of the solution was investigated using the shear deformation theory (SDT) as well as the classical plate theory (CPT). Table 1 shows the center (transverse) deflection and normal stress of a two-layer, cross-ply square plate (material 1) under suddenly applied load for various values of the time step:

$$\text{Material 1: } E_1/E_2 = 25,\ G_{12} = G_{13} = G_{23} = 0.5E_2,\ \nu_{12} = 0.25 \quad (25)$$

From the results presented in Table 1 it is clear that the time step between 1 and 5 μsec has no appreciable effect on the accuracy of the solutions. Furthermore, the shear deformation theory is less sensitive to the time step in the range considered (consistent with the estimate in equation (23)). The effect of the shear deformation on the response is significant, as can be seen from the amplitude and period of the center deflection (given in parentheses) shown in Table 1. The center deflection in SDT is about 30 percent larger compared to that in CPT. In all of the subsequent cases to be discussed, a time increment of 5μsec was used.

The first example is concerned with a two-layer cross-ply (0 deg/90 deg) square plate under suddenly applied transverse load (the boundary conditions and the spatial distribution of the loading are obvious). The problem was also analyzed using the finite element method [24]; the present solution and the finite element solution [24] for center deflection, center normal stress, corner inplane shear stress, and transverse shear stress at the midside are compared in Table 2. The solutions are in excellent agreement with each other. The

Table 1 Effect of the time increment on the center (maximum) transverse deflection and normal stress for two-layer cross-ply (0 deg/90 deg, Material 1) square plate ($a/h = 5$) under suddenly applied sinusoidal loading

	$w,\sigma \diagdown \Delta t$	1	2	3	4	5	6	7	8
SDT	w	0.4609(98)[a]	0.4608(98)	0.4607(99)	0.4606(100)	0.4604(100)	0.4601(102)	0.4586(105)	0.4590(104)
	σ	357.7	357.3	358.9	359.8	357.8	357.6	357.5	358.2
CPT	w	0.3161(81)	0.3160(82)	0.3157(81)	0.3156(84)	0.3153(85)	0.3154(84)	0.3154(84)	0.3139(88)
	σ	314.9	314.7	312.8	312.8	310.7	307.4	305.9	305.0

[a] Values in the parentheses indicate the time (in μsec) at which the maximum center deflection occurred (CPT = classical plate theory; SDT = shear deformation theory).

Table 2 Comparison of transverse deflection and stresses obtained in the present study with those obtained by the finite-element method[a] for two-layer cross-ply square plate (Material 1) under suddenly applied transverse load

Time t	Center deflection, $\bar{w}$		Normal stress, $\bar{\sigma}_x$		Shear stress, $\bar{\sigma}_{xy}$		Shear stress, $\bar{\sigma}_{xz}$	
(μsec)	present	FES[a]	present	FES	present	FES	present	FES
10	0.0076	0.0076	4.038	3.920	0.190	0.182	0.699	0.679
20	0.0365	0.0365	28.48	27.66	1.611	1.555	2.252	2.190
40	0.1472	0.1474	113.6	110.3	8.506	8.243	5.891	5.730
60	0.2922	0.2925	227.2	220.7	16.47	15.95	12.34	12.00
80	0.4116	0.4119	319.1	309.9	23.85	23.11	16.34	15.89
100	0.4604	0.4606	357.8	347.3	26.27	25.43	18.94	18.40
120	0.4173	0.4172	323.1	313.5	24.12	23.34	15.96	16.19
140	0.3010	0.3006	233.0	225.8	17.05	16.47	12.58	12.21
160	0.1562	0.1558	119.6	115.6	8.848	8.533	6.533	6.327
180	0.0414	0.0410	30.40	29.23	2.029	1.939	2.233	2.155
200	0.0013	0.0013	0.742	0.702	0.248	0.242	0.564	0.548

[a] Finite element solution from [24] (obtained using 2 × 2 mesh of nine-node rectangular elements).

Table 3 Effect of layers, shear deformation, lamination scheme, and orthotropy on the center transverse deflection ($w \times 10^3$) of square plates subjected to suddenly applied transverse pulse loading (CP = cross-ply, (0 deg/90 deg/ . . .); AP = angle-ply (45 deg/ − 45 deg/ + . − . . .), $\gamma = E_1/E_2$, $q_0 = 10$ N/cm^2)

Lamination Scheme	Layers 1	2	3	4	5	6	7	8
CP-CPT	0.1272	0.3153	0.1272	0.1493	0.1272	0.1366	0.1272	0.1325
$\gamma = 25$	(55[a])	(85)	(55)	(60)	(55)	(55)	(55)	(55)
CP-SDT	0.3566	0.4604	0.3386	0.2947	0.2924	0.2809	0.2817	0.2765
$\gamma = 25$	(90)	(100)	(85)	(80)	(80)	(80)	(80)	(80)
CP-SDT	0.3233	0.3824	0.2985	0.2438	0.2463	0.2344	0.2366	0.2316
$\gamma = 40$	(85)	(90)	(80)	(75)	(75)	(70)	(70)	(70)
AP-SDT	–	0.3387	–	0.2277	–	0.2196	–	0.2170
$\gamma = 25$		(85)		(70)		(70)		(70)
AP-SDT	–	0.2826	–	0.1977	–	0.1922	–	0.1885
$\gamma = 40$		(80)		(65)		(65)		(65)

[a] Values in the parentheses denote the time (in μsec) at which the maximum center deflection occurred.

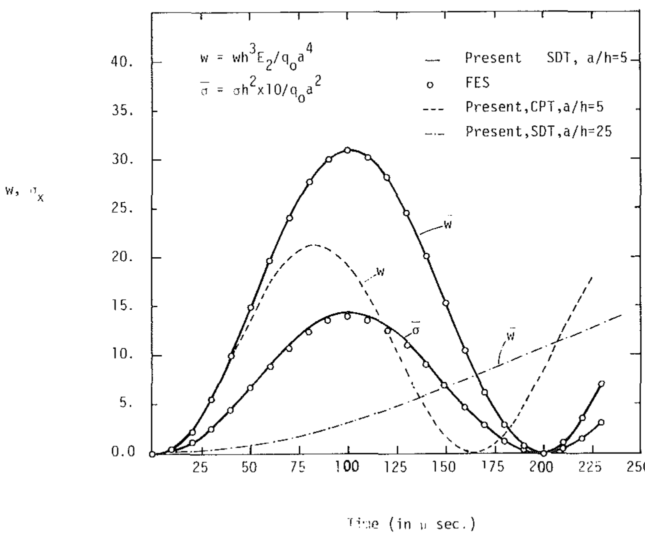

Fig. 1 Comparison of the present solution with the finite-element solution (FES) of two-layer cross-ply (0 deg/90 deg) square plate under suddenly applied sinusoidal loading ($E_1/E_2 = 25$)

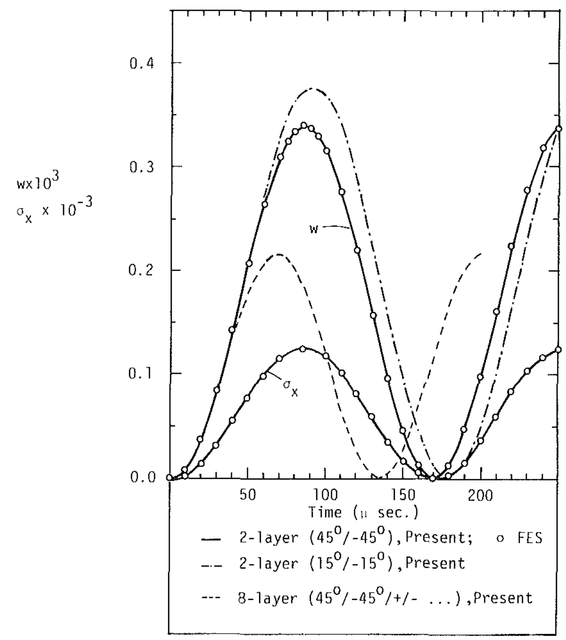

Fig. 2 Comparison of the present solution finite-element solution (FES) of angle-ply ($\theta/-\theta/\theta/-\theta$ . . .) square plates under suddenly applied sinusoidal loading ($q_0 = 1$kg/cm^2; $E_1/E_2 = 25$)

small difference in stresses is due to the fact that the stresses in the finite-element method are computed at the Gauss points.

Figure 1 shows plots of nondimensionalized center deflection and center stress for a two-layer cross-ply (0 deg/90 deg) square plate (Material 1). The present solutions with and without shear deformation are compared with the finite-element solutions of the shear deformation theory in Fig. 1 for h = 1 cm (i.e., $a/h = 25$). From Fig. 1 it is clear that the classical plate theory predicts significantly lower values of deflection and period. It is also apparent from the results of the shear deformation theory that the nondimensionalized deflection increases and the period decreases with increasing values of thickness of the plate. The effect of transverse shear and plate thickness on the amplitude and period of the deflection is clear.

Figure 2 shows plots of center deflection and normal stress (SDT) for angle-ply square plates (for Material 1 and data in equation (22)). The effect of layers (45 deg/ − 45 deg/ + / − ...) and lamination angle on the amplitude and period of deflection is apparent. Again the agreement between the present solution and the finite-element solution [24] is excellent.

To further investigate the effect of the layers, shear deformation, lamination scheme, and material orthotropy on the transverse deflection and normal stress, parametric studies were carried and the results are presented in Table 3. The values in the parentheses of Table 3 indicate the time (μsec) at which the maximum deflection occurs. As in the static analysis, the response of a two-layer construction is significantly different (i.e., larger deflection) when compared to single-layer or multilayered plates.

Figure 3 shows the effect of the angle ($\theta/-\theta$), aspect ratio, and material orthotropy on the center deflection of composite plates. The effect on the amplitude and period of the deflections is clearly nonlinear.

The last example is concerned with transient response of a two-layer (45 deg/ − 45 deg) square plate (Material 1) under impulsive loading,

$$q = 10H(t-t_0)\sin\frac{\pi x}{a}\sin\frac{\pi y}{a}, \ t_0 = 5\mu\text{sec}$$

where $H(t)$ denotes the Heavyside step function. Figure 4 shows plots of the center deflection and normal stress with respect to time. Since no damping is accounted for in the present study, the wave does not damp out with time.

Conclusions

The exact form of the spatial variation of solutions are presented herein for two different lamination schemes. The results also bring out the significance of including the transverse shear strains on the transient response of composite plates. Although the analysis presented herein is valid only for rectangular plates of two different lamination schemes and boundary conditions, and sinusoidal distribution of the transverse loading, the results should be of interest to numerical analysts in validating their numerical methods, and to experimentalists in interpreting their experimental findings (see, for example, [24–28]). Of course, duplicating any mathematical boundary conditions in an experiment is often a difficult task. The boundary conditions in equation (8), for example, can be simulated in an experiment by making a v-groove along the edges of the cross-ply plate to be tested, and then supporting the plate on knife edges so that motion along the edges is not restrained but motion perpendicular and transverse to the edges is restricted. On the other hand, simulation of boundary conditions of an experiment in a finite element model is relatively simple. With this in mind, the author has conducted finite-element analyses and preliminary results are included in [24]. It is also of practical importance to include damping, and nonlinearities due to large deflections and material behavior. The analysis presented herein can also be extended to certain shell theories.

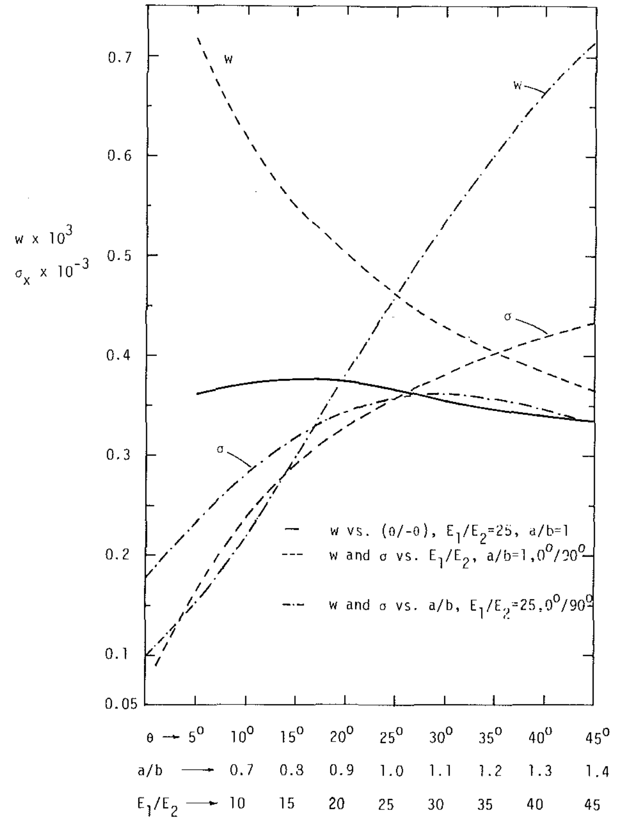

Fig. 3 Effect of lamination angle, aspect ratio, and material orthotropy on the solution of two layer plates under suddenly applied sinusoidal loading ($q_0 = 10\text{N/cm}^2$)

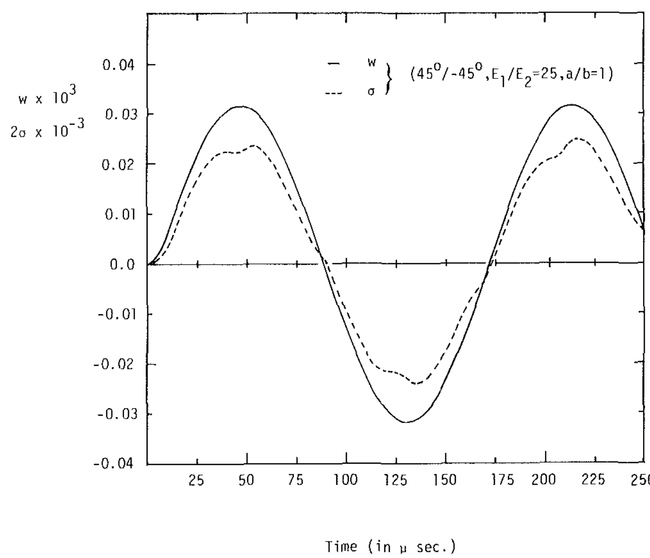

Fig. 4 Transient response of two-layer angle-ply (45 deg/ − 45 deg) square plate ($E_1/E_2 = 25$) under impulsive sinusoidally distributed transverse load (duration = 5μsec)

Acknowledgments

The results reported in the present study were obtained during an investigation supported by the Structural Mechanics Program of the Air Force Office of Scientific Research (AFOSR) through Grant AFOSR-81-0142. The support is gratefully acknowledged. It is also a pleasure to acknowledge the constructive comments of Professor L. E. Malvern of the University of Florida on an earlier version of the paper.

References

1 Reismann, H., and Lee, Y., "Forced Motions of Rectangular Plates," in: *Developments in Theoretical and Applied Mechanics*, Vol. 4, Frederick, D., ed., Pergamon Press, New York, 1969, pp. 3–18.

2 Reismann, H., "Forced Motion of Elastic Plates," ASME Journal of Applied Mechanics, Vol. 35, 1968, pp. 510–515.

3 Lee, Y., and Reismann, H., "Dynamics of Rectangular Plates," *International Journal of Engineering Science*, Vol. 7, 1969, pp. 93–113.

4 Rock, T., and Hinton, E., "Free Vibration and Transient Response of Thick and Thin Plates Using the Finite Element Method," *Earthquake Engineering and Structural Dynamics*, Vol. 3, 1974, pp. 51–63.

5 Hinton, E., Owen, D. R., and Shantaram, D., "Dynamic Transient Behavior of Thick and Thin Plates," *The Mathematics of Finite Elements and Applications II*, Whiteman, J. R., ed., Academic Press, New York, 1976.

6 Hinton, E., "The Dynamic Transient Analysis of Axisymmetric Circular Plates by the Finite Element Method," *Journal of Sound and Vibration*, Vol. 46, 1976, pp. 465–

7 Pica, A., and Hinton, E., "Transient and Pseudo-Transient Analysis of Mindlin Plates," *International Journal for Numerical Methods in Engineering*, Vol. 15, 1980, pp. 189–208.

8 Akay, H. U., "Dynamic Large Deflection Analysis of Plates Using Mixed Finite Elements," *Computers & Structures*, Vol. 11, 1980, pp. 1–11.

9 Moon, F. C., "Wave Surfaces due to Impact on Anisotropic Plates," *Journal of Composite Materials*, Vol. 6, 1972, pp. 62–79.

10 Moon, F. C., "One-dimensional Transient Waves in Anisotropic Plates," ASME Journal of Applied Mechanics, Vol. 40, 1973, pp. 485–490.

11 Chow, T. S., "On the Propagation of Flexural Waves in an Orthotropic Laminated Plate and its Response to an Impulsive Load," *Journal of Composite Materials*, Vol. 5, 1971, pp. 306–319.

12 Wang, A. S. D., Chou, P. C., and Rose, J. L., "Strongly Coupled Stress Waves in Heterogeneous Plates," *AIAA Journal*, Vol. 10, 1972, pp. 1088–1090.

13 Sun, C. T., "Propagation of Shock Waves in Anisotropic Composite Plates," *Journal of Composite Materials*, Vol. 7, 1973, pp. 366–382.

14 Sun, C. T., and Whitney, J. M., "Forced Vibrations of Laminated Composite Plates in Cylindrical Bending," *Journal of the Acoustical Society of America*, Vol. 55, No. 5, 1974, pp. 1003–1008.

15 Sun, C. T., and Whitney, J. M., "Dynamic Response of Laminated Composite Plates," *AIAA Journal*, Vol. 13, No. 10, 1975, pp. 1250–1260.

16 Whitney, J. M., and Sun, C. T., "Transient Response of Laminated Composite Plates Subjected to Transverse Dynamic Loading," *Journal of the Acoustical Society of America*, Vol. 61, No. 1, 1977, pp. 101–104.

17 Mindlin, R. D., and Goodman, L. E., "Beam Vibrations With Time-Dependent Boundary Conditions," ASME Journal of Applied Mechanics, Vol. 17, 1950, pp. 377–380.

18 Yang, P. C., Norris, C. H., and Stavsky, Y., "Elastic Wave Propagation in Heterogeneous Plates," *International Journal of Solids and Structures*, Vol. 2, 1966, pp. 665–684.

19 Whitney, J. M., and Pagano, N. J., "Shear Deformation in Heterogeneous Anisotropic Plates," ASME Journal of Applied Mechanics, Vol. 37, 1970, pp. 1031–1036.

20 Reddy, J. N., and Chao, W. C., "A Comparison of Closed-Form and Finite Element Solutions of Thick, Laminated, Anisotropic Rectangular Plates," *Nuclear Engineering and Design*, Vol. 61, 1981, pp. 153–167.

21 Bathe, K. J., and Wilson, E. L., *Numerical Methods in Finite Element Analysis*, Prentice-Hall, Englewood Cliffs, N.J., 1976.

22 Leech, J. W., "Stability of Finite Difference Equations for the Transient Response of a Flat Plate," *AIAA Journal*, Vol. 3, No. 9, 1965, pp. 1772–1773.

23 Tsui, T. Y., and Tong, P., "Stability of Transient Solution of Moderately Thick Plate by Finite Difference Method," *AIAA Journal*, Vol. 9, 1971, pp. 2062–2063.

24 Reddy, J. N., "Dynamic (Transient) Analysis of Layered Anisotropic Composite-Material Plates," Department of Engineering Science and Mechanics, Report No. VPI-E-81-24, Virginia Polytechnic Institute, Blacksburg, Va., 1981.

25 Ross, C. A., and Sierakowski, R. L., "Studies on the Impact Resistance of Composite Plates," *Composites*, Vol. 4, 1973, pp. 157–161.

26 Sierakowski, R. L., Malvern, L. E., Ross, C. A., and Strickland, W. S., "Failure of Composite Plates Subjected to Dynamic Loads," *Proceedings of the Army Symposium on Solid Mechanics*, 1976, pp. 9–25.

27 Malvern, L. E., Sierakowski, R. L., Ross, C. A., and Cristescu, N., "Impact Failure Mechanics in Fiber-Reinforced Composite Plates," *Proceedings of the IUTAM Symposium on High Velocity Deformation of Solids*, Kawata, K., and Shioiri, J., eds., Tokyo, Aug. 24–27, 1977.

28 Takeda, N., and Sierakowski, R. L., "Localized Impact Problems of Composite Laminates," *Shock and Vibration Digest*, Vol. 12, No. 8, 1980, pp. 3–10.

APPENDIX 1

Elements of the Operator Matrix in Equation (7):

$$L_{11}=A_{11}d_{11}+2A_{16}d_{12}+A_{66}d_{22}+Pd_{tt},$$
$$L_{12}=(A_{12}+A_{66})d_{12}+A_{16}d_{11}+A_{26}d_{22},\ L_{13}=0,$$
$$L_{14}=B_{11}d_{11}+2B_{16}d_{12}+B_{66}d_{22}+Rd_{tt},$$
$$L_{15}=(B_{12}+B_{66})d_{12}+B_{16}d_{11}+B_{26}d_{22}=L_{24},$$
$$L_{22}=2A_{26}d_{12}+A_{22}d_{22}+A_{66}d_{11}+Pd_{tt},\ L_{23}=0$$
$$L_{25}=2B_{26}d_{12}+B_{22}d_{22}+B_{66}d_{11}+Rd_{tt},$$
$$L_{33}=-A_{44}d_{11}-2A_{45}d_{12}-A_{55}d_{22}+Pd_{tt},$$
$$L_{34}=A_{44}d_1-A_{45}d_2$$
$$L_{35}=-A_{45}d_1-A_{55}d_2,\ L_{44}=D_{11}d_{11}+2D_{16}d_{12}+D_{66}d_{22}-A_{44}+Id_{tt},$$
$$L_{45}=(D_{12}+D_{66})d_{12}+D_{16}d_{11}+D_{26}d_{22}-A_{45},$$
$$L_{55}=2D_{26}d_{12}+D_{22}d_{22}+D_{66}d_{11}+Id_{tt}-A_{55}$$

where $d_i=\partial/\partial x_i$, $d_{ij}=\partial^2/\partial x_i\partial x_j\ (i,j=1,2)$, and $d_{tt}=\partial^2/\partial t^2$.

$$M_{11}=M_{22}=M_{33}=P,\ M_{44}=M_{55}=I,$$
$$M_{ij}=0 \text{ for } i\neq j\ (i,j=1,2,\ldots,5),$$

$F_3=q$, $F_i=0$ for all other $i=1,2,4,5$.

Elements of the Coefficient Matrix in Equation (13):

$$C_{11}=A_{11}\alpha^2+A_{66}\beta^2,\ C_{12}=(A_{12}+A_{66})\alpha\beta$$
$$C_{13}=0,\ C_{14}=\alpha^2B_{11}+B_{66}\beta^2,\ C_{15}=(B_{12}+B_{66})\alpha\beta$$
$$C_{22}=A_{22}\beta^2+A_{66}\alpha^2,\ C_{23}=0,\ C_{24}=C_{15},$$
$$C_{25}=B_{22}\beta^2+B_{66}\alpha^2,\ C_{33}=\alpha^2A_{44}+\beta^2A_{55},$$
$$C_{34}=\alpha A_{44},\ C_{35}=\beta A_{55},\ C_{44}=D_{11}\alpha^2+D_{66}\beta^2+A_{44},$$
$$C_{45}=(D_{12}+D_{66})\alpha\beta,\ C_{55}=D_{66}\alpha^2+D_{22}\beta^2+A_{55}.$$

Elements of the Stiffness Matrix in Equation (17):

$$K_{11}=(A_{11}\alpha^2+A_{66}\beta^2),\ K_{12}=\alpha\beta(A_{12}+A_{66}),$$
$$K_{13}=0,\ K_{14}=(\alpha^2B_{16}+\beta^2B_{26})/h,\ K_{15}=2\alpha\beta B_{16}/h,$$
$$K_{22}=(\alpha^2A_{66}+\beta^2A_{22}),\ K_{23}=0,\ K_{24}=2\alpha\beta B_{26}/h,$$
$$K_{25}=(\alpha^2B_{16}+\beta^2B_{26})/h,\ K_{33}=(\beta^2A_{55}+\alpha^2A_{44}),$$
$$K_{34}=\alpha A_{44}/h,\ K_{35}=\beta A_{55}/h,$$
$$K_{44}=(\alpha^2D_{66}+\beta^2D_{22}+A_{44})/h^2,$$
$$K_{45}=\alpha\beta(D_{12}+D_{66})/h^2,\ K_{55}=(\alpha^2D_{11}+\beta^2D_{66}+A_{55})/h^2,$$
$$F_3=Q_{mn},\ F_1=F_2=F_4=F_5=0.$$

Nonlinear Theory for Flexural Motions of Thin Elastic Plate

Part 3: Numerical Evaluation of Boundary Layer Solutions

N. Sugimoto
Research Associate,
Department of Mechanical Engineering,
Faculty of Engineering Science,
Osaka University,
Toyonaka, Osaka 560, Japan

The boundary layer solutions previoulsy obtained in Part 2 of this series for the cases of the built-in edge and the free edge are evaluated numerically. For the built-in edge, a characteristic penetration depth of the boundary layer toward the interior region is given by 0.13 ϵh, ϵh being the normalized thickness of the plate, while for the free edge, it is given by 0.32 ϵh. Thus the boundary layer for the free edge penetrates more deeply toward the interior region than that for the built-in edge. The first-order stress distribution in each boundary layer is displayed. For the built-in edge, the stress singularity appears on the edge. It is shown that, in the boundary layer, the shearing and normal stresses become comparable with the bending stresses. Similarly for the free edge, the shearing stress also becomes comparable with the twisting stress. It should be remarked that, in the boundary layer, the shearing or the normal stress plays a primarily important role as the bending or the twisting stress. But the former decays toward the interior region and remains higher order than the latter. Finally owing to these numerical results, the coefficients involved in the "reduced" boundary conditions for the built-in edge are evaluated for the various plausible values of Poisson's ratio.

Introduction

This series of papers [1, 2] deals with a comprehensive theory for flexural motions of a thin elastic plate in which the effect of finite thickness and that of small but finite deformation are taken into account. In developing the theory, the plate is treated as composed of two regions, one being the interior region away from the edge and the other the boundary layer region adjacent to the edge. In Part 1 [1], the higher-order equations were derived for the flexural motions in the interior region. In its subsequent paper, Part 2 [2], the boundary layer theory near the edge was developed and the reduced boundary conditions relevant to the higher-order equations were derived for the three typical edge conditions; built-in edge, free edge, and hinged edge. The concern of Part 2 was mainly focused on the derivation of the reduced boundary conditions and explicit stress distribution in the boundary layer for each edge condition is left untouched. The purpose of this paper is to obtain the boundary layer solutions numerically and to display the resulting stress distribution in both cases of the built-in edge and the free edge. For the hinged edge, no boundary layer is assumed to develop and therefore this case is excluded here. Also the numerical values of the coefficients involved in the reduced boundary conditions for the built-in edge are evaluated for the various plausible values of Poisson's ratio. In this paper as well, the same notations are used in common with the previous two papers.

As already seen in Part 2, the boundary layer problem and the interior problem are mutually interrelated. Indeed the boundary layer solutions affect the interior solutions through the reduced boundary conditions. Conversely, the interior solutions affect the boundary layer solutions through their values at the boundary of the interior region. For a given plate problem, the boundary layer problem is solved after the interior problem is first solved under the appropriate reduced boundary conditions to that problem. As far as the first-order boundary layer problem is concerned, however, this interrelation is rather simple because the boundary layer solutions merely undergo a change of scale factor determined by the interior solutions at the boundary. In this paper, we are mainly concerned with the numerical results of the first-order problem. The computations for the higher-order problems can be carried out, if necessary, in the same way as presented in this paper.

The boundary layer solutions[1] $\tilde{\varphi}^{(1)}$ for the built-in edge and $\tilde{\psi}^{(1)}$ for the free edge decay exponentially away from the edge toward the interior region. Being consistent with the earlier assumption made in Part 2, a penetration depth of the boundary layer toward the interior region is of the order of

Contributed by the Applied Mechanics Division for Publication in the JOURNAL OF APPLIED MECHANICS.

Discussion on this paper should be addressed to the Editorial Department, ASME, United Engineering Center, 345 East 47th Street, New York, N.Y. 10017, and will be accepted until two months after final publication of the paper itself in the JOURNAL OF APPLIED MECHANICS. Manuscript received by ASME Applied Mechanics Division, January, 1981; final revision, December 1981.

[1] Here the penetration depth is roughly defined as the width by which $\tilde{\varphi}^{(1)}$ or $\tilde{\psi}^{(1)}$ decays by the factor e.

the normalized thickness of the plate ϵh.[1] For the built-in edge, the characteristic penetration depth is given by 0.13 ϵh, while for the free edge, it is given by 0.32 ϵh. Thus the boundary layer for the free edge penetrates more deeply toward the interior region than that for the built-in edge. The first-order stress distribution in the boundary layer is displayed for both edge conditions. The pattern of distribution in each condition remains unchanged except the scale factor aforementioned whatever the interior solutions may be. In this sense, the pattern of distribution is characteristic of each edge condition. For the built-in edge, the stress singularity appears on the edge (more specifically, on the intersections between the plate surfaces and the edge surface). Of course, the stresses near the intersections are mainly determined by this stress singularity. Except in the vicinity of the stress singularity, the bending stresses K_{yy} and K_{xx} do not differ appreciably from those at the boundary of the interior region. But it is displayed that, in the boundary layer, the shearing stress K_{yz} and the normal stress K_{zz} become comparably important with the bending stresses and they decay toward the interior region. Similarly for the free edge, on the other hand, it is also displayed that the shearing stress K_{xz} becomes important as well as the twisting stress K_{xy}. Thus in the boundary layer, the shearing or the normal stress plays a primarily important role as the bending or the twisting stress and cannot be essentially neglected.

Numerical Results

1 Case of Built-in Edge. In Part 2, the first-order boundary layer problem for the built-in edge condition is posed for $\tilde{\varphi}^{(1)}$ as the plane strain problem:

$$\tilde{\varphi}^{(1)}_{,\eta\eta\eta\eta} + 2\tilde{\varphi}^{(1)}_{,\eta\eta\zeta\zeta} + \tilde{\varphi}^{(1)}_{,\zeta\zeta\zeta\zeta} = 0, \tag{1}$$

with the boundary conditions

$$\eta = 0, \quad (1-\sigma)\tilde{\varphi}^{(1)}_{,\eta\eta} - \sigma\tilde{\varphi}^{(1)}_{,\zeta\zeta} = 2\sigma/(1-\sigma)w^{(0)}_{,yy}\zeta,$$

$$(1-\sigma)\tilde{\varphi}^{(1)}_{,\eta\eta\eta} + (2-\sigma)\tilde{\varphi}^{(1)}_{,\eta\zeta\zeta} = 0,$$

$$\eta \to \infty, \ \tilde{\varphi}^{(1)} \to 0, \quad \text{and} \quad \zeta = \pm h/2, \quad \tilde{\varphi}^{(1)} = \tilde{\varphi}^{(1)}_{,\zeta} = 0, \tag{2}$$

where $w^{(0)}_{,yy}$ is evaluated at $y = 0$ in the interior region. The explicit procedure to solve this problem by the Laplace transform method is given in Appendix B of Part 2. This case corresponds to that with $\alpha = [2\sigma/(1-\sigma)^2]w^{(0)}_{,yy}$ and $\beta = 0$. First $\tilde{\varphi}^{(1)}$ and $\tilde{\varphi}^{(1)}_{,\eta}$ at $\eta = 0$ are assumed to be

$$\tilde{\varphi}^{(1)}(0,\zeta) = \frac{2\sigma h^3}{(1-\sigma)^2} w^{(0)}_{,yy}\left\{ \sum_{n=1,3,5}^{\infty} A'_n \cos\left[n\pi\left(\frac{\zeta}{h} + \frac{1}{2}\right)\right] + A'_S\phi^{(s)}\left(\frac{\zeta}{h}\right)\right\},$$

$$\tilde{\varphi}^{(1)}_{,\eta}(0,\zeta) = \frac{2\sigma h^2}{(1-\sigma)^2} w^{(0)}_{,yy}\left\{ \sum_{n=1,3,5}^{\infty} B'_n \cos\left[n\pi\left(\frac{\zeta}{h} + \frac{1}{2}\right)\right] + B'_S\phi^{(s)}_{,\eta}\left(\frac{\zeta}{h}\right)\right\}, \tag{3}$$

with

$$\phi^{(s)}(\zeta/h) = (1/2 - \zeta/h)^{\lambda+1} - (1/2 + \zeta/h)^{\lambda+1} + (\lambda+1)\zeta/h,$$

$$\phi^{(s)}_{,\eta}(\zeta/h) = (1/2 - \zeta/h)^{\lambda} - (1/2 + \zeta/h)^{\lambda} + \lambda\zeta/h, \tag{4}$$

where A'_n, $B'_n (n = 1,3,5,\ldots)$, A'_s, and B'_s are real constants to be determined later and λ $(0 < \lambda < 1)$[2] denotes the power of the stress singularity at the corner. This λ is given by the solution of the following characteristic equation for the corner singularity with one side built-in and the other free (see the Appendix):

$$\sin^2(\pi\lambda/2) = 4(1-\sigma)^2/(3-4\sigma) - \lambda^2/(3-4\sigma). \tag{5}$$

According to the aforementioned Laplace transform method, $\tilde{\varphi}^{(1)}$ can easily be obtained by the inversion formula, which can be expressed in the form of the Papkovich-Fadle eigenfunction expansion [3,4]:

$$\tilde{\varphi}^{(1)} = \frac{2\sigma h^3}{(1-\sigma)^2} w^{(0)}_{,yy}\phi^{(1)} = -\frac{2\sigma h^3}{(1-\sigma)^2} w^{(0)}_{,yy} \sum_{k=1}^{\infty} C_k \Phi_k(\zeta)\exp(-q_k\eta/h) + \text{complex conjugate}, \tag{6}$$

with C_k and Φ_k $(k = 1,2,3,\ldots)$ given by

$$C_k = \sum_{n=1,3,5}^{\infty} \frac{\cot^2(q_k/2)}{[q_k^2 - (n\pi)^2]^2}\left\{\left[q_k^3 - \frac{(2-\sigma)}{(1-\sigma)}(n\pi)^2 q_k\right]A'_n - \left[q_k^2 + \frac{\sigma}{(1-\sigma)}(n\pi)^2\right]B'_n\right\}$$
$$+ \left[\frac{\hat{\phi}^{(s)}_{1,\zeta}(q_k)}{2\sin^2(q_k/2)} - \cot^2\left(\frac{q_k}{2}\right)\hat{\phi}^{(s)}_1(q_k)\right]A'_S - \left[\frac{\hat{\phi}^{(s)}_{2,\zeta}(q_k)}{2\sin^2(q_k/2)} - \cot^2\left(\frac{q_k}{2}\right)\hat{\phi}^{(s)}_2(q_k)\right]B'_S + \frac{1}{2q_k^3},$$

$$\Phi_k(\zeta) = \cos(q_k/2)\sin(q_k\zeta/h) - 2\sin(q_k/2)(\zeta/h)\cos(q_k\zeta/h), \ (k = 1,2,3,\ldots) \tag{7}$$

where q_k $(\neq 0;\ k = 1,2,3,\ldots)$ are the roots of the equation $\sin q = q$ in the first quadrant of the complex q plane and they are ordered as $0 < \operatorname{Re} q_1 < \operatorname{Re} q_2 \ldots$. The real coefficients A'_n, B'_n $(n = 1,3,5\ldots)$, A'_s, and B'_s involved in C_k are determined by the following complex simultaneous equations in infinite dimensions:

$$\sum_{n=1,3,5}^{\infty} \frac{\cot^2(q_k/2)}{[q_k^2 - (n\pi)^2]^2}\left\{\left[q_k^3 - \frac{(2-\sigma)}{(1-\sigma)}(n\pi)^2 q_k\right]A'_n + \left[q_k^2 + \frac{\sigma}{(1-\sigma)}(n\pi)^2\right]B'_n\right\}$$
$$+ \left[\frac{\hat{\phi}^{(s)}_{1,\zeta}(q_k)}{2\sin^2(q_k/2)} - \cot^2\left(\frac{q_k}{2}\right)\hat{\phi}^{(s)}_1(q_k)\right]A'_S + \left[\frac{\hat{\phi}^{(s)}_{2,\zeta}(q_k)}{2\sin^2(q_k/2)} - \cot^2\left(\frac{q_k}{2}\right)\hat{\phi}^{(s)}_2(q_k)\right]B'_S$$
$$= -\frac{1}{2q_k^3}, (k = 1,2,3,\ldots), \tag{8}$$

where the definitions of $\hat{\phi}^{(s)}_{i,\zeta}(q_k)$ and $\hat{\phi}^{(s)}_i(q_k)$ $(i = 1,2)$ are referred to Appendix B of Part 2. By virtue of these equations, C_k can take a simpler form as

$$C_k = \sum_{n=1,3,5}^{\infty} \frac{2\cot^2(q_k/2)}{[q_k^2 - (n\pi)^2]^2}\left[q_k^3 - \frac{(2-\sigma)}{1-\sigma)}(n\pi)^2 q_k\right]A'_n + 2\left[\frac{\hat{\phi}^{(s)}_{1,\zeta}(q_k)}{2\sin^2(q_k/2)} - \cot^2\left(\frac{q_k}{2}\right)\hat{\phi}^{(s)}_1(q_k)\right]A'_S + \frac{1}{q_k^3}. \tag{9}$$

The simultaneous equations in infinite dimensions (8) are solved by truncating them into finite dimensions. Setting

[2] In this paper, λ is used for the power of the stress singularity, not for Lamé constant.

Table 1 Table of coefficients A_n', B_n', A_S', and B_S' for $\sigma = 1/3$ ($E-n = 10^{-n}$)

	N = 48	N = 52	N = 56	N = 60	N = 64	N = 68	N = 72
A_1'	-0.3547E-1	-0.3559E-1	-0.3566E-1	-0.3572E-1	-0.3577E-1	-0.3579E-1	-0.3580E-1
A_3'	-0.1992E-2	-0.1104E-2	-0.1108E-2	-0.1111E-2	-0.1114E-2	-0.1115E-2	-0.1115E-2
A_5'	-0.2048E-3	-0.2061E-3	-0.2071E-3	-0.2079E-3	-0.2085E-3	-0.2088E-3	-0.2089E-3
A_7'	-0.6535E-4	-0.6586E-4	-0.6628E-4	-0.6659E-4	-0.6681E-4	-0.6694E-4	-0.6697E-4
A_9'	-0.2726E-4	-0.2752E-4	-0.2773E-4	-0.2789E-4	-0.2800E-4	-0.2807E-4	-0.2808E-4
A_{11}'	-0.1337E-4	-0.1352E-4	-0.1365E-4	-0.1374E-4	-0.1386E-4	-0.1384E-4	-0.1385E-4
A_{13}'	-0.7312E-5	-0.7411E-5	-0.7490E-5	-0.7550E-5	-0.7592E-5	-0.7616E-5	-0.7623E-5
B_1'	0.8496E-1	0.8519E-1	0.8537E-1	0.8551E-1	0.8562E-1	0.8568E-1	0.8571E-1
B_3'	0.2507E-2	0.2542E-2	0.2570E-2	0.2592E-2	0.2608E-2	0.2619E-2	0.2623E-2
B_5'	0.2726E-3	0.2869E-3	0.2984E-3	0.3074E-3	0.3142E-3	0.3186E-3	0.3206E-3
B_7'	-0.3229E-5	-0.4542E-5	-0.1085E-4	0.1582E-4	0.1953E-4	0.2198E-4	0.2312E-4
B_9'	-0.4822E-4	-0.4337E-4	-0.3940E-4	-0.3626E-4	-0.3391E-4	-0.3234E-4	-0.3160E-4
B_{11}'	-0.5068E-4	-0.4740E-4	-0.4470E-4	-0.4256E-4	-0.4092E-4	-0.3983E-4	-0.3930E-4
B_{13}'	-0.4456E-4	-0.4222E-4	-0.4029E-4	-0.3873E-4	-0.3755E-4	-0.3675E-4	-0.3635E-4
A_S'	0.2381E+0	0.2388E+0	0.2394E+0	0.2398E+0	0.2401F+0	0.2403E+0	0.2403E+0
B_S'	-0.1330E+0	-0.1335E+0	-0.1339E+0	-0.1342E+0	-0.1344E+0	-0.1346E+0	-0.1347E+0
A_S'/B_S'	-0.1790E+1	-0.1789E+1	-0.1788E+1	-0.1787E+1	-0.1786E+1	-0.1785E+1	-0.1784E+1

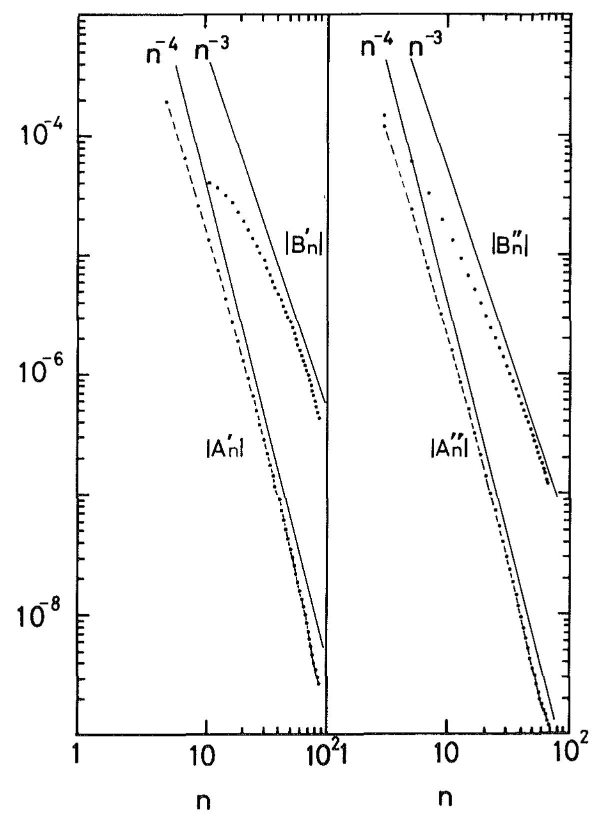

Fig. 1

other terms than the first $2N$ unknowns A_n', B_n' ($n=1,3,5,\ldots,2N-3$), A_s', and B_s' to be zero, and taking the first N complex equations ($k=1,2,3,\ldots,N$), the real simultaneous equations for $2N$ unknowns are solved. Increasing the number of unknowns $2N$, the coefficients are calculated until convergence is reached. In numerical computation of the integrals in $\hat{\phi}_{i,\zeta}^{(s)}(q_k)$ and $\hat{\phi}_i^{(s)}(q_k)(i=1,2)$, Simpson's rule is employed with the division 4000 in the interval $0 \leq \zeta/h \leq 1/2$. For a plausible value of Poisson's ratio $\sigma = 1/3$ ($\lambda = 0.68998353$ from (5)), Table 1 shows how the first 16 coefficients A_n', B_n' ($n=1,3,5,\ldots,13$), A_s', and B_s' converge as N increases from 48 to 72. It is found from this that the greatest terms A_s' and B_s' converge with the relative error or order of 10^{-3}. The accuracy of computation for each N is also checked as follows. From the boundary conditions at $\zeta = \pm h/2$, A_n', B_n' ($n=1,3,5,\ldots$), A_s', and B_s' must satisfy the relations

$$\sum_{n=1,3,5}^{\infty} A_n' + (1-\lambda)A_s'/2 \equiv S_A' = 0, \tag{10}$$

and

$$\sum_{n=1,3,5}^{\infty} B_n' + (1-\lambda/2)B_s' \equiv S_B' = 0. \tag{11}$$

Substituting the coefficients calculated into S_A' and S_B' (the upper limit of the summation is then taken as $N-1$ instead of infinity), it is found that $|S_A'|$ always remains less than 3×10^{-7}, while $|S_B'|$ is less than 3×10^{-4}. Comparing S_A' and S_B' with the respective greatest term in the left-hand side of (10) and (11), the relative error is considered to be of the order of 10^{-3}. In addition to this, the ratio of A_s'/B_s' is also checked. From the analysis of the stress singularity at the corner (see Appendix), A_s'/B_s' must converge to -1.77750 for $\sigma = 1/3$. As can be seen from Table 1, this ratio is regarded to converge to the limiting value with the relative error 3×10^{-3}. Thus it is found that this computation is correct with the relative error of the order of 10^{-3}. Figure 1 shows how $|A_n'|$ and $|B_n'|$ calculated at $N=72$ decay as n increases. It indicates that $|A_n'|$ decays as n^{-4}, while $|B_n'|$ decays as n^{-3}. Since they decrease more rapidly than n^{-2}, the Fourier series in $\tilde{\varphi}^{(1)}(0,\zeta)$ and $\tilde{\varphi}_{,\eta}^{(1)}(0,\zeta)$ converge uniformly over $-1/2 \leq \zeta \leq 1/2$. Furthermore the stresses derived from them also converge uniformly.

We now seek the stresses derived from $\phi^{(1)}$. Noting that $\phi^{(1)}$ is odd with respect to ζ, therefore $\phi_{,\eta\eta}^{(1)}$ and $\phi_{,\zeta\zeta}^{(1)}$ are odd, while $\phi_{,\eta\zeta}^{(1)}$ is even, these stress components are displayed in Figs. 2–4 over the half range of ζ, i.e., $0 \leq \zeta/h \leq 1/2$. In these figures, attention should be paid to the stress singularity at the corner $\eta = 0$ and $\zeta/h = 1/2$. Here the stresses along $\eta = 0$ are calculated by (3), not by (6), since the term by term differentiation of (6) is found in admissible. From (6), $\phi^{(1)}$

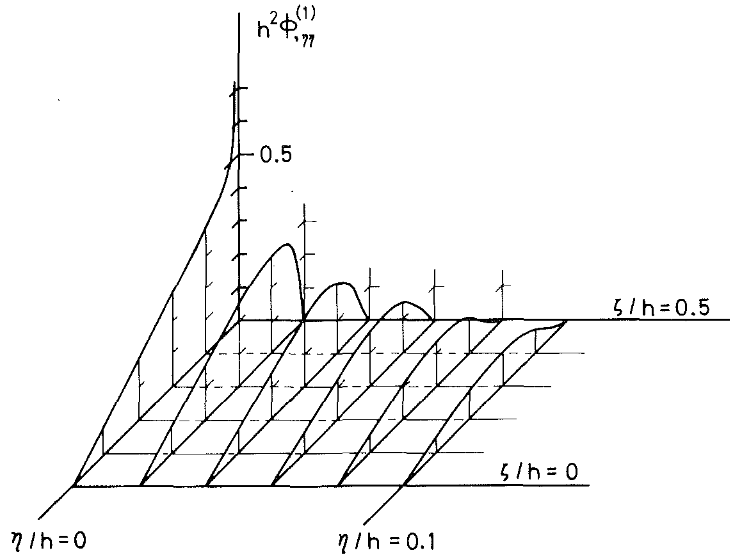

Fig. 2

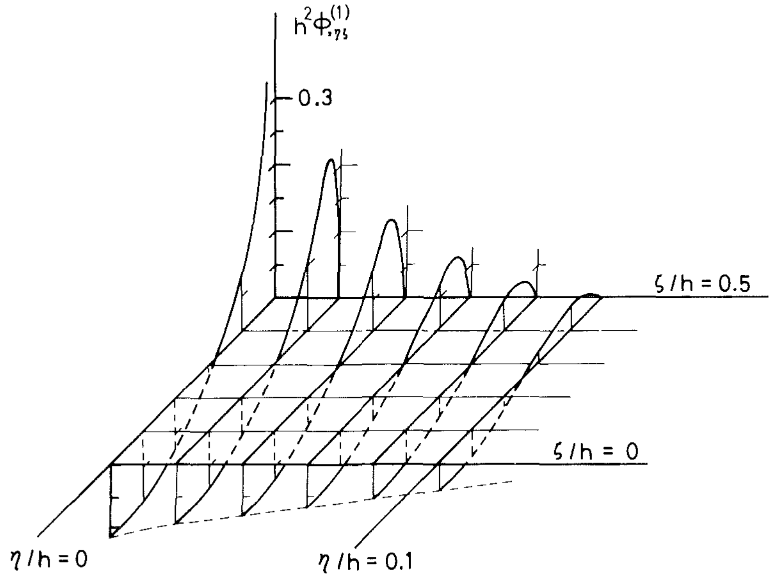

Fig. 3

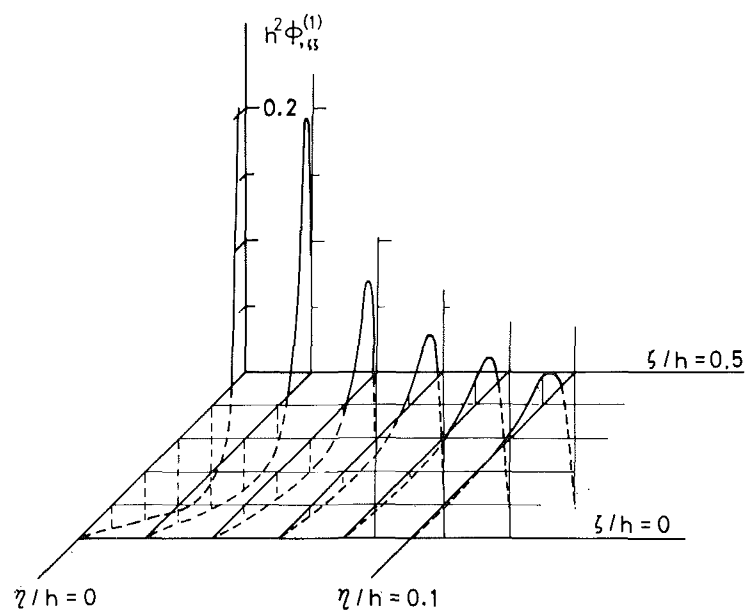

Fig. 4

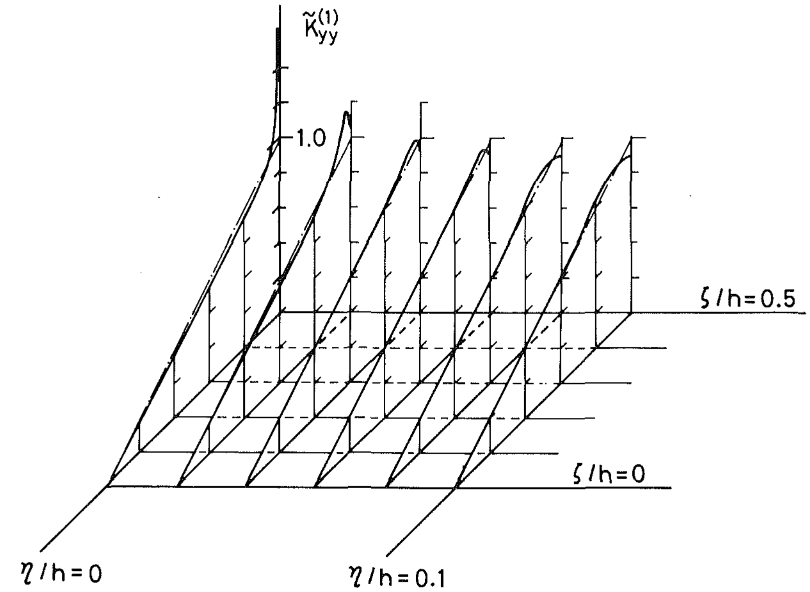

Fig. 5

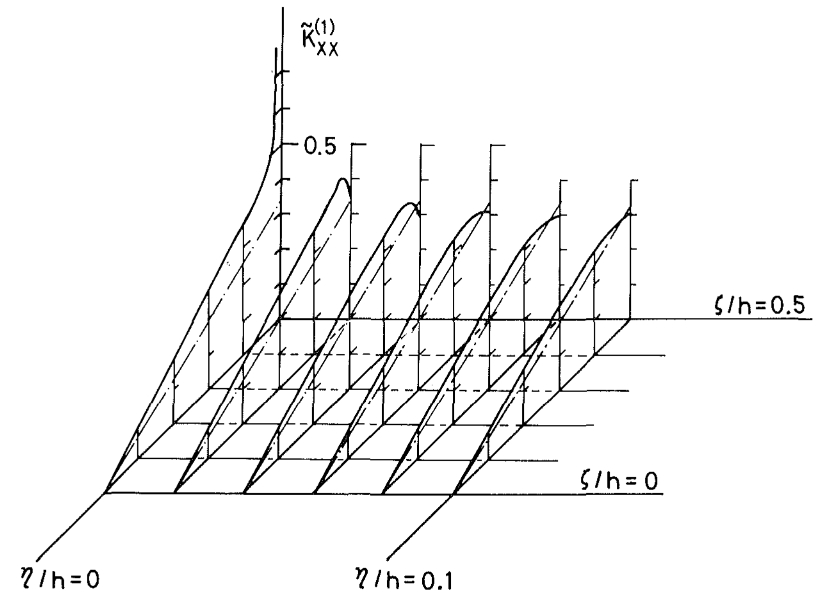

Fig. 6

and its derivatives decay exponentially as η/h increases. A characteristic penetration depth is determined by the inverse of Re q_1 ($\cong$ 7.5) of the most slowly decreasing function $\exp(-q_1\eta/h)$ and therefore $\eta/h \sim 0.13$, i.e., $y \sim 0.13\ \epsilon h$. This result is consistent with the earlier assumption made in Part 2 that the penetration depth of the boundary layer toward the interior region is of the order of the normalized thickness ϵh.

It should be remembered here that the actual first-order stresses in the boundary layer are given by (17) and (22) in Part 2:

$$
\begin{aligned}
\tilde{K}^{(1)}_{yy} &= 2c[\zeta/h + \sigma/(1-\sigma)h^2\phi^{(1)}_{,\zeta\zeta}],\\
\tilde{K}^{(1)}_{yz} &= -2c\sigma/(1-\sigma)h^2\phi^{(1)}_{,\eta\zeta}, \quad \tilde{K}^{(1)}_{zz} = 2c\sigma/(1-\sigma)h^2\phi^{(1)}_{,\eta\eta},\\
\tilde{K}^{(1)}_{xx} &= 2c\sigma[\zeta/h + \sigma/(1-\sigma)h^2(\phi^{(1)}_{,\eta\eta} + \phi^{(1)}_{,\zeta\zeta})],\\
\tilde{K}^{(1)}_{xy} &= \tilde{K}^{(1)}_{xz} = 0,
\end{aligned}
\tag{12}
$$

where $c = -hw^{(0)}_{,yy}/(1-\sigma)$ represents the stress $\tilde{K}^{(1)}_{yy}$ at the upper surface $\zeta/h = 1/2$ as $\eta/h \to \infty$ (i.e., at the boundary of the interior region). From these expressions, the first-order stresses in the boundary layer depend on the interior solutions through the scale factor $w^{(0)}_{,yy}$. Except for this factor, the pattern of the stress distribution is characteristic of the built-in edge condition. In Fig. 5 and Fig. 6, $\tilde{K}^{(1)}_{yy}$ and $\tilde{K}^{(1)}_{xx}$ are displayed in which c is set equal to unity and σ is 1/3. The contribution of $\phi^{(1)}_{,\zeta\zeta}$ and $\phi^{(1)}_{,\eta\eta}$ to $\tilde{K}^{(1)}_{yy}$ and $\tilde{K}^{(1)}_{xx}$ is small, because of the factor $\sigma/(1-\sigma)$, compared with the term ζ/h except in the vicinity of the corners $\eta = 0$ and $\zeta/h = \pm 1/2$. But near the corners, $\tilde{K}^{(1)}_{yy}$ and $\tilde{K}^{(1)}_{xx}$ are determined mainly by the stress singularity. Noting that for $\sigma = 1/3$, $\tilde{K}^{(1)}_{yz} = -ch^2\phi^{(1)}_{,\eta\zeta}$, and $\tilde{K}^{(1)}_{zz} = ch^2\phi^{(1)}_{,\eta\eta}$, the similar graphical representations for $\tilde{K}^{(1)}_{yz}$ and $\tilde{K}^{(1)}_{zz}$ are given by Fig. 3 and Fig. 2, respectively. It is to be remarked here that the first-order shearing stress $\tilde{K}^{(1)}_{yz}$ and normal stress $\tilde{K}^{(1)}_{zz}$ become comparable with the bending stresses $\tilde{K}^{(1)}_{yy}$ and $\tilde{K}^{(1)}_{xx}$ and decay toward the interior region. Thus it is found that, in the boundary layer for the built-in edge, the shearing and normal stresses play an essential role as the bending stresses.

Proceeding to the second-order problem, the boundary layer solution $\tilde{\varphi}^{(2)}$ is sought in a similar manner to that for $\tilde{\varphi}^{(1)}$. This case corresponds to the case with $\alpha = [2\sigma/(1-\sigma)^2]\, w^{(1)}_{,yy}$ and $\beta = -[2(2-\sigma)/(1-\sigma)^2]w^{(0)}_{,yyy}$ in Part 2. To obtain

Table 2 Table of coefficients A_n'', B_n'', A_S'', and B_S'' for $\sigma = 1/3$ ($E-n = 10^{-n}$)

	N = 48	N = 52	N = 56	N = 60	N = 64	N = 68	N = 72
A_1''	-0.2149E-2	-0.2137E-2	-0.2128E-2	-0.2119E-2	-0.2111E-2	-0.2103E-2	-0.2096E-2
A_3''	0.1157E-3	0.1163E-3	0.1168E-3	0.1172E-3	0.1176E-3	0.1180E-3	0.1183E-3
A_5''	0.2369E-4	0.2383E-4	0.2395E-4	0.2406E-4	0.2416E-4	0.2426E-4	0.2434E-4
A_7''	0.7617E-5	0.7675E-5	0.7724E-5	0.7768E-5	0.7808E-5	0.7845E-5	0.7882E-5
A_9''	0.3152E-5	0.3182E-5	0.3207E-5	0.3229E-5	0.3250E-5	0.3269E-5	0.3287E-5
A_{11}''	0.1528E-5	0.1545E-5	0.1560E-5	0.1573E-5	0.1585E-5	0.1595E-5	0.1607E-5
A_{13}''	0.8247E-6	0.8357E-6	0.8452E-6	0.8536E-6	0.8612E-6	0.8683E-6	0.8753E-6
B_1''	0.4378E-2	0.4357E-2	0.4340E-2	0.4325E-2	0.4311E-2	0.4298E-2	0.4285E-2
B_3''	0.1603E-3	0.1572E-3	0.1545E-3	0.1522E-3	0.1501E-3	0.1480E-3	0.1460E-3
B_5''	0.6604E-4	0.6480E-4	0.6371E-4	0.6274E-4	0.6186E-4	0.6102E-4	0.6019E-4
B_7''	0.3579E-4	0.3512E-4	0.3454E-4	0.3402E-4	0.3353E-4	0.3307E-4	0.3262E-4
B_9''	0.2190E-4	0.2149E-4	0.2113E-4	0.2080E-4	0.2050E-4	0.2021E-4	0.1992E-4
B_{11}''	0.1448E-4	0.1421E-4	0.1396E-4	0.1374E-4	0.1354E-4	0.1334E-4	0.1315E-4
B_{13}''	0.1011E-4	0.9925E-5	0.9756E-5	0.9601E-5	0.9455E-5	0.9314E-5	0.9173E-5
A_S''	0.1287E-1	0.1279E-1	0.1272E-1	0.1266E-1	0.1261E-1	0.1255E-1	0.1250E-1
B_S''	-0.7237E-2	-0.7193E-2	-0.7154E-2	-0.7120E-2	-0.7090E-2	-0.7060E-2	-0.7032E-2
A_S''/B_S''	-0.1778E+1	-0.1778E+1	-0.1778E+1	-0.1778E+1	-0.1778E+1	-0.1778E+1	-0.1778E+1

Table 3 Table of coefficients κ_1, κ_2, and κ_3 for various values of Poisson's ratio

	σ = 0.25	σ = 0.3	σ = 0.32	σ = 1/3	σ = 0.35
κ_1	0.006627	0.01064	0.01268	0.01420	0.01630
κ_2	0.01058	0.01349	0.01476	0.01566	0.01679
κ_3	0.2772	0.2992	0.3089	0.3156	0.3245

$\tilde{\varphi}^{(2)}$, A_n'', B_n'' ($n=1,3,5,\ldots$), A_s'', and B_s'' are calculated. Table 2 shows the first 16 coefficients for $\sigma = 1/3$ as N varies from 48–72. Also Fig. 1 shows the decay behavior of $|A_n''|$ and $|B_n''|$ calculated at $N=72$ as n increases. In this computation as well, the accuracy is assured at the same level as for A_n', B_n', A_s', and B_s' with the relative error of the order of 10^{-3}. The second-order stresses would be computed from these numerical values, but they are omitted here.

Finally owing to these numerical results, the coefficients κ_1, κ_2, and κ_3 involved in the reduced boundary conditions for the built-in edge can be evaluated:

$$\kappa_1 = \frac{24\sigma^2}{(1-\sigma)^2}\left[\sum_{n=1,3,5}^{\infty}\frac{B_n'}{(n\pi)^2} - c_2 B_S'\right],$$

$$\kappa_2 = \frac{\sigma}{40(1-\sigma)} - \frac{24\sigma(2-\sigma)}{(1-\sigma)^2}\left[\sum_{n=1,3,5}^{\infty}\frac{A_n'}{(n\pi)^2} - c_1 A_S'\right],$$

$$\kappa_3 = \frac{8+\sigma}{40(1-\sigma)} + \frac{24\sigma(2-\sigma)}{(1-\sigma)^2}\left[\sum_{n=1,3,5}^{\infty}\frac{B_n''}{(n\pi)^2} - c_2 B_S''\right], \tag{13}$$

with

$$c_1 = \int_0^{1/2}\xi\phi^{(s)}(\xi)d\xi, \text{ and } c_2 = \int_0^{1/2}\xi\phi^{(s)}_{,\eta}(\xi)d\xi, \tag{14}$$

where for example $c_1 = -0.01471$ and $c_2 = -0.04713$ for $\sigma = 1/3$. In Table 3, these coefficients are given for the various plausible values of Poisson's ratio.

2 Case of Free Edge. Next we examine the boundary layer solutions in the case of the free edge. There first appears the torsion boundary layer. The stress function $\tilde{\psi}^{(1)}$ has already been given in Part 2 as

$$\tilde{\psi}^{(1)} = 8w^{(0)}_{,xy}h^2\sum_{M=0}^{\infty}\frac{(-1)^m}{\pi^3(2m+1)^3}\cos \times[\pi(2m+1)\zeta/h]\exp[-\pi(2m+1)\eta/h] \equiv w^{(0)}_{,xy}h^2\psi^{(1)}, \tag{15}$$

where $w^{(0)}_{,xy}$ is evaluated at $y = 0$ in the interior region. This stress function also decays exponentially as η/h increases and its characteristic penetration depth is given by $\eta/h \sim 0.32$, i.e., $y \sim 0.32\,\epsilon h$. From this, the penetration depth for the free edge is about three times longer than that for the built-in edge. Thus the boundary layer for the free edge penetrates more deeply toward the interior region than that for the built-in edge.

Let us calculate the stresses in the boundary layer. The first-order stresses in this case are given by (17) and (22) in Part 2:

$$\tilde{K}^{(1)}_{xy} = c(2\zeta/h + h\psi^{(1)}_{,\zeta}) \quad \tilde{K}^{(1)}_{xz} = -ch\psi^{(1)}_{,\eta},$$
$$\tilde{K}^{(1)}_{yy} = \tilde{K}^{(1)}_{yz} = \tilde{K}^{(1)}_{zz} = 0, \quad \tilde{K}^{(1)}_{xx} = -2(1+\sigma)w^{(0)}_{,xx}\zeta, \tag{16}$$

where $c = -hw^{(0)}_{,xy}$ represents the stress $\tilde{K}^{(1)}_{xy}$ at the upper surface $\zeta/h = 1/2$ as $\eta/h \to \infty$ and $w^{(0)}_{,xx}$ is also evaluated at $y = 0$ in the interior region. In this free-edge condition, the first-order shearing stress $\tilde{K}^{(1)}_{xz}$ appears only in the boundary layer and it becomes important as well as the twisting stress $\tilde{K}^{(1)}_{xy}$. Graphical representations for $\tilde{K}^{(1)}_{xy}$ and $\tilde{K}^{(1)}_{xz}$ are shown in Fig. 7 and Fig. 8 where c is set equal to unity.

Acknowledgments

The author is grateful to Professor T. Kakutani for stimulating discussions and for kind inspection of the original manuscript. The author is also grateful to the editor and the reviewers for useful comments which led to the improvement of the manuscript.

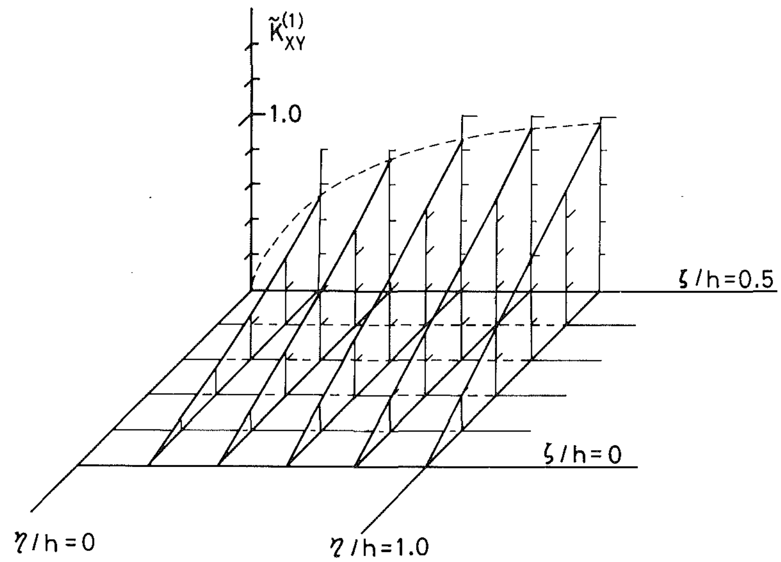

Fig. 7

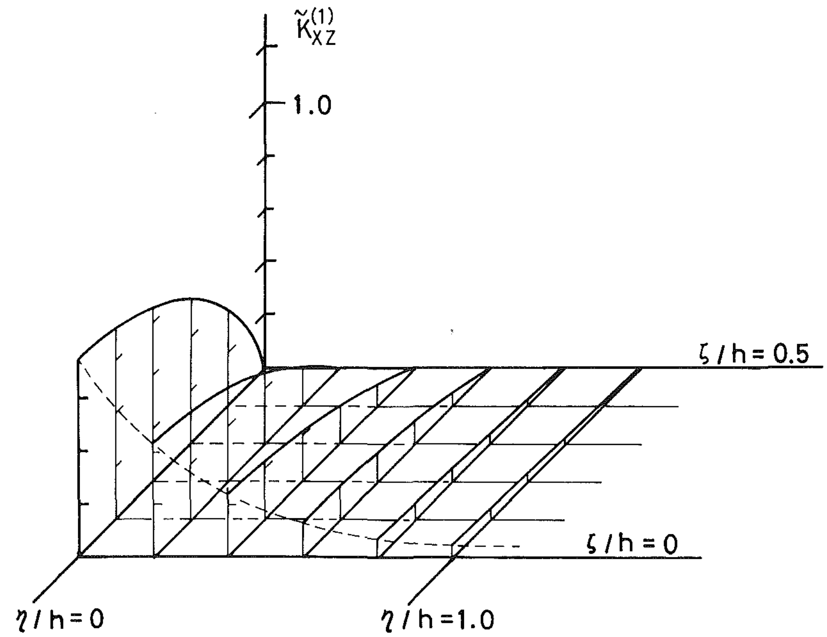

Fig. 8

This work has been partially supported by THE SAKKOKAI FOUNDATION, Tokyo, Japan.

All the computations were carried out with the computer NEAC 900 at the Computer Center of Osaka University.

References

1 Sugimoto, N., "Nonlinear Theory for Flexural Motions of Thin Elastic Plate Part 1: Higher Order Theory," ASME JOURNAL OF APPLIED MECHANICS, Vol. 48, 1981, pp. 377–382.

2 Sugimoto, N., "Nonlinear Theory for Flexural Motions of Thin Elastic Plate Part 2: Boundary Layer Theory near the Edge," ASME JOURNAL OF APPLIED MECHANICS, Vol. 48, 1981, pp. 383–390.

3 Papkovitsch, P. F., "Über eine Form der Lösung des byharmonischen Problems für das Rechteck," *Comptes Rendus (Doklady) de l'Académie des Sciences de l'URSS*, Vol. 27, 1940, pp. 334–338.

4 Fadle, J., "Die Selbstspannungs Eigenwertfunctionen der quadratischen Scheibe," *Ingenieur Archiv*, Vol. 11, 1941, pp. 125–149.

5 Williams, M. L., "Stress Singularities Resulting from Various Boundary Conditions in Angular Corners of Plate in Extension," ASME JOURNAL OF APPLIED MECHANICS, Vol. 19, 1952, pp. 526–528.

APPENDIX

Here we briefly summarize the results on the stress singularity at two corners $\eta = 0$ and $\zeta = \pm h/2$. A detailed discussion is given in reference [5].

At the corners, there appears the same type of stress singularity as that at the vertex of a right wedge with one side built-in and the other free in a plane strain. Although, in the present formulation, the displacements are prescribed along $\eta = 0$ over $-h/2 \leq \zeta \leq h/2$, there appears the stress singularity which satisfy the homogeneous boundary conditions, i.e., no displacements along $\eta = 0$ and no stresses along $\zeta = \pm h/2$. In the following, only the corner $\eta = 0$ and $\zeta = h/2$ is considered as an example.

We take the local polar coordinate system r and θ with the origin at the corner $\eta = 0$ and $\zeta = h/2$ so that the free edge corresponds to $\theta = 0$ and the built-in edge to $\theta = -\pi/2$. Near the corner, the local behavior of $\tilde{\varphi}^{(1)}$ for the stress singularity can be expressed as

$$\tilde{\varphi}^{(1)} = r^{\lambda+1} f(\theta) = r^{\lambda+1} \{ a_1 \sin[(\lambda+1)\theta] + a_2 \cos[(\lambda+1)\theta] + a_3 \sin[(\lambda-1)\theta] + a_4 \cos[(\lambda-1)\theta] \}, \tag{17}$$

where a_i $(i = 1,2,3,4)$ are constants which should be determined so as to satisfy the homogeneous boundary conditions along both sides in the vicinity of the corner. On introducing this expression into the stress and displacement components in the plane strain case, and imposing the boundary conditions ($\sigma_{rr} = \sigma_{\theta\theta} = 0$, at $\theta = 0$ and $u_r = u_\theta = 0$ at $\theta = -\pi/2$), the nontrivial condition for a_i yields the characteristic equation (5) for λ. Then the constants a_i are determined as

$$a_1 = (\lambda-1)A, \quad a_3 = -(\lambda+1)A, \quad a_2 = -a_4 = B,$$

and

$$A/B = [\lambda + 2(1-\sigma)]\cot(\pi\lambda/2) / \{(\lambda+1)[\lambda - 1 + 2(1-\sigma)\}. \tag{18}$$

Thus the asymptotic expressions for $\tilde{\varphi}^{(1)}$ and $\tilde{\varphi}^{(1)}_{,\eta}$ near the corner along the edge $\eta = 0$ are given by

$$\tilde{\varphi}^{(1)} = -2r^{\lambda+1} [\lambda A/B \cos(\pi\lambda/2) + \sin(\pi\lambda/2)]B,$$
$$\tilde{\varphi}^{(1)}_{,\eta} = r^{-1} \tilde{\varphi}^{(1)}_{,\theta} = -2r^{\lambda} [(\lambda^2-1)A/B \sin(\pi\lambda/2) - \lambda\cos(\pi\lambda/2)]B. \tag{19}$$

Since $r = h/2 - \zeta$ along $\eta = 0$, comparison of these expressions with $\alpha h^3 A_s'(1/2 - \zeta/h)^{\lambda+1}$ and $\alpha h^2 B_s'(1/2 - \zeta/h)^{\lambda}$ in (3), α being $[2\sigma/(1-)^2] \times w^{(0)}_{,yy}$, yields the ratio A_s'/B_s'

$$\frac{A_s'}{B_s'} = \frac{\lambda A/B \cos(\pi\lambda/2) + \sin(\pi\lambda/2)}{(\lambda^2-1)A/B \sin(\pi\lambda/2) - \lambda\cos(\pi\lambda/2)}, \tag{20}$$

and similarly A_s''/B_s'' is given by (20).

The Axisymmetrical Steady-State Response of Internally Damped Annular Double-Plate Systems

T. Irie
Professor.

G. Yamada
Associate Professor.

Y. Muramoto
Graduate Student.

Department of Mechanical Engineering,
Hokkaido University,
Kita-13, Nishi-8, Kita-ku,
Sapporo, 060 Japan

The axisymmetrical steady-state response of an internally damped, annular double-plate system interconnected by several springs uniformly distributed along concentric circles to a sinusoidally varying force is determined by the transfer matrix technique. Once the transfer matrix of an annular plate has been determined analytically, the response of the system is obtained by the product of the transfer matrices of each plate and the point matrices at each connecting circle. By the application of the method, the driving-point impedance, transfer impedance, and force transmissibility are calculated numerically for a free-clamped system and a simply supported system.

1 Introduction

This paper presents an analysis of the axisymmetrical steady-state response of an internally damped, annular double-plate system interconnected by several springs uniformly distributed along concentric circles under a sinusoidally varying force, in which the transfer matrix method is used. Though a number of papers are available on the vibration of circular or annular plates, only a few papers have been presented for the vibration and the forced response of double-plate or multiplate systems. Kunukkasseril and Radhakrishnan [1] studied the free vibration of an elastically connected, rectangular multiplate system, and Kunukkasseril and Swamidas [2, 3] also studied elastically connected, circular double-plate or multiplate systems. Chonan [4, 5] studied the free vibration of circular or annular multiplate systems subjected to radial tension. However, these studies were confined to undamped double-plate or multiplate systems interconnected by uniformly distributed springs, and no papers have been presented for the response of the damped annular double-plate systems reported here, except for the study of Swamidas and Kunukkasseril [6] treating an undamped circular or annular double-plate system elastically connected along concentric circles. Although there are many studies of composite and sandwich plates, which are collected in the monograph of Bert [7], these are not directly concerned in this study.

For the purpose of this study, the Mindlin equations of transverse vibration of an internally damped annular plate are written in a matrix differential equation of the first-order by use of the transfer matrix of the plate. The matrix is obtained conveniently by a series type solution to the matrix equation and the steady-state response of the system is determined by the product of the transfer matrices of each plate and the point matrices at each connecting circle. In this paper, elastic moduli of internally damped plates and springs are assumed to be complex quantities. This assumption is justified by the results of experimental measurement [8].

By the application of the present method, the driving-point impedance, transfer impedance, and force transmissibility are calculated numerically for a free-clamped, annular double-plate system and a simply supported, annular double-plate system interconnected by several springs of the same stiffness located at equal radial intervals.

The transfer matrix method of this paper is very simple and clear as an analytical process, and has significant computational advantages [9, 10]. The method is also applicable for annular double-plate systems governed by partial differential equations for which separation of variables is possible, including an unsymmetrical response of the system.

2 Mindlin Equations of an Internally Damped Annular Plate and the Solution

With the outer and inner radii denoted by a and b, respectively, the polar coordinates (r, θ) are taken in the middle surface of an annular plate. The steady-state

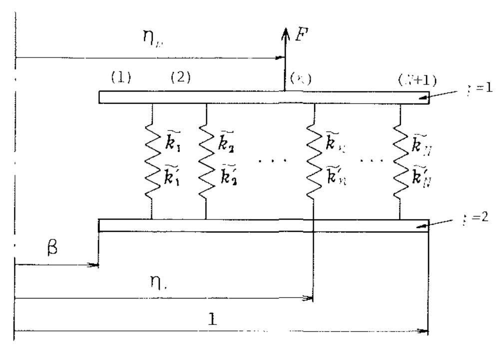

Fig. 1 Annular double-plate system driven by a sinusoidally varying concentric force

Contributed by the Applied Mechanics Division for publication in the JOURNAL OF APPLIED MECHANICS.

Discussion on this paper should be addressed to the Editorial Department, ASME, United Engineering Center, 345 East 47th Street, New York, N.Y. 10017, and will be accepted until two months after final publication of the paper itself in the JOURNAL OF APPLIED MECHANICS. Manuscript received by ASME Applied Mechanics Division, June, 1981.

deflection, moments, and forces of the plate under a sinusoidally varying force are written as

$$w^* = awe^{j\omega t}, \quad (M_r^*, M_\theta^*) = \frac{D}{a}(M_r, M_\theta)e^{j\omega t}$$

$$Q_r^* = \frac{D}{a^2}Q_r e^{j\omega t}, \quad F^* = \frac{D_1}{a^2}Fe^{j\omega t} \tag{1}$$

where the variables w, M_r, M_θ, Q_r, and F without the asterisk* are all dimensionless quantities. The quantity D is the flexural rigidity of the plate expressed as $D = Eh^3/12(1-\nu^2)$. For simplicity of the analysis, the following dimensionless variables are also introduced:

$$\eta = \frac{r}{a}\left(\beta = \frac{b}{a}\right), \quad \alpha = \frac{h}{a}$$

$$\lambda^4 = \frac{\rho h a^4 \omega^2}{D} \quad \text{(frequency parameter)} \tag{2}$$

$$[A(\eta)] = \begin{bmatrix} 0 & -1 & 0 & \dfrac{\alpha^2}{6(1-\nu)K^2(1+j\delta_G)} \\ 0 & -\dfrac{\nu}{\eta} & \dfrac{1}{1+j\delta_G} & 0 \\ 0 & (1+j\delta_E)\dfrac{1-\nu^2}{\eta^2} - \dfrac{\alpha^2\lambda^4}{12} & -\dfrac{1-\nu}{\eta} & 1 \\ -\lambda^4 & 0 & 0 & -\dfrac{1}{\eta} \end{bmatrix} \tag{8}$$

where ρ is the mass per unit volume and ω is the circular frequency. The Young's modulus and shear modulus of internally damped plate are considered to be the complex quantities

$$\tilde{E} = E(1+j\delta_E), \quad \tilde{G} = G(1+j\delta_G) \tag{3}$$

where E and G express the real parts of $\tilde{E}$ and $\tilde{G}$, respectively, and δ_E and δ_G are constants representing the ratios of the imaginary to the real parts of them at any frequencies ω.

The equations of axisymmetrical vibration of the plate based on the Mindlin plate theory are written as [11, 12]

$$\frac{dQ_r}{d\eta} + \frac{Q_r}{\eta} + \lambda^4 W = 0$$

$$\frac{dM_r}{d\eta} + \frac{M_r - M_\theta}{\eta} - Q_r + \frac{\alpha^2}{12}\lambda^4\psi = 0 \tag{4}$$

The components of the moment and shearing force are given by

$$M_r = (1+j\delta_E)\left(\frac{d\psi}{d\eta} + \frac{\nu}{\eta}\psi\right), \quad M_\theta = (1+j\delta_E)\left(\nu\frac{d\psi}{d\eta} + \frac{\psi}{\eta}\right)$$

$$Q_r = \frac{6(1-\nu)K^2}{\alpha^2}(1+j\delta_G)\left(\psi + \frac{dW}{d\eta}\right) \tag{5}$$

in terms of the transverse deflection W and the angular rotation ψ of the normal to the middle surface in radial direction. The quantity K^2 is the shear coefficient which assumes the value $\pi^2/12$.

Upon eliminating the variable M_θ, (4) and (5) are written as a matrix differential equation

$$\frac{d}{d\eta}\{Z(\eta)\} = [A(\eta)]\{Z(\eta)\} \tag{6}$$

where

$$\{Z(\eta)\} = \{W\ \psi\ M_r\ Q_r\}^T \tag{7}$$

and

The state vector $\{Z(\eta)\}$ is expressed as

$$\{Z(\eta)\} = [T(\eta)]\{Z(\eta_0)\} \quad (\eta > \eta_0) \tag{9}$$

by use of the transfer matrix $[T(\eta)]$. The substitution of (9) into (6) yields the equation

$$\frac{d}{d\eta}[T(\eta)] = [A(\eta)][T(\eta)] \tag{10}$$

The matrix $[T(\eta)]$ is determined by the power series solution to (10) as follows:

$$[T(\eta)] = \exp([M(\eta)])$$

$$= [I] + \frac{1}{1!}[M(\eta)] + \frac{1}{2!}[M(\eta)]^2 + \ldots \tag{11}$$

where

$$[M(\eta)] = \int_{\eta_0}^{\eta} [A(\eta)]d\eta$$

$$= \begin{bmatrix} 0 & -\eta & 0 & \dfrac{\alpha^2}{6(1-\nu)K^2(1+j\delta_G)}\eta \\ 0 & -\nu\ln\eta & \dfrac{\eta}{1+j\delta_E} & 0 \\ 0 & -(1+j\delta_E)\dfrac{1-\nu^2}{\eta} - \dfrac{\alpha^2\lambda^4}{12}\eta & -(1-\nu)\ln\eta & \eta \\ -\lambda^4\eta & 0 & 0 & -\ln\eta \end{bmatrix}_{\eta_0}^{\eta} \tag{12}$$

Numerical difficulty arises in the calculation of $[T(\eta)]$ given by (11) if the radial interval is too long. However, it can be overcome by subdividing each radial interval into a number of small intervals and calculating the transfer matrix in each interval. The entire structure matrix is obtained by assembling the matrices in these intervals.

3 Axisymmetric Response of an Annular Double-Plate System to a Sinusoidally Varying Concentric Force

Figure 1 shows an annular double-plate system interconnected by several springs uniformly distributed along concentric circles. At the radius $\eta = \eta_n$ where the two plates are interconnected by a spring, we have the continuity and equilibrium relations

$$
\begin{aligned}
&W_p(\eta_n+0)=W_p(\eta_n-0), \quad \psi_p(\eta_n+0)=\psi_p(\eta_n-0)\\
&M_{r,p}(\eta_n+0)=M_{r,p}(\eta_n-0)+(-1)^p\tilde{\kappa}'_{p,n}\{\psi_2(\eta_n)-\psi_1(\eta_n)\}\\
&Q_{r,p}(\eta_n+0)=Q_{r,p}(\eta_n-0)+(-1)^p\tilde{\kappa}_{p,n}\{W_2(\eta_n)-W_1(\eta_n)\}
\end{aligned} \tag{13}
$$

where $\tilde{\kappa}_{p,n}$ and $\tilde{\kappa}'_{p,n}$ express the translational and rotational stiffnesses of internally damped spring, respectively, which are also assumed to be the complex quantities

$$
\begin{aligned}
\tilde{\kappa}_{p,n}&=\frac{a^3}{D_p}\kappa_n^*(1+j\delta_{\kappa,n})=\kappa_{p,n}(1+j\delta_{\kappa,n})\\
\tilde{\kappa}'_{p,n}&=\frac{a}{D_p}\kappa_n'^*(1+j\delta'_{\kappa,n})=\kappa'_{p,n}(1+j\delta'_{\kappa,n})
\end{aligned} \tag{14}
$$

Here, the subscripts $p = 1, 2$ express the upper and lower plates, respectively. When the upper plate is driven by a force F uniformly distributed along a concentric circle of radius $\eta = \eta_F$, we have the relations

$$
\begin{aligned}
&W_1(\eta_F+0)=W_1(\eta_F-0), \qquad \psi_1(\eta_F+0)=\psi_1(\eta_F-0)\\
&M_{r,1}(\eta_F+0)=M_{r,1}(\eta_F-0), \qquad Q_{r,1}(\eta_F+0)=Q_{r,1}(\eta_F-0)+F
\end{aligned} \tag{15}
$$

The boundary conditions of each plate are written as

$$
\begin{aligned}
M_r=Q_r=0 &\quad \text{at a free edge}\\
W=M_r=0 &\quad \text{at a simply supported edge}\\
W=\psi=0 &\quad \text{at a clamped edge}
\end{aligned} \tag{16}
$$

The relations (13) can be written as

$$
\begin{Bmatrix} Z_{1,n+1}\\ Z_{2,n+1}\end{Bmatrix}_{(\eta_n+0)}=\begin{bmatrix} K_1 & -K'_1\\ -K'_2 & K_2\end{bmatrix}_n\begin{Bmatrix} Z_{1,n}\\ Z_{2,n}\end{Bmatrix}_{(\eta_n-0)} \tag{17}
$$

by using the point matrices

$$
[K_p]_n=\begin{bmatrix} 1 & 0 & 0 & 0\\ 0 & 1 & 0 & 0\\ 0 & (1+j\delta_{\kappa',n})\kappa'_{p,n} & 1 & 0\\ (1+j\delta_{\kappa,n})\kappa_{p,n} & 0 & 0 & 1\end{bmatrix}
$$

$$
[K'_p]_n=\begin{bmatrix} 0 & 0 & 0 & 0\\ 0 & 0 & 0 & 0\\ 0 & (1+j\delta_{\kappa',n})\kappa'_{p,n} & 0 & 0\\ (1+j\delta_{\kappa,n})\kappa_{p,n} & 0 & 0 & 0\end{bmatrix} \tag{18}
$$

are also written as

$$
\begin{Bmatrix} Z_{1,n}\\ Z_{2,n}\end{Bmatrix}_{(\eta_F+0)}=\begin{Bmatrix} Z_{1,n}\\ Z_{2,n}\end{Bmatrix}_{(\eta_F-0)}+\begin{Bmatrix} F_1\\ 0\end{Bmatrix} \tag{19}
$$

by use of the force vector $\{F_1\} = \{0\,0\,0\,F\}^T$. At an arbitrary radius, the response of the system is expressed as

$$
\begin{aligned}
\begin{Bmatrix} Z_{1,m}\\ Z_{2,m}\end{Bmatrix}_{(\eta)}&=\begin{bmatrix} T_1 & 0\\ 0 & T_2\end{bmatrix}_{(\eta_{m-1},\eta)}\prod_{i=1}^{m-1}\begin{bmatrix} K_1 & -K'_1\\ -K'_2 & K_2\end{bmatrix}_i\begin{bmatrix} T_1 & 0\\ 0 & T_2\end{bmatrix}_{(\eta_{i-1},\eta_i)}\begin{Bmatrix} Z_{1,1}\\ Z_{2,1}\end{Bmatrix}_{(\beta)}\\
&=\begin{bmatrix} \bar{T}_1 & \bar{T}'_1\\ \bar{T}'_2 & \bar{T}_2\end{bmatrix}_{(\beta,\eta)}\begin{Bmatrix} Z_{1,1}\\ Z_{2,1}\end{Bmatrix}_{(\beta)} \qquad (\eta_F>\eta\geqq\beta)
\end{aligned} \tag{20}
$$

and

$$
\begin{aligned}
\begin{Bmatrix} Z_{1,m}\\ Z_{2,m}\end{Bmatrix}_{(\eta)}&=\begin{bmatrix} T_1 & 0\\ 0 & T_2\end{bmatrix}_{(\eta_{m-1},\eta)}\prod_{i=n}^{m-1}\begin{bmatrix} K_1 & -K'_1\\ -K'_2 & K_2\end{bmatrix}_i\begin{bmatrix} T_1 & 0\\ 0 & T_2\end{bmatrix}_{(\eta_{i-1},\eta_i)}\begin{Bmatrix} Z_{1,n}\\ Z_{2,n}\end{Bmatrix}_{(\eta_F+0)}\\
&=\begin{bmatrix} \bar{T}_1 & \bar{T}'_1\\ \bar{T}'_2 & \bar{T}_2\end{bmatrix}_{(\eta_F,\eta)}\begin{Bmatrix} Z_{1,n}\\ Z_{2,n}\end{Bmatrix}_{(\eta_F+0)} \qquad (1\geqq\eta>\eta_F)
\end{aligned} \tag{21}
$$

where $[\bar{T}_p]_{(\eta_F,\eta)}$ and $[\bar{T}'_p]_{(\eta_F,\eta)}$ marked with an overbar, — express the products of the transfer matrices and the point matrices. Upon substituting the equations obtained by taking $\eta = \eta_F - 0$ in (20) and $\eta = 1 - 0$ in (21) into (19), we have

$$
\begin{bmatrix} \bar{T}_1 & \bar{T}'_1\\ \bar{T}'_2 & \bar{T}_2\end{bmatrix}^{-1}_{(\eta_F,1)}\begin{Bmatrix} Z_{1,N+1}\\ Z_{2,N+1}\end{Bmatrix}_{(1)}=\begin{bmatrix} \bar{T}_1 & \bar{T}'_1\\ \bar{T}'_2 & \bar{T}_2\end{bmatrix}_{(\beta,\eta_F)}\begin{Bmatrix} Z_{1,1}\\ Z_{2,1}\end{Bmatrix}_{(\beta)}+\begin{Bmatrix} F_1\\ 0\end{Bmatrix} \tag{22}
$$

A half of the elements of $\{Z_{1,N+1}\ Z_{2,N+1}\}^T_{(1)}$ and $\{Z_{1,1}\ Z_{2,1}\}^T_{(\beta)}$ are zero by a given set of the boundary conditions (16), and other unknown elements are determined by (22). The

Table 1 Resonant frequencies of a free-clamped, undamped annular double-plate system interconnected by a spring at the free edge: $\nu = 0.3$, $\beta = 0.2$, $\alpha_1 = 0.05$, $\alpha_2/\alpha_1 = 1.0$, $\kappa = 200$, $\kappa' = 0$

Number of division	$\lambda_1^{(i)}$	$\lambda_1^{(o)}$	$\lambda_2^{(i)}$	$\lambda_2^{(o)}$	$\lambda_3^{(i)}$
1	2.395	4.720	5.801	7.648	9.543
4	2.283	4.585	5.610	7.564	9.431
8	2.273	4.583	5.609	7.562	9.434
12	2.272	4.582	5.609	7.562	9.434
20	2.271	4.582	5.609	7.561	9.434
Exact solution	2.271	4.582	5.609	7.561	9.434

axisymmetrical response of any annular double-plate system is determined by (20) and (21).

The normalized transfer impedance is expressed as

$$|Z_p(\eta)| = \frac{2D_1\eta_F F}{(1-\beta^2)D_p\lambda_p^4\,|W(\eta)|} \tag{23}$$

The driving-point impedance is given only by replacing the variable η in (23) with the variable η_F. The force transmissibility at the supports is given by

$$|T_{R,p}| = \frac{\eta D_p\,|Q_{r,p}|}{\eta_F D_1 F} \tag{24}$$

The method of this paper can be applied to annular double-plate systems under any combination of boundary conditions. Here, two examples will be explained.

Example 1: A Free-Clamped Annular Double-Plate System Driven at the Free Edge

Consider a free-clamped annular double-plate system interconnected by several springs of the same stiffness located at equal radial intervals. Upon taking $\eta = \eta_F = 1$ in (20), we have

$$\begin{Bmatrix} Z_{1,N+1} \\ Z_{2,N+1} \end{Bmatrix}_{(1)} = \prod_{i=1}^{N} \begin{bmatrix} K_1 & -K_1' \\ -K_2' & K_2 \end{bmatrix}_i \begin{bmatrix} T_1 & 0 \\ 0 & T_2 \end{bmatrix}_{(\eta_{i-1},\eta_i)} \begin{Bmatrix} Z_{1,1} \\ Z_{2,1} \end{Bmatrix}_{(\beta)} \tag{25}$$

By the boundary conditions (16), we have

$$\begin{bmatrix} \bar{T}_{1,33} & \bar{T}_{1,34} & \bar{T}'_{1,33} & \bar{T}'_{1,34} \\ \bar{T}_{1,43} & \bar{T}_{1,44} & \bar{T}'_{1,43} & \bar{T}'_{1,44} \\ \bar{T}'_{2,33} & \bar{T}'_{2,34} & \bar{T}_{2,33} & \bar{T}_{2,34} \\ \bar{T}'_{2,43} & \bar{T}'_{2,44} & \bar{T}_{2,43} & \bar{T}_{2,44} \end{bmatrix}_{(\beta,1)} \begin{Bmatrix} M_{r,1} \\ Q_{r,1} \\ M_{r,2} \\ Q_{r,2} \end{Bmatrix}_{(\beta)} = \begin{Bmatrix} 0 \\ F \\ 0 \\ 0 \end{Bmatrix} \tag{26}$$

with only the elements of $[\bar{T}_p]_{(\beta,1)}$ and $[\bar{T}'_p]_{(\beta,1)}$ necessary for the calculation. The unknown variables $\{M_{r,1}\ Q_{r,1}\ M_{r,2}\ Q_{r,2}\}^T_{(\beta)}$ at the clamped edge are determined by (26).

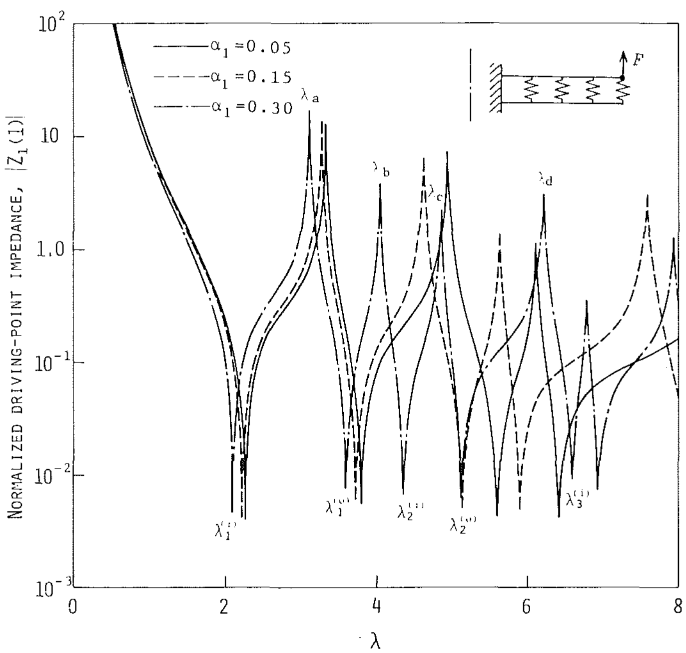

Fig. 2 Normalized driving-point impedance of a free-clamped, annular double-plate system driven at the free edge: $\nu = 0.3$, $\beta = 0.2$, $\alpha_2/\alpha_1 = 1.0$, $N = 4$, $\kappa = 10$, $\kappa' = 1.0$, $\delta_E = \delta_G = \delta_\kappa = \delta_\kappa{}' = 0.01$

Example 2: A Simply Supported Annular Double-Plate System Driven at a Concentric Circle of Any Radius

Consider a simply supported annular double-plate system interconnected by several springs of the same stiffness located at equal radial intervals. In this case (20) and (21), respectively, are written as

$$\begin{Bmatrix} Z_{1,n} \\ Z_{2,n} \end{Bmatrix}_{(\eta_F-0)} = \prod_{i=0}^{n-1} \begin{bmatrix} T_1 & 0 \\ 0 & T_2 \end{bmatrix}_{(\eta_i,\eta_{i+1})} \begin{bmatrix} K_1 & -K_1' \\ -K_2' & K_2 \end{bmatrix}_i \begin{Bmatrix} Z_{1,0} \\ Z_{2,0} \end{Bmatrix}_{(\beta)} \tag{27}$$

and

$$\begin{Bmatrix} Z_{1,N} \\ Z_{2,N} \end{Bmatrix}_{(1)} = \prod_{i=n}^{N-1} \begin{bmatrix} K_1 & -K_1' \\ -K_2' & K_2 \end{bmatrix}_i \begin{bmatrix} T_1 & 0 \\ 0 & T_2 \end{bmatrix}_{(\eta_{i-1},\eta_i)} \begin{Bmatrix} Z_{1,n} \\ Z_{2,n} \end{Bmatrix}_{(\eta_F+0)} \tag{28}$$

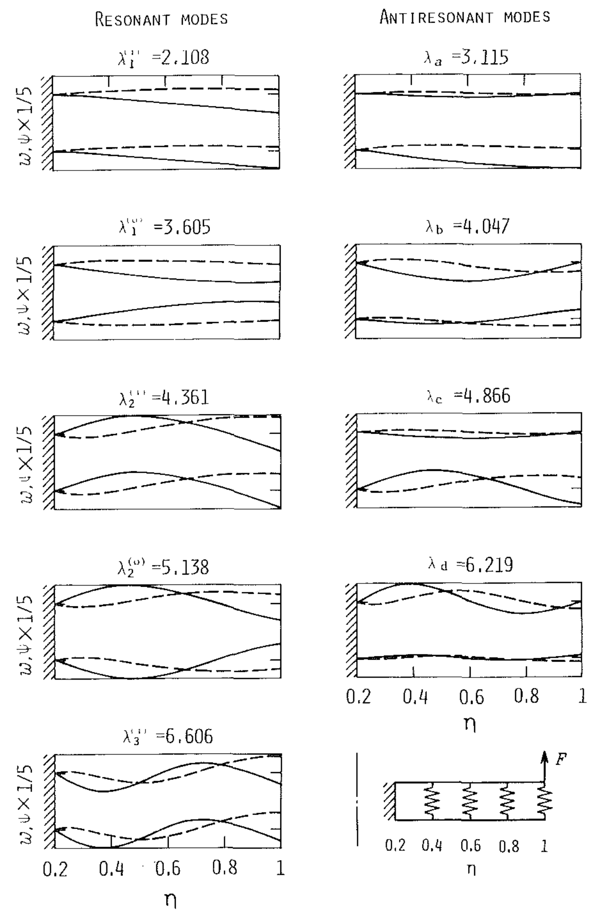

Fig. 3 Resonant and antiresonant mode shapes of a free-clamped, undamped annular double-plate system driven at the free edge: $\nu = 0.3$, $\beta = 0.2$, $\alpha_1 = 0.05$, $\alpha_2/\alpha_1 = 1.0$, $N = 4$, $\kappa = 10$, $\kappa' = 1.0$, —— W, ------ ψ

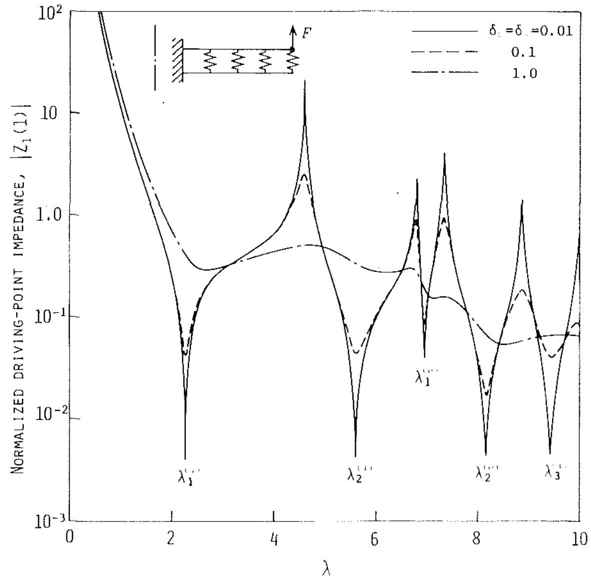

Fig. 4 Normalized driving-point impedance of a free-clamped, annular double-plate system driven at the free edge: $\nu=0.3$, $\beta=0.2$, $\alpha_1=0.05$, $\alpha_2/\alpha_1=1.0$, $N=4$, $\kappa=200$, $\kappa'=0$, $\delta_\kappa=0.01$

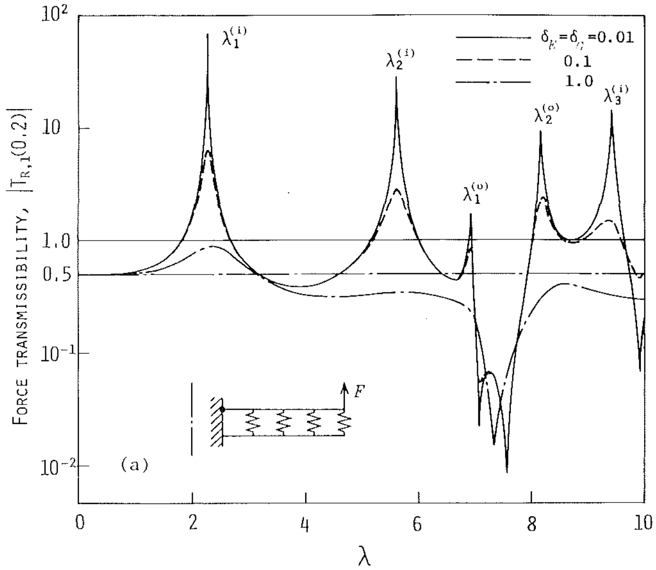

Fig. 6(*a*)

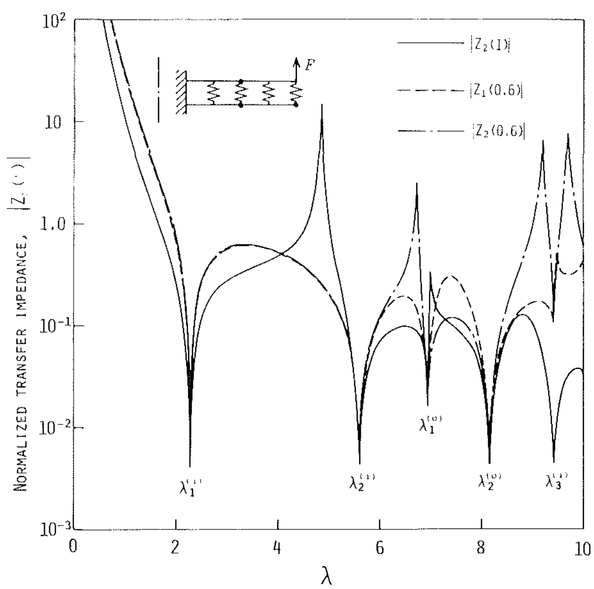

Fig. 5 Normalized transfer impedance of a free-clamped, annular double-plate system driven at the free edge: $\nu=0.3$, $\beta=0.2$, $\alpha_1=0.05$, $\alpha_2/\alpha_1=1.0$, $N=4$, $\kappa=200$, $\kappa'=0$, $\delta_E=\delta_G=\delta_\kappa=0.01$

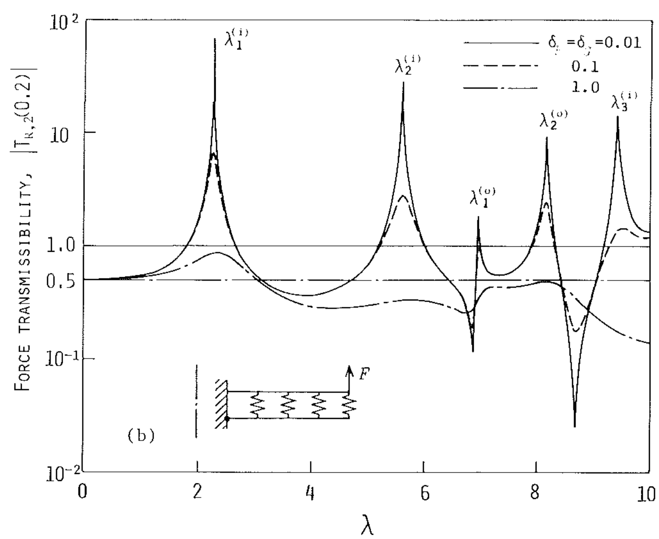

Fig. 6(*b*)

Fig. 6 Force transmissibility of a free-clamped, annular double-plate system driven at the free edge: $\nu=0.3$, $\beta=0.2$, $\alpha_1=0.05$, $\alpha_2/\alpha_1=1.0$, $N=4$, $\kappa=200$, $\kappa'=0$, $\delta_\kappa=0.01$

By arranging the equation obtained by the substitution of (27) and (28) into (22), the following equation is derived:

$$\begin{bmatrix} \bar{R}_{1,11} & \bar{R}_{1,12} & \bar{R}'_{1,12} & \bar{R}'_{1,14} \\ \bar{R}_{1,21} & & & \cdot \\ \bar{R}_{1,31} & & & \cdot \\ \bar{R}_{1,41} & & & \cdot \\ \bar{R}'_{2,11} & & & \cdot \\ \bar{R}'_{2,21} & & & \cdot \\ \bar{R}'_{2,31} & & & \cdot \\ \bar{R}'_{2,41} & \cdot & \cdot & \bar{R}_{2,44} \end{bmatrix}_{(\eta_F,1)} \begin{Bmatrix} W_1 \\ \psi_1 \\ \psi_2 \\ Q_{r,2} \end{Bmatrix}_{(1)} - \begin{bmatrix} \bar{T}_{1,11} & \bar{T}_{1,12} & \bar{T}'_{1,12} & \bar{T}'_{1,14} \\ \bar{T}_{1,21} & & & \cdot \\ \bar{T}_{1,31} & & & \cdot \\ \bar{T}_{1,41} & & & \cdot \\ \bar{T}'_{2,11} & & & \cdot \\ \bar{T}'_{2,21} & & & \cdot \\ \bar{T}'_{2,31} & & & \cdot \\ \bar{T}'_{2,41} & \cdot & \cdot & \bar{T}_{2,44} \end{bmatrix}_{(\beta,\eta_F)} \begin{Bmatrix} W_1 \\ \psi_1 \\ \psi_2 \\ Q_{r,2} \end{Bmatrix}_{(\beta)} = \begin{Bmatrix} 0 \\ 0 \\ 0 \\ F \\ 0 \\ 0 \\ 0 \\ 0 \end{Bmatrix} \tag{29}$$

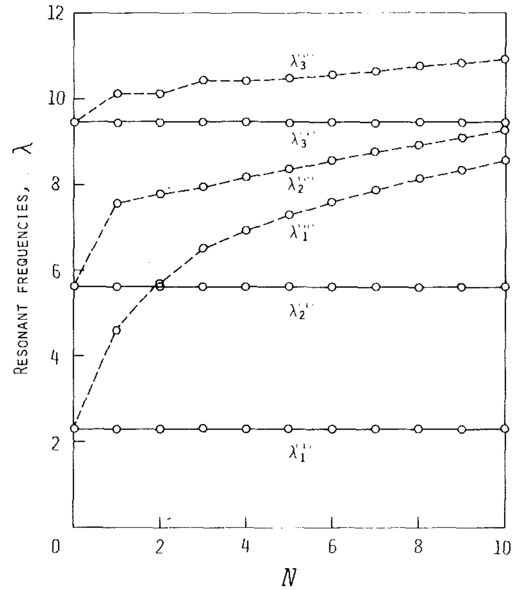

Fig. 7 Resonant frequencies of free-clamped, undamped annular double-plate system: $\nu = 0.3$, $\beta = 0.2$, $\alpha_1 = 0.05$, $\alpha_2/\alpha_1 = 1.0$, $\kappa = 200$, $\kappa' = 0$

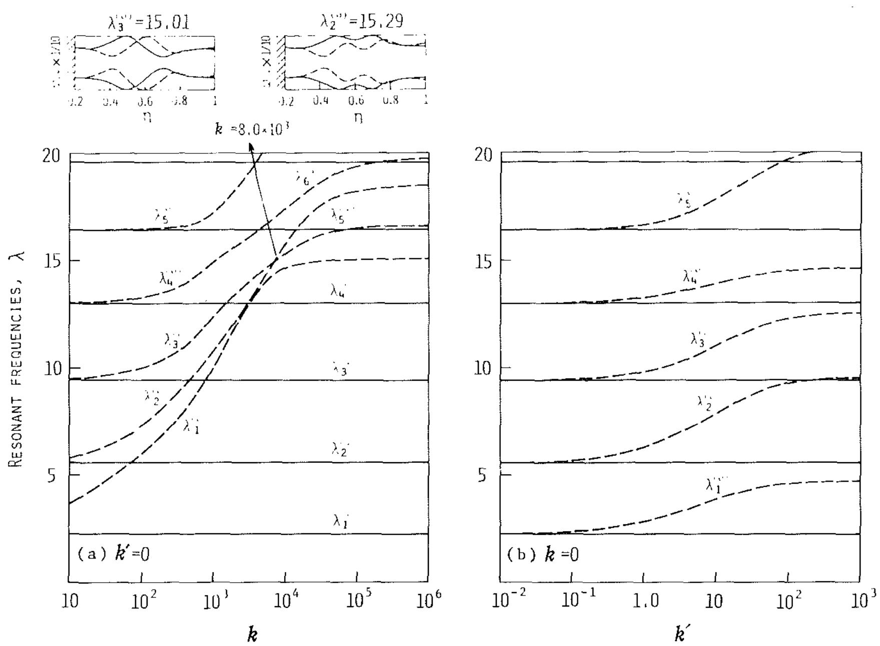

Fig. 8 Resonant frequencies of free-clamped, undamped annular double-plate system: $\nu = 0.3, \beta = 0.2, \alpha_1 = 0.05, \alpha_2/\alpha_1 = 1.0$, $N = 4$; (a) $\kappa' = 0$, (b) $\kappa = 0$

where

$$\begin{bmatrix} \bar{R}_1 & \bar{R}_1' \\ \bar{R}_2' & \bar{R}_2 \end{bmatrix}_{(\eta_F, 1)} = \begin{bmatrix} \bar{T}_1 & \bar{T}_1' \\ \bar{T}_2' & \bar{T}_2 \end{bmatrix}^{-1}_{(\eta_F, 1)} \tag{30}$$

4 Numerical Calculation and Discussion

In this section, the present method is applied to a free-clamped, annular double-plate system and a simply supported, annular double-plate system interconnected by several springs of the same stiffness located at equal radial intervals, and the axisymmetrical steady-state response to a sinusoidally varying concentric force is calculated numerically. For metals and nonmetals, the assumption that δ_E is nearly equal in value to δ_G over a broad frequency range, is well justified from the results of experimental measurement [8]. Though the dynamic moduli and damping factors depend on the frequency for practical materials, it was assumed for the purposes of the calculations presented here that δ_E, δ_G, δ_k, and δ_k' are constant for all frequencies.

Table 1 shows the resonant frequencies of a free-clamped, undamped annular double-plate system obtained by the present method using the transfer matrix versus the number of subdivided radial intervals in the calculation of the transfer matrix of the plate together with the exact values obtained by the solution using the Bessel functions. With an increase in number of the subdivided intervals, the values obtained here are in good agreement with the exact ones.

Figures 2–6 show the response of a free-clamped, annular double-plate system composed of two annular plates of the

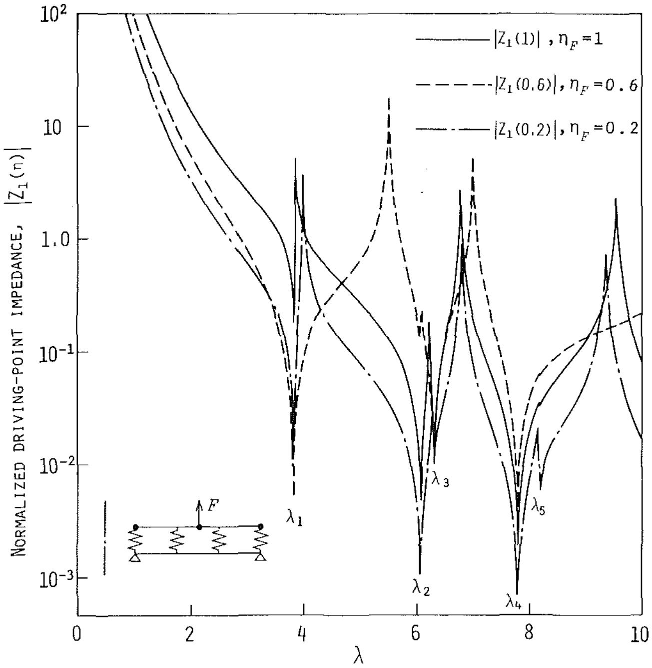

Fig. 9 Normalized driving-point impedance of a simply supported, annular double-plate system driven at a concentric circle: $\nu = 0.3$, $\beta = 0.2$, $\alpha_1 = 0.05$, $\alpha_2/\alpha_1 = 1.0$, $N = 4$, $\kappa = 200$, $\kappa' = 0$, $\delta_E = \delta_G = \delta_\kappa = 0.01$

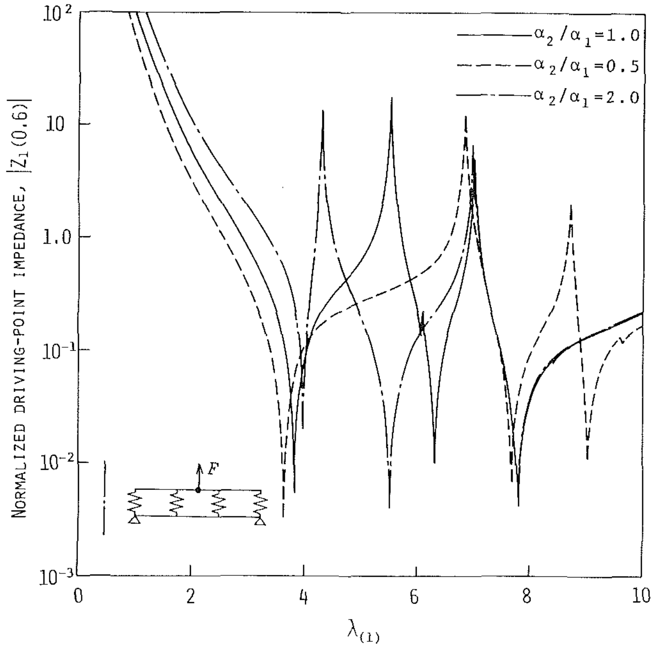

Fig. 11 Normalized driving-point impedance of simply supported, annular double-plate systems driven at a concentric circle: $\nu = 0.3$, $\beta = 0.2$, $\alpha_1 = 0.05$, $N = 4$, $\kappa = 200$, $\kappa' = 0$, $\delta_E = \delta_G = \delta_\kappa = 0.01$, $\eta_F = 0.6$

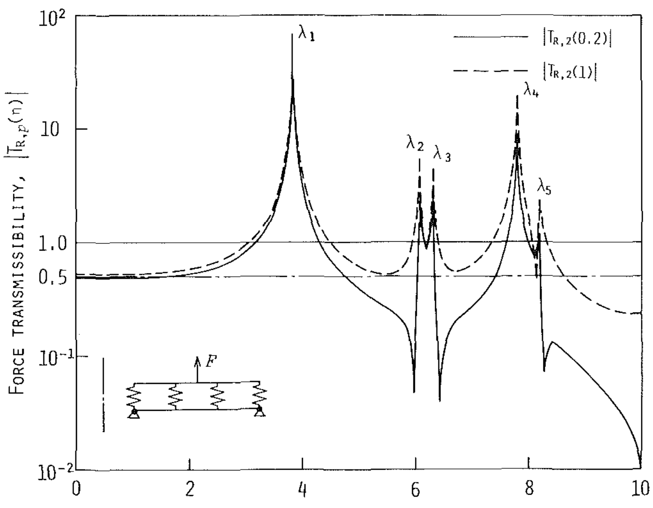

Fig. 10 Force transmissibility of a simply supported, annular double-plate system at a concentric circle: $\nu = 0.3$, $\beta = 0.2$, $\alpha_1 = 0.05$, $\alpha_2/\alpha_1 = 1.0$, $N = 4$, $\kappa = 200$, $\kappa' = 0$, $\delta_E = \delta_G = \delta_\kappa = 0.01$, $\eta_F = 0.6$

same dimensions which are interconnected by four springs and are driven at the free edge of the upper plate.

Figure 2 shows the normalized driving-point impedance of the system. Within the frequency range of the figure, some resonant peaks appear at the natural frequencies (the frequency parameters) of the system and also some antiresonant peaks appear at the frequencies between adjacent resonant ones. With an increase of the thickness ratio α_1, the resonant and antiresonant frequencies become smaller monotonically.

Figure 3 shows the deflection and angular rotation of an undamped annular double-plate system at the resonant frequencies $\lambda_1^{(i)}$, $\lambda_1^{(o)}$, $\lambda_2^{(i)}$, . . . and antiresonant frequencies λ_a, λ_b, λ_c, . . . presented in Fig. 2. Here, the superscripts (i) and (o) attached to λ_n express the inphase and out-of-phase vibrations, respectively. In the inphase vibrations, the transverse deflection and angular rotation of each plate have the same values, respectively, and hence there are no relative deflection and rotation between the plates. In the out-of-phase vibrations, the deflection and rotation are symmetrical with respect to the central surface between two plates. At the antiresonance, the deflection of the plate is extremely small at the driving point and hence the distinctive antiresonant behaviors appear.

Figure 4 shows the normalized driving-point impedance of the system. With an increase of the internal damping ratios δ_E and δ_G, the distinctive resonant and antiresonant behaviors vanish, which is also seen in the case when the damping ratio δ_κ of the springs increases. The resonant frequencies of damped system are usually smaller than those of undamped system calculated from the frequency equation obtained by taking F in (26) as zero. However, the difference between them is very small for the system with small damping treated here.

Figure 5 shows the normalized transfer impedance of the system monitored at $\eta = 0.6$ of the upper plate or at $\eta = 1$ and 0.6 of the lower plate marked with • at the upper-most figure. Though the resonant behaviors are not so much affected by the location of the monitored points, the antiresonant behaviors change irregularly.

Figure 6(a) and (b) show the force transmissibility of the upper and lower plates, respectively. With an increase of the damping ratios, the magnitude of the transmissibility becomes smaller and the frequency range where the transmissibility of each plate is less than 0.5 becomes more wide, which indicates the possibility of vibration isolation.

Figures 7 and 8 show the resonant frequencies of a free-clamped undamped system presented in Figs. 4–6. The resonant frequencies of the inphase vibration are not affected at all by the number and the stiffness of springs, because relative deflection and rotation do not arise between the upper and lower plates. The resonant frequencies of the out-of-phase vibration become larger monotonically with an increase of the number and the stiffness of springs. In this case, frequency crossing arises between the $\lambda_2^{(0)}$- and $\lambda_3^{(0)}$-modes for $k \fallingdotseq 8.0 \times 10^3$, where the deflection and rotation of the plates become considerably irregular as shown in the top figures.

Figures 9–11 show the response of simply supported, annular double-plate systems interconnected by four springs and are driven at a concentric circle. Figure 9 shows the normalized driving-point impedance of the system composed of two plates with the same thickness. With the variation of the location of the driving-point, the magnitude of the impedance changes irregularly, although the resonant frequencies remain constant.

Figure 10 shows the force transmissibility of the system at the inner and outer edges of the lower plate. The magnitude of the transmissibility of the system at the outer edge is larger than that at the inner edge. Within a certain frequency range, the transmissibility is less than 0.5.

Figure 11 shows the normalized driving-point impedance of the systems composed of two plates with different thickness, where the frequency parameter $\lambda_{(1)} = \rho h_1 a^4 \omega^2 / D_1$ is taken as the axis of abscissa. With the variation of the depth ratio h_2/h_1, the resonant and antiresonant frequencies and also the magnitude of the impedance change irregularly.

The numerical computations presented here were carried out on a HITAC M-200H computer of the Hokkaido University Computing Center.

References

1 Kunukkasseril, V. X., and Radhakrishnan, S., "Free Vibrations of Elastically Connected Multi-Plate Systems," *Proceedings of the Conference of the Indian Society for Theoretical and Applied Mechanics*, 1970, pp. 441–458.

2 Kunukkasseril, V. X., and Swamidas, A. S. J., "Normal Modes of Elastically Connected Circular Plates," *Journal of Sound and Vibration*, Vol. 30, No. 1, 1973, pp. 99–108.

3 Swamidas, A. S. J., and Kunukkasseril, V. X., "Free Vibration of Elastically Connected Circular Plate Systems," *Journal of Sound and Vibration*, Vol. 39, No. 2, 1975, pp. 229–235.

4 Chonan, S., "The Free Vibrations of Elastically Connected Circular Plate Systems with Elastically Restrained Edges and Radial Tensions," *Journal of Sound and Vibration*, Vol. 49, No. 1, 1976, pp. 129–136.

5 Chonan, S., "Resonance Frequencies and Mode Shapes of Elastically Restrained, Prestressed Annular Plates Attached Together by Flexible Cores," *Journal of Sound and Vibration*, Vol. 67, No. 4, 1979, pp. 487–500.

6 Swamidas, A. S. J., and Kunukkasseril, V. X., "Vibration of Circular Double-Plate Systems," *The Journal of the Acoustical Society of America*, Vol. 63, No. 6, 1978, pp. 1832–1840.

7 Bert, C. W., "Recent Research in Composite and Sandwich Plate Dynamics," *The Shock and Vibration Digest*, Vol. 11, No. 10, 1979, pp. 13–23.

8 Kerlin, R. L., and Snowdon, J. C., "Driving-Point Impedances of Cantilever Beams—Comparison of Measurement and Theory," *The Journal of the Acoustical Society of America*, Vol. 47, No. 1 (Part 2), 1970, pp. 220–228.

9 Irie, T., Yamada, G., and Aomura, S., "Free Vibration of a Mindlin Annular Plate of Varying Thickness," *Journal of Sound and Vibration*, Vol. 66, No. 2, 1979, pp. 187–197.

10 Irie, T., Yamada, G., and Aomura, S., "The Steady-State Response of a Rotating Damped Disk of Variable Thickness," ASME Journal of Applied Mechanics, Vol. 47, No.4, 1980, pp. 896–900.

11 Mindlin, R. D., and Deresiewicz, H., "Thickness-Shear and Flexural Vibrations of a Circular Disk," *Journal of Applied Physics*, Vol. 25, No. 10, 1954, pp. 1329–1332.

12 Deresiewicz, H., and Mindlin, R. D., "Axially Symmetric Flexural Vibrations of a Circular Disk," ASME Journal of Applied Mechanics, Vol. 22, No. 1, 1955, pp. 86–88.

On the Instability of Rotating Shafts Due to Internal Damping

L. L. Bucciarelli
Associate Professor,
School of Engineering,
Massachusetts Institute of Technology,
Cambridge, Mass. 02139

Internal damping in rotating shafts can lead to dynamic instability – the unbounded growth over time of the off-axis displacement of the spinning shaft in whirl. In analyzing this phenomenon, some authors have phrased the instability criterion in terms of energies dissipated through internal and external damping. One such study has claimed that instability ensues when the rate of work done by internal damping equals that done by external damping. This analysis shows that this criterion is wrong and explains why it fails. It also provides a clear picture of how internal forces can act to produce instability by coupling the motion of spin with motion in whirl.

Introduction

By providing a way for kinetic energy of spin to be transformed into kinetic and potential energy of whirl, internal damping in rotating shafts can lead to unbounded growth of the off-axis shaft displacement with time. Crandall [1] has published a clear analysis of the basic phenomenon using a planar model of a rotor which carries around an elastically supported point mass subject also to internal and external viscous damping. The work of Thomson, Younger, and Gordon [2] is often cited as a paradigmatic analysis of a system that more closely resembles the shaft-disk assemblies encountered in the world of rotating machinery. In this concise study of the whirl stability of a pendulous supported flywheel, the authors first determine the whirl states as a function of spin speed – how the whirl frequencies and associated mode shapes depend on the gyroscopic effects of the rotary inertias of the flywheel. All of this is well and good. They then go on to investigate the stability of these whirl states with hysteretic, internal damping and viscous, external damping present. They obtain a criterion for instability by equating the rate of work by internal hysteresis to the rate of energy dissipation through the viscous, external damper.

The main object of this analysis is to show that this criterion is wrong and to explain why it fails. At the same time, through the analysis of a relatively simple yet realistic model, this study provides, in the spirit of [1], a clear picture of how the forces arising from internal friction act to produce instability. This is accomplished without having recourse to the introduction of artificial forces as in [3]. Finally it accounts explicitly for all energy sources, sinks, and transformations and yields a correct decision rule for stability in terms of these quantities; a rule compatible with the results obtained by others from equilibrium considerations [3–9].

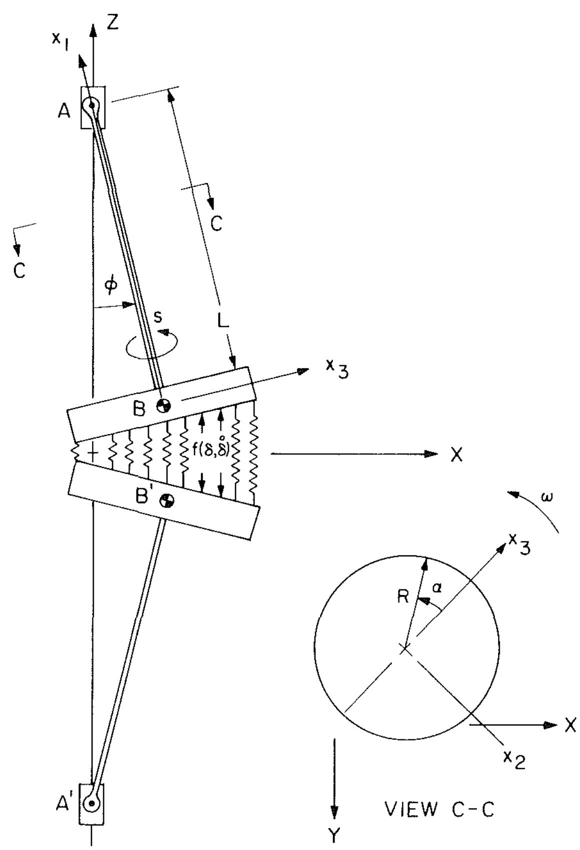

Fig. 1 Shaft-disk assembly

Contributed by the Applied Mechanics Division for publication in the JOURNAL OF APPLIED MECHANICS.

Discussion on this paper should be addressed to the Editorial Department, ASME, United Engineering Center, 345 East 47th Street, New York, N.Y. 10017, and will be accepted until two months after final publication of the paper itself in the JOURNAL OF APPLIED MECHANICS. Manuscript received by ASME Applied Mechanics Division, March 1981; final revisions, October, 1981.

Equations of Motion

Figure 1 shows the system under consideration. The rotating shaft-disk assembly is designed to spin about the vertical axis, Z, with the centers of mass of the two disks lying on that axis. Motion in whirl, where the mass centers move off that axis is also possible as indicated in the figure. Points A and A' are fixed in space, gravity is neglected (its effect could be taken into account without altering the essential results of this analysis), and all internal elastic restoring forces and all nonconservative damping forces are assumed to be generated within the intervening medium BB'. An external viscous damper (not shown) connects point B (and B') to ground.

The x_1 x_2 x_3 axes are a moving coordinate system with the x_1 axis lying along the shaft AB and the x_3 axis in the plane defined by the shaft and the Z axis. Motion of the rigid body AB (due to symmetry we need only consider half of the system), is expressed in terms of the angle ϕ, the spin relative to the x_1 axis, s, and the angular velocity of the plane of the shaft about the Z axis, ω. The angular velocity of the moving coordinate frame is then

$$\boldsymbol{\omega} = (\omega\cos\phi)\mathbf{x}_1 + (\mathring{\phi})\mathbf{x}_2 + (\omega\sin\phi)\mathbf{x}_3$$

and the absolute angular velocity of the system is

$$\boldsymbol{\Omega} = (\omega\cos\phi + s)\mathbf{x}_1 + (\mathring{\phi})\mathbf{x}_2 + (\omega\sin\phi)\mathbf{x}_3 .$$

The equations of motion are found to be

$$J\overset{\circ}{\overline{(\omega\cos\phi + s)}} = M_1 + T \tag{1}$$

$$(I + ML^2)\overset{\circ\circ}{\phi} - (I + ML^2)\omega^2\sin\phi\cos\phi + J(\omega\cos\phi + s)\,\omega\sin\phi$$
$$= M_2 - C_e L^2\mathring{\phi} - KL^2\sin\phi\{(2L^2/R^2)(1-\cos\phi) + \cos\phi\} \tag{2}$$

$$(I + ML^2)\overset{\circ}{\overline{(\omega\sin\phi)}} + (I + ML^2)\omega\mathring{\phi}\cos\phi - J\mathring{\phi}(\omega\cos\phi + s)$$
$$= M_3 - C_e L^2\,\omega\sin\phi \tag{3}$$

In obtaining these, the internal, conservative restoring forces within BB' have been modeled as a rotationally symmetric distribution of linear elastic springs of stiffness $K(L^2/\pi R^2)$ per radian of arc affixed at the disk's outer radius, R. The effect of the linear viscous external damper, which acts to retard the motion of point B, appears on the right-hand side of equations (2) and (3). M_1, M_2, and M_3 are the components of the internal moment about A due to internal damping within the layer BB'. I is the moment of inertia of the disk about the x_2 or x_3 axis, J is that about the x_1 axis, and M is the mass of the system.

The analysis has not been restricted to small deflections. Large deflections are considered in order to ensure the coupling of motion about the spin axis, x_1, with motion in whirl. The gyroscopic effects of the rotary inertias I and J are also considered. If the latter are neglected and if the internal damping is taken as linear-viscous, a case considered in the following, then (2) and (3) define the motion of a point mass, M, moving in a horizontal plane – a problem considered in references [1] and [9]. To get the equations of motion studied in [1] requires a transformation to rectangular cartesian coordinates and the small deflection assumption to the extent of setting $\cos\phi = 1$. To get the system of [9] requires admitting the possibility of an eccentric mass, i.e., allowing for an offset of the elastic axis from the mass center.

Whirl States

Whirl frequencies are obtained from the preceding system of equations by seeking nontrivial solutions for constant ϕ ignoring all internal as well as external damping forces. For constant whirl-rate, equations (1) and (3) are identically satisfied and equation (2) yields a quadratic equation for ω.

$$(1 + I/ML^2)\omega^2 - (J\Omega\omega/ML^2\cos\phi)$$
$$-(K/M)\{1 + (2L^2/R^2)(1-\cos\phi)/\cos\phi\} = 0. \tag{4}$$

The absolute angular velocity of the system about the x_1 axis has been defined as Ω, i.e.,

$$\Omega \equiv \omega\cos\phi + s. \tag{5}$$

For a given Ω and ϕ, equation (4) yields two real roots, one positive, the other negative. The former, assuming s is positive, corresponds to a forward whirl motion, the latter to retrograde whirl. For a more complex system – say, with N degrees of freedom – the equivalent linearized set of equations to (2) and (3) presents an eigenvalue problem of $2N$ real roots, N positive forward whirl frequencies, and N negative retrograde whirl frequencies. The associated mode shapes, the eigenvectors, take the place of the condition ϕ = a constant [10].

Stability of Whirl States

Stability of both the forward and retrograde whirl states may be studied by developing first-integrals of the equations of motion, identifying the terms so obtained with forms of energy, seeking conditions that lead to a monotonic increase in the energy associated with whirl. Multiplying equation (1) by Ω yields the first-integral

$$\mathring{E}_s = M_1(\omega\cos\phi + s) + T(\omega\cos\phi + s)$$

where $E_s = 1/2\,J\Omega^2$ is the kinetic energy rotation about the x_1 axis.

Multiplying (2) by $\mathring{\phi}$, equation (3) by $\omega\sin\phi$, and adding the two first integrals so obtained gives

$$\mathring{E}_w = M_2\mathring{\phi} + M_3\,\omega\sin\phi - C_e L^2(\mathring{\phi}^2 + \omega^2\sin^2\phi)$$

where

$$E_w = \frac{1}{2}\,(I + ML^2)(\mathring{\phi}^2 + \omega^2\sin^2\phi)$$
$$+\ \frac{1}{2}\,KL^2\left[\sin^2\phi + \frac{2L^2}{R^2}(1-\cos\phi)^2\right]$$

is the kinetic and potential energy of the system associated with motion of the moving coordinate frame, e.g., whirl motion.

Consider now the moment components due to the internal nonconservative forces: for ease of visualization, and with but a small, not irrecoverable loss in generality, the mechanism responsible for these forces is taken to be axisymmetrically distributed at the disk's outer radius, R, as was the elastic restoring force. The elemental damping force, f, a force per unit radian of arc assumed to be positive when acting upward on the disk B, is permitted to depend on the change, δ, and rate of change, $\mathring{\delta}$, in the length of the elements themselves. Integrating around the disk gives

$$M_1 = -m\sin\phi; \quad M_3 = +m\cos\phi \tag{6}$$

$$M_2 = +m_2\cos\phi + F_\delta L\sin\phi \tag{7}$$

where

$$m \equiv R\int_{\alpha=0}^{2\pi} f(\delta,\mathring{\delta})\sin\alpha d\alpha \tag{8}$$

$$m_2 \equiv R\int_{\alpha=0}^{2\pi} f(\delta,\mathring{\delta})\cos d\alpha \tag{9}$$

and

$$F_\delta \equiv \int_{\alpha=0}^{2\pi} f(\delta,\mathring{\delta})d\alpha \tag{10}$$

With these, the foregoing energy equations may be written

$$\mathring{E}_s = -m\omega\sin\phi\cos\phi - ms\sin\phi + T\Omega$$

$$\mathring{E}_w = +m\omega\sin\phi\cos\phi + m_2\mathring{\phi}\cos\phi$$
$$-C_e L^2(\mathring{\phi}^2 + \omega^2\sin^2\phi) + F_\delta L\mathring{\phi}\sin\phi$$

Two further relationships will prove useful: summing the two preceding equations yields an expression for the rate of change of the total energy of the system, namely

$$\mathring{E}_t = m_2\mathring{\phi}\cos\phi - ms\sin\phi + F_\delta L\mathring{\phi}\sin\phi$$
$$-C_e L^2(\mathring{\phi}^2 + \omega^2\sin^2\phi) + T\Omega$$

With δ given by

$$\delta = R\cos\alpha\sin\phi + L(1-\cos\phi)$$

and hence,

$$\mathring{\delta} = R\mathring{\phi}\cos\phi\cos\alpha - Rs\sin\phi\sin\alpha + L\mathring{\phi}\sin\phi$$

the sum of the first three terms on the right-hand side of this last equation is found to be equal to the rate of work done by the internal damping forces, W_i. That is,

$$\mathring{W}_i \equiv \int_{\alpha=0}^{2\pi} f(\delta,\mathring{\delta})\mathring{\delta}d\alpha = m_2\mathring{\phi}\cos\phi - ms\sin\phi + F_\delta L\mathring{\phi}\sin\phi$$

For motion in the neighborhood of a whirl state, with $\mathring{\phi}=0$, ω fixed by (4), and with the applied torque, T, set to zero (stability criteria should stand independent of an arbitrary external influence), the preceding relationships simplify to

$$\mathring{E}_s = -m\omega\sin\phi\cos\phi + \mathring{W}_i \quad (11)$$

$$\mathring{E}_w = +m\omega\sin\phi\cos\phi - C_e L^2\omega^2\sin^2\phi \quad (12)$$

$$\mathring{E}_t = +\mathring{W}_i - C_e L^2\omega^2\sin^2\phi \quad (13)$$

and

$$\mathring{W}_i = -ms\sin\phi \quad (14)$$

It might appear that equation (13) justifies the stability criterion of Thomson et al. [2], that is, instability ensues and the total energy of the system grows without bound, when the rate of work done by the internal damping forces exceeds the power extracted from the system through the external viscous damper. But this is wrong. If the internal nonconservative forces are truly dissipative then $\mathring{W}_i$ will be negative – the rate of work done *by* the internal damping *on* the system is truly power dissipated through that mechanism, e.g., mechanical energy transformed into heat. To derive a correct stability condition the spin and whirl energy equations must be considered.

Assuming for the moment that s is positive, with $\mathring{W}_i$ negative it follows from equation (14) that m must be positive. Equations (11) and (12) then imply that if ω is positive, i.e., forward whirl, then energy flows from spin to whirl at a rate given by

$$m\omega\sin\phi\cos\phi$$

If, on the other hand, ω is negative i.e., retrograde whirl, then energy flows in the opposite direction and the energy associated with whirl motion must decrease with time. In both cases additional energy of spin is dissipated through the damper at the rate $\mathring{W}_i$. Thus, retrograde whirl states are always stable and forward whirl states are stable so long as the foregoing rate of exchange of energy remains less than the power dissipated through the external damper. If the former exceeds the latter, then, according to (12), the energy of whirl grows without bound.

To illustrate the argument, two kinds of damping, hysteretic and linear viscous, are considered in the next section.

Hysteretic Internal Damping

For the case of hysteretic damping, the case considered in [2], the damping force in each circumferential element might vary with displacement as shown in Fig. 2. Assume as is customary [3] as well as [2], that this relationship is frequency independent and that the energy dissipated per cycle, the shaded area in the figure, is proportional to the square of the maximum displacement, $R\sin\phi$. Letting ΔE_i be the magnitude of that area, an energy per radian of arc, following [2], one can write

$$\Delta E_i = 2\pi\gamma(1/2)(KL^2/\pi R^2)R^2\sin^2\phi = \gamma KL^2\sin^2\phi \quad (15)$$

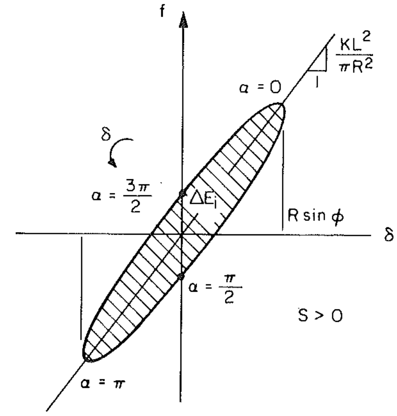

Fig. 2 Internal force-displacement relationship

where γ is a constant of proportionality.

To evaluate the moment m, or M_1 and M_3, the integral (8) around the disk over $\alpha = 0$, 2π may be transformed into an integral around the hysterisis loop. With

$$d\delta = -R\sin\phi\sin\alpha d\alpha$$

equations (6) and (8) yield

$$M_1 = \oint_\delta f(\delta)d\delta$$

where the direction of integration around the loop, for the case when s is positive is indicated in Fig. 2. In this case the damping element instantaneously located at $\alpha=\pi/2$ is experiencing unloading, that at $\alpha = 3\pi/2$ loading. On the other hand, if s is negative, the element at $\pi/2$ is subject to loading while that at $3\pi/2$, unloading. In the latter case the direction of integration around the hysterisis loop reverses from that shown in the figure, the foregoing integral changes sign. (Note that Fig. 2 shows the force acting on the dissipative elements within the layer BB', i.e., the equal and opposite reaction to the force acting on the disk B.) M_1 is thus expressible in terms of the area contained within the hysterisis loop according to

$$M_1 = -\Delta E_i sgn(s) \quad \text{where} \quad sgn(s) = \begin{cases} +1 & s>0 \\ 0 & s=0 \\ -1 & s<0 \end{cases}$$

The energy relationships then may be written

$$\mathring{E}_s = -\Delta E_i sgn(s)\omega\cos\phi + \mathring{W}_i$$

$$\mathring{E}_w = +\Delta E_i sgn(s)\omega\cos\phi - C_e L^2\omega^2\sin^2\phi$$

and

$$\mathring{W}_i = -\Delta E_i sgn(s)s = -\Delta E_i|s|\cdot$$

Thus $\mathring{W}_i$ is always negative, regardless of ω and s and only the forward whirl modes may prove unstable. Retrograde whirl is always stable and forward whirl stable as long as

$$\Delta E_i sgn(s)\,\omega\cos\phi < C_e L^2\omega^2\sin^2\phi$$

Using (15) this may be written

$$(1/\gamma)\,(C_e/K)\{\omega/[\cos\phi\, sgn(s)]\} > 1.0$$

The criterion applied in [2], setting W_i equal to the power dissipated through the external damper would give

$$(1/\gamma)(C_e/K)\left\{\omega/\left(\frac{\Omega}{\omega}-1\right)\right\} > 1.0$$

Note that this faulty criterion does not rule out the possibility of instability of retrograde whirl modes.

Linear Viscous Internal Damping

For the case of linear viscous internal damping, the damping force, f, may be expressed as

$$f(\delta,\mathring{\delta}) = -(C_i L^2/\pi R^2)\mathring{\delta}$$

Note that if $\mathring{\delta}$ is positive, the distance between the disks is increasing, then the force on disk B is retarding, hence, the negative sign. With $\mathring{\delta}$ as previously derived, equations (8) and (9) give

$$m = +C_i L^2 s \sin\phi$$
$$m_2 = -C_i L^2 \mathring{\phi} \cos\phi$$

and the energy relationships for motion in the vicinity of the whirl states ($\mathring{\phi} = 0$) are then

$$\mathring{E}_s \;=\; -C_i L^2 s\omega \sin^2\phi\cos\phi - \mathring{W}_i$$
$$\mathring{E}_w \;=\; +C_i L^2 s\omega \sin^2\phi\cos\phi - C_e L^2\omega^2\sin^2\phi$$

and

$$\mathring{W}_i \;=\; -C_i L^2 s^2 \sin^2\phi$$

Thus, as in the case of hysteretic damping, the rate of work done by the internal damping is always negative, i.e., dissipative, retrograde whirl is never unstable, and forward whirl is stable so long as the following condition is met:

$$C_e\omega > C_i s\cos\phi$$

This stability criterion corresponds to results obtained by others using equilibrium considerations [1, 7, 9]. It is not difficult to take the differential equations governing the motion of a mass point that appear in these studies, develop first-integrals, and state the stability criterion in terms of the energy expressions so obtained. (See [1], for example.)

Discussion of Results

It has been demonstrated that the instability criterion of reference [2] is incorrect. The source of this error may lie in [7]. In his analysis of instability caused by velocity-independent, internal friction, Bolotin, after determining the conditions for solutions to the differential equations governing the motion of a mass point to grow exponentially with time, interprets the stability rule so obtained in terms of the energy dissipated *per cycle* by internal friction and by external friction. That is, the stability criterion he obtains from force equilibrium considerations is dressed up and masquerades as an energy condition. There is a certain amount of ambiguity in this, for there are two different cycles involved in his argument and in the energy form of his stability criterion. The cycle appropriate to the calculation of the energy dissipated by internal friction is that which occurs in one revolution of the shaft relative to the moving coordinate system, that is in time $2\pi/s$. For the external damping, the cycle is that which occurs in one revolution of whirl, i.e, in one revolution of the moving coordinate system relative to ground. This occurs in the time $2\pi/\omega$. Equating these two energies per cycle, while it may be another way of presenting a correct criterion obtained by other means, is clearly *not* the same as setting the rate of work done by hysterisis to the rate of work done by external damping as was done in [2].

It is the transfer of energy from spin to whirl through the coupling term, the first term on the right-hand side of equations (11) and (12), that is responsible for instability. If the rate of transfer exceeds the rate at which energy is extracted from whirl motion by means of the external damper then the off-axis shaft displacement will grow unbounded in time. The energy dissipated through internal damping is truly dissipated and it is best not to suggest that this power flow out of the system is responsible for instability.

References

1 Crandall, S. H., "Physical Explanations of the Destabilizing Effect of Damping in Rotating Parts," NASA CP 2133, May 1980, pp. 369-382.

2 Thomson, W. T., Younger, F. C., and Gordon, H. S., "Whirl Stability of the Pendulously Supported Flywheel System," ASME JOURNAL OF APPLIED MECHANICS, Vol. 44, June 1977, pp. 322-328.

3 Timoshenko, S., *Vibration Problems in Engineering*, 3rd ed., D. Van Nostrand Co., N.J., 1961.

4 Kimball, A. L., "Internal Friction as a Cause of Shaft Whirling," *Philosophical Magazine*, Series 6, Vol. 49, 1925, p. 724

5 Den Hartog, J. P., *Mechanical Vibrations*, 4th ed., McGraw-Hill, New York, 1956.

6 Smith, D. M., "The Motion of a Rotor Carried by a Flexible Shaft in Flexible Bearings," *Proc. Royal Society* (London), Series A, Vol. 142, 1933, pp. 92-118.

7 Bolotin, V. V., *Non-conservative Problems of the Theory of Elastic Stability*, Macmillan, New York, 1963, pp. 146-156.

8 Ehrich, F. F., "Shaft Whirl Induced by Rotor Internal Damping," ASME JOURNAL OF APPLIED MECHANICS, Vol. 31, June 1964, pp. 279-282.

9 Torby, J., "The Effect of Structural Damping Upon the Whirling of Rotor," ASME JOURNAL OF APPLIED MECHANICS, Vol. 46, June 1979, pp. 469-470.

10 Bucciarelli, L. L., and Rangarajan, A., "Dynamic Analysis of a Magnetically Suspended Energy Storage Wheel," Paper presented at the Flywheel Technology Symposium, Scottsdale, Arizona, Oct. 26-30, 1980.

Z. -M. Ge
Associate Professor.

Y. -H. Cheng
Graduate Student.

Engineering Mechanics Department,
Shanghai Jiaotong University,
Shanghai, People's Republic of China

Extended Kane's Equations for Nonholonomic Variable Mass System

An extension of Kane's equations of motion for nonholonomic variable mass systems is presented. As an illustrative example, equations of motion are formulated for a rocket car.

Introduction

In 1979, Ge [1] derived three forms of equations of motion for linearly nonholonomic, variable mass systems, namely, generalized Ferrers' equations, generalized Hamel's equations, and generalized Appell's equations. The present paper contains a generalization of Kane's equations [2–4]. The new equations apply to nonholonomic variable mass systems and are simpler than any of the others, a fact that becomes readily apparent when they are used in an illustrative example.

Derivation

Consider a system S of N variable mass particles $P_1, \ldots, P_N$, whose configuration in an inertial reference frame R^* is characterized by n generalized coordinates $q_1, \ldots, q_n$, which is subject to constraints represented by m linear nonholonomic constraint equations of the form

$$\sum_{i=1}^{n} A_{is}\dot{q}_i + B_s = 0 \quad (s=1, \ldots, m) \tag{1}$$

where A_{is} and B_s $(i=1, \ldots, n;\ s=1, \ldots, m)$ are functions of $q_1, \ldots, q_n$ and the time t. The number of degrees of freedom of S is $k=n-m$. Proceeding as in reference [2], one can introduce k generalized speeds $u_1, \ldots, u_k$ such that equation (1) is satisfied whenever $\dot{q}_1, \ldots, \dot{q}_n$ satisfy the kinematical equations

$$\dot{q}_i = \sum_{r=1}^{k} C_{ir}u_r + D_i \quad (i=1, \ldots, n) \tag{2}$$

where C_{ir} and D_i are functions of $q_1, \ldots, q_n$ and t; and the velocity of P_i in R^* can be written as

$$\mathbf{V}^{P_i} = \sum_{r=1}^{k} \mathbf{V}_r^{P_i} u_r + \mathbf{V}_t^{P_i} \quad (i=1, \ldots, N)$$

where $\mathbf{V}_r^{P_i}$ is called the rth partial velocity of P_i in R^*. Now, for each variable mass particle P_i of mass $m_i(t)$, we have the fundamental dynamical equation[1]

$$\mathbf{R}_i - m_i\mathbf{a}^{P_i} + \mathbf{C}^{P_i}\dot{m}_i = 0 \quad (i=1, \ldots, N) \tag{3}$$

where $\mathbf{R}_i$ is the resultant of all contact and body forces acting on P_i, $\mathbf{a}^{P_i}$ is the acceleration of P_i, $\dot{m}_i$ is the time-derivative of m_i, and $\mathbf{C}^{P_i}$ is the difference between the velocity of matter being separated from P_i and the velocity of P_i itself. Taking the dot product of equations (3) with $\mathbf{V}_r^{P_i}$, and summing from 1–N, we have

$$\sum_{i=1}^{N} \mathbf{V}_r^{P_i} \cdot \mathbf{R}_i + \sum_{i=1}^{N} \mathbf{V}_r^{P_i} \cdot (-m_i\mathbf{a}^{P_i}) + \sum_{i=1}^{N} \mathbf{V}_r^{P_i} \cdot \mathbf{C}^{P_i}\dot{m}_i = 0 \quad (r=1, \ldots, k) \tag{4}$$

and, after defining F_r, F_r^*, and F_r', called the generalized active force, the generalized inertia force, and the generalized thrust for S in R^*, respectively, as

$$F_r \triangleq \sum_{i=1}^{N} \mathbf{V}_r^{P_i} \cdot \mathbf{R}_i \quad (r=1, \ldots, k) \tag{5a}$$

$$\mathbf{F}_r^* \triangleq \sum_{i=1}^{N} \mathbf{V}_r^{P_i} \cdot (-m_i\mathbf{a}^{P_i}) \quad (r=1, \ldots, k) \tag{5b}$$

$$Fr' \triangleq \sum_{i=1}^{N} \mathbf{V}_r^{P_i} \cdot \mathbf{C}^{P_i}\dot{m}_i \quad (r=1, \ldots, k) \tag{5c}$$

one can replace equation (4) with

$$F_r + F_r^* + F_r' = 0 \quad (r=1, \ldots, k) \tag{6}$$

These equations are called the *Kane's equations for nonholonomic variable mass systems.*

If system S consists of L particles $P_1, \ldots, P_L$ of variable mass $\lambda_1, \ldots, \lambda_L$, respectively, M particles $Q_1, \ldots, Q_M$ of constant mass $\mu_1, \ldots, \mu_M$, respectively, and N rigid bodies $R_1, \ldots, R_N$, then

$$F_r = \sum_{i=1}^{L} \mathbf{V}_r^{P_i} \cdot \mathbf{R}_i + \sum_{i=1}^{M} \mathbf{V}_r^{Q_i} \cdot \mathbf{R}_j + \sum_{s=1}^{N} (F_r)_{R_s}$$

Contributed by the Applied Mechanics Division for publication in the JOURNAL OF APPLIED MECHANICS.

Discussion on this paper should be addressed to the Editorial Department, ASME, United Engineering Center, 345 East 47th Street, New York, N.Y. 10017, and will be accepted until two months after final publication of the paper itself in the JOURNAL OF APPLIED MECHANICS. Manuscript received by ASME Applied Mechanics Division, August, 1981; final revision, November, 1981.

[1] When some matter is being added to P_i while other matter is being separated from P_i, equation (3) must be augmented with a term similar to the last term in equation (3).

$$F_r^* = \sum_{i=1}^{L} \mathbf{V}_r^{Pi} \cdot (-\lambda_i \mathbf{a}^{Pi})$$

$$+ \sum_{j=1}^{M} \mathbf{V}_r^{Qj} (-\mu_\pi \mathbf{a}^{QJ}) + \sum_{s=1}^{N} (F_r^*)_{R_s}$$

$$F_r' = \sum_{i=1}^{L} \mathbf{V}_r^{Pi} \cdot \mathbf{C}^{Pi} \lambda_i$$

where $(F_r)_{R_s}$ and $(F^*)_{R_s}$ are, respectively, the contributions of $R_1, \ldots, R_N$ to F_r and F_r^*. The methods for evaluating these have been presented in detail in reference [3]. Moreover, if some of $R_1, \ldots, R_N$ form gyrostats, one can evaluate their contributions to F_r and F_r^* by using formulas available in reference [3].

Application to Rocket Car

Figure 1 represents an idealized model of a jet racing car which is propelled by a rocket engine at point P, the rocket engine being treated as a variable mass particle at P. The vehicle consists of the particle at P, the body A_2, which contains the rear axle, the front axle A_1, pivoted on A_2 at point Q, and four wheels B_i $(i=1,2,3,4,)$. B_1, B_2, and A_1, form a gyrostat G_1, while B_3, B_4, and A_2 form a gyrostat G_2. Points Q and C are presumed to be the mass centers of G_1 and G_2, respectively.

Geometrically, the system is characterized by the dimensions L, l, a, b, r_1, and r_2 shown in Fig. 1. We introduce $\mathbf{g}_1$, $\mathbf{g}_2$, $\mathbf{g}_3$ and $\mathbf{g}'$, $\mathbf{g}'$, $\mathbf{g}'$ as two dextral sets of mutually perpendicular unit vectors fixed on A_1 and A_2, respectively, and we let M_1, M_2, and $m(t)$ denote the masses of G_1, G_2, and the particle at P, respectively. Furthermore, we let I_1 be the moment of inertia of G_1 about the axis parallel to $\mathbf{g}_2$ and passing through Q, I_2 the moment of inertia of G_2 about the axis parallel to $\mathbf{g}_2'$ and passing through C, J_1 the axial moment of inertia either of B_1 or of B_2, and J_2 that of either of B_3 or B_4.

Generalized coordinates that suffice for the description of the configuration of the system are q_1 and q_2, Cartesian coordinates of Q; q_3, an attitude angle for A_2; q_4, measuring the relative orientation of A_1 and A_2; and q_{4+i} $(i=1,2,3,4,)$, rotation angles of wheels $B_1, \ldots, B_4$; hence $n=8$.

Since, as will be shown, $k=2$, we need two generalized speeds. We define these as

$$u_1 \triangleq {}^{A_2}\omega^{A_1} \cdot \mathbf{g}_2 \tag{7}$$

and

$$u_2 \triangleq \mathbf{V}^Q \cdot \mathbf{g}_3 \tag{8}$$

where ${}^{A_2}\omega^{A_1}$ denotes the angular velocity of A_1 in A_2, so that

$$^{A_2}\omega^{A_1} = \dot{q}_4 \mathbf{g}_2 \tag{9}$$

while $\mathbf{V}^Q$ is the velocity of Q, so that

$$\mathbf{V}^Q = \dot{q}_1 \mathbf{n}_1 + \dot{q}_2 \mathbf{n}_2 \tag{10}$$

where $\mathbf{n}_1$ and $\mathbf{n}_2$ are unit vectors directed as shown in Fig. 1. It thus follows directly from equations (7) and (9) that

$$u_1 = \dot{q}_4 \tag{11}$$

and from equations (8) and (10) that

$$u_2 = \dot{q}_1 C_{3+4} + \dot{q}_2 S_{3+4} \tag{12}$$

where C_{3+4} and S_{3+4} denote $\cos(q_3+q_4)$ and $\sin(q_3+q_4)$, respectively.

Six additional independent equations linear in $\dot{q}_1, \ldots, \dot{q}_8$ result from imposing the requirement that $B_1, \ldots, B_4$ roll without slipping. For example, in order for the point of B_1 that is in contact with the support to have zero velocity, the two equations

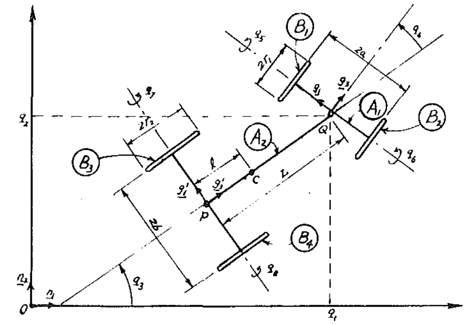

Fig. 1

$$\dot{q}_1 S_{3+4} - \dot{q}_2 C_{3+4} = 0 \tag{13}$$

and

$$\dot{q}_1 C_{3+4} + \dot{q}_2 S_{3+4} - a(\dot{q}_3 + \dot{q}_4) - r_1 \dot{q}_5 = 0 \tag{14}$$

must be satisfied. Hence we have eight equations linear in $\dot{q}_1, \ldots, \dot{q}_8$, and, solving them for these variables, we obtain

$$\left.\begin{aligned}
&\dot{q}_1 = u_2 C_{3+4}, \dot{q}_2 = u_2 S_{3+4}, \dot{q}_3 = \frac{1}{L} u_2 S_4, \dot{q}_4 = u_1 \\
&\dot{q}_5 = \frac{1}{r_1}\left[\left(1 - \frac{a}{L} S_4\right) u_2 - a u_1\right] \\
&\dot{q}_6 = \frac{1}{r_1}\left[\left(1 + \frac{a}{L} S_4\right) u_2 + a u_1\right] \\
&\dot{q}_7 = \frac{1}{r_2}\left(C_4 - \frac{b}{L} S_4\right) u_4, \dot{q}_8 = \frac{1}{r_2}\left(C_4 + \frac{b}{L} S_4\right) u_2
\end{aligned}\right\} \tag{15}$$

These are the kinematical equation playing the roles of equation (2). Moreover, the velocities of Q, C, and P now can be expressed as

$$\mathbf{V}^Q = u_2 \mathbf{g}_3, \mathbf{V}^C = u_2 \left(C_4 \mathbf{g}_3' + \frac{l}{L} S_4 \mathbf{g}_1'\right), \mathbf{V}^P = u_2 C_4 \mathbf{g}_3' \tag{16}$$

while the angular velocities of A_1 and A_2 are given by

$$\omega^{A_1} = \frac{1}{L}(L u_1 + u_2 S_4) \mathbf{g}_2, \omega^{A_2} = \frac{1}{L} u_2 S_4 \mathbf{g}_2' \tag{17}$$

The partial velocities of Q, C, and P, and the partial angular velocities of A_1 and A_2, formed by reference to equations (16) and (17), are

$$\mathbf{V}_1^Q = 0, \mathbf{V}_2^Q = \mathbf{g}_3, \mathbf{V}_1^C = 0, \mathbf{V}_2^C = \frac{l}{L} S_4 \mathbf{g}_1' + C_4 \mathbf{g}_3'$$
$$\mathbf{V}_1^P = 0, \mathbf{V}_2^P = C_4 \mathbf{g}_3'$$

$$\omega_1^{A_1} = \mathbf{g}_2, \omega_2^{A_1} = \frac{1}{L} S_4 \mathbf{g}_2, \omega_1{}^{A_2} = 0, \omega_2^{A_2} = \frac{1}{L} S_4 \mathbf{g}_2'$$

Differentiation of equations (16) and (17) with respect to t produces [with the aid of equation (15)] the accelerations and angular accelerations

$$a^P = \frac{1}{L} u_2^2 S_4 C_4 \mathbf{g}_1' + (\dot{u}_2 C_4 - u_1 u_2 S_4) \mathbf{g}_3' \triangleq a_1^P \mathbf{g}_1' + a_3^P \mathbf{g}_3'$$

$$\begin{aligned}
\mathbf{a}^C = {} & \frac{1}{L}(u_2^2 S_4 C_4 + \dot{u}_2 l S_4 + l u_1 u_2 C_4) \mathbf{g}_1' \\
& + \left(\dot{u}_2 C_4 - u_1 u_2 S_4 - \frac{l}{L^2} u_2^2 S_4^2\right) \mathbf{g}_3' \triangleq a_1^C \mathbf{g}_1' + a_3^C \mathbf{g}_3'
\end{aligned}$$

$$\mathbf{a}^Q = \left(\frac{1}{L} u_2^2 S_4 + u_1 u_2\right) \mathbf{g}_1 + \dot{u}_2 \mathbf{g}_3 \triangleq a_1^Q \mathbf{g}_1 + \dot{u}_2 \mathbf{g}_3$$

$$\alpha^{A_1} = \frac{1}{L}(\dot{u}_2 S_4 + u_1 u_2 C_4 + L \dot{u}_1) \mathbf{g}_2 \triangleq \alpha^{A_1} \mathbf{g}_2$$

$$\alpha^{A_2} = \frac{1}{L}(\dot{u}_2 S_4 + u_1 u_2 C_4) \mathbf{g}_2' \triangleq \alpha^{A_2} \mathbf{g}_2{}'$$

There are no forces contributing to generalized active forces. The contribution of a gyrostat G to generalized inertia force, denoted by $(F_r^*)_G$, can be found by using the relationship

$$(F_r^*)_G = (F_r^*)_{GR} + (F_r^*)_{GI} \tag{18}$$

where

$$(F_r^*)_{GR} = \mathbf{V}_r^G \cdot \mathbf{F}_G^* + \omega_r^A \cdot \mathbf{T}_G^* \tag{19}$$

$$(F_r^*)_{GI} = -J\{\omega_r^A[\ddot{q}_k\mathbf{g}_1 + \dot{q}_k(\omega_3^A\mathbf{g}_2 - \omega_2^A\mathbf{g}_3)] + C_{kr}(\dot{\omega}_1^A + \ddot{}_k)\} \tag{20}$$

The physical significance of each term of equations (18)-(20) has been given in reference [3].

For the gyrostat G_1, equation (19) yields

$$(F_1^*)_{G_1R} = -I_1\alpha^{A_1}, (F_2^*)_{G_1R} = -M_1\dot{u}_2 - \frac{1}{L}I_1\alpha^{A_1}S_4 \tag{21}$$

It is noted that G_1 contains two rotors, so that equation (20) leads to

$$(F_1^*)_{G_1I} = -J_1(C_{51}\ddot{q}_5 + C_{61}\ddot{q}_6),$$
$$(F_2^*)_{G_1I} = -J_1(C_{52}\ddot{q}_5 + C_{62}\ddot{q}_6) \tag{22}$$

Here, $\ddot{q}_5$ and $\ddot{q}_6$ can be evaluated from q_5 and $\dot{q}_6$ given in equation (15), and C_{kr} $(k=5,6,;\ r=1,2)$ may be obtained from equation (15):

$$C_{51} = -\frac{a}{r_1}, C_{52} = \frac{1}{r_1}\left(1 - \frac{a}{L}S_4\right), C_{61} = \frac{a}{r_1}, C_{62} = \frac{1}{r_1}\left(1 + \frac{a}{L}S_4\right)$$

According to equation (18), we have

$$\left.\begin{aligned}(F_1^*)_{G_1} &= -I_1\alpha^{A_1} - J_1(C_{51}\ddot{q}_5 + C_{61}\ddot{q}_6)\\ (F_2^*)_{G_1} &= -M_1\dot{u}_2 - \frac{1}{L}I_1\alpha^{A_1}S_4 - J_1(C_{52}\ddot{q}_5 + C_{62}\ddot{q}_6\end{aligned}\right\} \tag{23}$$

Similarly, for G_2 we find

$$\left.\begin{aligned}(F_1^*)_{G_2} &= -J_2(C_{71}\ddot{q}_7 + C_{81}\ddot{q}_8)\\ (F_2^*)_{G_2} &= -M_2\left(a_3^C C_4 + \frac{l}{L}a_1^C S_4\right)\\ &- \frac{1}{L}I_2\alpha^{A_2}S_4 - J_2(C_{72}\ddot{q}_7 + C_{82}\ddot{q}_8)\end{aligned}\right\} \tag{24}$$

The contributions of P to F_r^* are

$$(F_1^*)_P = 0, (F_2^*)_P = -m(t)a_3^P C_4 \tag{25}$$

The generalized inertia forces now can be formulated as

$$F_r^* = (F_r^*)_{G_1} + (F_r^*)_{G_2} + (F_r^*)_P (r=1,2) \tag{26}$$

We assume that the velocity of the material ejected at P relative to A_2 is $-C(t)\mathbf{g}_3'$, where $C(t)$ is positive. Then the generalized thrust, formed in accordance with equation (5c), is

$$F_1' = 0, F_2' = -C(t)\dot{m}C_4 \tag{27}$$

Substituting from equations (26) and (27) into equation (6) and using equations (23)-(25), one arrives at the following equations of motion of the car:

$$\left.\begin{aligned}L\dot{u}_1 + u_1u_2C_4 + \dot{u}_2S_4 = 0\\ \sigma\dot{u}_1S_4 + \pi u_1u_2C_4S_4 + (\tau + \tau_1S_4^2 + \tau_2C_4^2)\dot{u}_2 + C(t)\dot{m}C_4 = 0\end{aligned}\right\}$$

where

$$\sigma = \frac{1}{L}\left(I_1 + \frac{2a^2J_1}{r_1^2}\right), \tau = M_1 + \frac{2J_1}{r_1^2}, \tau_2 = m(t) + M_2 + \frac{2J_2}{r_2^2}$$

$$\tau_1 = \frac{1}{L^2}\left(I_1 + I_2 + M_2l^2 + \frac{2a^2J_1}{r_1^2} + \frac{2b^2J_2}{r_2^2}\right), \pi = \tau_1 - \tau_2$$

Conclusion

The reader can vertify that the formulation of equations of motion for the system just considered becomes a very laborious task when it is based on any of the classical equations, such as Lagrange's equations, Hamel's equations, etc., rather than on equation (6). Thus it appears that Kane's equations furnish a more effective tool for the formulation of equations of motion than do the other methods, not only for constant mass systems, but also for variable mass holonomic or nonholonomic systems.

References

1 Ge, Z. -M., "Equations of Motion for Nonholonomic Variable Mass Systems and Their Application to a Control System," *Journal of Shanghai Jiaotong University*, No. 4, 1979, pp. 1-22.

2 Kane, T. R., "Dynamics of Nonholonomic Systems," ASME JOURNAL OF APPLIED MECHANICS, Vol. 28, 1961, pp. 574-578.

3 Kane, T. R., "Nonholonomic Multibody Systems Containing Gyrostats," Dynamics of Multibody Systems, Symposium Munich, Germany, Aug. 29-Sept. 3, 1977, pp. 97-107.

4 Kane, T. R., and Levinson, D. A., "Formulation of Equations of Motion for Complex Spacecraft," *Journal of Guidance and Control*, Vol. 3, No. 2, 1980, pp. 99-112.

Journal of Applied Mechanics

Design Data and Methods

Torsion of Multihole Circular Cylinders[1]

A. K. Naghdi[2]

Introduction

The problem of torsion of cylindrical bars with a row of equally spaced circular cavities is investigated. Both cases of cylinders with or without a central cutout are considered. In the case of a multihole bar with a central circular hole, the combination of eigenfunctions of Laplace's equation in bipolar and polar coordinate systems is utilized. Extensive and very accurate numerical results for shear stresses and torsional rigidities are presented. Some of these results are compared with those given by a previous investigator.

Method of Solution

The problem of torsion of circular cylindrical bars having eccentric as well as central circular holes was first solved by Ling [1]. He employed functions defined by Howland [2]. Later, Kuo and Conway [3, 4] used the same technique for the solution of the problem of torsion of cylinders whose eccentric and central circular cavities are reinforced with circular bars of different material. Recently, a method of solving Laplace's equation in a multiply connected circular region was introduced by the author [5]. This latter technique, although not used in this investigation, provides valuable information for comparison. The advantage of the new technique presented in this investigation is believed to be the remarkably accurate solutions it produces as compared to the computer time it requires.

Consider circular cylindrical bars whose cross sections contain N eccentric, equally spaced circular holes. The two cases of the cylindrical bars with or without a central cutout are analyzed [see Figs. 1(*a*) and 1(*b*)]. According to St. Venant's theory of torsion of prismatic bars [6], Laplace's equation

$$\nabla^2 \psi = 0 \tag{1}$$

must be satisfied in the multiply connected region, and the boundary conditions

$$\psi = \frac{1}{2}\rho^2 \qquad \text{on the outer boundary,} \quad \rho = 1 \tag{2}$$

$$\left.\begin{aligned}&\psi = \frac{1}{2}\rho^2 + K_m\\ &m = 1, 2, 3, \ldots\ldots, N+1\end{aligned}\right\} \qquad \text{on each inner boundary} \tag{3}$$

has to be fulfilled. Here in relation (2) $\rho = r/R$ is the dimensionless polar coordinate measured from the center of the main circle, and K_m are constants to be determined. In addition, it is required that the following conditions be satisfied [6]:

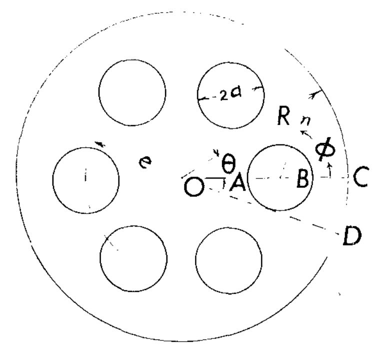

Fig. 1(*a*) Cylinder with equally spaced circular cylindrical holes

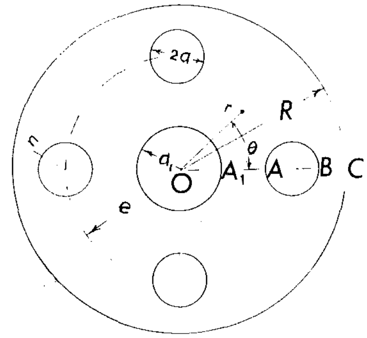

Fig. 1(*b*) Cylinder with equally spaced circular cylindrical holes and a central circular cylindrical cavity

Fig. 1

[1] The author wishes to thank the Department of Computing Services of IUPUI and the Indiana University Computing Network for providing CDC 6600 Computer time for this investigation.

[2] Professor of Aeronautical-Astronautical Engineering and Mathematical Sciences, Purdue University, School of Engineering and Technology, Indianapolis, Ind. 46205.

Manuscript received by ASME Applied Mechanics Division, May 1981; final revision, September, 1981.

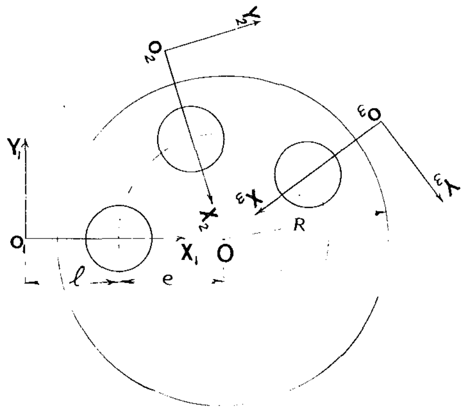

Fig. 2 Utilization of multibipolar coordinate systems in the solution of torsion of multihole cylinders

$$\oint_{C_m} \frac{d\psi}{dn}\, ds = 0, \quad m = 1,2,3,\ldots\ldots,N+1, \tag{4}$$

in which C_m is the boundaries of the inner holes, ds is the element of arc length, and n is the normal direction associated with each inner cutout [see Figs. 1(a), 1(b)]. Since the constant 1/2 is a solution of Laplace's equation, relations (1–4) may be rewritten as follows:

$$\nabla^2\psi_1 = 0,\ \psi_1 = \psi - \frac{1}{2}, \tag{1'}$$

$$\psi_1 = 0 \quad \text{on the outer boundary } \rho = 1, \tag{2'}$$

$$\psi_1 = \frac{1}{2}\rho^2 + K_m - \frac{1}{2} \quad \text{on each inner boundary,} \tag{3'}$$

$$\oint_{C_m} \frac{d\psi_1}{dn}\, ds = 0, \quad m = 1,2,3,\ldots\ldots,N+1. \tag{4'}$$

The following series solution with each term consisting of number of solutions of Laplace's equation in a multibipolar coordinate system is now introduced:

$$\left.\begin{aligned}\bar{\psi}_1 = \sum_{n=1}^{\infty} \bar{A}_n \{ & [e^{n\eta_1} - e^{n(2\beta-\eta_1)}]\cos n\xi_1 \\ & + [e^{n\eta_2} - e^{n(2\beta-\eta_2)}]\cos n\xi_2 + \cdots + [e^{n\eta_N} \\ & - e^{n(2\beta-\eta_N)}]\cos n\xi_N \}\end{aligned}\right\} \tag{5}$$

in which ξ_i and η_i are the bipolar coordinates measured with respect to rectangular coordinates X_i and Y_i system (see Fig. 2), and are given by [7]:

$$\left.\begin{aligned} & \xi_i = \text{Arctan}\ \frac{2\bar{C}\bar{Y}_i}{\bar{X}_i^2 + \bar{Y}_i^2 - \bar{C}^2}, \\ & \eta_i = \frac{1}{2} ln \frac{(\bar{X}_i + \bar{C})^2 + \bar{Y}_i^2}{(\bar{X}_i - \bar{C})^2 + \bar{Y}_i^2} \\ & \bar{X}_i = \frac{X_i}{R},\ \bar{Y}_i = \frac{Y_i}{R}, \quad i = 1,2,3,\ldots\ldots.,N. \end{aligned}\right\} \tag{6}$$

Here in equation (5)β is the common value of all η_i on the outer boundary of the cylinder, and is obtained from [7]:

$$\left.\begin{aligned} & \beta = \cosh^{-1}(\bar{a}\cosh\alpha + \bar{e}), \\ & \bar{a} = \frac{a}{R},\quad \bar{e} = \frac{e}{R},\quad \alpha = \cosh^{-1}\left[\frac{1-\bar{a}^2-\bar{e}^2}{2\bar{a}\bar{e}}\right]. \end{aligned}\right\} \tag{7}$$

It is seen that each term in the series solution (5) automatically satisfies conditions (2′) and (4′), and that it is periodical in the circumferential direction with the period of $2\pi/N$. The solution (5) shall be utilized for the problem of a multihole cylinder without a central hole.

The only remaining condition to be satisfied is (3′). Considering the symmetry, the common constant $K_1 = K_2 = \text{---} = K_N = \bar{K}$ shall be evaluated along with $\bar{A}_1$, $\bar{A}_2$, ----, $\bar{A}_n$ by satisfying the condition (3′) on one half of the boundary of one of the inner circular cutouts.

The solutions of Laplace's equation in polar coordinates $\rho = r/R$, θ satisfying conditions (2′) and (4′) are obtained in the usual way. Thus, it is found

Table 1 Comparison of the values of $\bar{\tau}_{z\theta}$ along radial lines BC, OD, and $\theta = \pi/N$ [see Fig. 1(a)], obtained from the present investigation, (pre.) with those from reference [5]. $\bar{a} = 0.1$, $\bar{e} = 0.6$, $N = 4$.

$\rho = \frac{r}{R}$		0.75	0.80	0.85	0.90	0.95
$\bar{\tau}_{Z\theta}$ along BC	pre.	1.005174	0.944174	0.945219	0.970959	1.008754
	[5]	1.005175	0.944173	0.945217	0.970956	1.008752
$\rho = \frac{r}{R}$		1/6	2/6	3/6	4/6	5/6
$\bar{\tau}_{Z\theta}$ along OD	pre.	0.171101	0.369953	0.504343	0.487211	0.878751
	[5]	0.171102	0.369952	0.504341	0.487206	0.878750
$\bar{\tau}_{Z\theta}$ along $\theta = \pi/N$	pre.	0.161095	0.295598	0.429248	0.605069	0.791715
	[5]	0.161096	0.295598	0.429248	0.605070	0.791715

Table 2 Comparison of the values of shear stresses and torsional rigidities obtained in the present investigation with those given by reference [1] for the case of $\bar{a} = 2/7$, $\bar{e} = 3/7$, $N = 2$ [see Fig. 1(a)].

	$\bar{\tau}_{Z\theta}\|_B$	$\bar{\tau}_{Z\theta}\|_C$	$\bar{\tau}_{Z\theta}\|_A$	$\bar{\tau}_{Z\theta}\Big\|_{\theta=\frac{\pi}{2}}^{\rho=1}$	$\bar{D}/(\pi/2)$
present investigation	1.19880	1.18549	0.396801	0.91614	0.871216
reference [1]	1.194	1.185	−0.392	0.916	0.8809

Table 3 Comparison of the values of shear stresses and torsional rigidities obtained in the present investigation with those given by reference [1] for the case of two eccentric holes and a central cutout with $\bar{a}=0.2$, $\bar{e}=0.6$, $\bar{a}_1=0.2$ [see Fig. 1(*b*)].

present	$\bar{\tau}_{Z\theta}\|_B$	$\bar{\tau}_{Z\theta}\|_C$	$\bar{\tau}_{Z\theta}\|_A$	$\bar{\tau}_{Z\theta}\|_{A_1}$	$\bar{D}/(\pi/2)$
investigation	1.54667	1.30794	1.03328	0.45887	0.86802
reference [1]	1.547	1.308	−1.033	0.459	0.8093

Table 4 The values of dimensionless shear stress $\bar{\tau}_{z\theta}$ along the radial lines *BC*, *OA* [see Fig. 1(*a*)] and along the line $\theta=30$ deg for the case of $a/R=0.1$, $e/R=0.6$, and $N=6$ – cylinder without a central hole (R = cylinder radius, e = eccentricity of holes, a = eccentric hole radius, N = no. of holes).

ρ along BC	$\bar{\tau}_{z\theta}$	ρ along OA	$\bar{\tau}_{z\theta}$	ρ along $\theta=30$ deg	$\bar{\tau}_{z\theta}$
0.7	1.231	0.	0.	0.	0.
0.775	0.932	0.125	0.125	0.25	0.243
0.85	0.921	0.250	0.257	0.50	0.375
0.925	0.968	0.375	0.435	0.75	0.673
1.00	1.035	0.50	0.999	1.00	0.971

Table 5 The values of dimensionless shear stress $\bar{\tau}_{z\theta}$ along the radial lines *BC*, A_1A, [see Fig. 1(*b*)] and along the line $\theta=30$ deg for the case of $a/R=0.1$, $e/R=0.8$, $a_1/R=0.5$ and $N=6$ – cylinder with a central hole (R = cylinder radius, e = eccentricity of holes, a = eccentric hole radius, a_1 = central hole radius, N = no. of eccentric holes).

ρ along BC	$\bar{\tau}_{z\theta}$	ρ along A_1A	$\bar{\tau}_{z\theta}$	ρ along $\theta=30°$	$\bar{\tau}_{z\theta}$
0.900	1.792	0.500	0.602	0.900	0.767
0.917	1.590	0.533	0.639	0.917	0.786
0.933	1.472	0.567	0.696	0.933	0.805
0.950	1.404	0.600	0.776	0.950	0.824
0.967	1.368	0.633	0.894	0.967	0.842
0.983	1.354	0.667	1.086	0.983	0.861
1.000	1.357	0.700	1.463	1.000	0.880

Table 6 The values of $\bar{\tau}_{z\theta}$ along the line *BC* for the cases of multihole cylinders without a central cutout for various a/R, e/R and N (R = cylinder radius, e = eccentricity of holes, a = eccentric hole radius, N = no. of holes).

$a/R=0.1$, $e/R=0.6$, $N=4$		$a/R=0.1$, $e/R=0.6$, $N=6$		$a/R=0.125$, $e/R=0.7$ $N=3$		$a/R=0.125$, $e/R=0.7$, $N=5$		$a/R=0.15$, $e/R=0.7$, $N=4$	
ρ	$\bar{\tau}_{z\theta}$	ρ	$\bar{\tau}_{z\theta}$	ρ	$\bar{\tau}_{z\theta}$	ρ	$\bar{\tau}_{z\theta}$	ρ	$\bar{\tau}_{z\theta}$
0.700	1.281	0.700	1.231	0.825	1.603	0.825	1.522	0.85	1.628
0.775	0.962	0.775	0.932	0.869	1.321	0.869	1.259	0.889	1.408
0.850	0.945	0.850	0.921	0.913	1.229	0.913	1.176	0.925	1.320
0.925	0.989	0.925	0.968	0.956	1.212	0.956	1.163	0.963	1.295
1.000	1.054	1.000	1.035	1.000	1.232	1.000	1.186	1.000	1.307

Table 7 The values of $\bar{\tau}_{z\theta}$ along the line *BC* for the cases of multihole cylinders with a central cutout for various a/R, e/R, a_1/R, and N (R = cylinder radius, e = eccentricity of holes, a = eccentric hole radius, a_1 = central hole radius, N = no. of eccentric holes).

$a/R=0.1$, $e/R=0.6$, $a_1/R=0.3$, $N=4$		$a/R=0.1$, $e/R=0.6$, $a_1/R=0.3$, $N=6$		$a/R=0.125$, $e/R=0.7$, $a_1/R=0.4$, $N=5$		$a/R=0.1$, $e/R=0.8$, $a_1/R=0.5$, $N=6$		$a/R=0.15$, $e/R=0.7$, $a_1/R=0.4$, $N=4$	
ρ	$\bar{\tau}_{z\theta}$	ρ	$\bar{\tau}_{z\theta}$	ρ	$\bar{\tau}_{z\theta}$	ρ	$\bar{\tau}_{z\theta}$	ρ	$\bar{\tau}_{z\theta}$
0.70	1.282	0.70	1.232	0.825	1.522	0.900	1.792	0.850	1.634
0.75	1.006	0.75	0.971	0.854	1.316	0.917	1.590	0.875	1.466
0.80	0.945	0.80	0.916	0.883	1.219	0.933	1.472	0.900	1.374
0.85	0.946	0.85	0.921	0.913	1.176	0.950	1.404	0.925	1.324
0.90	0.971	0.90	0.949	0.942	1.162	0.967	1.368	0.950	1.302
0.95	1.009	0.95	0.989	0.971	1.167	0.983	1.354	0.975	1.299
1.00	1.054	1.00	1.035	1.000	1.186	1.000	1.357	1.000	1.310

$$\psi_1^* = \sum_{J=1}^{\infty} A_J^* (\rho^{NJ} - \bar{\rho}^{NJ}) \cos NJ\theta. \tag{8}$$

The function $\psi_1 = \bar{\psi}_1 + \psi_1^*$ is suitable for the case of the problem of torsion of a multihole cylinder with a central cutout. The unknown constants of integration A_1^*, A_2^*, ---A_j^*, ---$\bar{A}_1$, $\bar{A}_2$, ---$\bar{A}_n$--- along with $\bar{K}$ and $K^*=K_{N+1}$ are evaluated by applying the inner boundary condition (3′) on one half of one of the eccentric holes and $1/2N$ of the boundary of the central cutout. For this purpose, p terms in the series solution are retained, and the boundary condition(s) are satisfied at q points ($q>p$) of the boundary (or boundaries) under consideration. This procedure leads to a set of $q\times p$ linear algebraic equations which are normalized and solved approximately by the method of least square error [8]. For a case of a cylinder with only eccentric holes, using 35 by 24 equations, the maximum value of relative error in satisfaction of the inner boundary condition is of the order of 10^{-12}. This

Table 8 The effect of closeness of the eccentric holes to the outer boundary: dimensionless shear stresses $\bar{\tau}_{z\theta}|_B$ and $\bar{\tau}_{z\theta}|_C$ [See Fig. 1(*a*)] versus e/R for the case of $a/R=0.125$, $N=3$ – cylinder without a central hole (R = cylinder radius, e = eccentricity of holes, a = eccentric hole radius, N = no. of holes).

e/R	$\bar{\tau}_{z\theta}\|_B$	$\bar{\tau}_{z\theta}\|_C$
0.70	1.603	1.232
0.75	1.789	1.382
0.80	2.101	1.708

Table 9 The values of dimensionless torsional rigidities $\bar{D}$ for various a/R, e/R, N and for the cases of cylinders without a central hole (R = cylinder radius, e = eccentricity of holes, a = eccentric hole radius, N = no. holes).

a/R	e/R	N	$\bar{D}$
0.100	0.6	4	1.482
0.100	0.6	6	1.444
0.125	0.7	3	1.422
0.125	0.7	5	1.337
0.150	0.7	4	1.293

Table 10 The values of dimensionless torsional rigidities $\bar{D}$ for various a/R, e/R, a_1/R, N and for the cases of cylinders with a central hole (R = cylinder radius, e = eccentricity of holes, a = eccentric hole radius, a_1 = central hole radius, N = no. of eccentric holes).

a/R	e/R	a_1/R	N	$\bar{D}$
0.100	0.6	0.3	4	1.460
0.100	0.6	0.3	6	1.410
0.100	0.8	0.5	6	1.199
0.125	0.7	0.4	3	1.369
0.125	0.7	0.4	5	1.262
0.150	0.7	0.4	4	1.208

remarkable accuracy shows how rapidly the series solution (5) converges. Thus, for ordinary engineering approximations much smaller sets of linear equations can be utilized.

The values of dimensionless shear stress $\bar{\tau}_{z\theta}=\tau_{z\theta}/G\alpha_1 R^2$ and torsional rigidity $\bar{D}=T/G\alpha_1 R^4$ are determined from the obtained solution [6]. Here α_1 is the angle of twist per unit length, G is modulus of shear, and T is the applied torque. The nondimensional torsional rigidity $\bar{D}$ is evaluated by a highly accurate eight-order polynomial approximation for numerical integration [8].

In Table 1 the values of $\bar{\tau}_{z\theta}$ along various radial directions are compared with those calculated from the technique of reference [5]. In Tables 2 and 3 the values of dimensionless shear stresses and torsional rigidities are compared with those given by Ling [1]. It is seen that most of the values of $\bar{\tau}_{z\theta}$ in Tables 2 and 3 agree closely. The disagreement of the signs for the shear stresses at point A is believed to be due to the difference between the convention signs of $\tau_{z\theta}$ and $\tau_{z\phi}$. However, the values of $\bar{D}/(\pi/2)$ in Tables 2 and 3 disagree. In view of the comparison of our results with those of the independent technique of reference [5] (Table 1), the correctness of the values of $\bar{D}/(\pi/2)$ given by Ling [1] is doubtful. In Tables 4 and 5 the values of nondimensional shear stresses $\bar{\tau}_{z\theta}$ have been presented for various ρ and θ, and for the cases of multihole cylinders with or without a central circular cavity. In Tables 6 and 7 the variations of dimensionless stress $\bar{\tau}_{z\theta}$ along the lines BC [see Figs. 1(*a*), 1(*b*)] are presented for multihole cylinder cases with or without a central hole, and having 3, 4, 5, and 6 eccentric holes. In Table 8 the effect of nearness of the eccentric holes to the outer boundary is demonstrated. Finally, in Tables 9 and 10 the values of torsional rigidity $\bar{D}$ for various geometrical dimensions are presented.

References

1 Ling, C. B., "Torsion of a Circular Tube With Longitudinal Circular Holes," *Quart. Appl. Math.*, Vol. 5, No. 2, pp. 168–181, July, 1947.

2 Howland, R. C. J., "Potential Functions With Periodicity in One Coordinate," *Proceedings of The Cambridge Philosophical Society*, London, England, Vol. 30, pp. 315–326, 1935.

3 Kuo, Y. -M., and Conway, H. D., "Torsion of Cylinders With Multiple Reinforcement," *Journal of Engineering Mechanics Division*, ASCE, Vol. 100, EM2, Proc. Paper 10460, pp. 221–234 Apr., 1974.

4 Kuo, Y. -M., and Conway, H. D., "The Torsion of Composite Tubes and Cylinders," *International Journal of Solids and Structures*, Vol. 9, pp. 1553–1566 1973.

5 Naghdi, A. K., "Closed Form Eigenfunctions of Laplace's Equation In Multiply Connected Regions and Applications," *Proceedings of The 16th Midwestern Mechanics Conference: Developments In Mechanics*, Vol. 10, pp. 131–135, 1979.

6 Sokolnikoff, S., *Mathematical Theory of Elasticity*, McGraw-Hill, New York, 1956.

7 Bateman, H., *Partial Differential Equations of Mathematical Physics*, Dover Publications, New York, 1944.

8 Hildebrand, F. B., *Introduction to Numerical Analysis*, McGraw-Hill, New York, 1956.

Journal of Applied Mechanics

Brief Notes

A Brief Note is a short paper that presents a specific solution of technical interest in mechanics but which does not necessarily contain new general methods or results. A Brief Note should not exceed 1500 words *or equivalent* (a typical one-column figure or table is equivalent to 250 words; a one line equation to 30 words). Brief Notes will be subject to the usual review procedures prior to publication. After approval such Notes will be published as soon as possible. The Notes should be submitted to the Technical Editor of the JOURNAL OF APPLIED MECHANICS. Discussions on the Brief Notes should be addressed to the Editorial Department, ASME, United Engineering Center, 345 East 47th Street, New York, N. Y. 10017, or to the Technical Editor of the JOURNAL OF APPLIED MECHANICS. Discussions on Brief Notes appearing in this issue will be accepted until two months after publication. Readers who need more time to prepare a Discussion should request an extension of the deadline from the Editorial Department.

Stability of Nonparallel Developing Flow in an Annulus to Asymmetric Disturbances

V. K. Garg[1]

Linear spatial stability of the nonparallel developing flow in a concentric annulus shows that the asymmetric disturbance with an azimuthal wave number equal to unity is more unstable than the axisymmetric disturbance at all axial locations. Also, in the near entry region, the critical Reynolds number corresponding to the parallel flow theory is as much as three times that due to the nonparallel theory for some values of the annular diameter ratio.

Introduction

Almost all practical applications of flow through ducts involve the developing flow rather than the fully developed flow. However, while the stability of fully developed flow in a concentric annulus has been thoroughly studied [1-3], that of the axially developing flow has not been examined. One possible reason for this may be the fact that the developing flow is not a parallel flow but changes, though slowly, in the downstream direction. It is known [4], however, that even this slow variation affects the stability characteristics considerably. An additional complication is the fact [5] that Squire's theorem [6] is not applicable to axisymmetric flows. We, therefore, examine the linear spatial stability of the nonparallel, axially developing flow in a concentric annulus to asymmetric disturbances.

Analysis

For the flow of an incompressible, Newtonian fluid in the inlet region of a circular, concentric annulus of inner and outer radii a and b, respectively, we define the following dimensionless variables

$$X=\frac{2x}{b-a},\quad R=\frac{2r}{b-a},\quad T=\frac{2tu_a}{b-a},\quad P=\frac{\hat{p}}{\rho u_a{}^2} \tag{1}$$

$$U=\frac{\hat{u}}{u_a},\ V=\frac{\hat{v}\sqrt{\mathrm{Re}}}{u_a},\quad \mathrm{Re}=\frac{u_a(b-a)}{2\nu},$$

where x and r are the axial and radial coordinates measured, respectively, from the inlet section and the axis of the annulus, $\hat{u}$ and $\hat{v}$ are the axial and radial components of velocity at any point (x,r) and at any time t, u_a is the average velocity of the flow, $\hat{p}$ is the pressure at any section x, ρ and ν are, respectively, the density and kinematic viscosity of the fluid, and Re is the Reynolds number of the flow.

Consider an infinitesimal asymmetric disturbance with dimensionless velocity components $u(X,R,\theta,T)$, $v(X,R,\theta,T)$, and $w(X,R,\theta,T)$, and dimensionless pressure $p(X,R,\theta,T)$ superimposed on the main flow. Here θ is the azimuthal coordinate of the cylindrical coordinate system. It is well known that for the developing flow the velocity components $U(X,R)$ and $V(X,R)$ are slowly varying functions of X. To express this slow variation we introduce another independent variable X_1 along X direction such that $X_1=\epsilon X$, where ϵ is a small dimensionless parameter that characterizes the nonparallelism of the flow; $\epsilon=0$ implies a truly parallel flow. For reasons given in [4], ϵ is taken as $\mathrm{Re}^{-1/2}$ in the near-inlet region. The disturbance is taken to be of the type

$$u=\{u_0(x_1,R)+\epsilon u_1(X_1,R)+\epsilon^2u_2(X_1,R)+\ \ldots\ \}e^{i\eta}, \tag{2}$$

and similar expressions for v, w, and p, with

$$\frac{\partial\eta}{\partial T}=-\omega,\quad \frac{\partial\eta}{\partial X}=k_0(X_1),\quad \text{and}\ \frac{\partial\eta}{\partial\theta}=n,$$

where ω is the dimensionless frequency of the disturbance, n is the azimuthal wave number, the real part of k_0 is the axial wave number, and its imaginary part is the spatial growth rate for parallel-flow stability. Substituting for u,v, etc., from equation (2) in the linearized governing equations, using the transformation relations between (X,T) and (X_1,η) planes, equating the like powers of ϵ, and denoting a derivative with respect to R by D, we get

Order ϵ^0:

$$\begin{aligned}
L_u(u_0) &\equiv D^2u_0+\frac{Du_0}{R}-Au_0-\mathrm{Re}v_0DU-ik_0p_0=0,\\
L_v(v_0) &\equiv Dv_0+\frac{v_0}{R}+ik_0u_0+\frac{inw_0}{R}=0,\\
L_w(w_0) &\equiv D^2w_0+\frac{Dw_0}{R}-\left(A+\frac{1}{R^2}\right)w_0\\
&\quad+\frac{2inv_0}{R^2}-\frac{inp_0}{R}=0,\\
L_p(p_0) &\equiv Dp_0+Av_0+ik_0Du_0+\frac{in}{R}Dw_0+\frac{inw_0}{R^2}=0,
\end{aligned} \tag{3}$$

where $A=n^2/R^2+k_0^2+i\mathrm{Re}\ (k_0U-\omega)$, p_0 stands for $\mathrm{Re}p_0$ with the boundary conditions $u_0=v_0=w_0=0$ at $R=R_1$ and R_2, where $R_1=2a/(b-a)$ and $R_2=2b/(b-a)$.

[1] Professor, Department of Mechanical Engineering Indian Institute of Technology, Kanpur 208016, India, Mem. ASME. Currently Visiting Professor, Department of Mathematical Sciences, Rensselaer Polytechnic Institute, Troy, New York 12181.

Manuscript received by ASME Applied Mechanics Division May, 1981; final revision, October, 1981.

Order ϵ^1:

$$
\begin{aligned}
L_u(u_1) &= \mathrm{Re}\left(U\frac{\partial u_0}{\partial X_1} + VDu_0 + u_0\frac{\partial U}{\partial X_1}\right) + \frac{\partial p_0}{\partial X_1} \\
&\quad -2ik_0\frac{\partial u_0}{\partial X_1} - iu_0\frac{dk_0}{dX_1}, \\
L_v(v_1) &= -\frac{\partial u_0}{\partial X_1}, \\
L_w(w_1) &= \mathrm{Re}\left(U\frac{\partial w_0}{\partial X_1} + VDw_0 + \frac{Vw_0}{R}\right) \\
&\quad -2ik_0\frac{\partial w_0}{\partial X_1} - iw_0\frac{dk_0}{dX_1}, \qquad (4) \\
L_p(p_1) &= -\mathrm{Re}\left(U\frac{\partial v_0}{\partial X_1} + VDv_0 + v_0DV\right) \\
&\quad -\frac{\partial^2 u_0}{\partial X_1 \partial R} + 2ik_0\frac{\partial v}{\partial X_1} + iv_0\frac{dk_0}{dX_1},
\end{aligned}
$$

with the boundary conditions

$$u_1 = v_1 = w_1 = 0 \text{ at } R = R_1 \text{ and } R_2.$$

For given values of ω, Re, $U(X_1,R)$, and $V(X_1,R)$, the solution of (3) may be expressed as

$$
\begin{aligned}
u_0 &= B(X_1)\beta_1(R;X_1), v_0 = B(X_1)\beta_2(R;X_1), \\
w_0 &= B(X_1)\beta_3(R;X_1), \text{ and } p_0 = B(X_1)\beta_4(R;X_1),
\end{aligned}
$$

where β_1, β_2, etc., are the eigenfunctions. The amplitude function $B(X_1)$ is given by

$$\frac{dB}{dX_1} = -ik_1(X_1)B \qquad (5)$$

where $ik_1 = b_2(X_1)/b_1(X_1)$, and b_1 and b_2 involve quadratures of the eigenfunctions of the original and adjoint problems. Thus, to the first approximation

$$u = B_0\beta_1(R;X_1) \exp\left[i\textstyle\int(k_0+\epsilon k_1)dX - i\omega T + in\theta\right], \qquad (6)$$

and similarly for v, w, and p, where B_0 is a constant.

Computational Procedure

The main flow velocity field was found using an implicit finite-difference technique [7]. This yields the velocity components U and V as functions of $\bar{X} = X/\mathrm{Re}$ and R. Equations (3) were integrated using the fourth-order, Runge-Kutta method. Convergence to the eigenvalue, k_0, was achieved by means of Muller's technique [8]. With k_0 and eigenfunctions known, a procedure similar to the foregoing was used to solve the adjoint problem

$$
\begin{aligned}
&D^2u^* + \frac{Du^*}{R} + ik_0p^* - (A + k_0^2)u^* - \frac{nk_0w^*}{R} = 0, \\
&DV^* + \frac{v^*}{R} + ik_0u^* + \frac{inw^*}{R} = 0, \\
&D^2w^* + \frac{Dw^*}{R} - \left(A + \frac{n^2+1}{R^2}\right)w^* \\
&\quad - \frac{nk_0u^*}{R} + \frac{2inv^*}{R^2} + \frac{inp^*}{R} = 0, \qquad (7) \\
&Dp^* + \mathrm{Re}u^*DU - Av^* - \frac{2inw^*}{R^2} = 0,
\end{aligned}
$$

with the boundary conditions

$$u^* = v^* = w^* = 0 \text{ at } R = R_1 \text{ and } R_2,$$

the difference being that no iteration is necessary since the adjoint problem has the same eigenvalue as the original problem. Calculations were performed on a DEC 1090 computer that carries 17 digits in double precision mode. Step size for the Runge-Kutta method was taken as 0.005 and selective application of the Gram-Schmidt orthonormalization technique was used to keep the solution vectors linearly independent during numerical integration; details are available in [9].

Table 1 Radial distance R_w (from the inner wall) where g_w has the maximum value

$\bar{X}$	R_w	
	$\gamma = 0.01$	$\gamma = 0.1$
0.008	1.8 -1.83[a]	0.16 -0.2
0.012	1.775-1.805	0.18-0.21
0.020	1.745-1.785	1.75-1.785
0.028	1.735-1.765	1.725-1.765

$\bar{X}$	R_w	
	$\gamma = 0.4$	$\gamma = 0.8$
0.004	0.135-0.16	0.125-0.14
0.006	0.145-0.165	0.135-0.15
0.008	0.155-0.17	0.145-0.155
0.012	1.825-1.85	1.84 -1.85

[a]varies slightly with Re and ω.

Results

Growth rates based on the axial, radial, and tangential components of disturbance velocity and on the energy density E of the disturbance following [10] were obtained at several axial locations. Defining the growth rate of a complex flow quantity Q as

$$g_Q \equiv \frac{1}{|Q|}\frac{\partial |Q|}{\partial X},$$

it is easy to see that the growth rate based on w is given by

$$g_w(X,R) = -\alpha_i + \frac{\epsilon}{|\beta_3|}\frac{\partial|\beta_3|}{\partial X_1},$$

where α_i is the imaginary part of $(k_0 + \epsilon k_1)$. Similar relations hold for g_u and g_v. The growth rate of energy density E of the disturbance where

$$E = \frac{1}{2}\int_{R_1}^{R_2} 2\pi R(\overline{u^2} + \overline{v^2} + \overline{w^2})dR,$$

is given by

$$g_E(X) \equiv \frac{1}{2}E^{-1}\frac{dE}{dX} = -\alpha_i + \frac{\epsilon}{2C}\frac{\partial C}{\partial X_1}$$

where

$$C = \int_{R_1}^{R_2}(|\beta_1|^2 + |\beta_2|^2 + |\beta_3|^2)RdR.$$

Since the velocity field was obtained at a given $\bar{X}$ instead of X, all growth rates have been obtained for a given $\bar{X}$ value, and are, hereafter, referred to as functions of $\bar{X}$. Amongt $g_E(\bar{X})$, $g_u(\bar{X},R)$, $g_v(\bar{X},R)$, and $g_w(\bar{X},R)$, it was found that the maximum value of g_w is the largest at a given $\bar{X}$. Results are therefore presented for g_w only. It is also known that for the nonparallel flow stability, one gets different wave numbers for different disturbance properties. It was found, however, that the modified wave numbers are little different from the parallel flow wave number given by the real part of k_0. Therefore, the modified wave numbers, though computed, are not reported here.

Since g_w is a function of both the axial and radial coordinates, the maximum value of g_w, occurring at say R_w, was selected for a given axial location to limit the number of neutral curves. Typical values of R_w are listed in Table 1. It may be noted that the values of R_w are close to those corresponding to the boundary layer edge of either the inner or the outer wall depending on the axial location $\bar{X}$ and the diameter ratio $\gamma = a/b$. For four values of $\gamma(=0.01, 0.1, 0.4,$ and 0.8) and several axial locations ($\bar{X}=0.004$, 0.006, 0.008, 0.012, 0.02, 0.028), the growth rate $g_w(\bar{X},R_w)$ was plotted against the disturbance dimensionless frequency ω with Re as a parameter. The azimuthal wave number n was taken to be unity. From these plots (not shown here) neutral curves (Fig. 1) were obtained. These curves show that for any value of γ, the range of unstable frequencies diminishes as the flow develops. Also, at a given axial location (fixed $\bar{X}$), the flow becomes unstable at a lower Reynolds number in (generally) a smaller diameter ratio annulus.

Figure 2 shows the variation of critical Reynolds number Re_c based on $g_w(\bar{X},R_w)$ and the parallel flow theory against $\bar{X}$ with γ as a parameter. It also contains the $\mathrm{Re}_c - \bar{X}$ curve for the pipe flow ($\gamma=0$) for comparison with $\gamma=0.01$ case. It is obvious that the nonparallel effects reduce the critical Reynolds number considerably for any γ and $\bar{X}$. In fact, the behavior of $\mathrm{Re}_c - \bar{X}$ curves appear to be quite different with the inclusion of nonparallel effects. Table 2 highlights some of these differences. For the sake of comparison, results were also found for an axisymmetric disturbance ($n=0$). The analysis simplifies considerably in this case and one can, in fact, work in terms of the disturbance stream function ψ (see [4] for the pipe flow case). It was found that while g_v and g_ψ were little different from each other except very close to the entry section ($\bar{X} \leq 0.002$), they were larger than both g_u and g_E for $n=0$. Also, for given $\bar{X}$ and γ, both g_v and g_ψ had their maxima at one radial location, say R_v. Table 2 also lists values of Re_c(for $n=0$) corresponding to g_v $(\bar{X},R_v)$ and the parallel-flow theory together with values of R_v. It is in-

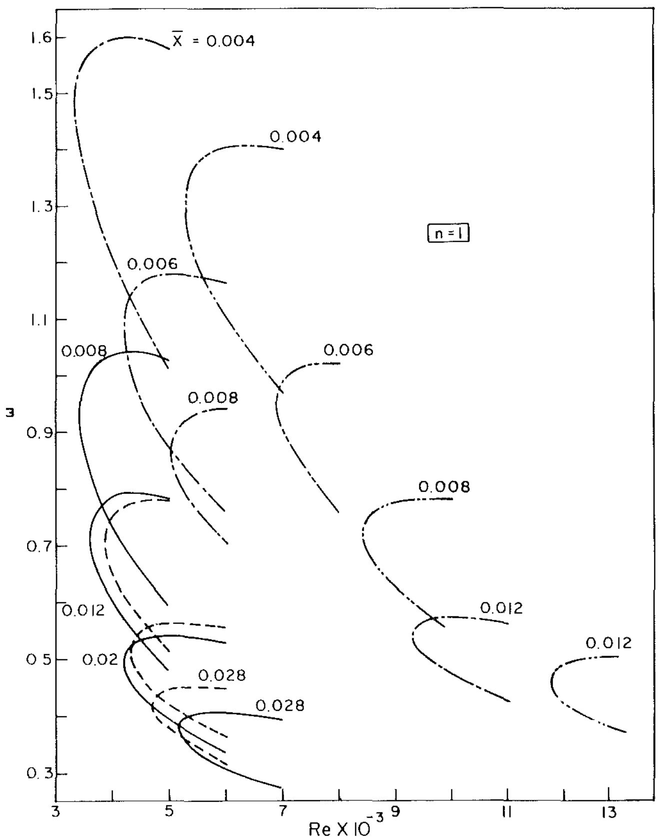

Fig. 1 Neutral curves based on g_w $(\bar{X},R_w)$ for various γ and $\bar{X}$. ____, $\gamma=0.01$; _ _ _ _, $\gamma=0.1$; _ _ _ _ $\gamma=0.4$; _ _ _ _ _, $\gamma=0.8$.

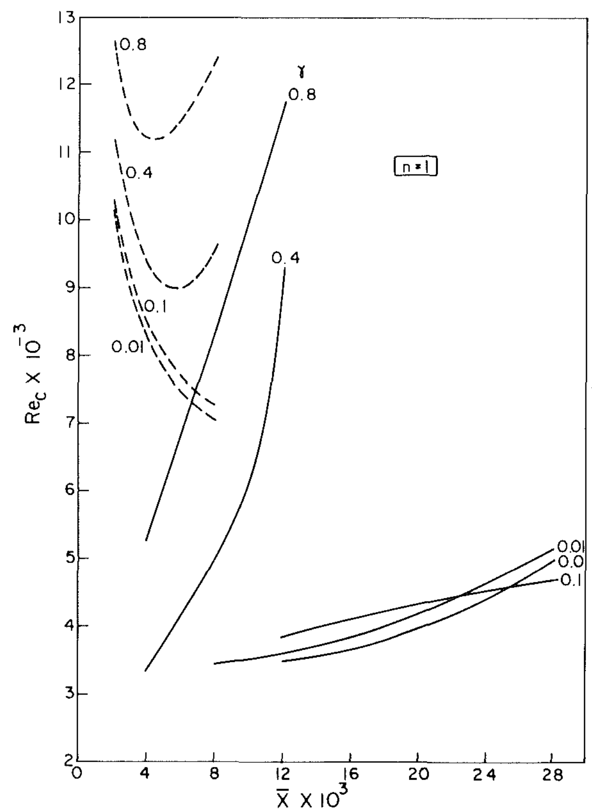

Fig. 2 Critical Reynolds number versus $\bar{X}$. ___, based on $g_w(\bar{X},R)$; _ _ _, based on parallel-flow theory.

Table 2 Critical Reynolds numbers

γ	$\bar{X}$	Re_c based on $g_w(\bar{X},R_w)$ $(n=1)$	Re_c based on $g_v(\bar{X},R_v)$ $(n=0)$	R_v	Re_c based on parallel-flow theory $n=1$	Re_c based on parallel-flow theory $n=0$
0.01	0.008	3440	5800	0.22[a]	7050	6500
0.1	0.008	2400	6250	0.35	7275	7050
0.4	0.004	3330	7800	0.44	9350	9250
	0.006	4200	7700	0.51	9000	8650
	0.008	5000	8200	0.56	9650	9000
0.8	0.004	5270	10000	0.7	11200	11200
	0.006	6880	10850	0.78	11550	11500
	0.008	8400	12100	0.85	12425	11100

[a] mean value (from the inner wall) as R_v changes a little with Re and ω.

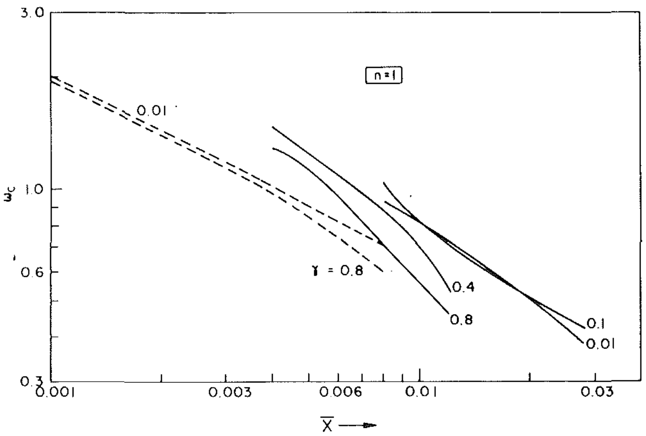

Fig. 3 Critical frequency versus $\bar{X}$. ——, based on g_w $(\bar{X},R_w)$; – – –, based on parallel-flow theory.

teresting to note from this Table that while developing flow in the annulus, taken as a parallel flow, is less unstable to asymmertic disturbance ($n=1$) in comparison to the axisymmetric disturbance ($n=0$), the reverse is true when nonparallel effects are taken into account.

Figure 3 shows the variation of critical frequency ω_c corresponding to $g_w(\bar{X},R_w)$ and the parallel flow theory for $n=1$ against $\bar{X}$ with γ as a parameter. It is observed that the nonparallel effects increase the critical frequency for all $\bar{X}$ and γ. However, in comparison to the large drop in critical Reynolds number, the critical frequency is only slightly increased by the nonparallel effects.

Conclusions

The nonparallel developing flow in a circular concentric annulus is found to be more unstable to asymmetric disturbances with an azimuthal wave number equal to unity than to the axisymmetric disturbances. The present results show that for such disturbances, the parallel flow theory overpredicts the critical Reynolds number by as much as 203 percent at $\bar{X}=0.008$ for $\gamma=0.1$. Thus considering the developing flow in ducts to be parallel for stability analysis is highly improper.

Acknowledgments

Assistance of Dr. S. C. Gupta in carrying out some computations for the axisymmetric case is gratefully acknowledged.

References

1 Mott, J. E., and Joseph, D. D., "Stability of Parallel Flow Between Concentric Cylinders," *Physics of Fluids*, Vol. 11, 1968, pp. 2065–2073.

2 Mahadevan, R., and Lilley, G. M., "The Stability of Axial FLow Between Concentric Cylinders to Asymmetric Disturbances," AGARD CP224, 1977.

3 Garg, V. K., "Spatial Stability of Concentric Annular Flow," *Journal of Physical Society of Japan*, Vol. 49, 1980, pp. 1577–1583.

4 Garg, V. K., and Gupta, S. C., "Stability of Developing Flow in a Pipe-Nonparallel Effects," ASME Journal of Applied Mechanics, Vol. 48, 1981, pp. 243–248.

5 Spielberg, K., and Timan, H., "On Three and Two-Dimensional Disturbances of Pipe Flow," ASME Journal of Applied Mechanics, Vol. 28, 1960, pp. 381–389.

6 Squire, H. B., "On the Stability for Three-Dimensional Disturbances of Viscous Fluid Flow Between Parallel Walis," *Proceedings of the Royal Society*, London, Series A, Vol. 142, 1933, pp. 621–628.

7 Gupta, S. C., and Garg, V. K., "Developing Flow in a Concentric Annulus," *Computer Methods in Applied Mechanics and Engineering*, Vol. 27, 1981, pp. 27–35.

8 Muller, D. E., "A Method for Solving Algebraic Equations Using an Automatic Computer," *Mathematical Tables and Other Aids to Computation*, Vol. 10, 1956, pp. 208–215.

9 Garg, V. K., "Improved Shooting Techniques for Linear Boundary Value Problems," *Computer Methods in Applied Mechanics and Engineering*, Vol. 22, 1980, pp. 87–99.

10 Shen, S. F., "Some Considerations on the Laminar Stability of Time-Dependent Basic Flows," *Journal of Aeronautical Sciences*, Vol. 28, 1961, pp. 397–404.

Free Out-of-Plane Vibration of Arcs

T. Irie,[1] G. Yamada,[1] and K. Tanaka[1]

Introduction

The vibration theory of beams has great importance in many engineering applications such as in the design of machines and structures. Therefore, a considerable number of papers are available on the out-of-plane vibration of arcs or curved beams, as well as straight beams. The fundamental equations of arcs or curved beams have been presented together with the solution to them in the book of Love [1]. Takahashi [2], Volterra and Morell [3, 4], Chang and Volterra [5], and Suzuki, Aida, and Takahashi [6] studied the free out-of-plane vibration of arcs and curved beams on the basis of the classical beam theory in which the rotatory inertia and shear deformation are not taken into account. Recently, Rao [7], Kirkhope [8], Suzuki and Takahashi [9], and Davis, Henshell, and Warburton [10] have analyzed rings and curved beams, and Irie, Yamada, and Takahashi [11, 12] have analytically studied arcs and curved beams of variable cross section. These recent studies have been based on the Timoshenko beam theory in which both of the rotatory inertia and shear deformation are taken into account.

This paper presents an analysis of the free out-of-plane vibration of elastic arcs governed by the Timoshenko beam theory and by the specialized theories in which either or both of the rotatory inertia and shear deformation are taken into account. For this purpose, the equations of out-of-plane vibration of an arc are written in a matrix differential equation of the first-order by use of the transfer matrix of the arc. The transfer matrix is conveniently expressed as the series type solution to the equation, and the frequency equations are derived by the boundary conditions. The natural frequencies (the eigenvalues of vibration) of some arcs are calculated numerically by the application of the method and are compared with one another, from which the effects of the rotatory inertia and shear deformation on the vibration are studied.

Theoretical Consideration

We consider a uniform arc of radius of curvature of the neutral axis R. With the angular coordinate denoted by θ and with the opening angle by α, the $X-$, $Y-$, and $Z-$ axes are taken in radial, transverse, and tangential directions, respectively, as shown in Fig. 1.

1. Timoshenko equations (TM).

On the assumption that the shear center of the cross section coincides with the centroid, the equation of translational motion of the arc is written as

$$\frac{dQ_y^*}{Rd\theta}+\rho A\omega^2 v^*=0 \qquad (1)$$

and the equations of rotation are

$$-\frac{dM_x^*}{Rd\theta}+\frac{T^*}{R}-Q_y^*+\rho I_x\omega^2\varphi=0 \qquad (2)$$

[1] Professor, Associate Professor, and Instructor, respectively, Department of Mechanical Engineering, Hokkaido University, Kita-13, Nishi-8, Kita-ku, Sapporo, 060 Japan

Manuscript received by ASME Applied Mechanics Division, May, 1981; final revision, September, 1981.

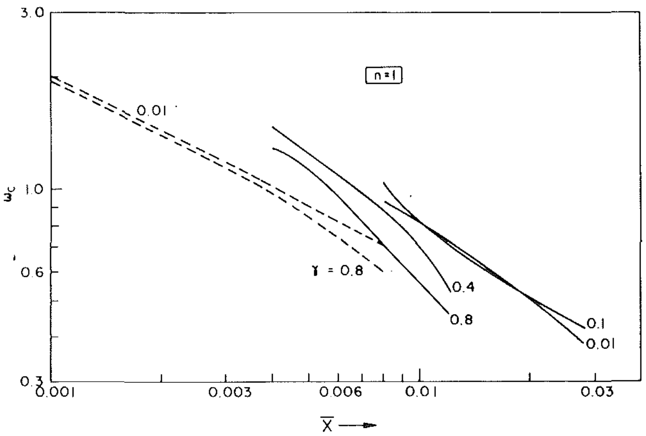

Fig. 3 Critical frequency versus $\bar{X}$. ——, based on g_w $(\bar{X},R_w)$; – – –, based on parallel-flow theory.

teresting to note from this Table that while developing flow in the annulus, taken as a parallel flow, is less unstable to asymmertic disturbance ($n=1$) in comparison to the axisymmetric disturbance ($n=0$), the reverse is true when nonparallel effects are taken into account.

Figure 3 shows the variation of critical frequency ω_c corresponding to $g_w(\bar{X},R_w)$ and the parallel flow theory for $n=1$ against $\bar{X}$ with γ as a parameter. It is observed that the nonparallel effects increase the critical frequency for all $\bar{X}$ and γ. However, in comparison to the large drop in critical Reynolds number, the critical frequency is only slightly increased by the nonparallel effects.

Conclusions

The nonparallel developing flow in a circular concentric annulus is found to be more unstable to asymmetric disturbances with an azimuthal wave number equal to unity than to the axisymmetric disturbances. The present results show that for such disturbances, the parallel flow theory overpredicts the critical Reynolds number by as much as 203 percent at $\bar{X}=0.008$ for $\gamma=0.1$. Thus considering the developing flow in ducts to be parallel for stability analysis is highly improper.

Acknowledgments

Assistance of Dr. S. C. Gupta in carrying out some computations for the axisymmetric case is gratefully acknowledged.

References

1 Mott, J. E., and Joseph, D. D., "Stability of Parallel Flow Between Concentric Cylinders," *Physics of Fluids*, Vol. 11, 1968, pp. 2065–2073.

2 Mahadevan, R., and Lilley, G. M., "The Stability of Axial FLow Between Concentric Cylinders to Asymmetric Disturbances," AGARD CP224, 1977.

3 Garg, V. K., "Spatial Stability of Concentric Annular Flow," *Journal of Physical Society of Japan*, Vol. 49, 1980, pp. 1577–1583.

4 Garg, V. K., and Gupta, S. C., "Stability of Developing Flow in a Pipe-Nonparallel Effects," ASME JOURNAL OF APPLIED MECHANICS, Vol. 48, 1981, pp. 243–248.

5 Spielberg, K., and Timan, H., "On Three and Two-Dimensional Disturbances of Pipe Flow," ASME JOURNAL OF APPLIED MECHANICS, Vol. 28, 1960, pp. 381–389.

6 Squire, H. B., "On the Stability for Three-Dimensional Disturbances of Viscous Fluid Flow Between Parallel Walis," *Proceedings of the Royal Society*, London, Series A, Vol. 142, 1933, pp. 621–628.

7 Gupta, S. C., and Garg, V. K., "Developing Flow in a Concentric Annulus," *Computer Methods in Applied Mechanics and Engineering*, Vol. 27, 1981, pp. 27–35.

8 Muller, D. E., "A Method for Solving Algebraic Equations Using an Automatic Computer," *Mathematical Tables and Other Aids to Computation*, Vol. 10, 1956, pp. 208–215.

9 Garg, V. K., "Improved Shooting Techniques for Linear Boundary Value Problems," *Computer Methods in Applied Mechanics and Engineering*, Vol. 22, 1980, pp. 87–99.

10 Shen, S. F., "Some Considerations on the Laminar Stability of Time-Dependent Basic Flows," *Journal of Aeronautical Sciences*, Vol. 28, 1961, pp. 397–404.

Free Out-of-Plane Vibration of Arcs

T. Irie,[1] G. Yamada,[1] and K. Tanaka[1]

Introduction

The vibration theory of beams has great importance in many engineering applications such as in the design of machines and structures. Therefore, a considerable number of papers are available on the out-of-plane vibration of arcs or curved beams, as well as straight beams. The fundamental equations of arcs or curved beams have been presented together with the solution to them in the book of Love [1]. Takahashi [2], Volterra and Morell [3, 4], Chang and Volterra [5], and Suzuki, Aida, and Takahashi [6] studied the free out-of-plane vibration of arcs and curved beams on the basis of the classical beam theory in which the rotatory inertia and shear deformation are not taken into account. Recently, Rao [7], Kirkhope [8], Suzuki and Takahashi [9], and Davis, Henshell, and Warburton [10] have analyzed rings and curved beams, and Irie, Yamada, and Takahashi [11, 12] have analytically studied arcs and curved beams of variable cross section. These recent studies have been based on the Timoshenko beam theory in which both of the rotatory inertia and shear deformation are taken into account.

This paper presents an analysis of the free out-of-plane vibration of elastic arcs governed by the Timoshenko beam theory and by the specialized theories in which either or both of the rotatory inertia and shear deformation are taken into account. For this purpose, the equations of out-of-plane vibration of an arc are written in a matrix differential equation of the first-order by use of the transfer matrix of the arc. The transfer matrix is conveniently expressed as the series type solution to the equation, and the frequency equations are derived by the boundary conditions. The natural frequencies (the eigenvalues of vibration) of some arcs are calculated numerically by the application of the method and are compared with one another, from which the effects of the rotatory inertia and shear deformation on the vibration are studied.

Theoretical Consideration

We consider a uniform arc of radius of curvature of the neutral axis R. With the angular coordinate denoted by θ and with the opening angle by α, the $X-$, $Y-$, and $Z-$ axes are taken in radial, transverse, and tangential directions, respectively, as shown in Fig. 1.

1. Timoshenko equations (TM).

On the assumption that the shear center of the cross section coincides with the centroid, the equation of translational motion of the arc is written as

$$\frac{dQ_y^*}{Rd\theta}+\rho A\omega^2 v^*=0 \tag{1}$$

and the equations of rotation are

$$-\frac{dM_x^*}{Rd\theta}+\frac{T^*}{R}-Q_y^*+\rho I_x\omega^2\varphi=0 \tag{2}$$

[1] Professor, Associate Professor, and Instructor, respectively, Department of Mechanical Engineering, Hokkaido University, Kita-13, Nishi-8, Kita-ku, Sapporo, 060 Japan

Manuscript received by ASME Applied Mechanics Division, May, 1981; final revision, September, 1981.

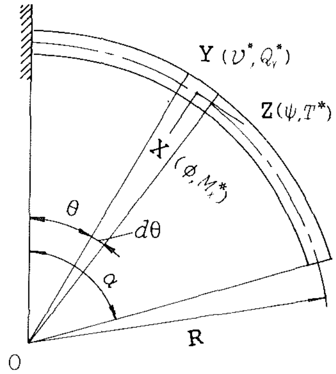

Fig. 1 Circular arc

$$\frac{dT^*}{Rd\theta} + \frac{M_x^*}{R} + \rho J_z \omega^2 \psi = 0 \tag{3}$$

where ρ is the mass per unit volume, A is the cross-sectional area, I_x and J_z, respectively, are the second moment and polar moment of area of the arc, and ω is the circular frequency. On the basis of the Timoshenko beam theory, the bending moment and torsional moment, respectively, are given by

$$M_x^* = \frac{EI_x}{R}\left(-\psi - \frac{d\varphi}{d\theta}\right), \quad T^* = \frac{GC_z}{R}\left(-\varphi + \frac{d\psi}{d\theta}\right) \tag{4, 5}$$

and the shearing force is

$$Q_y^* = \kappa GA\left(\varphi + \frac{dv^*}{Rd\theta}\right) \tag{6}$$

in terms of the transverse deflection v^*, the angle of rotation φ due to pure bending and the angle of torsion ψ. Here, the sets of variables (φ, M_x^*), (v^*, Q_y^*), and (ψ, T^*) are defined to be of positive sign in the $X-$, $Y-$ and $Z-$directions, respectively. The quantity E is Young's modulus, G is the shear modulus and C_z is the St. Venant torsional constant of the cross section. The parameter κ is the numerical factor depending on the shape of cross section, which is 0.85 for rectangular cross section and 0.89 for circular cross section for an arc of Poisson's ratio $\nu = 0.3$ [13].

The boundary conditions of the arc are written as $M_x^* = Q_y^* = T^* = 0$ at free end, $v^* = M_x^* = T^* = 0$ at hinged end, and $\varphi = v^* = \psi = 0$ at clamped end, respectively.

Equations (1)–(6) can be written in a matrix differential equation

$$\frac{d}{d\theta}\{Z(\theta)\} = [M]\{Z(\theta)\} \tag{7}$$

where

$$\{Z(\theta)\} = \{\varphi \;\; v \;\; \psi \, M_x Q_y T\}^T \tag{8}$$

and

$$[M] = \begin{bmatrix} 0 & 0 & -1 & -1 & 0 & 0 \\ -1 & 0 & 0 & 0 & \frac{E}{kG}\frac{1}{s_x^2} & 0 \\ 1 & 0 & 0 & 0 & 0 & \frac{1}{\mu} \\ \Lambda^2 \frac{1}{s_x^2} & 0 & 0 & 0 & -1 & 1 \\ 0 & -\Lambda^2 & 0 & 0 & 0 & 0 \\ 0 & 0 & -\Lambda^2\left(\frac{1}{s_x^2} + \frac{1}{s_y^2}\right) - 1 & & 0 & 0 \end{bmatrix} \tag{9}$$

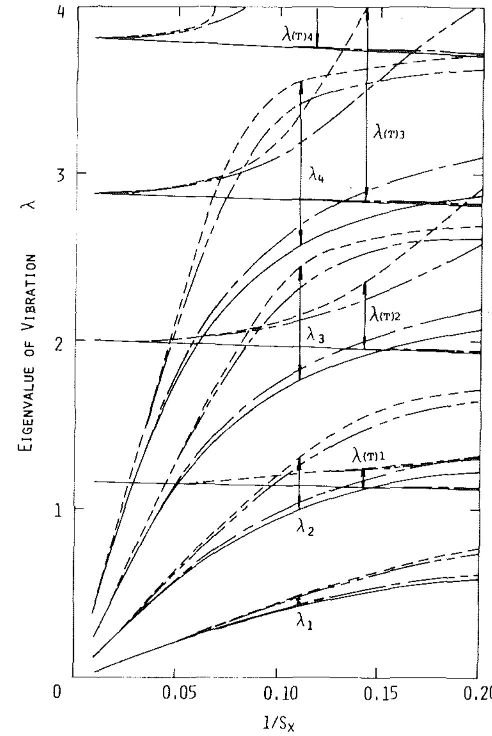

Fig. 2(a) Clamped-clamped arc

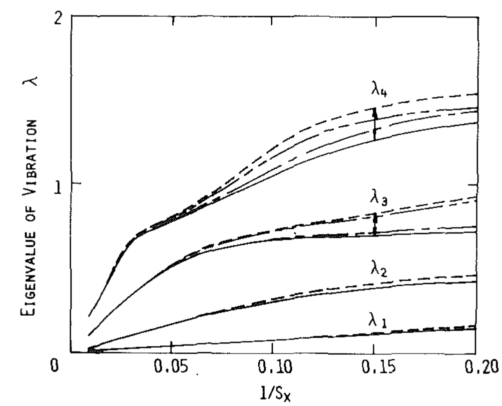

Fig. 2(b) Free-clamped arc

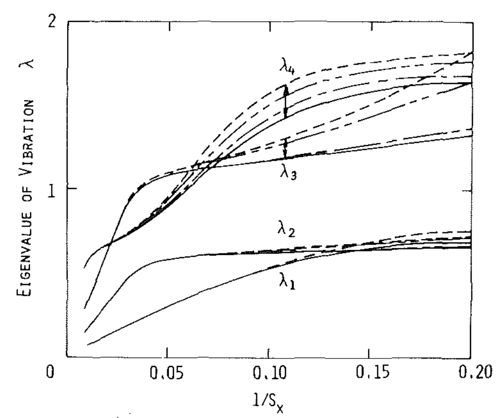

Fig. 2(c) Hinged-hinged arc

Fig. 2 Eigenvalues λ of out-of-plane vibration of arcs: $\nu = 0.3$, $\kappa = 0.89$, $\alpha = 120$ deg ——; (TM), — — —; (NI), — - — —; (NS), — — — — —; (BE)

Here, for simplicity of the analysis, the following dimensionless variables have been introduced:

$$v = \frac{1}{R} v^*, \quad (M_x, T) = \frac{R}{EI_x}(M_x^*, T^*), \quad Q_y = \frac{R^2}{EI_x} Q_y^* \tag{10}$$

$$s_x^2 = \frac{AR^2}{I_x}, \quad s_y^2 = \frac{AR^2}{I_y}, \quad \mu = \frac{GC_z}{EI_x} \tag{11}$$

and

$$\Lambda^2 = \frac{\rho A R^4 \omega^2}{EI_x} \tag{12}$$

The quantities s_x and s_y are the slenderness ratios, μ is the rigidity ratio of the arc and Λ denotes a frequency parameter.

2. Equations without rotatory inertia taken into account (NI).

When the rotatory inertia of the arc is not taken into account, the equations of vibration are also given by (7) in which the element M_{41} of the matrix $[M]$ is taken as zero.

3. Equations without shear deformation taken into account (NS).

In this case, the equations are given by (7) in which the element M_{25} is taken as zero.

4. Bernoulli-Euler equations (classical beam theory) (BE).

In the classical beam theory in which both of the rotatory inertia and shear deformation are not taken into account, the equations are given by (7) in which both of the elements M_{41} and M_{25} are taken as zero.

The state vector $\{Z(\theta)\}$ can be expressed as

$$\{Z(\theta)\} = [T(\theta)]\{Z(\theta)\} \quad (\theta > 0) \tag{13}$$

by using the transfer matrix $[T(\theta)]$ of the arc. The substitution of (13) into (7) yields

$$\frac{d}{d\theta}[T(\theta)] = [M][T(\theta)] \tag{14}$$

The transfer matrix can be conveniently expressed as the power series type solution to (14),

$$\begin{aligned}[T(\theta)] &= \exp([M]\theta) \\ &= [I] + \frac{1}{1!}[M]\theta + \frac{1}{2!}[M]^2\theta^2 + \ldots \\ &\qquad + \frac{1}{n!}[M]^n\theta^n + \ldots \end{aligned} \tag{15}$$

Numerical difficulty arises in the calculation of $[T(\theta)]$ given by (15) if the opening angle α is too large. However, it can be overcome by subdividing the arc into 5–10 small elements at most and calculating the transfer matrices for each element. The entire structure matrix is obtained by assembling the matrices of these elements.

The substitution of (13) into a given set of the boundary conditions yields the frequency equation of the arc with only the elements of the matrix $[T(\alpha)]$ necessary for the calculation.

Numerical Calculation and Discussion

Figure 2 shows the first four eigenvalues $\lambda = \Lambda/s_x$ of vibration of clamped-clamped, free-clamped, and hinged-hinged arcs with the angle $\alpha = 120$ deg obtained by the method. The eigenvalues λ of these vibrations become larger in that order for the TM-, NI-, NS-, and BE-vibrations according that the rotatory inertia or shear deformation is or is not taken into account. The eigenvalues of the NI-vibration are comparatively near to those of the TM-one, and the values

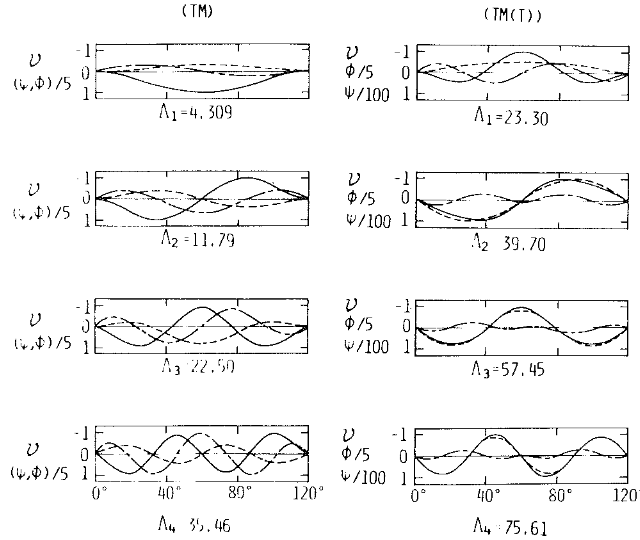

Fig. 3 Mode shapes of a clamped-clamped arc: $\nu = 0.3$, $\kappa = 0.89$, $s_x = s_y = 20$, $\alpha = 120$ deg. ——— ;v , — — — — ; ψ, ——— — ——— ; φ

of the NS-vibration are near to those of the BE-one. The difference among these eigenvalues is large in higher modes, and becomes larger with a decrease of the slenderness ratio s_x. Only in clamped-clamped arcs, torsion type vibrations [(T)-vibrations], with the frequencies $\lambda(T)_1$, $\lambda(T)_2$, . . . in which the angle of torsion is dominant arise besides usual bending type vibrations in which the transverse deflection is dominant, as seen in Fig. 3. The eigenvalues λ of the arcs become larger monotonically with a decrease of the ratio s_x, except for the TM(T)- and NI(T)-vibrations of clamped-clamped arcs. In general, the eigenvalues of free-clamped and hinged-hinged arcs are smaller than those of clamped-clamped arcs, and the eigenvalues of the fourth modes change in a wave-like manner with the variation of the ratio s_x.

References

1 Love, A. E. H., *A Treatise on the Mathematical Theory of Elasticity*, fourth ed., Dover Publications, New York, 1944.

2 Takahashi, S., "Vibration of a Circular Arc Bar (Perpendicular to its Plane)," *Bulletin of the JSME*, Vol. 6, No. 24, 1963, pp. 674–681.

3 Volterra, E., and Morell, J. D., "Lowest Natural Frequency of Elastic Arc for Vibrations outside the Plane of Initial Curvature," ASME JOURNAL OF APPLIED MECHANICS, Vol. 28, No. 4, 1961, pp. 624–627.

4 Volterra, E., and Morell, J. D., "Lowest Natural Frequencies of Elastic Hinged Arcs," *The Journal of the Acoustical Society of America*, Vol. 33, No. 12, 1961, pp. 1787–1790.

5 Chang. T. C., and Volterra, E., "Upper and Lower Bounds for Frequencies of Elastic Arcs," *The Journal of the Acoustical Society of America*, Vol. 46, No. 5 (Part 2), 1969, pp. 1165–1174.

6 Suzuki, K., Aida, H., and Takahashi, S., "Vibrations of Curved Bars Perpendicular to their Planes," *Bulletin of the JSME*, Vol. 21, No. 162, 1978, pp. 1685–1695.

7 Rao, S. S., "Effects of Transverse Shear and Rotatory Inertia on the Coupled Twist-Bending Vibrations of Circular Rings," *Journal of Sound and Vibration*, Vol. 16, No. 4, 1971, pp. 551–566.

8 Kirkhope, J., "Out-of-Plane Vibration of Thick Circular Ring," *ASCE Journal of the Engineering Mechanics Division*, Vol. 102, No. EM2, 1976, pp. 239–247.

9 Suzuki, K., and Takahashi, S., "Out-of-Plane Vibrations of Curved Bars Considering Shear Deformation and Rotatory Inertia," *Transactions of the Japan Society of Mechanical Engineers* (in Japanese), Vol. 46, No. 411, 1980, pp. 1319–1325.

10 Davis, R., Henshell, R. D., and Warburton, G. B., "Curved Beam Finite Elements for Coupled Bending and Torsional Vibration," *Earthquake Engineering and Structural Dynamics*, Vol. 1, No. 2, 1972, pp. 165–175.

11 Irie, T., Yamada, G., and Takahashi, I., "Out-of-Plane Vibration of Arc Bar of Variable Cross-Section," *Bulletin of the JSME*, Vol. 23, No. 181, 1980, pp. 1200–1205.

12 Irie, T., Yamada, G., and Takahashi, I., "The Steady State Out-of-Plane Response of a Timoshenko Curved Beam with Internal Damping," *Journal of Sound and Vibration*, Vol. 71, No. 1, 1980, pp. 145–156.

13 Cowper, G. R., "The Shear Coefficient in Timoshenko's Beam Theory," ASME JOURNAL OF APPLIED MECHANICS, Vol. 33, No. 2, 1966, pp. 335–340.

Effects of a Rigid Circular Inclusion on States of Twisting and Shearing in Shallow Spherical Shells[1]

E. Reissner[2] and J. E. Reissner[3]

Introduction

An earlier paper on the subject of this Note [1] has complemented known results for transverse twisting and inplane shearing of flat plates by asymptotic results for the corresponding problems of spherical shells, for the case of shells which are thin enough to fall within the scope of the asymptotic solution procedure. The present Note extends the work in [1] by reducing the problem of the determination of stress concentration factors to a problem of solving four simultaneous linear equations, with the coefficients in these four equations being certain combinations of Kelvin functions of the second order, and by then deducing numerical values of stress concentration factors in the entire range of values of the parameter $\mu = \sqrt{12(1-\nu^2)}a/\sqrt{Rh}$, involving wall thickness h and radius R of the shell, as well as Poisson's ratio ν and the radius a of the rigid inclusion.

Differential Equations and Boundary Conditions

As in [1] we consider a shallow spherical shell, with middle surface equation $z = H - r^2/2R$ relative to base plane polar coordinates r, θ, and with differential equations $RB\nabla^4 K - \nabla^2 w = 0$ and $RD\nabla^4 w + \nabla^2 K = 0$, where $D = Eh^3/12(1-\nu^2)$ and $B = 1/Eh$. To be obtained are solutions of the two differential equations in the domain $a \le r \le \infty$, with boundary conditions $w = w,_r = u_r = u_\theta = 0$ at the inner edge $r = a$ of the shell, and with conditions for $r \to \infty$ or the form $w \to Pr^2 \sin 2\theta/4(1-\nu)D$, $K \to 0$ for the problem of transverse twisting, and $w \to 0$, $K \to -1/2Sr^2 \sin 2\theta$ for the problem of membrane shearing.

In accordance with the analysis in [1], appropriate expressions for w and K are of the form $w = \phi + \chi$, $K = \psi - RD\nabla^2\chi$ where

$$\phi = -\frac{Pa^2 \sin 2\theta}{2(1-\nu)D}\left(\frac{1}{2}\frac{r^2}{a^2} + c_1\frac{a^2}{r^2}\right),$$
$$\psi = \frac{Pa^2 \sin 2\theta}{2(1-\nu)\sqrt{DB}}\left(c_2\frac{a^2}{r^2}\right), \tag{1}$$

$$\phi = Sa^2\sqrt{\frac{B}{D}}\sin 2\theta\left(c_1\frac{a^2}{r^2}\right),$$
$$\psi = -Sa^2 \sin 2\theta\left(\frac{1}{2}\frac{r^2}{a^2} + c_2\frac{a^2}{r^2}\right), \tag{2}$$

respectively, and

$$\chi = \left(\frac{-Pa^2}{2(1-\nu)D},\quad Sa^2\sqrt{\frac{B}{D}}\right)(c_3 ker_2 \lambda r + c_4 kei_2 \lambda r)\sin 2\theta, \tag{3}$$

respectively, where $\lambda^4 = 1/R^2BD$ and where the four constants of integration c_n are to be determined by means of the four stipulations that $\phi + \chi = 0$, $\phi,_r + \chi,_r = 0$, $(1-\nu)BR\psi,_r + \lambda^{-4}(\nabla^2\chi),_r - \int\phi dr = 0$, and $(1-\nu)BR\,\psi,_\theta + \lambda^{-4}(\nabla^2\chi),_\theta - r\int(\int\phi,_\theta dr)r^{-2}dr = 0$ for $r = a$.

Determination of the Stress Concentration Factors k_b and k_m.

The introduction of ϕ, ψ, and χ from (1)–(3) into the four boundary conditions for $r = a$ gives, with the help of certain transformations involving the Kelvin functions $ker_2\mu$ and $kei_2\mu$, where $\mu = \lambda a$, the following systems of four simultaneous equations for the four quantities c_1, c_2^+, c_3, c_4, where $c_2^+ = c_2$ for the problem of membrane shear, and $c_2^+ = c_2 + \mu^2/12(1+\nu)$ for the problem of transverse twisting.

c_1	c_2^+	c_3	c_4	TT	MS
1	0	$ker_2\mu$	$kei_2\mu$	$-\frac{1}{2}$	0
-2	0	$\mu ker_2'\mu$	$\mu kei_2'\mu$	-1	0
$\frac{1}{2}\frac{\mu^2}{1+\nu}$	4	$-kei_2\mu$	$ker_2\mu$	0	$-\frac{1}{2}$
$\frac{\mu^2}{1+\nu}$	-2	$-\mu kei_2'\mu$	$\mu ker_2'\mu$	0	-1

In contrast to the problems of the circular hole [2], where the concentrations of stress involve the edge values of the tangential resultants and couples $N_{\theta\theta}$ and $M_{\theta\theta}$, the problems of the rigid circular insert involve the edge values of the radial resultants and couples N_{rr} and M_{rr}, in the form [1]

$$k_b = \left(\frac{2}{P}, \frac{hS}{6}\right)M_{rr}\left(a, \frac{\pi}{4}\right),\ k_m = \left(\frac{h}{3P}, \frac{6}{hS}\right)N_{rr}\left(a, \frac{\pi}{4}\right). \tag{4}$$

The numerical determination of the values of k_b and k_m is facilitated by observing that the defining relations for M_{rr} and N_{rr}, in conjunction with the boundary conditions for $r = a$, imply that *when* $r = a$ *then*

$$M_{rr} = -D\nabla^2\chi,\ N_{rr} = \frac{\int(\int\phi,_{\theta\theta}dr)r^{-2}dr - r^{-1}\int\phi dr}{(1+\nu)BR}, \tag{5}$$

and therewith, for the problem of transverse twisting

$$k_b = -\frac{\mu^2}{1-\nu}(c_3 kei_2\mu - c_4 ker_2\mu),\ k_m = \frac{\mu^2(1+2c_1)}{\sqrt{12(1-\nu^2)}}, \tag{6}$$

and for the problem of membrane shear

$$k_b = \frac{\sqrt{3}\mu^2}{\sqrt{1-\nu^2}}(c_3 kei_2\mu - c_4 ker_2\mu),\ k_m = -\frac{\mu^2 c_1}{1+\nu}. \tag{7}$$

Description of Numerical Procedure

The values of the zero-order Kelvin functions and their derivatives for $\mu \le 100$ were obtained, as in [2], from IMSL subroutines [3]. For larger μ, these functions were obtained from the asymptotic expressions in Nosova [4].[4] While we obtained numerical results up to $\mu = 1000$ we have included only one of them, for $\mu = 200$, in Table 1. As in [2], the form of the system of equations to be solved for the unknowns c_i is such as to make the expressions for the stress-concentration factors in terms of the c_i invariant to any factor multiplying all Kelvin functions and derivatives appearing, and we deleted the factors $\exp(-\mu\sqrt{2})$ from the asymptotic expressions and so prevented underflow problems for larger μ. The second-order Kelvin functions and derivatives were obtained by the usual linear recursion relations [4, 5].

Discussion of Results

Tables 1 and 2 summarize the consequences of a numerical evaluation of equations (6) and (7) on the basis of a solution of the four by four systems of equations for the coefficients c_n. Our numerical calculations confirm the previously stated nature of the one-term asymptotic results for sufficiently large values of μ,[5] and they furthermore brought to our attention

[1] The work of the first-named author has been supported by the Office of Naval Research.

[2] Department of Applied Mechanics and Engineering Sciences, University of California, San Diego, La Jolla, Calif. 92093. Fellow ASME.

[3] Department of Physical Science, Pembroke State University, Pembroke, N.C. 28372.

Manuscript received by ASME Applied Mechanics Division, August, 1981.

[4] We found that equation (28) for kei' in [4] is in error by a factor of -1.

[5] After making a correction in the earlier formula for k_b for the problem of membrane shear, which should have been $k_b \approx \mu^2/2(1-\nu)$ in place of the expression $\mu^2/2(1+\nu)$ in equation (38) in [1].

Table 1 Stress concentration factors for tranverse twisting

μ	k_b			k_m		
	$\nu=0$	$\nu=1/3$	$\nu=1/2$	$\nu=0$	$\nu=1/3$	$\nu=1/2$
0	4.0	6.0	8.0	0.0	0.0	0.0
0.1	4.016	6.024	8.032	0.013	0.019	0.025
0.3	4.140	6.214	8.289	0.082	0.117	0.146
0.5	4.377	6.582	8.790	0.186	0.256	0.316
0.8	4.908	7.413	9.924	0.389	0.514	0.624
1.0	5.362	8.123	10.89	0.552	0.714	0.858
1.5	6.780	10.34	13.91	1.053	1.306	1.538
2.0	8.545	13.08	17.63	1.689	2.034	2.361
2.5	10.61	16.28	21.97	2.463	2.902	3.333
3.0	12.96	19.90	26.87	3.376	3.916	4.461
3.5	15.59	23.93	32.31	4.429	5.076	5.747
4.0	18.47	28.36	38.28	5.625	6.385	7.195
4.5	21.62	33.18	44.76	6.963	7.845	8.806
5.0	25.02	38.38	51.76	8.443	9.455	10.58
6.0	32.60	49.92	67.28	11.83	13.13	14.62
7.0	41.18	62.99	84.83	15.80	17.41	19.37
8.0	50.78	77.56	104.4	20.34	22.30	24.69
9.0	61.38	93.65	126.0	25.46	27.80	30.72
10.0	72.98	111.9	149.5	31.15	33.92	37.42
15.0	146.0	221.7	297.4	68.272	73.65	80.88
20.0	244.1	369.7	495.4	119.8	128.7	141.0
25.0	367.2	555.3	743.4	185.8	199.0	217.8
50.0	1358	2045	2733	732.2	780.4	857.6
75	2973	4473	5973	1639	1744	1902
100	5214	7838	10460	2907	3091	3369
200	20430	30680	40920	11590	12310	13340
Asympt.						
10	50.00	75.00	100.0	28.87	30.60	33.30
100	5000	7500	10000	2887	3060	3333
200	20000	30000	40000	11550	12240	13330

Table 2 Stress concentration factors for membrane shear

μ	k_b			k_m		
	$\nu=0$	$\nu=1/3$	$\nu=1/2$	$\nu=0$	$\nu=1/3$	$\nu=1/2$
0	0.0	0.0	0.0	1.333	1.500	1.600
0.1	0.028	0.045	0.058	1.332	1.497	1.596
0.3	0.144	0.228	0.297	1.321	1.479	1.574
0.5	0.275	0.434	0.563	1.305	1.453	1.541
0.8	0.451	0.713	0.920	1.280	1.411	1.488
1.0	0.561	0.870	1.119	1.263	1.385	1.454
1.5	0.769	1.176	1.502	1.227	1.327	1.383
2.0	0.919	1.391	1.766	1.198	1.282	1.329
2.5	1.030	1.547	1.955	1.175	1.247	1.287
3.0	1.116	1.665	2.096	1.156	1.219	1.254
3.5	1.183	1.756	2.205	1.140	1.197	1.227
4.0	1.238	1.829	2.291	1.128	1.179	1.206
4.5	1.282	1.888	2.360	1.118	1.164	1.188
5.0	1.320	1.937	2.418	1.109	1.151	1.173
8.0	1.457	2.114	2.622	1.075	1.102	1.116
10.0	1.508	2.171	2.694	1.062	1.084	1.096
20.0	1.615	2.309	2.844	1.033	1.044	1.052
50.0	1.684	2.392	2.937	1.014	1.018	1.021
100.0	1.708	2.421	2.968	1.007	1.009	1.010
Asympt 10.0 100.0 200.0	1.732	2.449	3.0	1.0	1.0	1.0

the fact that it should have been $k_b(0)=4/(1-\nu)$ for the problem of transverse twisting, and $k_m(0)=4/(3-\nu)$ for the problem of membrane shear, in place of the corresponding formulas with factors 2 and 8, respectively, in [1].

Additionally, our numerical calculations indicate, consistent with the results reported in [2], the existence of appreciable percentage differences between the exact numerical results and the consequences of the one-term asymptotic formulas, up to μ-values of about 100. They furthermore indicate that the surmise in [1] that these asymptotic results "apply when the parameter μ is sufficiently large, say larger than about 10, ... " must be considered as being in part too optimistic, considering the fact that when $\mu=10$ the differences between asymptotic and exact results are of the order of 10 percent for the problem membrane shear and for the values of k_m for transverse twisting, but that insofar as the values of k_b for this latter problem are concerned there remain differences of the order of 40 to 50 percent which decay to about 4 to 5 percent when $\mu=100$ and to about 2 percent when $\mu=200$.

References

1 Reissner, E., "On the Influence of a Rigid Circular Inclusion on the Twisting and Shearing of a Shallow Spherical Shell," ASME JOURNAL OF APPLIED MECHANICS, Vol. 47, 1980, 586–589.

2 Reissner, J. E., "Effects of a Circular Hole on States of Uniform Twisting and Shearing in Shallow Spherical Shells," ASME JOURNAL OF APPLIED MECHANICS, Vol. 48, Sept. 1981, pp. 674–676.

3 IMSL, The International Mathematical and Statistical Libraries, Inc. Houston, Texas, 1979.

4 Nosova, L. N., *Tables of Thomson Functions and Their First Derivatives*, Pergamon Press, New York, 1961.

5 Abramowitz, M., and Stegun, J. A., *Handbook of Mathematical Tables*, Dover Publications, New York, 1965.

Spatial Bifurcation of a Prestressed Rod

P. Vielsack[1]

Let us assume a straight elastic rod of length l with flexural rigidities A and B and torsional rigidity C. These and the following quantities refer to the principal system of flexure and torsion. The corresponding unit vectors $\mathbf{e}_1$ and $\mathbf{e}_2$ coincide with both principal axes of the cross section, and $\mathbf{e}_3$ is directed along the tangent to the center line of the rod (Fig. 1).

As an example for prestresses we imagine that the rod is heated partially on its surface, parallel to the center line. Then the rod tends to become a circular arch in the $\mathbf{e}_2-\mathbf{e}_3$ – plane with constant precurvature κ about the $\mathbf{e}_1$ – axis. Now, if temperature-induced strains are prevented there will again result an ideal straight rod this time, however, with prestresses. The intensity of these stresses is proportional to and thus can be measured by the magnitude of the precurvature κ of the unconstrained arch. If, in addition, external conservative compressing forces are applied at both ends of the rod, we are interested in the influence of the prestresses on buckling.

The starting point of the consideration are Kirchhoff's general equations in tensor notation [1]

$$\begin{aligned}\dot{\mathbf{F}}+\omega\times\mathbf{F}&=-\mathbf{q},\\ \dot{\mathbf{M}}+\omega\times\mathbf{M}+\mathbf{e}_3\times\mathbf{F}&=-\mathbf{m},\\ \mathbf{J}\cdot(\omega-\omega_0)&=\mathbf{M},\end{aligned}\tag{1}$$

where $\mathbf{q}$ or $\mathbf{m}$ are the external, continuous force vector or moment vector, respectively, $\mathbf{F}$ or $\mathbf{M}$ are the internal force vector or moment vector, respectively, ω_0 or ω are the rotational vector of the principal system of coordinates in the state without tension or the loaded state, respectively, and $\mathbf{J}$ is a diagonal tensor with elements A, B, and C. A dot indicates differentiation with respect to the arc length s of the center line. Considering only problems with vanishing continuous loadings

$$\begin{aligned}\mathbf{q}&=\mathbf{0},\\ \mathbf{m}&=\mathbf{0},\end{aligned}\tag{2}$$

we can specify boundary conditions for the components of the rotational vector ω. If s_0 is the arbitrarily chosen origin of the arc length s we get

$$\omega(s_0)=\omega(s_0+2l/n);\quad n=1,2\ldots\tag{3}$$

which corresponds to periodic solutions of the nonlinear system of equations (1). A global equilibrium condition yields

$$\mathbf{F}^2(s_0)=N^2\tag{4}$$

for the internal forces with $N=$const. As mentioned in the foregoing, we have to consider the special problem of a circular arch with

$$\omega_0=[\kappa,0,0]^T\tag{5}$$

[1] Professor of Mechanics, Department of Civil Engineering, University of Karlsruhe, Karlsruhe, Federal Republic of Germany.

Manuscript received by ASME Applied Mechanics Division, July 1981; final revision, September 1981.

Table 1 Stress concentration factors for tranverse twisting

μ	k_b			k_m		
	$\nu=0$	$\nu=1/3$	$\nu=1/2$	$\nu=0$	$\nu=1/3$	$\nu=1/2$
0	4.0	6.0	8.0	0.0	0.0	0.0
0.1	4.016	6.024	8.032	0.013	0.019	0.025
0.3	4.140	6.214	8.289	0.082	0.117	0.146
0.5	4.377	6.582	8.790	0.186	0.256	0.316
0.8	4.908	7.413	9.924	0.389	0.514	0.624
1.0	5.362	8.123	10.89	0.552	0.714	0.858
1.5	6.780	10.34	13.91	1.053	1.306	1.538
2.0	8.545	13.08	17.63	1.689	2.034	2.361
2.5	10.61	16.28	21.97	2.463	2.902	3.333
3.0	12.96	19.90	26.87	3.376	3.916	4.461
3.5	15.59	23.93	32.31	4.429	5.076	5.747
4.0	18.47	28.36	38.28	5.625	6.385	7.195
4.5	21.62	33.18	44.76	6.963	7.845	8.806
5.0	25.02	38.38	51.76	8.443	9.455	10.58
6.0	32.60	49.92	67.28	11.83	13.13	14.62
7.0	41.18	62.99	84.83	15.80	17.41	19.37
8.0	50.78	77.56	104.4	20.34	22.30	24.69
9.0	61.38	93.65	126.0	25.46	27.80	30.72
10.0	72.98	111.9	149.5	31.15	33.92	37.42
15.0	146.0	221.7	297.4	68.272	73.65	80.88
20.0	244.1	369.7	495.4	119.8	128.7	141.0
25.0	367.2	555.3	743.4	185.8	199.0	217.8
50.0	1358	2045	2733	732.2	780.4	857.6
75	2973	4473	5973	1639	1744	1902
100	5214	7838	10460	2907	3091	3369
200	20430	30680	40920	11590	12310	13340
Asympt.						
10	50.00	75.00	100.0	28.87	30.60	33.30
100	5000	7500	10000	2887	3060	3333
200	20000	30000	40000	11550	12240	13330

Table 2 Stress concentration factors for membrane shear

μ	k_b			k_m		
	$\nu=0$	$\nu=1/3$	$\nu=1/2$	$\nu=0$	$\nu=1/3$	$\nu=1/2$
0	0.0	0.0	0.0	1.333	1.500	1.600
0.1	0.028	0.045	0.058	1.332	1.497	1.596
0.3	0.144	0.228	0.297	1.321	1.479	1.574
0.5	0.275	0.434	0.563	1.305	1.453	1.541
0.8	0.451	0.713	0.920	1.280	1.411	1.488
1.0	0.561	0.870	1.119	1.263	1.385	1.454
1.5	0.769	1.176	1.502	1.227	1.327	1.383
2.0	0.919	1.391	1.766	1.198	1.282	1.329
2.5	1.030	1.547	1.955	1.175	1.247	1.287
3.0	1.116	1.665	2.096	1.156	1.219	1.254
3.5	1.183	1.756	2.205	1.140	1.197	1.227
4.0	1.238	1.829	2.291	1.128	1.179	1.206
4.5	1.282	1.888	2.360	1.118	1.164	1.188
5.0	1.320	1.937	2.418	1.109	1.151	1.173
8.0	1.457	2.114	2.622	1.075	1.102	1.116
10.0	1.508	2.171	2.694	1.062	1.084	1.096
20.0	1.615	2.309	2.844	1.033	1.044	1.052
50.0	1.684	2.392	2.937	1.014	1.018	1.021
100.0	1.708	2.421	2.968	1.007	1.009	1.010
Asympt 10.0 100.0 200.0	1.732	2.449	3.0	1.0	1.0	1.0

the fact that it should have been $k_b(0)=4/(1-\nu)$ for the problem of transverse twisting, and $k_m(0)=4/(3-\nu)$ for the problem of membrane shear, in place of the corresponding formulas with factors 2 and 8, respectively, in [1].

Additionally, our numerical calculations indicate, consistent with the results reported in [2], the existence of appreciable percentage differences between the exact numerical results and the consequences of the one-term asymptotic formulas, up to μ-values of about 100. They furthermore indicate that the surmise in [1] that these asymptotic results "apply when the parameter μ is sufficiently large, say larger than about 10, ... " must be considered as being in part too optimistic, considering the fact that when $\mu=10$ the differences between asymptotic and exact results are of the order of 10 percent for the problem membrane shear and for the values of k_m for transverse twisting, but that insofar as the values of k_b for this latter problem are concerned there remain differences of the order of 40 to 50 percent which decay to about 4 to 5 percent when $\mu=100$ and to about 2 percent when $\mu=200$.

References

1 Reissner, E., "On the Influence of a Rigid Circular Inclusion on the Twisting and Shearing of a Shallow Spherical Shell," ASME Journal of Applied Mechanics, Vol. 47, 1980, 586–589.

2 Reissner, J. E., "Effects of a Circular Hole on States of Uniform Twisting and Shearing in Shallow Spherical Shells," ASME Journal of Applied Mechanics, Vol. 48, Sept. 1981, pp. 674–676.

3 IMSL, The International Mathematical and Statistical Libraries, Inc. Houston, Texas, 1979.

4 Nosova, L. N., *Tables of Thomson Functions and Their First Derivatives*, Pergamon Press, New York, 1961.

5 Abramowitz, M., and Stegun, J. A., *Handbook of Mathematical Tables*, Dover Publications, New York, 1965.

Spatial Bifurcation of a Prestressed Rod

P. Vielsack[1]

Let us assume a straight elastic rod of length l with flexural rigidities A and B and torsional rigidity C. These and the following quantities refer to the principal system of flexure and torsion. The corresponding unit vectors $\mathbf{e}_1$ and $\mathbf{e}_2$ coincide with both principal axes of the cross section, and $\mathbf{e}_3$ is directed along the tangent to the center line of the rod (Fig. 1).

As an example for prestresses we imagine that the rod is heated partially on its surface, parallel to the center line. Then the rod tends to become a circular arch in the $\mathbf{e}_2-\mathbf{e}_3-$plane with constant precurvature κ about the $\mathbf{e}_1-$axis. Now, if temperature-induced strains are prevented there will again result an ideal straight rod this time, however, with prestresses. The intensity of these stresses is proportional to and thus can be measured by the magnitude of the precurvature κ of the unconstrained arch. If, in addition, external conservative compressing forces are applied at both ends of the rod, we are interested in the influence of the prestresses on buckling.

The starting point of the consideration are Kirchhoff's general equations in tensor notation [1]

$$\begin{aligned}\dot{\mathbf{F}}+\boldsymbol{\omega}\times\mathbf{F}&=-\mathbf{q},\\ \dot{\mathbf{M}}+\boldsymbol{\omega}\times\mathbf{M}+\mathbf{e}_3\times\mathbf{F}&=-\mathbf{m},\\ \mathbf{J}\cdot(\boldsymbol{\omega}-\boldsymbol{\omega}_0)&=\mathbf{M},\end{aligned}\tag{1}$$

where $\mathbf{q}$ or $\mathbf{m}$ are the external, continuous force vector or moment vector, respectively, $\mathbf{F}$ or $\mathbf{M}$ are the internal force vector or moment vector, respectively, ω_0 or ω are the rotational vector of the principal system of coordinates in the state without tension or the loaded state, respectively, and $\mathbf{J}$ is a diagonal tensor with elements A, B, and C. A dot indicates differentiation with respect to the arc length s of the center line. Considering only problems with vanishing continuous loadings

$$\begin{aligned}\mathbf{q}&=\mathbf{0},\\ \mathbf{m}&=\mathbf{0},\end{aligned}\tag{2}$$

we can specify boundary conditions for the components of the rotational vector $\boldsymbol{\omega}$. If s_0 is the arbitrarily chosen origin of the arc length s we get

$$\omega(s_0)=\omega(s_0+2l/n);\quad n=1,2\ldots\tag{3}$$

which corresponds to periodic solutions of the nonlinear system of equations (1). A global equilibrium condition yields

$$\mathbf{F}^2(s_0)=N^2\tag{4}$$

for the internal forces with $N=\text{const}$. As mentioned in the foregoing, we have to consider the special problem of a circular arch with

$$\omega_0=[\kappa,0,0]^T\tag{5}$$

[1] Professor of Mechanics, Department of Civil Engineering, University of Karlsruhe, Karlsruhe, Federal Republic of Germany.

Manuscript received by ASME Applied Mechanics Division, July 1981; final revision, September 1981.

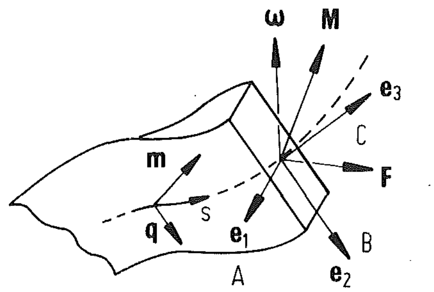

Fig. 1 Deformed rod

Once equation (5) is specified, the nonlinear boundary value problem is analogous to the problem of stationary periodic motions of a heavy gyrostat [2]. This is a system of two rigid bodies, the so-called carrier, and a symmetric rotor fixed on the carrier. This system is suspended as a pendulum at a point on one principal axis of inertia of the total system.

In the particular case characterized by (5), we consider a heavy gyrostat in which the rotor axis is directed along the principal axis of inertia mentioned in the foregoing. Then the following special and simple motion exists: the carrier does not move at all and the rotor rotates with constant angular velocity, its axis being in a vertical position. Using the analogy, we can therefore construct as a solution of the rod problem,

$$\begin{aligned} \mathbf{M} &= [-\kappa A, 0, 0]^T, \\ \omega &= [0,0,0]^T, \\ \mathbf{F} &= [0,0,-N]^T. \end{aligned} \tag{6}$$

Equation (6) describes the special state of equilibrium of an originally circular arch bent by moments $M_1 = -\kappa A$ into a straight form and compressed by forces $F_3 = -N$. To investigate the uniqueness of this configuration we apply in the sense of bifurcation theory small perturbations to each quantity in question. Thus it is evident that bifurcation theory in elasticity is analogous to the theory of small oscillations in the field of kinetics. Inserting the new state of equilibrium

$$\begin{aligned} \mathbf{M} &= [-\kappa A + \bar{M}_1, \bar{M}_2, \bar{M}_3]^T, \\ \omega &= [\bar{\omega}_1, \bar{\omega}_2, \bar{\omega}_3]^T, \\ \mathbf{F} &= [\bar{F}_1, \bar{F}_2, -N+\bar{F}_3]^T \end{aligned} \tag{7}$$

into the boundary value problem, equating only linear terms in all perturbations, and eliminating the lateral forces $\bar{F}_1$ and $\bar{F}_2$, and the torsion $\bar{\omega}_3$ we get three linear decoupled boundary value problems in scalar notation. The first one is

$$\dot{\bar{F}}_3 = 0; \quad \bar{F}_3(s_0) = 0. \tag{8}$$

This confirms the well-known assumption of buckling theory, that the normal forces do not change at the bifurcation point. The second one is the classical eigenvalue problem

$$A\ddot{\bar{\omega}}_1 + N\bar{\omega}_1 = 0; \quad \bar{\omega}_1(0) = \bar{\omega}_1(l) = 0 \tag{9}$$

for plane buckling. This is analogous to a small pendulum motion of the carrier. It confirms the well-known analogy between the plane motion of a pendulum and the plane buckling of a straight and untwisted rod. If we choose the second Euler-case the critical load is

$$N_1 = A\left(\frac{\pi}{l}\right)^2. \tag{10}$$

Evidently, plane buckling is not influenced by the prestresses considered. The third one is also an eigenvalue problem

$$B\ddot{\bar{\omega}}_2 + \left(N + \frac{(A\kappa)^2}{C}\right)\bar{\omega}_2 = 0; \quad \bar{\omega}_2(0) = \bar{\omega}_2(l) = 0, \tag{11}$$

which describes lateral buckling. In the sense of the analogy we get a precessional motion of the carrier, i.e., a spatial motion of the rotor axis with constant angular velocity on a circular cone about the vertical.

The buckling phenomenon of the rod can best be discussed for a rod with equal flexural rigidities $A = B$. As an example we take a rod with circular cross section, for which the ratio can be given easily: $A/C = 1 + \nu$ (ν = Poisson's constant). Such a rod without prestresses is free to buckle in any direction normal to its center line. In the case considered, however, buckling always occurs in the direction normal to the original plane of the arch combined with a torsional movement of the cross sections. If we suppose, for instance, fork bearings in (11), we arrive at a spatial buckling load

$$N_2 = N_1\left(1 - (1+\nu)\left(\frac{\kappa l}{\pi}\right)^2\right). \tag{12}$$

For nonvanishing prestresses we thus have a smaller critical load than Euler's.

References

1 Vielsack, P., "The Analogy Between Elastic Rods and Rigid Body Motions, Part I: Nonlinear Theory", *SM-Archives*, Vol. 4, 1979 pp. 347–377.

2 Wittenburg, J., *Dynamics of Systems of Rigid Bodies*, Stuttgart, Teubner, 1977.

Two-Dimensional Theory of Incompressible Flow Over Inlets

M. K. Huang[1]

On the basis of the assumption of incompressible inviscid fluid, a linearized solution has been derived for the two-dimensional flow over an inlet of general form. The theory can be used to estimate the external drag of the inlets with sharp lips at subsonic speeds.

1 Introduction

To reduce the wave drag at supersonic speeds, the air inlet with sharp lips is often used on a supersonic aircraft. It is well known that the external drag of the inlet consists of the pressure drag and the additive drag in inviscid flow. If there is no separation and no shock wave in the flow, it can be shown that the external drag is just equal to zero (See [1, 2]). This statement applies to the inlet of round lip without flow separation. For the inlet with sharp lip, however, the flow separation may happen and the external drag must be increased because of the loss of the suction at the lip. In view of the fact that the pressure drag including the lip suction just cancels the additive drag in subsonic flow, the magnitude of the external drag has to be equal to that of the lost suction at the lip, i.e.,

$$D_e = X_s \tag{1}$$

To my knowledge, there has been no simple method to estimate the suction for an inlet with general form. This paper will give an analytical solution to this problem for two-dimensional inlets with very general form in incompressible flow. For high subsonic or supersonic oncoming flow, the related problem is quite difficult because of the existence of the transonic flow field. One cannot solve it in analytical form. Some numerical methods (See [3–5]) have been developed for this purpose.

[1] Visiting Scholar, Department of Aerospace Engineering Sciences, University of Colorado, Boulder, Colo. 80309; on leave from Nanjing Aeronautical Institute, China.

Manuscript received by ASME Applied Mechanics Division, February 1981; final revision, August, 1981.

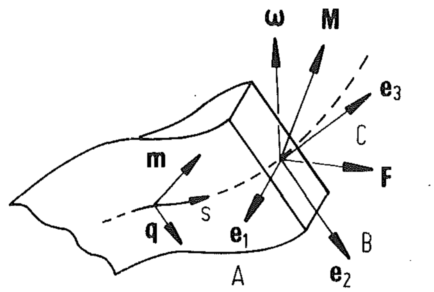

Fig. 1 Deformed rod

Once equation (5) is specified, the nonlinear boundary value problem is analogous to the problem of stationary periodic motions of a heavy gyrostat [2]. This is a system of two rigid bodies, the so-called carrier, and a symmetric rotor fixed on the carrier. This system is suspended as a pendulum at a point on one principal axis of inertia of the total system.

In the particular case characterized by (5), we consider a heavy gyrostat in which the rotor axis is directed along the principal axis of inertia mentioned in the foregoing. Then the following special and simple motion exists: the carrier does not move at all and the rotor rotates with constant angular velocity, its axis being in a vertical position. Using the analogy, we can therefore construct as a solution of the rod problem,

$$\begin{aligned}\mathbf{M} &= [-\kappa A, 0, 0]^T,\\ \omega &= [0,0,0]^T,\\ \mathbf{F} &= [0,0,-N]^T.\end{aligned} \tag{6}$$

Equation (6) describes the special state of equilibrium of an originally circular arch bent by moments $M_1 = -\kappa A$ into a straight form and compressed by forces $F_3 = -N$. To investigate the uniqueness of this configuration we apply in the sense of bifurcation theory small perturbations to each quantity in question. Thus it is evident that bifurcation theory in elasticity is analogous to the theory of small oscillations in the field of kinetics. Inserting the new state of equilibrium

$$\begin{aligned}\mathbf{M} &= [-\kappa A + \bar{M}_1, \bar{M}_2, \bar{M}_3]^T,\\ \omega &= [\bar{\omega}_1, \bar{\omega}_2, \bar{\omega}_3]^T,\\ \mathbf{F} &= [\bar{F}_1, \bar{F}_2, -N + \bar{F}_3]^T\end{aligned} \tag{7}$$

into the boundary value problem, equating only linear terms in all perturbations, and eliminating the lateral forces $\bar{F}_1$ and $\bar{F}_2$, and the torsion $\bar{\omega}_3$ we get three linear decoupled boundary value problems in scalar notation. The first one is

$$\dot{\bar{F}}_3 = 0; \quad \bar{F}_3(s_0) = 0. \tag{8}$$

This confirms the well-known assumption of buckling theory, that the normal forces do not change at the bifurcation point. The second one is the classical eigenvalue problem

$$A\ddot{\bar{\omega}}_1 + N\bar{\omega}_1 = 0; \quad \bar{\omega}_1(0) = \bar{\omega}_1(l) = 0 \tag{9}$$

for plane buckling. This is analogous to a small pendulum motion of the carrier. It confirms the well-known analogy between the plane motion of a pendulum and the plane buckling of a straight and untwisted rod. If we choose the second Euler-case the critical load is

$$N_1 = A\left(\frac{\pi}{l}\right)^2. \tag{10}$$

Evidently, plane buckling is not influenced by the prestresses considered. The third one is also an eigenvalue problem

$$B\ddot{\bar{\omega}}_2 + \left(N + \frac{(A\kappa)^2}{C}\right)\bar{\omega}_2 = 0; \quad \bar{\omega}_2(0) = \bar{\omega}_2(l) = 0, \tag{11}$$

which describes lateral buckling. In the sense of the analogy we get a precessional motion of the carrier, i.e., a spatial motion of the rotor axis with constant angular velocity on a circular cone about the vertical.

The buckling phenomenon of the rod can best be discussed for a rod with equal flexural rigidities $A = B$. As an example we take a rod with circular cross section, for which the ratio can be given easily: $A/C = 1 + \nu$ (ν = Poisson's constant). Such a rod without prestresses is free to buckle in any direction normal to its center line. In the case considered, however, buckling always occurs in the direction normal to the original plane of the arch combined with a torsional movement of the cross sections. If we suppose, for instance, fork bearings in (11), we arrive at a spatial buckling load

$$N_2 = N_1\left(1 - (1+\nu)\left(\frac{\kappa l}{\pi}\right)^2\right). \tag{12}$$

For nonvanishing prestresses we thus have a smaller critical load than Euler's.

References

1 Vielsack, P., "The Analogy Between Elastic Rods and Rigid Body Motions, Part I: Nonlinear Theory", *SM-Archives*, Vol. 4, 1979 pp. 347–377.

2 Wittenburg, J., *Dynamics of Systems of Rigid Bodies*, Stuttgart, Teubner, 1977.

Two-Dimensional Theory of Incompressible Flow Over Inlets

M. K. Huang[1]

On the basis of the assumption of incompressible inviscid fluid, a linearized solution has been derived for the two-dimensional flow over an inlet of general form. The theory can be used to estimate the external drag of the inlets with sharp lips at subsonic speeds.

1 Introduction

To reduce the wave drag at supersonic speeds, the air inlet with sharp lips is often used on a supersonic aircraft. It is well known that the external drag of the inlet consists of the pressure drag and the additive drag in inviscid flow. If there is no separation and no shock wave in the flow, it can be shown that the external drag is just equal to zero (See [1, 2]). This statement applies to the inlet of round lip without flow separation. For the inlet with sharp lip, however, the flow separation may happen and the external drag must be increased because of the loss of the suction at the lip. In view of the fact that the pressure drag including the lip suction just cancels the additive drag in subsonic flow, the magnitude of the external drag has to be equal to that of the lost suction at the lip, i.e.,

$$D_e = X_s \tag{1}$$

To my knowledge, there has been no simple method to estimate the suction for an inlet with general form. This paper will give an analytical solution to this problem for two-dimensional inlets with very general form in incompressible flow. For high subsonic or supersonic oncoming flow, the related problem is quite difficult because of the existence of the transonic flow field. One cannot solve it in analytical form. Some numerical methods (See [3–5]) have been developed for this purpose.

[1] Visiting Scholar, Department of Aerospace Engineering Sciences, University of Colorado, Boulder, Colo. 80309; on leave from Nanjing Aeronautical Institute, China.

Manuscript received by ASME Applied Mechanics Division, February 1981; final revision, August, 1981.

2 Theory

We consider a two-dimensional inlet with a ramp as shown in Fig. 1, where U_o is oncoming flow velocity, U_i the downstream velocity inside the inlet, and BL, CK, and FK are the straight lines parallel to the axis x. Assume that the flow is incompressible, inviscid, and irrotational so that the complex variable method can be used. The flow field in physical plane can be considered as the superposition of the basic flow with uniform speed U_o and the perturbation with the velocity components u and v in the directions of x and y, respectively. Under the assumption of small perturbation, the boundary conditions can be applied on the cut $LBACK$ which is parallel to the x axis and on the x axis itself, as shown in Fig. 2(a). The boundary conditions can be formulated as

$$\left.\begin{aligned} &v=U_o\left(\frac{dy}{dx}\right)_{\text{cowl}} && \text{on } BAC,\\ &v=U_o\left(\frac{dy}{dx}\right)_{\text{ramp}} && \text{on } EF,\\ \text{and}\quad &v=0 && \text{on } CKF \text{ and } ELB. \end{aligned}\right\} \qquad (2)$$

We denote the complex velocity of the perturbation by $\bar{W} = u-iv$. To determine $\bar{W}$, we first use the transformation (See [6])

$$z-ih=[h/(a+k)\pi]\{\zeta-a-(a+k)\log[(\zeta+k)/(a+k)]\} \qquad (3)$$

to map the upper half of the physical plane $z=x+iy$ with cut LAK into the upper half of the plane $\zeta=\xi+i\eta$, as shown in Fig. 2(b). Here a and k are determined by

$$\left.\begin{aligned} &(a+k)\log[(k+1)/(k-1)]=2\\ &c=[h/(a+k)\pi]\{1-a-(a+k)\log[(1+k)/(a+k)]\} \end{aligned}\right\} \qquad (4)$$

where c is defined in Fig. 1. According to the calculation, the constant k has the value very close to 1. For instance, $k=1.0001$ and 1.000001 correspond to $c/h=2.10$ and 3.45, respectively. Then we only need to solve the boundary value problem of analytical functions on the half plane. The solution can be given by the Schwartz's formula as

$$\bar{W}=-\frac{1}{\pi}\int_{-1}^{1}\frac{U_o\left(\dfrac{dy}{dx}\right)_{\text{cowl}}}{t-\zeta}\,dt-\frac{1}{\pi}\int_{e}^{f}\frac{U_o\left(\dfrac{dy}{dx}\right)_{\text{ramp}}}{t-\zeta}\times dt+\frac{N_o}{\pi(\zeta-a)} \qquad (5)$$

where the last term on the right-hand side is a doublet which simulates the singularity of square root at the lip and does not violate the boundary conditions that the first two terms have already satisfied.

To determine the strength of the singularity N_o, we take a circle with the radius tended to infinity as a control surface in the physical plane which has been extended symmetrically into the lower half, as shown in Fig. 3. The mass conservation law gives the identity

$$\int_{S_1}\mathbf{v}\cdot\mathbf{n}\,ds=2[U_iH+(U_o-U_i)h_1] \qquad (6)$$

where $\mathbf{v}$ is the vector of the perturbation velocity and $\mathbf{n}$ the unit outward normal to the control surface S_1. Equation (6) shows that there exists a source at infinity of the physical plane with the rate of volume flux equal to $2[U_iH+(U_o-U_i)h_1]$, so that the expansion of $\bar{W}$ should contain the term

$$[U_iH+(U_o-U_i)h_1]/(\pi z) \qquad (7)$$

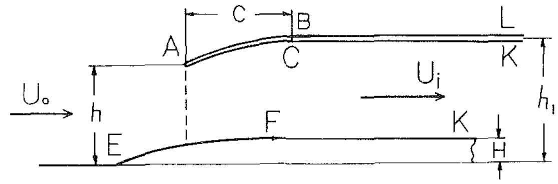

Fig. 1 Typical two-dimensional inlet

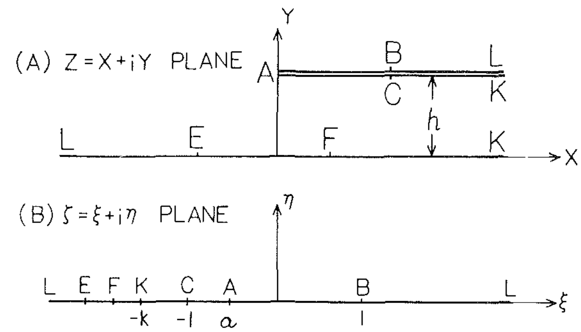

Fig. 2 Physical plane $z=x+iy$ and transformation plane $\zeta=\xi+i\eta$

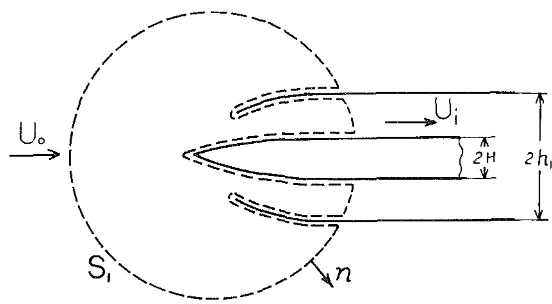

Fig. 3 Sketch of the control surface

After expanding the expression (5) and comparing with the expression (7), we obtain

$$N_o=\pi(a+k)U_o\left[\left(1-\frac{U_i}{U_o}\right)\frac{h_1}{h}-\frac{1}{2\pi}\left(\log\frac{k+1}{k-1}\right)\left(\int_{-1}^{1}\left(\frac{dy}{dx}\right)_{\text{cowl}}dt+\int_{e}^{f}\left(\frac{dy}{dx}\right)_{\text{ramp}}dt\right)+\frac{U_iH}{U_oh}\right] \qquad (8)$$

At the lip of the inlet, we have the approximation

$$\frac{\bar{W}}{U_o}\sim\frac{h^{1/2}N_o}{(2\pi)^{1/2}\pi(a+k)U_o(z-ih)^{1/2}} \qquad (9)$$

This can be used to determine the strength of the singularity at the lip. With the same method as that for the calculation of the leading edge suction in thin wing theory [8], the suction coefficient can be obtained as

$$C_s=X_s/(q_oA_c)=(m_s-m)^2 \qquad (10)$$

where $A_c=h$ represents the capture area of the inlet, q_o is the dynamic pressure of free stream; m, the mass-flow ratio of the inlet, is defined by

$$m=[U_i(h_1-H)]/(U_oh) \qquad (11)$$

and m_s is given by

$$m_s=\frac{h_1}{h}-\frac{1}{2\pi}\log\left(\frac{k+1}{k-1}\right)\left[\int_{-1}^{1}\left(\frac{dy}{dx}\right)_{\text{cowl}}dt+\int_{e}^{f}\left(\frac{dy}{dx}\right)_{\text{ramp}}dt\right] \qquad (12)$$

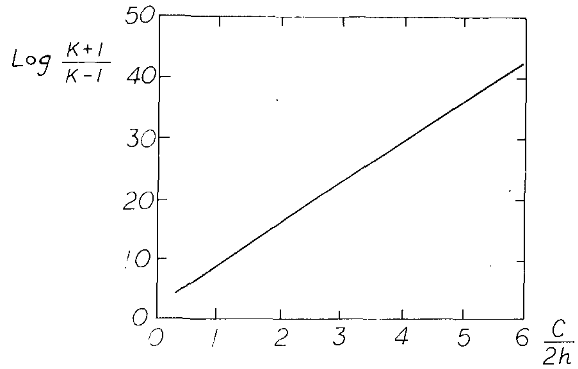

Fig. 4 log $[(k+1)/(k-1)]$ as a function of $c/(2h)$

Here m_s can be considered as such mass-flow ratio that there exists smooth flow without separation at the sharp lip.

The relationship between log $[(k+1)/(k-1)]$ and $c/(2h)$ is given in Fig. 4, and the integral $\int_{-1}^{1} (dy/dx)_{\text{cowl}}\, dt$ as a function of $c/(2h)$ is given in Fig. 5 for the cowls with straight and parabolic shapes. For the calculation of the second integral in equation (12), we need to know the relationship between x and t on the ramp, which is given in Fig. 6.

3 Applicaton and Discussion

As the first example we consider the simplest case with $h=h_1$ and $H=0$. We have $m_s=1$ and

$$C_s=(1-m)^2 \tag{13}$$

This is exactly the same as that for Pitot-inlet with constant section at low speeds (See [7]). The subsonic version for such an inlet has been given in [2]. We can see from the comparison between equations (10) and (13) that the expression of C_s in terms of m for general inlets can be obtained from equation (13) by $(1+m-m_s)$ insteady of m. This approach is exact in our approximation for incompressible flow and could be considered as a reasonable approximation for subsonic flow.

The second example is shown in Fig. 7. With the use of Figs. 4–6 the computation result is shown by the solid line in Fig. 7. Here the dashed line shows the result for the ramp surface of all 5 deg.

In conclusion, it should be noted that:

1. What the inside wall of an inlet corresponds to is only a little part of the real axis in ζ plane, so that there is only a little contribution of the inside shape to the two integrals in equation (12). Thus, the inside shape of the inlet has only a little effect on the results.

2. The theory is based on the assumption of small perturbation. One might suppose that the results obtained would be applicable only to the case that U_i is close to U_o. However, in view of the previous conclusion, and the fact that the exact mass conservation law was used in equation (6), the results should also apply to the case of rather small mass-flow ratio, which has been proved for the first example.

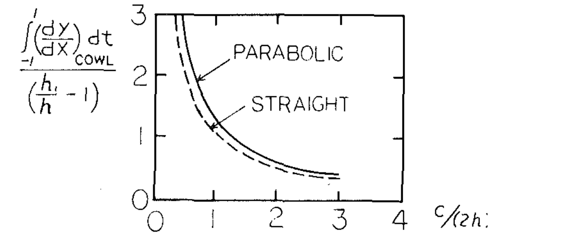

Fig. 5 The integral $\int_{-1}^{1} (dy/dx)_{\text{cowl}}\, dt$ for the cowls with parabolic and straight shapes

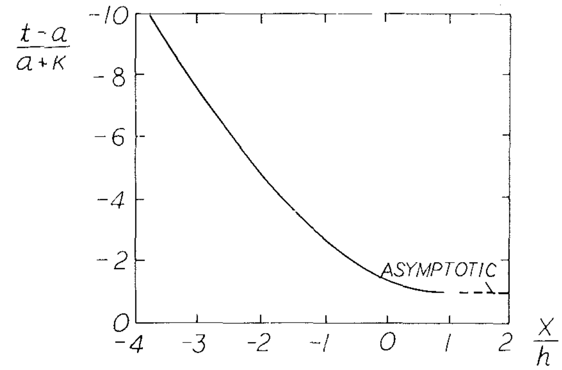

Fig. 6 $(t-a)/(a+k)$ as a function of x/h

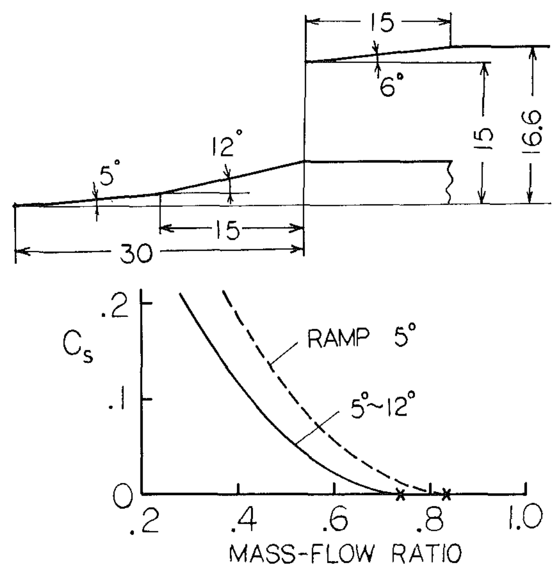

Fig. 7 Examples

References

1 Donovan, A. F., and Lawrence, H. R., "Aerodynamic Components of Aircraft at High Speeds," *High Speed Aerodynamics and Jet Propulsion*, Vol. VII, Section D, 1957.

2 Fradenburgh, E. A., and Wyatt, D. D., "Theoretical Performance Characteristics of Sharp-Lip Inlets at Subsonic Speeds," NACA Report 1193, 1954.

3 Bansod, P., "Supersonic Flow About Ducted Bodies With Subsonic Internal Boundaries," *J. of Aircraft*, Vol. 12, No. 6, 1975, pp. 531–538.

4 Reyhner, T. A., "Cartesian Mesh Solution for Axisymmetric Transonic Potential Flow Around Inlets," *AIAA Journal*, Vol. 15, No. 5, 1977, pp. 624–631.

5 Caughey, D. A., and Jameson, A., "Accelerated Iterative Calculation of Transonic Nacelle Flow Fields," *AIAA Journal*, Vol. 15, No. 10, 1977, pp. 1474–1480.

6 Lissaman, P. B. S., "A Linear Theory for the Jet Flap in Ground Effect," *AIAA Journal*, Vol. 6, No. 7, 1968, pp. 1356–1362.

7 Kuchemann, D., and Weber, J., *Aerodynamics of Propulsion*, McGraw-Hill, 1953.

8 Sears, W. R., "General Theory of High Speed Aerodynamics," *High Speed Aerodynamics and Jet Propulsion*, Vol. VI, Section D, 1954.

Mode III Dynamic Stress Intensity for Two Colinear Cracks at a Bimaterial Interface

R. L. Ryan[1] and S. Mall[1]

Introduction

The harmonic stress intensity produced by a pair of colinear

[1] Department of Mechanical Engineering, University of Maine, Orono, Me., 04469.

Manuscript received by ASME Applied Mechanics Division, September, 1981; final revision, November, 1981.

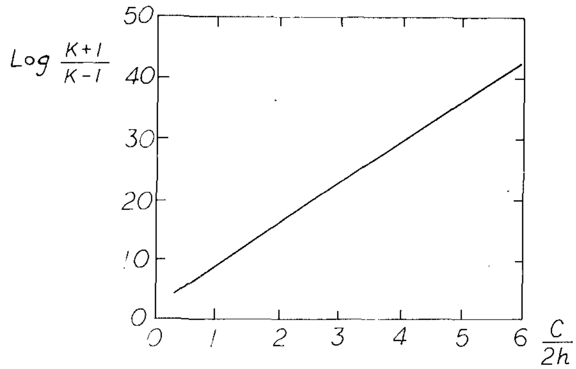

Fig. 4 log $[(k+1)/(k-1)]$ as a function of $c/(2h)$

Here m_s can be considered as such mass-flow ratio that there exists smooth flow without separation at the sharp lip.

The relationship between log $[(k+1)/(k-1)]$ and $c/(2h)$ is given in Fig. 4, and the integral $\int_{-1}^{1} (dy/dx)_{\text{cowl}}\, dt$ as a function of $c/(2h)$ is given in Fig. 5 for the cowls with straight and parabolic shapes. For the calculation of the second integral in equation (12), we need to know the relationship between x and t on the ramp, which is given in Fig. 6.

3 Applicaton and Discussion

As the first example we consider the simplest case with $h = h_1$ and $H = 0$. We have $m_s = 1$ and

$$C_s = (1-m)^2 \tag{13}$$

This is exactly the same as that for Pitot-inlet with constant section at low speeds (See [7]). The subsonic version for such an inlet has been given in [2]. We can see from the comparison between equations (10) and (13) that the expression of C_s in terms of m for general inlets can be obtained from equation (13) by $(1 + m - m_s)$ insteady of m. This approach is exact in our approximation for incompressible flow and could be considered as a reasonable approximation for subsonic flow.

The second example is shown in Fig. 7. With the use of Figs. 4–6 the computation result is shown by the solid line in Fig. 7. Here the dashed line shows the result for the ramp surface of all 5 deg.

In conclusion, it should be noted that:

1. What the inside wall of an inlet corresponds to is only a little part of the real axis in ζ plane, so that there is only a little contribution of the inside shape to the two integrals in equation (12). Thus, the inside shape of the inlet has only a little effect on the results.

2. The theory is based on the assumption of small perturbation. One might suppose that the results obtained would be applicable only to the case that U_i is close to U_o. However, in view of the previous conclusion, and the fact that the exact mass conservation law was used in equation (6), the results should also apply to the case of rather small mass-flow ratio, which has been proved for the first example.

References

1 Donovan, A. F., and Lawrence, H. R., "Aerodynamic Components of Aircraft at High Speeds," *High Speed Aerodynamics and Jet Propulsion*, Vol. VII, Section D, 1957.

2 Fradenburgh, E. A., and Wyatt, D. D., "Theoretical Performance Characteristics of Sharp-Lip Inlets at Subsonic Speeds," NACA Report 1193, 1954.

3 Bansod, P., "Supersonic Flow About Ducted Bodies With Subsonic Internal Boundaries," *J. of Aircraft*, Vol. 12, No. 6, 1975, pp. 531–538.

4 Reyhner, T. A., "Cartesian Mesh Solution for Axisymmetric Transonic Potential Flow Around Inlets," *AIAA Journal*, Vol. 15, No. 5, 1977, pp. 624–631.

5 Caughey, D. A., and Jameson, A., "Accelerated Iterative Calculation of Transonic Nacelle Flow Fields," *AIAA Journal*, Vol. 15, No. 10, 1977, pp. 1474–1480.

6 Lissaman, P. B. S., "A Linear Theory for the Jet Flap in Ground Effect," *AIAA Journal*, Vol. 6, No. 7, 1968, pp. 1356–1362.

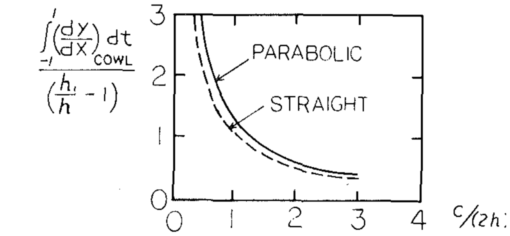

Fig. 5 The integral $\int_{-1}^{1} (dy/dx)_{\text{cowl}}\, dt$ for the cowls with parabolic and straight shapes

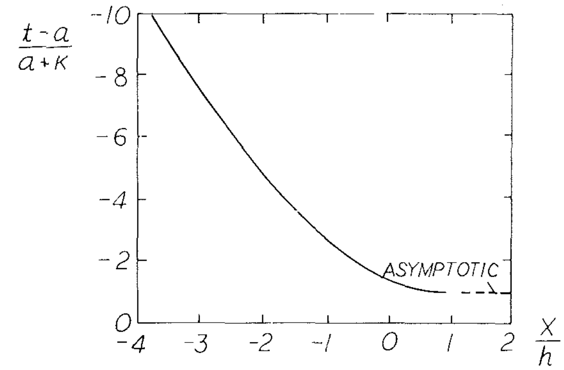

Fig. 6 $(t-a)/(a+k)$ as a function of x/h

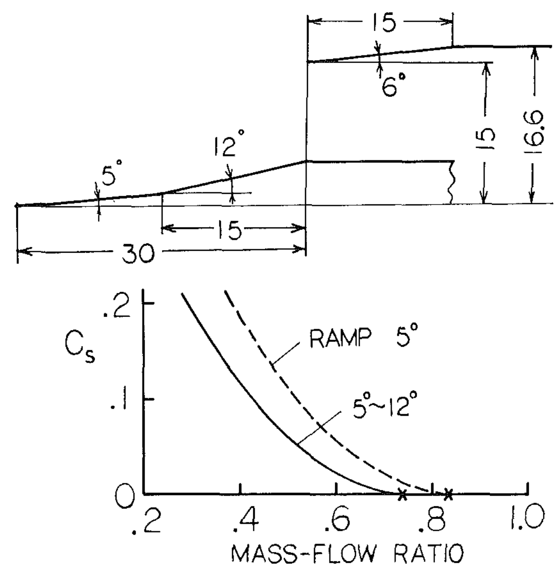

Fig. 7 Examples

7 Kuchemann, D., and Weber, J., *Aerodynamics of Propulsion*, McGraw-Hill, 1953.

8 Sears, W. R., "General Theory of High Speed Aerodynamics," *High Speed Aerodynamics and Jet Propulsion*, Vol. VI, Section D, 1954.

Mode III Dynamic Stress Intensity for Two Colinear Cracks at a Bimaterial Interface

R. L. Ryan[1] and S. Mall[1]

Introduction

The harmonic stress intensity produced by a pair of colinear

[1] Department of Mechanical Engineering, University of Maine, Orono, Me., 04469.

Manuscript received by ASME Applied Mechanics Division, September, 1981; final revision, November, 1981.

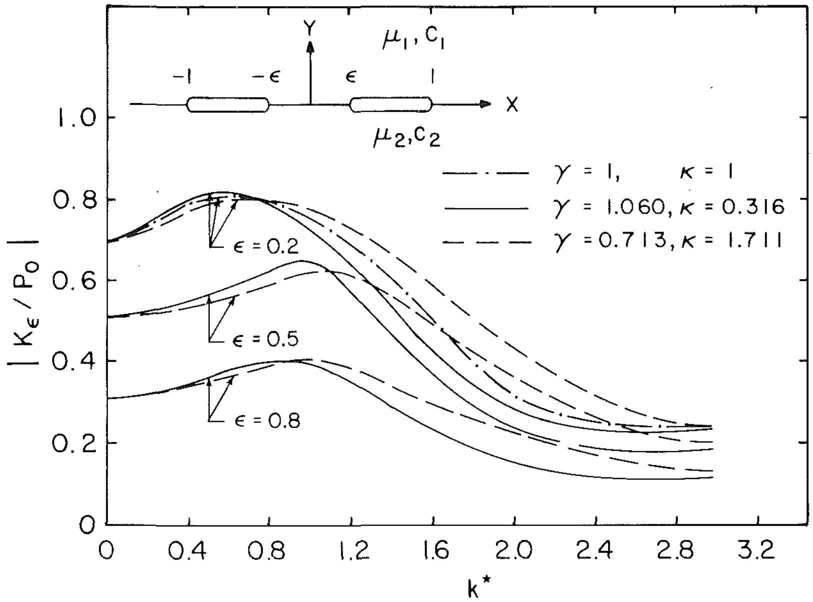

Fig. 1 Normalized stress intensity at inner edge of crack

cracks at a bimaterial interface is considered. The effects of frequency as well as inertia and rigidity ratios on the stress intensities at the crack tips are determined. Additionally, the results for a single crack are obtained as a limiting case.

Formulation

The geometry of two dissimilar materials with a pair of colinear cracks along the interface is shown in Fig. 1. The composite is assumed to be excited by a harmonic plane shear wave generated from deep within material 2 and at normal incidence with the cracks. On account of symmetry with respect to the plane $x=0$ we consider only the portion of the composite $0 \le x < \infty$. Hereafter the subscript $j=1, 2$ refers to material 1 ($y>0$) and 2 ($y<0$), respectively.

Let w_j represent the antiplane displacement associated with the waves scattered by the cracks, and let $\tau_{ij} = \mu_j w_{j,i}$, $i=x,y$ represent the associated stress components. Omitting the time factor $e^{-i\omega t}$, the problem for determining w_j may be specified as follows

$$\nabla^2 w_j + k_j{}^2 w_j = 0 \tag{1}$$

$$\tau_{y1} = \tau_{y2} = \tau(x), \quad 0<x<\infty, \quad y=0 \tag{2}$$

$$\tau(x) = -p_0, \quad \epsilon<x<1, \quad y=0 \tag{3}$$

$$w_1 = w_2, \quad 0 \le x \le \epsilon, \quad 1<x<\infty, \quad y=0 \tag{4}$$

$$\tau_{xj} = 0, \quad x=0. \tag{5}$$

In (1) $k_j = w/c_j$ is the wave number of material j, and in (3) p_0 is the stress induced by the incident wave. In addition, w_j must satisfy the radiation condition as well as the usual crack-tip conditions.

By use of Fourier cosine transforms, it may be shown that equation (1) and conditions (2)–(5) reduce to the following integral equation

$$\frac{1}{\pi}\int_\epsilon^1 \frac{w'(s)}{s-x}\,ds + \frac{1}{\pi}\int_\epsilon^1 w'(s)\left[\frac{1}{s+x} + k_2 P(s,x,k_2)\right]ds$$

$$= \frac{-p_0}{\mu_1}(1+\kappa), \quad \epsilon<x<1 \tag{6}$$

where

$$w'(s) = \frac{\partial}{\partial s}[w_1(s,0) - w_2(s,0)] \tag{7}$$

$$P(s,x,k_2) = L[k_2(s-x)] + L[k_2(s+x)] \tag{8}$$

$$L(k_2 s) = \int_0^\infty \xi^{-1}[(1+\kappa)R(\xi) - \xi]\sin(k_2 s\xi)\,d\xi \tag{9}$$

$$R(\xi) = \alpha_1\alpha_2/(\alpha_2 + \kappa\alpha_1), \quad \kappa = \mu_1/\mu_2, \tag{10}$$

in which $\alpha_1 = (\xi^2 - \gamma^2)^{1/2}$, $\alpha_2 = (\xi^2 - 1)^{1/2}$, and $\gamma = k_1/k_2 = c_2/c_1$. In addition, for single valuedness $w'(s)$ is subject to the constraint condition

$$\int_\epsilon^1 w'(s)\,ds = 0, \quad \epsilon>0. \tag{11}$$

Equations (6) and (11) can be treated numerically by the Gauss-Chebyshev technique [3]. First, however, the equations are transformed to the new set of variables

$$(z,t) = \frac{2}{1-\epsilon}(x,s) - \frac{1+\epsilon}{1-\epsilon}; \quad w'(s) = v(t) \tag{12}$$

In terms of the new variables (6) and (11) become

$$\frac{1}{\pi}\int_{-1}^1 \frac{v(t)}{t-z}\,dt + \frac{1}{\pi}\int_{-1}^1 v(t)\left[\frac{1}{t+z+\nu} + k^* P^*(t,z,k^*)\right]$$

$$dt = -(1+\kappa)p_0/\mu_1, \quad |z|<1 \tag{13}$$

$$\int_{-1}^1 f(t)\,dt = 0 \tag{14}$$

where $k^* = (1-\epsilon)/2\,k_2$, $\nu = 2(1+\epsilon)/(1-\epsilon)$, and

$$P^*(t,z,k^*) = L[k^*(t-z)] + L[k^*(t+z+\nu)]. \tag{15}$$

Next, putting

$$v(t) = -(1+\kappa)p_0/\mu_1 u(t)(1-t^2)^{-1/2} \tag{16}$$

where $u(t)$ is bounded, and applying the Gauss-Chebyshev technique gives the algebraic system

$$\frac{1}{N}\sum_1^N u_p\left\{\frac{1}{t_p - z_q} + \frac{1}{t_p + z_q + \nu} + k^* P_{pq}{}^*\right\} = 1, \quad q=1,2, \ldots, N-1, \tag{17}$$

$$\sum_1^N u_p = 0. \tag{18}$$

where $t_p = \cos[\pi(2p-1)/2N]$, $z_q = \cos\pi q/N$, $u_p = u(t_p)$, and $p_{pq}{}^* = p^*(t_p, z_q, k^*)$. By choosing N sufficiently large, the algebraic system may be made to approximate equations (13) and (14) to any desired degree of accuracy. For the case $\epsilon = 0$ ($\nu = 2$) the algebraic system must be modified slightly to avoid

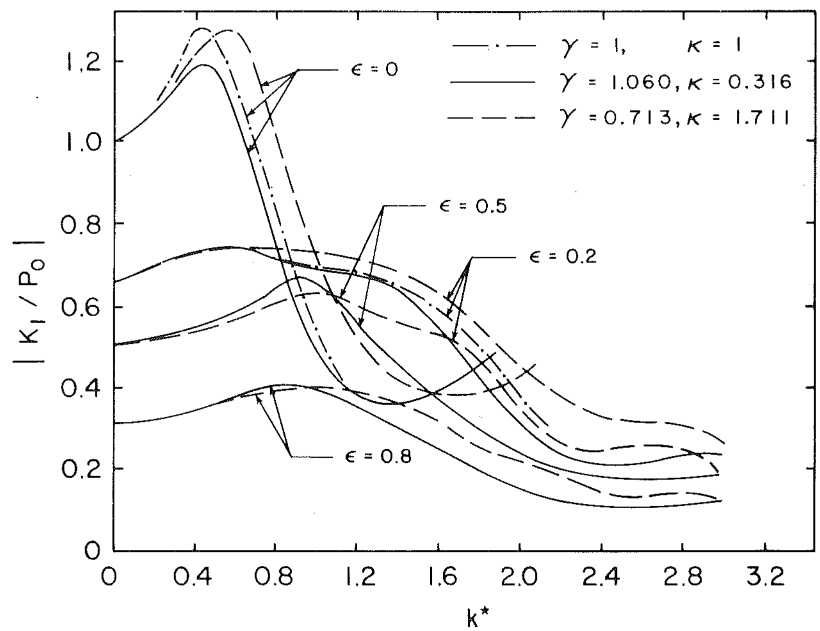

Fig. 2 Normalized stress intensity at outer edge of crack

a stress or dislocation singularity at $z=-1$ ($x=0$). Such a singularity is removed if the constraint condition (14) is replaced by the condition $v(-1)=0$. This condition is approximated by setting $u_N=0$.

Once the system is solved for u_p the stress intensities may be determined as follows

$$|K_\epsilon/p_0| = \left(\frac{1-\epsilon}{2}\right)^{1/2} |u(-1)$$

$$|K_1/p_0| = \left(\frac{1-\epsilon}{2}\right)^{1/2} |u(1)| \tag{19}$$

Numerical Results and Discussion

The algebraic system (17–18) was solved by a complex computer program using $N=20$; the kernels $P_{pg}{}^*$ were approximated by Simpson's rule using 90 subdivisions. We considered the following cases: (*a*) $\gamma=\kappa=1$, (*b*) $\gamma=1.060$, $\kappa=0.316$, and (*c*) $\gamma=0.713$, $\kappa=1.711$. Case (*a*) corresponds to a homogeneous material, whereas cases (*b*) and (*c*) correspond to composites of aluminum/steel and wrought iron/copper, respectively, with material properties as given in [1]. The stress intensity was computed for each case for $\epsilon=0$, 0.2, 0.5, 0.8. Results for case (*a*) have been previously reported by Mal [2] for $\epsilon=0$, and by Itou [4] for other values of ϵ. Accordingly, only partial results for case (*a*) are shown in Figs. 1 and 2. These results agree to within about 3 percent with those previously reported. By comparison with case (*a*) the results of cases (*b*) and (*c*) illustrate the effects of inertia and rigidity ratios. It is seen that for the values considered, these ratios exert a relatively mild influence, giving a maximum difference of about 6 percent in the peak intensity compared to the homogeneous case. The results for $\epsilon=0$ have been previously reported by Srivastava et al. [1]. Their results, however, predict peak intensities of approximately 2.4 and 2.2 for case (*b*) and case (*c*), respectively, giving a maximum difference of about 85 percent compared to the homogeneous case. If the results of [1] are in error, a possible source lies in the fact that equations (3.15) and (3.16) of [1] are not valid for $u>t$. In addition, it is noted that the comparison between the exact and approximate stress intensities as shown in [1], Fig. 2, are apparently inconsistent with a similar comparison reported by Mal [5], Fig. 2.

References

1 Srivastava, K. N., Palaiya, R. M., and Karaulis, D. S., "Interaction of Antiplane Shear Waves by a Griffith Crack at the Interface of Two Bonded Dissimilar Elastic Half Spaces," *International Journal of Fracture*, Vol. 16, No. 4, 1980, pp. 349–358.

2 Mal, A. K., "Interaction of Elastic Waves with a Griffith Crack," *International Journal of Engineering Science*, Vol. 8, 1970, pp. 763–776.

3 Erdogan, F., and Gupta, G. D., "On the Numerical Solution of Singular Integral Equations," *Quarterly of Applied Mathematics*, Vol. 30, 1972, pp. 525–534.

4 Itou, S., "Diffraction of an Antiplane Shear Wave by Two Coplanar Griffith Cracks in an Infinite Elastic Medium," *International Journal of Solids and Structures*, Vol. 16, 1980, pp. 1147–1153.

5 Mal, A. K., "A Note on the Low Frequency Diffraction of Elastic Waves by a Griffith Crack," *International Journal of Engineering Science*, Vol. 10, 1972, pp. 609–612.

Wind Tunnel Corrections for Lifting Thin Airfoils

A. Plotkin[1]

Introduction

A detailed review of the subject of subsonic wind tunnel wall corrections is given in Garner et al. [1]. For the idealized problem of steady two-dimensional incompressible potential flow, Tomotika [2] and Havelock [3] used conformal mapping to obtain the exact solutions for flow past a flat plate and elliptic cylinder, respectively, placed between parallel walls. Goldstein [4] used conformal transformations and power series expansions to obtain an approximate solution for the thick cambered airfoil. In the foregoing references, the complicated exact solution is also expanded in a series in the ratio of chord to tunnel height. More recently, accurate numerical solutions using panel methods (surface singularity distributions) are readily obtainable. An early example of this approach is given in Giesing [5].

In the situation where the airfoil disturbance and the chord-to-tunnel height ratio are both small, analytical results can be obtained directly with the use of thin-airfoil theory and an

[1] Professor, Department of Aerospace Engineering, University of Maryland, College Park, Md. 20742. Mem. ASME.

Manuscript received by ASME Applied Mechanics Division, August, 1981.

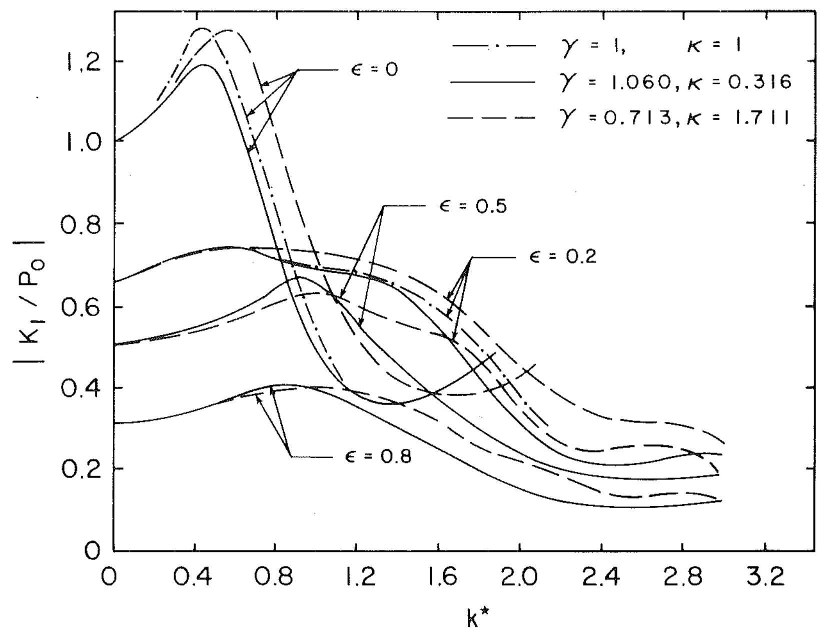

Fig. 2 Normalized stress intensity at outer edge of crack

a stress or dislocation singularity at $z=-1$ ($x=0$). Such a singularity is removed if the constraint condition (14) is replaced by the condition $v(-1)=0$. This condition is approximated by setting $u_N=0$.

Once the system is solved for u_p the stress intensities may be determined as follows

$$|K_\epsilon/p_0| = \left(\frac{1-\epsilon}{2}\right)^{1/2} |u(-1)$$

$$|K_1/p_0| = \left(\frac{1-\epsilon}{2}\right)^{1/2} |u(1)| \tag{19}$$

Numerical Results and Discussion

The algebraic system (17–18) was solved by a complex computer program using $N=20$; the kernels $P_{pg}{}^*$ were approximated by Simpson's rule using 90 subdivisions. We considered the following cases: (*a*) $\gamma=\kappa=1$, (*b*) $\gamma=1.060$, $\kappa=0.316$, and (*c*) $\gamma=0.713$, $\kappa=1.711$. Case (*a*) corresponds to a homogeneous material, whereas cases (*b*) and (*c*) correspond to composites of aluminum/steel and wrought iron/copper, respectively, with material properties as given in [1]. The stress intensity was computed for each case for $\epsilon=0$, 0.2, 0.5, 0.8. Results for case (*a*) have been previously reported by Mal [2] for $\epsilon=0$, and by Itou [4] for other values of ϵ. Accordingly, only partial results for case (*a*) are shown in Figs. 1 and 2. These results agree to within about 3 percent with those previously reported. By comparison with case (*a*) the results of cases (*b*) and (*c*) illustrate the effects of inertia and rigidity ratios. It is seen that for the values considered, these ratios exert a relatively mild influence, giving a maximum difference of about 6 percent in the peak intensity compared to the homogeneous case. The results for $\epsilon=0$ have been previously reported by Srivastava et al. [1]. Their results, however, predict peak intensities of approximately 2.4 and 2.2 for case (*b*) and case (*c*), respectively, giving a maximum difference of about 85 percent compared to the homogeneous case. If the results of [1] are in error, a possible source lies in the fact that equations (3.15) and (3.16) of [1] are not valid for $u>t$. In addition, it is noted that the comparison between the exact and approximate stress intensities as shown in [1], Fig. 2, are apparently inconsistent with a similar comparison reported by Mal [5], Fig. 2.

References

1 Srivastava, K. N., Palaiya, R. M., and Karaulis, D. S., "Interaction of Antiplane Shear Waves by a Griffith Crack at the Interface of Two Bonded Dissimilar Elastic Half Spaces," *International Journal of Fracture*, Vol. 16, No. 4, 1980, pp. 349–358.

2 Mal, A. K., "Interaction of Elastic Waves with a Griffith Crack," *International Journal of Engineering Science*, Vol. 8, 1970, pp. 763–776.

3 Erdogan, F., and Gupta, G. D., "On the Numerical Solution of Singular Integral Equations," *Quarterly of Applied Mathematics*, Vol. 30, 1972, pp. 525–534.

4 Itou, S., "Diffraction of an Antiplane Shear Wave by Two Coplanar Griffith Cracks in an Infinite Elastic Medium," *International Journal of Solids and Structures*, Vol. 16, 1980, pp. 1147–1153.

5 Mal, A. K., "A Note on the Low Frequency Diffraction of Elastic Waves by a Griffith Crack," *International Journal of Engineering Science*, Vol. 10, 1972, pp. 609–612.

Wind Tunnel Corrections for Lifting Thin Airfoils

A. Plotkin[1]

Introduction

A detailed review of the subject of subsonic wind tunnel wall corrections is given in Garner et al. [1]. For the idealized problem of steady two-dimensional incompressible potential flow, Tomotika [2] and Havelock [3] used conformal mapping to obtain the exact solutions for flow past a flat plate and elliptic cylinder, respectively, placed between parallel walls. Goldstein [4] used conformal transformations and power series expansions to obtain an approximate solution for the thick cambered airfoil. In the foregoing references, the complicated exact solution is also expanded in a series in the ratio of chord to tunnel height. More recently, accurate numerical solutions using panel methods (surface singularity distributions) are readily obtainable. An early example of this approach is given in Giesing [5].

In the situation where the airfoil disturbance and the chord-to-tunnel height ratio are both small, analytical results can be obtained directly with the use of thin-airfoil theory and an

[1] Professor, Department of Aerospace Engineering, University of Maryland, College Park, Md. 20742. Mem. ASME.

Manuscript received by ASME Applied Mechanics Division, August, 1981.

expansion technique due to Keldysh and Lavrentiev [6]. This approach was used in Plotkin and Kennell [7] to obtain the lift coefficient due to thickness and angle of attack for a thin airfoil in ground affect. In this Note, expressions for the lift coefficient of a flat plate and parabolic arc airfoil at the center of a wind tunnel will be derived which are linear in angle of attack and camber ratio and in the form of a series expansion in the chord-to-tunnel height ratio.

Problem Formulation and Method of Solution

The problem under consideration is the steady two-dimensional incompressible potential flow of a uniform stream of speed U past a zero-thickness airfoil of chord $2c$. The midchord of the airfoil is located at the center of a wind tunnel with height $2hc$. All lengths are normalized by c and speeds by U. A cartesian coordinate system is introduced with origin at midchord, x aligned with the stream, and y normal to it.

The airfoil is described by the equation

$$y = -\alpha x + \beta \eta(x) \tag{1}$$

where $\beta = 0(\alpha)$. The velocity field is characterized by a velocity potential Φ which is normalized by Uc. A perturbation velocity potential ϕ is introduced such that

$$\Phi = x + \phi \tag{2}$$

and the first-order, thin-airfoil mathematical problem for ϕ (linear in α and β) is

$$\nabla^2 \phi = 0 \tag{3}$$

$$\phi_y = 0 \qquad y = \pm h \tag{4}$$

$$\phi_y = -\alpha + \beta \eta'(x) \qquad y = \pm 0, \ -1 \le x \le 1 \tag{5}$$

$$\nabla \phi \to 0 \qquad x \to \pm\infty \tag{6}$$

If the disturbance to the stream is modeled by vortices of strength $\gamma(x)$ per unit length, normalized by U, and if the images of these singularities in the wind tunnel walls are added, the perturbation complex potential becomes

$$f = \phi + i\psi = \frac{i}{2\pi} \int_{-1}^{1} \gamma(\xi) \log \tanh[\pi(z-\xi)/4h] \, d\xi \tag{7}$$

where ψ is the stream function and $z = x + iy$. This satisfies equations (3), (4), and (6). Substitution into the body boundary condition (5) leads to the following integral equation for the vorticity:

$$\int_{-1}^{1} \gamma(\xi) K(x-\xi) \, d\xi = 2\pi(\alpha - \beta \eta'(x)) \tag{8}$$

where the kernel function is

$$K(x) = (\pi/4h)[\coth(\pi x/4h) - \tanh(\pi x/4h)] \tag{9}$$

Keldysh and Lavrentiev [6] suggest the following expansion scheme with h^{-1} as the expansion parameter:

$$K(x) = x^{-1} + h^{-1} \sum_{0}^{\infty} K_n (x/h)^n$$
$$\gamma(x) = \sum_{0}^{\infty} h^{-n} \gamma_n(x) \tag{10}$$

Equation (10) is substituted into equation (8) and terms with like powers of h^{-1} are collected. The following system of equations for the unknown $\gamma_n(x)$ is obtained:

$$\int_{-1}^{1} \frac{\gamma_0(\xi)}{x-\xi} d\xi = 2\pi(\alpha - \beta \eta'(x))$$

$$\int_{-1}^{1} \frac{\gamma_n(\xi)}{x-\xi} d\xi = -\int_{-1}^{1} \sum_{m=0}^{n-1} K_m (x-\xi)^m \gamma_{n-m-1}(\xi) \, d\xi$$
$$n \ge 1 \equiv f_n(x) \tag{11}$$

The solution is not unique until the Kutta condition at the trailing edge is satisfied. The solution of equations (11) is then

$$\gamma_n(x) = \frac{1}{\pi^2} \left(\frac{1-x}{1+x}\right)^{1/2} \int_{-1}^{1} \left(\frac{1+\xi}{1-\xi}\right)^{1/2} \frac{f_n(\xi)}{\xi - x} d\xi \tag{12}$$

The singular integrals are to be considered in the Cauchy principal value sense. It is seen that only K_m with odd subscripts are nonzero and the first two are

$$K_1 = -\pi^2/24 \qquad K_3 = 7\pi^4/5760 \tag{13}$$

Results

Consider first the case of a flat plate at angle of attack α. This is represented by $y = -\alpha x$ in equation (1). The first three terms in the vorticity expansion are found to be

$$\gamma_0 = 2\alpha\left(\frac{1-x}{1+x}\right)^{1/2}$$
$$\gamma_2 = \frac{\pi^2\alpha}{12}\left(\frac{1-x}{1+x}\right)^{1/2}\left(x + \frac{3}{2}\right) \tag{14}$$
$$\gamma_4 = \frac{-\pi^4\alpha}{2880}\Big) \frac{1-x}{1+x}\Big)^{1/2}\left(7x^3 + \frac{35x^2}{2} + \frac{29x}{2} + 12\right)$$

The lift coefficient is given by

$$C_L = \int_{-1}^{1} \gamma(x) \, dx \tag{15}$$

and therefore for the flat plate

$$C_L = 2\pi\alpha\left\{1 + \frac{\pi^2}{24h^2} - \frac{11\pi^4}{7680h^4} + 0(h^{-6})\right\} \tag{16}$$

Note that γ_0 gives the result for a flat plate in an infinite fluid with lift coefficient $2\pi\alpha$. Note also that h is the ratio of tunnel height to chord. The solution is identical to that in reference [2]for terms linear in α.

Consider next the case of a cambered airfoil at zero angle of attack represented by $y = \beta\eta(x)$ in equation (1). β is a measure of the disturbance near to the foil. To carry out the expansion, it is necessary to choose a camber shape. The parabolic arc airfoil is selected and is given by

$$y = \beta(1-x^2) \tag{17}$$

The first three terms in the vorticity expansion are

$$\gamma_0 = 4\beta(1-x^2)^{1/2}$$
$$\gamma_2 = (\pi^2\beta/12)(1-x^2)^{1/2} \tag{18}$$
$$\gamma_4 = \frac{-\pi^4\beta}{2880}\left(\frac{1-x}{1+x}\right)^{1/2}\left(7x^3 + 7x^2 + \frac{15x}{4} + \frac{15}{4}\right)$$

The lift coefficient is

$$C_L = 2\pi\beta\left\{1 + \frac{\pi^2}{48h^2} - \frac{\pi^4}{46080h^4} + 0(h^{-6})\right\} \tag{19}$$

Discussion

Wall-interference corrections to the first-order, thin-airfoil lift have been obtained directly for incompressible flow using a regular perturbation expansion in h^{-1}, the chord-to-tunnel height ratio. It is important to realize that this problem contains two small expansion parameters and that therefore the utility of the result is related to their relative magnitude. To illustrate this point, consider the expansion in h^{-1} of the exact solution of Tomotika [2] for the flat plate. It is

$$C_L = 2\pi \sin\alpha\left\{1+\frac{\pi^2}{24h^2}(1+\sin^2\alpha)\right.$$

$$\left.\frac{-\pi^4}{7680h^4}(11-53\sin^2\alpha-22\sin^4\alpha)+0(h^{-6})\right\} \qquad (20)$$

as given in Garner et al. [1]. If $\alpha = 0(h^{-1})$, for example, it would be incorrect to keep the $0(h^{-4})$ term in equation (16) since we have neglected the $0(\alpha^2/h^2)$ term from equation (20) by considering only terms linear in α.

References

1 Garner, H. C., et al., "Subsonic Wind Tunnel Wall Corrections," *AGARDograph*, Vol. 109, 1966, Chapter II.

2 Tomotika, S., "The Lift of a Flat Plate Placed in a Stream Between Two Parallel Walls and Some Allied Problems," *Aero. Res. Inst.* (Tokyo) Report 170, 1934.

3 Havelock, T. H., "The Lift and Moment on a Flat Plate in a Stream of Finite Width," *Proceedings of the Royal Society, Series A*, Vol. 166, 1938, pp. 178–196.

4 Goldstein, S., "Two-Dimensional Wind-Tunnel Interference," *ARC R and M*, 1902, 1942.

5 Giesing, J. P., "Potential Flow About Two-Dimensional Airfoils," Douglas Aircraft Company Report No. LB 31946, Dec. 1965.

6 Keldysh, M. V., and Lavrentiev, M. A., "On the Motion of a Wing Under the Surface of a Heavy Fluid," *CAHI*, Moscow, 1935; *translation in* Science Translation Service, STS-75, Cambridge, Mass., 1949.

7 Plotkin, A., and Kennell, C. G., "Thickness-Induced Lift on a Thin Airfoil in Ground Effect," *AIAA Journal*, Vol. 19, No. 11, 1981, pp. 1484–1486.

Analysis of the Weibull Distribution Function

K. T. Chang[1]

Weibull originally introduced his distribution function based on a chain links model and, as such, found wide application in ceramics engineering analysis. A general criticism of his formulation had been that the function lacked theoretical justification – that the selection of the functional form was based on intuitive empirical reasoning. This paper proposes a proof of the correctness of the Weibull function, and in so doing, also explicitly defines the expected behavior of a population that fits the distribution.

We consider two sets of sample bars of the same ceramic material, manufactured by the same process. They are geometrically similar, but have two distinctively different sizes. It is assumed that the two sample sets contain a similar distribution of flaws, so that each elemental volume of the material, taken from either sample set, may be assigned the same probabilities of failure as a function of the local tensile stress. A failure of the weakest volume, of course, constitutes a total failure of the sample.

Now the two sets of samples are tested in simple tension, in nearly as possible identical conditions. Cumulative failure distributions are obtained as a function of the nominal applied stress for each set. We expect the following results:

(*i*) The stress levels at which samples begin to fail would be different according to size, the large samples failing at lower stress levels than the small samples.

(*ii*) Although the stress levels are different, the shape of the failure distribution curves should be similar in appearance.

At this point, we need to more precisely define what is

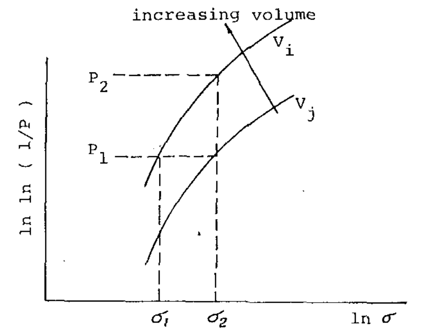

Fig. 1 Properties of nonlinear distribution function on Weibull paper

meant by "similar distributions." For the large samples, we select two failure percentiles N_1, N_2 (for example, 80 percent and 20 percent), and the corresponding stresses are $\sigma_l(N_1)$ and $\sigma_l(N_2)$, the ratio is

$$\frac{\sigma_l(N_1)}{\sigma_l(N_2)} = r_l(N_1, N_2)$$

Similarly, we determine the stress ratio for the small samples

$$\frac{\sigma_s(N_1)}{\sigma_s(N_2)} = r_s(N_1, N_2)$$

The condition for the two distributions to be similar is then

$$r_l(N_1, N_2) = r_s(N_1, N_2) \qquad (1)$$

for any and all choices of the percentiles N_1 and N_2.

On Weibull paper, we arbitrarily draw a curve to represent the faliure distribution of the large samples. Then, using simple probability theory, the failure distribution for the small samples can easily be plotted. It then becomes apparent that, except for Weibull straight lines, the condition for similarity is violated; we therefore will have established that the Weibull function applies to populations satisfying condition (*ii*) mentioned in the foregoing.

We assume a distribution function in the general form

$$F(\sigma) = 1 - e^{-\phi(\sigma)} (= 1 - P) \qquad (2)$$

where $F(\sigma)$ is the probability of failure of an elemental volume of the test material. Let each large sample contain "i" unit volumes, then

$$F_l(\sigma) = 1 - e^{-i\phi(\sigma)} \qquad (3)$$

In Fig. 1 we sketch a curve (in this case, concave downward), which corresponds to some selection of $\phi(\sigma)$ yet to be determined. Let each small sample contain "j" unit volumes, then

$$F_s(\sigma) = 1 - e^{-j\phi(\sigma)} \qquad (4)$$

At stress equal to σ_2 the probability of survival of the small samples are

$$P_1 = e^{-j\phi(\sigma_2)}$$

For large samples,

$$P_2 = e^{-i\phi(\sigma_2)}$$

therefore

$$P_2 = P_1^{\,i/j} \qquad (5)$$

Since i/j is constant, the vertical separation of V_i and V_j is constant $(= ln i/j)$, therefore V_j is obtained by moving V_i down a fixed distant parallel to the vertical axis. Now the horizontal separation $(= ln \sigma_2/\sigma_1)$ becomes variable, except when the curves are inclined parallel straight lines. Therefore we have shown that any nonlinear distribution on Weibull paper violates the similarity condition.

Another way to look at the Weibull distribution is to postulate a test on samples of uniform size. After testing all samples to failure, the results may be plotted on Weibull

[1] The Garrett Corporation, Los Angeles, Calif. 90009.

Manuscript received by ASME Applied Mechanics Division, May 1980; final revision, November, 1981.

$$C_L = 2\pi \sin\alpha \left\{ 1 + \frac{\pi^2}{24h^2}(1+\sin^2\alpha) \right.$$

$$\left. \frac{-\pi^4}{7680h^4}(11 - 53\sin^2\alpha - 22\sin^4\alpha) + 0(h^{-6}) \right\} \quad (20)$$

as given in Garner et al. [1]. If $\alpha = 0(h^{-1})$, for example, it would be incorrect to keep the $0(h^{-4})$ term in equation (16) since we have neglected the $0(\alpha^2/h^2)$ term from equation (20) by considering only terms linear in α.

References

1 Garner, H. C., et al., "Subsonic Wind Tunnel Wall Corrections," *AGARDograph*, Vol. 109, 1966, Chapter II.

2 Tomotika, S., "The Lift of a Flat Plate Placed in a Stream Between Two Parallel Walls and Some Allied Problems," *Aero. Res. Inst.* (Tokyo) Report 170, 1934.

3 Havelock, T. H., "The Lift and Moment on a Flat Plate in a Stream of Finite Width," *Proceedings of the Royal Society, Series A*, Vol. 166, 1938, pp. 178-196.

4 Goldstein, S., "Two-Dimensional Wind-Tunnel Interference," *ARC R and M*, 1902, 1942.

5 Giesing, J. P., "Potential Flow About Two-Dimensional Airfoils," Douglas Aircraft Company Report No. LB 31946, Dec. 1965.

6 Keldysh, M. V., and Lavrentiev, M. A., "On the Motion of a Wing Under the Surface of a Heavy Fluid," *CAHI*, Moscow, 1935; *translation in* Science Translation Service, STS-75, Cambridge, Mass., 1949.

7 Plotkin, A., and Kennell, C. G., "Thickness-Induced Lift on a Thin Airfoil in Ground Effect," *AIAA Journal*, Vol. 19, No. 11, 1981, pp. 1484-1486.

Analysis of the Weibull Distribution Function

K. T. Chang[1]

Weibull originally introduced his distribution function based on a chain links model and, as such, found wide application in ceramics engineering analysis. A general criticism of his formulation had been that the function lacked theoretical justification – that the selection of the functional form was based on intuitive empirical reasoning. This paper proposes a proof of the correctness of the Weibull function, and in so doing, also explicitly defines the expected behavior of a population that fits the distribution.

We consider two sets of sample bars of the same ceramic material, manufactured by the same process. They are geometrically similar, but have two distinctively different sizes. It is assumed that the two sample sets contain a similar distribution of flaws, so that each elemental volume of the material, taken from either sample set, may be assigned the same probabilities of failure as a function of the local tensile stress. A failure of the weakest volume, of course, constitutes a total failure of the sample.

Now the two sets of samples are tested in simple tension, in nearly as possible identical conditions. Cumulative failure distributions are obtained as a function of the nominal applied stress for each set. We expect the following results:

(*i*) The stress levels at which samples begin to fail would be different according to size, the large samples failing at lower stress levels than the small samples.

(*ii*) Although the stress levels are different, the shape of the failure distribution curves should be similar in appearance.

At this point, we need to more precisely define what is meant by "similar distributions." For the large samples, we select two failure percentiles N_1, N_2 (for example, 80 percent and 20 percent), and the corresponding stresses are $\sigma_l(N_1)$ and $\sigma_l(N_2)$, the ratio is

$$\frac{\sigma_l(N_1)}{\sigma_l(N_2)} = r_l(N_1, N_2)$$

Similarly, we determine the stress ratio for the small samples

$$\frac{\sigma_s(N_1)}{\sigma_s(N_2)} = r_s(N_1, N_2)$$

The condition for the two distributions to be similar is then

$$r_l(N_1, N_2) = r_s(N_1, N_2) \quad (1)$$

for any and all choices of the percentiles N_1 and N_2.

On Weibull paper, we arbitrarily draw a curve to represent the faliure distribution of the large samples. Then, using simple probability theory, the failure distribution for the small samples can easily be plotted. It then becomes apparent that, except for Weibull straight lines, the condition for similarity is violated; we therefore will have established that the Weibull function applies to populations satisfying condition (*ii*) mentioned in the foregoing.

We assume a distribution function in the general form

$$F(\sigma) = 1 - e^{-\phi(\sigma)} (= 1 - P) \quad (2)$$

where $F(\sigma)$ is the probability of failure of an elemental volume of the test material. Let each large sample contain "*i*" unit volumes, then

$$F_l(\sigma) = 1 - e^{-i\phi(\sigma)} \quad (3)$$

In Fig. 1 we sketch a curve (in this case, concave downward), which corresponds to some selection of $\phi(\sigma)$ yet to be determined. Let each small sample contain "*j*" unit volumes, then

$$F_s(\sigma) = 1 - e^{-j\phi(\sigma)} \quad (4)$$

At stress equal to σ_2 the probability of survival of the small samples are

$$P_1 = e^{-j\phi(\sigma_2)}$$

For large samples,

$$P_2 = e^{-i\phi(\sigma_2)}$$

therefore

$$P_2 = P_1^{\,i/j} \quad (5)$$

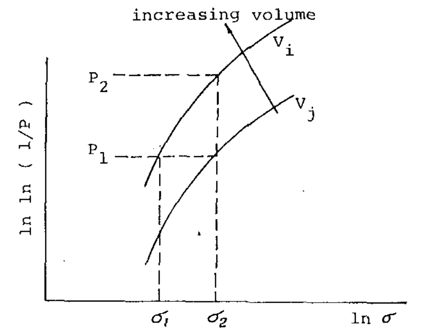

Fig. 1 Properties of nonlinear distribution function on Weibull paper

Since i/j is constant, the vertical separation of V_i and V_j is constant $(= ln\,i/j)$, therefore V_j is obtained by moving V_i down a fixed distant parallel to the vertical axis. Now the horizontal separation $(= ln\sigma_2/\sigma_1)$ becomes variable, except when the curves are inclined parallel straight lines. Therefore we have shown that any nonlinear distribution on Weibull paper violates the similarity condition.

Another way to look at the Weibull distribution is to postulate a test on samples of uniform size. After testing all samples to failure, the results may be plotted on Weibull

[1] The Garrett Corporation, Los Angeles, Calif. 90009.

Manuscript received by ASME Applied Mechanics Division, May 1980; final revision, November, 1981.

paper as a single straight line. However, it is also possible to observe that, at, say the 20 percentile point, the remaining 80 percent of the samples in fact have a smaller percentage of defective volumes in them than in the original set of samples. Disregarding the "high strength" portion of each remaining sample, in effect we have a new set of samples with smaller volume of previous failure probabilities. The next failure then can be either a continuation of the first cumulative failure curve, or the first failure in a new population with smaller sizes. Thus, a single straight line, or a family of parallel straight lines, can equally well represent the same test results, according to interpretation. The similarity assumption proposed earlier is seen to be no more than a requirement of *self-consistency* in the behavior of the samples.

It is also possible to derive the Weibull distribution in a formal mathematical sense[2]. From equations (3) and (4), at a selected percentile N_1, one can write

$$\phi(\sigma_1(N_1)) = -\frac{lnN_1}{i}$$

$$\phi(\sigma_s(N_1)) = -\frac{lnN_1}{j}$$

Similar expressions can be written for N_2. Now imposing the similarity condition (1), also denoting by ψ the inverse function of ϕ:

$$\frac{\psi\left(-\frac{lnN_1}{i}\right)}{\psi\left(-\frac{lnN_2}{i}\right)} = \frac{\psi\left(-\frac{lnN_1}{j}\right)}{\psi\left(-\frac{lnN_2}{j}\right)}$$

Thus, in general, $\psi(\alpha A)/\psi(\alpha B)$ is independent of α. Specifically,

$$\frac{\psi(\alpha A)}{\psi(\alpha B)} = \frac{\psi(A)}{\psi(B)} = \text{constant}$$

Differentiating the first quotient with respect to α,

$$\psi(\alpha B)\psi'(\alpha A)A - \psi(\alpha A)\psi'(\alpha B)B = 0$$

Separating variables,

$$\frac{\psi'(\alpha A)A}{\psi(\alpha A)} = \frac{\psi'(\alpha B)B}{\psi(\alpha B)}$$

Again, this expression holds true for all values of α, so that $\psi'(\alpha A)/\psi(\alpha A)$ can be written, without loss of generality, to $\psi'(A)/\psi(A)$; where $\psi' = d\psi(\alpha A)/d(\alpha A)$ now becomes $\psi' = d\psi(A)/dA$. This gives

$$\frac{\psi'(A)}{\psi(A)} \bullet A = \text{ constant } = k_1$$

Integrating,

$$ln\psi(A) = k_1 lnA + lnk_2$$

or,

$$\psi(A) = k_2 A^{k_1}$$

so that,

$$\phi(\psi) = \left(\frac{\psi}{k_2}\right)^{k_1/1}$$

which is the Weibull distribution.

Referring again to Fig. 1, for equal probability of survival P_1 on the two curves V_i and V_j,

$$P_1 = e^{-i\phi(\sigma_1)} = e^{-j\phi(\sigma_2)}$$

or

$$\frac{\phi_2}{\phi_1} = \frac{i}{j} = \text{ constant} \tag{6}$$

Equation (6) can be satisfied by a nonunique choice of the form of the function ϕ, the distinguishing property of Weibull's choice,

$$\phi(x) = \left(\frac{x - x_u}{x_0}\right)^m$$

$$F(x) = 1 - e^{-\left(\frac{x-x_u}{x_0}\right)^m} \tag{7}$$

is that

$$\frac{x_2 - x_u}{x_1 - x_u} = \sqrt[m]{\frac{i}{j}} \tag{8}$$

or the modified stress ratio is constant along V_i versus V_j, independent of the value of the percentile $F(X)$ in equation (7).

If two sets of samples are identical except in size (size is here generalized to be a basic building block of the phenomenon under observation, it is a parameter whose enumeration differentiates the sets of samples), and the only size effect is a constant shift of the x-variable, we may feel justified to say that these two sets of samples are self-consistent, or they belong to the same population that exhibits a self-consistent characteristic.

As pointed out by Weibull, any distribution may be represented by a sum of simple (linear) distributions. If we encounter data that are curved on Weibull paper, it can far more easily be explained on the basis of the samples not belonging to a single self-consistent population, than to arbitrarily impose a complex curve formulation and attempt to discover a logical new distribution function. Weibull's analysis of the statures for adult males born in the British Isles, for example, showed that the distribution could be represented by two self-consistent populations. An interested historian might research the immigration of people to the British Isles prior to 1917, and identify two major populations. By not using linear distributions, the opportunity for understanding the phenomenon may be forever lost.

References

1 Weibull W. "A Statistical Distribution Function of Wide Applicability," ASME Journal of Applied Mechanics, Vol. 18, 1951, pp. 293–297.

2 Weibull W. "A Survey of Statistical Effects in the Field of Material Failure", *Applied Mechanic Surveys*, Macmillan, 1966, pp. 397–400.

[2]This approach was suggested by a reviewer of the ASME Journal of Applied Mechanics.

Influence of End-Wall Friction on the Flow Rates of Granular Materials in Wedge-Shaped Hoppers

M. Sayed[1] and S. B. Savage[2]

Nomenclature

b = effective aperture width
d = particle diameter

[1]Research Assistant, Department of Civil Engineering and Applied Mechanics, McGill University, Montreal, Quebec, Canada H3A 2K6.

[2]Professor, Department of Civil Engineering and Applied Mechanics, McGill University, Montreal, Quebec, Canada H3A 2K6. Mem. ASME.

Manuscript received by ASME Applied Mechanics Division, April, 1981; final revision, November, 1981.

paper as a single straight line. However, it is also possible to observe that, at, say the 20 percentile point, the remaining 80 percent of the samples in fact have a smaller percentage of defective volumes in them than in the original set of samples. Disregarding the "high strength" portion of each remaining sample, in effect we have a new set of samples with smaller volume of previous failure probabilities. The next failure then can be either a continuation of the first cumulative failure curve, or the first failure in a new population with smaller sizes. Thus, a single straight line, or a family of parallel straight lines, can equally well represent the same test results, according to interpretation. The similarity assumption proposed earlier is seen to be no more than a requirement of *self-consistency* in the behavior of the samples.

It is also possible to derive the Weibull distribution in a formal mathematical sense[2]. From equations (3) and (4), at a selected percentile N_1, one can write

$$\phi(\sigma_1(N_1)) = -\frac{lnN_1}{i}$$

$$\phi(\sigma_s(N_1)) = -\frac{lnN_1}{j}$$

Similar expressions can be written for N_2. Now imposing the similarity condition (1), also denoting by ψ the inverse function of ϕ:

$$\frac{\psi\left(-\frac{lnN_1}{i}\right)}{\psi\left(-\frac{lnN_2}{i}\right)} = \frac{\psi\left(-\frac{lnN_1}{j}\right)}{\psi\left(-\frac{lnN_2}{j}\right)}$$

Thus, in general, $\psi(\alpha A)/\psi(\alpha B)$ is independent of α. Specifically,

$$\frac{\psi(\alpha A)}{\psi(\alpha B)} = \frac{\psi(A)}{\psi(B)} = \text{constant}$$

Differentiating the first quotient with respect to α,

$$\psi(\alpha B)\psi'(\alpha A)A - \psi(\alpha A)\psi'(\alpha B)B = 0$$

Separating variables,

$$\frac{\psi'(\alpha A)A}{\psi(\alpha A)} = \frac{\psi'(\alpha B)B}{\psi(\alpha B)}$$

Again, this expression holds true for all values of α, so that $\psi'(\alpha A)/\psi(\alpha A)$ can be written, without loss of generality, to $\psi'(A)/\psi(A)$; where $\psi' = d\psi(\alpha A)/d(\alpha A)$ now becomes $\psi' = d\psi(A)/dA$. This gives

$$\frac{\psi'(A)}{\psi(A)} \cdot A = \text{constant} = k_1$$

Integrating,

$$ln\psi(A) = k_1 lnA + lnk_2$$

or,

$$\psi(A) = k_2 A^{k_1}$$

so that,

$$\phi(\psi) = \left(\frac{\psi}{k_2}\right)^{k_1/1}$$

which is the Weibull distribution.

Referring again to Fig. 1, for equal probability of survival P_1 on the two curves V_i and V_j,

$$P_1 = e^{-i\phi(\sigma_1)} = e^{-j\phi(\sigma_2)}$$

or

$$\frac{\phi_2}{\phi_1} = \frac{i}{j} = \text{constant} \tag{6}$$

Equation (6) can be satisfied by a nonunique choice of the form of the function ϕ, the distinguishing property of Weibull's choice,

$$\phi(x) = \left(\frac{x - x_u}{x_0}\right)^m$$

$$F(x) = 1 - e^{-\left(\frac{x-x_u}{x_0}\right)^m} \tag{7}$$

is that

$$\frac{x_2 - x_u}{x_1 - x_u} = \sqrt[m]{\frac{i}{j}} \tag{8}$$

or the modified stress ratio is constant along V_i versus V_j, independent of the value of the percentile $F(X)$ in equation (7).

If two sets of samples are identical except in size (size is here generalized to be a basic building block of the phenomenon under observation, it is a parameter whose enumeration differentiates the sets of samples), and the only size effect is a constant shift of the x-variable, we may feel justified to say that these two sets of samples are self-consistent, or they belong to the same population that exhibits a self-consistent characteristic.

As pointed out by Weibull, any distribution may be represented by a sum of simple (linear) distributions. If we encounter data that are curved on Weibull paper, it can far more easily be explained on the basis of the samples not belonging to a single self-consistent population, than to arbitrarily impose a complex curve formulation and attempt to discover a logical new distribution function. Weibull's analysis of the statures for adult males born in the British Isles, for example, showed that the distribution could be represented by two self-consistent populations. An interested historian might research the immigration of people to the British Isles prior to 1917, and identify two major populations. By not using linear distributions, the opportunity for understanding the phenomenon may be forever lost.

References

1 Weibull W. "A Statistical Distribution Function of Wide Applicability," ASME JOURNAL OF APPLIED MECHANICS, Vol. 18, 1951, pp. 293–297.

2 Weibull W. "A Survey of Statistical Effects in the Field of Material Failure", *Applied Mechanic Surveys*, Macmillan, 1966, pp. 397–400.

[2]This approach was suggested by a reviewer of the ASME JOURNAL OF APPLIED MECHANICS.

Influence of End-Wall Friction on the Flow Rates of Granular Materials in Wedge-Shaped Hoppers

M. Sayed[1] and S. B. Savage[2]

Nomenclature

b = effective aperture width
d = particle diameter

[1]Research Assistant, Department of Civil Engineering and Applied Mechanics, McGill University, Montreal, Quebec, Canada H3A 2K6.

[2]Professor, Department of Civil Engineering and Applied Mechanics, McGill University, Montreal, Quebec, Canada H3A 2K6. Mem. ASME.

Manuscript received by ASME Applied Mechanics Division, April, 1981; final revision, November, 1981.

f = function of ϕ and ψ_w
g = gravitational acceleration
J = nondimensional plane flow rate
J' = corrected nondimensional flow rate
L = hopper length
r_0 = radius at the aperture
r_2 = radius at the upper stress-free surface
S = aperture width
u = radial velocity
W = mass flow rate
α = momentum coefficient
ϵ = end-wall friction angle
δ = side-wall friction angle
ρ = bulk density of the granular material
σ = mean stress
σ_1 = major principal stress
σ_r = radial normal stress
σ_z = lateral normal stress
σ_θ = circumferential normal stress
$\tau_{r\theta}, \tau_{zr}$ = shear stresses
ϕ = angle of friction of the granular material
ψ = angle between σ_1 and the r-axis
ψ_w = ψ at the inclined side walls

Introduction

The flow of granular materials in wedge-shaped hoppers (Fig. 1) is usually modeled as a two-dimensional flow between two infinitely long inclined planes (a review of previous work may be found in reference [1]). Analyses developed by the authors [1], which neglected the friction on the vertical end walls, tended to overestimate the experimental hopper flow rates. From physical considerations it would seem almost certain that including end-wall friction in these analyses would bring them in closer agreement with the experimental measurements. (One is not *absolutely* certain because as is noted in references [1], there exists both theoretical and experimental evidence that under certain conditions, increases in wall friction can actually *increase* the flow rate.) The present Note extends one of the theoretical analyses of reference [1] to examine the effects of such end-wall friction on predicted flow rates.

Governing Equations

Reference [1] presented two approximate solutions for stress and velocity fields in wedge-shaped hoppers, both of which were based on the method of integral relations. One, called Analysis I, made use of the linear momentum equations in both the r and θ directions. Based on the information learned from this analysis, Savage and Sayed [1] devised a second and much simpler approach called Analysis II, which made use of only one linear momentum equation, the radial momentum equation averaged over the width of the hopper. The two approaches, Analysis I and II, were found to yield results that were very close to each other; evidently the simple Analysis II was so constructed as to include the essential features present in the more complete theory.

For simplicity in the present paper, we shall develop an extension of the more straightforward Analysis II of reference [1].

Following the analysis presented in reference [1], the granular material is treated as a continuum obeying the Mohr-Coulomb yield criterion which is satisfied by expressing the stresses in terms of σ and ψ as follows,

$$\begin{aligned} \sigma_r &= \sigma(1+\sin\phi\cos 2\psi) \\ \sigma_\theta &= \sigma(1-\sin\phi\cos 1\psi) \\ \tau_{r\theta} &= \tau_{\theta r} = \sigma\sin\phi\sin 2\psi \end{aligned} \quad (1)$$

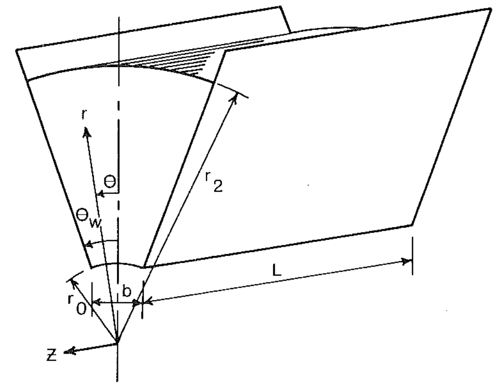

Fig. 1 Definition sketch of flow in wedge-shaped hopper

The flow is assumed radial with constant bulk density. An investigation of the compressibility of the flow near the aperture may be found in reference [1]. With the foregoing assumptions, the equations of continuity and balance of linear momentum in the r-directions become,

$$\frac{\partial}{\partial r}(\rho r u) = 0 \quad (2)$$

$$\frac{\partial \sigma_r}{\partial r} + \frac{1}{r}\frac{\partial \tau_{r\theta}}{\partial \theta} + \frac{\sigma_r - \sigma_\theta}{r} + \frac{\partial \tau_{zr}}{\partial z} + \rho g \cos\theta = -\rho u \frac{\partial u}{\partial r} \quad (3)$$

The term $\partial\tau_{zr}/\partial z$ in equation (3) accounts for the deviation from the two-dimensional stress field caused by the vertical end walls. Note that in the foregoing we have assumed the stress field to be three-dimensional but the deformation or flow field to be two-dimensional. The vertical side walls are thus considered to be sufficiently rough to generate finite shear stresses τ_{zr} but not rough enough to cause the material to shear on surfaces other than those perpendicular to the r-θ plane. The granular material slips on the vertical end walls even though shear stresses exist there. Such two-dimensional flow fields are commonly observed in hopper-flow visualization experiments in which the hopper is initially loaded with layers of different colored granular material and then discharged.

Analysis

The present analysis is based on an approximate two-dimensional theory termed Analysis II in reference [1]. Only a brief outline of this Analysis (which takes $\tau_{zr} = 0$) is given here. The normal stress σ_θ is assumed to have an average value $\bar{\sigma}_\theta$ depending only on the radial coordinate r. Substituting equations (1) and (2) in equation (3) and integrating from $\theta = 0$ to $\theta = \theta_w$, the r-momentum equation (3) is transformed into an ordinary differential equation. The resulting solution of the stress distribution is

$$\frac{\bar{\sigma}_\theta}{\rho g r_0} = \kappa\left(\frac{r}{r_0}\right)^\eta + \left[\frac{\sin\theta_w}{\theta_w - 2f\theta_w + \tan\delta}\right]\left(\frac{r}{r_0}\right) + \frac{1}{g r_0^3}\left[\frac{\alpha\lambda^2}{1+f+(\tan\delta)/\theta_w}\right]\left(\frac{r_0}{r}\right)^2 \quad (4)$$

where

$$f = \frac{4}{(2\psi_w - \pi)\cos\phi}\left\{\tan^{-1}\left[\frac{(1+\sin\phi)\tan\psi_w}{\cos\phi}\right] - \pi/2\right\} - 1 \quad (5)$$

and

$$\eta = [1+f+(\tan\delta)/\theta_w]/f \quad (6)$$

The constants κ and λ are determined from the boundary conditions at the upper and lower stress-free surfaces.

$$\bar{\sigma}_\theta(r_2) = \bar{\sigma}_\theta(r_0) = 0$$

The assumption of the lower stress-free surface to be at $r = r_0$ = constant, and the effect of this approximation on the flow rates is discussed in [1]. It was found there that flow rate solutions based on this approximate boundary condition were close to those in which the shape of the stress-free surface at the exit was explicitly determined. The nondimensional aperture velocity is

$$\frac{u_0}{\sqrt{gb}} = \left[\frac{1+f+(\tan\delta)/\theta_w}{\alpha[(2-4f)\theta_w + 2\tan\delta]}\right]^{1/2} \tag{8}$$

where b is the effective aperture width $(S-kd)$, and k is of order one.

The preceding expression for $u_0/\sqrt{gb}$ is different from the nondimensional flow rate J, which should be defined as

$$J = \frac{W}{\rho L g^{1/2} b^{3/2}} = \left(\frac{\theta_w}{\sin\theta_w}\right)\frac{u_0}{\sqrt{gb}} \tag{9}$$

(Note that in [1] the expressions for the nondimensional flow rates given by equations (33) and (41) are in error; these expressions are in fact $u_0/\sqrt{gb}$ and not J.)

Now the effects of the vertical end walls will be accounted for by including the term $\partial\tau_{zr}/\partial z$ in equation (3) in the analysis. Considering the material to reach yield in all three dimensions and assuming that the shear stresses developed on the vertical end walls are small, the lateral (z-direction) normal stress may be taken approximately equal to the major principal stress,

$$\sigma_z \simeq \sigma_1 = \sigma(1+\sin\phi) \tag{10}$$

This assumption is reminiscent of the Haar-von Kármán hypothesis for axisymmetric flow. It is reasonable for small end-wall friction coefficient ϵ, i.e., for small ϵ/ϕ. Thus integrating $\partial\tau_{zr}/\partial_z$ across the hopper gives

$$\frac{1}{\theta_w}\int_0^{\theta_w} \frac{\partial\tau_{zr}}{\partial_z}\, d\theta \cong \frac{-\bar{\sigma}_\theta}{L}(1+f)(1+\sin\theta)\tan\epsilon \tag{11}$$

where we have taken $\partial\tau_{zr}/\partial\theta \simeq \sigma z_w\,(\tan\epsilon)/(L/2)$ and used approximations similar to those in [1]. Integrating equation (3) from $\theta = 0$ to $\theta = \theta_w$, and using equation (11) yields,

$$fr\frac{d\bar{\sigma}_\theta}{dr} + \left[f - 1 - \frac{\tan\delta}{\theta_w} + M\left(\frac{r}{r_0}\right)\right]\bar{\sigma}_\theta = \rho g\frac{\sin\theta_w}{\theta_w} r + \frac{\alpha\lambda^2}{r^2} \tag{12}$$

where

$$M = \frac{-r_0}{L}(1+f)(1+\sin\phi)\tan\epsilon \tag{13}$$

Equation (12) was integrated numerically using a predictor corrector method. Starting with the initial conditions at the upper stress-free surface and assuming a value for the parameter λ, integration continued to the radius at which $\bar{\sigma}_\theta = \sigma = 0$, corresponding to the aperture.

The assumption (10) is true for small values of ϵ/ϕ and thus for small values of the shear stress τ_{zr}. Consequently, the term $M\,(r/r_0)\,\bar{\sigma}_\theta$ is small compared to the other terms in equation (12). This makes it possible to obtain a closed-form approximate solution by using the two-dimensional value of $\bar{\sigma}_\theta$ [equation (4)] to estimate the term $M\,(r/r_0)\,\bar{\sigma}_\theta$. The resulting expression for the stress distribution is

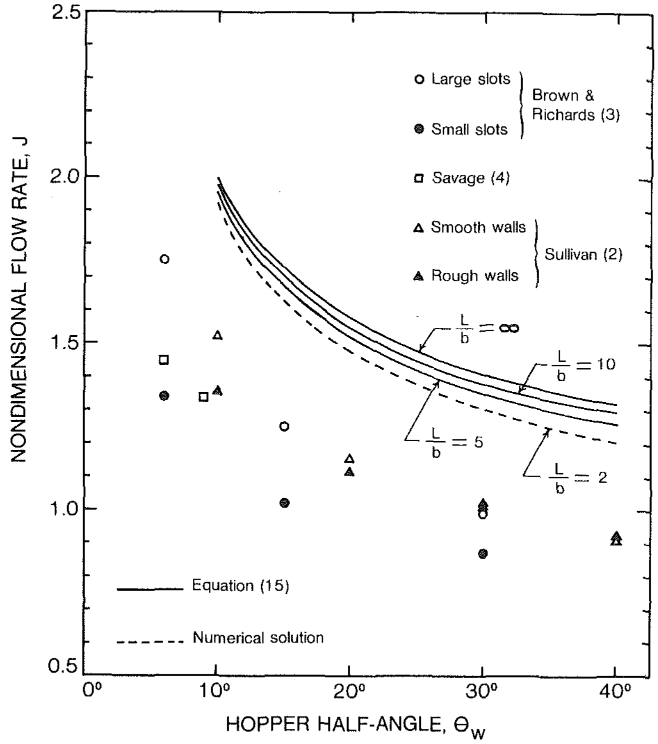

Fig. 2 Nondimensional flow rates, approximate solution [equation (15)], numerical solution for ϕ = 38 deg, δ = 22 deg, and ϵ = 14 deg

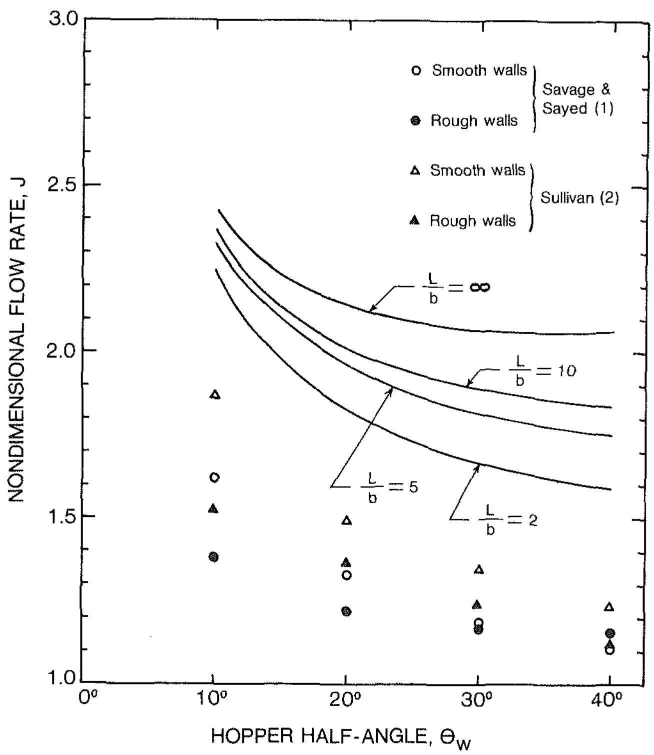

Fig. 3 Nondimensional flow rates, numerical solution for ϕ = 23 deg, δ = 14 deg, and ϵ = 9 deg

$$\frac{\bar{\sigma}_\theta}{\rho g r_0} = \kappa\left(\frac{r}{r_0}\right)^\eta\left[1 + \frac{M}{f}\left(\frac{r}{r_0}\right)\right] + \left[\frac{\sin\theta_w}{\theta_w - 2f\theta_w + \tan\delta}\right]\left[1 - \frac{M(r/r_0)}{3f - 1 - \dfrac{\tan\delta}{\theta_w}}\right]\left(\frac{r}{r_0}\right) + \frac{1}{g{r_0}^3}\left[\frac{\alpha\lambda^2}{1+f+(\tan\delta)/\theta_w}\right]\left[1 - \frac{M(r/r_0)}{1 + \dfrac{\tan\delta}{\theta_w}}\right]\left(\frac{r_0}{r}\right)^2 \tag{14}$$

Applying the boundary conditions (7), the nondimensional flow rate for large heads ($r_2 >> r_0$) becomes

$$J' = J\left[\frac{(1+\tan\delta/\theta_w)(3f-1-\tan\delta/\theta_w-M)}{\left(3f-1-\dfrac{\tan\delta}{\theta_w}\right)\left(1+\dfrac{\tan\delta}{\theta_w}+M\right)}\right]^{1/2} \tag{15}$$

Results and Discussion

This analysis is intended only for small values of the end-wall shear stresses τ_{zr}, i.e., for small values of the parameter M corresponding to small side-wall friction coefficients ϵ and length-to-aperture width ratio (L/b). Figure 2 shows typical predicted nondimensional flow rates J' for ϕ = 38 deg, δ = 22 deg, and ϵ = 14 deg, and the experimental results of Sullivan [2], Brown and Richards [3], and Savage [4]. The closed-form and numerical solutions were almost identical except for L/b = 2, where only numerical solutions could be obtained. Reductions of J' due to end-wall friction are moderate and the magnitude of the reductions decrease rapidly for increasing L/b. The values of J' for ϕ = 23 deg, δ = 14 deg, and ϵ = 9 deg could be obtained only numerically and are shown in Fig. 3, compared to the experimental results of the authors [1] and Sullivan [2]. The reductions of J' in this case are larger than those of ϕ = 38 deg.

The experimental values in reference [1] for ϕ = 23 deg were obtained by averaging the measured flow rates corresponding to different values of L/b ranging from 6.8–16. As might be expected for this limited range of L/b, only slight differences of the flow rates occurred and no clear dependence on L/b could be observed. The experimental flow rates of Brown and Richards [3] for sand ($\phi \simeq$ 38 deg) were higher for large slots (and small L/b) than for small slots (and large L/b). Apparently those flow rates were influenced by factors other than the vertical end-wall friction. One likely reason for the reduction of flow rates from small slots could be the intermittent arching phenomenon which is related to the particle diameter-to-slot width ratio. The values of L/b for the experiments of references [2] and [4] were not available.

The preceding results indicate that the inclusion of end-wall friction in the analysis brings the theoretical values of nondimensional flow rate closer to the experimental values. Further reductions due to compressibility and nonuniform velocity distribution near the aperture (see reference [1]), would result in a good agreement.

Acknowledgment

The authors are indebted to the Natural Science and Engineering Research Council of Canada (NSERC) for financial support during the course of this work.

References

1 Savage, S. B., and Sayed, M., "Gravity Flow of Cohesionless Granular Materials in Wedge-Shaped Hoppers," Mechanics Applied to the Transport of Bulk Materials, ASME AMD-31, 1979.

2 Sullivan, W. N., "Heat Transfer to Flowing Granular Media," Ph.D. Thesis, California Institute of Technology, Pasadena, Calif., 1972.

3 Brown, R. L., and Richards, J. C., "Principles of Powder Mechanics," 1st ed., Pergamon Press, Oxford, 1970.

4 Savage, S. B., "Some Considerations of Flow of Cohesionless Granular Solids," Ph.D. Thesis, McGill University, Montreal, 1967.

A Note on a No-Slip Interface Crack

L. M. Keer[1] and K. P. Meade[2]

Introduction

In [1] the adhesive fracture of an interdigitated or very rough surface was investigated by considering an interface crack with no-slip zones. Solutions of this type are motivated by problems in internal artificial human joints. The material (PMMA) forming the bond between the articulating surface and the bone does not adhere to the bone, but rather forms a mechanical interlock. It was found that for practical values of parameters representing a PMMA/ cancellous bone interface, the no-slip zones will generally extend throughout the entire crack region.

Results from experiments performed to study the characteristics of the PMMA/bone interface were reported in [2]. During the experiments the crack was observed to inititate from the tip of the notch in the test specimen at about 60 percent of the maximum applied load. This means that after the crack had started propagating, the structure increased its load-carrying capacity. Since adhesion between PMMA and cancellous bone is small and thus would be lost under minimal applied loads, it was suggested that the mechanical interlocking of the PMMA and the trabecular structure could be responsible for the increased load resistance as the crack opened.

In this Note, an interface crack with no tangential slip is considered where the strengthening mechanism due to the mechanical interlocking between the crack surfaces is simulated by relating the load on the crack surfaces to the crack opening displacement in a nonlinear manner. A nonlinear integral equation results and is solved using the method of successive approximations. The solution shows the effects of mechanical interlocking on the crack opening displacement and stress-intensity factor.

Formulation

Two linearly elastic, homogeneous, isotropic half planes are perfectly bonded along the interface, y = 0, except for the region $|x| < a$ where adhesion is lost. In this region the materials are mechanically interlocked so that no relative tangential slip between the crack surfaces can occur. The geometry and coordinate system are as depicted in Fig. 1 of [1].

The boundary conditions on y = 0 are:

$$\sigma_{xy}^1 = \sigma_{xy}^2, \quad \sigma_{yy}^1 = \sigma_{yy}^2, \quad u_x^1 = u_x^2, \quad 0 \leq |x| < \infty \tag{1}$$

$$u_y^1 = u_y^2 \quad a < |x| < \infty \tag{2}$$

$$\sigma_{xy}^1 = \sigma_{xy}^2 = 0, \quad \sigma_{yy}^1 = \sigma_{yy}^2 = -P(V(x)) \quad |x| < a \tag{3}$$

where

$$V(x) \equiv u_y^1(x,0) - u_y^2(x,0) \tag{4}$$

and the function $P(\cdot)$, representing the load applied to the crack surfaces, is as yet unspecified. The superscripts are used to distinguish the two materials.

Following Mak et al. [1], the boundary value problem may be reduced to the solution of the following integral equation:

$$V(x) = -\alpha^{-1}\int_0^a P(V(x_0))K(x_0,x) \quad dx_0, \tag{5}$$

where

$$K(x_0,x) = \frac{2}{\pi}\log\{[(1-(x_0/a)^2)^{1/2} + (1-(x/a)^2)^{1/2}] \,/\, |(x_0/a)^2 - (x/a)^2|^{1/2}\} \tag{6}$$

[1]Professor, Department of Civil Engineering, Northwestern University, Evanston, Ill. 60201. Mem. ASME.

[2]Graduate Student, Department of Civil Engineering, Northwestern University, Evanston, Ill. 60201. Student Mem. ASME.

Manuscript received by ASME Applied Mechanics Division, September, 1981; final revision, December 1981.

Applying the boundary conditions (7), the nondimensional flow rate for large heads ($r_2 >> r_0$) becomes

$$J' = J\left[\frac{(1+\tan\delta/\theta_w)(3f-1-\tan\delta/\theta_w - M)}{\left(3f-1-\dfrac{\tan\delta}{\theta_w}\right)\left(1+\dfrac{\tan\delta}{\theta_w}+M\right)}\right]^{1/2} \tag{15}$$

Results and Discussion

This analysis is intended only for small values of the end-wall shear stresses τ_{zr}, i.e., for small values of the parameter M corresponding to small side-wall friction coefficients ϵ and length-to-aperture width ratio (L/b). Figure 2 shows typical predicted nondimensional flow rates J' for ϕ = 38 deg, δ = 22 deg, and ϵ = 14 deg, and the experimental results of Sullivan [2], Brown and Richards [3], and Savage [4]. The closed-form and numerical solutions were almost identical except for $L/b = 2$, where only numerical solutions could be obtained. Reductions of J' due to end-wall friction are moderate and the magnitude of the reductions decrease rapidly for increasing L/b. The values of J' for ϕ = 23 deg, δ = 14 deg, and ϵ = 9 deg could be obtained only numerically and are shown in Fig. 3, compared to the experimental results of the authors [1] and Sullivan [2]. The reductions of J' in this case are larger than those of ϕ = 38 deg.

The experimental values in reference [1] for ϕ = 23 deg were obtained by averaging the measured flow rates corresponding to different values of L/b ranging from 6.8–16. As might be expected for this limited range of L/b, only slight differences of the flow rates occurred and no clear dependence on L/b could be observed. The experimental flow rates of Brown and Richards [3] for sand ($\phi \simeq$ 38 deg) were higher for large slots (and small L/b) than for small slots (and large L/b). Apparently those flow rates were influenced by factors other than the vertical end-wall friction. One likely reason for the reduction of flow rates from small slots could be the intermittent arching phenomenon which is related to the particle diameter-to-slot width ratio. The values of L/b for the experiments of references [2] and [4] were not available.

The preceding results indicate that the inclusion of end-wall friction in the analysis brings the theoretical values of non-dimensional flow rate closer to the experimental values. Further reductions due to compressibility and nonuniform velocity distribution near the aperture (see reference [1]), would result in a good agreement.

Acknowledgment

The authors are indebted to the Natural Science and Engineering Research Council of Canada (NSERC) for financial support during the course of this work.

References

1 Savage, S. B., and Sayed, M., "Gravity Flow of Cohesionless Granular Materials in Wedge-Shaped Hoppers," Mechanics Applied to the Transport of Bulk Materials, ASME AMD-31, 1979.

2 Sullivan, W. N., "Heat Transfer to Flowing Granular Media," Ph.D. Thesis, California Institute of Technology, Pasadena, Calif., 1972.

3 Brown, R. L., and Richards, J. C., "Principles of Powder Mechanics," 1st ed., Pergamon Press, Oxford, 1970.

4 Savage, S. B., "Some Considerations of Flow of Cohesionless Granular Solids," Ph.D. Thesis, McGill University, Montreal, 1967.

A Note on a No-Slip Interface Crack

L. M. Keer[1] and K. P. Meade[2]

Introduction

In [1] the adhesive fracture of an interdigitated or very rough surface was investigated by considering an interface crack with no-slip zones. Solutions of this type are motivated by problems in internal artificial human joints. The material (PMMA) forming the bond between the articulating surface and the bone does not adhere to the bone, but rather forms a mechanical interlock. It was found that for practical values of parameters representing a PMMA/ cancellous bone interface, the no-slip zones will generally extend throughout the entire crack region.

Results from experiments performed to study the characteristics of the PMMA/bone interface were reported in [2]. During the experiments the crack was observed to initiate from the tip of the notch in the test specimen at about 60 percent of the maximum applied load. This means that after the crack had started propagating, the structure increased its load-carrying capacity. Since adhesion between PMMA and cancellous bone is small and thus would be lost under minimal applied loads, it was suggested that the mechanical interlocking of the PMMA and the trabecular structure could be responsible for the increased load resistance as the crack opened.

In this Note, an interface crack with no tangential slip is considered where the strengthening mechanism due to the mechanical interlocking between the crack surfaces is simulated by relating the load on the crack surfaces to the crack opening displacement in a nonlinear manner. A nonlinear integral equation results and is solved using the method of successive approximations. The solution shows the effects of mechanical interlocking on the crack opening displacement and stress-intensity factor.

Formulation

Two linearly elastic, homogeneous, isotropic half planes are perfectly bonded along the interface, $y = 0$, except for the region $|x| < a$ where adhesion is lost. In this region the materials are mechanically interlocked so that no relative tangential slip between the crack surfaces can occur. The geometry and coordinate system are as depicted in Fig. 1 of [1].

The boundary conditions on $y = 0$ are:

$$\sigma_{xy}^1 = \sigma_{xy}^2, \quad \sigma_{yy}^1 = \sigma_{yy}^2, \quad u_x^1 = u_x^2, \quad 0 \le |x| < \infty \tag{1}$$

$$u_y^1 = u_y^2 \quad a < |x| < \infty \tag{2}$$

$$\sigma_{xy}^1 = \sigma_{xy}^2 = 0, \quad \sigma_{yy}^1 = \sigma_{yy}^2 = -P(V(x)) \quad |x| < a \tag{3}$$

where

$$V(x) \equiv u_y^1(x,0) - u_y^2(x,0) \tag{4}$$

and the function $P(\cdot)$, representing the load applied to the crack surfaces, is as yet unspecified. The superscripts are used to distinguish the two materials.

Following Mak et al. [1], the boundary value problem may be reduced to the solution of the following integral equation:

$$V(x) = -\alpha^{-1}\int_0^a P(V(x_0))K(x_0,x) \quad dx_0, \tag{5}$$

where

$$K(x_0,x) = \frac{2}{\pi}\log\{[(1-(x_0/a)^2)^{1/2} + (1-(x/a)^2)^{1/2}] \,/\, |(x_0/a)^2 - (x/a)^2|^{1/2}\} \tag{6}$$

[1] Professor, Department of Civil Engineering, Northwestern University, Evanston, Ill. 60201. Mem. ASME.

[2] Graduate Student, Department of Civil Engineering, Northwestern University, Evanston, Ill. 60201. Student Mem. ASME.

Manuscript received by ASME Applied Mechanics Division, September, 1981; final revision, December 1981.

and the symbol "log" indicates the natural logarithm. The constant α has the same definition as in [1].

In addition to preventing relative tangential slip, the mechanical interlocking between the crack surfaces may offer resistance to opening the crack [2]. Assuming this is the case, $P(\cdot)$ is taken as

$$P(V(x_0)) = \begin{cases} -P_0 + kV(x_0) - \gamma(V(x_0))^3 & 0 \le V(x_0) \le v \\ -P_0 & V(x_0) > v \end{cases} \tag{7}$$

where $-P_0$ is a constant applied pressure tending to open the crack. The quantity v represent the magnitude of the crack-opening displacement at which the mechanical interlocks would "fail" in the sense of no longer offering resistance to opening the crack. Also, v would necessarily be less than or equal to 2δ where δ is the average physical interdigitation height [1]. The constants k and γ characterize the material response of the mechanical interlocks in tension.

The form of equation (7) indicates that when the mechanical interlocking between the crack surfaces offers resistance to opening the crack, it behaves as a "nonlinear spring." Thus as the crack opening displacement increases there is an increased load resistance followed by a "softening" phase and then ultimately the interlocking "fails."

The constants k and γ are estimated in the following manner. Since the interlocking is assumed to resist the crack opening, the maximum value of this resistance, σ_R, is set equal to some fraction of the tensile strength of the interface, i.e., $\sigma_R = \epsilon\sigma_T$ where $0 < \epsilon < 1$ and σ_T is the tensile strength of the interface. For a PMMA/ cancellous bone interface the tensile strength is given as 1.8 MPa [2]. This assumption, together with equation (7) and the assumption that the interlocking "fails" in the sense described in the foregoing gives

$$k = \frac{3\sqrt{3}\sigma_R}{2v} = \frac{3\sqrt{3}\epsilon\sigma_T}{2v}, \quad \gamma = \frac{3\sqrt{3}\sigma_R}{2v^3} = \frac{3\sqrt{3}\epsilon\sigma_T}{2v^3}$$

Numerical Solution

Substituting equation (7) into equation (5) and introducing the dimensionless quantities $\xi = x/a$, $\xi_0 = x_0/a$, $W(\xi) = V(a\xi)/2\delta$, $\bar{P} = P_0 a/2\delta\alpha$, $\bar{k} = ka/\alpha$, $\bar{\gamma} = 4\delta^2\gamma a/\alpha$, and $\bar{v} = v/2\delta$ gives

$$W(\xi) = \bar{P}(1-\xi^2)^{1/2} - \int_0^1 N[W(\xi_0)]K(\xi_0,\xi)d\xi_0 \tag{8}$$

where

$$N[W(\xi_0)] = \begin{cases} \bar{k}W(\xi_0) - \bar{\gamma}[W(\xi_0)]^3 & 0 \le W(\xi_0) \le \bar{v} \\ 0 & W(\xi_0) > \bar{v} \end{cases} \tag{9}$$

Equation (8) is a nonlinear integral equation whose solution is determined using the method of successive approximations. The equation is written in the form

$$W_n(\xi) = \bar{P}(1-\xi^2)^{1/2} - \int_0^1 N[W_{n-1}(\xi_0)]K(\xi_0,\xi) \quad d\xi_0 \tag{10}$$

The first approximation, $W_0(\xi_0)$, is taken to be zero which gives

$$W_1(\xi) = \bar{P}(1-\xi^2)^{1/2} \tag{11}$$

i.e., the solution for the case where the mechanical interlocking offers no resistance to opening the crack. This agrees with equation (13) of [1]. Subsequent approximations are obtained numerically until a convergence criterion is satisfied.

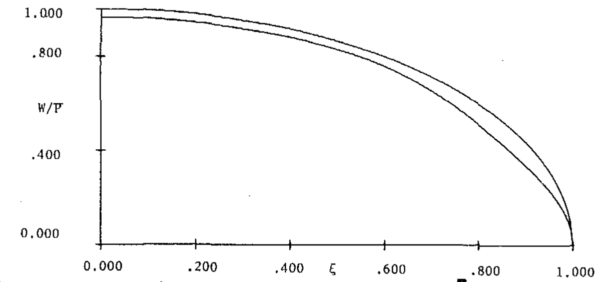

Fig. 1 Normalized crack opening displacement, $\bar{P}$ = 0.050. Upper curve is solution from [1]; lower curve is present analysis.

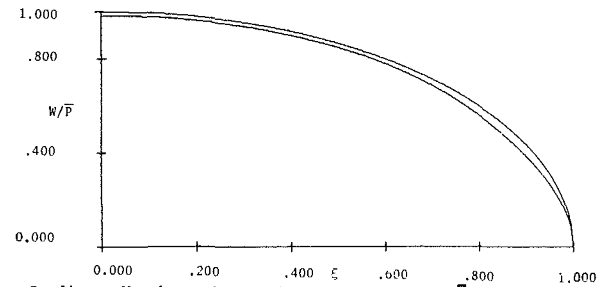

Fig. 2 Normalized crack opening displacement, $\bar{P}$ = 0.075. Upper curve is solution from [1]; lower curve is present analysis.

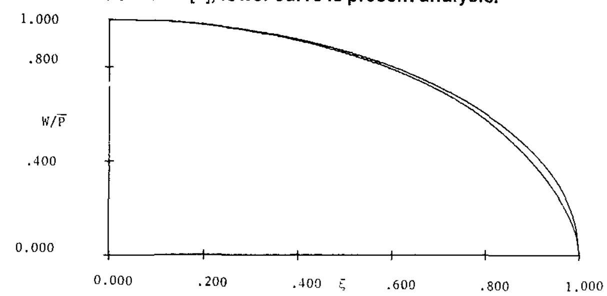

Fig. 3 Normalized crack opening displacement, $\bar{P}$ = 0.100. Upper curve is solution from [1]; lower curve is present analysis.

Table 1 Normalized stress-intensity factors

$\bar{P}$	0.050	0.075	0.100	0.200	0.300	0.400	0.500
K_I	0.87	0.93	0.92	0.96	0.98	0.98	0.98

Results and Discussion

Numerical results for the crack-opening displacement and stress-intensity factor are presented for $\bar{k} = 0.2436$, $\bar{\gamma} = 0.9744$, $\epsilon = 0.5$, $v/a = 0.10$, $\bar{v} = 0.5$, and $0 \le \bar{P} \le 0.500$.

For $\bar{P} = 0.050$ and 0.075, the effect of the mechanical interlocking on the crack-opening displacement is seen throughout the entire crack region (see Figs. 1 and 2). As the load is increased, the effect of the interlocking becomes concentrated near the crack tip (see Fig. 3). In all cases the crack-opening displacement is diminished due to the presence of the interlocking.

Table 1 shows that for $\bar{P} = 0.050$ the stress-intensity factor is 13 percent less than it would have been in the absence of the interlocking. This effect is seen to decay with an increase in the load to the point where there is only a 2 percent reduction in K_I for $\bar{P} = 0.500$.

Both results, the reduction of the crack-opening displacement and the stress-intensity factor, are consistent with the strengthening mechanism proposed by Mak [2].

Acknowledgment

The authors are grateful to partial support from the National Science Foundation, Grant 14EA-8117106.

References

1 Mak, A. F., Keer, L. M., Chen, S. H., Lewis, J. L., "A No-Slip Interface Crack," ASME Journal of Applied Mechanics, Vol. 47, 1980, pp. 347–350.

2 Mak, A. F., "Fracture Mechanics of the PMMA/Cancellous Bone Interface," Ph.D. Thesis, Northwestern University, Aug. 1980.

Pure Bending of Elliptic Ring Sector

H. A. Lang[1]

Introduction

The problem solved in this Brief Note is shown in Fig. 1. A ring sector is subjected to pure bending couples, M. The cross section is an ellipse defined by the equation $b^2x^2 + a^2y^2 = a^2b^2$ where a and b are the axes of the ellipse. The toroidal radius is R.

The method of analysis is particularly simple because it avoids the use of elliptic coordinates. Two methods of solution are available. The method of Göhner [1] and the method of toroidal elasticity (reference [2]). The method of Göhner is used because it is the simpler. Numerical results are listed in Table 1 for five values of the ratio b/a.

The analysis is limited to determining the first correction to the initial stress state for pure bending of an elliptic ring sector.

Analysis

The initial state for pure bending of an elliptic ring sector may be taken as:

$$\sigma_x = \sigma_y = \tau_{xy} = 0$$

and $\sigma_\theta = -cEx$, which is the stress distribution for pure bending of prismatical bars. Göhner [1] has developed the next equations which are:

$$\frac{\partial \sigma_x}{\partial x} - \frac{\partial \tau_{xy}}{\partial y} - \frac{cEx}{R} = 0$$

$$\frac{\partial \tau_{xy}}{\partial x} - \frac{\partial \sigma_y}{\partial y} = 0 \qquad (1)$$

These are the two equilibrium equations. In addition, the stress compatibility equations are:

$$\Delta\sigma_x + \frac{1}{1+\nu}\,\frac{\partial^2 \oplus}{\partial x^2} = 0$$

$$\Delta\sigma_y + \frac{1}{1+\nu}\,\frac{\partial^2 \oplus}{\partial y^2} = 0$$

$$\Delta\sigma_\theta + \left(\frac{2+\nu}{1+\nu}\right)\frac{cE}{R} = 0 \qquad (2)$$

$$\Delta\tau_{xy} - \frac{1}{1+\nu}\,\frac{\partial^2 \oplus}{\partial x \partial y} = 0$$

where:

$$\Delta \quad \text{denotes} \quad \frac{\partial^2}{\partial x^2} + \frac{\partial^2}{\partial y^2}$$

and

$$\oplus = \sigma_x + \sigma_y + \sigma_\theta$$

Next we introduce a stress function ϕ, such that

$$\sigma_x = \frac{cE}{2b^2R}\left[b^2x^2 + a^2y^2 - a^2b^2\right] + \frac{\partial^2\phi}{\partial y^2}$$

$$\sigma_y = \frac{\partial^2\phi}{\partial x^2} \qquad (3)$$

$$\tau_{xy} = \frac{\partial^2\phi}{\partial x \partial y}$$

[1] Director, LANG-Research West, Santa Monica, Calif. 90403.

Manuscript received by ASME Applied Mechanics Division, May 1981; final revision, November, 1981.

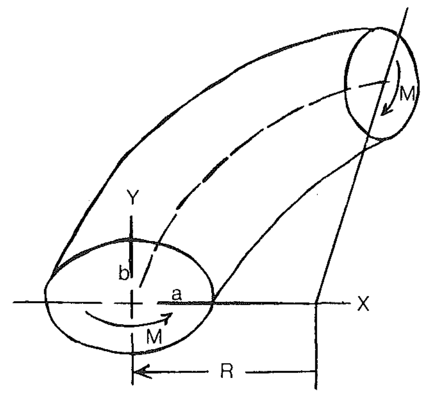

Fig. 1 Pure bending of ring section of elliptic cross section

Both equilibrium equations are identically satisfied.

The sum of the first three compatibility equations is

$$\Delta\oplus = -\frac{cE}{R}$$

Subtracting

$$\Delta\sigma_\theta = -\left(\frac{2+\nu}{1+\nu}\right)\frac{cE}{R}$$

so that (4)

$$\Delta(\sigma_x + \sigma_y) = \frac{1}{1+\nu}\,\frac{cE}{R}$$

Since

$$\sigma_x + \sigma_y = \frac{cE}{2b^2R}\,(b^2x^2 + a^2y^2 - a^2b^2) + \Delta\phi$$

$$\Delta(\sigma_x + \sigma_y) = \frac{cE}{b^2R}\,[a^2 + b^2] + \Delta\Delta\phi$$

and

$$\Delta\Delta\phi = \frac{cE(-\nu b^2 - (1+\nu)a^2)}{Rb^2(1+\nu)} \qquad (5)$$

Selecting for the stress function, ϕ, the expression

$$\phi = \frac{cEA_0}{64R}\,(b^2x^2 + a^2y^2 - a^2b^2)^2 \qquad (6)$$

we find

$$\Delta\Delta\phi = \frac{cEA_0}{R}\left[\frac{(a^2+b^2)^2 + 2(b^4 + a^4)}{8}\right]$$

Comparing with equation (5), the constant A_0 is:

$$A_0 = \frac{-8((1+\nu)a^2 + \nu b^2)}{b^2(1+\nu)[(a^2+b^2)^2 + 2(a^4+b^4)]} \qquad (7)$$

Finally, take

$$\sigma_\theta = \frac{cE}{R}\,[c_0 + c_1x^2 + c_2y^2]$$

and adjust c_0 so there is no resultant force on a cross section

$$N = 0 = \iint \sigma_\theta\, dxdy = \frac{cE}{R}\iint (c_0 + c_1x^2 + c_2y^2)\,dxdy$$

$$0 = \left[abc_0 + c_1\frac{a^3b}{4} + c_2\frac{ab^3}{4}\right]$$

or

$$c_0 = -\left[\frac{c_1a^2}{4} + \frac{c_2b^2}{4}\right] \qquad (8)$$

It remains to determine c_1 and c_2 from the compatibility equation. The last compatibility equation is identically satisfied.

Table 1 Numerical results

$b\rightarrow$	Multiplier	$0.5a$	$0.75a$	a	$1.5a$	$2a$
A_0	$\frac{cE}{Ra^4}$	−9.1789	−3.1666	−1.2308	−0.01507	−0.0625
c_1	$\frac{cE}{R}$	−1.0752	−1.0897	−1.0923	−1.4160	−1.0635
c_2	$\frac{cE}{R}$	0.1907	0.2051	0.1500	−0.1959	0.1790
c_0	$\frac{cEa^2}{R}$	0.2569	0.2436	0.2212	0.4642	0.0864
k_0	$\frac{a}{R}$	0.3102	0.3656	0.6381	0.0239	0.8178
$(c_0-c_1a^2)$	$\frac{cEa^2}{R}$	−0.8183	−0.8461	−0.8711	−0.9518	−0.9766
(σ_θ) (inner)	$\frac{cEa^2}{R}$	−0.0717	−0.1252	−0.1538	−0.0095	−0.1304

Equation (6) satisfies the boundary conditions which reduce to

$$\phi=0 \text{ and } \frac{\partial\phi}{\partial n}=0$$

Noting that the stresses are:

$$\sigma_x=\frac{cE}{2b^2R}[b^2x^2+a^2y^2-a^2b^2]$$

$$+\frac{cEA_0a^2}{16R}[3a^2y^2+b^2x^2-a^2b^2]$$

$$\sigma_y=\frac{cEA_0}{16b^2R}[3b^2x^2+a^2y^2-a^2b^2],$$

$$\tau_{xy}=\frac{cEA_0}{8R}(a^2b^2xy)$$

$$\sigma_\theta=\frac{cE}{R}\left[c_1\left(x^2-\frac{a^2}{4}\right)+c_2\left(y^2-\frac{b^2}{4}\right)\right]$$

The first compatibility equation reduces to

$$\frac{2+\nu}{1+\nu}+\frac{a^2}{b^2}+\frac{A_0a^2}{8}\left[\frac{3a^2(1+\nu)+h^2(2+\nu)}{(1+\nu)}\right]$$

$$+\frac{3}{8}\frac{A_0b^4}{1+\nu}+\frac{2c_1}{1+\nu}=0$$

from which

$$c_1=-\frac{a^2}{2b^2}(1+\nu)-\left(\frac{2+\nu}{2}\right)$$

$$-\frac{A_0}{16}[3a^4(1+\nu)+a^2b^2(2+\nu)+3b^4]$$

The second compatibility equation is:

$$\frac{a^2}{b^2(1+\nu)}+\frac{3}{8}\frac{A_0a^4}{(1+\nu)}+\frac{2c_2}{1+\nu}$$

$$+\frac{A_0b^2}{8(1+\nu)}[3b^2(1+\nu)+(2+\nu)a^2]=0$$

from which

$$c_2=-\frac{a^2}{2b^2}-\frac{A_0}{16}[3b^4(1+\nu)+a^2b^2(2+\nu)+3a^4]$$

Then, using equation (8),

$$c_0=\frac{a^4(1+\nu)+a^2b^2(3+\nu)}{8b^2}+\frac{A_0}{64}[3(1+\nu)(a^6+b^6)$$

$$+(5+\nu)a^4b^2+(5+\nu)a^2b^4]$$

Determination of the Constant, c

The constant c is determined by the moment equation

$$M=\iint-\sigma_\theta x\,dx\,dy$$

or

$$M_0=\iint-\sigma_{\theta_0}x\,dx\,dy=\frac{cEba^3\pi}{4}$$

For the more complete solution

$$M_1=\iint\sigma_{\theta_1}x\,dx\,dy=\frac{cE}{5R}(3a^2b^3c_2-c_1a^4b)$$

and

$$M=M_0+M_1$$

To the first approximation

$$cE=\frac{4M}{\pi ba^3}$$

To the next approximation

$$cE=\frac{4M}{\pi ba^3}\Big/\left[1+\frac{1}{5R}\left(\frac{3b^2c_2}{a}-c_1a\right)\right]$$

We write this as

$$cE=\frac{4M}{\pi ba^3}\left(\frac{1}{1+k_0}\right)$$

where:

$$k_0=\frac{4}{5\pi aR}[3b^2c_2-c_1a^2]$$

Numerical results for the constants A_0, c_1, c_2, c_0, and k_0 are given in Table 1 together with the value of stress σ_θ at the innermost point. The initial state of stress is omitted from Table 1.

Results for Stress at Inner Point ($x=a$)

Using the results of Table 1, we have

$$\sigma_\theta - cEa + cE(c_0 - c_1 a^2)$$

$$= -cEa\left[1 + \frac{c_1 a^2 - c_0}{a}\right]$$

For $b = 0.5a$

$$\sigma_\theta = -\frac{4M}{\pi b a^3}\left[\frac{1 + 0.8133\,\frac{a}{R}}{1 + 0.3102\,\frac{a}{R}}\right]$$

$$= -\frac{4M}{\pi b a^3}\left[1 + 0.5081\,\frac{a}{R} + \ldots.\right]$$

For $b = a$

$$\sigma_\theta = -\frac{4M}{\pi b a^3}\left[\frac{1 + 0.8711\,\frac{a}{R}}{1 + 0.6381\,\frac{a}{R}}\right]$$

$$= -\frac{4M}{\pi b a^3}\left[1 + 0.233\,\frac{a}{R} + \ldots.\right]$$

For $b = 2a$

$$\sigma_\theta = -\frac{4M}{\pi b a^3}\left[\frac{1 + 0.9766\,\frac{a}{R}}{1 + 0.8178\,\frac{a}{R}}\right]$$

$$= -\frac{4M}{\pi b a^3}\left[1 + 0.1588\,\frac{a}{R} + \ldots.\right]$$

References

1 Timoshenko, S., and Goodier, J. N., *Theory of Elasticity,* 2nd Ed., McGraw-Hill, 1951, pp. 395-398.

2 Lang, H. A., "Stress Analysis of Pressurized Elbows for Nuclear Components Using Toroidal Elasticity," *Fourth International Conference on Pressure Vessel Technology,* London, England, 1980, *Proceedings,* Vol. II, pp. 251-260.

Journal of Applied Mechanics

Discussion

The Vibrating Beam With Nonhomogeneous Boundary Conditions[1]

H. D. Fisher[2]. The author is to be congratulated for presenting a new solution method (subsequently designated the E method) for a class of time-dependent boundary value problems. The purpose of this discussion is to explore the generality of the E method and to present a detailed comparison of it with the widely used Mindlin-Goodman method (denoted here the M-G method) which is the author's reference [1]. The discusser was motivated to investigate the present problem by related research [1-3] in second-order systems.

The range of applicability of the E method is readily ascertained by expressing (1.2 – here the first number refers to the author's paper and the second to the numbered equation in that paper) and the last of the boundary conditions as

$$y(x,t) = Y(x,t) + F(x)\,T(t) + G(x)\,t\dot{T}(t) \tag{1}$$

and

$$y_{xx}(\pi,t) = \beta R(t) \tag{2}$$

where β is an arbitrary constant, $T(t)$ and $R(t)$ are time-dependent functions, and $\cdot$ denotes the derivative with respect to time. Taking the required derivatives of (1) and substituting into (1.1), gives (1.3) and the previously derived coupled system

$$F''''(X) - F(X) = 2G(X) \tag{3}$$

$$G''''(X) - G(X) = 0 \tag{4}$$

if, and only if,

$$\ddot{T}(t) + \alpha^2 T(t) = 0 \tag{5}$$

Thus from (5)

$$T(t) = A_1 \sin\alpha t + A_2 \cos\alpha t \tag{6}$$

where A_1 and A_2 are arbitrary constants. Substituting into the initial boundary conditions gives the earlier equations constraining Y, F, and G with the exception that the final restriction on F is replaced by

$$F''(\pi) = \beta \tag{7}$$

This substitution also discloses that

$$R(t) = T(t) \tag{8}$$

Equation (8) demonstrates that the E method, which requires that (3) and (4) be satisfied, is applicable exclusively to beam responses produced by sinusoid excitation.

Following the author's procedure, the solution to the problem described in the foregoing is given by (1) with

$$Y(x,t) = \sum_{n=1}^{\infty} (A_{4n} \sin\alpha n^2 t + A_{5n} \cos\alpha n^2 t) \sin nx \tag{9}$$

$$F(x) = A_3 \sin x + \frac{\beta}{2}\left(\frac{\sinh x}{\sinh \pi} + \frac{x}{\pi}\cos x\right) \tag{10}$$

$$G(x) = \frac{\beta}{\pi}\sin x \tag{11}$$

Here A_3 is an arbitrary constant and

$$A_{4n} = \left(\frac{2}{\pi\alpha n^2}\right)\int_0^\pi Y_t(x,0)\,\sin nx\,dx \tag{12}$$

$$A_{5n} = \left(\frac{2}{\pi}\right)\int_0^\pi Y(x,o)\,\sin nx\,dx \tag{13}$$

with

$$Y(x,0) = -A_2 F(x) \tag{14}$$

$$Y_t(x,0) = -\alpha A_1 [F(x) + G(x)] \tag{15}$$

The author's solution for the case when $\beta = 4A\pi$ and $R(t) = \sin\alpha t$ is readily derived from (1) comparing (10) and the first of (1.5) yields

$$A_3 = -5A \tag{16}$$

and from (8) and (6)

$$A_1 = 1,\ A_2 = 0 \tag{17}$$

Employing (16) and (17) in (12)-(15) simplifies (1) to (1.6) as required.

To solve (1.1) subject to the boundary conditions given in the author's paper, the M-G method requires that

$$y(x,t) = Y(x,t) + H(x)\,T(t) \tag{18}$$

with

$$H(x) = \frac{2A}{3}(x^3 - \pi^2 x) \tag{19}$$

and

$$T(t) = \sin\alpha t \tag{20}$$

Here $Y(x,t)$ satisfies the nonhomogeneous PDE

$$\alpha^2 Y_{xxxx}(x,t) + Y_{tt}(x,t) = \frac{2\alpha^2 A}{3}(x^3 - \pi^2 x)\sin\alpha t \tag{21}$$

together with the homogeneous boundary conditions (1.4) and the nonhomogeneous initial conditions

$$Y(x,0) = 0 \tag{22}$$

$$Y_t(x,0) = \frac{2\alpha A}{3}(\pi^2 x - x^3) \tag{23}$$

[1] Edstrom, C.R., and published in the September, 1981 issue of the ASME Journal of Applied Mechanics, Vol. 48, pp. 669-670.

[2] Consulting Engineer, Mechanical Design Department, Combustion Engineering, Inc., 1000 Prospect Hill Road, Windsor, Conn. 06095.

Inserting (19), (20), and the solution of (21)-(23) into (18) yields

$$y(x,t) = 8A\Bigg[\left(\frac{x^3-\pi^2x+6\sin x}{12}\right)\sin\alpha t + \frac{\alpha t\cos\alpha t\sin x}{2} + \sum_{n=2}^{\infty}\frac{(-1)^{n+1}}{n^3(n^4-1)}(n^2\sin\alpha n^2 t - \sin\alpha t)\sin nx\Bigg] \tag{24}$$

The equality of (1.6) and (24) follows since it can be shown that

$$\frac{2(x^3-\pi^2x)}{3} - 2x\cos x + 9\sin x - \frac{2\pi\sinh x}{\sinh\pi} = 8\sum_{n=2}^{\infty}\frac{(-1)^{n+1}\sin nx}{n^3(n^4-1)} \tag{25}$$

Because the *M-G* method has wider applicability than the *E* method, it remains the standard method of solution for beams subjected to time-dependent boundary excitation. However, for problems involving sinusoidal excitation only, the *E* method provides an alternate solution.

References

1 Fisher, H. D., Cepkaukas, M. M., and Chandra, S., "Solution of Time-Dependent Boundary Value Problems by the Boundary Operator Method," *International Journal of Solids and Structures*, Vol. 15, 1979, pp. 607–614.

2 Fisher, H. D., "Solution of a Generalized One-Dimensional Wave Equation by the Boundary Operator Method," *Journal of Sound and Vibration*, Vol. 79, No. 2, 1981, pp. 316–318.

3 Fisher, H. D., "A Generalized Wave Equation in Finite Domains," *Journal of the Engineering Mechanics Division, American Society of Civil Engineers*, Vol. 108, No. 1, 1982, pp. 155–163.

Author's Closure

H. D. Fisher's statement "that the *E* method is applicable exclusively to beam responses produced by sinusoid excitation" is not correct. The *E* method can be applied to boundary value problems with other boundary conditions. In the Brief Note it was not the author's intent to describe the most general case, but instead to show one illustration of the method. For more generality we have the following.

The existence of a form for the change of dependent variable depends on the properties of the functions that are prescribed on the boundaries. If these functions possess a finite number of linearly independent derivatives, then the form for the change of dependent variable should contain a linear combination of these functions and all of their linearly independent derivatives. However, in place of constants in this linear combination there should be functions of the variable held fixed on the boundary. Also, if the partial differential equation is separable as well as homogeneous, the particular product solutions can be determined. A comparison of these product solutions with the linear combination of the boundary functions and all of their derivatives will determine the need for either a bounded or unbounded form for the change of dependent variable. Thus, since the form for the change of dependent variable depends on the prescribed functions on the boundaries as well as the partial differential equation, the range of applicability of this method cannot be ascertained by generalizing the form of the change of dependent variable I used in the illustration of this method.

On the Formulation of Strain-Space Plasticity With Multiple Loading Surfaces[1]

J. Casey[2] and P. M. Naghdi[3]. We take exception to a number of points made in the paper of Yoder and Iwan [1], and especially to their claim that the stress-space and strain-space formulations of plasticity are equivalent. Although in [1] both single and multiple loading surfaces are employed, it suffices for the purpose of this discussion to consider only the case of single loading surfaces.

The possibility of using a strain-space (rather than a stress-space) formulation of plasticity has been mentioned by several authors in the past. However, the physical significance of the use of the strain-space formulation was first brought out in the paper of Naghdi and Trapp [2]. To elaborate, it was observed by Naghdi and Trapp [2] that the stress-space formulation of plasticity leads to unreliable results in any region such as that corresponding to the maximum point of engineering stress versus engineering strain curve for uniaxial tension of a typical ductile metal. After also observing that the stress-space formulation does not reduce directly to the theory of elastic-perfectly plastic materials, and that a separate formulation for the latter is required, Naghdi and Trapp [2] proposed an alternative strain-space formulation of plasticity which:

(*a*) is valid for the full range of elastic-plastic deformation; and

(*b*) includes as a special case, the theory of elastic-perfectly plastic materials.

The strain-space formulation was further elaborated in [3], which also contains a discussion of restrictions imposed on constitutive equations by a work assumption that was originally introduced in a strain-space setting by Naghdi and Trapp [4]. Additional related developments utilizing the strain-space formulation are contained in [5–7].

Yoder and Iwan [1, p. 774] state: "(Naghdi) did not establish equivalence between stress and strain space loading criteria . . . ." Actually, Naghdi and Trapp did undertake a comparison between the two independently postulated sets of loading criteria. They concluded that a correspondence between the two sets could be established for all conditions except that of loading from an elastic-plastic state. They observed [2, p. 792]: ". . . no general conclusion can be reached regarding the correspondence or equivalence of $\hat{g}>0$ (the loading criterion in strain space) and $\hat{f}>0$ (the loading criterion in stress space)."

Once a strain-space formulation is adopted, stress appears as a dependent variable, and it is conceivable that certain conditions in stress space might be induced by the conditions that are assumed in strain space. If this were indeed the case, then it would not be necessary, or even desirable, to postulate independent conditions in both strain space and stress space. This is the point of view that was taken by Casey and Naghdi [7], who showed that, in fact, the loading conditions in stress space are determined by those in strain space through the constitutive equations of the theory. However, the conditions induced in stress space during loading are not identical to those of the strain-space formulation, nor do they imply the loading conditions of the strain-space formulation[4].

[1] By P. S. Yoder and W. D. Iwan, and published in the December, 1981, issue of the ASME Journal of Applied Mechanics, Vol. 48, pp. 773–778.

[2] Department of Mechanical Engineering, University of Houston, Houston, Texas 77004.

[3] Department of Mechanical Engineering, University of California, Berkeley, Calif. 94720.

[4] For a summary of the relationship between the conditions in stress space and the loading criteria in strain space, see [7, Table 1].

Inserting (19), (20), and the solution of (21)-(23) into (18) yields

$$y(x,t)=8A\left[\left(\frac{x^3-\pi^2x+6\sin x}{12}\right)\sin\alpha t+\frac{\alpha t\cos\alpha t\sin x}{2}+\sum_{n=2}^{\infty}\frac{(-1)^{n+1}}{n^3(n^4-1)}(n^2\sin\alpha n^2t-\sin\alpha t)\sin nx\right] \tag{24}$$

The equality of (1.6) and (24) follows since it can be shown that

$$\frac{2(x^3-\pi^2x)}{3}-2x\cos x+9\sin x-\frac{2\pi\sinh x}{\sinh\pi}=8\sum_{n=2}^{\infty}\frac{(-1)^{n+1}\sin nx}{n^3(n^4-1)} \tag{25}$$

Because the *M-G* method has wider applicability than the *E* method, it remains the standard method of solution for beams subjected to time-dependent boundary excitation. However, for problems involving sinusoidal excitation only, the *E* method provides an alternate solution.

References

1 Fisher, H. D., Cepkaukas, M. M., and Chandra, S., "Solution of Time-Dependent Boundary Value Problems by the Boundary Operator Method," *International Journal of Solids and Structures*, Vol. 15, 1979, pp. 607–614.

2 Fisher, H. D., "Solution of a Generalized One-Dimensional Wave Equation by the Boundary Operator Method," *Journal of Sound and Vibration*, Vol. 79, No. 2, 1981, pp. 316–318.

3 Fisher, H. D., "A Generalized Wave Equation in Finite Domains," *Journal of the Engineering Mechanics Division, American Society of Civil Engineers*, Vol. 108, No. 1, 1982, pp. 155–163.

Author's Closure

H. D. Fisher's statement "that the *E* method is applicable exclusively to beam responses produced by sinusoid excitation" is not correct. The *E* method can be applied to boundary value problems with other boundary conditions. In the Brief Note it was not the author's intent to describe the most general case, but instead to show one illustration of the method. For more generality we have the following.

The existence of a form for the change of dependent variable depends on the properties of the functions that are prescribed on the boundaries. If these functions possess a finite number of linearly independent derivatives, then the form for the change of dependent variable should contain a linear combination of these functions and all of their linearly independent derivatives. However, in place of constants in this linear combination there should be functions of the variable held fixed on the boundary. Also, if the partial differential equation is separable as well as homogeneous, the particular product solutions can be determined. A comparison of these product solutions with the linear combination of the boundary functions and all of their derivatives will determine the need for either a bounded or unbounded form for the change of dependent variable. Thus, since the form for the change of dependent variable depends on the prescribed functions on the boundaries as well as the partial differential equation, the range of applicability of this method cannot be ascertained by generalizing the form of the change of dependent variable I used in the illustration of this method.

On the Formulation of Strain-Space Plasticity With Multiple Loading Surfaces[1]

J. Casey[2] and P. M. Naghdi[3]. We take exception to a number of points made in the paper of Yoder and Iwan [1], and especially to their claim that the stress-space and strain-space formulations of plasticity are equivalent. Although in [1] both single and multiple loading surfaces are employed, it suffices for the purpose of this discussion to consider only the case of single loading surfaces.

The possibility of using a strain-space (rather than a stress-space) formulation of plasticity has been mentioned by several authors in the past. However, the physical significance of the use of the strain-space formulation was first brought out in the paper of Naghdi and Trapp [2]. To elaborate, it was observed by Naghdi and Trapp [2] that the stress-space formulation of plasticity leads to unreliable results in any region such as that corresponding to the maximum point of engineering stress versus engineering strain curve for uniaxial tension of a typical ductile metal. After also observing that the stress-space formulation does not reduce directly to the theory of elastic-perfectly plastic materials, and that a separate formulation for the latter is required, Naghdi and Trapp [2] proposed an alternative strain-space formulation of plasticity which:

(*a*) is valid for the full range of elastic-plastic deformation; and

(*b*) includes as a special case, the theory of elastic-perfectly plastic materials.

The strain-space formulation was further elaborated in [3], which also contains a discussion of restrictions imposed on constitutive equations by a work assumption that was originally introduced in a strain-space setting by Naghdi and Trapp [4]. Additional related developments utilizing the strain-space formulation are contained in [5–7].

Yoder and Iwan [1, p. 774] state: "(Naghdi) did not establish equivalence between stress and strain space loading criteria . . . ." Actually, Naghdi and Trapp did undertake a comparison between the two independently postulated sets of loading criteria. They concluded that a correspondence between the two sets could be established for all conditions except that of loading from an elastic-plastic state. They observed [2, p. 792]: ". . . no general conclusion can be reached regarding the correspondence or equivalence of $\hat{g}>0$ (the loading criterion in strain space) and $\hat{f}>0$ (the loading criterion in stress space)."

Once a strain-space formulation is adopted, stress appears as a dependent variable, and it is conceivable that certain conditions in stress space might be induced by the conditions that are assumed in strain space. If this were indeed the case, then it would not be necessary, or even desirable, to postulate independent conditions in both strain space and stress space. This is the point of view that was taken by Casey and Naghdi [7], who showed that, in fact, the loading conditions in stress space are determined by those in strain space through the constitutive equations of the theory. However, the conditions induced in stress space during loading are not identical to those of the strain-space formulation, nor do they imply the loading conditions of the strain-space formulation[4].

[1] By P. S. Yoder and W. D. Iwan, and published in the December, 1981, issue of the ASME JOURNAL OF APPLIED MECHANICS, Vol. 48, pp. 773–778.

[2] Department of Mechanical Engineering, University of Houston, Houston, Texas 77004.

[3] Department of Mechanical Engineering, University of California, Berkeley, Calif. 94720.

[4] For a summary of the relationship between the conditions in stress space and the loading criteria in strain space, see [7, Table 1].

Geometrically, during loading the yield surface in strain space is always moving outward locally, whereas the corresponding yield surface in stress space may concurrently be moving outward, inward, or may be stationary. It should therefore be clear that the stress-space and strain-space formulations are not equivalent.

Our preference for choosing the loading criteria of strain space as primary in [7] was motivated by the limitations of the stress-space formulation that were mentioned in the foregoing. This leads [7] to a characterization of strain-hardening in terms of a rate-independent dimensionless quotient $\hat{f}/\hat{g}$ (with $\hat{g}>0$). A parallel analysis based on the possibility of taking the loading criteria of stress space as primary would lead to a characterization in terms of $\hat{g}/\hat{f}$ (with $\hat{f}>0$) – obviously, this characterization would be inappropriate if elastic-perfectly plastic behavior were also to be included, as indeed it must.

If the loading criteria of strain space are adopted as primary, then certain features of the work of Yoder and Iwan [1] may be obtained as a special case of that of Casey and Naghdi [7]. However, a demonstration of this requires considerable mathematical details; and, in the interest of keeping this discussion brief, the additional developments will be provided elsewhere. Finally, it may be emphasized that the basic theory of [2–7] is not limited to infinitesimal deformation and is valid for finite deformation of elastic-plastic materials.

References

1 Yoder, P. J., and Iwan, W. D., "On the Formulation of Strain-Space Plasticity With Multiple Loading Surfaces," ASME Journal of Applied Mechanics, Vol. 48, 1981, pp. 773–778.

2 Naghdi, P. M., and Trapp, J. A., "The Significance of Formulating Plasticity Theory With Reference to Loading Surfaces in Strain Space," *Int. J. Eng. Sci.*, Vol. 13, 1975, pp. 785–797.

3 Naghdi, P. M., "Some Constitutive Restrictions in Plasticity," *Proc. Symp. on Constitutive Equations in Viscoplasticity: Computational and Engineering Aspects*, AMD Vol. 20, 1976, pp. 79–93.

4 Naghdi, P. M., and Trapp, J. A., "Restrictions on Constitutive Equations of Finitely Deformed Elastic-Plastic Materials," *Quart. J. Mech. Appl. Math.*, Vol. 28, 1975, pp. 25–46.

5 Naghdi, P. M., and Trapp, J. A., "On the Nature of Normality of Plastic Strain Rate and Convexity of Yield Surfaces in Plasticity," ASME Journal of Applied Mechanics, Vol. 42, 1975, pp. 61–66.

6 Caulk, D. A., and Naghdi, P. M., "On the Hardening Response in Small Deformation of Metals," ASME Journal of Applied Mechanics, Vol. 45, 1978, pp. 755–764.

7 Casey, J., and Naghdi, P. M., "On the Characterization of Strain-Hardening in Plasticity," ASME Journal of Applied Mechanics, Vol. 48, 1981, pp. 285–296.

Authors' Closure

In view of Naghdi's pioneering efforts in the area of strain-space plasticity, we appreciate the careful attention that he and Casey have devoted to our recent paper [1]. It occurs to us that many of the points they raise in regard to the subject paper stem not so much from disagreements of substance as from the differing points of view from which we approach the matter of a strain-space formulation.

As noted in the introduction to [1], the analytical work documented therein was motivated in large part by the quest for more accurate and more efficient computational algorithms for plasticity. A follow-up paper [2], soon to appear, will present some numerical results intended to demonstrate the inherent superiority of the strain-space theory for computational applications. To keep this point from being obscured, it was decided to sidestep, for the time being, the question of finite deformations and cast the analysis of [1] and [2] within the traditional framework of the small-strain theory. Plasticity has, as a matter of fact, been extended to handle finite deformations in a number of different ways, as outlined by McMeeking and Rice [3]. Their recommendations on the matter, recently elaborated on by Hughes and Winget [4], do not precisely parallel those of Naghdi [5–7]. Naghdi's approach, therefore, appealing as it might be, is not the only possibility at hand, nor is it somehow inextricably linked to the concept of strain-space plasticity.

In describing the relationship between the stress and strain-space formulations, much of our language was influenced by a desire to address issues involved in the computational implementation of plasticity theory. So far as the authors know, previous computational algorithms for plasticity theory have been based on the notion of loading surfaces in stress space. This is true whether the algorithms were designed to deal with strain-hardening, perfectly plastic, or strain-softening behavior. Accordingly, it seemed natural to use the expression *stress-space plasticity* in a rather broad sense that includes whatever formulations might be necessary to describe these three cases in terms of stress-space loading surfaces. It appears in retrospect that some readers of [1] may have been confused concerning the intended scope of the presentation. It should be emphasized that constitutive law [Γ] as presented in the paper is appropriate only for the case of strain hardening ($\Delta>0$). The stress-space formulations applicable to perfect plasticity ($\Delta=0$) and to strain softening ($\Delta<0$) are omitted from [1] for brevity but may be found in reference [8].

Never was there any intention to suggest that the strain-hardening constitutive law [Γ] could be used interchangeably with [*C*] in cases of perfect plasticity or strain softening. The authors wholeheartedly agree with Casey and Naghdi that statement (γ), or $\hat{f} > 0$ in their notation, would be a most unacceptable criterion for loading in cases of perfect plasticity or strain softening. It was never claimed that the loading conditions induced in stress space were "identical" to those in strain space. That they could not be identical is obvious because, as Casey and Naghdi point out, during loading the relaxation surface in strain space is moving outward locally while the yield surface in stress space may be moving outward, inward, or may be stationary. This conclusion in fact follows directly from an extension of the concepts presented in the authors' paper [8]. This observation does not in any way conflict with the idea of "equivalence" as used by the authors.

The authors submit that [*C*] and [Γ], as specified in their paper, can be used interchangeably in cases of strain hardening provided the model parameters are interrelated through equations (18)–(20). In this regard it would perhaps be helpful to discuss in more detail the reasons for using the word *equivalence* to describe this relationship. It should be noted that $\boldsymbol{\sigma}^R$ and $\boldsymbol{\epsilon}^P$, as defined through equations (5) and (15), are merely alternative indications of the deviation from Hookean linearity. Until some assumptions are made regarding the manner in which they evolve as deformation proceeds, their use cannot in any way impose restrictions on the mechanical response. Similarly, the loading functions $\hat{F}$ and $\hat{\Phi}$ are powerless to influence the material behavior until either [*C*] or [Γ] is activated. Thus it is possible at any stage during the deformation to compute values for both D and Δ, based on the stress and strain history, without in any way influencing the relationship between the *next* stress and strain increments. Now, it is shown in [8] that if $\Delta>0$ and [*C*] is valid, then so is [Γ]. The scheme of the proof is as follows:

$$\begin{array}{rcl} (a) & \Rightarrow & (\alpha)\quad ; \\ (\beta) \text{ and } (\gamma) & \Rightarrow & (b) \text{ and } (c) \\ & \Rightarrow & (d) \\ & \Rightarrow & (\delta)\quad ; \\ \text{not } (\beta) \text{ or not } (\gamma) & \Rightarrow & \text{not } (b) \text{ or not } (c) \\ & \Rightarrow & (e) \\ & \Rightarrow & (\epsilon)\quad . \end{array}$$

In a similar way, if $\Delta > 0$, $[\Gamma] \Rightarrow [C]$. Analogous results can also be obtained for cases of perfect plasticity ($\Delta = 0$) and strain softening ($\Delta < 0$) [8] – provided the stress-space formulations are properly framed. This is what the authors mean by the word *equivalent*.

We apologize if the use of this word has proved misleading to some readers of the subject paper. The main point to be stressed is that in designing a computational algorithm for plasticity, one is at liberty to work from either the stress or strain-space version, whichever is more convenient, since the two approaches can, with certain restrictions, be made to yield the same physical behavior. The computational experience reported in [2] and [8] lends additional support to the interchangeability of these two formulations.

References

1 Yoder, P. J., and Iwan, W. D., "On Formulation of Strain-Space Plasticity With Multiple Loading Surfaces," ASME JOURNAL OF APPLIED MECHANICS, Vol. 48, 1981, pp. 773–778.

2 Yoder, P. J., and Iwan, W. D., "Computational Aspects of Strain Space Plasticity," accepted for publication in ASCE *J. Engineering Mechanics Div.*

3 McMeeking, R. M., and Rice, J. R., "Finite Element Formulation for Problems of Large Elastic-Plastic Deformation," *Int. J. Solids Structures*, Vol. 11, 1975, pp. 601–616.

4 Hughes, T. J. R., and Winget, J., "Finite Rotation Effects in Numerical Integration of Rate Constitutive Equations Arising in Large-Deformation Analysis," *Int. J. Numerical Methods in Engineering*, Vol. 15, 1980, pp. 1862–1867.

5 Naghdi, P. M., and Trapp, J. A., "The Significance of Formulating Plasticity Theory With Reference to Loading Surfaces in Strain Space," *Int. J. Eng. Sci.*, Vol. 13, 1975, pp. 785–797.

6 Naghdi, P. M., "Some Constitutive Restrictions in Plasticity," *Proc. Symp. on Constitutive Equations in Viscoplasticity: Computational and Engineering Aspects*, AMD Vol. 20, 1976, pp. 79–93.

7 Casey, J., and Naghdi, P. M., "On the Characterization of Strain-Hardening in Plasticity," ASME JOURNAL OF APPLIED MECHANICS, Vol. 48, 1981, pp. 285–296.

8 Yoder, P. J., "A Strain-Space Plasticity Theory and Numerical Implementation," Ph.D. Thesis, California Institute of Technology, 1981.

The Annular Membrane Under Axial Load[1]

Robert Schmidt.[2] Let us introduce auxiliary notations x, y, z, and p defined by

$$r_2^2 x = r^2, \quad 4Dy = r^2 N_r, \tag{1a,b}$$

$$2^{3/2} tz = [3(1-\nu^2)]^{1/2} r\beta, \tag{1c}$$

$$2^{5/2} \pi E t^4 p = [3(1-\nu^2)]^{3/2} r_2^2 P, \tag{1d}$$

where $D = Et^3/12(1-\nu^2)$, and the remaining symbols have the meaning assigned to them in the Note under discussion. With these notations, the nonlinear differential equations [1] governing moderately large axisymmetric deflections of circular plates become [2, 3]

$$x^2 y'' = -z^2, \quad x^2 z'' = yz + px, \tag{2a,b}$$

where primes denote derivatives with respect to x.

For a membrane, the foregoing equations reduce to

$$x^2 y'' = -z^2, \quad yz = -px, \tag{3a,b}$$

and finally to Schwerin's form [4]

$$y^2 y'' = -p^2, \tag{4}$$

which possesses closed-form general implicit and special explicit solutions [4, 5], both of which were published by Schwerin in 1929 [4].[3] Needless to say, Schwerin was rather proud of his discovery, which doubled the number of known closed-form solutions in the theory of slack membranes from one to two. The authors of the present Note have simply rediscovered Schwerin's special solution, which is valid for $\nu = 1/3$.

Much later, closed-form solutions, similar to Schwerin's, were obtained by Jahsman, Field, and Holmes [5] for a prestretched axisymmetrical membrane, and by E. Reissner for a spherical membrane.

References

1 Timoshenko, S., and Woinowsky-Krieger, S., *Theory of Plates and Shells*, 2nd ed., McGraw-Hill, New York, 1959.

2 Schmidt, R., "Large Deflections of a Clamped Circular Plate," *Journal of the Engineering Mechanics Division, Proc. ASCE*, Vol. 94, No. EM6, Dec. 1968, pp. 1603–1606.

3 Schmidt, R., "Finite Deflections of a Circular Plate Sealing an Incompressible Liquid," ASME JOURNAL OF APPLIED MECHANICS, Vol. 43, No. 4, Dec. 1976, pp. 694–695.

4 Schwerin, E., "Ueber Spannungen und Formaenderungen kreisring-foermiger Membranen," *Zeitschrift fuer technische Physik*, Vol. 10, No. 12, 1929, pp. 651–659.

5 Jahsman, W. E., Field, F. A., and Holmes, A. M. C., "Finite Deformations in a Prestressed, Centrally Loaded, Circular Elastic Membrane," *Proceedings of the Fourth U. S. National Congress of Applied Mechanics*, Vol. 1, 1962, pp. 585–594.

[3] It should be noted that equation (4) is analogous to the differential equation $r^2 \ddot{r} = \text{const.}$, describing the free fall of two spherical bodies toward each other.

[1] By D. J. Allman and E. H. Mansfield, and published in the December, 1981, issue of the ASME JOURNAL OF APPLIED MECHANICS, Vol. 48, pp. 975–976.

[2] Professor of Engineering Mechanics, Department of Mechanical Engineering, University of Detroit, Detroit, Mich. 48221. Mem. ASME.

The Annular Membrane Under Axial Load[1]

C. W. Bert[2]. The authors are to be congratulated for obtaining a closed-form solution for a nonlinear problem which has not been solved previously in the context of the Föppl theory [1] used. The limitations of the Föppl theory have been discussed by Junkin and Davis [2] in comparison with an exact membrane theory obtained from Budiansky's shell equations [3]. In reference [2], it was shown that Föppl's theory is valid only when the ratio of the deflection to the outside radius is small compared to unity. Nevertheless, using order-of-magnitude considerations, reference [2] obtained, for $\nu = 1/3$, a closed-form solution equivalent to that obtained by the authors.

[1] By D. J. Allman and E. H. Mansfield, and published in the December, 1981, issue of the ASME JOURNAL OF APPLIED MECHANICS, Vol. 48, 1981, pp. 975–976.

[2] Perkinson Professor of Engineering, School of Aerospace, Mechanical and Nuclear Engineering, The University of Oklahoma, Norman, Okla. 73019.

In a similar way, if $\Delta>0$, $[\Gamma] \Rightarrow [C]$. Analogous results can also be obtained for cases of perfect plasticity ($\Delta=0$) and strain softening ($\Delta<0$) [8] – provided the stress-space formulations are properly framed. This is what the authors mean by the word *equivalent*.

We apologize if the use of this word has proved misleading to some readers of the subject paper. The main point to be stressed is that in designing a computational algorithm for plasticity, one is at liberty to work from either the stress or strain-space version, whichever is more convenient, since the two approaches can, with certain restrictions, be made to yield the same physical behavior. The computational experience reported in [2] and [8] lends additional support to the interchangeability of these two formulations.

References

1 Yoder, P. J., and Iwan, W. D., "On Formulation of Strain-Space Plasticity With Multiple Loading Surfaces," ASME JOURNAL OF APPLIED MECHANICS, Vol. 48, 1981, pp. 773–778.

2 Yoder, P. J., and Iwan, W. D., "Computational Aspects of Strain Space Plasticity," accepted for publication in ASCE *J. Engineering Mechanics Div.*

3 McMeeking, R. M., and Rice, J. R., "Finite Element Formulation for Problems of Large Elastic-Plastic Deformation," *Int. J. Solids Structures*, Vol. 11, 1975, pp. 601–616.

4 Hughes, T. J. R., and Winget, J., "Finite Rotation Effects in Numerical Integration of Rate Constitutive Equations Arising in Large-Deformation Analysis," *Int. J. Numerical Methods in Engineering*, Vol. 15, 1980, pp. 1862–1867.

5 Naghdi, P. M., and Trapp, J. A., "The Significance of Formulating Plasticity Theory With Reference to Loading Surfaces in Strain Space," *Int. J. Eng. Sci.*, Vol. 13, 1975, pp. 785–797.

6 Naghdi, P. M., "Some Constitutive Restrictions in Plasticity," *Proc. Symp. on Constitutive Equations in Viscoplasticity: Computational and Engineering Aspects*, AMD Vol. 20, 1976, pp. 79–93.

7 Casey, J., and Naghdi, P. M., "On the Characterization of Strain-Hardening in Plasticity," ASME JOURNAL OF APPLIED MECHANICS, Vol. 48, 1981, pp. 285–296.

8 Yoder, P. J., "A Strain-Space Plasticity Theory and Numerical Implementation," Ph.D. Thesis, California Institute of Technology, 1981.

The Annular Membrane Under Axial Load[1]

Robert Schmidt.[2] Let us introduce auxiliary notations x, y, z, and p defined by

$$r_2^2 x = r^2, \quad 4Dy = r^2 N_r, \tag{1a,b}$$

$$2^{3/2} tz = [3(1-\nu^2)]^{1/2} r\beta, \tag{1c}$$

$$2^{5/2} \pi E t^4 p = [3(1-\nu^2)]^{3/2} r_2^2 P, \tag{1d}$$

where $D = Et^3/12(1-\nu^2)$, and the remaining symbols have the meaning assigned to them in the Note under discussion. With these notations, the nonlinear differential equations [1] governing moderately large axisymmetric deflections of circular plates become [2, 3]

$$x^2 y'' = -z^2, \quad x^2 z'' = yz + px, \tag{2a,b}$$

where primes denote derivatives with respect to x.

For a membrane, the foregoing equations reduce to

$$x^2 y'' = -z^2, \quad yz = -px, \tag{3a,b}$$

and finally to Schwerin's form [4]

$$y^2 y'' = -p^2, \tag{4}$$

which possesses closed-form general implicit and special explicit solutions [4, 5], both of which were published by Schwerin in 1929 [4].[3] Needless to say, Schwerin was rather proud of his discovery, which doubled the number of known closed-form solutions in the theory of slack membranes from one to two. The authors of the present Note have simply rediscovered Schwerin's special solution, which is valid for $\nu = 1/3$.

Much later, closed-form solutions, similar to Schwerin's, were obtained by Jahsman, Field, and Holmes [5] for a prestretched axisymmetrical membrane, and by E. Reissner for a spherical membrane.

References

1 Timoshenko, S., and Woinowsky-Krieger, S., *Theory of Plates and Shells*, 2nd ed., McGraw-Hill, New York, 1959.

2 Schmidt, R., "Large Deflections of a Clamped Circular Plate," *Journal of the Engineering Mechanics Division, Proc. ASCE*, Vol. 94, No. EM6, Dec. 1968, pp. 1603–1606.

3 Schmidt, R., "Finite Deflections of a Circular Plate Sealing an Incompressible Liquid," ASME JOURNAL OF APPLIED MECHANICS, Vol. 43, No. 4, Dec. 1976, pp. 694–695.

4 Schwerin, E., "Ueber Spannungen und Formaenderungen kreisring-foermiger Membranen," *Zeitschrift fuer technische Physik*, Vol. 10, No. 12, 1929, pp. 651–659.

5 Jahsman, W. E., Field, F. A., and Holmes, A. M. C., "Finite Deformations in a Prestressed, Centrally Loaded, Circular Elastic Membrane," *Proceedings of the Fourth U. S. National Congress of Applied Mechanics*, Vol. 1, 1962, pp. 585–594.

[3] It should be noted that equation (4) is analogous to the differential equation $r^2\ddot{r} = \text{const.}$, describing the free fall of two spherical bodies toward each other.

[1] By D. J. Allman and E. H. Mansfield, and published in the December, 1981, issue of the ASME JOURNAL OF APPLIED MECHANICS, Vol. 48, pp. 975–976.

[2] Professor of Engineering Mechanics, Department of Mechanical Engineering, University of Detroit, Detroit, Mich. 48221. Mem. ASME.

The Annular Membrane Under Axial Load[1]

C. W. Bert[2]. The authors are to be congratulated for obtaining a closed-form solution for a nonlinear problem which has not been solved previously in the context of the Föppl theory [1] used. The limitations of the Föppl theory have been discussed by Junkin and Davis [2] in comparison with an exact membrane theory obtained from Budiansky's shell equations [3]. In reference [2], it was shown that Föppl's theory is valid only when the ratio of the deflection to the outside radius is small compared to unity. Nevertheless, using order-of-magnitude considerations, reference [2] obtained, for $\nu = 1/3$, a closed-form solution equivalent to that obtained by the authors.

[1] By D. J. Allman and E. H. Mansfield, and published in the December, 1981, issue of the ASME JOURNAL OF APPLIED MECHANICS, Vol. 48, 1981, pp. 975–976.

[2] Perkinson Professor of Engineering, School of Aerospace, Mechanical and Nuclear Engineering, The University of Oklahoma, Norman, Okla. 73019.

Even in the context of the Föppl theory, the second of equations (2), is not quite correct, since it involves an extra derivative with respect to radius. The correct equation is

$$r\frac{d}{dr}\left[\frac{1}{r}\frac{d}{dr}\left(r\frac{d\Phi}{dr}\right)\right]+\frac{1}{2}Et\left(\frac{dw}{dr}\right)^2=0 \tag{1}$$

Then equation (6) becomes

$$c\beta^2(\beta-2)r^{\beta-2}+\frac{1}{2}Et\ k^2\alpha^2r^{2\alpha-2}=0 \tag{2}$$

Fortunately, the solution obtained by the authors, as manifested in their equations (3), (4), and (7), satisfies the preceding corrected equations and thus is still correct.

The lower order in equation (1) follows directly from the appropriate compatibility equation for this problem:

$$\frac{d}{dr}(r\epsilon_\theta)-\epsilon_r=-\frac{1}{2}\left(\frac{dw}{dr}\right)^2 \tag{3}$$

since the strain-displacement relations are:

$$\epsilon_r=\frac{du}{dr}+\frac{1}{2}\left(\frac{dw}{dr}\right)^2;\quad \epsilon_\theta=u/r \tag{4}$$

To compare results with an existing numerical solution [4] (not based on Föppl's theory), the authors' equations can be cast in the following dimensionless form

$$w_{\max}/r_2=(6f)^{1/3}(1-\rho^{2/3}) \tag{5}$$

$$(\sigma_r)_{\max}/E=(9/16)^{1/3}f^{2/3}\rho^{-2/3} \tag{6}$$

where $\rho=r_1/r_2$, $f=P/2\pi Etr_2$. It is interesting to note that although Lidin's analysis [4] is not based on Föppl's theory, Lidin obtained the same form of the variation of $w_{\max}/r_2$ and $(\sigma_r)_{\max}/E$ with f as in equations (5) and (6). However, there is some difference between the respective dependencies on ρ, as can be seen in the following tabulation:

	Values of $w_{\max}/r_2f^{1/3}$		Values of $(\delta_r)_{\max}/Ef^{2/3}$	
Radius ratio ρ	Allman & Mansfield	[4]	Allman & Mansfield	[4]
0.1	1.426	1.239	3.832	3.906
0.3	1.003	0.9042	1.842	1.735
0.5	0.6724	0.6849	1.310	1.201
0.7	0.3846	0.4287	1.047	0.8697
0.9	0.1233	0.2394	0.8856	0.5420

It is noted that Lidin's result is purportedly valid for any Poisson's ratio, yet it is independent of Poisson's ratio, which seems unusual from a physical viewpoint.

References

1 Föppl, A., *Vorlesungen über Technische Mechanik*, Vol., 5, B. G. Teubner Leipzig, 1907, p. 132.

2 Junkin, G. II, and Davis, R. T., "General Non-Linear Plate Theory Applied to a Circular Plate with Large Deflections," *Int. J. Non-Lin. Mech.*, Vol. 7, 1972, pp. 503–526.

3 Budiansky, B., "Notes on Nonlinear Shell Theory," ASME Journal of Applied Mechanics, Vol. 35, 1968, pp. 393–401.

4 Lidin, L., "Circular Elastic Membrane Loaded at Concentric Circle," *AIAA Journal*, Vol. 13, 1975, pp. 1242–1245.

Author's Closure

The authors are pleased to note the interest shown in their paper by Professor Bert and they are indebted to him for the valuable comparison of results with earlier work.

In response to his discussion, however, it must be restated here that the second of equations (2) is the correct Föppl equation (which is of fourth order) for the annular membrane under axial load. The third-order equation derived from first principles by Professor Bert is recognized as the first integral of the Föppl equation with the constant of integration zero, as is necessary for a solution of equation (6) to be obtained.

A subsequent paper [1] by the first author, which uses a variational formulation of Föppl's theory to obtain approximate solutions for the annular membrane under axial load, will also be published soon. Numerical results are presented there for a range of values of Poisson's ratio including the value of one-third considered in the present work.

References

1 Allman, D. J., "Variational Solutions for the Nonlinear Deflexion of an Annular Membrane Under Axial Load," to be published in *International Journal of Mechanical Sciences*.

Journal of Applied Mechanics

Book Reviews

The Physics of Deformation and Flow. By E. W. Billington and A. Tate. McGraw-Hill, New York, 1981. pp. xx–626. Price $59.00.

REVIEWED BY DANIEL C. DRUCKER[1]

This is a most unusual book of great value to those entering the field or changing the direction of their research. It is unusual because of its broad coverage from advanced mathematics to simple experiments, from linear and nonlinear fluids, and linear and nonlinear elastic solids to plastic solids, and because of its aim to bring together, in a meaningful way and at a high level, both macroscopic and microscopic physical behavior within a broad set of current continuum mechanics approaches. A remarkable compartmentalization of approach is employed without comment in a most successful innovation. Each major section is written primarily from the viewpoint of those who developed that specific area in its present form. The authors exercise judgment in the choices they make of inclusion or omission but then carefully display the mathematics and the physical arguments to represent the school of thought (as of June 1979) without the distraction of contrary viewpoints. Consequently there is much with which each expert will disagree but much more that will prove helpful in achieving greater understanding. Ample reference is made to the relevant literature needed to follow up on the background presented.

The work of Truesdell, Toupin, and Noll, to which extensive credit is given, is preceded by a mathematical introduction to scalars, vectors, and tensors. Yet this approach sits side by side with other sections from other points of view including both those that are primarily physically based and those that are reminiscent of Love and Lamb in their detailed writing of scalar equations. Appropriate sections are interspersed that give descriptions of electronic, atomic, and interatomic structure and forces, dislocations and dislocation structure of solids, molecular structure of fluids, statistical mechanics, and the results of basic continuum experiments. A full chapter is devoted to crystal plasticity between two chapters on continuum plasticity. Impact, dynamic plasticity, and shock waves receive the attention to be expected from the great interest of the authors in these fields, but the writing here is just as concise and effective as in the closing chapter on fracture, and throughout the book. The authors certainly have done well to provide the continuum mechanics background that would be of great help to materials scientists and engineers as well as the "useful reminder to those involved in continuum mechanics that the ultimate test of abstract theories lies in the laboratory."

[1] Dean, College of Engineering, University of Illinois at Urbana-Champaign, Urbana, Ill. 61801.

Biomechanics. Mechanical Properties of Living Tissues. By Y. C. Fung. Springer-Verlag, New York, Heidelberg, Berlin, 1981. 433 pages. Price $23.85.

REVIEWED BY RICHARD SKALAK[2]

Biomechanics has grown rapidly in the last decade and it is a pleasure to report that in this book an acknowledged leader in the field has set down a connected account of much of the progress that has been made in recent years. The book includes a good bit of anatomy, physiology, and analysis of systems, such as blood flow in tubes and muscle contraction, which entails more than just physical properties in the usual sense. The balance of materials presented serves the purposes of the book very well. It will be especially appreciated by students of biomechanics. It can be expected that physiologists will also find it of interest. Established workers in other branches of theoretical and applied mechanics who wish to have an authoritative and collected introduction to biomechanics will also find the book valuable. It will be a welcome textbook in courses in biomechanics.

This book has a number of features that make it especially pleasurable to read. First is the open style and the alternation of biological background and analytical representation that gives a degree of integration which has been often lacking in both the mechanical and biological literatures. Second, there is a most interesting historical introduction in Chapter 1 which points out that biomechanics is a fairly old subject. Although biomechanics is a relatively new word, which means the application of mechanics to biology, it turns out that the word mechanics is somewhat older than the word biology.

Third, the exercises given in small print at the end of each chapter are unique in the biomechanical literature. In many cases they add to the content of the book by the ideas they suggest and the impetus to have the reader work out some of the details. Finally, as befits the subject, it may be seen from the reference lists in each chapter that a large fraction of the literature cited has been written in the last decade. Professor Fung is one of the few people who has kept up with the development of biomechanics on so many different fronts in the last decade and could single-handedly write this book for us.

There are some items in this book that probably deserve special mention as they are distinct contributions to the literature. One of these is the discussion of extreme values in relation to red blood cell sizes. Another is the consideration of the mechanics and thermodynamics of biological tissues in a single format. The discussion of inversion of stress-strain relations is an original and interesting contribution.

[2] James Kip Finch Professor of Engineering Mechanics, Director, Bioengineering Institute, Department of Civil Engineering and Engineering Mechanics, Columbia University, New York, N. Y.. 10027.

One of the virtues of a book like this is that the different parts of the subject can be treated with a uniform vocabulary and approach. The basic definitions of stress, strain, strain rate, and viscoelasticity are given in Chapter 2. While this information may not be new to graduate students in applied mechanics, it is useful to have it written down and connected to biomechanics in an orderly way. Chapters 3, 4, and 5 deal with flow properties of blood, red blood cells, the deformability, and the rheology of blood in the microvessels. These chapters will give a fresh survey of the complicated field of blood cell properties and blood rheology. These chapters are a good example of Professor Fung's ability to set down the main facts in clear form. There is a good bit of advanced analysis in the literature which is not given here in any detail. Examples would be the solution of Stokes equations for various particles in capillary flow and the many different models that have been studies for wave propagation in blood flow. Presumably these will be covered in two later volumes which Professor Fung has promised in the introduction to the present book.

Bioviscoelastic fluids including protoplasm, mucous, saliva, cervical mucous, semen, and synovial fluid are treated in Chapter 6. Here again the main facts and adequate references are well summarized.

The next five chapters deal with soft tissues and are largely drawn from the research work of Professor Fung, his associates, and students. Chapter 7, on bioviscoelastic solids, is an especially long and important chapter. It contains informative descriptions of elastin collagen. It also contains general discussion of thermodynamics of elastic deformation, generalized viscoelastic relations, the complementary energy function, and inversion of stress-strain relationships. The idea of pseudoelasticity using a model of one elastic material in loading and another elastic material in unloading is developed. The reduced relaxation function is introduced and illustrated in this chapter by application to experimental data on rabbit mesentary. The notion of the reduced relaxation function is used repeatedly in the remainder of the book. It allows a reduction of a good deal of data on soft tissues which is highly nonlinear in its elastic behavior but linear in its viscoelastic response.

Chapter 8 deals with the mechanical properties of blood vessels. The arterial wall is another example in which the reduced relaxation function idea is useful. This chapter includes discussions of capillary blood vessels and the sheet flow in the alveolar walls of the lung which was developed by Professor Fung and his associates. The chapter closes with a discussion of the properties of the veins but does not go into the many interesting phenomena that occur when veins collapse. These will no doubt appear in later volumes.

The next three chapters, Chapters 9, 10, and 11 on skeletal muscle, heart muscle, and smooth muscles are like a minibook within the book, and surely represent a topic of great importance and particular interest. Here Professor Fung has tackled the difficult subject of describing the active contraction of muscles as well as their passive behavior when relaxed. Although some fault is found with Hill's classical three-element model, it is clear that the discussion is still an imcomplete one. These chapters show that the variety and complexity of muscles is very great and a complete description must take into account a variety of detailed anatomical features and biochemical influences. The chapter on smooth muscle is most interesting, probably because the spontaneous cyclic contraction has an air of independence and mystery about it.

The book closes with Chapter 12 on bone and cartilege. This is a comparatively short chapter but gives the main known facts about the structure, variability, and properites of bones. Although the strains are small because bones are stiff, the discussion of material properties is no less difficult than for soft tissues due to the complex heterogenity and anisotropy of bones. The questions of growth and resorption in bone are dealt with only briefly but at least more rationally than much of the literature. The last few sections on cartilege and lubrication of articular surfaces give the main effects leading to the very small coefficients of friction between typical articular cartilege surfaces. Synovial fluid was discussed previously in Chapter 6.

There are omissions which one could complain about except that the subject is so large that something must be omitted. Workers interested in the cornea or other parts of the eye or the ear will probably feel left out. One area which has received no mention is that of the brain and neutral system. This reviewer is convinced that neural mechanics is underdeveloped, say, compared to vascular mechanics and that the return on such development would be very much worthwhile. A discussion of teeth, the stiffness of their sockets, and the properties of the various components might also be of interest. Finally it should be pointed out that besides some data on frogs, almost all of properties discussed are of mammalian tissues. Fish, plants, seashells, and other interesting forms such as coral are not mentioned. Of course the inclusion of all of these topics might require another volume but people in agriculture and marine biology would probably like to see similar books for their fields.

This is a book that will surely be a standard text for some time. We will all be looking forward to seeing the two additional volumes which are promised in the Introduction. The next volume will be on the mechanics of circulation and respiration. A third volume on advanced biomechanics will include recent developments where advanced methods in contiuum mechanics and analysis have to be used. As Professor Fung has so aptly said in his preface, "Biomechanics at the level or current research cannot be bound by elementary mathematics." We will look forward to the forthcoming volumes to be as interesting and useful as the present first fine volume.

A Modern Course in Aeroelasticity. Edited by E. H. Dowell. By E. H. Dowell, H. C. Curtiss, Jr., R. H. Scanlan, and F. Sisto. Sijthoff and Noordhoff, Alpen aan den Rijn, The Netherlands, 1978. pp. v-464, Price $90.00.

REVIEWED BY R. M. BENNETT[3]

Aeroelasticity is an important hybrid field that treats the stability and response of flexible structures under fluid dynamic loading and includes the phenomena of flutter, divergence, buffeting, and gust response. The applications primarily involve aerospace vehicles but also include areas such as the civil engineering problems of the response of bridges, smoke stacks, and so forth, to wind loading. There are several well-known textbooks (references [1-4]) but they are several decades old and do not reflect recent developments and emphases. The two more recent books [5-6] are not available in English. This book is an effort to satisfy the need for a modern textbook.

Chapters 1-4 are by Prof. Dowell. After a brief introduction (Chapter 1, 2 pages), static aeroelasticity (Chapter 2, 44 pages) is considered. Deflection and divergence of a typical two-dimensional wing section are treated, followed by beam and surface representations of finite wings and by a brief section on the flow through flexible pipes. Chapter 3

[3] Aerospace Engineer, Unsteady Aerodynamics Branch, Loads and Aeroelasticity Division, NASA Langley Research Center, Hampton, Va. 23665.

One of the virtues of a book like this is that the different parts of the subject can be treated with a uniform vocabulary and approach. The basic definitions of stress, strain, strain rate, and viscoelasticity are given in Chapter 2. While this information may not be new to graduate students in applied mechanics, it is useful to have it written down and connected to biomechanics in an orderly way. Chapters 3, 4, and 5 deal with flow properties of blood, red blood cells, the deformability, and the rheology of blood in the microvessels. These chapters will give a fresh survey of the complicated field of blood cell properties and blood rheology. These chapters are a good example of Professor Fung's ability to set down the main facts in clear form. There is a good bit of advanced analysis in the literature which is not given here in any detail. Examples would be the solution of Stokes equations for various particles in capillary flow and the many different models that have been studies for wave propagation in blood flow. Presumably these will be covered in two later volumes which Professor Fung has promised in the introduction to the present book.

Bioviscoelastic fluids including protoplasm, mucous, saliva, cervical mucous, semen, and synovial fluid are treated in Chapter 6. Here again the main facts and adequate references are well summarized.

The next five chapters deal with soft tissues and are largely drawn from the research work of Professor Fung, his associates, and students. Chapter 7, on bioviscoelastic solids, is an especially long and important chapter. It contains informative descriptions of elastin collagen. It also contains general discussion of thermodynamics of elastic deformation, generalized viscoelastic relations, the complementary energy function, and inversion of stress-strain relationships. The idea of pseudoelasticity using a model of one elastic material in loading and another elastic material in unloading is developed. The reduced relaxation function is introduced and illustrated in this chapter by application to experimental data on rabbit mesentary. The notion of the reduced relaxation function is used repeatedly in the remainder of the book. It allows a reduction of a good deal of data on soft tissues which is highly nonlinear in its elastic behavior but linear in its viscoelastic response.

Chapter 8 deals with the mechanical properties of blood vessels. The arterial wall is another example in which the reduced relaxation function idea is useful. This chapter includes discussions of capillary blood vessels and the sheet flow in the alveolar walls of the lung which was developed by Professor Fung and his associates. The chapter closes with a discussion of the properties of the veins but does not go into the many interesting phenomena that occur when veins collapse. These will no doubt appear in later volumes.

The next three chapters, Chapters 9, 10, and 11 on skeletal muscle, heart muscle, and smooth muscles are like a minibook within the book, and surely represent a topic of great importance and particular interest. Here Professor Fung has tackled the difficult subject of describing the active contraction of muscles as well as their passive behavior when relaxed. Although some fault is found with Hill's classical three-element model, it is clear that the discussion is still an imcomplete one. These chapters show that the variety and complexity of muscles is very great and a complete description must take into account a variety of detailed anatomical features and biochemical influences. The chapter on smooth muscle is most interesting, probably because the spontaneous cyclic contraction has an air of independence and mystery about it.

The book closes with Chapter 12 on bone and cartilege. This is a comparatively short chapter but gives the main known facts about the structure, variability, and properites of bones. Although the strains are small because bones are stiff, the discussion of material properties is no less difficult than for soft tissues due to the complex heterogenity and anisotropy of bones. The questions of growth and resorption in bone are dealt with only briefly but at least more rationally than much of the literature. The last few sections on cartilege and lubrication of articular surfaces give the main effects leading to the very small coefficients of friction between typical articular cartilege surfaces. Synovial fluid was discussed previously in Chapter 6.

There are omissions which one could complain about except that the subject is so large that something must be omitted. Workers interested in the cornea or other parts of the eye or the ear will probably feel left out. One area which has received no mention is that of the brain and neutral system. This reviewer is convinced that neural mechanics is underdeveloped, say, compared to vascular mechanics and that the return on such development would be very much worthwhile. A discussion of teeth, the stiffness of their sockets, and the properties of the various components might also be of interest. Finally it should be pointed out that besides some data on frogs, almost all of properties discussed are of mammalian tissues. Fish, plants, seashells, and other interesting forms such as coral are not mentioned. Of course the inclusion of all of these topics might require another volume but people in agriculture and marine biology would probably like to see similar books for their fields.

This is a book that will surely be a standard text for some time. We will all be looking forward to seeing the two additional volumes which are promised in the Introduction. The next volume will be on the mechanics of circulation and respiration. A third volume on advanced biomechanics will include recent developments where advanced methods in contiuum mechanics and analysis have to be used. As Professor Fung has so aptly said in his preface, "Biomechanics at the level or current research cannot be bound by elementary mathematics." We will look forward to the forthcoming volumes to be as interesting and useful as the present first fine volume.

A Modern Course in Aeroelasticity. Edited by E. H. Dowell. By E. H. Dowell, H. C. Curtiss, Jr., R. H. Scanlan, and F. Sisto. Sijthoff and Noordhoff, Alpen aan den Rijn, The Netherlands, 1978. pp. v-464, Price $90.00.

REVIEWED BY R. M. BENNETT[3]

Aeroelasticity is an important hybrid field that treats the stability and response of flexible structures under fluid dynamic loading and includes the phenomena of flutter, divergence, buffeting, and gust response. The applications primarily involve aerospace vehicles but also include areas such as the civil engineering problems of the response of bridges, smoke stacks, and so forth, to wind loading. There are several well-known textbooks (references [1-4]) but they are several decades old and do not reflect recent developments and emphases. The two more recent books [5-6] are not available in English. This book is an effort to satisfy the need for a modern textbook.

Chapters 1-4 are by Prof. Dowell. After a brief introduction (Chapter 1, 2 pages), static aeroelasticity (Chapter 2, 44 pages) is considered. Deflection and divergence of a typical two-dimensional wing section are treated, followed by beam and surface representations of finite wings and by a brief section on the flow through flexible pipes. Chapter 3

[3] Aerospace Engineer, Unsteady Aerodynamics Branch, Loads and Aeroelasticity Division, NASA Langley Research Center, Hampton, Va. 23665.

(112 pages) presents dynamic aeroelasticity starting with the basic principles and equations for the typical wing section, and progressing to the analysis of complex structures and pipe flows. Chapter 4 (108 pages) is on nonsteady aerodynamics of lifting and nonlifting surfaces. It starts with the basic fluid equations and takes the reader through subsonic and supersonic flows over airfoils and wings. Consistent with the current state of the art, unsteady transonic flows are described by approximate methods.

Chapter 5 (14 pages), by Professor Sisto, discusses stall flutter. It gives an overview of the phenomena including a nonlinear mechanics description. In Chapter 6 (46 pages), Professor Scanlan gives a valuable and unique exposition of the aeroelastic problems of civil engineering structures such as divergence, vortex shedding, and flutter of bridges, and galloping of cables. Chapter 7 (56 pages) by Prof.Curtiss is on the aeroelastic problems of rotorcraft and gives a brief description of blade dynamics, stall flutter, and blade motion/body coupling. In Chapter 8 (28 pages), Prof. Sisto describes aeroelastic problems in turbomachines highlighting the special problems encountered in axial flow compressors.

Appendix I (8 pages) by Prof. Dowell, is a primer for structural response to random pressure fluctuations and gives a good resume of an application of modern spectral analysis techniques. Appendix II (38 pages, Prof. Dowell) gives some example problems that are pertinent to Chapters 2-4 and their solutions.

This book gives a good exposition of basic principles and a good overview of the diverse field of aeroelasticity from a modern point of view. As the title indicates, it is primarily directed as a textbook rather than to the practitioner. It supplements reference [1] rather than replacing it, however, as the range of topics considered are somewhat different. Further emphasis might have also been given to testing techniques and experimental results. The book is recommended and Profs. Dowell, Sisto, Scanlan, and Curtiss are to be commended for this addition to the literature.

References

1 Bisplinghoff, R. L., Ashley, H., and Halfman, R. L., *Aeroelasticity*, Addison-Wesley, Cambridge, Mass., 1955.

2 Bisplinghoff, R. L., Ashley, H., *Principles of Aeroelasticity*, Wiley, New York, 1962. (Also available in Dover Edition.)

3 Fung, Y. C., *An Introduction to the Theory of Aeroelasticity*, Wiley, New York, 1955. (Also available in Dover Edition.)

4 Scanlan, R. H., and Rosenbaum, R., *Introduction to the Study of Aircraft Vibration and Fluttter*, Macmillan, New York, 1951. (Also available in Dover Edition.)

5 Petre, A., *Theory of Aeroelasticity, Vol I Statics, Vol. II Dynamics*. (In Romanian) Bucharest, 1966.

6 Forsching, H.W., *Fundamentals of Aeroelasticity*. (In German), Springer-Verlag, Berlin, 1974.

The Calculus of Variations and Optimal Control. By George Leitmann. Plenum Press, New York, 1981, 311 pages. Price $35.00.

REVIEWED BY DANIEL TABAK[4]

A large variety of books covering the topics of calculus of variations and optimal control exists. Thus, a reader may naturally ask: what is so special about this book that would justify its addition to the practically oversaturated market? Once the book is read, the answer to this question becomes simple: it is not the contents of the book, but the way the book is written that makes it so special and outstanding. Before elucidating on this point, let us first look at the contents.

The book covers the basic theory of the calculus of variations and optimal control. It is accordingly divided into two parts; Part I, Calculus of Variations (Chapters 1-8) and Part II, Optimal Control (Chapters 9-17). Part I includes the topics of necessary conditions for an extremum, integration of the Euler-Lagrange equation, the inverse problem, the Weierstrass and Jacobi necessary conditions, and the corner conditions. Part II includes the topics of optimality principle, optimal trajectories, Maximum Principle, special cases of optimal control problems, sufficient conditions, feedback control, and optimization with vector-valued cost. The last topic makes the book just about unique contents-wise; very few books touch on it. Practically all chapters contain illustrative examples and exercises for students. A list of references, an extensive bibliography and and index are given at the end of the book.

The book contains a rigorous mathematical presentation of the basic theoretical results. At the same time it is very clearly written and easy to learn from and to teach with. (In fact, it has already been successfully used by this reviewer as a self-paced text for graduate students.) Its numerous solved examples and clear figures make it even more attractive to the reader. It contains some specific economic and aerospace application examples of optimal control implementation.

It is this particular combination of mathematical rigor with an excellent tutorial lucidity that makes the book so unique and its use so widely recommendable. The book can serve as a excellent primary text in optimal control for graduate students. Since it contains examples from many diverse areas, it is not restricted to any particular discipline. It can be used by students of engineering, mathematics, operations research, economics, and other related areas.

Mechanics of Wave Forces on Offshore Structures. By T. Sarpkaya and M. Isaacson. Van Nostrand Reinhold, New York, 1981. pp. xiv-651. Price $37.50.

REVIEWED BY J. V. WEHAUSEN[5]

The authors' purpose, as stated in the preface, is to bring into one place the extensive and widely dispersed literature on wave forces on offshore structures. They speak of the work as a text and suggest that it could be used for a graduate course in ocean engineering. Have they succeeded? In my opinion they have, provided that one takes account of their approach to the problem of expounding a large amount of material.

The book is divided into nine chapters, a short introduction discussing the nature of the engineering problems encountered in analyzing ocean structures, another short chapter reviewing the fundamental equations for an incompressible Newtonian fluid, and then seven chapters with the following titles: "Flow Separation and Time-Dependent Flows," "Wave Theories," "Wave Forces on Small Bodies," "Wave Forces on Large Bodies," "Random Waves and Wave Forces," "Dynamic Response of Framed Structures and Vortex-Induced Oscillations," and "Models and Prototypes."

Chapters may be read reasonably independently of one another, but may be considered self-contained only if one comes to the book with "a good background in mathematics and fluid mechanics," a prerequisite stated in the preface. With such a background, any serious reader will find this an invaluable guide to the current literature. Each chapter is followed by an extensive bibliography in which, with few exceptions, complete author, title, and source data are given, thus making it easy for the reader to locate referenced papers. Although developments within the chapters are not sufficiently detailed to allow one to avoid going back to the

[4]Professor, Department of Electrical Engineering, P.O. Box 653, Ben-Gurion University, Beer Sheva, Israel.

[5]Professor of Engineering Science, University of California, Naval Architecture and Offshore Engineering, Berkeley, Calif. 94720.

(112 pages) presents dynamic aeroelasticity starting with the basic principles and equations for the typical wing section, and progressing to the analysis of complex structures and pipe flows. Chapter 4 (108 pages) is on nonsteady aerodynamics of lifting and nonlifting surfaces. It starts with the basic fluid equations and takes the reader through subsonic and supersonic flows over airfoils and wings. Consistent with the current state of the art, unsteady transonic flows are described by approximate methods.

Chapter 5 (14 pages), by Professor Sisto, discusses stall flutter. It gives an overview of the phenomena including a nonlinear mechanics description. In Chapter 6 (46 pages), Professor Scanlan gives a valuable and unique exposition of the aeroelastic problems of civil engineering structures such as divergence, vortex shedding, and flutter of bridges, and galloping of cables. Chapter 7 (56 pages) by Prof.Curtiss is on the aeroelastic problems of rotorcraft and gives a brief description of blade dynamics, stall flutter, and blade motion/body coupling. In Chapter 8 (28 pages), Prof. Sisto describes aeroelastic problems in turbomachines highlighting the special problems encountered in axial flow compressors.

Appendix I (8 pages) by Prof. Dowell, is a primer for structural response to random pressure fluctuations and gives a good resume of an application of modern spectral analysis techniques. Appendix II (38 pages, Prof. Dowell) gives some example problems that are pertinent to Chapters 2-4 and their solutions.

This book gives a good exposition of basic principles and a good overview of the diverse field of aeroelasticity from a modern point of view. As the title indicates, it is primarily directed as a textbook rather than to the practitioner. It supplements reference [1] rather than replacing it, however, as the range of topics considered are somewhat different. Further emphasis might have also been given to testing techniques and experimental results. The book is recommended and Profs. Dowell, Sisto, Scanlan, and Curtiss are to be commended for this addition to the literature.

References

1 Bisplinghoff, R. L., Ashley, H., and Halfman, R. L., *Aeroelasticity*, Addison-Wesley, Cambridge, Mass., 1955.

2 Bisplinghoff, R. L., Ashley, H., *Principles of Aeroelasticity*, Wiley, New York, 1962. (Also available in Dover Edition.)

3 Fung, Y. C., *An Introduction to the Theory of Aeroelasticity*, Wiley, New York, 1955. (Also available in Dover Edition.)

4 Scanlan, R. H., and Rosenbaum, R., *Introduction to the Study of Aircraft Vibration and Fluttter*, Macmillan, New York, 1951. (Also available in Dover Edition.)

5 Petre, A., *Theory of Aeroelasticity, Vol I Statics, Vol. II Dynamics*. (In Romanian) Bucharest, 1966.

6 Forsching, H.W., *Fundamentals of Aeroelasticity*. (In German), Springer-Verlag, Berlin, 1974.

The Calculus of Variations and Optimal Control. By George Leitmann. Plenum Press, New York, 1981, 311 pages. Price $35.00.

REVIEWED BY DANIEL TABAK[4]

A large variety of books covering the topics of calculus of variations and optimal control exists. Thus, a reader may naturally ask: what is so special about this book that would justify its addition to the practically oversaturated market? Once the book is read, the answer to this question becomes simple: it is not the contents of the book, but the way the book is written that makes it so special and outstanding. Before elucidating on this point, let us first look at the contents.

The book covers the basic theory of the calculus of variations and optimal control. It is accordingly divided into two parts; Part I, Calculus of Variations (Chapters 1-8) and Part II, Optimal Control (Chapters 9-17). Part I includes the topics of necessary conditions for an extremum, integration of the Euler-Lagrange equation, the inverse problem, the Weierstrass and Jacobi necessary conditions, and the corner conditions. Part II includes the topics of optimality principle, optimal trajectories, Maximum Principle, special cases of optimal control problems, sufficient conditions, feedback control, and optimization with vector-valued cost. The last topic makes the book just about unique contents-wise; very few books touch on it. Practically all chapters contain illustrative examples and exercises for students. A list of references, an extensive bibliography and and index are given at the end of the book.

The book contains a rigorous mathematical presentation of the basic theoretical results. At the same time it is very clearly written and easy to learn from and to teach with. (In fact, it has already been successfully used by this reviewer as a self-paced text for graduate students.) Its numerous solved examples and clear figures make it even more attractive to the reader. It contains some specific economic and aerospace application examples of optimal control implementation.

It is this particular combination of mathematical rigor with an excellent tutorial lucidity that makes the book so unique and its use so widely recommendable. The book can serve as a excellent primary text in optimal control for graduate students. Since it contains examples from many diverse areas, it is not restricted to any particular discipline. It can be used by students of engineering, mathematics, operations research, economics, and other related areas.

[4]Professor, Department of Electrical Engineering, P.O. Box 653, Ben-Gurion University, Beer Sheva, Israel.

Mechanics of Wave Forces on Offshore Structures. By T. Sarpkaya and M. Isaacson. Van Nostrand Reinhold, New York, 1981. pp. xiv-651. Price $37.50.

REVIEWED BY J. V. WEHAUSEN[5]

The authors' purpose, as stated in the preface, is to bring into one place the extensive and widely dispersed literature on wave forces on offshore structures. They speak of the work as a text and suggest that it could be used for a graduate course in ocean engineering. Have they succeeded? In my opinion they have, provided that one takes account of their approach to the problem of expounding a large amount of material.

The book is divided into nine chapters, a short introduction discussing the nature of the engineering problems encountered in analyzing ocean structures, another short chapter reviewing the fundamental equations for an incompressible Newtonian fluid, and then seven chapters with the following titles: "Flow Separation and Time-Dependent Flows," "Wave Theories," "Wave Forces on Small Bodies," "Wave Forces on Large Bodies," "Random Waves and Wave Forces," "Dynamic Response of Framed Structures and Vortex-Induced Oscillations," and "Models and Prototypes."

Chapters may be read reasonably independently of one another, but may be considered self-contained only if one comes to the book with "a good background in mathematics and fluid mechanics," a prerequisite stated in the preface. With such a background, any serious reader will find this an invaluable guide to the current literature. Each chapter is followed by an extensive bibliography in which, with few exceptions, complete author, title, and source data are given, thus making it easy for the reader to locate referenced papers. Although developments within the chapters are not sufficiently detailed to allow one to avoid going back to the

[5]Professor of Engineering Science, University of California, Naval Architecture and Offshore Engineering, Berkeley, Calif. 94720.

sources, they provide a coherent exposition of the subjects treated together with sufficient information about the referenced papers so that one can decide whether or not he or she needs or wishes to consult them for further details. I do not see this as a textbook for even an advanced class, but it (or parts of it) could be used as a skeleton to be fleshed out by independent reading or supplementary lecturing.

To say that such an extensive work shows signs of hasty writing would be manifestly unfair. Still, it would have benefitted by some editorial attention, for it seems to me that it contains more misspelled and misused words and more awkward or obscure sentences than is normal. However, none of this really detracts from its usefulness. The typography also deserves comment. It is customary in mathematical text to set variables in italic type and operators in roman. Here everything is in roman. Although I was aware of this while reading, I did not find it any way confusing. If substantial costs in typesetting are thus effected, perhaps it should be used more widely, although I prefer the usual convention.

Although it might appear appropriate to compare the book under review with a similar one *Vagues et Ouvrages Petroliers en Mer,* by G. Susbielles and Chr. Bratu, Editions Technip, Paris, 1981), which appeared almost simultaneously, I think I should disqualify myself on the grounds of possible partiality. We are fortunate, however, to have two such treatises available.

Techniques of Finite Elements. by B. Irons and S. Ahmad, Wiley, New York, 1981. 529 pages. Price $30.95.

REVIEWED BY K. J. BATHE[6]

This is a valuable and enjoyable book to read for those who basically know already quite a bit about finite element methods. In a conversational style, the authors summarize their experiences about almost every topic of finite element techniques in linear structural analysis. Details are primarily given in the discussion of those methods that the authors have researched over the last two decades (and the authors are certainly well known in the finite element community for their research contributions). Two major topics are the frontal solution method and the semiloof elements, for which computer programs are also given; but the menu includes a large variety of topics, which can be appreciated by studying the titles of the 29 chapters: Overview; Basic Techniques; Shape Functions; Various Elastic Problems; Nodal Loads from Shape Function Routines; Problems of Management; Matrix-Structural Theory; The Matched Solution; Convergence – The Patch Test; Developing and Implementing Elements; How Nodes Hang Together: Front or Band?; Element Assembly and Equation Solving; A Frontal Solution Package; Roundoff Errors; Further Matrix-Structural Theory; Plate Bending; Shells; The Semiloof Beam and Shell; Symmetry; Sectorial Symmetry; Nonlinearity; Eigenvalues and Numerical Stability; Eigenvalues and Structural Problems; Non-Structural Problems; Implications of the Patch Test; Interpolation and Numerical Integration; Matrices; Vectors and Differential Geometry; and Stress and Strain.

Although quite detailed in some descriptions, the book is probably intended to be a strong subjective representation of finite element methods, and the authors have obviously not researched related literature to a high degree. The most notable contribution in this book is that the authors attempt to make the reader appreciate the structural and finite element principles from both a mathematical *and* a physical viewpoint. This is a very valuable endeavor and goes well with the conversational style of the book.

The readers most attracted to the volume will probably be finite element teachers and researchers who desire to obtain further insight into finite element techniques – the authors provide much valuable and thought-provoking material in that regard.

[6] Associate Professor, Department of Mechanical Engineering, Massachusetts Institute of Technology, Cambridge, Mass. 02139.

Hydrodynamic Stability. By P. Drazin and W. Reid. Cambridge University Press, 1981. 525 pages. Price $77.00.

REVIEWED BY F. H. BUSSE[7]

Over the past decades the subject of hydrodynamic stability has assumed a central role in theoretical fluid dynamics. In spite of some earlier doubts, stability theory has become an indispensable tool for the understanding of the onset of turbulence in fluid flow and applications of the theory in engineering, and physical and environmental sciences are growing rapidly. Several books on the subject have been published, but there is a continuing demand for clear exposition of its foundation and methods.

The book by Drazin and Reid goes the farthest in meeting this expectation. Faced with the large variety of stability problems, the authors decided to treat the most basic problems of stability in detail instead of attempting to cover all known hydrodynamic instabilities. Many of the examples neglected in the main text appear in the extensive problem sections at the end of most chapters. The book starts with a discussion of the simplest examples of hydrodynamic instability such as Benard convection and Taylor vortices. It then proceeds to the more complex problems of the stability of parallel shear flows. Both the inviscid problem of stability based on Rayleigh's equation and the viscous problem based on the Orr-Sommerfeld equation are discussed in considerable detail. Asymptotic methods are emphasized, but numerical methods are not neglected. A final chapter of the book reviews nonlinear aspects of stability theory. Readers interested in this area research may regret that only brief outlines of various methods and results are given in this chapter. But a more complete account of the nonlinear theory would probably have required a separate volume.

While the authors have approached their subject mainly from the applied mathematician's point of view, they have kept the use of mathematical formalism at a minimum. The book should thus be readily accessible to engineers and physicists. In fact, the examples treated in this book may serve as a suitable introduction to singular perturbation techniques such as matched asymptotic expansions. On the other hand, physical ideas are not always expressed quite as clearly. In the discussion of the Boussinesq approximation, for example, it is not evident that the smallness of the ratio between mechanical energy and thermal energy variations of a fluid parcel is the basis of this approximation. Stress-free boundary conditions are summarily described as unrealistic, even though they have been well approximated in the experiment of Goldstein and Graham (*Phys. Fluids*, 1969). The reader may also search in vain for heuristic physical ideas on the origin of shear flow instabilities such as those developed by Lin (1945) and Gill (1965).

But these minor criticisms should not distract from the impression that this book is likely to be the standard reference

[7] Professor, Department of Earth and Space Sciences, University of California, Los Angeles, Calif. 90024.

for most aspects of hydrodynamic stability theory for many years to come. The book can be recommended as a text for a graduate course in hydrodynamic stability. It is well produced and remarkably free of misprints. Its success should prompt the publisher to make it available soon in a more affordable paperback format.

The Theory of Thin-Walled Bars. By Atle Gjelsvik. Wiley, New York, 1981. pp. ix–248. Price $31.50.

REVIEWED BY D. H. HODGES[8]

The theory of bending and torsion of bars is important in the design of aircraft, spacecraft, wind turbines, buildings, bridges, and ships. Since a general theory of thin-walled bars is a relative latecomer to mechanics, textbooks that cover the theory in detail, unlike similar books for plate and shell theories, are not common. This book is the first English text in this field that the reviewer has encountered since Vlasov's *Thin-Walled Elastic Beams* was translated in 1961.

[8]Research Scientist, Rotorcraft Dynamics Division, Aeromechanics Laboratory, U.S. Army Research and Technology Laboratories (AVRADCOM), Ames Research Center, Moffett Field, Calif. 94035.

There are several features that make this book distinctive. First is the development of the bar equations from shell theory. This approach has the advantage of elucidating the physical meaning of certain assumptions that are commonly made in beam theories. Second is the development of the closed cross-section theory from an extension of open cross-section theory. The book has many example problems involving open and closed cross sections. Third is the enlightening discussion of the behavior of the analysis variables at junctions involving discontinuities.

The chapter entitled "Nonlinear Theory" is written clearly and for applications that demand arbitrarily large rotations, the necessary extension can be developed based on what is already given. Solutions for a wide variety of buckling problems are given in the chapter on buckling. Plasticity is covered in the final chapter. The book would be useful for graduate students and researchers in the area of thin-walled bars, especially because of the original material it contains, which is not available elsewhere in published form.